frontiers | Research Topics

Thermodynamics of Newtonian and non-Newtonian nanofluids with recent advancements

Edited by
Mustafa Inc, Noor Saeed Khan, Hammad Khalil and Ishak Hashim

Published in
Frontiers in Materials

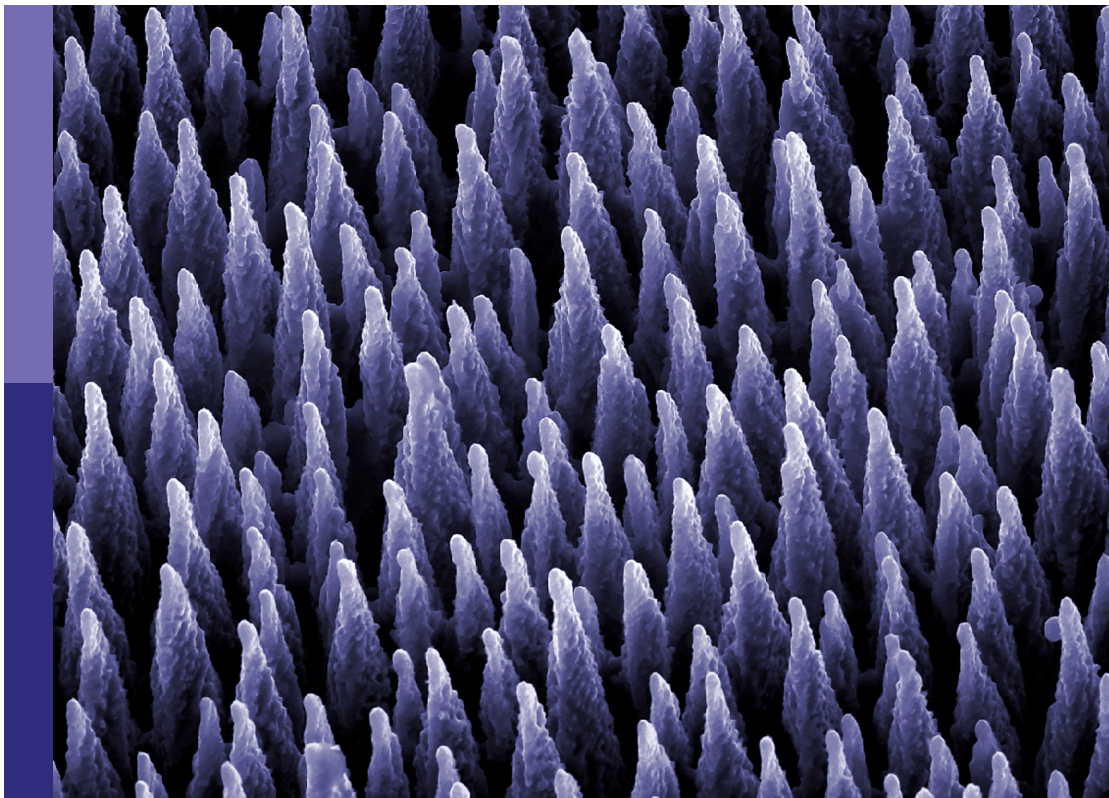

ISSN 1664-8714
ISBN 978-2-8325-4062-6
DOI 10.3389/978-2-8325-4062-6

About Frontiers

Frontiers is more than just an open access publisher of scholarly articles: it is a pioneering approach to the world of academia, radically improving the way scholarly research is managed. The grand vision of Frontiers is a world where all people have an equal opportunity to seek, share and generate knowledge. Frontiers provides immediate and permanent online open access to all its publications, but this alone is not enough to realize our grand goals.

Frontiers journal series

The Frontiers journal series is a multi-tier and interdisciplinary set of open-access, online journals, promising a paradigm shift from the current review, selection and dissemination processes in academic publishing. All Frontiers journals are driven by researchers for researchers; therefore, they constitute a service to the scholarly community. At the same time, the *Frontiers journal series* operates on a revolutionary invention, the tiered publishing system, initially addressing specific communities of scholars, and gradually climbing up to broader public understanding, thus serving the interests of the lay society, too.

Dedication to quality

Each Frontiers article is a landmark of the highest quality, thanks to genuinely collaborative interactions between authors and review editors, who include some of the world's best academicians. Research must be certified by peers before entering a stream of knowledge that may eventually reach the public - and shape society; therefore, Frontiers only applies the most rigorous and unbiased reviews. Frontiers revolutionizes research publishing by freely delivering the most outstanding research, evaluated with no bias from both the academic and social point of view. By applying the most advanced information technologies, Frontiers is catapulting scholarly publishing into a new generation.

What are Frontiers Research Topics?

Frontiers Research Topics are very popular trademarks of the *Frontiers journals series*: they are collections of at least ten articles, all centered on a particular subject. With their unique mix of varied contributions from Original Research to Review Articles, Frontiers Research Topics unify the most influential researchers, the latest key findings and historical advances in a hot research area.

Find out more on how to host your own Frontiers Research Topic or contribute to one as an author by contacting the Frontiers editorial office: frontiersin.org/about/contact

Thermodynamics of Newtonian and non-Newtonian nanofluids with recent advancements

Topic editors

Mustafa Inc — Firat University, Türkiye

Noor Saeed Khan — University of Education Lahore, Pakistan

Hammad Khalil — University of Education Lahore, Pakistan

Ishak Hashim — National University of Malaysia, Malaysia

Citation

Inc, M., Khan, N. S., Khalil, H., Hashim, I., eds. (2024). *Thermodynamics of Newtonian and non-Newtonian nanofluids with recent advancements*. Lausanne: Frontiers Media SA. doi: 10.3389/978-2-8325-4062-6

Table of contents

frontiers | Frontiers in Materials

TYPE Original Research
PUBLISHED 24 February 2023
DOI 10.3389/fmats.2023.1114665

OPEN ACCESS

EDITED BY
Noor Saeed Khan,
University of Education Lahore, Pakistan

REVIEWED BY
Ghulam Rasool,
Beijing University of Technology, China
Kanayo Kenneth Asogwa,
Nigeria Maritime University, Nigeria

*CORRESPONDENCE
Sayed M. Eldin,
sayed.eldin22@fue.edu.eg

SPECIALTY SECTION
This article was submitted to Colloidal Materials and Interfaces, a section of the journal Frontiers in Materials

RECEIVED 02 December 2022
ACCEPTED 07 February 2023
PUBLISHED 24 February 2023

CITATION
Ali Q, Amir M, Raza A, Khan U, Eldin SM, Alotaibi AM, Elattar S and Abed AM (2023), Thermal investigation into the Oldroyd-B hybrid nanofluid with the slip and Newtonian heating effect: Atangana–Baleanu fractional simulation. *Front. Mater.* 10:1114665. doi: 10.3389/fmats.2023.1114665

Thermal investigation into the Oldroyd-B hybrid nanofluid with the slip and Newtonian heating effect: Atangana–Baleanu fractional simulation

Qasim Ali[1], Muhammad Amir[1], Ali Raza[1,2], Umair Khan[3,4], Sayed M. Eldin[5]*, Abeer M. Alotaibi[6], Samia Elattar[7] and Ahmed M. Abed[8,9]

[1]Department of Mathematics, University of Engineering and Technology, Lahore, Pakistan, [2]School of Mathematics, Minhaj University, Lahore, Pakistan, [3]Department of Mathematical Sciences, Faculty of Science and Technology, Universiti Kebangsaan Malaysia, Selangor, Malaysia, [4]Department of Mathematics and Social Sciences, Sukkur IBA University, Sukkur, Sindh, Pakistan, [5]Center of Research, Faculty of Engineering, Future University in Egypt, New Cairo, Egypt, [6]Department of Mathematics, Faculty of Science, University of Tabuk, Tabuk, Saudi Arabia, [7]Department of Industrial & Systems Engineering, College of Engineering, Princess Nourah bint Abdulrahman University, Riyadh, Saudi Arabia, [8]Department of Industrial Engineering, College of Engineering, Prince Sattam Bin Abdulaziz University, Alkharj, Saudi Arabia, [9]Industrial Engineering Department, Faculty of Engineering, Zagazig University, Zagazig, Egypt

The significance of thermal conductivity, convection, and heat transportation of hybrid nanofluids (HNFs) based on different nanoparticles has enhanced an integral part in numerous industrial and natural processes. In this article, a fractionalized Oldroyd-B HNF along with other significant effects, such as Newtonian heating, constant concentration, and the wall slip condition on temperature close to an infinitely vertical flat plate, is examined. Aluminum oxide (Al_2O_3) and ferro-ferric oxide (Fe_3O_4) are the supposed nanoparticles, and water (H_2O) and sodium alginate ($C_6H_9NaO_7$) serve as the base fluids. For generalized memory effects, an innovative fractional model is developed based on the recently proposed Atangana–Baleanu time-fractional (AB) derivative through generalized Fourier and Fick's law. This Laplace transform technique is used to solve the fractional governing equations of dimensionless temperature, velocity, and concentration profiles. The physical effects of diverse flow parameters are discussed and exhibited graphically by Mathcad software. We have considered $0.15 \le \alpha \le 0.85, 2 \le Pr \le 9, 5 \le Gr \le 20, 0.2 \le \phi_1, \phi_2 \le 0.8, 3.5 \le Gm \le 8,\ 0.1 \le\ Sc\ \le 0.8$, and $0.3 \le \lambda_1, \lambda_2 \le 1.7$. Moreover, for validation of our present results, some limiting models, such as classical Maxwell and Newtonian fluid models, are recovered from the fractional Oldroyd-B fluid model. Furthermore, comparing the results between Oldroyd-B, Maxwell, and viscous fluid models for both classical and fractional cases, Stehfest and Tzou numerical methods are also employed to secure the validity of our solutions. Moreover, it is visualized that for a short time, temperature and momentum

Abbreviations: W_1, velocity $[ms^{-1}]$; β_1, volumetric coefficient of thermal expansion $[K^{-1}]$; g, acceleration due to gravity $[LT^{-2}]$; T_∞, temperature value away from the plate $[K]$; T_w, temperature on the plate $[K]$; C_∞, concentration value away from the plate $[kgm^{-3}]$; T, temperature $[K]$; C_w, concentration at the plate $[ML^{-3}]$; Gr, thermal Grashof number [-]; μ_{hbnf}, dynamic viscosity of hybrid nanofluid [-]; κ_{hbnf}, thermal conductivity of hybrid nanofluid [-]; Pr, Prandtl number [-]; λ_2, Maxwell parameter [-]; ϕ_1, ϕ_2, volumetric fractions [-]; Gm, mass Grashof number [-]; ρ_{hbnf}, density for hybrid nanofluid [-]; C_p, specific heat at constant pressure $[JM^{-1}K^{-1}]$; λ_1, Oldroyd parameter [-]; s, Laplace transformed variable [-]; α, γ, fractional parameters [-]. Note: this [-] characterizes the dimensionless quantity.

profiles are decayed for larger values of α, and this effect is reversed for a long time. Furthermore, the energy and velocity profiles are higher for water-based HNFs than those for the sodium alginate-based HNF.

KEYWORDS

fractionalized hybrid Oldroyd-B fluid, AB time-fractional derivative, Newtonian heating, Laplace transform method, hybrid nanofluid

1 Introduction

With the addition of nanometer-sized particles in various base fluids, thermophysical characteristics may improve in energy transfer schemes. This process signals an expansion in the thermal conductivity for base fluids, making it more reliable and ongoing. These significant fluids define nanofluids (NFs) with an extensive series of suggestions in several areas of science, as well as technology, with nuclear devices, heat exchangers, solar plates, vehicle heaters, and biotic and organic devices (Usman et al., 2018; Khan et al., 2022a; Khan et al., 2022b; Ahmed et al., 2022; Hassan et al., 2022; Khan et al., 2022c). First, Lee and Eastman presented the idea of NFs in 1995 (Lee et al., 1999). Numerous applications of NFs are discoursed by Kaufui et al. (Wong and Omar De Leon., 2010). Mahian et al. (2019) proposed important ideas and reflected novel innovations to completely explain the NFs. They were obsessed with innovative expansions in this field, comprehensive explanations of the thermophysical characteristics, and imitation of thermal transmission in NF flow. Waini et al. (2019) used a numerical scheme to discuss an unsteady thermal transmission flow past a shrinking sheet in an HNF. They presented different applications of NFs in numerous branches of science along with appreciated recommendations. NFs have achieved significant consideration from researchers due to their improved heat conversion characteristics. The rheological presentation of an NF using a revolving rheometer was proposed by Vallejo et al. (2019a). Different rheological characteristics of NFs are discussed in Vallejo et al. (2019b). Currently, NFs have been characterized as HNFs in several mechanisms (Rashad et al., 2018). HNFs are developed by mixing two dissimilar nanoparticles in the base liquid. Its main inspiration is to increase the thermal features of NFs. The variable thermal transmission of HNFs through magnetic influence was examined in Mohebbi et al. (2019). The heat transmission in the non-Newtonian HNF composed with entropy generation was discussed in Shahsavar et al., 2018). Furthermore, Farooq et al. (2018) deliberated on the entropy in the HNF flow in a stretching sheet.

Asogwa et al. (2021) discussed chemical reactions and heat sinks over a ramped temperature. The analytical solution of governing equations was found with the Laplace transform. Asogwa et al. (2022a) used the Laplace approach to discuss a water-based NF containing aluminum oxide and copper in a moving plate and proved that thermal absorption causes a decline in aluminum oxide NF's thermal and momentum profiles with a copper NF. Shankar Goud et al. (2022) used the Keller–box scheme for the numerical solution along with thermal effects, momentum, and solutal slip on the thermal transmission with a description of the magnetohydrodynamic (MHD) flow of Casson fluid and an exponential porous surface with Dufour, chemical reaction, and Soret impacts. Khan et al. (2022d) studied a fractionalized electro-osmotic flow based on the Caputo operator of a Casson NF containing sodium alginate nanoparticles over a vertical microchannel with MHD effects. They proved that the inclination angle boosts the velocity. Asogwa et al. (2022b) and Asogwa et al. (2022c) considered the stimulation significance of the thermal transmission with the MHD flow of a NF through an extending sheet with MATLAB bvp4c. Furthermore, they investigated the radiative features of the MHD flow with collective heat transportation characteristics on a reactive stretching surface with the Casson NF numerically using MATLAB bvp4c. Goud et al. (2022) applied the bvp4c scheme to study the convection flow *via* an infinite porous plate on thermal transmission, as well as mass transmission. Asogwa et al. (2022d) discussed the influences of the movement of nanoparticles in NFs by an exponentially enhanced Riga plate. Reddy et al. (2022) calculated the effect of activation energy on a second-grade MHD NF flow over a convectively curved heated stretched surface by considering the Brownian motion and generation/absorption, and thermophoresis. They have shown that velocity and thermal profiles suggestively increase with the concurrent increasing estimation of the fluid parameter.

The fractional calculus (FC) has obtained substantial consideration from experts in previous decades. The important inventions have newly been presented in the application of the FC, where new derivatives, as well as integral operators, are hired (Awan et al., 2019). The new anticipated operators contain the generalized Mittag–Leffler function (MLF), and these features intensify the innovative constructions to achieve numerous attractive properties that are recognized in important outcomes. Subsequently, Atangana and Dumitru (2016) anticipated, the innovative and applicable time-fractional operator, which is expansively hired in numerous branches of science and engineering. It is exposed that the MLF is a more operative and vigorous screening apparatus than the exponential and power laws, constructing the AB-fractional operator, in terms of Caputo, an effective arithmetic procedure to simulate progressively perilous complex tasks. Due to their extensive implications, such fractional models are extensively identified for deriving fractional differential equations (FDEs) with no manufactured irregularities, as for Caputo, Riemann–Liouville (RL), and Caputo–Fabrizio (CF) derivatives, because of their characteristic non-orientation (Ali et al., 2021; Ali et al., 2022a; Raza et al., 2022; Zhang et al., 2022). We also perceived interest in these fractional derivatives on the topic of mathematical approaches, although scientifically approximating these operators' outcomes to compute different problems (Martyushev and Sheremet, 2012; Ali et al., 2022b).

Batool et al. (2022) discussed the thermal and mass transmission processes of a micropolar NF under magnetic and buoyancy effects across an inclusion. Rasool et al. (2022a) examined the significance of the MHD Maxwell NF flow and obtained the solution to this problem by employing the homotopy analysis technique for diverse physical parameters. Moreover, they studied an electro-magneto-hydrodynamic NF flow in a permeable medium with heating

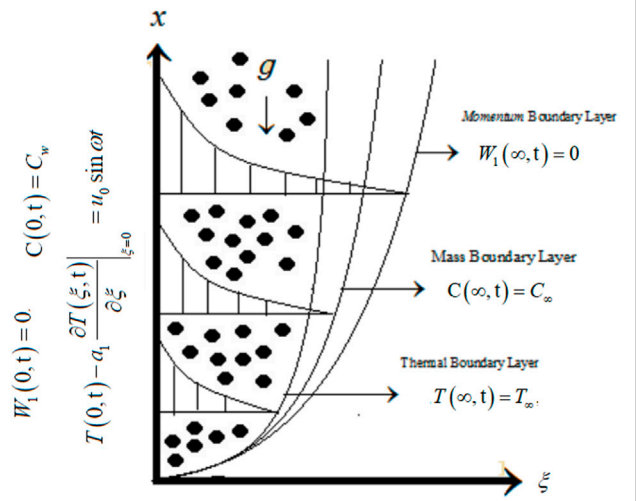

FIGURE 1
Physical flow.

boundary conditions. Furthermore, they applied Buongiorno's method for the flow of radiating thixotropic NFs over a horizontal surface by considering the retardational effects of Lorentz forces and using the influence of Brownian and thermophoresis diffusions (Rasool et al., 2022b; Rasool et al., 2023).

In this paper, a fractionalized Oldroyd-B HNF flow is examined by the recent definitions of the AB time-fractional derivative having a Mittage–Leffler kernel along with Newtonian heating, constant concentration, and the wall slip condition on temperature close to an infinite vertical flat plate. The AB fractional operator is introduced in the governing equations of temperature and diffusion by employing the generalized types of Fourier and Fick's law. The developed non-dimensional fractional model is solved using the Laplace transform method. Graphical illustrations are used to depict the physical behavior of fractional derivatives and the consequence of diverse flow parameters on velocity, thermal, and concentration fields. Furthermore, for validation of our attained results, some limiting cases are considered to recover fractional derivatives, as well as classical models of Maxwell and Newtonian fluids. The impacts of diverse flow parameters on variable profiles are achieved and presented graphically with significant conclusions.

2 Mathematical formulation based on a hybrid nanofluid

Consider an unsteady and an incompressible Oldroyd-B HNF flow close to an infinite vertical flat plate. Initially, consider that the fluid and plate are at a relaxation position, with constant temperature T_∞ and concentration C_∞. After some time, the plate is kept constant and the fluid begins to move with a temperature value $T(0,t)-a_1\frac{\partial T(0,t)}{\partial \xi}=u_0\sin\omega t$, where u_0 is a constant that signifies the dimension of velocity. At that time, the plate obtains a temperature T_w and concentration C_w, which persist constantly. We supposed that velocity, temperature, and concentration profiles are the only functions of ξ and t. The configuration of the problem is shown in Figure 1.

By Boussinesq's estimation (Ali et al., 2021), the governing equations for an Oldroyd-B HNF are discussed by Martyushev and Sheremet (2012). The equation of motion is as follows:

$$\rho_{hbnf}\left(1+\lambda_1\frac{\partial}{\partial t}\right)\frac{\partial W_1(\xi,t)}{\partial t}=\mu_{hbnf}\left(1+\lambda_2\frac{\partial}{\partial t}\right)\frac{\partial^2 W_1(\xi,t)}{\partial \xi^2}+g(\rho\beta_1)_{hbnf}\left(1+\lambda_1\frac{\partial}{\partial t}\right)\times(T(\xi,t)-T_\infty)+g(\rho\beta_2)_{hbnf}\left(1+\lambda_1\frac{\partial}{\partial t}\right)\times(C(\xi,t)-C_\infty). \quad (1)$$

The energy balance equation is as follows (Awan et al., 2019):

$$(\rho C_p)_{hbnf}\frac{\partial T(\xi,t)}{\partial t}=-\frac{\partial q}{\partial \xi}. \quad (2)$$

The Fourier law (Zhang et al., 2022) for thermal conduction is as follows:

$$q(\xi,t)=-\kappa_{hbnf}\frac{\partial T(\xi,t)}{\partial \xi}. \quad (3)$$

The diffusion equation (Awan et al., 2019) for

$$\frac{\partial C(\xi,t)}{\partial t}=-\frac{\partial j}{\partial \xi}. \quad (4)$$

The Fick law is as follows (Awan et al., 2019):

$$j(\xi,t)=-D_{hbnf}\frac{\partial C(\xi,t)}{\partial \xi}. \quad (5)$$

The appropriate initial and boundary conditions are as follows:

$$W_1(\xi,0)=0, T(\xi,0)=T_\infty, C(\xi,0)=C_\infty, \forall \xi\geq 0, \quad (6)$$

$$W_1(0,t)=0, T(0,t)-a_1\frac{\partial T(\xi,t)}{\partial \xi}\Big|_{\xi=0}=u_0\sin\omega t, C(0,t)=C_w, \quad (7)$$

$$W_1(\xi,t)\to 0, T(\xi,t)\to T_\infty, C(\xi,t)\to C_\infty \text{ as } \xi\to\infty. \quad (8)$$

Table 1 shows the properties of thermal and under-conversation fluids and nanoparticles.

$$\rho_{hbnf}=\rho_f(1-\phi_2)\times\left(\frac{\rho_{s_1}}{\rho_f}\phi_1+(1-\phi_1)\right)+\phi_2\rho_{s_2}\mu_{hbnf}=\frac{\mu_f}{(1-\phi_1)^{2.5}(1-\phi_2)^{2.5}}, (\rho C_p)_{hbnf}=(\rho C_p)_f(1-\phi_2)\times\left((1-\phi_1)+\phi_1\frac{(\rho C_p)_{s_1}}{(\rho C_p)_f}\right)+\phi_2(\rho C_p)_{s_2}, (\rho\beta_T)_{hbnf}=(1-\phi_2)(\rho\beta_T)_f\times\left((1-\phi_1)+\phi_1\frac{(\rho\beta_T)_{s_1}}{(\rho\beta_T)_f}\right)+\phi_2(\rho\beta_T)_{s_2}, \kappa_{hbnf}=\left(\frac{\kappa_{s_2}+(s-1)\kappa_{bf}-(s-1)\phi_2(\kappa_{bf}-\kappa_{s_2})}{\kappa_{s_2}+(s-1)\kappa_{bf}+\phi_2(\kappa_{bf}-\kappa_{s_2})}\right)\kappa_{bf}, \kappa_{bf}=\left(\frac{\kappa_{s_1}+(s-1)\kappa_f-(s-1)\phi_1(\kappa_f-\kappa_{s_1})}{\kappa_{s_1}+(s-1)\kappa_f+\phi_1(\kappa_f-\kappa_{s_1})}\right)\kappa_f. \quad (9)$$

TABLE 1 Thermal characteristics of base fluids and nanoparticles (Raza et al., 2022; Zhang et al., 2022).

Material	Water (H_2O)	Sodium alginate $(C_6H_9NaO_7)$	Aluminum oxide (Al_2O_3)	Ferro-ferric oxide (Fe_3O_4)
$\rho(M/L^3)$	997.1	898	3970	5180
$C_p(J/M\,K)$	4179	4175	765	670
$k(W/L\,K)$	0.613	0.6367	40	9.7
$\beta_T(K^{-1})$	21	23	0.85	0.9
σ	0.05	0.07	3.6×10^7	1×10^{-7}

The properties of a HNF are defined by Zhang et al. (2022).

TABLE 2 Numerical comparison of energy, concentration, and velocity profiles by different numerical methods.

ψ	$\theta(\psi,\eta)$ by Stehfest	$\theta(\psi,\eta)$ by Tzou	$\Phi(\psi,\eta)$ by Stehfest	$\Phi(\psi,\eta)$ by Tzou	$\mathbf{W}(\psi,\eta)$ by Stehfest	$\mathbf{W}(\psi,\eta)$ by Tzou
0.1	0.61263	0.61309	0.97297	0.9736	0.15292	0.15291
0.5	0.45242	0.45274	0.87168	0.87198	0.60469	0.60453
0.9	0.33289	0.33311	0.78055	0.7806	0.86701	0.86664
1.3	0.24413	0.24428	0.6986	0.69848	1.0032	1.0026
1.7	0.17849	0.1786	0.62496	0.62473	1.0553	1.0546
2.1	0.13014	0.13021	0.55882	0.55852	1.0522	1.0515
2.5	0.094641	0.094686	0.49946	0.49911	1.0137	1.0129
2.9	0.068661	0.06869	0.44621	0.44584	0.95349	0.95272
3.3	0.049701	0.04972	0.39847	0.39809	0.88123	0.8805
3.7	0.035902	0.035914	0.35568	0.35532	0.80356	0.80288
4.1	0.025884	0.025891	0.31737	0.31702	0.7 2499	0.72437
4.5	0.018627	0.018631	0.28306	0.28274	0.64852	0.64796
4.9	0.013381	0.013384	0.25237	0.25207	0.57605	0.57556

The following are a set of non-dimensional parameters:

$$\psi^\star = \frac{u_0}{\upsilon_f}\xi, \eta^\star = \frac{u_0^2}{\upsilon_f}\mathrm{t}, W^\star = \frac{W_1}{u_0}, \theta^\star = \frac{T-T_\infty}{T_w-T_\infty}, \Phi^\star = \frac{C-C_\infty}{C_w-C_\infty}, \mathrm{q}^\star = \frac{q}{q_0}, \mathrm{j}^\star = \frac{j}{j_0},$$
$$\lambda_1^* = \frac{u_0^2}{\upsilon_f}\lambda_1, \lambda_2^* = \frac{u_0^2}{\upsilon_f}\lambda_2, q_0 = \frac{\kappa_f(T_w-T_\infty)u_0}{\upsilon_f}, \mathrm{j}_0 = \frac{D_{nf}(C_w-C_\infty)u_0}{\upsilon_f},$$
$$Gr = \frac{g(\upsilon\beta_1)_f(T_w-T_\infty)}{u_0^3}, Gm = \frac{g(\upsilon\beta_2)_f(C_w-C_\infty)}{u_0^3}, \mathrm{Pr} = \frac{(\mu C_p)_f}{\kappa_f}, Sc = \frac{\upsilon_f}{D_f}. \tag{10}$$

By utilizing the aforementioned variables in Eqs. 1–8 and after dropping the * notation, we obtain

$$\Omega_1\left(1+\lambda_1\frac{\partial}{\partial\eta}\right)\frac{\partial W(\psi,\eta)}{\partial\eta} = \Omega_2\left(1+\lambda_2\frac{\partial}{\partial\eta}\right)\frac{\partial^2 W(\psi,\eta)}{\partial\psi^2} + \Omega_3\left(1+\lambda_1\frac{\partial}{\partial\eta}\right)Gr\;\theta(\psi,\eta) + \Omega_4\left(1+\lambda_1\frac{\partial}{\partial\eta}\right)Gm\;\Phi(\psi,\eta). \tag{11}$$

$$\Omega_5\mathrm{Pr}\frac{\partial\theta(\psi,\eta)}{\partial\eta} = -\frac{\partial q}{\partial\psi}. \tag{12}$$

$$q(\psi,\eta) = -\Omega_6\frac{\partial\theta(\psi,\eta)}{\partial\psi}. \tag{13}$$

$${}^{AB}D_\eta^\alpha\Phi(\psi,\eta) = -\frac{(1-\phi_1)(1-\phi_2)}{Sc}\frac{\partial j}{\partial\psi}, \tag{14}$$

$$j(\psi,\eta) = -\frac{\partial\Phi(\psi,\eta)}{\partial\psi}. \tag{15}$$

$$W(\psi,0) = 0, \theta(\psi,0) = 0, \Phi(\psi,0) = 0, \forall\psi \geq 0, \tag{16}$$

$$W(0,\eta) = 0, \theta(0,\eta) - a_1\frac{\partial\theta(\psi,\eta)}{\psi}\bigg|_{\psi=0} = \sin\omega\eta, \Phi(0,\eta) = 1, \forall\eta > 0, \tag{17}$$

$$W(\psi,\eta) \to 0, \theta(\psi,\eta) \to 0, \Phi(\psi,\eta) \to 0, \mathrm{as}, \psi \to \infty\,. \tag{18}$$

where

$$\Omega_1 = (1-\phi_2)\times\left((1-\phi_1)+\phi_1\frac{\rho_{s_1}}{\rho_f}\right)+\phi_2\frac{\rho_{s_2}}{\rho_f}, \Omega_2 = \frac{1}{(1-\phi_1)^{2.5}(1-\phi_2)^{2.5}},$$
$$\Omega_3 = (1-\phi_2)\times\left((1-\phi_1)+\phi_1\frac{(\rho\beta_1)_{s_1}}{(\rho\beta_1)_f}\right)+\phi_2\frac{(\rho\beta_1)_{s_2}}{(\rho\beta_1)_f},$$
$$\Omega_4 = (1-\phi_2)\times\left((1-\phi_1)+\phi_1\frac{(\rho\beta_2)_{s_2}}{(\rho\beta_2)_f}\right)+\phi_2\frac{(\rho\beta_2)_{s_2}}{(\rho\beta_2)_f},$$
$$\Omega_5 = (1-\phi_2)\times\left((1-\phi_1)+\phi_1\frac{(\rho C_p)_s}{(\rho C_p)_f}\right)+\phi_2\frac{(\rho C_p)_{s_2}}{(\rho C_p)_f},$$
$$\Omega_6 = \left(\frac{\kappa_{s_2}+(s-1)\kappa_{bf}-(s-1)\phi_2(\kappa_{bf}-\kappa_{s2})}{\kappa_{s_2}+(s-1)\kappa_{bf}+\phi_2(\kappa_{bf}-\kappa_s)}\right)\kappa_{bf},$$
$$\kappa_{bf} = \left(\frac{\kappa_{s_1}+(s-1)\kappa_f-(s-1)\phi_1(\kappa_f-\kappa_{s_1})}{\kappa_{s_1}+(s-1)\kappa_f+\phi_1(\kappa_f-\kappa_{s_1})}\right). \tag{19}$$

2.1 Fractional model based on a non-local kernel

Now, we develop a fractional Oldroyd-B HNF using Fourier and Fick's law based on the AB-fractional operator (Atangana and Dumitru, 2016), which is explained as the following expression for a function $f(\xi,t)$

$${}^{AB}D_t^{\gamma}f(\xi,t) = \frac{1}{1-\gamma}\int_0^t E_{\gamma}\left[\frac{\gamma(t-\tau)^{\gamma}}{1-\gamma}\right]f'(\xi,\tau)d\tau, 0<\gamma<1, \tag{20}$$

and the kernel Mittage–Leffler function $E_{\gamma}(\tau)$ is defined by

$$E_{\gamma}(\tau) = \sum_{r=0}^{\infty}\frac{\tau^{\gamma}}{\Gamma(r\gamma+1)}, 0<\gamma<1, \tau\in\mathbb{C}. \tag{21}$$

The Laplace transform is

$$L\{{}^{AB}D_t^{\gamma}f(\xi,t)\} = \frac{s^{\gamma}L\{f(\xi,t)\}-s^{\gamma-1}f(\xi,0)}{s^{\gamma}(1-\gamma)+\gamma}, \tag{22}$$

with

$$\lim_{\gamma\longrightarrow 1}{}^{AB}D_t^{\gamma}f(\xi,t) = \frac{\partial f(\xi,t)}{\partial t}. \tag{23}$$

The governing equations for the AB-fractional derivative are obtained by substituting the ordinary derivative with the AB derivative operator ${}^{AB}D_{\eta}^{\alpha}$ in Eqs. 11–15 as

$$\Omega_1\left(1+\lambda_1\frac{\partial}{\partial\eta}\right){}^{AB}D_{\eta}^{\alpha}W(\psi,\eta) = \Omega_2\left(1+\lambda_2\frac{\partial}{\partial\eta}\right)\frac{\partial^2W(\psi,\eta)}{\partial\psi^2}$$
$$+\Omega_3\left(1+\lambda_1\frac{\partial}{\partial\eta}\right)Gr\,\theta(\psi,\eta)+\Omega_4\left(1+\lambda_1\frac{\partial}{\partial\eta}\right)Gm\,\Phi(\psi,\eta), \tag{24}$$

$$\Omega_5\mathrm{Pr}\,{}^{AB}D_{\eta}^{\alpha}\theta(\psi,\eta) = -\frac{\partial q}{\partial\psi}, \tag{25}$$

$$q(\psi,\eta) = -\Omega_6\frac{\partial\theta(\psi,\eta)}{\partial\psi}. \tag{26}$$

$${}^{AB}D_{\eta}^{\alpha}\Phi(\psi,\eta) = -\frac{1}{Sc}\frac{\partial j}{\partial\psi}, \tag{27}$$

$$j(\psi,\eta) = -\frac{\partial\Phi(\psi,\eta)}{\partial\psi}. \tag{28}$$

3 Solution of the problem

3.1 Energy profile

Using the Laplace transform on Eqs. 25, 26 and corresponding conditions $(15)_2$-$(17)_2$, we have

$$\Omega_6\mathrm{Pr}\left(\frac{s^{\alpha}}{(1-\alpha)s^{\alpha}+\alpha}\right)\bar{\theta}(\psi,s) = -\frac{\partial\bar{q}}{\partial\psi}, \tag{29}$$

$$\bar{q}(\psi,s) = -\Omega_6\frac{\partial\bar{\theta}(\psi,s)}{\partial\psi}, \tag{30}$$

$$\bar{\theta}(0,s)-a_1\frac{\partial\bar{\theta}(\psi,s)}{\psi}\Big|_{\psi=0} = \frac{\omega}{s^2+\omega^2},$$
$$\bar{\theta}(\psi,s)\to 0, \text{as}, \psi\to\infty, \tag{31}$$

where $\bar{\theta}(\psi,s) = \int_0^{\infty}\theta(\psi,t)e^{-st}dt$ is the Laplace transform for $\theta(\psi,t)$, and s is the Laplace transform parameter (Ali et al., 2021).

The solution of Eq. (29) by using Eq. (30) and with conditions in Eq. (31) is

$$\bar{\theta}(\psi,s) = \frac{\omega}{(s^2+\omega^2)}\frac{1}{1+a\sqrt{\frac{\Pi s^{\alpha}}{(1-\alpha)s^{\alpha}+\alpha}}}\exp\left(-\psi\sqrt{\frac{\Pi s^{\alpha}}{(1-\alpha)s^{\alpha}+\alpha}}\right). \tag{32}$$

Eq. (32) can be written as

$$\bar{\theta}(\psi,s) = \frac{\omega}{(s^2+\omega^2)}\frac{1}{1+a\sqrt{\Lambda_1(s)}}\exp\left(-\psi\sqrt{\Lambda_1(s)}\right), \tag{33}$$

where $\Pi = \frac{\Omega_5\mathrm{Pr}}{\Omega_6}$ and $\Lambda_1(s) = \frac{\Pi s^{\alpha}}{(1-\alpha)s^{\alpha}+\alpha}$.

The Laplace inverse of Eq. (33) is shown numerically in Table 2.

3.2 Concentration field

By employing the Laplace transform on Eqs. 27, 28 with associated conditions defined in Eqs. $(15)_3$– $(17)_3$, we have

$$\frac{s^{\alpha}}{(1-\alpha)s^{\alpha}+\alpha}\bar{\Phi}(\psi,s) = -\frac{(1-\phi_1)(1-\phi_2)}{Sc}\frac{\partial\bar{j}(\psi,s)}{\partial\psi}, \tag{34}$$

$$\bar{j}(\psi,s) = -\frac{\partial\bar{j}(\psi,s)}{\partial\psi}. \tag{35}$$

$$\bar{\Phi}(0,s) = \frac{1}{s}, \bar{\Phi}(\psi,s)\to 0, \text{as}, \psi\to\infty. \tag{36}$$

The solution of Eq. (34) by using Eq. (35) and conditions in Eq. (36) is

$$\bar{\Phi}(\psi,s) = \frac{1}{s}\exp\left(-\psi\sqrt{\frac{Sc}{(1-\phi_1)(1-\phi_2)}\left(\frac{s^{\alpha}}{(1-\alpha)s^{\alpha}+\alpha}\right)}\right). \tag{37}$$

Eq. (37) may be written as

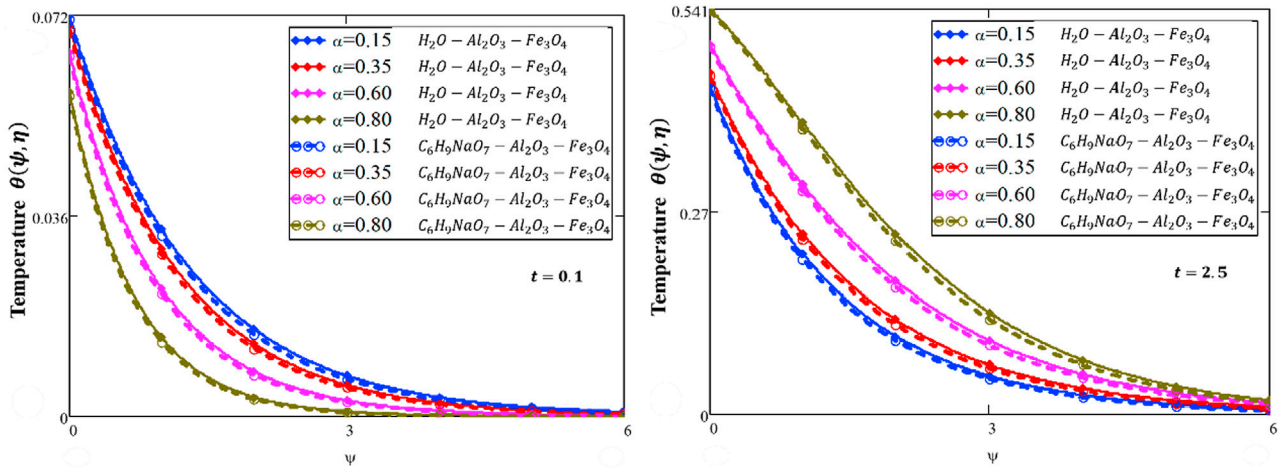

FIGURE 2
Simulation to explain the temperature for changing α when $Pr = 3$ and $\phi_1 = \phi_2 = 0.4$.

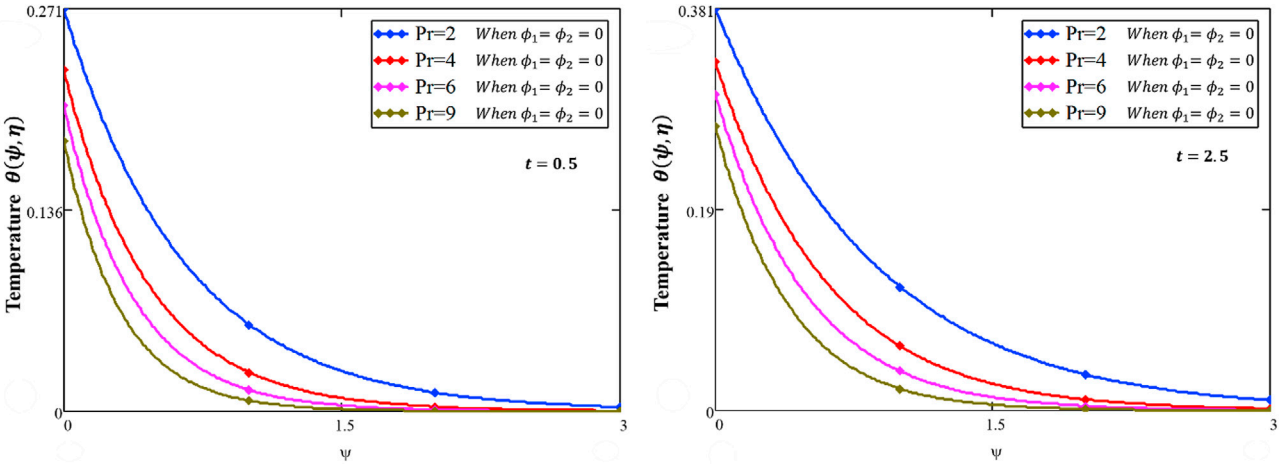

FIGURE 3
Simulation to explain the temperature for Pr when $\alpha = 0.4$.

$$\bar{\Phi}(\psi, s) = \frac{1}{s}\exp\left(-\psi\sqrt{\Lambda_2(s)}\right), \tag{38}$$

where $\Lambda_2(s) = \frac{Sc}{(1-\phi_1)(1-\phi_2)}\left(\frac{s^\alpha}{(1-\alpha)s^\alpha+\alpha}\right)$.

The Laplace inverse of Eq. (38) is computed numerically in Table 2 by invoking diverse numerical methods.

3.3 Momentum profile

Taking the Laplace transform on Eq. (24) with related conditions in Eqs. $(15)_1$– $(17)_1$, we have

$$\Omega_1(1+\lambda_1 s)\left(\frac{q^\alpha}{(1-\alpha)q^\alpha+\alpha}\right)\bar{W}(\psi, s) = \Omega_2(1+\lambda_2 s)\frac{\partial^2\bar{W}(\psi, s)}{\partial\psi^2} + \Omega_3(1+\lambda_1 s)Gr\bar{\theta}(\psi, s) + \Omega_4(1+\lambda_1 s)Gm\bar{\Phi}(\psi, s), \tag{39}$$

$$\bar{W}(0, s) = 0, \bar{W}(\psi, s) \to 0, \text{as}, \psi \to \infty\,. \tag{40}$$

By using temperature values from Eq. (37) and concentration from Eq. (38) and with conditions of Eq. (40), we obtain the solution of the velocity field for Eq. (40) as

$$\bar{W}(\psi, s) = \frac{\Lambda_4(s)Gr}{\Lambda_3(s)-\Lambda_1(s)}\frac{\omega}{s^s+\omega^2}\left[\frac{e^{-\psi\sqrt{\Lambda_1(s)}}}{1+a\sqrt{\Lambda_1(s)}} - \frac{e^{-\psi\sqrt{\Lambda_3(s)}}}{1+a\sqrt{\Lambda_1(s)}}\right] + \frac{\Lambda_5(s)Gm}{\Lambda_3(s)-\Lambda_2(s)}\left[\frac{e^{-\psi\sqrt{\Lambda_2(s)}}}{s} - \frac{e^{-\psi\sqrt{\Lambda_3(s)}}}{s}\right], \tag{41}$$

where
$b_1 = \frac{1+\lambda_1 s}{1+\lambda_2 s}$, $\Lambda_3(s) = b_1\frac{\Omega_1}{\Omega_2}\frac{s^\alpha}{(1-\alpha)s^\alpha+\alpha}$, $\Lambda_4(s) = b_1\frac{\Omega_3}{\Omega_2}$, and $\Lambda_5(s) = b_1\frac{\Omega_4}{\Omega_2}$.

Our achieved solutions of variable profiles are complex to find analytically. Different researchers employed varied numerical approaches; so to compute Laplace inversion, we

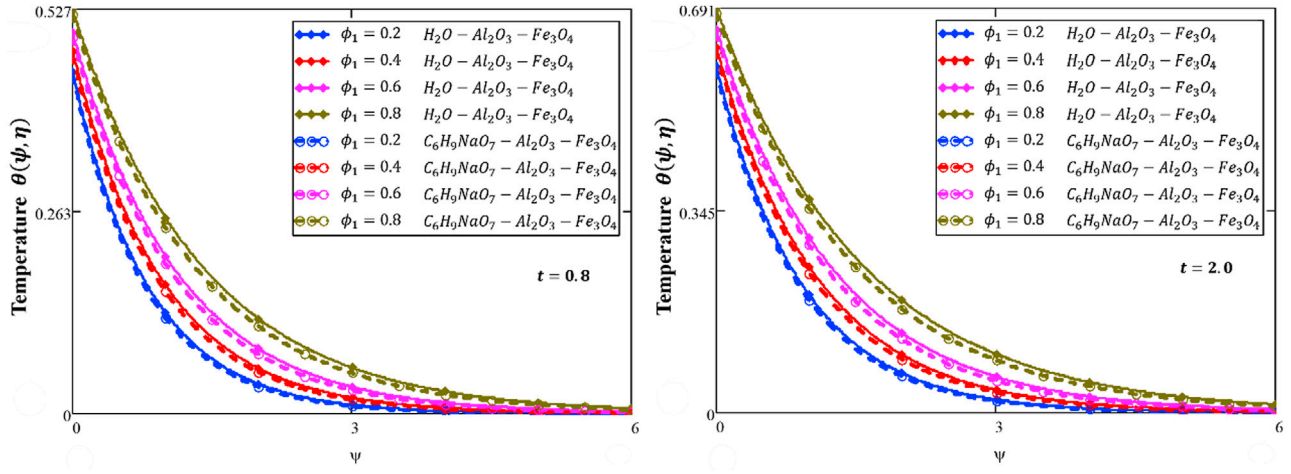

FIGURE 4
Simulation to explain the temperature for fluctuating ϕ_1 when $Pr = 6, \alpha = 0.4, and\ \phi_2 = 0.5$.

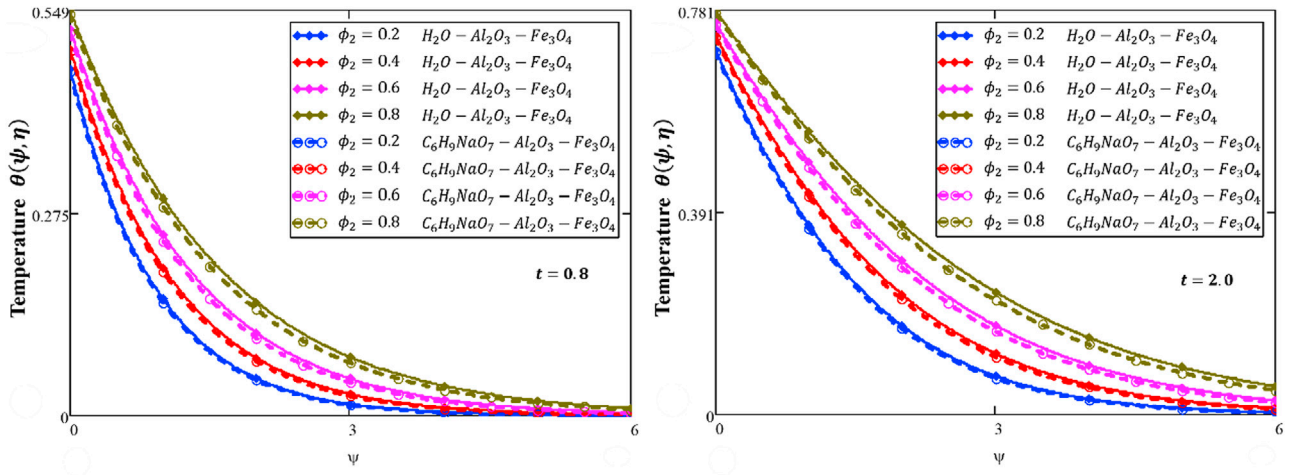

FIGURE 5
Simulation to explain the temperature for changing ϕ_2 when $Pr = 2, \alpha = 0.8, and\ \phi_1 = 0.2$.

also employed numerical techniques, i.e., Stehfest and Tzou numerical methods. These algorithms are defined as follows (Stehfest, 1970; Tzou, 2014):

$$W(\psi,\eta) = \frac{\ln(2)}{\eta}\sum_{m=1}^{M} w_m \bar{W}\left(\psi, \mathrm{m}\frac{\ln(2)}{\eta}\right), \tag{42}$$

where $w_m = (-1)^{m+\frac{M}{2}} \sum_{r=\left(\frac{q+1}{2}\right)}^{\min(q,\frac{M}{2})} \frac{r^{\frac{M}{2}}(2r)!}{\left(\frac{M}{2}-r\right)!r!(r-1)!(q-r)!(2r-q)!}$,

and

$$W(\psi,\eta) = \frac{e^{4.7}}{\eta}\left[\frac{1}{2}\bar{W}\left(\psi,\frac{4.7}{\eta}\right) + \mathrm{Re}\left\{\sum_{j=1}^{M}(-1)^j \bar{W}\left(\psi,\frac{4.7+j\pi i}{\eta}\right)\right\}\right]. \tag{43}$$

Case I. Classical Oldroyd-B fluid

By substituting $\alpha = 1$ in Eq. (41), the velocity solution takes the form as

$$\bar{W}(\psi,s) = \frac{\Omega_3\Omega_6(1+\lambda_1 s)Gr}{\Omega_1\Omega_6(1+\lambda_1 s) - \Omega_2\Omega_5\mathrm{Pr}(1+\lambda_2 s)}\frac{\omega}{s^2+\omega^2}$$
$$\left[\frac{e^{-\psi\sqrt{s\frac{\Omega_5\mathrm{Pr}}{\Omega_6}}}}{1+a\sqrt{s\frac{\Omega_5\mathrm{Pr}}{\Omega_6}}} - \frac{e^{-\psi\sqrt{\frac{1+\lambda_1 s}{1+\lambda_2 s}\frac{\Omega_1}{\Omega_2}s}}}{1+a\sqrt{s\frac{\Omega_5\mathrm{Pr}}{\Omega_6}}}\right] + \frac{\Omega_4 Sc(1+\lambda_1 s)Gm}{\Omega_1 Sc(1+\lambda_1 s) - \Omega_2(1+\lambda_2 s)}$$
$$\left[\frac{e^{-\psi\sqrt{\frac{s}{Sc}}}}{s} - \frac{e^{-\psi\sqrt{\frac{1+\lambda_1 s}{1+\lambda_2 s}\frac{\Omega_1}{\Omega_2}s}}}{s}\right]. \tag{44}$$

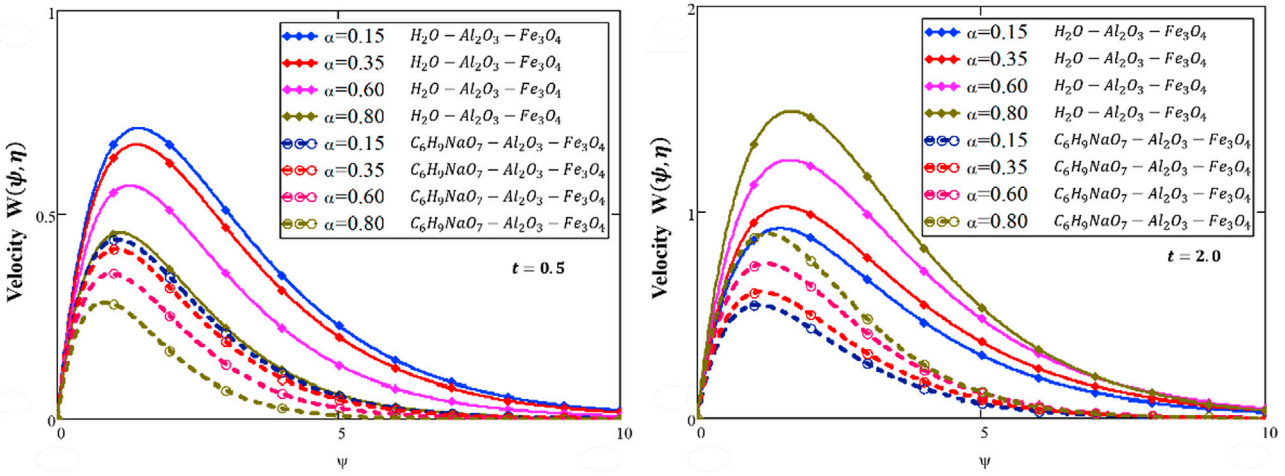

FIGURE 6
Simulation to explain the velocity for fluctuating α when $Pr = 3.2, \phi_1 = \phi_2 = 0.2, Gr = 8, Gm = 6.5, Sc = 0.5, \lambda_1 = 0.5$, and $\lambda_1 = 0.5$.

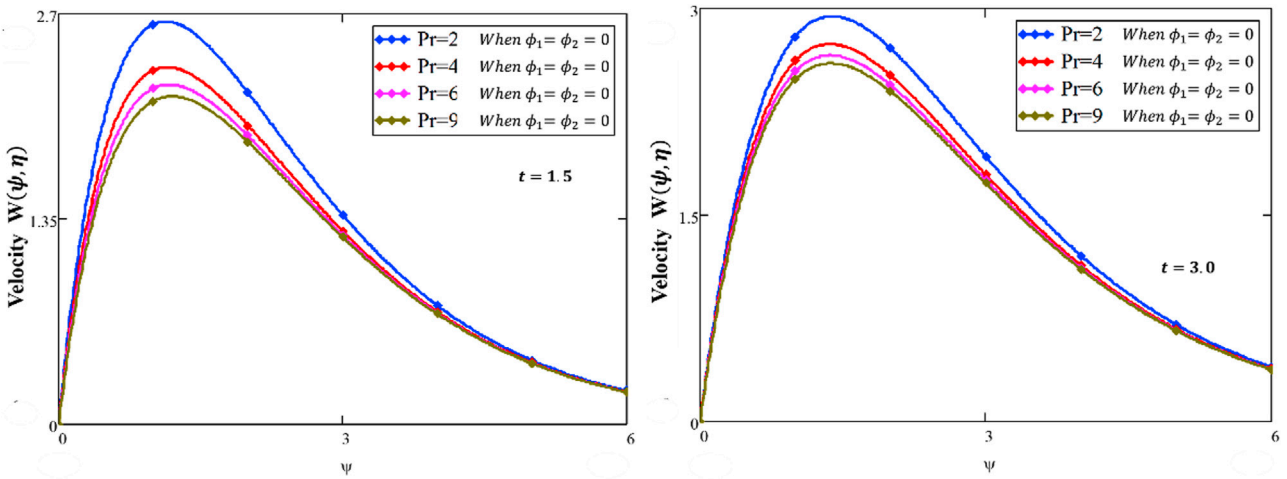

FIGURE 7
Simulation to explain the velocity for changing Pr when $\alpha = 0.5, Gr = 8, Gm = 6.5, Sc = 0.5, \lambda_1 = 0.5$, and $\lambda_1 = 0.3$.

Case II. Fractionalized Maxwell fluid

By substituting $\lambda_2 = 0$ in Eq. (41), the velocity solution converts as follows:

$$\bar{W}(\psi, s) = \frac{(1+\lambda_1 s)\left((1-\alpha)s^{\alpha}+\alpha\right)\Omega_3\Omega_6 Gr}{(1+\lambda_1 s)\Omega_1\Omega_6 s^{\alpha} - \Omega_5\Omega_2 \Pr s^{\alpha}} \frac{\omega}{s^{s}+\omega^2}$$
$$\frac{1}{1+a\sqrt{\frac{\Omega_5 \Pr}{\Omega_6}\frac{s^{\alpha}}{(1-\alpha)s^{\alpha}+\alpha}}}\left(\begin{array}{c} e^{-\psi\sqrt{\frac{\Omega_5 \Pr}{\Omega_6}\frac{s^{\alpha}}{(1-\alpha)s^{\alpha}+\alpha}}} - \\ e^{-\psi\sqrt{(1+\lambda_1 s)\frac{\Omega_1}{\Omega_2}\frac{s^{\alpha}}{(1-\alpha)s^{\alpha}+\alpha}}} \end{array}\right)$$
$$+\frac{(1+\lambda_1 s)\left((1-\alpha)s^{\alpha}+\alpha\right)\Omega_4 ScGm}{(1+\lambda_1 s)\Omega_1 Sc s^{\alpha} - \Omega_2 s^{\alpha}}\left(\begin{array}{c} \frac{e^{-\psi\sqrt{\frac{1}{Sc}\left(\frac{s^{\alpha}}{(1-\alpha)s^{\alpha}+\alpha}\right)}}}{s} - \\ \frac{e^{-\psi\sqrt{(1+\lambda_1 s)\frac{\Omega_1}{\Omega_2}\frac{s^{\alpha}}{(1-\alpha)s^{\alpha}+\alpha}}}}{s} \end{array}\right). \quad (45)$$

Case III. Ordinary Maxwell fluid

By substituting $\alpha = 1$ and $\lambda_2 = 0$ in Eq. (41), the velocity solution converts

$$\bar{W}(\psi, s) = \frac{(1+\lambda_1 s)\Omega_3\Omega_6 Gr}{(1+\lambda_1 s)\Omega_1\Omega_6 - \Omega_5\Omega_2 \Pr} \frac{\omega}{s^2+\omega^2}$$
$$\frac{1}{1+a\sqrt{s\frac{\Omega_5 \Pr}{\Omega_6}}}\left[e^{-\psi\sqrt{s\frac{\Omega_5 \Pr}{\Omega_6}}} - e^{-\psi\sqrt{(1+\lambda_1 s)\frac{\Omega_1}{\Omega_2}s}}\right]$$
$$+\frac{(1+\lambda_1 s)\Omega_4 ScGm}{(1+\lambda_1 s)\Omega_1 Sc - \Omega_2}\left[\frac{e^{-\psi\sqrt{\frac{s}{Sc}}}}{s} - \frac{e^{-\psi\sqrt{(1+\lambda_1 s)\frac{\Omega_1}{\Omega_2}s}}}{s}\right]. \quad (46)$$

Case IV. Fractionalized Newtonian fluid

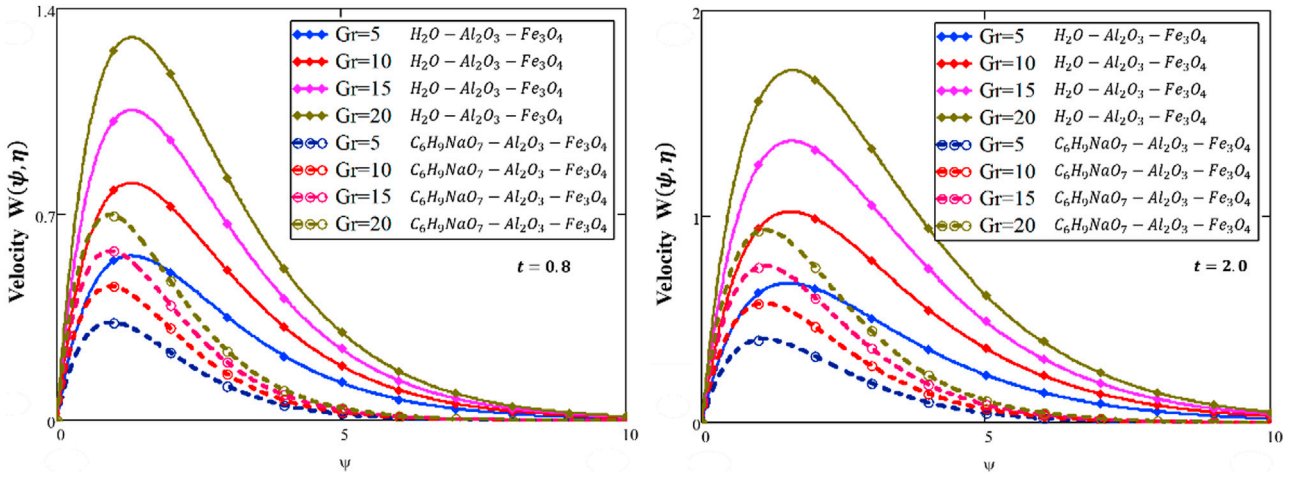

FIGURE 8
Simulation to explain the velocity for changing Gr when $\alpha = 0.4, Pr = 2.5, \phi_1 = \phi_2 = 0.2, Gm = 4.5, Sc = 0.8, \lambda_1 = 0.7, and\, \lambda_1 = 0.3$.

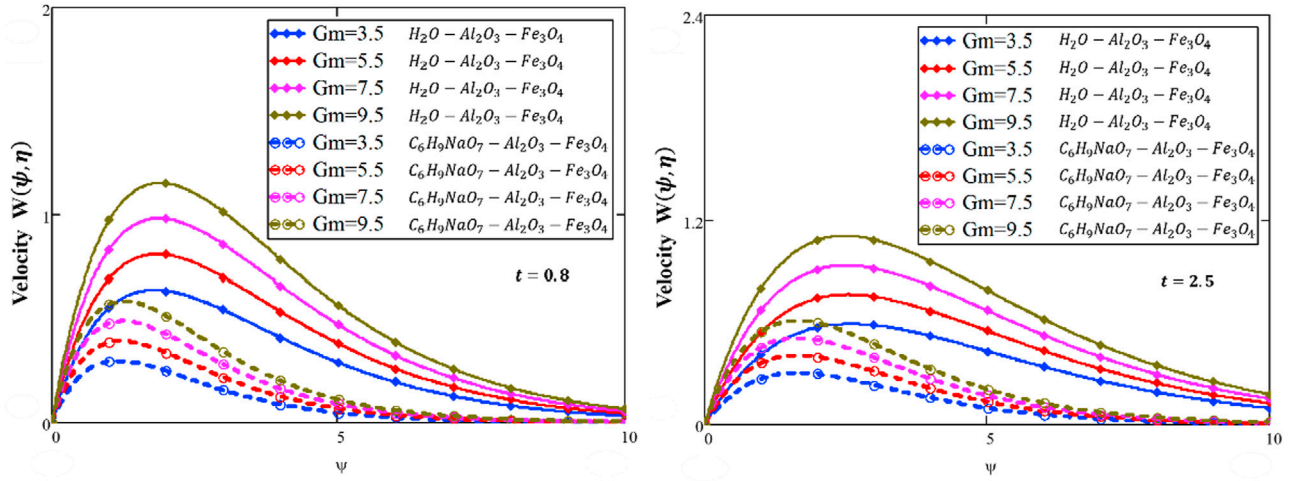

FIGURE 9
Simulation to explain the velocity for changing Gm when $\alpha = 0.4, Pr = 3.2, \phi_1 = \phi_2 = 0.3, Gr = 8, Sc = 0.2, \lambda_1 = 1.2, and\, \lambda_1 = 0.3$.

By substituting $\lambda_1 = 0$ in Eq. (45), the velocity solution converts

$$\bar{W}(\psi, s) = \frac{((1-\alpha)s^{\alpha} + \alpha)\Omega_3\Omega_6 Gr}{\Omega_1\Omega_6 s^{\alpha} - \Omega_5\Omega_2 \mathrm{Pr}\, s^{\alpha}} \frac{\omega}{s^s + \omega^2} \frac{1}{1 + a\sqrt{\frac{\Omega_5 \mathrm{Pr}}{\Omega_6}\frac{s^{\alpha}}{(1-\alpha)s^{\alpha}+\alpha}}} \left[\begin{matrix} e^{-\psi\sqrt{\frac{\Omega_5 \mathrm{Pr}}{\Omega_6}\frac{s^{\alpha}}{(1-\alpha)s^{\alpha}+\alpha}}} - \\ e^{-\psi\sqrt{\frac{\Omega_1}{\Omega_2}\frac{s^{\alpha}}{(1-\alpha)s^{\alpha}+\alpha}}} \end{matrix} \right] + \frac{((1-\alpha)s^{\alpha} + \alpha)\Omega_4 ScGm}{\Omega_1 Sc s^{\alpha} - \Omega_2 s^{\alpha}} \left[\frac{e^{-\psi\sqrt{\frac{1}{Sc}\left(\frac{s^{\alpha}}{(1-\alpha)s^{\alpha}+\alpha}\right)}}}{s} - \frac{e^{-\psi\sqrt{\frac{\Omega_1}{\Omega_2}\frac{s^{\alpha}}{(1-\alpha)s^{\alpha}+\alpha}}}}{s} \right]. \quad (47)$$

Case V. Ordinary Newtonian fluid

By substituting $\alpha = 1$ in Eq. (47), the velocity solution converts

$$\bar{W}(\psi, s) = \frac{\Omega_3\Omega_6 Gr}{\Omega_1\Omega_6 - \Omega_5\Omega_2 \mathrm{Pr}} \frac{\omega}{s^s + \omega^2} \frac{1}{1 + a\sqrt{\frac{\Omega_5 \mathrm{Pr}}{\Omega_6}}} \left[e^{-\psi\sqrt{\frac{\Omega_5 \mathrm{Pr}}{\Omega_6}}} - e^{-\psi\sqrt{\frac{\Omega_1}{\Omega_2}}} \right] + \frac{\Omega_4 ScGm}{\Omega_1 Sc - \Omega_2} \left[\frac{e^{-\psi\sqrt{\frac{1}{Sc}}}}{s} - \frac{e^{-\psi\sqrt{\frac{\Omega_1}{\Omega_2}}}}{s} \right]. \quad (48)$$

4 Discussion of results

In this article, the natural convection flow of the Oldroyd-B HNF flowing close to an infinite vertical flat plate is examined. Aluminum oxide–magnetite–water (Al_2O_3–Fe_3O_4–H_2O) and aluminum oxide–magnetite–sodium alginate (Al_2O_3–Fe_3O_4–$C_6H_9NaO_7$)-based HNFs are considered with an AB-fractional approach. The

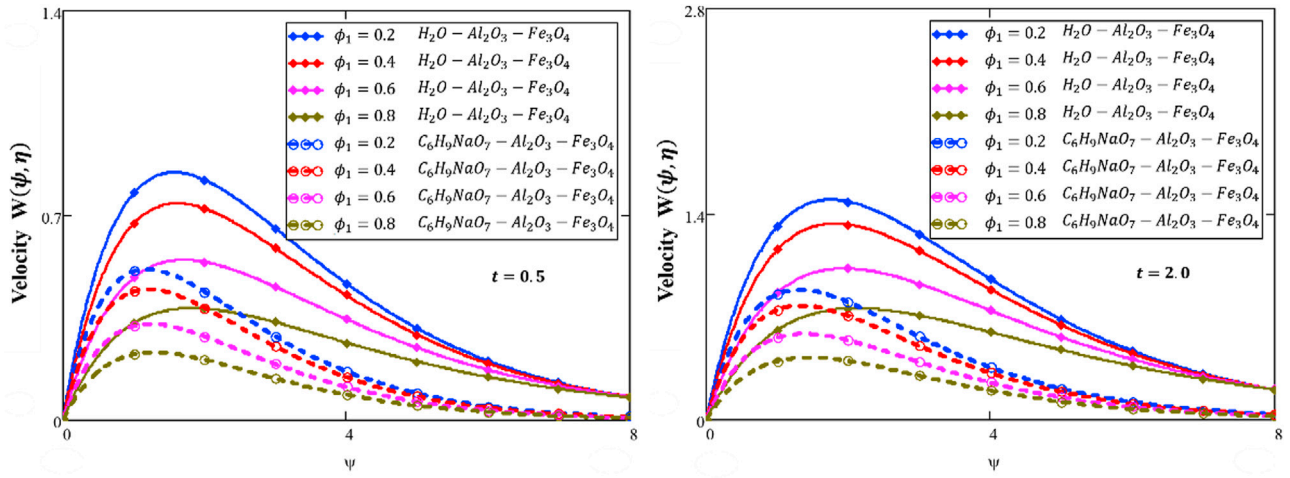

FIGURE 10
Simulation to explain the velocity for fluctuating ϕ_1 when $\alpha = 0.5, Pr = 3.2, \phi_2 = 0.3, Gr = 6, Gm = 8, Sc = 0.3, \lambda_1 = 0.7$, and $\lambda_1 = 1$.

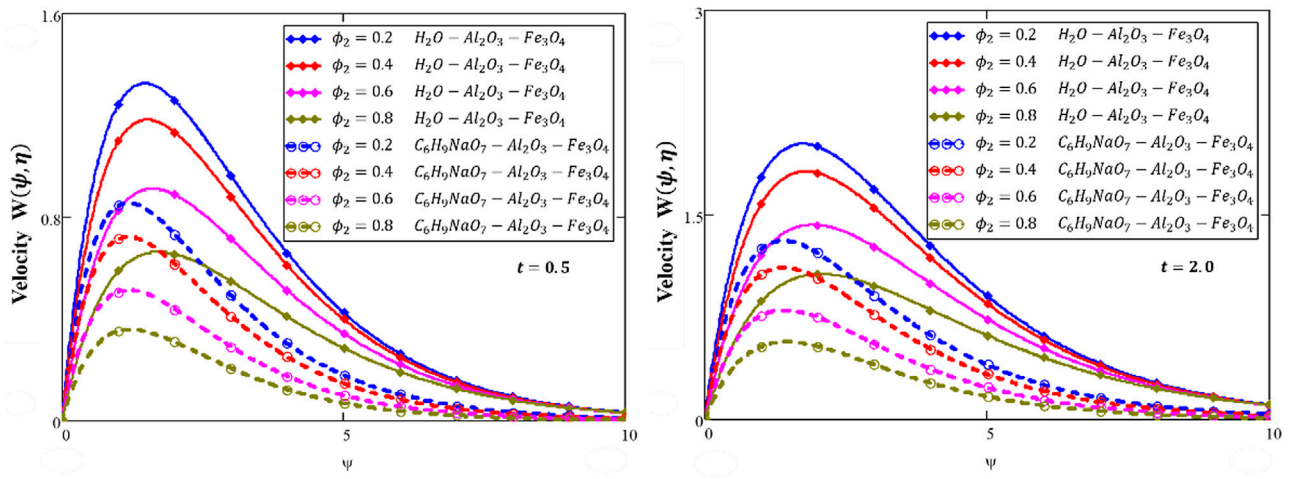

FIGURE 11
Simulation to explain the velocity for fluctuating ϕ_2 when $\alpha = 0.5, Pr = 3.2, \phi_1 = 0.2, Gr = 5, Gm = 6, Sc = 0.2, \lambda_1 = 1.7$, and $\lambda_1 = 1.3$.

solution of dimensionless fractional equations of energy, concentration, and momentum is obtained with the Laplace method. To observe from the physical perception, the impacts of fractional derivatives and different flow parameters on concentration, velocity, and temperature are measured and shown in Figures 2–15 graphically.

Figure 2 shows the influence of α on the temperature field. By setting other parameters constant and fluctuating the value of α, it is seen that for a small time, the temperature profile declined for larger values α and this effect is reversed for a greater time. We see that fluid characteristics can be measured by fractional parameters. For a different value of α, the temperature close to the plate is extreme. The temperature declines away from the plate and is asymptotic in the growing ξ direction, which satisfies our boundary conditions.

Figure 3 shows the thermal behavior for Pr. For large estimations of Pr, the temperature declines. Substantially, the heat conductivity increasing the estimations of Pr, manufacturing the fluid thicker, sources the least thickness of the heat boundary layer. Figures 4, 5 show the temperature behavior with ϕ_1 and ϕ_2. The temperature field represents an increasing function of ϕ_1 and ϕ_2. As expected, with greater values of ϕ_1 and ϕ_2, the capacity of the HNF expands to hold additional heat. Therefore, the heat conductivity of the NF increases and temperature increases at different times.

The fluid velocity declines as we increase α, as shown in Figure 6, when there is less time. For a long time, the velocity is enhanced. Physically, when α increases, the velocity and thermal boundary layer decline, and as a consequence, the velocity declines for a short time. Figure 7 shows the behavior of the

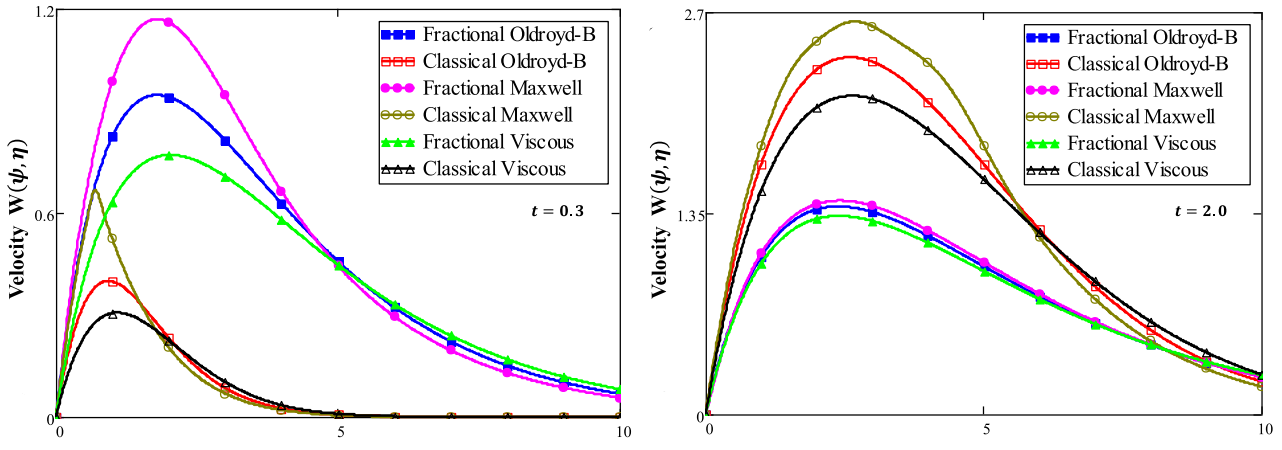

FIGURE 12
Simulation to explain the velocity for the different fluid models when $Pr = 3.2, \phi_1 = \phi_2 = 0.2, Gr = 8, Gm = 4.5, Sc = 0.1, \lambda_1 = 0.7, and\ \lambda_1 = 0.3$.

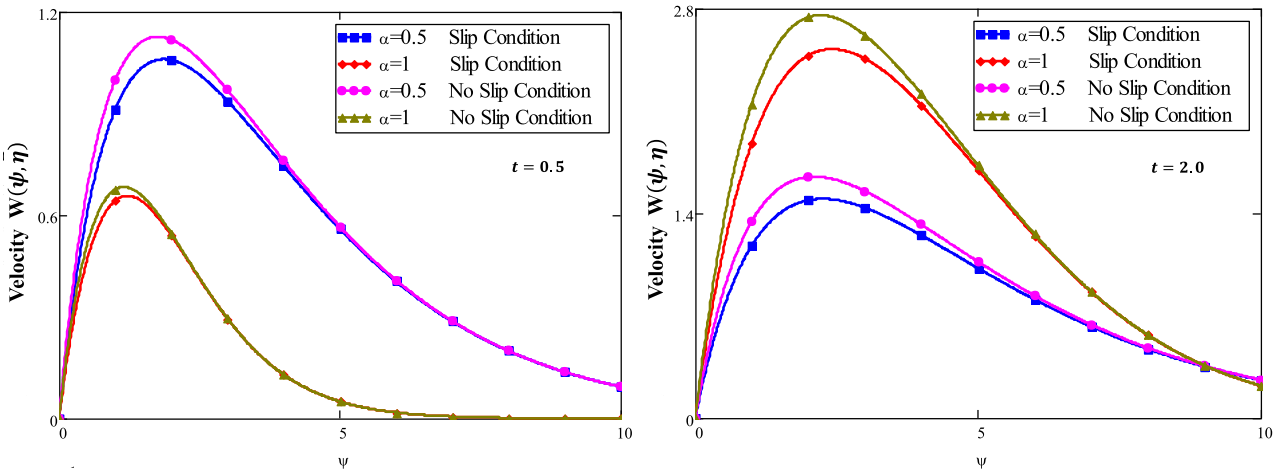

FIGURE 13
Simulation to clarify the velocity for the slip and no-slip condition when $Pr = 6.2, \phi_1 = \phi_2 = 0.2, Gr = 8, Gm = 4.5, Sc = 0.5, \lambda_1 = 0.7, and\ \lambda_1 = 0.3$.

velocity with *Pr*. The velocity field also decreases with increasing *Pr*. Enhancement in *Pr* decreases the thermal conductivity and increases the viscosity of the fluid because of which the momentum profile declines with *Pr*.

Figure 8 shows the influence of *Gr* on the momentum profile. By increasing *Gr*, the velocity profile is enhanced. Since *Gr* exhibits the buoyancy force that increases the natural convection, therefore the velocity grows. Figure 9 shows the impact of *Gm* on the velocity by considering the changing *Gm* with time. The ratio of the buoyant force and viscous force is named the mass Grashof number that sources unrestricted convection. Figure 9 shows that velocity is enhanced for enhancing *Gm*. Figures 10, 11 show the effect of ϕ_1 and ϕ_2 on velocity. The velocity decreases with increase in ϕ_1 and ϕ_2. This means that with the addition of nanoparticles to the base liquids, the resulting HNF becomes denser, so they become more viscous than the regular fluid. Also, the boundary layer of regular fluids is thinner than that of the HNF, and as a result, the velocity shows a declining behavior with increasing values of ϕ_1 and ϕ_2. Moreover, the impact of a water-based HNF has more progressive values as compared to that of the sodium alginate-based HNF on the profiles of energy and velocity.

Figure 12 shows a comparison of different fluid models. It is observed that the solutions of Maxwell nanofluids for both ordinary and fractional cases have developed curves as compared to Oldroyd-B and viscous nanofluids. Figure 13 shows the velocity for the slip

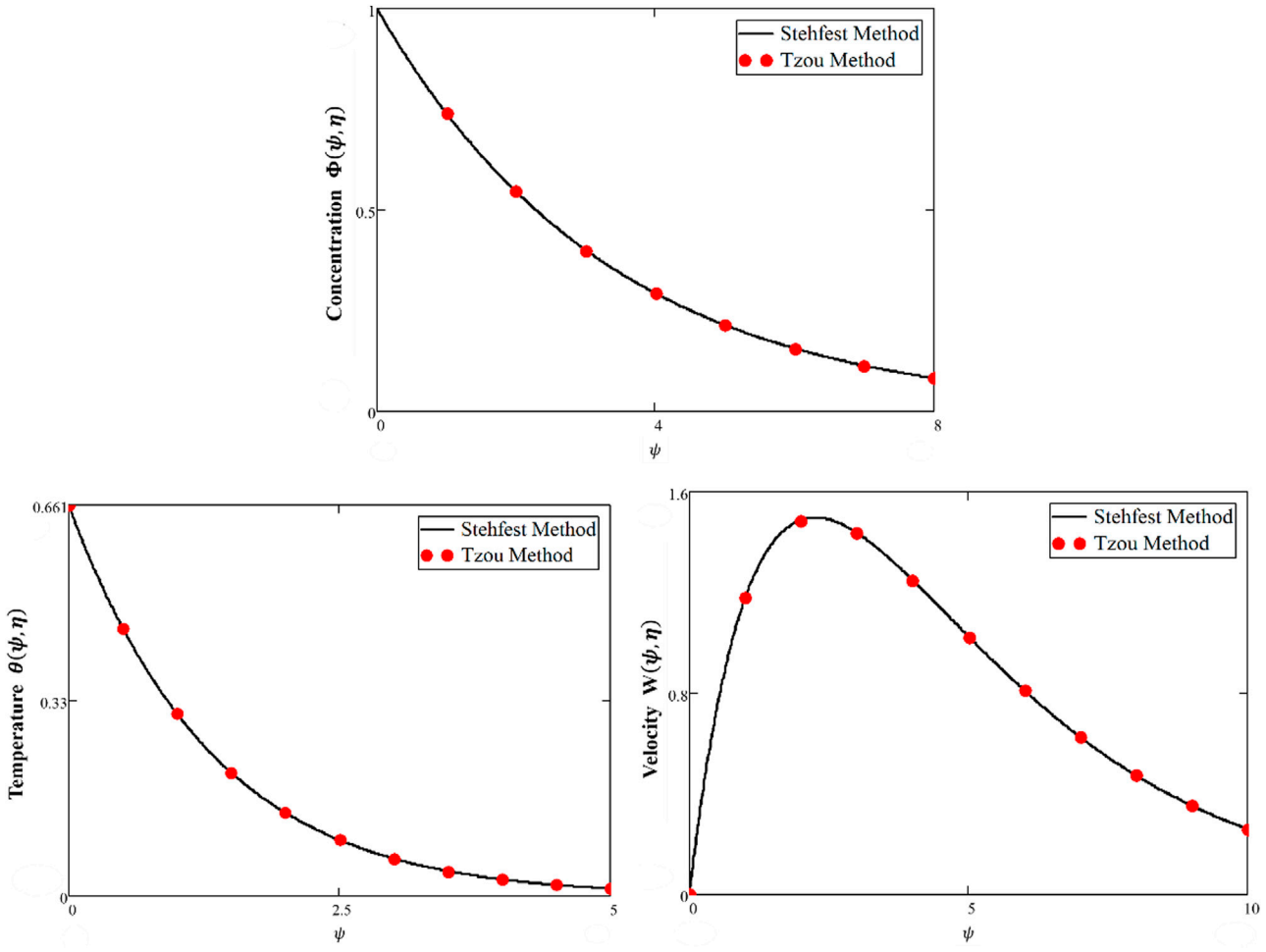

FIGURE 14
Simulation to explain the concentration, temperature, and velocity for the comparison of different inversion numerical algorithms.

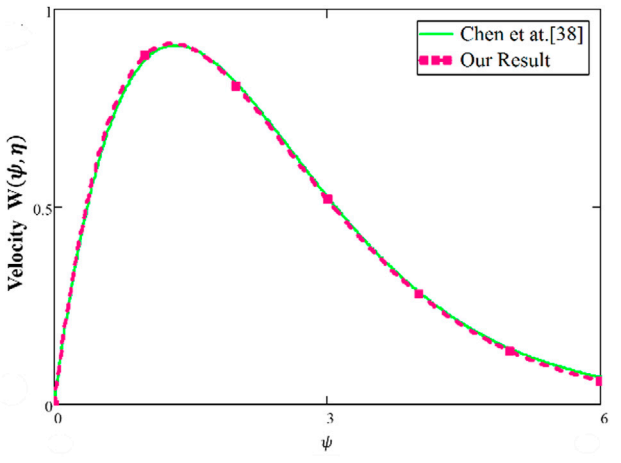

FIGURE 15
Comparison of our results with the results by Chen et al. (2022) for validation.

TABLE 3 Numerical results of the Nusselt number, Sherwood number, and skin friction.

α	t	Pr/Sc	Nu	Sh	C_f
0.3	0.5	5.0	0.3207866	0.45205	1.5162
0.4	0.5	5.0	0.3283006	0.45637	1.4984
0.5	0.5	5.0	0.3381411	0.46149	1.4724
0.5	0.3	5.0	0.214407	0.48954	1.4648
0.5	0.4	5.0	0.2783016	0.47409	1.4651
0.5	0.5	5.0	0.3381411	0.46149	1.4724
0.5	0.5	4.7	0.2101954	0.47599	1.4787
0.5	0.5	4.8	0.2116243	0.471	1.4765
0.5	0.5	4.9	0.2130279	0.46617	1.4744

and no-slip conditions. It can be seen that the slip condition shows a lesser profile for velocity than the no-slip conditions. Figure 14 shows the temperature and velocity behaviors for the comparison of

TABLE 4 Numerical results of comparisons of the velocity field.

ψ	Temperature by our result	Velocity by our result	Temperature by Chen et al. (2022)	Velocity by Chen et al. (2022)	Temperature difference (%)	Velocity difference (%)
0.1	0.2156	0.1693	0.2111	0.1648	2.1317	2.7306
0.6	0.1523	0.7126	0.1475	0.6964	3.2542	2.3262
1.1	0.1069	0.9015	0.1031	0.8917	3.6857	1.099
1.6	0.0747	0.8901	0.0721	0.8913	3.6061	0.1346
2.1	0.0519	0.7805	0.0504	0.7885	2.9762	1.0146
2.6	0.0359	0.6358	0.0352	0.6449	1.9886	1.4111
3.1	0.0247	0.4915	0.0246	0.4986	0.4065	1.424
3.6	0.017	0.365	0.0172	0.3701	1.1628	1.378
4.1	0.0116	0.2624	0.012	0.267	3.3333	1.7228

diverse numerical techniques (Stehfest and Tzou's algorithm). The overlapping of profiles shows that these algorithms are strongly validated with each other. Figure 15 shows the validation of our results with Chen et al. (2022). By overlapping both curves, it is observed from these graphs that our achieved results match those developed by Chen et al. (2022). The numerical comparison of energy, concentration, and velocity profiles by different numerical methods is shown in Table 2. Table 3 shows the numerical results of the Nusselt number, Sherwood number, and skin friction. The comparison of the momentum profile with the work of Chen et al. (2022) is shown in Table 4.

5 Conclusion

This article examines the investigations of the unsteady, convective flow of the Oldroyd-B HNF flowing over a flat plate with wall slip conditions on temperature and constant concentration. The model is developed using the AB-fractional operator and solved with the Laplace transform method. The Laplace inversion is computed with the well-known Stehfest and Tzou numerical schemes. Finally, the effect of diverse flow parameters is planned to estimate the physical clarification of the achieved results of governed equations. The main results from the previous section are summarized in the following:

- ❖ For a short time, the temperature and momentum profile decayed for a larger value of α, and this effect for both profiles is reversed for a longer time.
- ❖ By increasing Pr, the temperature and velocity show a decreasing behavior.
- ❖ By increasing Gm and Gr, the velocity profile is improved.
- ❖ The velocity decreases with increasing ϕ_1 and ϕ_2.
- ❖ The energy and velocity profiles are larger for a water-based HNF than those of the sodium alginate-based HNF.
- ❖ The graphs of Maxwell nanofluids for both classical and fractional models have more advanced curves than Oldroyd-B and viscous nanofluids.
- ❖ The slip condition shows a lower profile for velocity than the no-slip condition.
- ❖ The comparison of diverse numerical algorithms (Stehfest and Tzou) strongly validated our study's solutions.
- ❖ Chen et al. (2022), the overlapping of both curves validate the achieved results of our study.

6 Future recommendation

For extension of this fractional problem examined in this article, we idolized the following proposal based on investigation, approaches, extensions, and geometries, as demarcated in the following:

- The same problem can also be considered over a horizontal plate by using Prabhakar's time-fractional approach with an MHD effect in a porous medium.
- A comparative study of this study can be solved by the natural and Laplace transform methods.
- The same problem may be discussed by the Keller–box scheme.

Data availability statement

The original contributions presented in the study are included in the article/Supplementary Material; further inquiries can be directed to the corresponding author.

Author contributions

Conceptualization, SME, AR, QA, MA, and UK; methodology, SME, AR, and UK; software, MA, QA, SME, AR, and UK; validation, SME, AR, UK, SE, MA, and AhA; formal analysis, AbA, SE, AR, and AhA; investigation, UK, AbA, SE, and AhA; resources, AbA; data curation, QA; writing—original draft preparation, MA, SME, QA, UK,

AbA, SE, and AhA; writing—review and editing, AbA, QA, MA, and AhA; visualization, AR, AhA, and SE; supervision, UK; project administration, SE; funding acquisition, SE. All authors have read and agreed to the published version of the manuscript.

Funding

This work received support from Princess Nourah bint Abdulrahman University Researchers Supporting Project number (PNURSP2023R163), Princess Nourah bint Abdulrahman University, Riyadh, Saudi Arabia. In addition, this study is also funded by Prince Sattam bin Abdulaziz University project number (PSAU/2023/R/1444).

Acknowledgments

The authors are thankful for the support of Princess Nourah bint Abdulrahman University Researchers Supporting Project number (PNURSP2023R163), Princess Nourah bint Abdulrahman University, Riyadh, Saudi Arabia. Also, this work is supported *via* funding from Prince Sattam bin Abdulaziz University project number (PSAU/2023/R/1444).

Conflict of interest

The authors declare that the research was conducted in the absence of any commercial or financial relationships that could be construed as a potential conflict of interest.

Publisher's note

All claims expressed in this article are solely those of the authors and do not necessarily represent those of their affiliated organizations, or those of the publisher, the editors, and the reviewers. Any product that may be evaluated in this article, or claim that may be made by its manufacturer, is not guaranteed or endorsed by the publisher.

References

Ahmed, Awais, Alhowaity, Sawsan, and Mohamed, E. (2022). Ghoneim, fehmi gamaoun, elsayed tag-eldin, mansour F. Yassen, and mahnoor sarfraz. "Material and wave relaxation phenomena effects on the rheology of Maxwell nanofluids. *Front. Phys.* 10, 886.

Ali, Qasim, Al-Khaled, Kamel, Ijaz Khan, M., Khan, Sami Ullah, Ali, Raza, Oreijah, Mowffaq, et al. (2022). Diffusion phenomenon for natural convection flow of classical hartmann problem due to a cylindrical tube by generalized fourier's theories: A fractional analysis. *Int. J. Mod. Phys. B* 13, 2350104. doi:10.1142/s0217979223501047

Ali, Qasim, Al-Khaled, Kamel, Omar, Jiyan, Ali, Raza, Khan, Sami Ullah, Ijaz Khan, M., et al. (2022). Analysis for advection–diffusion problem subject to memory effects and local and nonlocal kernels: A fractional operators approach. *Int. J. Mod. Phys. B* 15, 2350099. doi:10.1142/s0217979223500996

Ali, Qasim, Riaz, Samia, Aziz Ullah, Awan, and Ali Abro, Kashif (2021). A mathematical model for thermography on viscous fluid based on damped thermal flux. *Z. für Naturforsch. A* 76 (3), 285–294. doi:10.1515/zna-2020-0322

Asogwa, Kanayo K., Bilal, Sardar M., Animasaun, Isaac L., and Mebarek-Oudina, Fateh M. (2021). Insight into the significance of ramped wall temperature and ramped surface concentration: The case of Casson fluid flow on an inclined Riga plate with heat absorption and chemical reaction. *Nonlinear Eng.* 10 (1), 213–230. doi:10.1515/nleng-2021-0016

Asogwa, Kanayo Kenneth, Goud, B. Shankar, Shah, Nehad Ali, and -Jin Yook, Se (2022). Rheology of electromagnetohydrodynamic tangent hyperbolic nanofluid over a stretching riga surface featuring dufour effect and activation energy. *Sci. Rep.* 12 (1), 14602. doi:10.1038/s41598-022-18998-9

Asogwa, Kanayo Kenneth, Goud, B. Shankar, Yanala Dharmendar Reddyand Ibe, Amarachukwu A. (2022). Suction effect on the dynamics of EMHD casson nanofluid over an induced stagnation point flow of stretchable electromagnetic plate with radiation and chemical reaction. *Results Eng.* 15 (2022), 100518. doi:10.1016/j.rineng.2022.100518

Asogwa, Kanayo Kenneth, Prasad, K. C. Rajendra, Kumar, Raman, Murtugudde, Gururaj, and Punith Gowda, R. J. (2022). Transient electromagnetohydrodynamic Nanofluid flow traveling through a moving Riga plate subject to radiation and heat absorption. *Int. J. Mod. Phys. B* 09, 2350168. doi:10.1142/s0217979223501680

Asogwa, Kanayo K., Mebarek-Oudina, F., and Animasaun, I. L. (2022). Comparative investigation of water-based Al2O3 nanoparticles through water-based CuO nanoparticles over an exponentially accelerated radiative Riga plate surface via heat transport. *Arabian J. Sci. Eng.* 47 (7), 8721–8738. doi:10.1007/s13369-021-06355-3

Atangana, Abdon, and Dumitru, Baleanu (2016). New fractional derivatives with nonlocal and non-singular kernel: Theory and application to heat transfer model. *arXiv Prepr. arXiv:1602.03408* 21.

Awan, Aziz Ullah, Shah, Nehad Ali, Ahmed, Najma, Ali, Qasim, and Riaz, Samia (2019). Analysis of free convection flow of viscous fluid with damped thermal and mass fluxes. *Chin. J. Phys.* 60, 98–106. doi:10.1016/j.cjph.2019.05.006

Batool, Saima, Rasool, Ghulam, Alshammari, Nawa, Khan, Ilyas, Kaneez, Hajra, and Hamadneh, Nawaf (2022). Numerical analysis of heat and mass transfer in micropolar nanofluids flow through lid driven cavity: Finite volume approach. *Case Stud. Therm. Eng.* 37 (2022), 102233. doi:10.1016/j.csite.2022.102233

Chen, C., Rehman, A. U., Riaz, M. B., Jarad, F., and Sun, X.-E. (2022). Impact of Newtonian heating via fourier and Fick's laws on thermal transport of Oldroyd-B fluid by using generalized mittag-leffler kernel. *Symmetry* 14 (4), 766. doi:10.3390/sym14040766

Farooq, U., Afridi, M. I., Qasim, M., and Lu, D. C. (2018). Transpiration and viscous dissipation effects on entropy generation in hybrid nanofluid flow over a nonlinear radially stretching disk. *Entropy* 20 (9), 668. doi:10.3390/e20090668

Goud, B. Shankar, Reddy, Y. Dharmendar, and Kenneth Asogwa, Kanayo (2022). Inspection of chemical reaction and viscous dissipation on MHD convection flow over an infinite vertical plate entrenched in porous medium with Soret effect. *Biomass Convers. Biorefinery* 29, 1–12. doi:10.1007/s13399-022-02886-3

Hassan, Ali, Hussain, Azad, Arshad, Mubashar, Gouadria, Soumaya, Jan, Awrejcewicz, Galal, Ahmed M., et al. (2022). Insight into the significance of viscous dissipation and heat generation/absorption in magneto-hydrodynamic radiative casson fluid flow with first-order chemical reaction. *Front. Phys.* 10, 605. doi:10.3389/fphy.2022.920372

Khan, Dolat, Kenneth Asogwa, Kanayo, Akkurt, Nevzat, Kumam, Poom, Watthayu, Wiboonsak, and Sitthithakerngkiet, Kanokwan (2022). Development of generalized fourier and Fick's law of electro-osmotic MHD flow of sodium alginate based casson nanofluid through inclined microchannel: Exact solution and entropy generation. *Sci. Rep.* 12 (1), 18646. doi:10.1038/s41598-022-21854-5

Khan, Muhammad Naveed, Ahammad, N. Ameer, Ahmad, Shafiq, and Mohamed Abdelghany, Elkotb (2022). Elsayed Tag-eldin, Kamel Guedri, Khaled A. Gepreel, and Mansour F. Yassen. "Thermophysical features of Ellis hybrid nanofluid flow with surface-catalyzed reaction and irreversibility analysis subjected to porous cylindrical surface. *Front. Phys.* 10, 795.

Khan, M. N., Alhowaity, S., Wang, Z., Alqahtani, A. M., Tag-eldin, E., and Yassen, M. F. (2022). Alqahtani, Elsayed Tag-eldin, and Mansour F. Yassen. "Significance of multiple solutions on the dynamics of ethylene glycol conveying gold and copper nanoparticles on a shrinking surface. *Front. Phys.* 10, 928.

Khan, Umar, Ahmed, Naveed, and Khan, Ilyas (2022). Heat transfer evaluation in MgZn6Zr/C8H18 [(Magnesium-Zinc-Zirconium)/Engine oil] with non-linear solar thermal radiations and modified slip boundaries over 3-dimensional convectively heated surface. *Front. Energy Res.* 12, 351.

Lee, S., Choi, S. U.-S, Li, S., and Eastman, J. A (1999). Measuring thermal conductivity of fluids containing oxide nanoparticles 2, 280–289.

Mahian, Omid, Kolsi, Lioua, Amani, Mohammad, Estellé, Patrice, Ahmadi, Goodarz, Kleinstreuer, Clement., et al. (2019). Recent advances in modeling and simulation of nanofluid flows-Part I: Fundamentals and theory. *Phys. Rep.* 790, 1–48. doi:10.1016/j.physrep.2018.11.004

Martyushev, Semen G., and Sheremet, Mikhail A. (2012). Characteristics of Rosseland and P-1 approximations in modeling nonstationary conditions of convection-radiation heat transfer in an enclosure with a local energy source. *J. Eng. Thermophys.* 21 (2), 111–118. doi:10.1134/s1810232812020026

Mohebbi, Rasul, Mehryan, S. A. M., Izadi, Mohsen, and Mahian, Omid (2019). Natural convection of hybrid nanofluids inside a partitioned porous cavity for application in solar power plants. *J. Therm. Analysis Calorim.* 137, 1719–1733. doi:10.1007/s10973-019-08019-9

Rashad, A. M., Chamkha, Ali J., Ismael, Muneer A., and Taha, Salah. (2018). Magnetohydrodynamics natural convection in a triangular cavity filled with a Cu-Al2O3/water hybrid nanofluid with localized heating from below and internal heat generation. *J. Heat Transf.* 140, 7. doi:10.1115/1.4039213, no.

Rasool, Ghulam, Ahammad, N. Ameer, Ali, Mohamed R., Shah, Nehad Ali, Wang, Xinhua, Shafiq, Anum, et al. (2023). Hydrothermal and mass aspects of MHD non-Darcian convective flows of radiating thixotropic nanofluids nearby a horizontal stretchable surface: Passive control strategy. *Case Stud. Therm. Eng.* 42 (2023), 102654. doi:10.1016/j.csite.2022.102654

Rasool, Ghulam, Shafiq, Anum, Hussain, Sajjad, Zaydan, Mostafa, Wakif, Abderrahim, Ali, J., et al. (2022). Significance of rosseland's radiative process on reactive Maxwell nanofluid flows over an isothermally heated stretching sheet in the presence of Darcy–forchheimer and Lorentz forces: Towards a new perspective on buongiorno's model. *Micromachines* 133, 368. doi:10.3390/mi13030368, no.

Rasool, G., Ali Shah, N., El-Zahar, E. R., and Wakif, A. (2022). Numerical investigation of EMHD nanofluid flows over a convectively heated riga pattern positioned horizontally in a Darcy-Forchheimer porous medium: Application of passive control strategy and generalized transfer laws. *Waves Random Complex Media* 17, 1–20.

Raza, A., Almusawa, M. Y., Ali, Q., Haq, A. U., Al-Khaled, K., and Sarris, I. E. (2022). Solution of water and sodium alginate-based casson type hybrid nanofluid with slip and sinusoidal heat conditions: A prabhakar fractional derivative approach. *Symmetry* 1412, 2658. doi:10.3390/sym14122658, no.

Reddy, S. C., Asogwa, K. K., Yassen, M. F., AdnanIqbal, Z., M-Eldin, S., et al. (2022). Dynamics of MHD second-grade nanofluid flow with activation energy across a curved stretching surface. *Front. ENERGY Res.* 10. doi:10.3389/fenrg.2022.1007159

Shahsavar, Amin, Moradi, Mehdi, and Bahiraei, Mehdi (2018). Heat transfer and entropy generation optimization for flow of a non-Newtonian hybrid nanofluid containing coated CNT/Fe3O4 nanoparticles in a concentric annulus. *J. Taiwan Inst. Chem. Eng.* 84, 28–40. doi:10.1016/j.jtice.2017.12.029

Shankar Goud, B., Dharmendar Reddy, Y., and Kenneth Asogwa, Kanayo (2022). Chemical reaction, Soret and Dufour impacts on magnetohydrodynamic heat transfer Casson fluid over an exponentially permeable stretching surface with slip effects. *Int. J. Mod. Phys. B*, 2350124. doi:10.1142/s0217979223501242

Stehfest, Harald. (1970). Algorithm 368: Numerical inversion of Laplace transforms [D5]. *Commun. ACM* 13 (1), 47–49. doi:10.1145/361953.361969

Tzou, Da Yu (2014). *Macro-to microscale heat transfer: The lagging behavior*.Hoboken, NJ, USA John Wiley & Sons.

Usman, M., Hamid, M., Zubair, T., Ul Haq, Rizwan, and Wang, Wei. (2018). Cu-AlO/Water hybrid nanofluid through a permeable surface in the presence of nonlinear radiation and variable thermal conductivity via LSM. *Int. J. Heat Mass Transf.* 126, 1347–1356. doi:10.1016/j.ijheatmasstransfer.2018.06.005

Vallejo, Javier P., Zyla, G., Fernandez-Seara, J., and Lugo, L. (2019). Influence of six carbon-based nanomaterials on the rheological properties of nanofluids. *Nanomaterials* 9 (2), 146. doi:10.3390/nano9020146

Vallejo, J. P., Álvarez-Regueiro, E., Cabaleiro, D., Fernández-Seara, J., Fernández, J., and Lugo, L. (2019). Functionalized graphene nanoplatelet nanofluids based on a commercial industrial antifreeze for the thermal performance enhancement of wind turbines. *Appl. Therm. Eng.* 152, 113–125. doi:10.1016/j.applthermaleng.2019.02.046

Waini, Iskandar, Ishak, Anuar, and Pop, Ioan (2019). Unsteady flow and heat transfer past a stretching/shrinking sheet in a hybrid nanofluid. *Int. J. heat mass Transf.* 136, 288–297. doi:10.1016/j.ijheatmasstransfer.2019.02.101

Wong, Kaufui V., and Omar De, Leon (2010). Applications of nanofluids: Current and future. *Adv. Mech. Eng.* 2, 519659. doi:10.1155/2010/519659

Zhang, Juan, Ali, Raza, Khan, Umair, Ali, Qasim, Zaib, Aurang, Weera, Wajaree, et al. (2022). Thermophysical study of Oldroyd-B hybrid nanofluid with sinusoidal conditions and permeability: A prabhakar fractional approach. *Fractal Fract.* 67, 357. doi:10.3390/fractalfract6070357, no.

frontiers | Frontiers in Materials

TYPE Original Research
PUBLISHED 28 February 2023
DOI 10.3389/fmats.2023.1132468

OPEN ACCESS

EDITED BY
Hammad Khalil,
University of Education Lahore, Pakistan

REVIEWED BY
Ali Zabihi,
Rowan University, United States
Aurang Zaib,
Federal Urdu University of Arts, Sciences and Technology Islamabad, Pakistan
Mustafa Turkyilmazoglu,
Hacettepe University, Türkiye
A. M. Rashad,
Aswan University, Egypt

*CORRESPONDENCE
Sayed M. Eldin,
sayed.eldin22@fue.edu.eg
Anwar Saeed,
anwarsaeed769@gmail.com

SPECIALTY SECTION
This article was submitted to Colloidal Materials and Interfaces, a section of the journal Frontiers in Materials

RECEIVED 27 December 2022
ACCEPTED 06 February 2023
PUBLISHED 28 February 2023

CITATION
Algehyne EA, Lone SA, Raizah Z, Eldin SM, Saeed A and Galal AM (2023), Chemically reactive hybrid nanofluid flow past a Riga plate with nonlinear thermal radiation and a variable heat source/sink.
Front. Mater. 10:1132468.
doi: 10.3389/fmats.2023.1132468

Chemically reactive hybrid nanofluid flow past a Riga plate with nonlinear thermal radiation and a variable heat source/sink

Ebrahem A. Algehyne[1,2], Showkat Ahmad Lone[3], Zehba Raizah[4], Sayed M. Eldin[5]*, Anwar Saeed[6]* and Ahmed M. Galal[7,8]

[1]Department of Mathematics, Faculty of Science, University of Tabuk, Tabuk, Saudi Arabia, [2]Nanotechnology Research Unit (NRU), University of Tabuk, Tabuk, Saudi Arabia, [3]Department of Basic Sciences, College of Science and Theoretical Studies, Saudi Electronic University, (Jeddah-M), Riyadh, Saudi Arabia, [4]Department of Mathematics, College of Science, King Khalid University, Abha, Saudi Arabia, [5]Center of Research, Faculty of Engineering, Future University in Egypt, New Cairo, Egypt, [6]Center of Excellence in Theoretical and Computational Science (TaCS-CoE), Science Laboratory Building, Faculty of Science, King Mongkut's University of Technology Thonburi (KMUTT), Bangkok, Thailand, [7]Department of Mechanical Engineering, College of Engineering in Wadi Alddawasir, Prince Sattam bin Abdulaziz University, Saudi Arabia, [8]Production Engineering and Mechanical Design Department, Faculty of Engineering, Mansoura University, Mansoura, Egypt

The suspension of nanoparticles in base liquids has found extensive applications in various industrial processes like nanomedicines, microsystem cooling, and energy conversion. Owing to its important applications, this article investigates the hybrid nanofluid flow over a three-dimensional stretching surface. The fluid is influenced by thermal radiation, chemical reaction, and a variable thermal source/sink. The set of equations that administer the fluid behavior has been transformed to dimensionless form by a suitable set of similarity transformations that are further solved by the homotopy analysis method. It was found that as the ratio parameter increased, the velocity of hybrid nanofluid velocity decreased along the primary direction and increased along the secondary direction. The temperature characteristic was augmented with greater values of nonlinear thermal radiation and source/sink factors. Growth in the chemically reactive factor and Schmidt number has an adverse effect on the concentration profile of the hybrid nanofluid flow. A comparative analysis of the current results and those established in the literature was conducted. A close agreement with those published results was found. It was noted that temperature and concentration increase more quickly for the $MoS_2 + MgO/H_2O$ hybrid nanofluid than the $MoS_2/H_2O, MgO/H_2O$ nanofluids.

KEYWORDS

nanofluid, hybrid nanofluid, Riga plate, thermal radiation, chemical reaction, variable heat source

1 Introduction

The heating and cooling of fluids is quite useful in industrial applications like power manufacturing and power transportation processes. Typical fluids have lower thermal conductivities because of their lower thermal flow characteristics. In contrast, the thermal conductivity of metals is higher. So, to create fluids with a desired level of thermal conductivity, solid nanoparticles are mixed with conventional fluids, as proposed by Choi (Choi and Eastman, 1995). Shah et al. (2020) mixed gold nanoparticles in blood, discussed the behavior of that fluid,

and concluded that the thermal characteristics were enhanced with improvements in the radiation factor and number of solid nanoparticles. Bhatti et al. (2022) studied the swimming behavior of microorganisms in a Williamson MHD nanofluid flow over rotating plates embedded in a permeable region and concluded that an increase in magnetic factor and nanoparticle volume fraction increased the temperature characteristics and decreased fluid velocity. Acharya et al. (2022) inspected the variations in hydrothermal nanofluid flow influenced by the diameters of nanoparticles and a nanolayer and showed that the nanolayer enhanced the thermal flow by 84.61%. Shahid et al. (2022) presented a numerical examination of nanofluid flow over a permeable surface using the influences of activation energy and bioconvection.

Mixing two different types of nanoparticles in a base fluid will enhance its thermal conductivities. This is called a hybrid nanofluid. Manzoor et al. (2021) studied the improvement of thermal transmission of a magnetized hybrid nanofluid flow over a stretching sheet and concluded that the temperature distributions were augmented with enhancements in volume fractions and magnetic factors. Khan et al. (2022a) examined the flow of a hybrid nanoliquid on a moving heated needle placed horizontally in the fluid and found that the thermal transmission was enlarged with an increase in Brownian motion, Eckert number, and volume fractions of nanoparticles. Waseem et al. (2021) examined the couple stress hybrid nanofluid flow over a vertically placed heated plate using heterogeneous and homogeneous reactions. They concluded that the skin friction increased with the increase in buoyance forces. Eid and Nafe (2022) examined the thermal conductivity and heat generation influences on MHD hybrid nanoliquid flow over a stretching surface with slip conditions. Zhang et al. (2022) analyzed the flow of hybrid nanoliquid past a stretching surface and concluded that the fluid moved faster with higher values of the Darcy number, while the motion of fluid was retarded with an increase in the magnetic factor. Ojjela (2022) investigated the thermal transportation of hybrid nanofluid using alumina and silica nanoparticles and compared the results with established studies. The related analyses can be seen in Zabihi et al. (2020a), Zabihi et al. (2020b), Wahid et al. (2020), Alhowaity et al. (2022), Khan et al. (2022b), and Zabihi et al. (2022).

Fluids that conduct electrically, like liquid metals, plasmas, and electrolytes, can be organized using magnetic fields. These flows have many applications in earthquakes, astrophysics, geophysics, and sensors. In such phenomena, magnetic and electric fields are used to control and direct the flow of fluids; these are called EMHD flow. Fluids flowing in electrically weak conducted fluids can be organized and controlled by applying an external electric field using a Riga plate, which is an electromagnetic surface with alternatively assembled electrodes. Such an arrangement produces hydrodynamic and electromagnetic behavior within the fluid flow on a surface. Lielausis (1961) constructed a Riga plate to control the fluid flow by producing a Lorentz effect along a wall. Shafiq et al. (2021) studied double stratification at the stagnant point in a Walters-B nanofluid past a radiative Riga plate. They observed that intensive retardation in thermal flow and concentration was found for double stratification, while stronger radiation values corresponded to a significant rise in temperature. Asogwa et al. (2022) compared two different nanofluid characteristics regarding the thermal, skin friction, and concentration past an exponentially accelerated Riga plate. They found that in the case of increased radiation, a CuO-based nanofluid behaved much better than a Al_2O_3-based nanofluid. Gangadhar et al. (2021) investigated the flow of a radiative EMHD fluid on a Riga plate due to heat convection using the modified Buongiorno model. Rahman et al. (2022) examined the effects of suction and magnetic factors on a nanofluid flow containing copper oxide, metal, alumina, and titanium dioxide nanoparticles over a spinning disc. Anuar et al. (2020) analyzed the magnetohydrodynamic effect on a nanofluid flow over a nonlinear extending surface. Kumar et al. (2017) investigated the influence of chemical reactions on the MHD three-dimensional nanofluid flow over a Riga plate.

Thermal radiation plays a fundamental role in the heat transport phenomenon. Many investigations have been made on the nanofluid flow with thermal radiation effects. Hayat et al. (2013) investigated the Jeffery liquid flow past a stretching sheet with the impact of thermal radiation and found that the skin friction and Sherwood number were amplified due to the higher radiation factor. Sabir et al. (2021) examined the Sutterby fluid flow with the influence of thermal radiation and concluded that higher strength of magnetic and radiation factors augmented the thermal characteristic and skin friction. Ijaz et al. (2021) simulated the effects of a thermal radiation magnetic field on a nanofluid flow containing gyrotactic microorganisms and concluded that the temperature- and space-based heat absorptions were more appropriate for cooling. Ali et al. (2021) inspected the influences of thermal radiation and magnetic field effects on the Darcy flow and observed that with an increase in the diameter of copper nanoparticles, the temperature distribution was increased. Saeed et al. (2021) investigated the Darcy–Forchheimer nanoliquid flow with thermal radiation and determined that the velocity profile reduced with the higher Darcy number, and temperature was increased with growth in the radiation factor. The impacts of thermal radiation, chemical reaction, and heat absorption/generation on MHD Maxwell nanofluid flow were examined by Tlili et al. (2020).

In many investigations, there may be reasonable thermal differences between the ambient fluid and the surface on which the fluid flows. This idea necessitates deliberation in the presence of thermal heat or a thermal sink that strongly affects the thermal flow rate of a fluid flow system. This idea is gaining more attention because of its expanding uses in production engineering problems where the heat transportation is substantial to enhance the quality of the final product. Khader and Sharma (2021) evaluated the time-based MHD liquid flow over a shrinking/stretching sheet using thermal radiation and a heat source and found that temperature declined with an expansion in the steadiness factor and the thermal buoyancy parameter, whereas it increased with higher values of the heat source. Tarakaramu et al. (2022) discussed the three-dimensional couple stress fluid flow past a stretching surface with nonlinear thermal radiation and heat source impacts. Ram et al. (2022) examined the mixed convection thermal and mass transportations in a magnetized fluid flow at a stagnant point of a stretching surface with a heat source. Haq et al. (2022) examined the mixed convective nanofluid flow past an irregular inclined sheet with a chemical reaction and heat source impact and found that velocity rises with the increases in the angle of inclination. Sharma et al. (2022) explored the effect of a thermal source on EMHD nanofluid flow over an extending surface. Saleh et al. (2022) analyzed the influence of the heat source on nanoliquid flow past a stretching surface and found that thermal distribution increased as the temperature-based heat source and space factors increased. Li et al. (2022) discussed the double

diffusion nanofluid flow with the influence of activation energy, a nonlinear heat source/sink, and convective conditions. Many similar studies can be seen in Alharbi et al. (2018), Alwawi et al. (2020), Hamarsheh et al. (2020), Sravanthi (2020), El-Zahar et al. (2021), Khan et al. (2021), Shamshuddin et al. (2021), El-Zahar et al. (2022), Thumma et al. (2022), Ullah et al. (2022), and Waini et al. (2022).

Apart from the aforementioned analyses, there is less work on the hybrid nanoliquid flow over a stretching surface. The surface of the plate is kept at a constant temperature and concentration. The nonlinear thermal radiation, variable heat source/sink, thermophoresis, Brownian motion, and chemical reaction impacts are considered to make this model novel. The mathematical formulation of the flow is presented in Section 2. Section 3 provides a semi-analytical solution to the flow problem. The validation of current results with published results is presented in Section 4. The discussion of the present results is presented in Section 5. Concluding remarks are presented in Section 6.

2 Problem formulation

Consider the flow of a hybrid nanofluid on a three-dimensional extending surface. The surface stretches along the x axis with a velocity $u_w(x) = a\,x$ and along the y axis with velocity $v_w(y) = by$, where a and b are positive fixed values. The flow in the system is induced by a Riga plate with $M = M_0(x)$ along the z direction. At the surface of the Riga plate, T_w is temperature and C_w is concentration, whereas, at the free surface, these quantities are given as T_∞ and C_∞. Nonlinear thermal radiation, the variable heat source/sink, thermophoresis, and chemical reaction effects are also considered. Using these assumptions, the leading equations can be written as follows (Ahmad et al., 2016; Muhammad et al., 2021; Alqarni, 2022; Shah et al., 2022):

$$\frac{\partial u}{\partial x}+\frac{\partial v}{\partial y}+\frac{\partial w}{\partial z}=0, \tag{1}$$

$$u\,\frac{\partial u}{\partial x}+v\,\frac{\partial u}{\partial y}+w\,\frac{\partial u}{\partial z}=\frac{\mu_{hnf}}{\rho_{hnf}}\frac{\partial^2 u}{\partial z^2}+\frac{1}{\rho_{hnf}}\frac{\pi j_0 M}{8}\exp\left(-\frac{\pi}{\alpha_0 z}\right), \tag{2}$$

$$u\frac{\partial v}{\partial x}+v\,\frac{\partial v}{\partial y}+w\,\frac{\partial v}{\partial z}=\frac{\mu_{hnf}}{\rho_{hnf}}\frac{\partial^2 v}{\partial z^2}, \tag{3}$$

$$u\frac{\partial T}{\partial x}+v\frac{\partial T}{\partial y}+w\frac{\partial T}{\partial z}=\frac{k_{hnf}}{\left(\rho C_p\right)_{hnf}}\frac{\partial^2 T}{\partial z^2}-\frac{1}{\left(\rho C_p\right)_{hnf}}\frac{\partial q_r}{\partial z}+\frac{1}{\left(\rho C_p\right)_{hnf}}q, \tag{4}$$

$$u\frac{\partial C}{\partial x}+v\frac{\partial C}{\partial y}+w\frac{\partial C}{\partial z}=D_B\frac{\partial^2 C}{\partial z^2}-K^*(C-C_\infty), \tag{5}$$

with boundary conditions:

$$\left\{\begin{array}{l} u=u_w(x)=ax,\quad v=v_w(y)=by,\quad T=T_w,\quad C=C_w\quad at\quad z=0 \\ u\to 0,\quad v\to 0,\quad T\to T_\infty\quad ,C\to C_\infty\quad as\quad z\to\infty \end{array}\right\} \tag{6}$$

As mentioned previously, $u, v,$ and w are the velocity components along the coordinate axes, M is the magnetic property of the plate surface due to the permanent magnet, and j_0 is the electrode current density.

The q_r (radiative heat flux) is defined as follows (Alqarni, 2022):

TABLE 1 Thermophysical characteristics of base fluid and nanoparticles (Mishra and Upreti, 2022).

Property	MgO	MoS_2	H_2O
ρ	3580	5.06×10^3	997.1
C_p	879	397.21	4179
k	30	904.4	0.613

$$q_r=-\frac{4\sigma^*}{3k^*}\frac{\partial T^4}{\partial z}=-\frac{16\sigma^*}{3k^*}\frac{\partial}{\partial z}\left(T^3\frac{\partial T}{\partial z}\right). \tag{7}$$

The variable heat source/sink term q is defined as follows (Khan et al., 2022c; Rawia et al., 2022):

$$q=\frac{u_w(x)k_{hnf}}{\nu_{hnf}x}\left(S_p(T_w-T_\infty)f'+H_s(T-T_\infty)\right). \tag{8}$$

In the aforementioned equation, S_p is the space factor and H_s is the heat sink/source factor.

Substituting Eqs 7, 8 in Eq. 4, we have

$$\begin{aligned} u\,\frac{\partial T}{\partial x}+w\,\frac{\partial T}{\partial z}+v\,\frac{\partial T}{\partial y}&=\frac{1}{\left(\rho C_p\right)_{hnf}}\left(k_{hnf}\,\frac{\partial^2 T}{\partial z^2}+\frac{16\,\sigma^*}{3\,k^*}\,\frac{\partial}{\partial z}\left(T^3\,\frac{\partial T}{\partial z}\right)\right)\\ &+\frac{1}{\left(\rho C_p\right)_{hnf}}\,\frac{u_w(x)k_{hnf}}{\nu_{hnf}x}\left(S_p(T_w-T_\infty)f'+H_s(T-T_\infty)\right). \end{aligned} \tag{9}$$

The thermophoresis models for a nanofluid and hybrid nanofluid are appended as follows (Acharya et al., 2020), while their numerical values are assumed in Table 1.

$$\left\{\begin{array}{l} \dfrac{\mu_{nf}}{\mu_f}=\dfrac{1}{(1-\phi)^{2.5}},\ \dfrac{\rho_{nf}}{\rho_f}=(1-\phi)+\phi\,\dfrac{\rho_s}{\rho_f},\ \dfrac{\left(\rho C_p\right)_{nf}}{\left(\rho C_p\right)_f}=(1-\phi)+\phi\dfrac{\left(\rho C_p\right)_s}{\left(\rho C_p\right)_f}, \\ \dfrac{k_{nf}}{k_f}=\dfrac{\left(k_s+2k_f\right)-2\phi\left(k_f-k_s\right)}{\left(k_s+2k_f\right)+\phi\left(k_f-k_s\right)},\quad \dfrac{\sigma_{nf}}{\sigma_f}=1+\dfrac{3\left(\dfrac{\sigma_s}{\sigma_f}-1\right)\phi}{\left(2+\dfrac{\sigma_s}{\sigma_f}\right)+\left(1-\dfrac{\sigma_s}{\sigma_f}\right)\phi}. \end{array}\right\} \tag{10}$$

$$\left\{\begin{array}{l} \dfrac{\sigma_{hnf}}{\sigma_f}=1+\dfrac{3\left(\dfrac{\phi_1\sigma_{s1}+\phi_2\sigma_{s2}}{\sigma_f}\right)-3\left(\phi_1+\phi_2\right)}{2+\left(\dfrac{\phi_1\sigma_{s1}+\phi_2\sigma_{s2}}{(\phi_1+\phi_2)\sigma_f}\right)-\left(\dfrac{\phi_1\sigma_{s1}+\phi_2\sigma_{s2}}{\sigma_f}-(\phi_1+\phi_2)\right)}, \\ \dfrac{\mu_{hnf}}{\mu_f}=\dfrac{1}{(1-\phi_1-\phi_2)^{2.5}},\ \dfrac{\rho_{hnf}}{\rho_f}=(1-\phi_1-\phi_2)+\phi_1\dfrac{\rho_{s1}}{\rho_f}+\phi_2\dfrac{\rho_{s2}}{\rho_f}, \\ \qquad \dfrac{\left(\rho C_p\right)_{hnf}}{\left(\rho C_p\right)_f}=(1-\phi_1-\phi_2)+\phi_1\dfrac{\left(\rho C_p\right)_{s1}}{\rho_f}+\phi_2\dfrac{\left(\rho C_p\right)_{s2}}{\rho_f}, \\ \dfrac{k_{hnf}}{k_f}=\dfrac{\dfrac{k_{s1}\phi_1+k_{s2}\phi_2}{\phi_1+\phi_2}+2k_f+2\left(k_{s1}\phi_1+k_{s2}\phi_2\right)-2\left(\phi_1+\phi_2\right)k_f}{\dfrac{k_{s1}\phi_1+k_{s2}\phi_2}{\phi_1+\phi_2}+2k_f-2\left(k_{s1}\phi_1+k_{s2}\phi_2\right)+\left(\phi_1+\phi_2\right)k_f}. \end{array}\right\} \tag{11}$$

The similarity variables are given as follows:

$$\left\{\begin{array}{l} u=a\,x\,f'(\xi), v=a\,y\,g'(\xi),\quad w=-\sqrt{av_f}\,(g(\xi)+f(\xi)), \\ \varphi(\xi)=\dfrac{C-C_\infty}{C_w-C_\infty},\quad \theta(\xi)=\dfrac{T-T_\infty}{T_w-T_\infty},\quad \xi=z\sqrt{\dfrac{a}{\nu_f}}. \end{array}\right\} \tag{12}$$

Employing Eq. 12, the governing equations are reduced as follows:

$$\frac{\mu_{hnf}/\mu_f}{\rho_{hnf}/\rho_f} f'''(\xi) + (g(\xi) + f(\xi))\, f''(\xi) - (f'(\xi))^2 + \frac{H}{\rho_{hnf}/\rho_f}\exp(-\xi\alpha) = 0, \tag{13}$$

$$\frac{\mu_{hnf}/\mu_f}{\rho_{hnf}/\rho_f} g'''(\xi) - (g'(\xi))^2 + (g(\xi) + f(\xi)) g''(\xi) = 0, \tag{14}$$

$$\left(\frac{k_{hnf}/k_f}{(\rho C_p)_{hnf}/(\rho C_p)_f} + \frac{N}{(\rho C_p)_{hnf}/(\rho C_p)_f}\{(1 + (\theta_w - 1)\theta(\xi))\theta(\xi)\}^3\right)\theta''(\xi) + \Pr(f(\xi) + g(\xi))\theta'(\xi) + \frac{(k_{hnf}/k_f)(\rho_{hnf}/\rho_f)}{\left((\rho C_p)_{hnf}/(\rho C_p)_f\right)((\mu_{hnf}/\mu_f))}\left(S_p f'(\xi) + H_s\theta(\xi)\right) = 0, \tag{15}$$

$$\frac{1}{Sc}\varphi''(\xi) + (f(\xi) + g(\xi))\varphi'(\xi) - \gamma\varphi(\xi) = 0, \tag{16}$$

with boundary conditions

$$\left\{\begin{array}{c} f(\xi = 0) = 0, \quad f'(\xi = 0) = 1, \quad f'(\xi \to \infty) = 0, \\ g(\xi = 0) = 0, \quad g'(\xi = 0) = S, \quad g'(\xi \to \infty) = 0, \\ \theta(\xi = 0) = 1, \quad \theta(\xi \to \infty) = 0, \\ \varphi(\xi = 0) = 1, \quad \varphi(\xi \to \infty) = 0. \end{array}\right\} \tag{17}$$

In the aforementioned equations, $\alpha\,(=\frac{\pi}{\alpha_0}\sqrt{\frac{\nu_f}{a}})$ is the EMHD material parameter, $H\,(=\frac{\mu j_0 M_0}{8a^2\rho_f})$ is the modified Hartmann number, $S\,(=\frac{b}{a})$ is the ratio parameter, $Sc\,(=\frac{\nu_f}{D_B})$ is the Schmidt number, $\Pr\,(=\frac{(\rho C_p)_f \nu_f}{k_f})$ is the Prandtl number, $N\,(=\frac{16\sigma^* T_\infty^3}{3k^* k_f})$ is the thermal radiation factor, $\theta_w\,(=\frac{T_w}{T_\infty})$ is the temperature ratio factor, and $\gamma\,(=\frac{K^*}{a})$ is the chemical reaction factor.

2.1 Quantities of interest

The main engineering quantities of interest, skin friction (C_{fx}; C_{fy}), Nusselt number (Nu_x), and Sherwood number (Sh_x), are specified as follows:

$$C_{fx} = \frac{\tau_{wx}}{\rho_f (u_w(x))^2}, \quad C_{fy} = \frac{\tau_{wy}}{\rho_f (v_w(y))^2}, \quad Nu_x = \frac{x q_w}{k_f (T_w - T_\infty)}, \quad Sh_x = \frac{x q_m}{D_B (C_w - C_\infty)}, \tag{18}$$

such that

$$\tau_{wx} = \mu_{hnf}\left.\frac{\partial u}{\partial z}\right|_{z=0}, \tau_{wy} = \mu_{hnf}\left.\frac{\partial v}{\partial z}\right|_{z=0}, q_w = -k_{hnf}\left.\frac{\partial T}{\partial z}\right|_{z=0} + q_r|_{z=0}, \quad q_m = -D_B\left.\frac{\partial C}{\partial z}\right|_{z=0}. \tag{19}$$

Using Eq. 12, we have

$$\left\{\begin{array}{c} \sqrt{\mathrm{Re}_x}\, C_{fx} = \frac{\mu_{hnf}}{\mu_f} f''(0), \sqrt{\mathrm{Re}_y}\, C_{fy} = \frac{\mu_{hnf}}{\mu_f} g''(0), \\ \frac{Nu_x}{\sqrt{\mathrm{Re}_x}} = -\left(\frac{k_{hnf}}{k_f} + N(1 + (\theta_w - 1)\theta(0))^3\right)\theta'(0), \frac{Sh_x}{\sqrt{\mathrm{Re}_x}} = -\varphi'(0). \end{array}\right\} \tag{20}$$

where $\mathrm{Re}_x\,(=\frac{u_w(x)x}{\nu_f})$ and $\mathrm{Re}_y\,(=\frac{v_w(y)y}{\nu_f})$ are the local Reynolds numbers.

3 Method of solution

To solve Eqs 13–16 with Eq. 17, we use the homotopy analysis approach (HAM) presented by Liao (1999) and Liao (2010). It is a semi-analytical approach used to find the solution of extremely nonlinear differential equations in the form of series solutions. It is a fast convergent approach for the solution of fluid problems. The initial guesses for this approach are given as follows:

$$f_0(\xi) = 1 - Exp[-\xi], \quad g_0(\xi) = S(1 - Exp[-\xi]), \quad \theta_0(\xi) = Exp[-\xi], \quad \varphi_0(\xi) = Exp[-\xi]. \tag{21}$$

The linear operators are specified as follows:

$$L_f(\xi) = \frac{\partial^3 f}{\partial\xi^3} - \frac{\partial f}{\partial\xi}, \quad L_g(\xi) = \frac{\partial^3 g}{\partial\xi^3} - \frac{\partial g}{\partial\xi}, \quad L_\theta(\xi) = \frac{\partial^2\theta}{\partial\xi^2} - \theta, \quad L_\varphi(\xi) = \frac{\partial^2\varphi}{\partial\xi^2} - \varphi, \tag{22}$$

with properties

$$\left\{\begin{array}{cc} L_f(\zeta_1 + \zeta_2 Exp[-\xi] + \zeta_3 Exp[\xi]) = 0, & L_g(\zeta_4 + \zeta_5 Exp[-\xi] + \zeta_6 Exp[\xi]) = 0, \\ L_\theta(\zeta_7 Exp[-\xi] + \zeta_8 Exp[\xi]) = 0, & L_\varphi(\zeta_9 Exp[-\xi] + \zeta_{10} Exp[\xi]) = 0, \end{array}\right\} \tag{23}$$

where $\zeta_1 - \zeta_{10}$ are the constants in general solution.

These are zeroth-order problems:

$$(1 - \mathrm{H})L_f(f(\xi;\mathrm{H}) - f_0(\xi)) = \mathrm{H}\hbar N_f(f(\xi;\mathrm{H}), g(\xi;\mathrm{H})), \tag{24}$$

$$(1 - \mathrm{H})L_g(g(\xi;\mathrm{H}) - g_0(\xi)) = \mathrm{H}\hbar N_g(g(\xi;\mathrm{H}), f(\xi;\mathrm{H})), \tag{25}$$

$$(1 - \mathrm{H})L_\theta(\theta(\xi;\mathrm{H}) - \theta_0(\xi)) = \mathrm{H}\hbar N_\theta(\theta(\xi;\mathrm{H}), f(\xi;\mathrm{H}), g(\xi;\mathrm{H})), \tag{26}$$

$$(1 - \mathrm{H})L_\varphi(\varphi(\xi;\mathrm{H}) - \varphi_0(\xi)) = \mathrm{H}\hbar N_\varphi(\varphi(\xi;\mathrm{H}), f(\xi;\mathrm{H}), g(\xi;\mathrm{H})), \tag{27}$$

$$\left\{\begin{array}{c} f(0;\mathrm{H}) = 0, \quad f'(0;\mathrm{H}) = 1, \quad f'(\infty;\mathrm{H}) = 0, \\ g(0;\mathrm{H}) = 0, \quad g'(0;\mathrm{H}) = S, \quad g'(\infty;\mathrm{H}) = 0, \\ \theta(0;\mathrm{H}) = 1, \quad \theta(\infty;\mathrm{H}) = 0, \\ \varphi(0;\mathrm{H}) = 1, \quad \varphi(\infty;\mathrm{H}) = 0, \end{array}\right\} \tag{28}$$

where $\mathrm{H} \in [0\ 1]$ is the embedding parameter and $\hbar$ is the non-zero auxiliary factor. The nonlinear operators can be written as follows:

$$N_f(f(\xi;\mathrm{H}), g(\xi;\mathrm{H})) = \frac{\mu_{hnf}/\mu_f}{\rho_{hnf}/\rho_f}\frac{\partial^3 f(\xi;\mathrm{H})}{\partial\xi^3} + (g(\xi;\mathrm{H}) + f(\xi;\mathrm{H}))\frac{\partial^2 f(\xi;\mathrm{H})}{\partial\xi^2} - \left(\frac{\partial f(\xi;\mathrm{H})}{\partial\xi}\right)^2 + \frac{H}{\rho_{hnf}/\rho_f}\exp(-\xi\alpha), \tag{29}$$

$$N_g(g(\xi;\mathrm{H}), f(\xi;\mathrm{H})) = \frac{\mu_{hnf}/\mu_f}{\rho_{hnf}/\rho_f}\frac{\partial^3 g(\xi;\mathrm{H})}{\partial\xi^3} - \left(\frac{\partial g(\xi;\mathrm{H})}{\partial\xi}\right)^2 + (g(\xi;\mathrm{H}) + f(\xi;\mathrm{H}))\frac{\partial^2 g(\xi;\mathrm{H})}{\partial\xi^2}, \tag{30}$$

$$N_\theta(\theta(\xi;\mathrm{H}), f(\xi;\mathrm{H}), g(\xi;\mathrm{H})) = \left(\frac{k_{hnf}/k_f}{(\rho C_p)_{hnf}/(\rho C_p)_f} + \frac{N}{(\rho C_p)_{hnf}/(\rho C_p)_f}\{(1 + (\theta_w - 1)\theta(\xi;\mathrm{H}))\theta(\xi;\mathrm{H})\}^3\right)\frac{\partial^2\theta(\xi;\mathrm{H})}{\partial\xi^2} + \Pr(f(\xi;\mathrm{H}) + g(\xi;\mathrm{H}))\frac{\partial\theta(\xi;\mathrm{H})}{\partial\xi} + \frac{(k_{hnf}/k_f)(\rho_{hnf}/\rho_f)}{\left((\rho C_p)_{hnf}/(\rho C_p)_f\right)((\mu_{hnf}/\mu_f))}\left(S_p\frac{\partial f(\xi;\mathrm{H})}{\partial\xi} + H_s\theta(\xi;\mathrm{H})\right). \tag{31}$$

$$N_{\varphi}(\varphi(\xi;\mathrm{H}), f(\xi;\mathrm{H}), g(\xi;\mathrm{H})) = \frac{1}{Sc}\frac{\partial^2\varphi(\xi;\mathrm{H})}{\partial\xi^2} + (f(\xi;\mathrm{H}) + g(\xi;\mathrm{H}))\frac{\partial\varphi(\xi;\mathrm{H})}{\partial\xi} - \gamma\varphi(\xi;\mathrm{H}). \tag{32}$$

For H = 0 and H = 1, we have

$$\left\{\begin{array}{ll} f(\xi;0) = f_0(\xi), & f(\xi;1) = f(\xi), \\ g(\xi;0) = g_0(\xi), & g(\xi;1) = g(\xi), \\ \theta(\xi;0) = \theta_0(\xi), & \theta(\xi;1) = \theta(\xi), \\ \varphi(\xi;0) = \varphi_0(\xi), & \varphi(\xi;1) = \varphi(\xi). \end{array}\right\} \tag{33}$$

Using a Taylor series expansion with respect to H, we have

$$\left\{\begin{array}{ll} f(\xi;\mathrm{H}) = f_0(\xi) + \sum_{m=1}^{\infty} f_m(\xi)\mathrm{H}^m, & f_m(\xi) = \frac{1}{m!}\frac{\partial^m f(\xi;\mathrm{H})}{\partial\xi^m} \\ g(\xi;\mathrm{H}) = g_0(\xi) + \sum_{m=1}^{\infty} g_m(\xi)\mathrm{H}^m, & g_m(\xi) = \frac{1}{m!}\frac{\partial^m g(\xi;\mathrm{H})}{\partial\xi^m} \\ \theta(\xi;\mathrm{H}) = \theta_0(\xi) + \sum_{m=1}^{\infty} \theta_m(\xi)\mathrm{H}^m, & \theta_m(\xi) = \frac{1}{m!}\frac{\partial^m \theta(\xi;\mathrm{H})}{\partial\xi^m} \\ \varphi(\xi;\mathrm{H}) = \varphi_0(\xi) + \sum_{m=1}^{\infty} \varphi_m(\xi)\mathrm{H}^m, & \varphi_m(\xi) = \frac{1}{m!}\frac{\partial^m \varphi(\xi;\mathrm{H})}{\partial\xi^m} \end{array}\right\}. \tag{34}$$

These are mth-order deformation problems:

$$L_f(f_m(\xi) - \chi_m f_{m-1}(\xi)) = \hbar R_m^f(\xi), \tag{35}$$

$$L_g(g_m(\xi) - \chi_m g_{m-1}(\xi)) = \hbar R_m^g(\xi), \tag{36}$$

$$L_\theta(\theta_m(\xi) - \chi_m \theta_{m-1}(\xi)) = \hbar R_m^\theta(\xi), \tag{37}$$

$$L_\varphi(\varphi_m(\xi) - \chi_m \varphi_{m-1}(\xi)) = \hbar R_m^\varphi(\xi), \tag{38}$$

$$\left\{\begin{array}{c} f_m(0) = f_m'(0) = f_m'(\infty) = 0 \\ g_m(0) = g_m'(0) = g_m'(\infty) = 0 \\ \theta_m(0) = \theta_m(\infty) = 0 \\ \varphi_m(0) = \varphi_m(\infty) = 0 \end{array}\right\}, \tag{39}$$

$$R_m^f(\xi) = \frac{\mu_{hnf}/\mu_f}{\rho_{hnf}/\rho_f} f_{m-1}''' + \sum_{n=0}^{m-1} g_{m-1-n} f_m'' + \sum_{n=0}^{m-1} f_{m-1-n} f_m'' - (f_{m-1}')^2 + \frac{H}{\rho_{hnf}/\rho_f}\exp(-\xi\alpha), \tag{40}$$

$$R_m^g(\xi) = \frac{\mu_{hnf}/\mu_f}{\rho_{hnf}/\rho_f} g_{m-1}''' - (g_{m-1}')^2 + \sum_{n=0}^{m-1} g_{m-1-n} g_m'' + \sum_{n=0}^{m-1} f_{m-1-n} g_m'', \tag{41}$$

$$R_m^\theta(\xi) = \left(\frac{k_{hnf}/k_f}{(\rho C_p)_{hnf}/(\rho C_p)_f} + \frac{N}{(\rho C_p)_{hnf}/(\rho C_p)_f}\{(1 + (\theta_w - 1)\theta_{m-1})\theta_{m-1}\}^3\right)\theta_{m-1}'' + \sum_{n=0}^{m-1} f_{m-1-n}\theta_m' + \sum_{n=0}^{m-1} g_{m-1-n}\theta_m' + \frac{(k_{hnf}/k_f)(\rho_{hnf}/\rho_f)}{\left((\rho C_p)_{hnf}/(\rho C_p)_f\right)\left((\mu_{hnf}/\mu_f)\right)}\left(S_p f_{m-1}'' + H_s\theta_{m-1}\right), \tag{42}$$

$$R_m^\varphi(\xi) = \frac{1}{Sc}\varphi_{m-1}'' + \sum_{n=0}^{m-1} g_{m-1-n}\varphi_m' + \sum_{n=0}^{m-1} f_{m-1-n}\varphi_m' - \gamma\varphi_{m-1}, \tag{43}$$

where

$$\chi_m = \left\{\begin{array}{ll} 0, & m \le 1 \\ 1, & m > 1 \end{array}\right. . \tag{44}$$

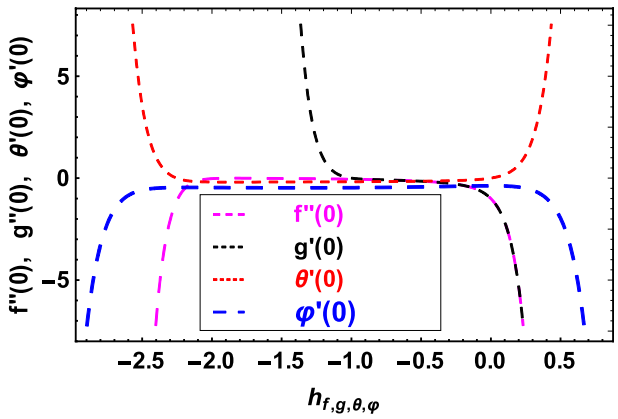

FIGURE 1
ħ– curves for $f''(0)$, $g''(0)$, $\theta'(0)$, and $\varphi'(0)$.

3.1 HAM convergence

HAM ensures the convergence of our series solution of the modeled equations. The auxiliary factor $\hbar$ plays a key role in adjusting and controlling the convergence region of the flow problem. To examine the convergence of our present model, we have plotted Figure 1. The convergence region of $f''(0)$ is $-2.0 \le \hbar_f \le 0.0$, $g''(0)$ is $-1.0 \le \hbar_g \le 0.0$, $\theta'(0)$ is $-2.3 \le \hbar_\theta \le 0.3$, and $\varphi'(0)$ is $-2.5 \le \hbar_\varphi \le 0.5$.

4 Validation

A comparative analysis was carried out, as shown in in Table 2, between the current results and the results given in Kumar et al. (2017), Anuar et al. (2020), and Shah et al. (2022). The current results have a close relationship with results previously published in the literature.

5 Results and discussion

This article investigates the EMHD flow of a hybrid nanofluid past a bi-directional extending surface. The fluid is influenced by nonlinear thermal radiation, chemical reactions, and a variable heat source. The set of equations that administered the fluid behavior has been transformed to dimensionless form by applying appropriate similarity variables. The impacts of various substantial parameters on the flow profiles are discussed in the following paragraphs.

Figure 2 depicts the influences of the Hartmann number on fluid velocity. It is observed that the higher values of H increase the velocity profile. The higher H intensity of the electric field enhances the parallel Lorentz force, and, as a result, the velocity of the hybrid nanofluid flow enhances. This shows that along the x-direction, the velocity gets support from the parallel Lorentz force. Therefore, the velocity profile of the hybrid nanofluid flow enhances with the greater H.

Figures 3, 4 show the impact of S on $f'(\xi)$ and $g'(\xi)$. It is observed that S is a retarding function of $f'(\xi)$ and an augmenting function of $g'(\xi)$. Physically, the increasing values of S support the

TABLE 2 Comparative analysis of common factors among current and previous results for $\phi_1 = \phi_2 = 0$.

S	$-f''(0)$				$-g''(0)$			
	Wang et al. (Shah et al., 2022)	Hayat et al. (Kumar et al., 2017)	Kumar et al. (Anuar et al., 2020)	Present value	Wang et al. (Shah et al., 2022)	Hayat et al. (Kumar et al., 2017)	Kumar et al. (Anuar et al., 2020)	Present value
0.0	1.0000	1.000000	1.00000	1.00000	0.0000	0.000000	0.00000	0.00000
0.25	1.0488	1.048810	1.04906	1.04881	0.1945	0.19457	0.19457	0.19457
0.5	1.0930	1.093095	1.09324	1.09309	0.4652	0.465205	0.46532	0.46520
0.75	1.1344	1.134500	1.13458	1.13450	0.7946	0.794620	0.79470	0.79462
1.0	1.1737	1.173721	1.17378	1.17372	1.1737	1.173721	1.17378	1.17372

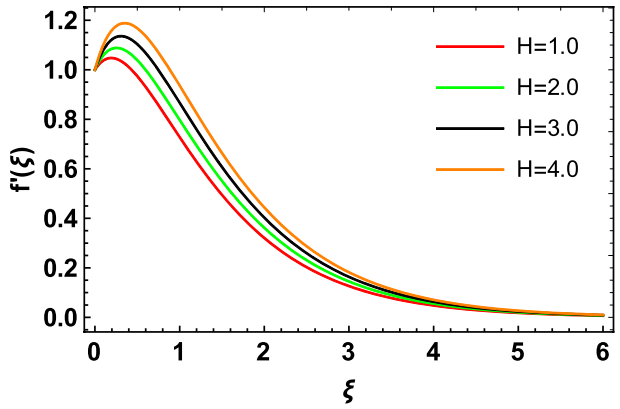

FIGURE 2
Impact of H on $f'(\xi)$.

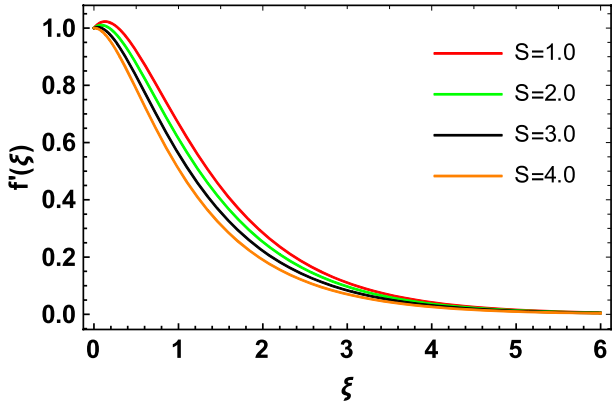

FIGURE 3
Impact of S on $f'(\xi)$.

skin friction at the surface of the Riga plate by extending more friction to the fluid motion in its opposite direction at the surface. The reason for this is that the ratio parameter S is in a direct relationship with the fluid velocity in the y-direction and in a reverse relationship in the x-direction. Hence, a retarding impact was noted in $f'(\xi)$, and an augmenting effect was observed in $g'(\xi)$.

The behavior of temperature flow due to the increase in the nonlinear thermal radiation factor N is depicted in Figure 5. We see that with the increase in N, the thermal profile increases. With growing values of N, maximum thermal diffusions occur at the surface of the Riga plate due to the electrical and magnetic characteristics at the surface. Hence, an increase in N results in an expansion in the thermal distribution, as depicted in Figure 5.

The influence of the space factor S_p and the heat source/sink factor H_S on temperature distribution is depicted in Figures 6, 7. Note that for the positive values of S_p and H_S, both behave as a heat generation source. Furthermore, the presence of a heat source factor discharges the energy to the fluid flow system. This released energy augments the temperature boundary layer, and consequently, the temperature distribution increases.

The effect of the chemical reactant factor γ on the concentration profile is shown in Figure 8. The higher chemical reaction factor reduces the concentration profile of the hybrid nanofluid flow.

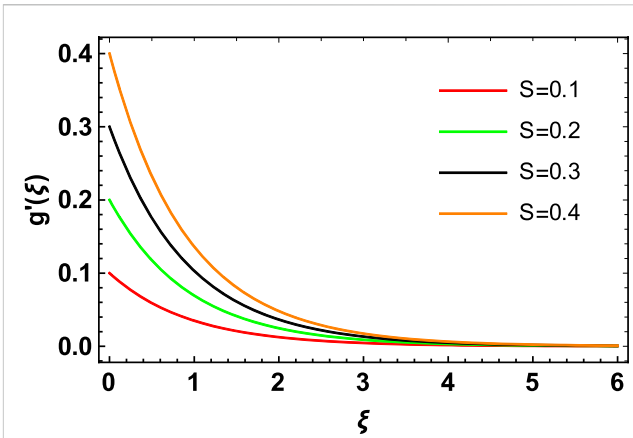

FIGURE 4
Impact of S on $g'(\xi)$.

The behavior of concentration characteristic in response to the variation in Schmidt number Sc is shown in Figure 9, which shows that the concentration profile reduces with the higher values of Sc. Note that Sc has an adverse impact upon the concentration

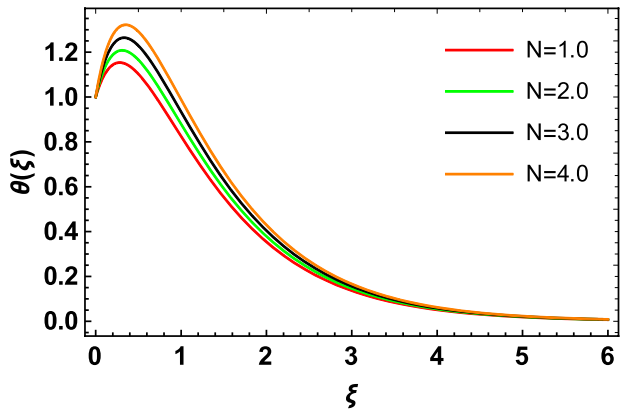

FIGURE 5
Impact of N on $\theta(\xi)$.

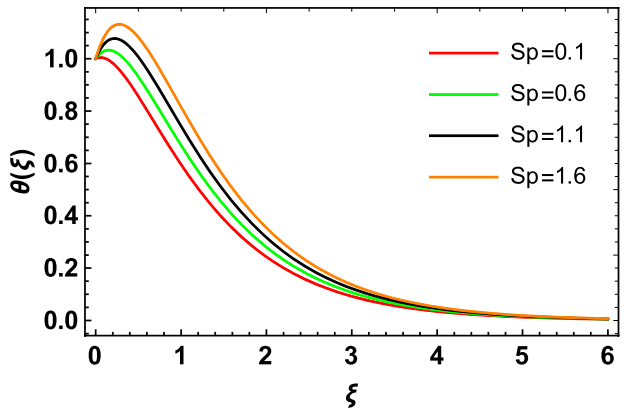

FIGURE 6
Impact of S_p on $\theta(\xi)$.

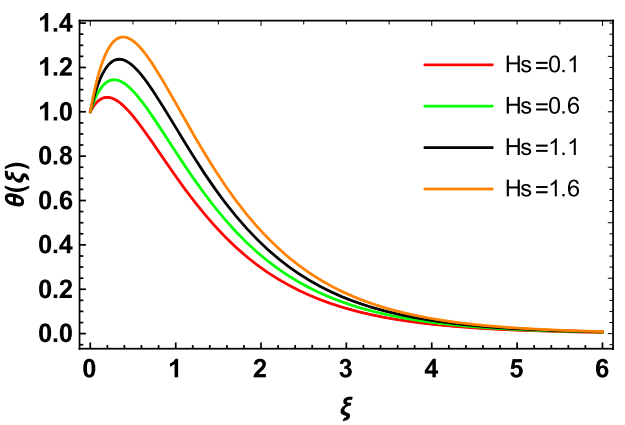

FIGURE 7
Impact of H_S on $\theta(\xi)$.

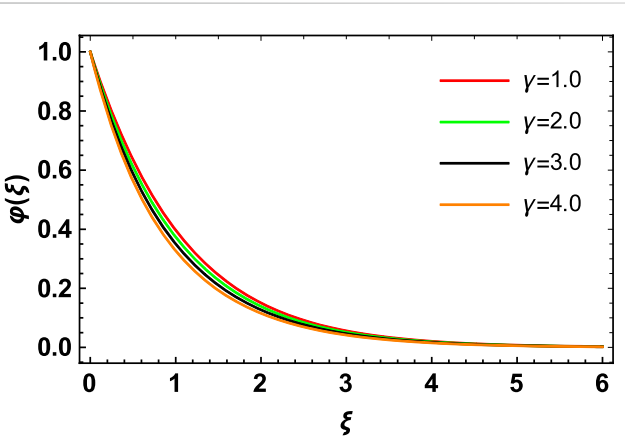

FIGURE 8
Impact of γ on $\varphi(\xi)$.

characteristics. Physically, with higher values of Sc, the mass diffusivity reduces, while the kinetic viscosity of fluid enhances, causing the declination in the mass profile. The fluid particles at the surface of the Riga plate with greater values of Sc defuse less, due to which less mass transmission occurs. As a result, the concentration characteristic diminishes gradually, as portrayed in Figure 9.

Figures 10, 11 depict the behavior of velocity profiles of the $MgO - H_2O$ nanofluid, the $MoS_2 - H_2O$ nanofluid, and the $MoS_2 - MgO/H_2O$ hybrid nanofluid. In the case of the $MgO - H_2O$ and $MoS_2 - H_2O$ nanofluids, there are the same variations in velocity characteristics at the surface of the Riga plate. However, in the case of the $MoS_2 - MgO/H_2O$ hybrid nanofluid, the behavior is different. Fluid motion is higher for the $MoS_2 - MgO/H_2O$ hybrid nanofluid flow than the $MoS_2 - H_2O$ and $MgO - H_2O$ nanofluid flows, as depicted in Figures 10, 11.

Similarly, from Figures 12, 13, we see that the behavior of temperature and concentration profiles for the $MgO - H_2O$, $MoS_2 - H_2O$,and $MoS_2 - MgO/H_2O$ hybrid nanofluids are quite

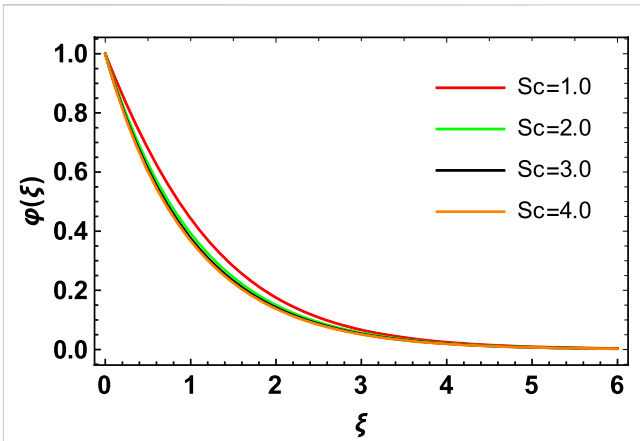

FIGURE 9
Impact of Sc on $\varphi(\xi)$.

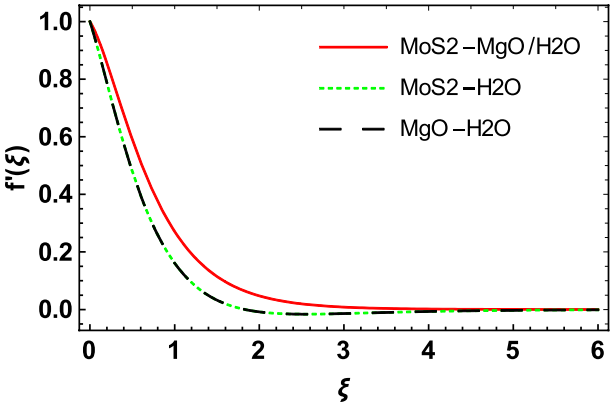

FIGURE 10
Velocity profile ($f'(\xi)$) for the comparison of $MoS_2 - MgO/H_2O$, $MoS_2 - H_2O$, and $MgO - H_2O$.

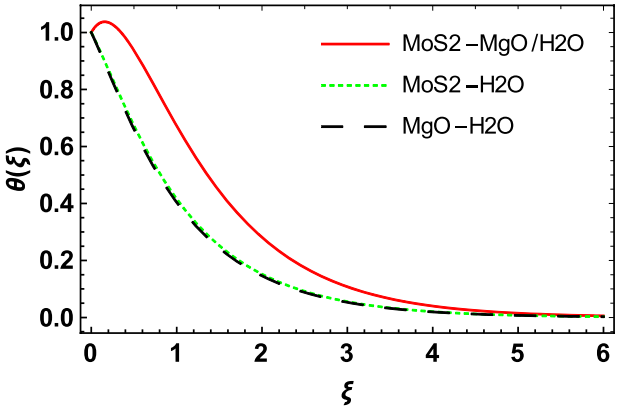

FIGURE 12
Temperature profile ($\theta'(\xi)$) for the comparison of $MoS_2 - MgO/H_2O$, $MoS_2 - H_2O$, and $MgO - H_2O$.

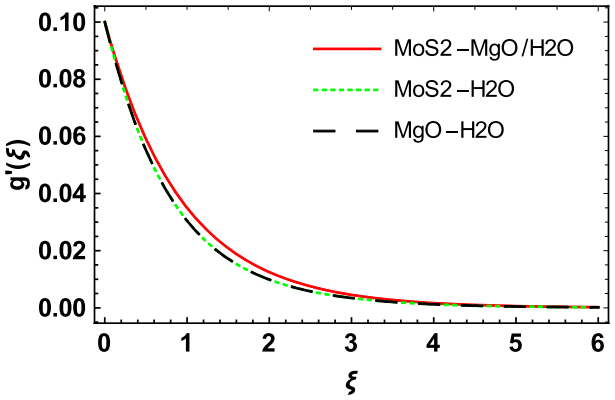

FIGURE 11
Velocity profile ($g'(\xi)$) for the comparison of $MoS_2 - MgO/H_2O$, $MoS_2 - H_2O$, and $MgO - H_2O$.

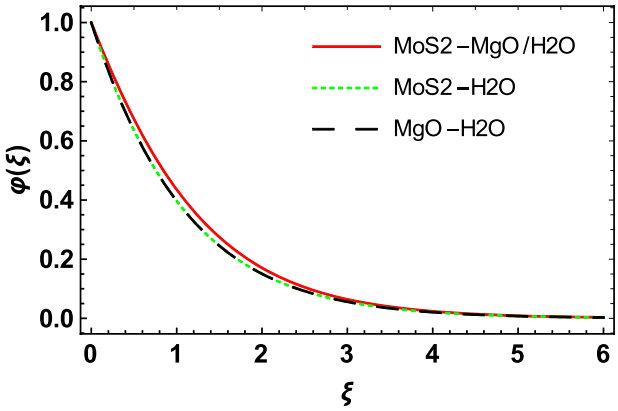

FIGURE 13
Concentration profile ($\varphi'(\xi)$) for the comparison of $MoS_2 - MgO/H_2O$, $MoS_2 - H_2O$, and $MgO - H_2O$.

different. For the $MgO - H_2O$ and the $MoS_2 - H_2O$ nanofluids, there are some variations in temperature and concentration characteristics at the surface of the Riga plate. However, in the case of the $MoS_2 - MgO/H_2O$ hybrid nanofluid flow, more heat transfer is offered to flow particles. Hence, the temperature is increased more in the case of the $MoS_2 - MgO/H_2O$ hybrid nanofluid flow, as depicted in Figure 12. The reason is that the hybrid nanofluid flow has greater thermal conductivity than the two other nanofluids. Similarly, the concentration boundary layer thickness is largest in the case of the $MoS_2 - MgO/H_2O$ hybrid nanofluid flow when compared to the $MgO - H_2O$ and $MoS_2 - H_2O$ nanofluids. Hence, the concentration profile is higher in the case of the $MoS_2 - MgO/H_2O$ hybrid nanofluid flow. The reason is that the hybrid nanofluid flow has more mass transfer rate than the other two nanofluids, as shown in Figure 13.

Table 1 portrays the numerical values of different thermophysical characteristics. Table 3 depicts the influences of nonlinear thermal radiation N, space factor S_p, and a heat source/sink factor H_S on the Nusselt number in the case of the $MgO - H_2O$ nanofluid, the $MoS_2 - H_2O$ nanofluid, and the $MgO - MoS_2/H_2O$ hybrid nanofluid. With growing values of N, the maximum thermal diffusions occur at the surface of the Riga plate due to the electric and magnetic characteristics at the surface. Hence, amplification in the values of N results in an increase in the Nusselt number. Similarly, an increase in the space factor S_p and heat source/sink factor H_S causes an increase in the Nusselt number. Growth in the Nusselt number in the case of the $MgO - MoS_2/H_2O$ hybrid nanofluid is greater than in the $MgO - H_2O$ and $MoS_2 - H_2O$ nanofluids. In Table 4, the impacts of the chemical reactant factor γ and the Schmidt number Sc are shown on the Sherwood number. With the increase in γ, the solutal molecules grow and cause mass diffusions. Hence, growth in γ causes a decline in the values of the Sherwood number. Similarly, with higher values of Sc, less mass transmission occurs; as a result, the Sherwood number decreases gradually.

TABLE 3 Impacts of different physical factors on the Nusselt number.

N	S_p	H_s	$\frac{Nu_x}{\sqrt{Re_x}}$		
			$MgO - H_2O$	$MoS_2 - H_2O$	$MgO - MoS_2/H_2O$
0.1			1.05455	1.05282	1.10516
0.2			1.14768	1.14586	1.19981
0.3			1.24278	1.24087	1.29642
	0.2		1.07391	1.07186	1.12650
	0.3		1.09323	1.09088	1.14723
	0.4		1.11260	1.10989	1.16823
		0.2	1.07391	1.07186	1.12650
		0.3	1.09323	1.09088	1.14723
		0.4	1.11260	1.10989	1.16823

TABLE 4 Influence of γ and Sc on the Sherwood number.

Sc	γ	$\frac{Sh_x}{\sqrt{Re_x}}$		
		$MgO - H_2O$	$MoS_2 - H_2O$	$MgO - MoS_2/H_2O$
0.1		0.98543	0.97584	1.05285
0.2		0.73236	0.72169	0.85410
0.3		0.45356	0.43864	0.57638
	0.2	1.53567	1.53567	1.67083
	0.3	1.50425	1.48536	1.65487
	0.4	1.47653	1.45369	1.63863

6 Conclusion

This work investigates hybrid nanofluid flow past a bi-directional stretching surface. The hybrid nanofluid flow is affected by thermal radiation, chemical reactions, and a variable thermal source/sink. The set of equations that administer the hybrid nanofluid flow behavior was transformed to a dimensionless form by suitable similarity transformations. After a comprehensive analysis, the following points are noted.

a) Because the increase in the Hartmann number augments the strength of the electrical field externally, the behavior of the wall Lorentz force increases the decrease in the velocity of the fluid.
b) The ratio parameter has a direct relationship with the hybrid nanofluid flow velocity in the y-direction and a reverse relationship in the x-direction. Hence, a retarding impact was noted on the primary velocity, and an augmenting effect was observed on the secondary velocity.
c) With growing values of the nonlinear thermal radiation factor, the maximum thermal diffusions occur at the surface of the Riga plate. Hence, augmentation of the radiation factor results in an increase in the thermal distribution.
d) The space factor and heat source/sink factor behave as a heat generator and a heat absorption point, respectively, in the flow system; hence, an increase in these factors increases the temperature of hybrid nanofluid flow.
e) Increases in the chemical reaction factor and the Schmidt number have an opposing effect on the concentration distribution of the hybrid nanofluid flow.
f) Temperature and concentration increase more rapidly for the hybrid nanofluid than the other two nanofluids.

Data availability statement

The original contributions presented in the study are included in the article/Supplementary Material; further inquiries can be directed to the corresponding authors.

Author contributions

EA and SL: conceptualization, methodology, software, reviewing and editing. ZR: data curation and writing—original draft preparation. SE: visualization and investigation. AS: software, validation, and supervision. AG: writing—reviewing and editing.

Acknowledgments

The author (ZR) extends her appreciation to the Deanship of Scientific Research at King Khalid University, Abha, Saudi Arabia, for funding this work through the Research Group Project under Grant Number (RGP.1/334/43).

Conflict of interest

The authors declare that the research was conducted in the absence of any commercial or financial relationships that could be construed as a potential conflict of interest.

Publisher's note

All claims expressed in this article are solely those of the authors and do not necessarily represent those of their affiliated organizations, or those of the publisher, the editors, and the reviewers. Any product that may be evaluated in this article, or claim that may be made by its manufacturer, is not guaranteed or endorsed by the publisher.

References

Acharya, N., Bag, R., and Kundu, P. K. (2020). On the impact of nonlinear thermal radiation on magnetized hybrid condensed nanofluid flow over a permeable texture. *Appl. Nanosci.* 10, 1679–1691. doi:10.1007/s13204-019-01224-w

Acharya, N., Mabood, F., Shahzad, S. A., and Badruddin, I. A. (2022). Hydrothermal variations of radiative nanofluid flow by the influence of nanoparticles diameter and nanolayer. *Int. Commun. Heat. Mass Transf.* 130, 105781. doi:10.1016/J.ICHEATMASSTRANSFER.2021.105781

Ahmad, A., Asghar, S., and Afzal, S. (2016). Flow of nanofluid past a Riga plate. *J. Magn. Magn. Mat.* 402, 44–48. doi:10.1016/j.jmmm.2015.11.043

Alharbi, S. O., Dawar, A., Shah, Z., Khan, W., Idrees, M., Islam, S., et al. (2018). Entropy generation in MHD eyring-powell fluid flow over an unsteady oscillatory porous stretching surface under the impact of thermal radiation and heat source/sink. *Appl. Sci.* 2, 2588. doi:10.3390/app8122588

Alhowaity, A., Bilal, M., Hamam, H., Alqarni, M. M., Mukdasai, K., and Ali, A. (2022). Non-Fourier energy transmission in power-law hybrid nanofluid flow over a moving sheet. *Sci. Rep.* 12, 10406. doi:10.1038/s41598-022-14720-x

Ali, L., Wang, Y., Ali, B., Liu, X., Din, A., and Al Mdallal, Q. (2021). The function of nanoparticle's diameter and Darcy-Forchheimer flow over a cylinder with effect of magnetic field and thermal radiation. *Case Stud. Therm. Eng.* 28, 101392. doi:10.1016/j.csite.2021.101392

. Alqarni, M. S. (2022). Thermo-bioconvection flow of Walter's B nanofluid over a Riga plate involving swimming motile microorganisms. *Aimspress. Com.* 7, 16231–16248. doi:10.3934/math.2022886

Alwawi, F., Alkasasbeh, H., Rashad, A., and Idris, R. (2020). MHD natural convection of Sodium Alginate Casson nanofluid over a solid sphere. *Results Phys.* 16, 102818. doi:10.1016/j.rinp.2019.102818

Anuar, N. S., Bachok, N., Turkyilmazoglu, M., Arifin, N. M., and Rosali, H. (2020). Analytical and stability analysis of MHD flow past a nonlinearly deforming vertical surface in Carbon Nanotubes. *Alex. Eng. J.* 59, 497–507. doi:10.1016/j.aej.2020.01.024

Asogwa, K. K., Mebarek-Oudina, F., and Animasaun, I. L. (2022). Comparative investigation of water-based Al_2O_3 nanoparticles through water-based CuO nanoparticles over an exponentially accelerated radiative Riga plate surface via heat transport. *Arab. J. Sci. Eng.* 47, 8721–8738. doi:10.1007/s13369-021-06355-3

Bhatti, M. M., Arain, M. B., Zeeshan, A., Ellahi, R., and Doranehgard, M. H. (2022). Swimming of Gyrotactic Microorganism in MHD Williamson nanofluid flow between rotating circular plates embedded in porous medium: Application of thermal energy storage. *J. Energy Storage.* 45, 103511. doi:10.1016/j.est.2021.103511

Choi, S. U. S., and Eastman, J. A. (1995). "Enhancing thermal conductivity of fluids with nanoparticles," in Int. Mech. Eng. Congr. Exhib. San Fr, CA United States, 12-17 Nov 1995.

Eid, M. R., and Nafe, M. A. (2022). Thermal conductivity variation and heat generation effects on magneto-hybrid nanofluid flow in a porous medium with slip condition. *Waves Random Complex Media* 32, 1103–1127. doi:10.1080/17455030.2020.1810365

El-Zahar, E. R., El Nasser Mahdy, A., Rashad, A. M., Saad, W., and Seddek, L. F. (2021). Unsteady MHD mixed convection flow of Non-Newtonian Casson hybrid nanofluid in the stagnation zone of sphere spinning impulsively. *Fluids* 6, 197. doi:10.3390/fluids6060197

El-Zahar, E., Rashad, A., Rashad, A. M., and Al-Juaydi, H. S. (2022). Studying massive suction impact on magneto-flow of a hybridized casson nanofluid on a porous continuous moving or fixed surface. *Symmetry* 14, 627. doi:10.3390/sym14030627

Gangadhar, K., Kumari, M. A., and Chamkha, A. J. (2021). EMHD flow of radiative second-grade nanofluid over a Riga plate due to convective heating: Revised buongiorno's nanofluid model. *Arab. J. Sci. Eng.* 47, 8093–8103. doi:10.1007/s13369-021-06092-7

Hamarsheh, A., Alwawi, F., Alkasasbeh, H. T., and Rashad, A. M. (2020). Heat transfer improvement in MHD natural convection flow of graphite oxide/carbon nanotubes-methanol based casson nanofluids past a horizontal circular cylinder. *Processes* 8, 1444. doi:10.3390/pr8111444

Haq, I., Bilal, M., Ahammad, N. A., Ghoneim, M. E., Ali, A., and Weera, W. (2022). Mixed convection nanofluid flow with heat source and chemical reaction over an inclined irregular surface. *ACS Omega* 7, 30477–30485. doi:10.1021/acsomega.2c03919

Hayat, T., Shehzad, S. A., and Alsaedi, A. (2013). Three-dimensional stretched flow of Jeffrey fluid with variable thermal conductivity and thermal radiation. *Appl. Math. Mech.* 34, 823–832. doi:10.1007/s10483-013-1710-7

Ijaz, M., Nadeem, S., Ayub, M., and Mansoor, S. (2021). Simulation of magnetic dipole on gyrotactic ferromagnetic fluid flow with nonlinear thermal radiation. *J. Therm. Anal. Calorim.* 143, 2053–2067. doi:10.1007/s10973-020-09856-9

Khader, M. M., and Sharma, R. P. (2021). Evaluating the unsteady MHD micropolar fluid flow past stretching/shirking sheet with heat source and thermal radiation: Implementing fourth order predictor–corrector FDM. *Math. Comput. Simul.* 181, 333–350. doi:10.1016/j.matcom.2020.09.014

Khan, A., Hassan, B., Ashraf, E. E., and Shah, S. Y. A. (2022). Thermally dissipative micropolar hybrid nanofluid flow over a spinning needle influenced by Hall current and gyrotactic microorganisms. *Heat. Transf.* 51, 1170–1192. doi:10.1002/htj.22347

Khan, U., Ishak, A., and Zaib, A. (2021). Hybrid nanofluid flow containing single-wall and multi-wall CNTs induced by a slender stretchable sheet. *Chin. J. Phys.* 74, 350–364. doi:10.1016/j.cjph.2021.10.009

Khan, U., Zaib, A., Ishak, A., Abu Bakar, S., Animasaun, I. L., and Yook, S-J. (2022). Insights into the dynamics of blood conveying gold nanoparticles on a curved surface when suction, thermal radiation, and Lorentz force are significant: The case of of Non-Newtonian Williamson fluid. *Math. Comput. Simul.* 193, 250–268. doi:10.1016/j.matcom.2021.10.014

Khan, U., Zaib, A., Ishak, A., Sherif, E.-S. M., Waini, I., Chu, Y.-M., et al. (2022). Radiative mixed convective flow induced by hybrid nanofluid over a porous vertical cylinder in a porous media with irregular heat sink/source. *Case Stud. Therm. Eng.* 30, 101711. doi:10.1016/j.csite.2021.101711

Kumar, K. G., Rudraswamy, N. G., and Gireesha, B. J. (2017). Effects of mass transfer on MHD three dimensional flow of a Prandtl liquid over a flat plate in the presence of chemical reaction. *Results Phys.* 7, 3465–3471. doi:10.1016/j.rinp.2017.08.060

Li, Y.-X., Alqsair, U. F., Ramesh, K., Khan, S. U., and Khan, M. I. (2022). Nonlinear heat source/sink and activation energy assessment in double diffusion flow of micropolar (non-Newtonian) nanofluid with convective conditions. *Arab. J. Sci. Eng.* 47, 859–866. doi:10.1007/s13369-021-05692-7

Liao, S. (2010). An optimal homotopy-analysis approach for strongly nonlinear differential equations. *Commun. Nonlinear Sci. Numer. Simul.* 15, 2003–2016. doi:10.1016/j.cnsns.2009.09.002

Liao, S.-J. (1999). An explicit, totally analytic approximate solution for Blasius' viscous flow problems. *Int. J. Non. Linear. Mech.* 34, 759–778. doi:10.1016/s0020-7462(98)00056-0

Lielausis, O. (1961). On a possibility to reduce the hydrodynamic resistance of a plate in an electrolyte. *Appl. Magnetohydrodyn.* 12, 143–146.

Manzoor, U., Imran, M., Muhammad, T., Waqas, H., and Alghamdi, M. (2021). Heat transfer improvement in hybrid nanofluid flow over a moving sheet with magnetic dipole. *Waves Random Complex Media*, 1–15. doi:10.1080/17455030.2021.1991602

Mishra, A., and Upreti, H. (2022). A comparative study of Ag–MgO/water and Fe3O4–CoFe2O4/EG–water hybrid nanofluid flow over a curved surface with chemical reaction using Buongiorno model. *Partial Differ. Equations Appl. Math.* 5, 100322. doi:10.1016/j.padiff.2022.100322

Muhammad, T., Waqas, H., Khan, S. A., Ellahi, R., and Sait, S. M. (2021). Significance of nonlinear thermal radiation in 3D Eyring–Powell nanofluid flow with Arrhenius activation energy. *J. Therm. Anal. Calorim.* 143, 929–944. doi:10.1007/s10973-020-09459-4

Ojjela, O. (2022). Numerical investigation of heat transport in Alumina–Silica hybrid nanofluid flow with modeling and simulation. *Math. Comput. Simul.* 193, 100–122. doi:10.1016/j.matcom.2021.09.022

Rahman, M., Sharif, F., Turkyilmazoglu, M., and Siddiqui, M. S. (2022). Unsteady three-dimensional magnetohydrodynamics flow of nanofluids over a decelerated rotating disk with uniform suction. *Pramana* 96, 170. doi:10.1007/s12043-022-02404-0

Ram, M. S., Spandana, K., Shamshuddin, M., and Salawu, S. O. (2022). Mixed convective heat and mass transfer in magnetized micropolar fluid flow toward stagnation point on a porous stretching sheet with heat source/sink and variable species reaction. *Int. J. Model. Simul.*, 1–13. doi:10.1080/02286203.2022.2112008

Rawia, N. A., Alib, A., Rubaa'ic, A. F. A., and Shafied, S. (2022). The effect of non-uniform heat source/sink on mixed convection flow of hybrid nanofluid over A stretching sheet. *Proceeding Sci. Math.* 7, 56.

Sabir, Z., Imran, A., Umar, M., Zeb, M., Shoaib, M., and Raja, M. A. Z. (2021). A numerical approach for 2-D Sutterby fluid-flow bounded at a stagnation point with an inclined magnetic field and thermal radiation impacts. *Therm. Sci.* 25, 1975–1987.

Saeed, A., Jawad, M., Alghamdi, W., Nasir, S., Gul, T., and Kumam, P. (2021). Hybrid nanofluid flow through a spinning Darcy–Forchheimer porous space with thermal radiation. *Sci. Rep.* 11, 16708. doi:10.1038/s41598-021-95989-2

Saleh, B., Madhukesh, J. K., Varun Kumar, R. S., Afzal, A., Abdelrhman, Y., Aly, A. A., et al. (2022). Aspects of magnetic dipole and heat source/sink on the Maxwell hybrid nanofluid flow over a stretching sheet. *Proc. Inst. Mech. Eng. Part E J. Process Mech. Eng.*, 09544089211056243.

Shafiq, A., Mebarek-Oudina, F., Sindhu, T. N., and Abidi, A. (2021). A study of dual stratification on stagnation point Walters' B nanofluid flow via radiative Riga plate: A statistical approach. *Eur. Phys. J. Plus.* 136, 407–424. doi:10.1140/epjp/s13360-021-01394-z

Shah, N. A., Wakif, A., El-Zahar, E. R., Ahmad, S., and Yook, S.-J. (2022). Numerical simulation of a thermally enhanced EMHD flow of a heterogeneous micropolar mixture comprising (60%)-ethylene glycol (EG),(40%)-water (W), and copper oxide nanomaterials (CuO). *Case Stud. Therm. Eng.* 35, 102046. doi:10.1016/j.csite.2022.102046

Shah, Z., Khan, A., Khan, W., Alam, M. K., Islam, S., Kumam, P., et al. (2020). Micropolar gold blood nanofluid flow and radiative heat transfer between permeable channels. *Comput. Methods Programs Biomed.* 186, 105197. doi:10.1016/j.cmpb.2019.105197

Shahid, A., Bhatti, M. M., Ellahi, R., and Mekheimer, K. S. (2022). Numerical experiment to examine activation energy and bi-convection Carreau nanofluid flow on an upper paraboloid porous surface: Application in solar energy. *Sustain. Energy Technol. Assessments.* 52, 102029. doi:10.1016/j.seta.2022.102029

Shamshuddin, M. D., Mabood, F., and Bég, O. A. (2021). Thermomagnetic reactive ethylene glycol-metallic nanofluid transport from a convectively heated porous surface with Ohmic dissipation, heat source, thermophoresis and Brownian motion effects. *Int. J. Model. Simul.*, 1–15.

Sharma, B. K., Kumar, A., Gandhi, R., and Bhatti, M. M. (2022). Exponential space and thermal-dependent heat source effects on electro-magneto-hydrodynamic Jeffrey fluid flow over a vertical stretching surface. *Int. J. Mod. Phys. B* 36, 2250220. doi:10.1142/s0217979222502204

Sravanthi, C. S. (2020). Second order velocity slip and thermal jump of Cu–water nanofluid over a cone in the presence of nonlinear radiation and nonuniform heat source/sink using homotopy analysis method. *Heat. Transf. - Asian Res.* 49, 86–102. doi:10.1002/HTJ.21600

Tarakaramu, N., Satya Narayana, P. V., Sivajothi, R., Bhagya Lakshmi, K., Harish Babu, D., and Venkateswarlu, B. (2022). Three-dimensional non-Newtonian couple stress fluid flow over a permeable stretching surface with nonlinear thermal radiation and heat source effects. *Heat. Transf.* 51, 5348–5367. doi:10.1002/htj.22550

Thumma, T., Mishra, S., Abbas, A. M., and Bhatti, M. M. (2022). Three-dimensional nanofluid stirring with non-uniform heat source/sink through an elongated sheet. *Appl. Math. Comput.* 421, 126927. doi:10.1016/j.amc.2022.126927

Tlili, I., Naseer, S., Ramzan, M., Kadry, S., and Nam, Y. (2020). Effects of chemical species and nonlinear thermal radiation with 3D Maxwell nanofluid flow with double stratification—An analytical solution. *Entropy* 22, 453. doi:10.3390/e22040453

Ullah, I., Alajlani, Y., Pasha, A. A., Adil, M., and Weera, W. (2022). Theoretical investigation of hybrid nanomaterials transient flow through variable feature of Darcy–Forchheimer space with exponential heat source and slip condition. *Sci. Rep.* 12, 15085. doi:10.1038/s41598-022-17988-1

Wahid, N. S., Arifin, N. M., Turkyilmazoglu, M., Hafidzuddin, M. E. H., and Abd Rahmin, N. A. (2020). "MHD hybrid Cu-Al_2O_3/water nanofluid flow with thermal radiation and partial slip past a permeable stretching surface: Analytical solution," in *J. Nano res.* (Switzerland: Trans Tech Publ).

Waini, I., Khan, U., Zaib, A., Ishak, A., and Pop, I. (2022). Inspection of TiO_2-$CoFe_2O_4$ nanoparticles on MHD flow toward a shrinking cylinder with radiative heat transfer. *J. Mol. Liq.* 361, 119615. doi:10.1016/J.MOLLIQ.2022.119615

Wang, C. Y. (1984). The three-dimensional flow due to a stretching flat surface. *Phys. Fluids.* 27, 1915–1917. doi:10.1063/1.864868

Waseem, M., Gul, T., Khan, I., Khan, A., Saeed, A., Ali, I., et al. (2021). Gravity-driven hydromagnetic flow of couple stress hybrid nanofluid with homogenous-heterogeneous reactions. *Sci. Rep.* 11, 17498–17512. doi:10.1038/s41598-021-97045-5

Zabihi, A., Akinshilo, A. T., Rezazadeh, H., Ansari, R., Sobamowo, M. G., and Tunç, C. (2022). Application of variation of parameter's method for hydrothermal analysis on MHD squeezing nanofluid flow in parallel plates. *Comput. Methods Differ. Equations.* 10, 580–594.

Zabihi, A., Ansari, R., Hosseini, K., Samadani, F., and Torabi, J. (2020). Nonlinear pull-in instability of rectangular nanoplates based on the positive and negative second-order strain gradient theories with various edge supports. *Z. Für Naturforsch. A* 75, 317–331. doi:10.1515/zna-2019-0356

Zabihi, A., Torabi, J., and Ansari, R. (2020). Effects of geometric nonlinearity on the pull-in instability of circular microplates based on modified strain gradient theory. *Phys. Scr.* 95, 115204. doi:10.1088/1402-4896/abba4e

Zhang, L., Bhatti, M. M., Michaelides, E. E., Marin, M., and Ellahi, R. (2022). Hybrid nanofluid flow towards an elastic surface with tantalum and nickel nanoparticles, under the influence of an induced magnetic field. *Eur. Phys. J. Spec. Top.* 231, 521–533. doi:10.1140/epjs/s11734-021-00409-1

Nomenclature

T_w surface temperature
u_w stretching velocity
M magnetic factor
q_r radiative heat flux
q variable heat source/sink
S_p **and** H_s space and heat factors
k^* Stefan–Boltzmann constant
Sc Schmidt number
N nonlinear thermal radiation
γ chemical reaction
C_p specific heat
MgO magnesium oxide
MoS_2 molybdenum disulfide
$(C_{fx}; C_{fy})$ skin frictions
v_f kinematic viscosity
$\theta(\xi)$ temperature profile
C_w surface concentration
E_{IJ} rate of deformation
j_0 electrode current density
ρ density
σ^* mean absorption coefficient
α EMHD factor
H modified Hartmann number
S ratio parameter
Pr Prandtl number
θ_w temperature ratio parameter
k thermal diffusivity
H_2O water
Nu_x Nusselt number
Sh_x Sherwood number
Re Reynold number
$f'(\zeta)$ velocity profile

frontiers | Frontiers in Materials

TYPE Original Research
PUBLISHED 03 March 2023
DOI 10.3389/fmats.2023.1132124

OPEN ACCESS

EDITED BY
Hammad Khalil,
University of Education Lahore, Pakistan

REVIEWED BY
Noreen Akbar,
National University of Sciences and Technology (NUST), Pakistan
Zhongliang Xie,
Northwestern Polytechnical University, China

*CORRESPONDENCE
Sayed M. Eldin,
sayed.eldin22@fue.edu.eg

SPECIALTY SECTION
This article was submitted to Colloidal Materials and Interfaces, a section of the journal Frontiers in Materials

RECEIVED 26 December 2022
ACCEPTED 13 February 2023
PUBLISHED 03 March 2023

CITATION
Algehyne EA, Lone SA, Raizah Z, Eldin SM, Saeed A and Galal AM (2023), Analysis of the electrically conducting magnetohydrodynamic hybrid nanofluid flow past a convectively heated stretching surface with suction/injection and non-linear thermal radiation. *Front. Mater.* 10:1132124. doi: 10.3389/fmats.2023.1132124

Analysis of the electrically conducting magnetohydrodynamic hybrid nanofluid flow past a convectively heated stretching surface with suction/injection and non-linear thermal radiation

Ebrahem A. Algehyne[1,2], Showkat Ahmad Lone[3], Zehba Raizah[4], Sayed M. Eldin[5]*, Anwar Saeed[6] and Ahmed M. Galal[7,8]

[1]Department of Mathematics, Faculty of Science, University of Tabuk, Tabuk, Saudi Arabia, [2]Nanotechnology Research Unit (NRU), University of Tabuk, Tabuk, Saudi Arabia, [3]Department of Basic Sciences, College of Science and Theoretical Studies, Saudi Electronic University, Jeddah-M, Riyadh, KSA, [4]Department of Mathematics, College of Science, King Khalid University, Abha, Saudi Arabia, [5]Center of Research, Faculty of Engineering, Future University in Egypt New Cairo, New Cairo, Egypt, [6]Center of Excellence in Theoretical and Computational Science (TaCS-CoE), Science Laboratory Building, Faculty of Science, King Mongkut's University of Technology Thonburi (KMUTT), Bang Mod, Thung Khru, Bangkok, Thailand, [7]Department of Mechanical Engineering, College of Engineering in Wadi Alddawasir, Prince Sattam bin Abdulaziz University, Saudi Arabia, [8]Production Engineering and Mechanical Design Department, Faculty of Engineering, Mansoura University, Mansoura, Egypt

Fluid flow through a porous media has many industrial applications such as water flowing through rocks and soil and purification of gas and oil mixed in rocks. Also, heat transfer enhancement has been introduced in various thermal and mechanical systems by improving the thermal conductance of base fluids. In this article, the flow of an electrically conducting water-based hybrid nanofluid comprising GO and Fe_3O_4 nanoparticles over an extending sheet using a porous medium has been investigated. The space-dependent heat source, Joule heating, Brownian motion, thermophoresis, thermal radiation, chemical reaction, and activation energy impacts are taken into account. For the solution of the modeled equations, the homotopy analysis method is considered. The homotopic convergence is shown with the help of a figure. This analysis is contrasted with previous outcomes and has found a great agreement. The impacts of embedded factors on different flow characteristics, skin friction coefficient, and Nusselt and Sherwood numbers are displayed using figures and tables. The outcomes of the present analysis show that the increasing magnetic and suction factors have reduced the fluid motion while amplifying the thermal profiles. Additionally, the suction factor has a reducing impact on both temperature and concentration profiles. The thermal profiles have increased with the increasing thermal Biot number, Eckert number, thermophoresis, and Brownian motion factors. The Nusselt numbers have increased with the increasing thermal Biot number and stretching factor but reduced with the increasing thermal radiation and temperature difference factors.

KEYWORDS

hybrid nanofluid, inclined magnetic field, Brownian motion and thermophoresis, space-dependent heat source, thermal radiation

1 Introduction

The selection of the coolant of different devices/equipment at the industrial level and for various engineering applications is one of the most challenging tasks. Recently, thermal flow enhancement has been introduced in various thermal and mechanical systems by improving the thermal conductance of base fluids. Different fluids which are considered as pure base fluids are engine/kerosene oil, water, ethylene glycol, *etc*. The suspension of non-size particles in a pure fluid has been familiarized by Choi and Eastman (1995) first to expand the thermal flow characteristics of the base fluid. Acharya et al. (2022) discussed the fluid flow and thermal phenomenon for a time-based MHD nanoliquid on a spinning surface and explored that the thermal properties of the nanofluid were enhanced by 84.61% in comparison to the normal fluid. Shah et al. (2020) mixed gold particles in blood to enhance its thermal properties by incorporating radiation and rotational effects in the flow system. Khan et al. (2021) introduced radiative effects in the revolving motion of an MHD nanofluid on a spinning cylinder and noticed a difference in temperature growth at the wall as well as on the surface of the cylinder. Bhatti et al. (2022) explored a bioconvective MHD Williamson nanofluid flowing amid two spinning circular surfaces placed in a penetrable medium. Hussain et al. (2022) solved numerically the radiative EMHD Williamson fluid flow on a stretching surface. Rasheed et al. (2022) discussed the Brownian three-dimensional motion of a thin-film nanofluid past a stretched and rotary sheet and found that the Nusselt number augmented with growth in magnetic and Brownian factors and the concentration of nanoparticles. Akbar et al. (2022) scrutinized the exact solution of an unsteady thermal conductive pressure on peristaltic transport with temperature nanofluid viscosity. Carbon nanotubes (CNTs) are grasped as nanoparticles in an irregular channel. Akram et al. (2022) investigated the electroosmotic flow of peristaltic transport of a nanofluid over a curved microchannel.

It has further been noticed experimentally that the thermal conductance of a base fluid can be additionally enhanced by suspending two unlike natures of nanoparticles in it and is characterized as a hybrid nanofluid. Chu et al. (2022) examined the impact of different nanoparticle shapes for unsteady hybrid nanofluid flow amid two plates of infinite length and determined that velocity weakened whereas the temperature of the fluid upsurged with augmentation in the number of hybrid nanoparticles. Zhang et al. (2022) examined the effects of magnetic field on hybrid nanoparticle flow over an elastic sheet and noticed that motion of the fluid propagated faster with progression in tantalum nanoparticles and the Darcy number while the temperature of the fluid declined with an upsurge in nickel and tantalum nanoparticle concentration. Guedri et al. (2022) discussed the trihybrid radiative nanofluid motion over a non-linear extended sheet using the impression of the Darcy–Forchheimer model and noticed that the heat of the fluid amplified with growth in Brownian, temperature ratio, and thermophoretic parameters. Salahuddin et al. (2022) examined flow and thermal behavior for a highly magnetized wavy heated cylinder on which hybrid nanofluids flow. Alrabaiah et al. (2022) estimated the bioconvective hybrid nanoparticles' flow in the cavity of a cone/disk using the influences of dissipation and microorganisms. Lone et al. (2022) explored MHD micro-rotational hybrid nanoparticles' flow past a flat plate using thermally radiated effects and mixed convection. Khan et al. (2022a) examined hybrid dissipative nanofluid flow on a heated revolving needle using microorganisms and Hall current effects. Maraj et al. (2017) studied the closed-form solution of mixed convective MHD carbon nanotube nanofluid flow in a rotating channel. In this study, one can see that temperature is the enhancing function against the improving estimations of the volume fraction parameter. Habib and Akbar (2021) proposed the incorporation of novel nanofluids in clinical isolates to battle *Staphylococcus aureus*. Akram et al. (2021) reported water-based hybrid (Ag–Au) nanofluids electroosmotically pumped through an inclined asymmetric microfluidic channel in a porous setting. With the help of the Debye–Hückel and lubrication linearization principles, the governing equations of the current model are linearized.

The study of electrically conducted fluids associated with magnetic effects such as salty water and plasma is called magnetohydrodynamics (MHD). Such fluids are crucial in many engineering and industrial applications, for instance, design of nuclear reactors, MHD generators, and flow meters. Asjad et al. (2022) explored the impact of activated energy and magnetic effects on a Williamson fluid using bioconvective effects on an exponentially stretched surface. Bejawada et al. (2022) inspected radiated MHD fluid motion on a non-linear inclined sheet using a permeable Forchheimer surface and concluded that the motion of liquid degenerated while temperature expanded with progression in the magnetic factor. Kodi and Mopuri (2022) discussed MHD time-based oscillatory fluid flow on an inclined surface using chemically reactive effects and thermal absorption. Usman et al. (2021) explored the impact of EMHD couple stress on a thin film hybrid nanoliquid flow on a gyratory surface and established that thermal conductance is better in case of hybrid nanoparticles. Venkata Ramudu et al. (2022) explored the impact of convective diffusion conditions on Casson MHD fluid motion on a stretched sheet and noticed that the Sherwood number upsurged while the Nusselt number declined with an escalation in the non-linear radiative factor. Sharma et al. (2022) deliberated theoretically on convection MHD liquid flow past a rotary extended disk and recognized that the Nusselt number augmented with progression in the magnetic factor at the lower disk. Same ideas can be seen in Waseem et al. (2021); Mahabaleshwar et al. (2022); Nagendramma et al. (2022); and Nazeer et al. (2022).

The experimental and theoretical investigations of fluid flow under the impact of Joule heating have been handled frequently in the literature. It plays a pivotal role in controlling the thermal flow effects. Shamshuddin and Eid (2022) discussed a higher-order reactive nanofluid in a convective extending sheet under the impact of Joule heating and mixed convection and proved that the Eckert

number supported the fluid motion and thermal characteristics, whereas growth in the magnetic factor declined the velocity and upsurged the Nusselt number. Wahid et al. (2022) examined an MHD nanofluid at the stagnant point of a shrinking surface with viscously dissipative Joule heating effects and noticed that 25% growth in melting effects augmented skin friction by 5%, whereas the flow phenomenon can be sustained as laminar by taking alumina nanoparticles as 2% instead of 1%. Xuan (2022) reviewed non-linear electro-kinetic fluid flow taking the effects of induced charge to Joule heating. Abbas et al. (2022) debated on the influence of the Darcy–Forchheimer model on dissipative MHD fluid flow using Joule heating effects on a porous sheet and explored that with progression in the thermal diffusion factor, the temperature, concentration, and velocity characteristics augmented. Khan et al. (2022b) examined the production of irreversibility for hydro-magnetic fluid flow using the Darcy–Forchheimer model and Joule heating effects and explained the thermal flow phenomenon both for prescribed thermal flux and surface temperatures. Waqas et al. (2022) deliberated on MHD nanoliquid flow on a radiated stretched surface using Joule heating as well as dissipative effects and noticed that the density of microbes degenerated with growth in the Peclet number. Saleem et al. (2022) discussed the bio-mathematical model for the flow of blood through an artery using Joule heating. Kumar et al. (2022) discussed numerically the chemically reactive MHD fluid slip flow with Joule heating on an exponentially extended sheet and explored that fluid motion weakened while the Nusselt number, as well as skin friction, amplified with an upsurge in magnetic effects. Xie et al. (2023a) designed experimental and numerical evaluations of a novel bearing's fluid–structure interaction lubricating abilities. Xie et al. (2023b) demonstrated the fluid–structure–acoustic coupling dynamics of a new water-lubricated bearing being studied theoretically and experimentally.

Thermal radiation is another main factor that plays a significant role in thermal flow analysis. Rehman et al. (2022) thermally inspected the radiated MHD Jeffery fluid flow with a comparative analysis upon plan/cylindrical surfaces and deduced that fluid flow on cylindrical surfaces has better thermal flow properties than on plain surfaces. For instance, the Nusselt number has greater values in case of cylindrical surfaces. Shaw et al. (2022) inspected MHD cross-liquid motion with effects of linear as well as non-linear heat radiations using an arbitrary Prandtl number and highlighted the thermal flow characteristics for Prandtl numbers within the interval $10^{-4} \le \mathrm{Pr} \le 10^{4}$ in case of the linear as well as non-linear thermal radiation factor. Bilal et al. (2022) explored the impact of heat radiation on liquid motion over a linear stretched surface and explained that with elevation in porosity and radiation factors, there is a growth in skin friction. Adnan (2022) discussed numerically the effects of radiative and convective thermal conduction on nanoliquid flow on a non-linear extended sheet and determined that fluid motion weakened with growth in the radiation factor, which, on the other hand, augmented both the Nusselt number and skin friction. Yaseen et al. (2022) discussed motion of hybrid nanoparticles amid two plates placed in parallel direction with the influence of the Darcy permeable medium and heat radiations effects and concluded that the Nusselt number augmented with progression in radiation and porosity factors. Ibrahim et al. (2022) debated on time-based viscously affected fluid flow using thermal radiations on a stretched plate. Ramesh et al. (2022) discussed CNT nanofluid flow on a gyratory sphere by employing the thermal radiation and thermophoretic effects.

Recently, thermal flow enhancement has been introduced in various thermal and mechanical systems by improving the thermal conductance of base fluids. Different fluids which are considered as base fluids are pure engine/kerosene oil, water, ethylene glycol, *etc.* This work investigates the flow of an electrically conducting hybrid nanofluid over an extending surface using a porous medium. The space-dependent heat source, Joule heating, Brownian motion, thermophoresis, thermal radiation, and chemically reactive activation energy impacts are taken into consideration. Section 2 comprises the main body of the study. Section 3 shows the homotopic solution of the model. The homotopic convergence is shown in Section 4. Section 5 shows the results and discussion part of the work. The final remarks are listed in Section 6.

2 Formulation of the problem

We consider the two-dimensional flow of an MHD hybrid nanofluid containing *GO* and Fe_3O_4 nanoparticles past a stretching sheet using porous media. A magnetic field of strength B_0 with an acute angle γ is employed for the hybrid nanofluid flow. The stretching velocity of the sheet is depicted by $u_w(x) = ax$. The surface of the sheet is kept with a constant temperature and concentration, T_w (such that $T_w < T_f$) and C_w, respectively, while the corresponding ambient temperature and concentration are T_∞ and C_∞, respectively. Here, T_f is the reference temperature. A geometrical representation of the flow problem is shown in Figure 1. Additionally, the space-dependent heat source, Joule heating, Brownian motion, thermal radiation, thermophoresis, chemical reaction, and activation energy impacts are taken into consideration. The leading equations are (Reddy et al., 2020; Dawar et al., 2022a)

$$\frac{\partial u}{\partial x} + \frac{\partial v}{\partial y} = 0, \tag{1}$$

$$u\frac{\partial u}{\partial x} + v\frac{\partial u}{\partial y} = \frac{\mu_{hnf}}{\rho_{hnf}}\frac{\partial^2 u}{\partial y^2} - \frac{\mu_{hnf}}{\rho_{hnf}}\frac{1}{K_p}u - \frac{\sigma_{hnf}}{\rho_{hnf}}B_0^2 u\sin^2(\alpha), \tag{2}$$

$$u\frac{\partial T}{\partial x} + v\frac{\partial T}{\partial y} = \frac{k_{hnf}}{(\rho C_p)_{hnf}}\frac{\partial^2 T}{\partial y^2} + \frac{(\rho C_p)_p}{(\rho C_p)_{hnf}}\left[D_B\frac{\partial C}{\partial y}\frac{\partial T}{\partial y} + \frac{D_T}{T_\infty}\left(\frac{\partial T}{\partial y}\right)^2\right] + \frac{\sigma_{hnf}}{(\rho C_p)_{hnf}}B_0^2 u^2\sin^2(\alpha) - \frac{1}{(\rho C_p)_{hnf}}\frac{\partial q_r}{\partial y} + \frac{Q}{(\rho C_p)_{hnf}}(T_f - T_\infty)\exp\left(-my\sqrt{\frac{a}{\nu_f}}\right), \tag{3}$$

$$v\frac{\partial C}{\partial y} + u\frac{\partial C}{\partial x} = \frac{D_T}{T_\infty}\frac{\partial^2 T}{\partial y^2} + D_B\frac{\partial^2 C}{\partial y^2} - K_r^2\left(\frac{T}{T_\infty}\right)^n (C - C_\infty)\exp\left(-\frac{E_a}{\kappa T}\right), \tag{4}$$

subject to the following boundary conditions (Dawar et al., 2022b):

$$\left\{\begin{array}{l} u = u_w(x)\lambda, v = v_w, D_B\frac{\partial C}{\partial y} + \frac{\partial T}{\partial y}\frac{D_T}{T_\infty} = 0, -\frac{\partial T}{\partial y}k_{hnf} = (T_f - T)h_f, y = 0 \\ u \to 0, C \to C_\infty, T \to T_\infty \text{ as } y \to \infty \end{array}\right\}, \tag{5}$$

where q_r is given as

$$q_r = -\frac{16\sigma^\star}{3K^\star}\left(T^3\frac{\partial T}{\partial y}\right). \tag{6}$$

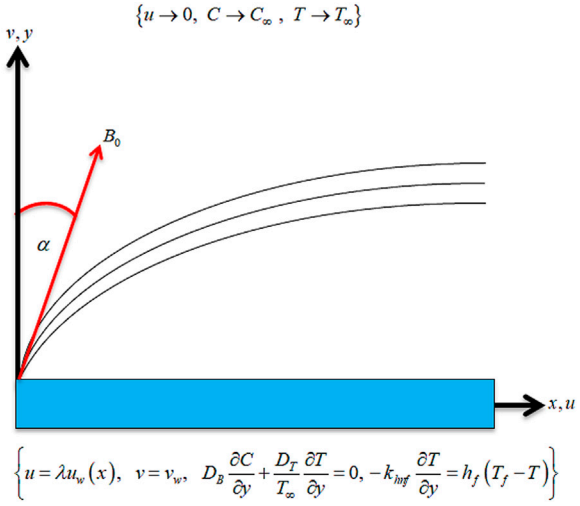

FIGURE 1
Flow geometry.

This can be reduced as

$$\frac{\partial q_r}{\partial \hat{y}} = -\frac{16\sigma^*}{3K^*}\left(3T^2\left(\frac{\partial T}{\partial y}\right)^2 + T^3\frac{\partial^2 T}{\partial y^2}\right). \tag{7}$$

So, Equation 3 can be written as

$$u\frac{\partial T}{\partial x} + v\frac{\partial T}{\partial y} = \frac{k_{hnf}}{(\rho C_p)_{hnf}}\frac{\partial^2 T}{\partial y^2} + \frac{(\rho C_p)_p}{(\rho C_p)_{hnf}}\left[D_B\frac{\partial C}{\partial y}\frac{\partial T}{\partial y} + \frac{D_T}{T_\infty}\left(\frac{\partial T}{\partial y}\right)^2\right]$$
$$+\frac{\sigma_{hnf}}{(\rho C_p)_{hnf}}B_0^2u^2\sin^2(\alpha) \quad + \frac{1}{(\rho C_p)_{hnf}}\frac{16\sigma^*}{3K^*}\left(3T^2\left(\frac{\partial T}{\partial y}\right)^2 + T^3\frac{\partial^2 T}{\partial y^2}\right)$$
$$+\frac{Q}{(\rho C_p)_{hnf}}(T_f - T_\infty)\exp\left(-my\sqrt{\frac{a}{\nu_f}}\right). \tag{8}$$

The thermophysical properties are defined as

$$\left\{\begin{array}{l} \frac{\mu_{hnf}}{\mu_f} = \frac{1}{(1-\nabla_1-\nabla_2)^{2.5}}, \frac{\rho_{hnf}}{\rho_f} = (1-\nabla_2-\nabla_1) + \frac{\rho_{p2}\nabla_2 + \rho_p\nabla_1}{\rho_f}, \\ \frac{(\rho C_p)_{hnf}}{(\rho C_p)_f} = (1-\nabla_1-\nabla_2) + \frac{(\rho C_p)_{p1}\nabla_1 + (\rho C_p)_{p2}\nabla_2}{(\rho C_p)_f}, \\ \frac{\sigma_{hnf}}{\sigma_f} = 1 + \frac{3\left(\frac{(\nabla_2\sigma_{p2} + \nabla_1\sigma_{p1})}{\sigma_f} - (\nabla_2+\nabla_1)\right)}{2 + \frac{(\nabla_2\sigma_{p2} + \nabla_1\sigma_{p1})}{(\nabla_2+\nabla_1)\sigma_f} - \frac{(\nabla_2\sigma_{p2} + \nabla_1\sigma_{p1})}{\sigma_f} + (\nabla_2+\nabla_1)}, \\ \frac{k_{hnf}}{k_f} = \frac{\frac{(\nabla_2 k_{p2} + \nabla_1 k_{p1})}{(\nabla_2+\nabla_1)} + 2k_f + 2(\nabla_2 k_{p2} + \nabla_1 k_{p1}) - 2(\nabla_2+\nabla_1)k_f}{\frac{(\nabla_2 k_{p2} + \nabla_1 k_{p1})}{(\nabla_2+\nabla_1)} + 2k_f - (\nabla_2 k_{p2} + \nabla_1 k_{p1}) + (\nabla_2+\nabla_1)k_f}. \end{array}\right\} \tag{9}$$

For the aboveproposed model, the similarity variables are defined as

$$u = af'(\eta)x, v = -f(\eta)\sqrt{a\nu_f}, \varphi(\eta) = \frac{C - C_\infty}{C_w - C_\infty}, \theta(\eta) = \frac{T - T_\infty}{T_f - T_\infty},$$
$$\eta = \sqrt{\frac{a}{\nu_f}}y. \tag{10}$$

Using Equation 10, the leading equations are reduced as

$$\frac{A_1}{A_2}f'''(\eta) - (f'(\eta))^2 + f''(\eta)f(\eta) - \frac{A_3}{A_2}M\sin^2(\alpha)f'(\eta)$$
$$- f'(\eta)\frac{A_1}{A_2}\gamma = 0, \tag{11}$$

$$A_4\theta''(\eta) + \left(Rd(\theta(\eta)(\theta_w - 1) + 1)^2(3(\theta'(\eta))^2(\theta_w - 1)\right.$$
$$\left.+(\theta(\eta)(\theta_w - 1) + 1)\theta''(\eta))\right) + A_5\Pr f(\eta)\theta'(\eta) + A_3\Pr Ec M(f'(\eta))^2\sin^2(\alpha)$$
$$+Nb\Pr\varphi'(\eta)\theta'(\eta) + Nt\Pr(\theta'(\eta))^2 + \Pr Q_e\exp(-m\eta) = 0, \tag{12}$$

$$\varphi''(\eta) + \frac{Nt}{Nb}\theta''(\eta) + Scf(\eta)\varphi'(\eta) - ScKr(1 + \delta\theta(\eta))^n$$
$$\exp\left(-\frac{E}{(1 + \delta\theta(\eta))}\right)\varphi(\eta) = 0, \tag{13}$$

$$\left\{\begin{array}{l} f'(\eta) = \lambda, f(\eta) = S, \frac{k_{hnf}}{k_f}\theta'(\eta) = Bi_T(\theta(\eta) - 1), Nt\theta'(\eta) + Nb\varphi'(\eta) = 0 \quad at \quad \eta = 0 \\ f'(\eta) = 0, \varphi(\eta) = 0, \theta(\eta) = 0 \quad \text{as} \quad \eta \to \infty \end{array}\right\}. \tag{14}$$

In the abovementioned equations, the embedded factors are defined as

$$\left\{\begin{array}{l} \Pr = \frac{(\mu C_p)_f}{k_f}, Rd = \frac{16\sigma^* T_\infty^3}{3k_f K^*}, Nb = \frac{(\rho C_p)_p D_B(C_w - C_\infty)}{(\rho C_p)_f \nu_f}, Bi_T = \frac{h_f}{k_f}\sqrt{\frac{\nu_f}{a}}, \\ Kr = \frac{K_r}{a}, Nt = \frac{(\rho C_p)_p D_T(T_f - T_\infty)}{(\rho C_p)_f \nu_f T_\infty}, \gamma = \frac{\mu_f}{aK_p\rho_f}, Sc = \frac{\nu_f}{D_B}, \theta_w = \frac{T_f}{T_\infty}, \delta = \frac{T_w - T_\infty}{T_\infty}, \\ M = \frac{\sigma_f B_0^2}{\rho_f a}, Q_e = \frac{Q}{a(\rho C_p)_f}, Ec = \frac{a^2x^2}{(C_p)_f(T_f - T_\infty)}, S = -\frac{v_w}{\sqrt{a\nu_f}}, E = \frac{E_a}{\kappa T_\infty}. \end{array}\right\} \tag{15}$$

In the abovementioned equations, Rd is the thermal radiation factor, Nb is the Brownian motion parameter, Pr is the Prandtl number, Kr is the chemical factor, Nt is the thermophoretic factor, γ is the porosity factor, Sc is the Schmidt number, Bi_T is the thermal Biot number, Ec is the Eckert number, Q_e is the heat source factor, M is the magnetic parameter, S is the suction/injection factor, E is the activation energy factor, and δ is the temperature difference parameter. Furthermore, A_1, A_2, A_3, A_4, and A_5 are defined as

$$\left\{\begin{array}{l} A_1 = \left[\frac{1}{(1-\nabla_1-\nabla_2)^{2.5}}\right], A_2 = \left[(1-\nabla_1-\nabla_2) + \frac{\rho_p\nabla_1 + \rho_{p2}\nabla_2}{\rho_f}\right], \\ A_5 = \left[(1-\nabla_1-\nabla_2) + \frac{(\rho C_p)_{p1}\nabla_1 + (\rho C_p)_{p2}\nabla_2}{(\rho C_p)_f}\right], \\ A_3 = \left[1 + \frac{3\left(\frac{(\nabla_2\sigma_{p2} + \nabla_1\sigma_{p1})}{\sigma_f} - (\nabla_2+\nabla_1)\right)}{2 + \frac{(\nabla_2\sigma_{p2} + \nabla_1\sigma_{p1})}{(\nabla_1+\nabla_2)\sigma_f} - \frac{(\nabla_2\sigma_{p2} + \nabla_1\sigma_{p1})}{\sigma_f} + (\nabla_2+\nabla_1)}\right], \\ A_4 = \left[\frac{\frac{k_{p1}\nabla_1 + k_{p2}\nabla_2}{\nabla_1+\nabla_2} + 2k_f + 2(k_{p1}\nabla_1 + k_{p2}\nabla_2) - 2(\nabla_1+\nabla_2)k_f}{\frac{k_{p1}\nabla_1 + k_{p2}\nabla_2}{\nabla_1+\nabla_2} + 2k_f - (k_{p1}\nabla_1 + k_{p2}\nabla_2) + (\nabla_1+\nabla_2)k_f}\right]. \end{array}\right\} \tag{16}$$

The quantities of interest such as C_{fx}, Nu_x, and Sh_x are defined as

$$C_{fx} = \frac{\tau_w}{\rho_f (u_w(x))^2}, Nu_x = \frac{xq_w}{k_f\left(T_f - T_\infty\right)}, Sh_x = \frac{xq_m}{D_B\left(C_f - C_\infty\right)}. \tag{17}$$

Here,

$$\tau_w\left(= \mu_{hnf}\frac{\partial u}{\partial y}\bigg|_{y=0}\right), q_w\left(= -k_{hnf}\frac{\partial T}{\partial y}\bigg|_{y=0}\right) + q_r\big|_{y=0}, q_m\left(= -D_B\frac{\partial C}{\partial y}\bigg|_{y=0}\right). \tag{18}$$

Eq. 18 is reduced as

$$C_{fx}\sqrt{\mathrm{Re}_x} = A_1 f''(0), \frac{Nu_x}{\sqrt{\mathrm{Re}_x}} = -A_4\left(1 + Rd\theta_w^3\right)\theta'(0), \frac{Sh_x}{\sqrt{\mathrm{Re}_x}} = -\varphi'(0). \tag{19}$$

Here, $\mathrm{Re}_x = \frac{\hat{u}_w(\hat{x})\hat{x}}{\hat{\nu}_{bf}}$ is the local Reynolds number.

3 Solution by HAM

The initial guesses are described as

$$\left\{\begin{array}{l} f_0(\eta) = (S+\lambda) - \lambda\exp(-\eta) \\ \theta_0(\eta) = \dfrac{Bi_T}{\left(k_{hnf}/k_f\right) + Bi_T}\exp(-\eta) \\ \varphi_0(\eta) = -\dfrac{Nt}{Nb}\theta_0(\eta) \end{array}\right\}. \tag{20}$$

The linear operators are defined as

$$\left\{\begin{array}{l} L_f(\eta) = f(\eta) + f'''(\eta) \\ L_\theta(\eta) = \theta''(\eta) + \theta(\eta) \\ L_\varphi(\eta) = \varphi''(\eta) + \varphi(\eta) \end{array}\right\}, \tag{21}$$

with the following properties:

$$\left\{\begin{array}{l} L_f(Z_1 + Z_2e^{-\eta} + Z_3e^{\eta}) = 0 \\ L_\theta(Z_4e^{-\eta} + Z_5e^{-\eta}) = 0 \\ L_\varphi(Z_6e^{-\eta} + Z_7e^{-\eta}) = 0 \end{array}\right\}, \tag{22}$$

where $Z_1 - Z_7$ are the arbitrary constants. The chart shown in Figure 2 explains the procedure of the homotopy analysis method (Liao, 1999; Liao, 2010).

4 HAM convergence

We are assured of the convergence of the series solution by the homotopy analysis approach. Our series solutions' convergence area is controlled and adjusted by the significant auxiliary parameter ħ. Because of this, we have displayed the ħ−curves in Figure 3. The acceptable value for the velocity profile is $-0.4 \le \hbar_f \le 0.1$, the temperature profile is $-0.41 \le \hbar_\theta \le 0.12$, and the concentration profile is $-0.65 \le \hbar_\varphi \le 0.2$.

5 Results and discussion

This section presents the discussion on the impacts of different embedded factors on the flow profiles of an electrically conducting hybrid nanofluid over an extending surface using a porous medium. The space-dependent heat source, Joule heating, Brownian motion, thermophoresis, thermal radiation, chemical reaction, and activation energy impacts are taken into consideration. Figure 4A shows the influence of the magnetic parameter M on the velocity profile ($f'(\eta)$). It is observed that the increasing M reduces $f'(\eta)$ significantly. Physically, when we increase M, an opposing force in the direction of fluid is created. This force is actually the Lorentz force, which resists the fluid particles' motion. This force slows down the motion of the flow particles and, thus, $f'(\eta)$ reduces. So, the velocity profile reduces with the increasing M. The effect of the suction/injection factor S on the velocity profile $f'(\eta)$ is depicted in Figure 4B. When $S > 0$, $f'(\eta)$ decreases. The heated fluid is physically forced away from the surface by the increased blowing factor, which causes the viscosity to drop and the fluid to accelerate. The momentum boundary layer is, however, thinned by the wall suction $S > 0$, which imposes a drag force near the surface. The impact of λ on the velocity profile $f'(\eta)$ is shown in Figure 4C. $f'(\eta)$ shows increasing conduct *via* λ. This is due to the fact that increasing λ decreases the viscous influence on the flow. As a result, rising

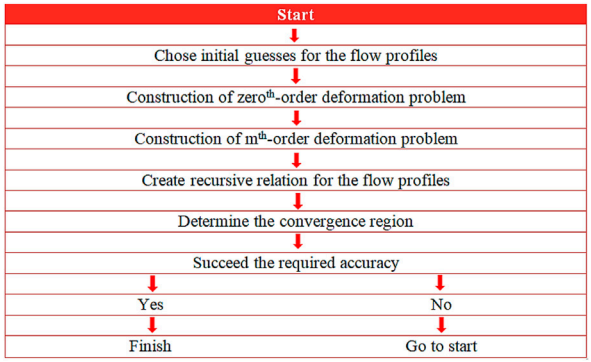

FIGURE 2
Flow chart of HAM.

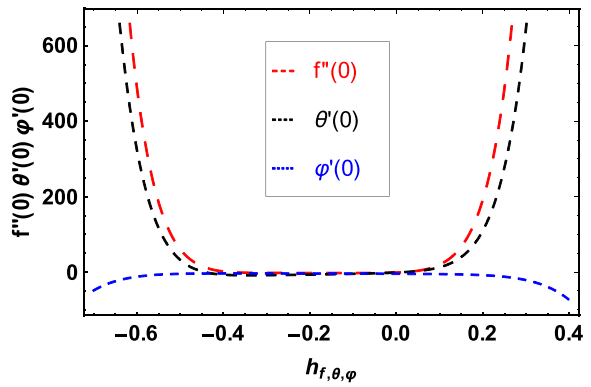

FIGURE 3
ħ−curves of $f''(0)$, $\theta'(0)$, and $\varphi'(0)$.

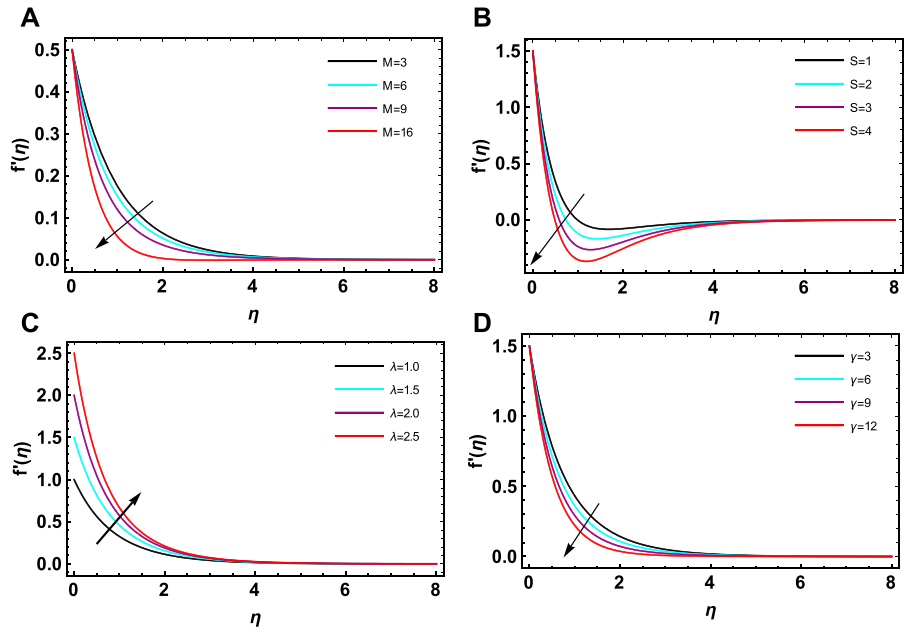

FIGURE 4
Impact of M on $f'(\eta)$. Impact of S on $f'(\eta)$. Impact of λ on $f'(\eta)$. Impact of γ on $f'(\eta)$.

λ reduces the thickness of the momentum boundary layer, and hence, $f'(\eta)$ increases. The effect of the porosity factor γ on $f'(\eta)$ is shown in Figure 4D. It has been seen that $f'(\eta)$ reduces with the upsurge in γ. This causes the motion of the fluid to reduce, which consequently reduces the thickness of the velocity boundary layer. So, $f'(\eta)$ declines with the inclement in γ. The consequence of M over the temperature profile $\theta(\eta)$ is shown in Figure 5A. According to this figure, the impact of the magnetic parameter results in the rise of $\theta(\eta)$ as M increases. It is also important to note that the application of M has a positive impact on the thickness of thermal boundary layers because the thickness increases in the presence of M. Figure 5B depicts how the injection/suction factor S affects the temperature profile $\theta(\eta)$. It is understandable that when S increases, the thickness of the thermal boundary layer decreases. In addition, the rate of deformation from the wall towards the fluid accelerates with the increasing S. The effect of the Brownian motion factor Nb on $\theta(\eta)$ is displayed in Figure 5C. Increasing Nb improves $\theta(\eta)$. Additionally, Nb has an increasing effect on the thermal boundary layer. According to the definition, when Nb grows, $\theta(\eta)$ rises because the fluid particles have more kinetic energy. The influence of Nt on $\theta(\eta)$ is shown in Figure 5D. From Figure 5D, we can see that $\theta(\eta)$ increases due to the rising Nt. Figure 5E displays the variation in the temperature profile $\theta(\eta)$ due to Ec. It is seen that $\theta(\eta)$ rises as Ec increases. To understand the thermal performance of fluid flow, Ec is important. By raising Ec, the rising intermolecular interaction will increase the kinetic energy, which will increase $\theta(\eta)$ and allow Ec to be utilized as a hot agent. Figure 5F and Figure 5G show how the radiation factor Rd and the temperature ratio factor θ_w affect the temperature profile $\theta(\eta)$. By increasing θ_w and Rd, the fluid temperature rises significantly. Physically, the fluid particles are supported and activated by the rise in θ_w and Rd as a result of obtaining thermal energy. The temperature of the boundary layer rises as a result of this. Increasing the thermal diffusion and thermal distribution, in turn, causes the boundary layer thickness to grow and its temperature to rise. Figure 5H shows how the temperature profile $\theta(\eta)$ is influenced by the space-dependent heat source parameter Q_e. $\theta(\eta)$ increases when we raise Q_e. Physically, when$Q_e > 0$, the thermal boundary layer produces energy which causes augmentation in $\theta(\eta)$. Figure 5I illustrates the influence of the thermal Biot number Bi_T on the temperature profile $\theta(\eta)$. When Bi_T increases, $\theta(\eta)$ also increases. Physically, an enhancement in Bi_T results in more supported convection, which causes the increasing conduct in $\theta(\eta)$. Therefore, higher values of Bi_T increase the thermal boundary layer thickness, which, in turn, results in higher $\theta(\eta)$. The influence of Nb on the concentration profile $\varphi(\eta)$ is shown in Figure 6A. $\varphi(\eta)$ significantly decreases with higher values of Nb. Physically, the increasing Nb produces the random movement of the nanoparticles in fluid; as a result, $\varphi(\eta)$ reduces. Figure 6B portrays the impact of the thermophoresis factor Nt on $\varphi(\eta)$. It is observed that the increasing Nt increases $\varphi(\eta)$. Physically, a rise in Nt is followed by an upsurge in the thermal energy, which promotes the liquid's temperature. As a result, the kinetic energy increases, and more collisions happen, which is enough to make the distribution of the concentration of nanoparticles large under the influence of Nt. The effect of activation energy E on the concentration profile $\varphi(\eta)$ is seen in Figure 6C. $\varphi(\eta)$ increases when E increases. Increasing values of E diverge from the modified Arrhenius function, which increases the rate of generative chemical reactions. The concentration is increased as a result. The impact of the Schmidt number Sc on the concentration profile $\varphi(\eta)$ is exhibited in Figure 6D. $\varphi(\eta)$ decreases as Sc increases. The concentration boundary layer gets thinner because higher values of

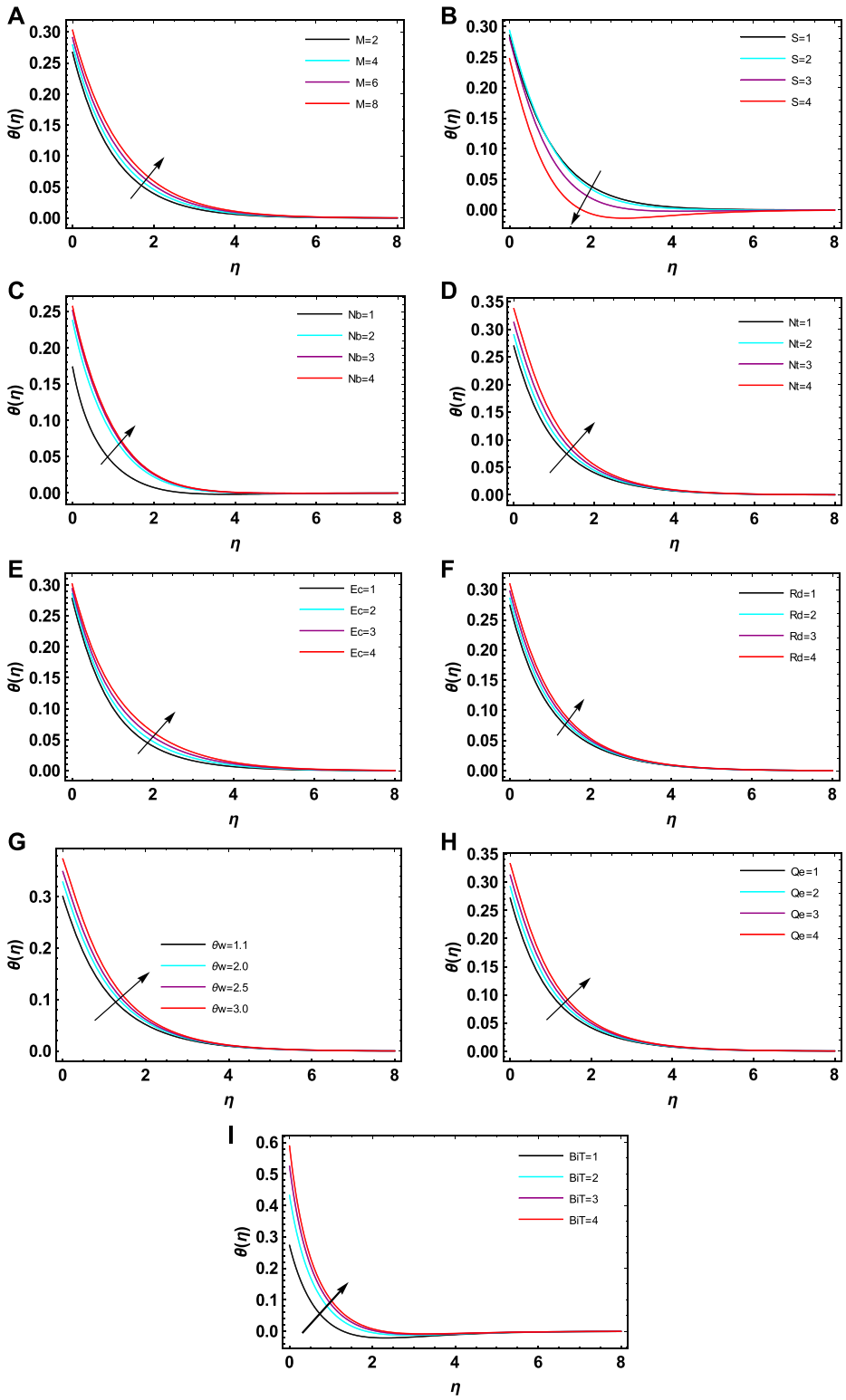

FIGURE 5
(A) Impact of *M* on θ(η). **(B)** Impact of *S* on θ(η). **(C)** Impact of *Nb* on θ(η). **(D)** Impact of *Nt* on θ(η). **(E)** Impact of *Ec* on θ(η). **(F)** Impact of *Rd* on θ(η). **(G)** Impact of θ_w on θ(η). **(H)** Impact of Q_e on θ(η). **(I)** Impact of Bi_T on θ(η).(a)(b)

TABLE 1 Thermophysical properties of the base fluid and nanoparticles (Acharya, 2021).

Base fluid/nanoparticles	$\widehat{\rho}[kgm^{-3}]$	$\widehat{C}_p[Jkg^{-1}K^{-1}]$	$\widehat{k}[Wm^{-1}K^{-1}]$	$\widehat{\sigma}[\Omega^{-1}m^{-1}]$
H_2O	997	4180	0.6071	0.05
Fe_3O_4	5180	670	9.7	25000
GO	2250	2100	2500	1×107

TABLE 2 Numerical comparison of the present results of $-\theta'(0)$ with published results for different values of Pr.

Pr	0.07	0.2	0.7	2.0	7.0
Reddy Gorla and Sidawi (1994)	0.0656	0.1691	0.4539	0.9114	1.8905
Hamad (2011)	0.06565	0.16909	0.45391	0.91136	1.89540
Present analysis	0.0655603	0.1690911	0.4539129	0.9113608	1.8954075

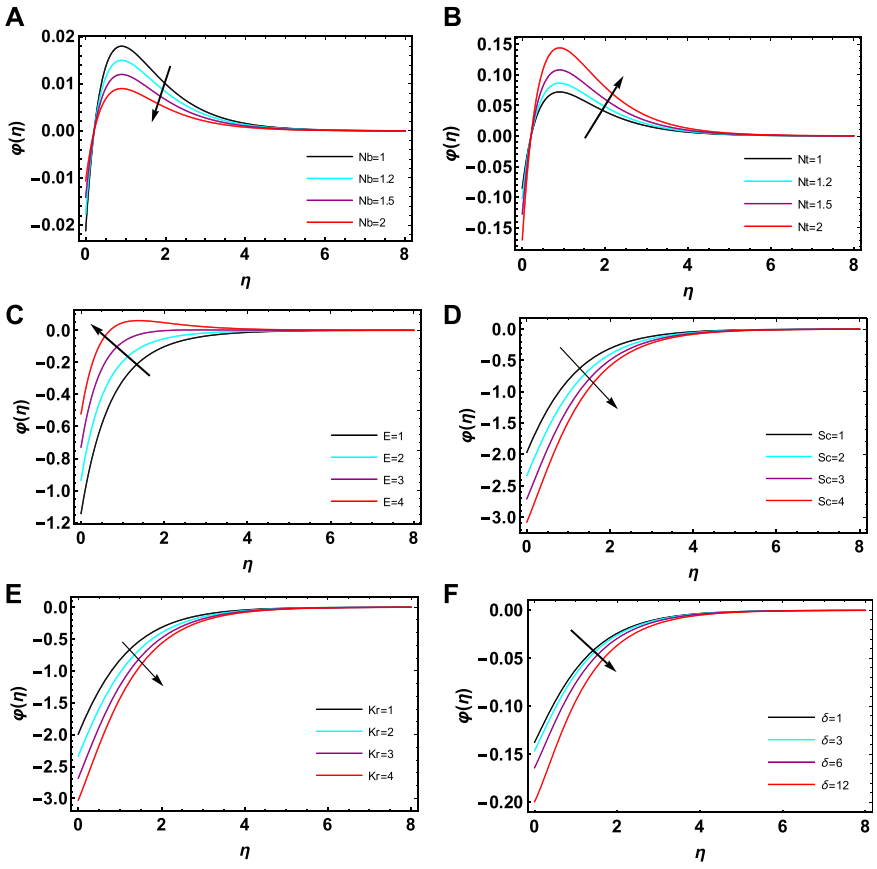

FIGURE 6
(A) Impact of *Nb* on $\varphi(\eta)$. **(B)** Impact of *Nt* on $\varphi(\eta)$. **(C)** Impact of *E* on $\varphi(\eta)$. **(D)** Impact of *Sc* on $\varphi(\eta)$. **(E)** Impact of *Kr* on $\varphi(\eta)$. **(F)** Impact of δ on $\varphi(\eta)$.

Sc result in a faster mass transfer rate. So, $\varphi(\eta)$ shows a decreasing impact against *Sc*. Figure 6E shows how the chemical reaction factor *Kr* affects the concentration profile $\varphi(\eta)$. It is obvious that $\varphi(\eta)$ decreases as *Kr* increases. The effect of the temperature difference parameter δ on the concentration profile $\varphi(\eta)$ is seen in Figure 6F. $\varphi(\eta)$ shows diminishing behavior when the temperature difference values are increased. Physically, a greater δ causes a decrease in molecular diffusivity, which lowers $\varphi(\eta)$. Table 1 shows the thermophysical

TABLE 3 Numerical values of skin friction for different values of M and λ.

M	λ	C_{fx}
0		2.66295
2		3.592403
4		4.361124
6		5.013328
0.5	0.5	2.884460
	0.7	3.037357
	1.5	3.584330
	2	3.887307

TABLE 4 Numerical value of the Nusselt number for different values of Rd, θ_w, Bi_T, M, and λ.

Rd	θ_w	Bi_T	M	λ	Nu_x
0					0.223108
0.5					0.217800
1					0.212663
	1.1				0.219903
	2				0.213570
	3				0.199832
		0.8			0.317610
		1.6			0.507121
		2.4			0.631193
			0		0.229551
			2		0.218854
			4		0.211617
				0.5	0.218854
				1.5	0.230718
				2.5	0.237256

properties of the base fluid and nanoparticles. The comparison of the present results with published results are shown in Table 2. The values of C_{fx} are shown in Table 3 for different stretching ratio parameters λ and magnetic field parameters M. We determined the negative values for C_{fx}. When friction force is negative, it indicates that the sheet is causing the fluid to move more slowly. In terms of quality, the effects of λ and M on C_{fx} caused by the flow are equivalent. In other words, C_{fx} is the decreasing function of M and λ. The numerical values of the Nusselt number Nu_x and Sherwood number Sh_x are shown in Tables 4 and Table 5 for various values of Rd, θ_w, Bi_T, M, and λ. Nu_x, in this case, increases for high values of Bi_T and λ while decreasing for larger values of Rd, θ_w, and M. Sh_x is the increasing function of Bi_T, and M is a decreasing function of Rd, θ_w, and λ.

TABLE 5 Numerical value of the Sherwood number for different values of Rd, θ_w, Bi_T, M, and λ.

Rd	θ_w	Bi_T	M	λ	Sh_x
0					0.917714
0.5					0.918590
1					0.919767
	1.1				0.918178
	2				0.919489
	3				0.922369
		0.8			0.902139
		1.6			0.871120
		2.4			0.850935
			0		1.038050
			2		0.919386
			4		0.836986
				0.5	0.918386
				1.5	1.245928
				2.5	1.511233

6 Conclusion

In this article, the authors have presented an electrically conducting hybrid nanofluid flow over an extending surface using a porous medium. The homotopic approach is tackled for the solution of the modeled equations. The space-dependent heat source, Joule heating, Brownian motion, thermophoresis, thermal radiation, and chemically reactive activated energy impacts are used. The following are the concluding points of this study:

- The growing magnetic and suction factors reduced the velocity profiles, while they enlarged the thermal profiles by magnetic factor. Additionally, the suction factor has a reducing impression on the thermal profile.
- Motion of the fluid reduced with the increasing porosity factor, while it increased with the increasing stretching factor.
- The thermal profiles increased with the increasing thermal Biot number, Eckert number, thermophoresis, space-based heat source, Brownian motion, and non-linear thermal radiation factors.
- The concentration profiles reduced with the increasing Brownian motion, chemical reaction, and temperature difference factors, while they were increased by the activation energy factor.
- The magnetic and stretching factors augmented the surface drag coefficient.
- The Nusselt numbers increased with the increasing thermal Biot number and stretching factor, while they reduced with the

increasing thermal radiation and temperature difference factors.

- The Sherwood numbers increased with the thermal Biot number and magnetic factor, while they reduced with the increasing thermal radiation, temperature difference, and stretching factors.

Data availability statement

The original contributions presented in the study are included in the article/Supplementary Material; further inquiries can be directed to the corresponding author.

Author contributions

EA and SL: conceptualization, methodology, software reviewing, and editing. ZR: data curation and writing—original draft preparation. SE: visualization and investigation. AS: software, validation, and supervision. AG: writing—reviewing and editing.

Acknowledgments

The author ZR extends her appreciation to the Deanship of Scientific Research at King Khalid University, Abha, Saudi Arabia, for funding this work through the Research Group Project under Grant Number RGP.1/334/43.

Conflict of interest

The authors declare that the research was conducted in the absence of any commercial or financial relationships that could be construed as a potential conflict of interest.

Publisher's note

All claims expressed in this article are solely those of the authors and do not necessarily represent those of their affiliated organizations, or those of the publisher, the editors, and the reviewers. Any product that may be evaluated in this article, or claim that may be made by its manufacturer, is not guaranteed or endorsed by the publisher.

References

Abbas, A., Jeelani, M. B., and Alharthi, N. H. (2022). Darcy–Forchheimer relation influence on MHD dissipative third-grade fluid flow and heat transfer in porous medium with joule heating effects: A numerical approach. *Processes* 10, 906. doi:10.3390/pr10050906

Acharya, N., Mabood, F., Shahzad, S. A., and Badruddin, I. A. (2022). Hydrothermal variations of radiative nanofluid flow by the influence of nanoparticles diameter and nanolayer. *Int. Commun. Heat. Mass Transf.* 130, 105781. doi:10.1016/J.ICHEATMASSTRANSFER.2021.105781

Acharya, N. (2021). Spectral quasi linearization simulation on the hydrothermal behavior of hybrid nanofluid spraying on an inclined spinning disk. *Partial Differ. Equations Appl. Math.* 4, 100094. doi:10.1016/J.PADIFF.2021.100094

Adnan, W. Ashraf (2022). Numerical thermal featuring in γAl2O3-C2H6O2 nanofluid under the influence of thermal radiation and convective heat condition by inducing novel effects of effective Prandtl number model (EPNM). *Adv. Mech. Eng.* 14, 168781322211065. doi:10.1177/16878132221106577

Alrabaiah, H., Bilal, M., Khan, M. A., Muhammad, T., and Legas, E. Y. (2022). Parametric estimation of gyrotactic microorganism hybrid nanofluid flow between the conical gap of spinning disk-cone apparatus. *Sci. Rep.* 12, 59–14. doi:10.1038/s41598-021-03077-2

Akbar, N. S., Maraj, E. N., Noor, N. F. M., and Habib, M. B. (2022). Exact solutions of an unsteady thermal conductive pressure driven peristaltic transport with temperature-dependent nanofluid viscosity. *Case Stud. Therm. Eng.* 35, 102124. doi:10.1016/j.csite.2022.102124

Akram, J., Akbar, N. S., and Tripathi, D. (2021). A theoretical investigation on the heat transfer ability of water-based hybrid (Ag–Au) nanofluids and Ag nanofluids flow driven by electroosmotic pumping through a microchannel. *Arab. J. Sci. Eng.* 46, 2911–2927. doi:10.1007/s13369-020-05265-0

Akram, J., Akbar, N. S., Alansari, M., and Tripathi, D. (2022). Electroosmotically modulated peristaltic propulsion of TiO2/10W40 nanofluid in curved microchannel. *Int. Commun. Heat. Mass Transf.* 136, 106208. doi:10.1016/j.icheatmasstransfer.2022.106208

Asjad, M. I., Zahid, M., Inc, M., Baleanu, D., and Almohsen, B. (2022). Impact of activation energy and MHD on Williamson fluid flow in the presence of bioconvection. *Alex. Eng. J.* 61, 8715–8727. doi:10.1016/j.aej.2022.02.013

Bejawada, S. G., Reddy, Y. D., Jamshed, W., Nisar, K. S., Alharbi, A. N., and Chouikh, R. (2022). Radiation effect on MHD Casson fluid flow over an inclined non-linear surface with chemical reaction in a Forchheimer porous medium. *Alex. Eng. J.* 61, 8207–8220. doi:10.1016/j.aej.2022.01.043

Bhatti, M. M., Arain, M. B., Zeeshan, A., Ellahi, R., and Doranehgard, M. H. (2022). Swimming of Gyrotactic Microorganism in MHD Williamson nanofluid flow between rotating circular plates embedded in porous medium: Application of thermal energy storage. *J. Energy Storage.* 45, 103511. doi:10.1016/j.est.2021.103511

Bilal, M., Saeed, A., Gul, T., Kumam, W., Mukhtar, S., and Kumam, P. (2022). Parametric simulation of micropolar fluid with thermal radiation across a porous stretching surface. *Sci. Rep.* 12, 2542–2611. doi:10.1038/s41598-022-06458-3

Choi, S. U. S., and Eastman, J. A. (1995). "Enhancing thermal conductivity of fluids with nanoparticles," in Proceedings of the Int. Mech. Eng. Congr. Exhib, San Fr. CA, United States, 12-17 Nov 1995.

Chu, Y., Bashir, S., Ramzan, M., and Malik, M. Y. (2022). Model-based comparative study of magnetohydrodynamics unsteady hybrid nanofluid flow between two infinite parallel plates with particle shape effects. *Math. Methods Appl. Sci.* 22, 8234. doi:10.1002/mma.8234

Dawar, A., Islam, S., Shah, Z., Mahmuod, S. R., and Lone, S. A. (2022). Dynamics of inter-particle spacing, nanoparticle radius, inclined magnetic field and nonlinear thermal radiation on the water-based copper nanofluid flow past a convectively heated stretching surface with mass flux condition: A strong suction case. *Int. Commun. Heat. Mass Transf.* 137, 106286. doi:10.1016/j.icheatmasstransfer.2022.106286

Dawar, A., Said, N. M., Islam, S., Shah, Z., Mahmuod, S. R., and Wakif, A. (2022). A semi-analytical passive strategy to examine a magnetized heterogeneous mixture having sodium alginate liquid with alumina and copper nanomaterials near a convectively heated surface of a stretching curved geometry. *Int. Commun. Heat. Mass Transf.* 139, 106452. doi:10.1016/j.icheatmasstransfer.2022.106452

Guedri, K., Khan, A., Sene, N., Raizah, Z., Saeed, A., and Galal, A. M. (2022). Thermal flow for radiative ternary hybrid nanofluid over nonlinear stretching sheet subject to Darcy–forchheimer phenomenon. *Math. Probl. Eng.* 2022, 1–14. doi:10.1155/2022/3429439

Hamad, M. A. A. (2011). Analytical solution of natural convection flow of a nanofluid over a linearly stretching sheet in the presence of magnetic field. *Int. Commun. Heat. Mass Transf.* 38, 487–492. doi:10.1016/j.icheatmasstransfer.2010.12.042

Habib, M. B., and Akbar, N. S. (2021). New trends of nanofluids to combat *Staphylococcus aureus* in clinical isolates. *J. Therm. Anal. Calorim.* 143, 1893–1899. doi:10.1007/s10973-020-09502-4

Hussain, S. M., Jamshed, W., Pasha, A. A., Adil, M., and Akram, M. (2022). Galerkin finite element solution for electromagnetic radiative impact on viscid Williamson two-phase nanofluid flow via extendable surface. *Int. Commun. Heat. Mass Transf.* 137, 106243. doi:10.1016/j.icheatmasstransfer.2022.106243

Ibrahim, M., Saeed, T., and Zeb, S. (2022). Numerical simulation of time-dependent two-dimensional viscous fluid flow with thermal radiation. *Eur. Phys. J. Plus.* 137, 609. doi:10.1140/epjp/s13360-022-02813-5

Khan, A., Saeed, A., Gul, T., Mukhtar, S., Ali, I., and Jawad, M. (2021). Radiative swirl motion of hydromagnetic Casson nanofluid flow over rotary cylinder using Joule dissipation impact. *Phys. Scr.* 96, 045206. doi:10.1088/1402-4896/abdf83

Khan, A., Hassan, B., Ashraf, E. E., and Shah, S. Y. A. (2022). Thermally dissipative micropolar hybrid nanofluid flow over a spinning needle influenced by Hall current and gyrotactic microorganisms. *Heat. Transf.* 51, 1170–1192. doi:10.1002/htj.22347

Khan, S. A., Khan, M. I., Alsallami, S. A. M., Alhazmi, S. E., Alharbi, F. M., and El-Zahar, E. R. (2022). Irreversibility analysis in hydromagnetic flow of Newtonian fluid with joule heating: Darcy-forchheimer model. *J. Pet. Sci. Eng.* 212, 110206. doi:10.1016/j.petrol.2022.110206

Kodi, R., and Mopuri, O. (2022). Unsteady MHD oscillatory Casson fluid flow past an inclined vertical porous plate in the presence of chemical reaction with heat absorption and Soret effects. *Heat. Transf.* 51, 733–752. doi:10.1002/htj.22327

Kumar, D., Sinha, S., Sharma, A., Agrawal, P., and Kumar Dadheech, P. (2022). Numerical study of chemical reaction and heat transfer of MHD slip flow with Joule heating and Soret–Dufour effect over an exponentially stretching sheet. *Heat. Transf.* 51, 1939–1963. doi:10.1002/htj.22382

Liao, S.-J. (1999). An explicit, totally analytic approximate solution for Blasius' viscous flow problems. *Int. J. Non. Linear. Mech.* 34, 759–778. doi:10.1016/s0020-7462(98)00056-0

Lone, S. A., Alyami, M. A., Saeed, A., Dawar, A., Kumam, P., and Kumam, W. (2022). MHD micropolar hybrid nanofluid flow over a flat surface subject to mixed convection and thermal radiation. *Sci. Rep.* 12, 17283–17314. doi:10.1038/s41598-022-21255-8

Liao, S. (2010). An optimal homotopy-analysis approach for strongly nonlinear differential equations. *Commun. Nonlinear Sci. Numer. Simul.* 15, 2003–2016. doi:10.1016/J.CNSNS.2009.09.002

Mahabaleshwar, U. S., Vishalakshi, A. B., and Hatami, M. (2022). MHD micropolar fluid flow over a stretching/shrinking sheet with dissipation of energy and stress work considering mass transpiration and thermal radiation. *Int. Commun. Heat. Mass Transf.* 133, 105966. doi:10.1016/j.icheatmasstransfer.2022.105966

Maraj, E. N., Akbar, N. S., Iqbal, Z., and Azhar, E. (2017). Framing the MHD mixed convective performance of CNTs in rotating vertical channel inspired by thermal deposition: Closed form solutions. *J. Mol. Liq.* 233, 334–343. doi:10.1016/j.molliq.2017.03.041

Nagendramma, V., Durgaprasad, P., Sivakumar, N., Rao, B. M., Raju, C. S. K., Shah, N. A., et al. (2022). Dynamics of triple diffusive free convective MHD fluid flow: Lie Group transformation. *Mathematics* 10, 2456. doi:10.3390/math10142456

Nazeer, M., Hussain, F., Khan, M. I., El-Zahar, E. R., Chu, Y.-M., Malik, M. Y., et al. (2022). Retracted: Theoretical study of MHD electro-osmotically flow of third-grade fluid in micro channel. *Appl. Math. Comput.* 420, 126868. doi:10.1016/j.amc.2021.126868

Ramesh, G. K., Madhukesh, J. K., Shah, N. A., and Yook, S.-J. (2022). Flow of hybrid CNTs past a rotating sphere subjected to thermal radiation and thermophoretic particle deposition. *Alex. Eng. J.* 64, 969–979. doi:10.1016/j.aej.2022.09.026

Rasheed, H. U., Khan, W., Khan, I., Alshammari, N., and Hamadneh, N. (2022). Numerical computation of 3D Brownian motion of thin film nanofluid flow of convective heat transfer over a stretchable rotating surface. *Sci. Rep.* 12, 1–14.

Rehman, K. U., Shatanawi, W., and Al-Mdallal, Q. M. (2022). A comparative remark on heat transfer in thermally stratified MHD Jeffrey fluid flow with thermal radiations subject to cylindrical/plane surfaces. *Case Stud. Therm. Eng.* 32, 101913. doi:10.1016/j.csite.2022.101913

Reddy Gorla, R. S., and Sidawi, I. (1994). Free convection on a vertical stretching surface with suction and blowing. *Appl. Sci. Res.* 52, 247–257. doi:10.1007/bf00853952

Reddy, S. R. R., Reddy, P. B. A., and Chamkha, A. J. (2020). Heat transfer analysis OFMHD CNTS nanofluid flow over a stretching sheet. *Spec. Top. Rev. Porous Media Int. J.* 11, 133–147. doi:10.1615/specialtopicsrevporousmedia.2020030647

Salahuddin, T., Siddique, N., Khan, M., and Chu, Y. (2022). A hybrid nanofluid flow near a highly magnetized heated wavy cylinder. *Alex. Eng. J.* 61, 1297–1308. doi:10.1016/j.aej.2021.06.014

Saleem, A., Akhtar, S., and Nadeem, S. (2022). Bio-mathematical analysis of electro-osmotically modulated hemodynamic blood flow inside a symmetric and nonsymmetric stenosed artery with joule heating. *Int. J. Biomath.* 15, 2150071. doi:10.1142/s1793524521500716

Shah, Z., Khan, A., Khan, W., Alam, M. K., Islam, S., Kumam, P., et al. (2020). Micropolar gold blood nanofluid flow and radiative heat transfer between permeable channels. *Comput. Methods Programs Biomed.* 186, 105197. doi:10.1016/j.cmpb.2019.105197

Shaw, S., Samantaray, S., Misra, A., Nayak, M. K., and Makinde, O. D. (2022). Hydromagnetic flow and thermal interpretations of Cross hybrid nanofluid influenced by linear, nonlinear and quadratic thermal radiations for any Prandtl number. *Int. Communiction Heat Mass Transf.* 130, 105816. doi:10.1016/j.icheatmasstransfer.2021.105816

Shamshuddin, M. D., and Eid, M. R. (2022). Nth order reactive nanoliquid through convective elongated sheet under mixed convection flow with joule heating effects. *J. Therm. Anal. Calorim.* 147, 3853–3867. doi:10.1007/s10973-021-10816-0

Sharma, K., Kumar, S., Narwal, A., Mebarek-Oudina, F., and Animasaun, I. L. (2022). Convective MHD fluid flow over stretchable rotating disks with dufour and Soret effects. *Int. J. Appl. Comput. Math.* 8, 159–212. doi:10.1007/s40819-022-01357-7

Usman, M., Gul, T., Khan, A., Alsubie, A., and Ullah, M. Z. (2021). Electromagnetic couple stress film flow of hybrid nanofluid over an unsteady rotating disc. *Int. Commun. Heat. Mass Transf.* 127, 105562. doi:10.1016/j.icheatmasstransfer.2021.105562

Venkata Ramudu, A. C., Anantha Kumar, K., Sugunamma, V., and Sandeep, N. (2022). Impact of Soret and Dufour on MHD Casson fluid flow past a stretching surface with convective–diffusive conditions. *J. Therm. Anal. Calorim.* 147, 2653–2663. doi:10.1007/s10973-021-10569-w

Wahid, N. S., Arifin, N. M., Pop, I., Bachok, N., and Hafidzuddin, M. E. H. (2022). MHD stagnation-point flow of nanofluid due to a shrinking sheet with melting, viscous dissipation and Joule heating effects. *Alex. Eng. J.* 61, 12661–12672. doi:10.1016/j.aej.2022.06.041

Waqas, M., Sadiq, M. A., and Bahaidarah, H. M. S. (2022). Gyrotactic bioconvection stratified flow of magnetized micropolar nanoliquid configured by stretchable radiating surface with Joule heating and viscous dissipation. *Int. Commun. Heat. Mass Transf.* 138, 106229. doi:10.1016/j.icheatmasstransfer.2022.106229

Waseem, M., Gul, T., Khan, I., Khan, A., Saeed, A., Ali, I., et al. (2021). Gravity-driven hydromagnetic flow of couple stress hybrid nanofluid with homogenous-heterogeneous reactions. *Sci. Rep.* 11, 17498–17512. doi:10.1038/s41598-021-97045-5

Xie, Z., Jiao, J., and Yang, K. (2023). Theoretical and experimental study on the fluid-structure-acoustic coupling dynamics of a new water lubricated bearing. *Tribol. Int.* 177, 107982. doi:10.1016/j.triboint.2022.107982

Xie, Z., Jiao, J., and Wrona, S. (2023). The fluid-structure interaction lubrication performances of a novel bearing: Experimental and numerical study. *Tribol. Int.* 179, 108151. doi:10.1016/j.triboint.2022.108151

Xuan, X. (2022). Review of nonlinear electrokinetic flows in insulator-based dielectrophoresis: From induced charge to Joule heating effects. *Electrophoresis* 43, 167–189. doi:10.1002/elps.202100090

Yaseen, M., Rawat, S. K., Shafiq, A., Kumar, M., and Nonlaopon, K. (2022). Analysis of heat transfer of mono and hybrid nanofluid flow between two parallel plates in a Darcy porous medium with thermal radiation and heat generation/absorption. *Symmetry (Basel)* 14, 1943. doi:10.3390/sym14091943

Zhang, L., Bhatti, M. M., Michaelides, E. E., Marin, M., and Ellahi, R. (2022). Hybrid nanofluid flow towards an elastic surface with tantalum and nickel nanoparticles, under the influence of an induced magnetic field. *Eur. Phys. J. Spec. Top.* 231, 521–533. doi:10.1140/epjs/s11734-021-00409-1

Nomenclature

a Constant

B_0 Magnetic field strength

$(C_p)_f$, $(C_p)_{hnf}$ Specific heat for the base fluid and hybrid nanofluid

D_B, D_T Brownian and thermophoresis diffusion coefficients

h_f Thermal transmission coefficient

k_p, k_f, k_{hnf} Thermal conductivities of the nanoparticles, base fluid, and hybrid nanofluid

K_p Permeability of the porous medium

Q Heat source coefficient

q_m Mass flux at the surface

q_w, q_r Surface and radiative heat fluxes

T_f, T_w, T_∞ Reference, wall, and ambient temperatures

u, v Velocity component

x, y Coordinates

τ_w Shear stress

λ Stretching parameter

$(\rho C_p)_p$, $(\rho C_p)_f$, $(\rho C_p)_{hnf}$ Heat capacitance of the nanoparticles, base fluid, and hybrid nanofluid

μ_p, μ_f, μ_{hnf} Dynamic viscosities of the nanoparticles, base fluid, and hybrid nanofluid

ρ_p, ρ_f, ρ_{hnf} Densities of the nanoparticles, base fluid, and hybrid nanofluid

σ_p, σ_f, σ_{hnf} Electrical conductivities of the nanoparticles, base fluid, and hybrid nanofluid

α Angle of inclination

$\mathbf{\nabla}_1$, $\mathbf{\nabla}_2$ Volumetric fraction of the first and second nanoparticle

Pr Prandtl number

Rd Radiation factor

Nb Brownian motion factor

Nt Thermophoretic factor

Kr Chemical factor

γ Porosity factor

Sc Schmidt number

Bi_T Thermal Biot number

M Magnetic factor

Q_e Exponential heating factor

Ec Eckert number

θ_w Thermal difference factor

E Activation energy factor

δ Temperature difference parameter

frontiers | Frontiers in Materials

TYPE Original Research
PUBLISHED 07 March 2023
DOI 10.3389/fmats.2023.1138249

OPEN ACCESS

EDITED BY
Mustafa Inc,
Firat University, Türkiye

REVIEWED BY
Zailan Siri,
University of Malaya, Malaysia
Mustafa Turkyilmazoglu,
Hacettepe University, Türkiye

*CORRESPONDENCE
Zareen A. Khan,
zakhan@pnu.edu.sa

SPECIALTY SECTION
This article was submitted to Colloidal Materials and Interfaces, a section of the journal Frontiers in Materials

RECEIVED 05 January 2023
ACCEPTED 22 February 2023
PUBLISHED 07 March 2023

CITATION
Ullah N, Khan Marwat DN and Khan ZA (2023), Analysis of unsteady thin film flows over the porous and moving surfaces of variable thickness: Unsteady and non-linear kinematics of sheet. *Front. Mater.* 10:1138249. doi: 10.3389/fmats.2023.1138249

Analysis of unsteady thin film flows over the porous and moving surfaces of variable thickness: Unsteady and non-linear kinematics of sheet

Naeem Ullah[1], Dil Nawaz Khan Marwat[1] and Zareen A. Khan[2]*

[1]Department of Mathematics, Faculty of Technologies and Engineering Sciences, Islamia College Peshawar, University Campus, Peshawar, Pakistan, [2]Department of Mathematical Sciences, College of Science, Princess Nourah bint Abdulrahman University, Riyadh, Saudi Arabia

Thin film flows over porous and moving sheets of variable thickness have been reconsidered here. New and multiple dimensions of classical problems of such type flow are analyzed. Here, we categorically emphasized on the nature and kinds of injection (suction) and moving velocities of the sheet, whereas, variable size of the sheet is also taken into account. We formed and investigated different cases and checked different options for kinematics of sheet, variable sizes of thin film and that of sheet. All possible cases of exact similarities are noticed by which the system of partial differential equations and boundary conditions are exactly transformed into ordinary differential equations. The final systems of exact equations are solved by **bvp4c** technique. The present simulations are exactly matched with the previously published analyses for special choices of functions and parameters. Strict behavioral changes have been observed in the velocity profiles by changing the nature of sheet's kinematics.

KEYWORDS

stretching/shrinking and porous sheet, unsteady flow of thin film, sheet of variable thickness, injection/suction, deformation of thin film

1 Introduction

The global nature of thin film and its technological uses have been identified in many physical and engineering problems. Therefore, the understanding of its mechanics is important in many applications. Most of the industrial systems and the different processes associated with them have been explained through concepts of on thin film flow. The thin film technology is the foundation of amazing development in solid state electronics. Therefore, the scientists worked hard and ascertained the usefulness of the optical properties of metal films, its technical advantages and the human interests associated with the characteristics of two dimensional solid, whereas, it has vast applications in industry and technology of thin films. A typical thin film flow consists of an expanse of metals, partially bounded by a solid or gas or liquid substrate with a (free) surface where the metals such as the liquids are exposed to another fluid (usually a gas and most often air in applications). Stretching/shrinking problem of thin film has one of the most common and stringent applications in industries. On the other hand, shrinking films are widely used for packing of industrial products in factories, whereas, unwanted heat is also produced during this phenomenon and

in most cases, it does not affect the flow mechanism during the flow processes. Furthermore, shrinking phenomenon has been frequently used for analyzing the flow in small and narrow pores in order to measure the capillary effects during osmosis processes. The shrinking and swelling properties of agricultural clay soil and boilers are most serious issues, therefore, the most relevant and significant variations in hydraulic and mechanical properties of these soils will eventually disturb the flow, transport and thermodynamics behaviors, whereas, agricultural progresses and environmental improvements are not possible without the perfect simulations of such circumstances. Thin film flow has played significant role in many physical problems of human uses. Most of the engineering systems are composed of heat exchangers, which are commonly used for cooling of machineries, devices and surfaces, as well as it also plays significant role in lubrication processes between small rotating parts, to coat sheets, walls and surfaces and to clean see water by removing oil slicks from it. The formation of tear film in the eyes and mucus linings of the airways and lungs are the uses of thin film flow in biological systems. A thin film is a layer of material ranging from fractions of a nanometer (monolayer) to several micrometers in thickness. Thin films are used for the coating of the household mirror which typically has a thin metal coating on the back of the glass to form a reflective interface.Certainly, we provided concrete investigations of thin film flow over surfaces through which injection and suction can take place, whereas, we came across the evidences where stretching and shrinking flow contribute to such flow. Furthermore, we also emphasized that thin film flow maintained on surfaces of a variable thickness. More specifically, we presented the detailed history and the latest developments in the analysis of thin film flows. Sakiadis (Sakiadis, 1961a; Sakiadis, 1961b) solved a modeled problem of fluid motion maintained over a stretching plate, whereas, the sheet moved with a constant speed. A new model of variable stretching velocity is presented by Crane (Crane, 1970). The classical simulations of Sakiadis (Sakiadis, 1961a; Sakiadis, 1961b) played a key role in the formulation of flow problems over a stretching sheet. However, the work of Sakiadis was generalized and refined by many researchers, whereas, Crane (Crane, 1970) extended the work of Sakiadis for variable stretching velocity and solved the governing non-linear boundary layer equations exactly in the closed form. The remarkable ideas of Crane and Sakiadis have been highly obliged and adopted by researchers for different situations and types of fluids. This section is mainly categorized on the bases of physical flow models, appeared in the literature time to time. They clearly described the fluid motion heat and mass transfer in certain systems. Tremendous improvements have been made in the notable work of Sakiadis and Crane by introducing thermal and mass diffusion characteristics in the previous problems of them, and a special model is developed on the bases of previous studies for thin film flows. Sparrow (Sparrow and Gregg, 1959) treated thin film condensation by using the approach of boundary-layer approximation. He produced remarkable results on the behavior of a thin film over a stretching surface. Wang (1990) investigated unsteady thin film flow on a stretching plate within a boundary layer. Tan et al. (1990) found interesting solutions for the transport of heat in a thin film by assuming a spatially periodic temperature along the plate. Burelbach et al. (1990) verified the work of (Tan et al., 1990) by performing experiments. Dandapat and Ray (1994) presented an accurate model for thermo-capillary process in a thin film flow on a rotating disk. Andersson et al. (1996) explained the idea of a thin film flow on the transient stretching plate for power law fluid. Dandapat et al. (2003) analyzed the diffusion of heat in a thin film flow on the stretching plate moving with time dependent velocity. Dandapat and Maity (2006) studied the unsteady thin film flow over stretching plate and they found the boundary layer type solution and it is confirmed that the two layers (thin film and boundary layer) are exactly matched at certain points. Dandapat et al. (2006) emphasized on the solution for a variable thin film on stretching sheet, whereas, the film thickness is strictly changed with both space and time variables in this case. However, Chen (2006) found the consequences of heat transfer in the flow of a thin film over a transient stretching sheet for power law fluids by considering viscous dissipation term in the modeled equations. Wang (2006) presented analytical solutions to the problem of a thin film, maintained on a transient stretching plate. Andersson et al. (2000) solved the problem of heat diffusion in a thin film flow over a transient stretching plate. Liu and Andersson (2008) presented the generalized concept for the model problem of Andersson et al. (2000) and they studied the diffusion of heat in a thin film, driven by a transient stretching plate. Abbas et al. (2008) modified the approach of Wang (2006) by considering a thin film flow of a non-newtonian second grade fluid on an unsteady stretching surface. Santra and Dandapat (2009) investigated to remove the constraints of planarity and linear stretching for the transport of heat and thermo capillarity. Noor et al. (2010) also extended the modeled problem of Wang (2006) and they found a solution for MHD flows and generalized surface temperature. Mostly recently, flow of different fluids have been discussed over a porous and deforming surfaces in different research articles e.g., see (Ali et al., 2022; Turkyilmazoglu, 2022a; Turkyilmazoglu, 2022b; Krishna et al., 2022; Siddiqui and Turkyilmazoglu, 2022). In these research article the authors have emphasized on the fluid motion, maintained over surfaces of different structure behavior of kinematics of surfaces, types of fluids and mechanism which affects the motion of fluids in advanced setups. All these mechanism have been analyses on flow in these papers very intelligently. In the present work, we have analyzed the new and multiple dimensions of classical problems of thin film flow over a moving and porous sheet of variable thickness. By taken into account the nature and kinds of injection (suction) and moving velocities of the sheet, we categorically emphasized the behavior of thin film flow. Different cases are checked for the non-unifrom kinematics of the sheet of variable size and thin film. All the previous cases of such simulation, already used in the literature, have been recovered easily from the present simulations. The present system of partial differential equations and boundary conditions are transformed into ordinary differential equations on the basis of these new variables, and the final system is solved by **bvp4c** technique. The classical problems of this film flow have been retrieved from one case for special choice of the parameters values. Furthermore, we obtained the published results of (Wang, 1990; Andersson et al., 2000; Dandapat et al., 2003; Liu and Andersson, 2008) in such situations. Note that the classical simulations of this film flow problem contain two parameters, whereas, we dealt with seven different parameters in of present simulations.

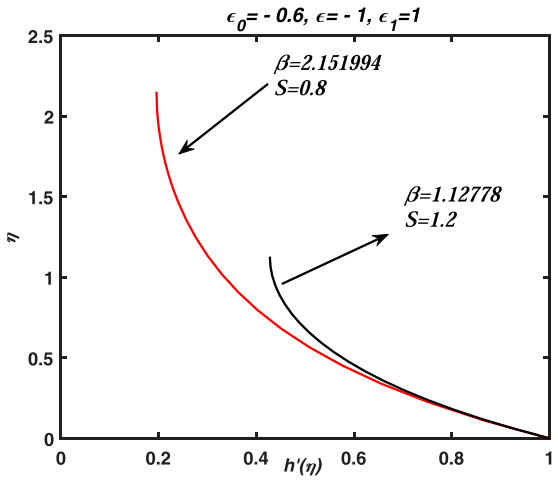

FIGURE 1
Two profiles of $h'(\eta)$ or axial velocity are graphed for two different values of β and S. Note that the parameter β and S are used by Anderson et al. (Andersson et al., 2000) and the graphs are exactly matched with the published work of them. Moreover, these profiles are obtained from the numerical solution of Eqs. **17**, **18** for the parameters values given in the title of this figure. These profiles are also reported in papers (Wang, 1990; Dandapat et al., 2003; Liu and Andersson, 2008).

2 Formulation of the problem

The flow of viscous thin film is taken over a porous sheet of variable thickness and the plate is moved in both forward and backward directions with variable velocity, whereas, the injection and suction velocities of the fluid through the porous sheet are non-uniform. Note that we explored different kinds of non-linear forms of five quantities associated with the geometry of sheet, structure of thin film along with the nature of boundary layer and the field variables, defined at the two surfaces in such a way that they exactly transformed the BVP of PDEs into BVP of ODEs. As a result we have obtained a generalized version of thin film flow in such circumstances. We need to evaluate the behavior of thin film within a momentum boundary layer. The constitutive equations, which have governed the flow of viscous thin film and used for the simulation of most complex problem, are the continuity and momentum equations. The boundary layer form of these governing equations is presented here and they are demonstrated in many research articles, e.g., see (Andersson et al., 2000; Dandapat et al., 2003; Liu and Andersson, 2008):

$$\frac{\partial u}{\partial x}+\frac{\partial v}{\partial y}=0, \tag{1}$$

$$\frac{\partial u}{\partial t}+u\frac{\partial u}{\partial x}+v\frac{\partial u}{\partial y}=\nu\frac{\partial^2 u}{\partial y^2}. \tag{2}$$

The porous sheet of variable thickness has the abilities to move in its own plane at either direction. The axial and normal velocities are prescribed at the surface of the sheet, so we imposed the following boundary conditions at the variable surface of the sheet and thin film:

$$u=U(x,t),v=V(x,t),y=f(x,t),v=w(x,t)\frac{Dr(x,t)}{Dt},\frac{\partial u}{\partial y}=0,$$
$$y=r(x,t). \tag{3}$$

Note that $U(x,t)$ defines the motion of the sheet at its own plane in both forward and backward directions, whereas, V indicates the fluid's velocity, which enters/leaves through the porous surface of the sheet. On the other hand $w(x,t)$ is controlling parameter for the rate of deformation of the thin film. Similarly $f(x,t)$ represents the variable thickness of sheet and $r(x,t)$ is used for variable size of the thin film. Moreover, $\frac{D}{Dt}$ is the material time derivative and it is defined as $\frac{D}{Dt}=\frac{\partial}{\partial t}+(\mathbf{V}.\nabla)$ where $\mathbf{V}=(u,v)$, $\nabla=(\frac{\partial}{\partial x},\frac{\partial}{\partial y})$. Note that $u(v)$ is the velocity component in $x(y)$ direction. Next our aim is to find the similarity transformation for generalized problem presented in Eqs. (1–3). For this reason, we defined the velocity components u, v and the similarity variable (η) in view of the boundaries inputs and independent variables as:

$$u=p(x,t)g(\eta),\ v=q(x,t)h(\eta),\ \text{where}\ \eta=\frac{y-f(x,t)}{r(x,t)} \tag{4}$$

In the above Eq. **4**, $g(\eta)$ and $h(\eta)$ are the representatives of the velocity components u and v, respectively. The above similarity variables/transformations are substituted into the governing PDEs in Eqs. **1**, **2** then we get the following Eqs. **5**, **6**. In this system, the coefficients of ODEs are variable and they are depending upon the independent quantities x and t. We have focused on the self similar solutions of the problem and they can be easily achieved if all these variable coefficients in the system of ODE's should independent of x and t. We tried to avail all such choices and exhaust all options for searching these self similar solutions, therefore, we proceed as:

$$h'+\alpha_1 g-\alpha_2 g'-\alpha_3\eta g'=0, \tag{5}$$

$$g''-\alpha_4 hg'+\alpha_5 g'-\alpha_6 g+\alpha_7\eta g'+\alpha_8 gg'-\alpha_9 g^2+\alpha_{10}\eta gg'=0. \tag{6}$$

The different coefficients in Eqs. **5**, **6** have the final form as:

$$\alpha_1=\frac{r(x,t)p_x(x,t)}{q(x,t)},\quad \alpha_2=\frac{p(x,t)f_x(x,t)}{q(x,t)},\quad \alpha_3=\frac{p(x,t)r_x(x,t)}{q(x,t)},$$
$$\alpha_4=\frac{q(x,t)r(x,t)}{\nu},\ \alpha_5=\frac{r(x,t)f_t(x,t)}{\nu},\quad \alpha_6=\frac{r^2(x,t)p_t(x,t)}{\nu p(x,t)},$$
$$\alpha_7=\frac{r(x,t)r_t(x,t)}{\nu},\quad \alpha_8=\frac{p(x,t)r(x,t)f_x(x,t)}{\nu},\ \alpha_9=\frac{r^2(x,t)p_x(x,t)}{\nu},$$
$$\alpha_{10}=\frac{p(x,t)r(x,t)r_x(x,t)}{\nu}, \tag{7}$$

where the subscripts x and t are used for the partial derivatives w.r.t. to that specific independent variable. Note that each of these coefficients contain either p,r,f and q or their partial derivatives, whereas, the functions are further expressed by introducing the following relations:

$$p(x,t)=A_1\left(C_2(t)+S_0(x,t)\right)^{\frac{\delta_2}{\delta_2+\delta_3}},$$
$$r(x,t)=A_2C_1(t)\left(C_2(t)+S_0(x,t)\right)^{\frac{\delta_3}{\delta_2+\delta_3}}, \tag{8}$$
$$f(x,t)=C_3(t)+A_3C_1(t)\left(C_2(t)+S_0(x,t)\right)^{\frac{\delta_3}{\delta_2+\delta_3}},$$

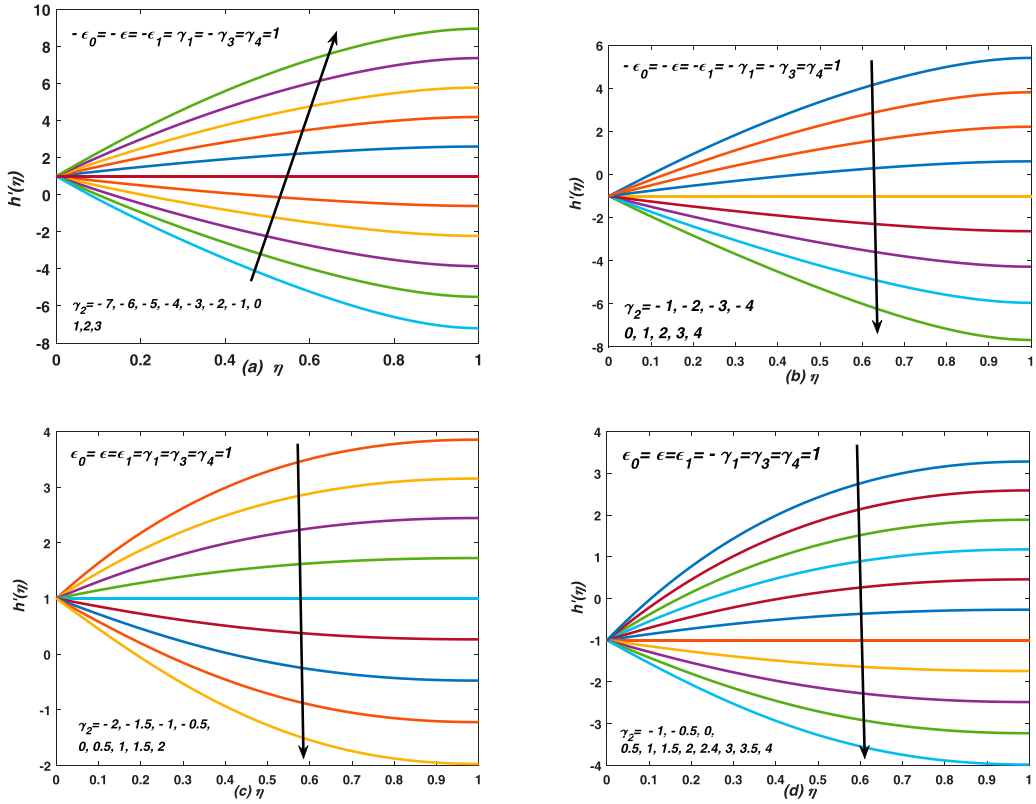

FIGURE 2
Flow behaviour of thin film has observed when the sheet, boundary layer and film are either compressed or expanded simultaneously. **(A)** Velocity profiles of squeezed flow of thin film have been graphed for the flow over a stretching sheet with suction and injection through its surface. **(B)**Velocity profiles of squeezed flow of thin film have been graphed for the flow over a shrinking sheet with suction and injection through its surface. **(C)** Velocity profiles of expanded flow of thin film have been graphed for the flow over a stretching sheet with suction and injection through its surface. **(D)** Velocity profiles of expanded flow of thin film have been graphed for the flow over a shrinking sheet with suction and injection through its surface.

where $S_0(x,t) = \frac{\delta_2}{C_1(t)} \int q(x,t)dx$. The three quantities p, r and f are expressed in term of q and some other variable constants $C_1(t), C_2(t), C_3(t)$, whereas, δ_2 and δ_3 has determined the non-linear nature of these three quantities. Furthermore, for $C_3(t) = 0$ and $A_3 = 0$, we may obtain a thin film flow on a flat plate. Note that, in view of the values of $p(x,t)$, $r(x,t)$ and $f(x,t)$, defined in Eq. 8, the values of different coefficient of Eq. 5 i.e., α_1, α_2, α_3 become, which are independent of x and t.

$$\alpha_1 = \frac{A_1 A_2 \delta_2^2}{\delta_2 + \delta_3}, \quad \alpha_2 = \frac{A_1 A_3 \delta_2 \delta_3}{\delta_2 + \delta_3}, \quad \alpha_3 = \frac{A_1 A_2 \delta_2 \delta_3}{\delta_2 + \delta_3}. \tag{9}$$

The BCs in Eq. 3 are simplified in view of the transformation in Eq. 4 as:

$$g(\eta) = \gamma_1 \quad \text{and} \quad h(\eta) = \gamma_2, \quad \text{when} \quad \eta = 0, \quad h(\eta) = \gamma_3, \quad g'(\eta) = 0 \quad \text{when} \quad \eta = \gamma_4 \tag{10}$$

where $\gamma_1 = \frac{U(x,t)}{p(x,t)}$, $\gamma_2 = \frac{V(x,t)}{q(x,t)}$, $\gamma_3 = \frac{w(x,t)}{q(x,t)} \frac{Dr}{Dt}$ and $\gamma_4 = \frac{r(x,t) - f(x,t)}{r(x,t)}$. In order to get the said (proclaimed) objectives, we have classified the problem into following cases.

3 Case I

The characteristic normal-velocity of the fluid through the porous surface is taken function of time t only, whereas, the other function p of variable nature has become dependent on both x and t, similarly $f(x,t)$ is varied with t only. All the variables and constants in Eq. 8 are fixed as:

$$\delta_3 = 0, \; C_2(t) = a_1 C_1(t)^{-2}, \; q(x,t) = C_1'(t), \; C_3(t) = C_1(t),$$
$$C_1(t) = a_0 \sqrt{\left(1 + \frac{2\nu\alpha t}{a_0^2}\right)}. \tag{11}$$

In view of these values, Eq. 8 takes the form:

$$p(x,t) = \frac{A_1 (a_1 + \nu\alpha\delta_2 x)}{a_0^2 \left(1 + \frac{2\nu\alpha t}{a_0^2}\right)},$$
$$r(x,t) = A_2 a_0 \sqrt{\left(1 + \frac{2\nu\alpha t}{a_0^2}\right)}, \tag{12}$$
$$f(x,t) = (1 + A_3) a_0 \sqrt{\left(1 + \frac{2\nu\alpha t}{a_0^2}\right)}.$$

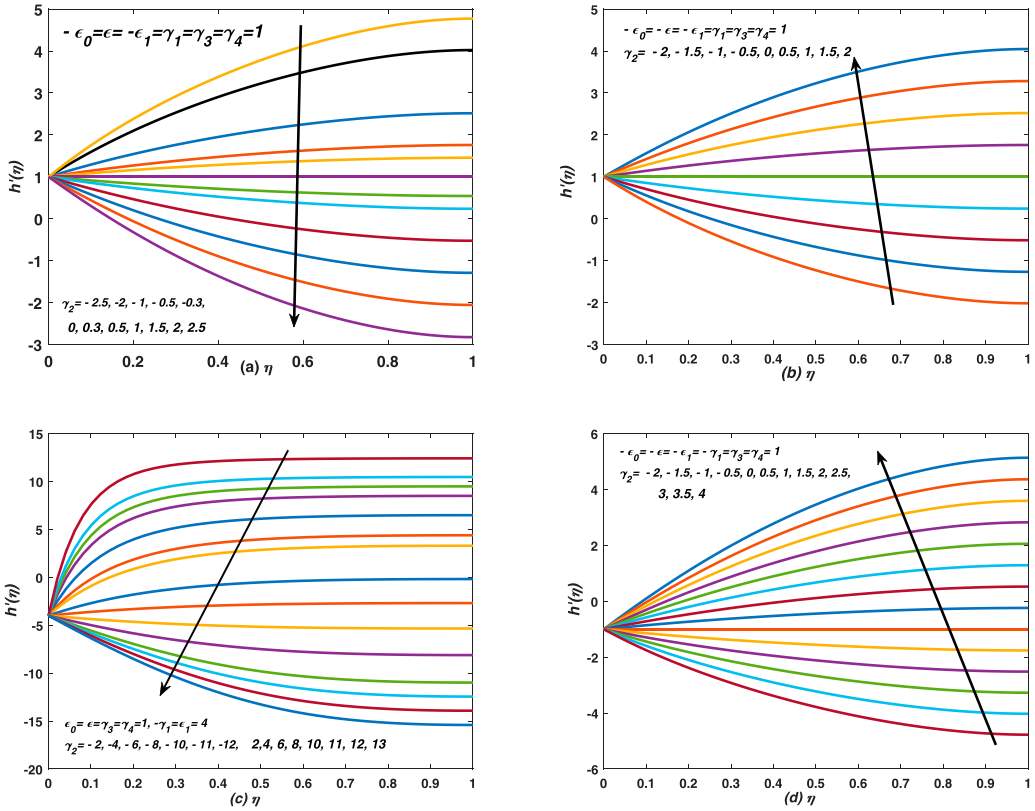

FIGURE 3
Flow behaviour of thin film has observed when the boundary layer is expanded/compressed with the deformation of film and sheet. **(A)** The axial velocity of deforming (both contraction and expansion can take place) thin film has been studied over a porous, stretched and compressed sheet in the presence of squeezed boundary layer. **(B)** Velocity profiles of thin film flow are drawn for flow over a stretching and porous sheet, whereas, the boundary layer is compressed. As a consequence, the sheet and thin film are also squeezed. Furthermore, the thin film is expanded *via* external stresses. **(C)** Velocity profiles of expanded flow of thin film are graphed for the flow over a shrinking sheet with suction and injection through its porous surface. **(D)** Velocity profiles of thin film flow are drawn for the flow over a shrinking and porous sheet, whereas, the boundary layer is compressed. As a consequence, the sheet and thin film are also squeezed. Furthermore, the thin film is expanded *via* external stresses.

Note that $p(x,t)$ depends upon the coordinate x and time t, whereas, $r(x,t)$ and $f(x,t)$ depend on t only. Moreover, the values of different quantities in Eq. 12 are substituted into Eq. 7 and all the different coefficients of this equation are reduced into the following simplest form:

$$\alpha_1 = A_1A_2\delta_2,\quad \alpha_2 = \quad \alpha_3 = \quad \alpha_8 = \quad \alpha_{10} = 0,\quad \alpha_4 = \alpha A_2,$$
$$\alpha_5 = \alpha A_2\left(1+A_3\right),\quad \alpha_6 = -2\alpha(A_2)^2, \alpha_7 = \alpha(A_2)^2,\quad \alpha_9 = \alpha A_1(A_2)^2\delta_2. \tag{13}$$

Moreover, all the above coefficients are independent of space variable x and the time variable t, whereas, the continuity and momentum equations of non-uniform coefficients take the form:

$$A_1A_2\delta_2 g(\eta) + h'(\eta) = 0. \tag{14}$$

$$\alpha A_2\left(A_2 g(\eta)\left(2 - A_1\delta_2 g(\eta)\right) + \left(1 + A_3 + A_2\eta - h(\eta)\right)g'(\eta)\right) + g''(\eta) = 0. \tag{15}$$

In view of the variable, defined in Eq. 12, the BCs in Eq. 10 are converted into the following form:

$$g(\eta) = \gamma_1 \quad \text{and} \quad h(\eta) = \gamma_2, \quad \text{when} \quad \eta = 0, \quad h(\eta) = \gamma_3, \quad g'(\eta) = 0 \quad \text{when} \quad \eta = \gamma_4, \tag{16}$$

Now, Eq. 14 is solved for $g(\eta)$ as $= -\frac{1}{A_1A_2\delta_2}h'(\eta)$ and it is substituted into Eqs. 15, 16, we obtained the following system:

$$h'''(\eta) + 2\epsilon_0 h'(\eta) + \epsilon h''(\eta) + \epsilon_1 h''(\eta) + \epsilon_0\eta h''(\eta) - \epsilon h(\eta)h''(\eta) + \epsilon h'(\eta)^2 = 0. \tag{17}$$

$$h'(\eta) = \gamma_1 \quad \text{and} \quad h(\eta) = \gamma_2, \quad \text{when} \quad \eta = 0, \quad h(\eta) = \gamma_3, \quad h''(\eta) = 0 \quad \text{when} \quad \eta = \gamma_4, \tag{18}$$

where $\epsilon = A_2\alpha$, $\epsilon_0 = A_2\epsilon$, $\epsilon_1 = A_3\epsilon$, $\gamma_1 = \frac{U_0a_0^2}{a_1A_1}$, $\gamma_2 = \frac{a_0V_0}{\alpha\nu}$, $\gamma_3 = A_2w_0$, and $\gamma_4 = \frac{A_2-A_3-1}{A_2}$. Eqs. 17, 18 are similar equation and they only depend upon the similarity variable η, whereas, the system contains the only unknown function $h(\eta)$. Moreover, the injection and suction velocity V is defined by $V = V_0(1+\frac{2\alpha\nu}{a_0^2}t)^{\frac{-1}{2}}$, whereas, the stretching(shrinking) velocity is expressed as $U = \frac{U_0(1+\frac{\nu a\delta_2 x}{a_1})}{1+\frac{2\nu at}{a_0^2}}$. Similarly, the controlling function for the thin film thickness is taken as $w = (\frac{w_0}{1+\beta_0(1+\frac{2\nu at}{a_0^2})^{\frac{-3}{4}}(1+\frac{\nu a\delta_2 x}{a_1})})$, where $\beta_0 = \frac{\delta_2a_0U_0^2}{A_2a_1}$. Remember that for this choice of $U(x,t)$, $V(x,t)$ and $w(x,t)$ all of the boundary

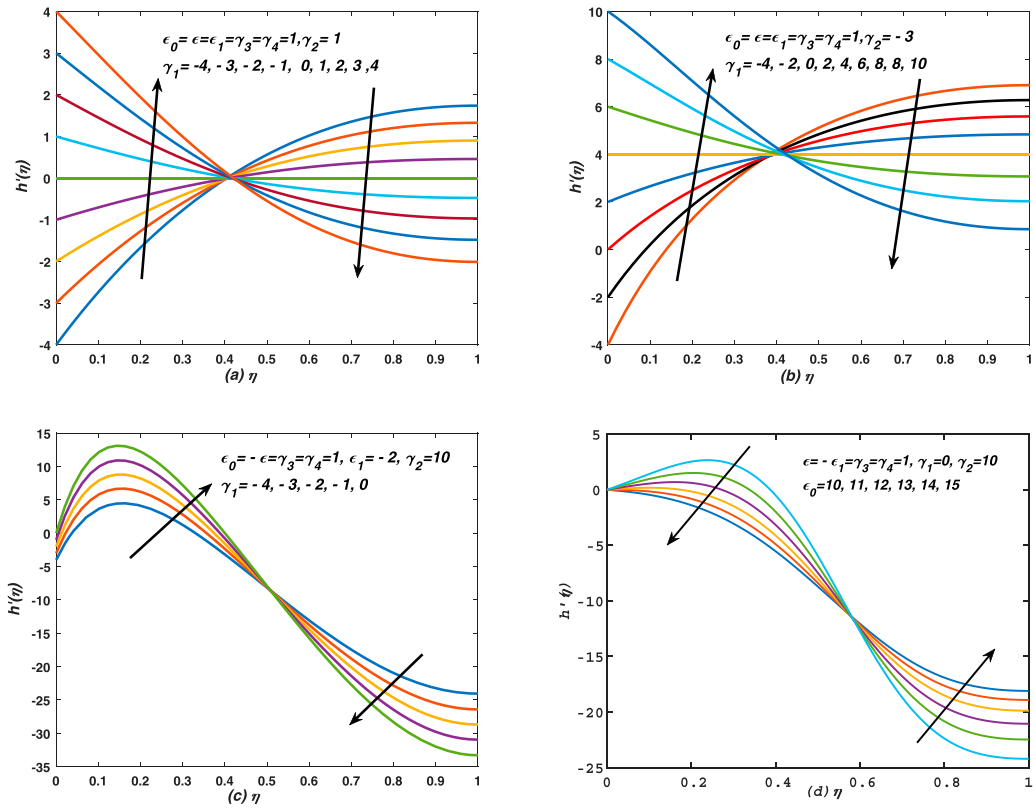

FIGURE 4
Flow bahaviour of thin film has observed for different values of (**i**) stretching/shrinking parameters and (**ii**) sudden expansion of the boundary layer. **(A)** Velocity profiles of expanded flow of thin film are graphed for the flow over a stretching and shrinking sheet with injection through porous plate. **(B)** Velocity profiles of expanded flow of thin film are graphed for the flow over a stretching and shrinking sheet with suction through porous plate. **(C)** An over shoot in the velocity profiles of deformed thin film flow has observed near the surface of the sheet. The sheet is compressed, whereas, the thin film is squeezed *via* external stresses. **(D)** Effects of boundary layer's expansion of thin film and squeezing of sheet are seen on the axial velocity of thin film flow over a non-stretching(non-shrinking) sheet with the injection velocity through the plate.

conditions including the boundary itself become exact similar (Hussan et al., 2012).

3.1 Comparison of the present simulations with the previously published work

We have taken the governing equations and the relevant data of four different published papers and compared the present simulated equations and their results with that benchmark solutions. In the first phase, the parameters in Eqs. 17, 18 are fixed as; $\alpha = \frac{-2}{S}, A_2 = \frac{S}{2}, A_3 = -1, w_0 = 1$, whereas, the boundary conditions in Eq. 18 take the form: $h(0) = 0$ and $h'(0) = 1$, $h(1) = \frac{S}{2}$, $h''(1) = 0$, where S is the unsteadiness parameter, used in the published papers (Wang, 1990; Andersson et al., 2000; Dandapat et al., 2003; Liu and Andersson, 2008). Note that, for these choices of parameters value, we exactly recovered equations number (9, 11a, 11b and 11c) of (Andersson et al., 2000) from Eqs. 17, Eq. 18. Furthermore, the graph of paper (Andersson et al., 2000) i.e., Figure 2, Figure 3 are retrieved from the numerical solutions of Eq. 17, Eq. 18 of the present paper for different values of parameter S. On the other hand these four papers demonstrate unsteady thin film flow over a stretching sheet, whereas, the stretching velocity and variation in the film thickness, taken in these classical papers, have certain known types, therefore, the claim of generalized simulation for a thin film flow over a moving and porous sheet/surface/plate of variable size is clearly justified in the comparative analysis. Eventually, the governing equations and associated boundary conditions of the simplified problem in these four papers have the form $F''' = S(F' + \frac{\eta}{2}F'') + (F')^2 - FF''$, $F'(0) = 1$; $F(0) = 0$, $F(\beta) = \frac{S\beta}{2}$, $F''(\beta) = 0$. Note that the different quantities used in these equations have the meaning, i.e., F, η, S and β are representing the dimensionless stream function, similarity variable, unsteadiness parameter and value of η at free surface, respectively.

Note that Figure 2 and Figure 3 of Andersson et al. (2000) have been graphed for $S = 0.8(1.2)$ and $\beta = 2.151,994(1.12778)$ and the two values of skin friction coefficient for the mentioned parameters values are determined as: $ff''(0) = -1.24581$ and -1.27917, respectively, whereas, this data is exactly obtained from the numerical solution of Eqs. 17, 18 for special values of the parameters as discussed above and demonstrated in **Figure 1** below.

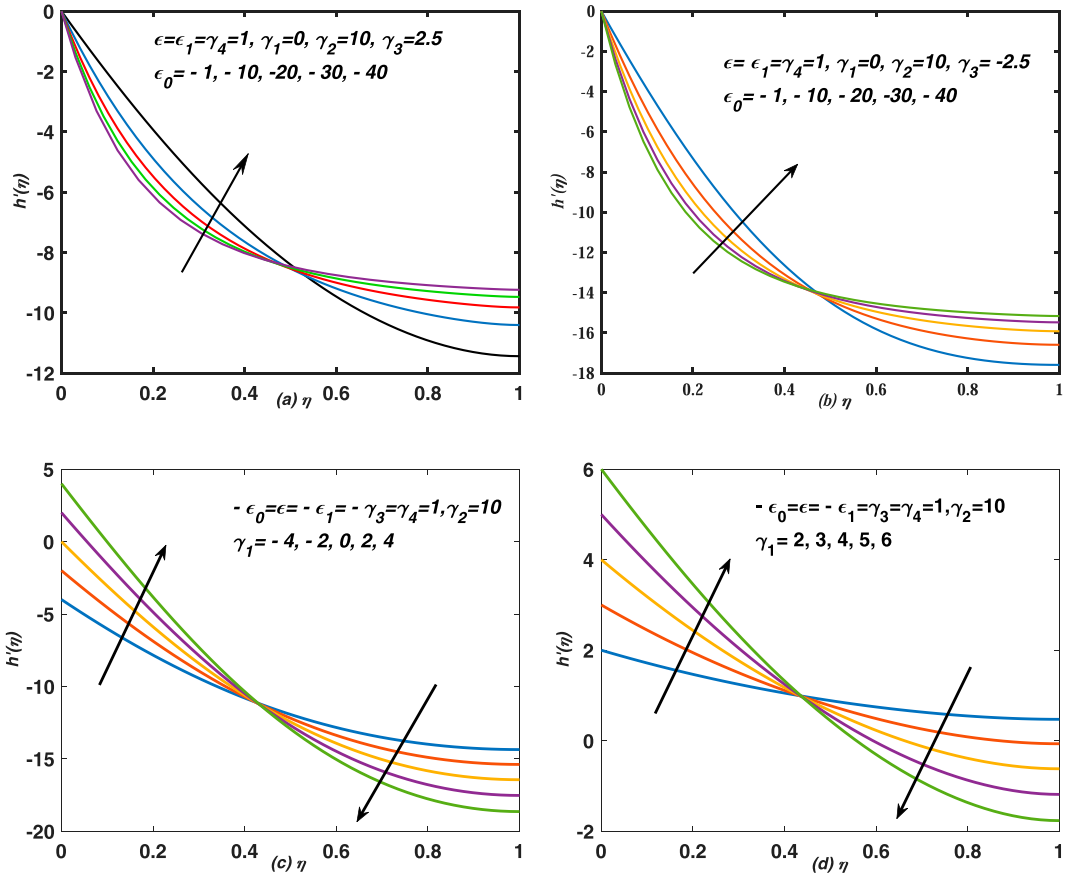

FIGURE 5
Decreasing behaviour of velocity profiles is observed against η for different values of (**i**) γ_1 (**ii**) $\epsilon_0 < 0$ (sudden compression of boundary layer).**(A)** Effects of boundary layer's compression and expansion of both thin film and sheet are seen on the axial velocity of thin film flow over a non-stretching (non-shrinking) sheet with the injection velocity through plate. **(B)** Effects of boundary layer's compression, deformation of thin film and expansion of sheet are seen on the axial velocity of thin film flow over a non-stretching (non-shrinking) sheet with the injection velocity through the plate. **(C)** Effects of shrinking are seen on the axial velocity of thin film flow over a non-stretching (non-shrinking) sheet with the injection velocity through the plate. **(D)** Effects of stretching are seen on the axial velocity of thin film flow over a non-stretching (non-shrinking) sheet with the injection velocity through the plate.

Remember that the simulated problem of Andersson et al. (2000) is independent of $\epsilon_0, \epsilon, \epsilon_1, \gamma_1, \gamma_2, \gamma_3$, and γ_4, whereas, these parameters arose in the present simulations and they played significant role in thin film flow analysis.

3.2 General analysis of the numerical solution of Eq. 17 and Eq. 18 and evaluation of the shear stress

The simulated problem in Eq. 17 and Eq. 18 contains seven parameters and each of them is corresponding to some physical settings, therefore, different values have been assigned to these parameter and they are associated with multiple functions of some physical activity. So effects of all these parameters have been observed on the axial velocity component and shear stress at the surface of the plate. The shear stress is usually expressed by τ and generally defined for two dimensional flow as $\tau = \mu(\frac{\partial u}{\partial y} + \frac{\partial v}{\partial x})$, where μ, u and v are defined earlier. By substituting values of u and v from Eq. 4, whereas, the values of $p(x,t)$, $q(x,t)$, $f(x,t)$ and $r(x,t)$ are expressed in Eq. 11 and Eq. 12 and finally the shear stress τ is obtained as $\tau = \mu\frac{p(x,t)}{r(x,t)}g'(\eta)$. The shear stress at the wall and its dimensionless form gives the skin frictions coefficient, which is obtained at the sheet of non-uniform thickness as: $g'(0) = \frac{r(x,t)}{\mu p(x,t)}\tau|_{y=f(x)}$. From Eq. 14, we get: $g(\eta) = -\frac{1}{A_1A_2\delta_2}h'(\eta)$ then the skin friction becomes $-\frac{1}{A_1A_2\delta_2}h''(0) = \frac{r(x,t)}{\mu p(x,t)}\tau|_{y=f(x)}$ and after scaling it, we have, i.e., $-h''(0) = \frac{r(x,t)}{\mu p(x,t)}A_1A_2\delta_2\tau|_{y=f(x)}$.

4 Graphs of the numerical solution and their discussion

In this paper, we have simulated the thin film flow over a porous and moving sheet of non-uniform thickness. At the first place, we introduced new function for the velocity components, and they have been strictly changed with the similarity variable. In the later stage, we imposed certain conditions on the boundaries inputs and field variables, defined at the free surface and on the face of the plate. In such situations, we obtained multiple set of ODEs

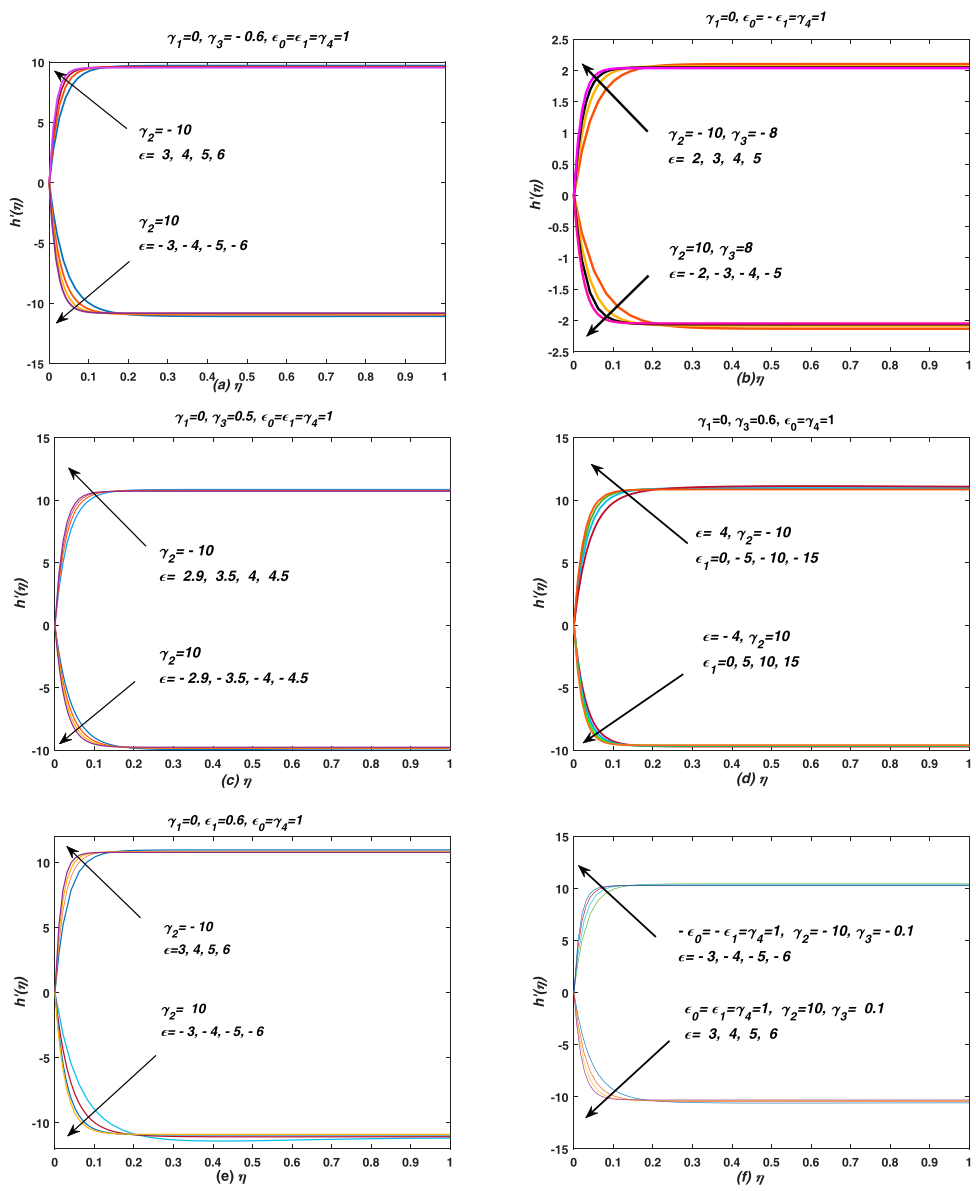

FIGURE 6
The boundary layer behaviour of thin film flow has observed when the flow is maintained over a non-stretching($\gamma_1 = 0$)/non-shrinking sheet. **(A)** The film is expanded ($\gamma_3 > 0$)/compressed ($\gamma_3 < 0$) slowly by external stresses and it is expanded ($\epsilon > 0$)/squeezed($\epsilon < 0$) *via* boundary layer. Note that the upper (lower) set of profiles is drawn for expanding sheet/boundary-layer and suction (injection) cases. **(B)** The film is expanded ($\gamma_3 > 0$)/compressed ($\gamma_3 < 0$) quickly by external stresses and it is expanded ($\epsilon > 0$)/squeezed($\epsilon < 0$) *via* boundary layer. Note that the upper (lower) set of profiles is drawn for contracted sheet ($\epsilon_1 < 0$), expended boundary-layer ($\epsilon_0 > 0$) and suction (injection) cases. **(C)** The film is expanded ($\gamma_3 > 0$)/compressed ($\gamma_3 < 0$) by external stresses and it is expanded ($\epsilon > 0$)/squeezed($\epsilon < 0$) *via* boundary layer. Note that the upper (lower) set of profiles is drawn for expanding sheet/boundary layer and suction (injection) cases. **(D)** The film is expanded ($\gamma_3 > 0$) by external stresses and it is expanded ($\epsilon > 0$)/squeezed($\epsilon < 0$) *via* boundary layer. Note that the upper (lower) set of profiles is drawn for contracting (expanding) sheet and suction (injection) cases. **(E)** The film is squeezed ($\gamma_3 < 0$)/expanded ($\gamma_3 > 0$) by external stresses and it is expanded ($\epsilon > 0$)/squeezed($\epsilon < 0$) *via* boundary layer. Note that the upper (lower) set of profiles is drawn for suction (injection) case. **(F)** The upper(lower) set of profiles is drawn for squeezing(expanding) and suction(injection) cases.

(problems) along with boundary conditions, however, we explained only those cases which give the exact self similar problem. As a result, a special case has been appeared, and is converted easily into the classical cases of thin film flows under certain constraints on the parameters. Moreover, this special situation of the present simulation has been shown in Eq. 17 and Eq. 18, whereas, the system is solved numerically for different choices of the parameters value. Note that each set of specific value of the parameters represents some proper physical senario; Figure 2; Figure 3; Figure 4 Figure 5; Figure 6) show the profiles of axial velocity against the similarity variable, which are obtained from the numerical solution of Eq. 17 and Eq. 18, whereas, the profiles in these figures are drawn for different values of γ_2 (injection/suction), γ_1 (stretching/shrinking), ϵ_0 (deformation of boundary layer) and ϵ (deformation of thin film *via* deformation of boundary layer). The deformation (both expansion and squeezing can be take place) of both thin film and

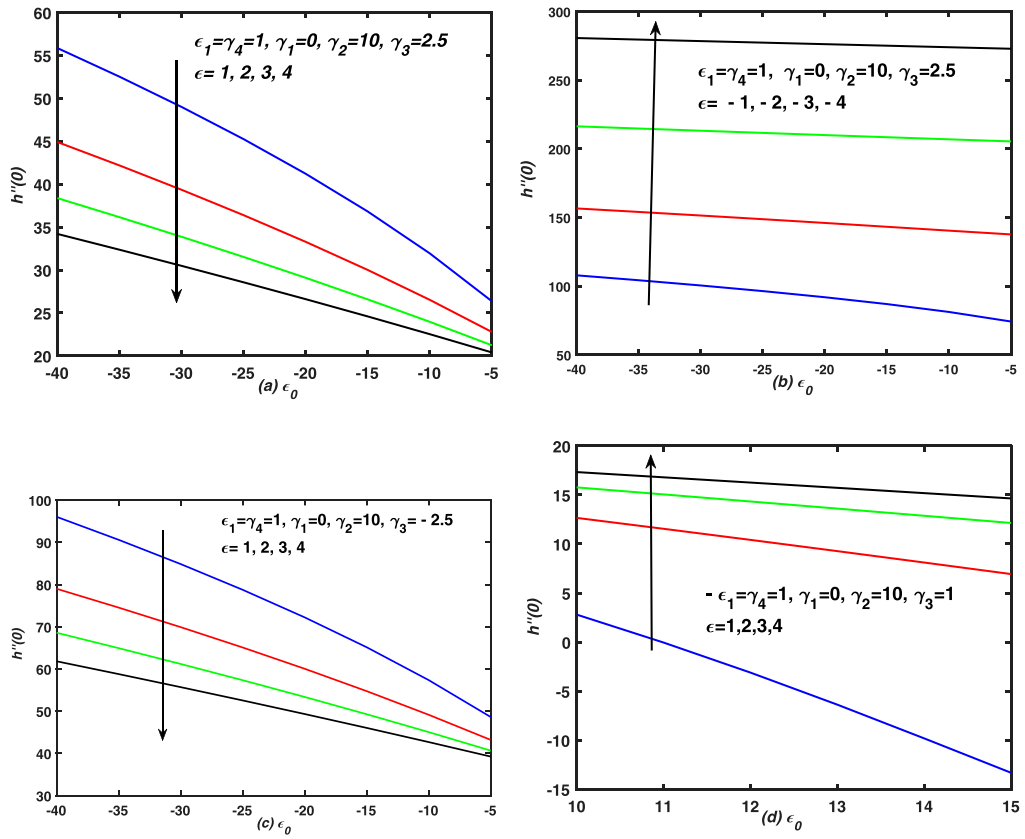

FIGURE 7
The linear and non-linear behaviour of skin friction is graphed against the compressed and expanded boundary layers. Note that the stretching and shrinking velocities are taken zero in this case. **(A)** Skin friction coefficient is plotted against compressed boundary layer (ϵ_0) for different values of expansion of thin film ϵ. It is the case of expanding film and injection through plate. **(B)** Skin friction coefficient is plotted against compressed boundary layer (ϵ_0) for different values of expansion of thin film ϵ. It is the case of deforming film and injection through plate. **(C)** Skin friction coefficient is plotted against compressed boundary layer (ϵ_0) for different values of expansion of thin film ϵ. It is the case of squeezing film and expanding plate with injection. **(D)** Skin friction coefficient is plotted against compressed boundary layer (ϵ_0) for different values of expansion of thin film ϵ. It is the case of expanding film and squeezing plate with injection.

sheet have been measured in term of deformation of the boundary layer, whereas, the self or direct deformation of thin film through some external stresses has played significant role during the flow process. In Figure 3A, the squeezing of the boundary layer and sheet have been considered and the flow is maintained over a stretching sheet. Note that the pure (over all) expansion and squeezing cases have been discussed for the flow over a stretching (shrinking) and porous sheet. The term over all deformation (squeezing or contraction) has been used for the simultaneous deformation (squeezing or contraction) of the boundary layer, thin film and that of the sheet. Moreover, the film is deformed (squeezed and expanded) in two different ways (i) deformation due to boundary layer and deformation due to other external stresses. Note that the velocity profiles in Figure 2 are decreased (increased) against η and different values of γ_2, whereas, the increasing (decreasing) behaviour of the velocity profiles is observed against η for injection (suction). The profiles have been risen suddenly (gradually) and dropped in case of expansion (contraction) of film and boundary layer for both stretching and shrinking sheet flows. However, massive injection occurs through the porous sheet and stretching velocity of the sheet is taken in these observations. In this Figure 2, effects of injection and suction are seen on the axial velocity and it has changed uniformly with the variation of this parameter. It is worthy noticeable that thin film is expanded by two means in this situation 1) external stresses 2) deformation of boundary layer. Moreover, for different values of γ_2, the axial velocity at the free surface of thin film gives non-uniform values, whereas, it remains fixed, i.e., zero at the sheet for each value of γ_2. Note that for non-zero value of ϵ_0 (when the boundary layer deforms), the profiles of $h'(\eta)$ intersect in between the free surface and plate, whereas, the common point is moving to left and right, depending upon the values of the parameters (see Figure 4; Figure 5). The large negative values of ϵ_0 show that the boundary layer has compressed extremely towards sheet. On the other hand, ϵ_0 measures the deformation of the boundary layer, which may expand and compressed simultaneously. Similarly ϵ measure deformation of the thin film and depends upon the boundary layer. Finally ϵ_1 defines deformation of sheet and it depends on the deformation of thin film. Remember that the nature of velocity is changed from increasing (decreasing) to decreasing (increasing) with the variation of parameters. The profiles in Figure 3 are decreased (increased) against η and different values of γ_2 (both injection and suction cases are taken). The increasing

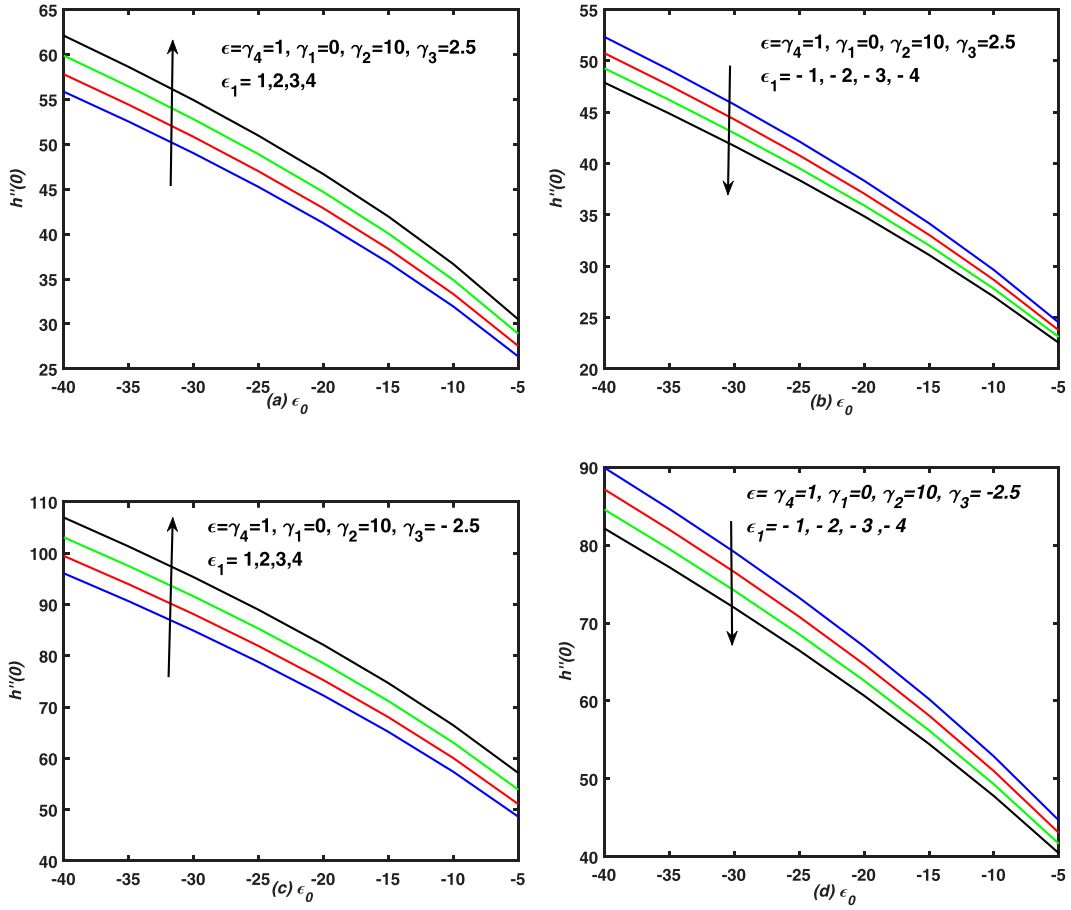

FIGURE 8
The linear and non-linear behaviour of skin friction is graphed against the compressed boundary layers. **(A)** Skin friction coefficient is plotted against compressed boundary layer (ϵ_0) for different values of deformation of sheet ϵ_1. It is the case of expanding film and injection through sheet. **(B)** Skin friction coefficient is plotted against compressed boundary layer (ϵ_0) for different values of deformation of sheet ϵ_1. It is the case of deforming film and injection through sheet. **(C)** Skin friction coefficient is plotted against compressed boundary layer (ϵ_0) for different values of deformation of sheet ϵ_1. It is the case of squeezing film and injection through sheet. **(D)** Skin friction coefficient is plotted against compressed boundary layer (ϵ_0) for different values of deformation of sheet ϵ_1. It is the case of squeezing film and injection through sheet.

(decreasing) behaviour of the velocity profiles is observed against η for injection (suction) in these plots. Each profiles in these figures is increased and decreased gradually, whereas, it is increased suddenly and the profiles have shown boundary layer patterns for large injection and expanded boundary layer when the flow is maintained over an expanded and contracting sheet. The profiles in Figure 4A,B have shown increasing (decreasing) behaviour against η for $\gamma_1 < 0$ ($\gamma_1 > 0$). In these two plots, the analysis has carried out for the expanded flow of thin film with suction and injection. Moreover, an overshoot in the velocity profiles is observed at Figure 4C,D for $\gamma_1 < 0$ and $\epsilon_0 > 0$. Note that the overshooting values have been seen increased (decreased) for large suction (deformation). Note that the overshoots in the profiles are observed for the flow over a compressed sheet. The velocity profiles are decreased against η in Figure 5 for the flow over a non-stretching (non-shrinking) sheet with an injection velocity. In Figures 5A,B the boundary layer shrinking is compressed more rapidly, and no stretching is taken into account and the sheet is equipped with injection velocity, whereas, in Figure 5C,D, injection is combined with stretching and shrinking. In Figures 5A,B, the velocity is decreased from zero to some fixed value against η, whereas, it is increased in the vicinity of plate and then decreased uniformly against η. In Figure 4; Figure 5, the profiles have a common point of intersection between the interval (0, 1) on $\eta - axis$, whereas, the profiles are linear (non-linear) on the left (right) of point of intersection and the graphs have shown asymptotic behavior on the right of the point. Moreover, the part of profiles on the left (right) are increased or decreased suddenly (gradually) against η. The reason is that the injection and expansion (which supports the injection) of sheet are assisting the flow in normal direction, whereas, the viscous nature of the fluid reduces or slow downs the impact of injection, and the velocity adopts non-linear nature after the point of intersection. In some cases overshoots in the velocity profiles have been seen and it is obvious fact that injection supports the flow in the normal direction. Note that the response of h' to γ_1 between zero and the point of intersection is opposite to the response between the point of intersection and 1. In Figures 4A–D, the point of intersections for different values of γ_1 are (0.42857, 0.50282), (0.40816, 4.1703), (0.5102, −8.7341),

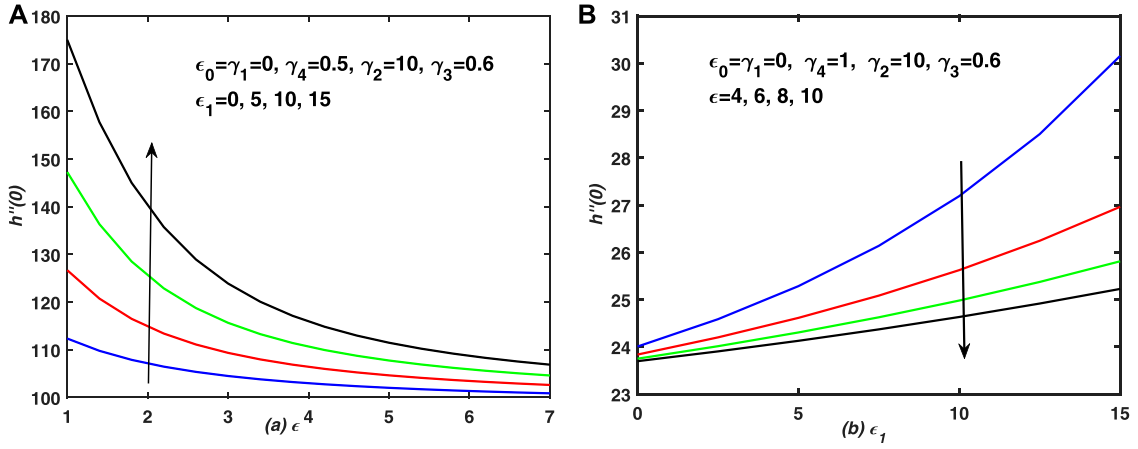

FIGURE 9
The increasing, decreasing and behaviour of skin friction is graphed against the expansion of sheet/thin film for different cases of expanding of thin film/sheet. **(A)** Skin friction coefficient is plotted against the expansion of sheet (ϵ) for different values of deformation of sheet ϵ_1. It is the case of expanding film and sheet with injection. **(B)** Skin friction coefficient is plotted against the expansion of sheet (ϵ_1) for different values of deformation of sheet ϵ_1. It is the case of expanding film and sheet with injection.

(0.58163, −11.5064), respectively, whereas, the point of intersection moves, this means that it varies depending upon the value of the parameters. Note that for certain ranges of the parameters value, the point of intersection disappears as shown in Figures 4A–D. In Figures 5A–D, the point of intersections for ϵ_0 and γ_1 are (0.4898, −8.4287), (0.45918, −13.881), (0.42857, −11.1422), (0.42857, 1.0577), respectively, whereas, the point of intersection moves, this means that it depends upon the set of parameters values. The profiles in these two figures, i. e., Figure 4; Figure 5) have shown the linear (non-linear), increasing (decreasing) and asymptotic behaviors against γ_1 and ϵ_0 before (after) point of intersection. It is observed that the point of intersection moves to the right/left and upward (downward) with the changes in the parameters value who supported (resisted) injection. Note that the surface deformation has played significant role in supporting and opposing the injection rate.

In Figure 6, the velocity profiles are asymptotic near the free surface for large injection/suction in the presence of squeezing (expanded) thin film flow, maintained over a non-stretching and non-shrinking sheet. Note that overshoot in velocity profiles is observed near the surface of plate for large shrinking (quick expansion of boundary layer) over a sheet with injection in case of expanding film (see Figures 4C,D). It happens because the injection provides extra momentum to the flows. Moreover, the film and surface deformations have minimum effect on the flow behaveiour in this special circumstances. The profiles of axial velocity in Figure 5A,B showed odd behavior, however, in case of squeezing film, the velocity profiles have been dropped more rapidly for compressing thin films as compared to its profile for expanding thin film. Furthermore, these observations are recorded in Figure 6A–D. Note that in all subplots of Figure 6, the boundary layer gets thinner and steaks to the sheet, whereas, it penetrates more quickly in case of squeezing thin film flow over an impermeable, shrinking and expanding sheet and these observations are noted in Figure 6E. A thin boundary layer is observed near the surface of the permeable (injection case) and non-stretching non-shrinking sheet, whereas, the boundary thickness is increased in case of flow over an impermeable and non-stretching and non-shrinking plate.On the other hand, Figure 7; Figure 8; Figure 9 show the profiles of skin friction against ϵ_0 (the boundary layer expansion and compression are taken) for different values of ϵ (both expansion and squeezing of thin film *via* boundary layer are considered) in the presence of deformation of thin films. Note that the profiles are drawn for the flow over a non-stretching and non-shrinking sheet with injection. The profiles are linear for squeezed and expanded thin film, whereas, they are decreased non-linearly against ϵ_0 when the expanding thin film is moved rapidly. On the other hand, the profiles are straight lines for expansion of film *via* external stresses through the boundary layer in the presence of shrinking sheet and they are decreased linearly. Furthermore, the experiment is repeated and the skin friction coefficient is graphed against ϵ_0 (compressed boundary layer is taken) for different values of stretching, shrinking and deformation of walls in Figure 8. In all these figures, the profile of skin friction are decreased rapidly and non-linearly against suction. In Figure 9A the skin friction is decreased linearly and quickly against injection for large stretching in case of expanding film. Whereas, the profiles are increased quickly and non-linearly against shrinking for abrupt expansion of surface in case of squeezing film. Moreover, the profiles are converge to a fixed value (i.e. 10) in each case and they converged asymptotically to 100 against ϵ. Finally, the profiles exhibit increasing (decreasing) behaveiour against ϵ_1 (ϵ) for non-stretching and non-shrinking plate, uniform boundary layer and rapid expansion of the boundary, respectively. In Figure 9B, the skin friction shows increasing and decreasing behaveiour against ϵ (expanding film) and ϵ_1 (expanding sheet) respectively. The profiles are decreased (increased) non-linearly for different values of ϵ and ϵ_1 in these two subplots. Note that the profiles show divergent behavior against ϵ_1 for small values of it (weak expansion of thin film) and they varied linearly against ϵ_1 for large values of it (expansion of thin film).

5 Conclusion

In this paper, we analyzed the flow of viscous thin film over a variably porous and moving sheet of non-uniform thickness. The non-uniform nature of thin film and thickness of the porous and moving sheet are major aspects of the present simulated flow model. The continuity law and boundary layer momentum equation are simplified in view of the generalized boundary conditions, imposed at sheet and free surface of thin film. A set of new variables is introduced for the velocity components and similarity variables, whereas, multiple constraints have been imposed on the set of transformations and they consequently provided multiple problems of self similar nature. A special case is formed from this transformation which is then converted into the classical problem for specific choice of the parameters value. So the results are exactly matched with the published work of (Wang, 1990; Andersson et al., 2000; Dandapat et al., 2003; Liu and Andersson, 2008). Moreover, the detailed discussion of this special case is also provided in view of new transformation. The problem is classified into several cases in which both steady and unsteady behaviors of the problem have been studied, whereas, the additional information and observation are also obtained from the present investigations. However, we restrict ourselves only to one case due to the length of the paper. Moreover, combined and individual effects of injection, suction, stretching, shrinking, deformation of both thin film and sheet have been seen on the axial velocity and skin friction. A narrow momentum boundary layer is observed over an permeable non-stretching and non-shrinking and expanding sheet of non-uniform thickness for the flow of thin film. Moreover, linear, non-linear, uniform, non-uniform, both sudden and gradual increasing and decreasing responses of the skin friction are observed for the different types of the boundary inputs. In nut shell three types of deformations are focused in this investigations, i.e., deformation of thin film, sheet and boundary layer. Moreover, two types of variations have been observed in the thickness of thin film. One is due to the surface stresses, whereas, the second one appears due to the changes in boundary layer. Significant changes in the flow behavior have been noted due to the variation of thin film, boundary layer and sheet thicknesses and these observations have been recorded in different graphs.

Data availability statement

The raw data supporting the conclusions of this article will be made available by the authors, without undue reservation.

Author contributions

There are three authors in this manuscript and each one has contributed properly. The mathematical model has been proposed by DK, all the numerical computations and their graphs have been carried out by NU. The discussion of graphs and their physical interpretation has been given by DK and ZK. The literature review and comparison of the present simulations with the classical data has been established by NU. The final review and amendments in the manuscript has been carried out by ZK.

Acknowledgments

Princess Nourah bint Abdulrahman University Researchers Supporting Project number (PNURSP 2023R8). Princess Nourah bint Abdulrahman University Riyadh, Saudi Arabia.

Conflict of interest

The authors declare that the research was conducted in the absence of any commercial or financial relationships that could be construed as a potential conflict of interest.

Publisher's note

All claims expressed in this article are solely those of the authors and do not necessarily represent those of their affiliated organizations, or those of the publisher, the editors and the reviewers. Any product that may be evaluated in this article, or claim that may be made by its manufacturer, is not guaranteed or endorsed by the publisher.

References

Abbas, Z., Hayat, T., Sajid, M., and Asghar, S. (2008). Unsteady flow of a second grade fluid film over an unsteady stretching sheet. *Math. Comput. Model.* 48 (3-4), 518–526. doi:10.1016/j.mcm.2007.09.015

Ali, A., Marwat, D. N. K., and Ali, A. (2022). Analysis of flow and heat transfer over stretching/shrinking and porous surfaces. *J. Plastic Film Sheeting* 38 (1), 21–45. doi:10.1177/87560879211025805

Andersson, H. I., Aarseth, J. B., Braud, N., and Dandapat, B. S. (1996). Flow of a power law fluid film on an unsteady stretching surface. *J. Newt. Fluid Mech.* 62 (1), 1–8. doi:10.1016/0377-0257(95)01392-x

Andersson, H. I., Aarseth, J. B., and Dandapat, B. S. (2000). Heat transfer in a liquid film on an unsteady stretching surface. *Int. J. Heat Mass Transf.* 43 (1), 69–74. doi:10.1016/s0017-9310(99)00123-4

Burelbach, J. P., Bankoff, S. G., and Davis, S. H. (1990). Steady thermocapillary flows of thin liquid layers. II. Experiment. . *Phys. Fluids A Fluid Dyn.* 2 (3), 322–333. doi:10.1063/1.857782

Chen, C. H. (2006). Effect of viscous dissipation on heat transfer in a non-Newtonian liquid film over an unsteady stretching sheet. *J. Newt. Fluid Mech.* 135 (2-3), 128–135. doi:10.1016/j.jnnfm.2006.01.009

Crane, L. J. (1970). Flow past a stretching plate. *Z. für Angew. Math. Phys. ZAMP* 21 (4), 645–647. doi:10.1007/bf01587695

Dandapat, B. S., Kitamura, A., and Santra, B. (2006). Transient film profile of thin liquid film flow on a stretching surface. *Z. für Angew. Math. Phys. ZAMP* 57 (4), 623–635. doi:10.1007/s00033-005-0040-7

Dandapat, B. S., and Maity, S. (2006). Flow of a thin liquid film on an unsteady stretching sheet. *Phys. fluids* 18 (10), 102101. doi:10.1063/1.2360256

Dandapat, B. S., and Ray, P. C. (1994). The effect of thermocapillarity on the flow of a thin liquid film on a rotating disc. *J. Phys. D Appl. Phys.* 27 (10), 2041–2045. doi:10.1088/0022-3727/27/10/009

Dandapat, B. S., Santra, B., and Andersson, H. I. (2003). Thermocapillarity in a liquid film on an unsteady stretching surface. *Int. J. Heat Mass Transf.* 46 (16), 3009–3015. doi:10.1016/s0017-9310(03)00078-4

Hussan, M., Mustafa, N., and Asghar, S. (2012). Mass transfer analysis for unsteady thin film flow over stretched heated plate. *Int. J. Phys. Sci.* 7 (12), 1903–1909. doi:10.5897/IJPS11.1674

Krishna, M. V., Ahammad, N. A., and Algehyne, E. A. (2022). Unsteady MHD third-grade fluid past an absorbent high-temperature shrinking sheet packed with silver nanoparticles and non-linear radiation. *J. Taibah Univ. Sci.* 16 (1), 585–593. doi:10.1080/16583655.2022.2087396

Liu, I. C., and Andersson, H. I. (2008). Heat transfer in a liquid film on an unsteady stretching sheet. *Int. J. Therm. Sci.* 47 (6), 766–772. doi:10.1016/j.ijthermalsci.2007.06.001

Noor, N. F. M., Abdul-Aziz, O., and Hashim, I. (2010). MHD flow and heat transfer in a thin liquid film on an unsteady stretching sheet by the homotopy analysis method. *Int. J. Numer. Methods Fluids* 63 (3), 357–373. doi:10.1002/fld.2078

Sakiadis, B. C. (1961). Boundary-layer behavior on continuous solid surfaces: I. Boundary-Layer equations for two-dimensional and axisymmetric flow. *AIChE J.* 7 (1), 26–28. doi:10.1002/aic.690070108

Sakiadis, B. C. (1961). Boundary-layer behavior on continuous solid surfaces: II. The boundary layer on a continuous flat surface. *AIChE J.* 7 (2), 221–225. doi:10.1002/aic.690070211

Santra, B., and Dandapat, B. S. (2009). Unsteady thin-film flow over a heated stretching sheet. *Int. J. Heat Mass Transf.* 52 (7-8), 1965–1970. doi:10.1016/j.ijheatmasstransfer.2008.09.036

Siddiqui, A. A., and Turkyilmazoglu, M. (2022). Slit flow and thermal analysis of micropolar fluids in a symmetric channel with dynamic and permeable. *Int. Commun. Heat Mass Transf.* 132, 105844. doi:10.1016/j.icheatmasstransfer.2021.105844

Sparrow, E. M., and Gregg, J. L. (1959). A boundary-layer treatment of laminar-film condensation. *J. Heat Transf.* 81 (1), 13–18. doi:10.1115/1.4008118

Tan, M. J., Bankoff, S. G., and Davis, S. H. (1990). Steady thermocapillary flows of thin liquid layers. I. Theory. *I. Theory. Phys. Fluids A Fluid Dyn.* 2 (3), 313–321. doi:10.1063/1.857781

Turkyilmazoglu, M. (2022). Asymptotic suction/injection flow induced by a uniform magnetohydrodynamics free stream couple stress fluid over a flat plate. *J. Fluids Eng.* 144 (3), 52417. doi:10.1115/1.4052417

Turkyilmazoglu, M. (2022). Radially expanding/contracting and rotating sphere with suction. *Int. J. Numer. Methods Heat Fluid Flow* 32, 3439–3451. doi:10.1108/HFF-01-2022-0011

Wang, C. (2006). Analytic solutions for a liquid film on an unsteady stretching surface. *Heat Mass Transf.* 42 (8), 759–766. doi:10.1007/s00231-005-0027-0

Wang, C. Y. (1990). Liquid film on an unsteady stretching surface. *Q. Appl. Math.* 48 (4), 601–610. doi:10.1090/qam/1079908

10.3389/fmats.2023.1138249

Nomenclature

$\alpha_1, \alpha_2, \alpha_3, \alpha_4, \alpha_5, \alpha_6, \alpha_7, \alpha_8, \alpha_9, \alpha_{10}$ variable coefficients
$\frac{D}{Dt}$ material time derivative
F dimensionless stream function
$f(x, t)$ variable thickness of sheet
$g(\eta)$ represent the velocity component v
$h(\eta)$ represent the velocity component u
$r(x, t)$ variable size of the thin film
S unsteadiness parameter
t time variable
u, v velocity components in $x(y)$ directions
U stretching(shrinking) velocity
V injection(suction) velocity
w controlling parameter for the deformation of thin film
x, y Cartesian Coordinates

Greek letters

η similarity variables
τ shear stress
β value of similarity variable at the surface of thin film
ϵ_0 boundary layer deformation
ϵ deformation of thin film due to boundary layer
ϵ_1 deformation of sheet
γ_1 stretching and shrinking parameter
γ_2 injection and suction parameter
γ_3 dimensionless normal velocity at the surface of the film
γ_4 value of similarity variable at surface of thin film

frontiers | Frontiers in Materials

TYPE Original Research
PUBLISHED 13 March 2023
DOI 10.3389/fmats.2023.1139284

OPEN ACCESS

EDITED BY
Hammad Khalil,
University of Education Lahore, Pakistan

REVIEWED BY
A. M. Rashad,
Aswan University, Egypt
Dharmendra Tripathi,
National Institute of Technology
Uttarakhand, India

*CORRESPONDENCE
Kottakkaran Sooppy Nisar,
n.sooppy@psau.edu.sa
Naeem Ullah,
naeemullah1989@gmail.com

SPECIALTY SECTION
This article was submitted to Colloidal Materials and Interfaces, a section of the journal Frontiers in Materials

RECEIVED 06 January 2023
ACCEPTED 20 February 2023
PUBLISHED 13 March 2023

CITATION
Ullah U, Shah SIA, Nisar KS, Khan H, Ullah N and Yousaf M (2023), Numerical computation for dual stratification of slip flow of sutterby nanofluids with heat generation features.
Front. Mater. 10:1139284.
doi: 10.3389/fmats.2023.1139284

Numerical computation for dual stratification of slip flow of sutterby nanofluids with heat generation features

Ubaid Ullah[1], Syed Inayat Ali Shah[1], Kottakkaran Sooppy Nisar[2,3]*, Hamid Khan[1], Naeem Ullah[1]* and Muhammad Yousaf[4]

[1]Department of Mathematics, Faculty of Technologies and Engineering Sciences, Islamia College University Peshawar, Peshawar, KP, Pakistan, [2]Department of Mathematics, College of Arts and Sciences, Wadi Aldawaser, Prince Sattam bin Abdulaziz University, Abdulaziz, Saudi Arabia, [3]School of Technology, Woxsen University, Hyderabad, Telangana, India, [4]Department of Mathematics, University of Malakand, Chakdara, KP, Pakistan

The current communication, manifest mathematical modelling and numerical computations of Sutterby nanofluids with radiant heat assessment subject to heat generation/absorption. The thermophoresis and Brownian motion effects are incorporated *via* the Buongiorno model in flow governing equations. Moreover, the present analysis reveals the impacts of thermal stratification, velocity slip, and a magnetic field on flow phenomena. The non-Newtonian nature is modelled using Sutterby fluid. The proposed model is formulated mathematically through basic partial differential equations relating mass, momentum, energy, and nanoparticle concentration conservations using boundary layer theory. We adapted the generated governed equations to ordinary differential equations utilizing similarity variables mechanism. Numerical treatment for the reduced system of ordinary differential equations is performed using the built-in MATLAB code bvp4c. The impacts of distinct characterizing parameters on velocity, temperature, and concentration profiles are determined and analyzed *via* graphs. The existence of velocity slip parameter, fluid flow is significantly dwindle, while the surface friction growth is sophisticated. Brownian and thermophoresis mechanisms degrade the heat transmission rate and escalate the mass flux. The thermal and solutal stratification exhibits opposite conduct for thermal and concentration of the nanoparticles.

KEYWORDS

Double stratification, activation energy, heat generating, Sutterby fluid, Darcy porous medium, dual stratification, slip flow, MHD

1 Introduction

In the era of ever-increasing high demand for the improved thermal capabilities of ordinary fluids, like water, glycol, ethylene, etc., nanotechnology is an opening gate for a revolutionary modernized world. Nanofluids are a new generation of heat enhancement fluids with tiny metallic particles (1–100 nm) mixed in the ordinary fluids, thereby enhancing their thermal characteristics significantly. These particles consist of different

metals (copper, gold, silver, titanium, etc.) or their oxides. They have novel implications in biomedical and engineering sciences, along with other industrial processes where heat transfer enhancement is prominent. The nanofluids have a wide range of uses in transportation, nuclear reactors, vehicle thermal applications, solar-based science, imaging and sensing applications, food packaging, etc. Choi (Choi, 1995) was the first to describe this type of fluid, which he dubbed "nanofluids". Xuan and Li (Xuan and Li, 2000) developed preparatory techniques for multiple sampling nanoparticles, and their thermophysical properties, such as, shape, amount, attributes, and dimensions were investigated. Buongiorno (Buongiorno, 2006) discussed the significance of a heterogeneous scientific mixture of nanomaterial processing stimulus and heat transport limits. Later, Kuznetsov an d Nield (Kuznetsov and Nield, 2010) conducted an analytic study for natural convective flow of viscous nanofluids across a vertical flat surface. Makinde and Aziz (Makinde and Aziz, 2011) discussed the convective heat transport for boundary layer flow of nanofluid generated by a linearly stretched surface. In another study, Mustafa et al. (Mostafa et al., 2011) reported an analytic investigation for stagnation-point flow of nanofluid using Buongiorno model. After that, Ibrahim et al. (Ibrahim et al., 2013) gave numerical solutions for MHD stagnation point flow generated by stretching surface in the presence of nanoparticles. The comprehensive analysis of literature in the framework of nanofluids flow and heat transport characteristics can be found in the works of (Hamad and Ferdows (Hamad and Ferdows, 2012), Kalidas Das (Das, 2012), Bachok et al. (Bachok et al., 2012), Turkyilamzoglu (Turkyilmazoglu, 2012), and Alsaedi et also (Effect of heat generation, 2012), etc.).

The fundamental manifestation of Navier-Stoke's theory of fluid dynamics is the no-slip boundary condition. However, there seem to be cases when this scenario is inappropriate. Specifically, for several non-Newtonian fluids and nanofluids, the no-slip boundary condition is inadequate, as certain polymer melts frequently exhibit microscopic wall slip, which is governed in general by a non-linear and monotone relationship between slip velocity and traction. Micro electromechanical systems (MEMS) have developed numerous microfluidic devices in the medical, physical, biological, chemical, engineering, and energy domains in recent years. The physical aspects of microscale flow and heat transmission, which may differ from macroscale flow, must be thoroughly understood to meet the technical needs. In an earlier studies, Andersson (Andersson, 2002) conducted the investigations that considered the slip boundary condition during the flow over a stretching sheet. He gave the exact solutions for modelled flow equations. Wang (Wang, 2002) gave the exact similarity solution for flow equations driven by a stretching geometry with partial slip condition. Again, Wang (Wang, 2006) researched at stagnation slip flow and heat transfer on a moving plate. Later, Wu (Wu, 2008) suggested a new second-order slip model based on the linear Boltzmann equation's. Similarly, Fang et al. (Fang et al., 2009) used mathematical methods to study slip magnetohydrodynamics viscous flow over a stretching sheet. Some notable research works showcasing the innovative properties of velocity slip during fluid flows can found in the references (Sutterby, 1965; Sutterby, 1966; Aziz, 2010; Fang et al., 2010; Hayat et al., 2011; Mahantesh et al., 2012).

The stratification phenomenon in fluids has recently attracted a lot of attention in heat and mass transport assessment, and it is a mechanism that occurs as a result of temperature, concentration, and density fluctuations in various fluids. In fact, due to its prevalence in geophysical flows such as oceans, rivers, ponds, solar ponds, and thermal energy storage technologies, evaluating the flow through a double stratified media is an essential fluid topic. Hayat et al. (Hayat et al., 2015) evaluate a dual stratified radiative flow of reactive species Oldroyd-B fluid in the presence of mixed convection. Hayat et al. (Hayat et al., 2017) report an assessment of chemical reactions in mixed convective squeezing fluid flows with thermal radiation. Muhammad et al. (Rehman et al., 2016) demonstrate a dual stratified flow of squeezed viscous fluid utilizing modified Fick's and Fourier's theories. The stagnation point Magnetohydrodynamic flowing of reactive chemical Powell-Eyring nano-fluid through dual stratified substrate with thermal radiation was established by Ramzan et al. (Ramzan et al., 2017). Some applications of thermal radiation and chemical reaction of various stratified flows in physiology and industry can be seen in literature (Mahanthesh et al., 2016; Rehman et al., 2016; Daniel et al., 2017; Muhammad et al., 2017; Bég et al., 2020; Lin and Ghaffari, 2021; Rehman et al., 2021; Unyong et al., 2021; Nandi et al., 2022). However Rashid et al. studied the unsteady slip flow amicroplor nanofluid over an impulsively stretched vertical surface see (El-Hakiem and Rashad, 2007; El-Kabeir et al., 2007; El-Kabeir et al., 2010; Chamkha et al., 2011; Tlili et al., 2019; Reddy et al., 2020; Nabwey et al., 2022). Furthermore, Tripathi et al. investigated the peristaltic pumping of hybrid nanofluids throught an asymmetric microchannel in the presence of electromagnetic field see (Akram et al., 2020a; Akram et al., 2020b; Prakash et al., 2020; Tripathi et al., 2020; Akram et al., 2021; Tripathi et al., 2021; Akram et al., 2022; Prakash et al., 2022; Saleem et al., 2022).

In any of the aforementioned analyses, the Sutterby fluid model was never used in conjunction with thermal radiation and a heat generating or absorbing source. The constitutive equations of Sutterby fluid are used in mathematical modelling to achieve this goal. The Sutterby fluid framework illustrates diluted polymer solutions and is one of the non-Newtonian fluid models used to study the rheological properties of various materials. As a result, the current effort is to investigate the heat-producing/absorbing Sutterby fluid flow across horizontal geometry with thermal radiation, as well as double stratification near thermal radiation. As an outcome, the influence of different flow, heat, and mass transport attributes is reported. Nusselt and Sherwood values, as well as drag force (skin friction coefficient), are visually assessed *versus* numerous emerging parameters.

2 Model development

As shown in **Figure 1**, an incompressible two-dimensional flow of non-Newtonian Sutterby fluid with heat and mass transport past an infinite flat surface is deliberated. The stretching surface has the linear velocity $u_w(x) = ax$, where a is constant. Non-linearly varying thermal radiation, velocity slip, heat generation/absorption are also incorporated in this analysis. The thermal stratification mechanism is studied by considering the surface temperature $T_w(x) = T_0 + m_1 x$ and ambient temperature $T_\infty(x) = T_0 + m_2 x$, respectively. Similarly, the surface concentration $C_w(x) = C_0 + m_1 x$

and free stream concentration $C_\infty(x) = C_0 + m_2 x$, is taken to discuss the solutal stratification. A magnetic force of intensity B_0 is applied parallel to the plate's y-axis, which is perpendicular to it. The induced magnetic field created by the velocity of an electrically conducting fluid is supposed to be insignificant in this case. The fluid is supposed to be grayish, generating, and absorbent but quasi medium, and the optically thick radiating limit is taken into account in this study, where the radiant heat flux term can be reduced using the Rosselant estimation. The use of Cartesian coordinates (x,y) to study the flow under discussion is acceptable because the x-axis runs parallel to the stretched sheet and the y-axis runs perpendicular to it. The following are the rheological equations that characterize the incompressible flow of Sutterby fluid:

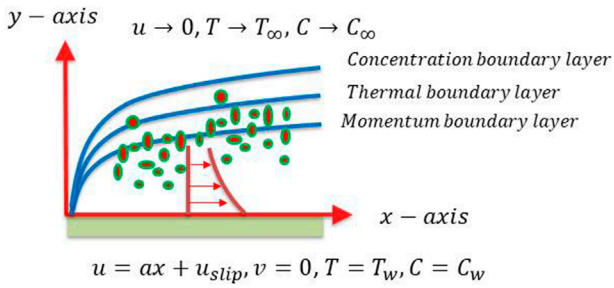

FIGURE 1
The physical model and coordinate systems.

2.1 Sutterby fluid model

The Cauchy stress tensor for Sutterby fluid (Sutterby, 1965; Sutterby, 1966) is expressed as

$$\tau = -pI + \mu S \tag{1}$$

where extra stress tensor has the form

$$S = \mu_0 \left(\frac{sinh^{-}1(\beta\dot{\gamma})}{\beta\dot{\gamma}} \right) A_1 \tag{2}$$

The shear rate can be defined as:

$$\dot{\gamma} = \sqrt{\left(\frac{1}{2} tr(A_1)^2 \right)} \tag{3}$$

where μ_0 is dynamic viscosity, B is the fluid parameter, n denoted the power-law index and "tr" means trace. For $Sinh^{-1}$ function, the second order approximation is considered as:

$$sinh^{-}1(\beta\dot{\gamma}) \approx \beta\dot{\gamma} - \frac{(\beta\dot{\gamma})^3}{6} \tag{4}$$

As a result, the stress tensor takes the form:

$$S = \mu_0 \left[1 - \frac{(\beta\dot{\gamma})^2}{6} \right]^n A_1 \tag{5}$$

For two-dimensional steady flow, we take the velocity field of the form

$$V = (u(x,y), v(x,y), 0] \tag{6}$$

In view of Eq. 4, the shear rate takes the form.

The extra stress components are expressed as below

$$\dot{\gamma} = \left[2\left(\frac{\partial u}{\partial x} \right)^2 + \left(\frac{\partial u}{\partial y} + \frac{\partial v}{\partial x} \right)^2 + 2\left(\frac{\partial u}{\partial x} \right)^2 \right]^{\frac{1}{2}} \tag{7}$$

The extra stress components are expressed as below

$$S_{xx} = -P + 2\mu_0 \left(1 - \frac{(\beta\dot{\gamma})^2}{6} \right)^n \frac{\partial u}{\partial y} \tag{8}$$

$$S_{xy} = \mu_0 \left(1 - \frac{(\beta\dot{\gamma})^2}{6} \right)^n \left(\frac{\partial u}{\partial y} + \frac{\partial v}{\partial x} \right) \tag{9}$$

$$S_{yy} = -P + 2\mu_0 \left(1 - \frac{(\beta\dot{\gamma})^2}{6} \right)^n \frac{\partial v}{\partial y} \tag{10}$$

Based on the above restrictions and involving boundary layer approximations, the prevailing equations for Sutterby nanofluids using the Buongiorno model are given as

$$\frac{\partial u}{\partial x} + \frac{\partial v}{\partial y} = 0 \tag{11}$$

$$u\frac{\partial u}{\partial x} + v\frac{\partial u}{\partial y} = \nu\left(1 - \frac{\beta^2}{6}\frac{\partial u}{\partial y}^2 \right)^n \frac{\partial^2 u}{\partial y^2} - \frac{n\nu\beta^2}{6}\left(1 - \frac{\beta^2}{6} \right) \times \left(\frac{\partial u}{\partial y}^n - 1 \right)\left(\frac{\partial u}{\partial y}^2 \right)\frac{\partial^2 u}{\partial y^2} - \frac{\sigma B0^2 u}{\rho}, \tag{12}$$

$$u\frac{\partial T}{\partial x} + v\frac{\partial T}{\partial y} = \alpha\frac{\partial^2 T}{\partial y^2} + \tau_{np}\left(D_B\frac{\partial C}{\partial y} \right)\frac{\partial T}{\partial y} + \frac{D_T}{T_\infty}\left(\frac{\partial T}{\partial y} \right)^2 - \frac{1}{\rho C_p}\left(\frac{16\sigma^* T_\infty}{3kk^*} \right)\frac{\partial^2 T}{\partial y^2} + Q_1(T - T_\infty), \tag{13}$$

$$u\frac{\partial T}{\partial x} + v\frac{\partial C}{\partial y} = D_B\frac{\partial^2 c}{\partial y^2} + \frac{D_T}{T_\infty}\frac{\partial^2 T}{\partial y^2}, \tag{14}$$

The associated boundary conditions

$$u = u_w + L\left[1 - \frac{B^2}{6}\left(\frac{\partial u}{\partial y} \right)^2 \right]^2 \left(\frac{\partial u}{\partial y} \right), \quad v = 0, T = T_w, \quad C = C_w aty = 0 \tag{15}$$

$$u \to U_\infty, T \to T_\infty, C \to \infty \; as \; y \to \infty \tag{16}$$

2.2 Transformations

The dimensionless form of the modelled problem is obtained by utilizing the following dimensionless variables:

$$\psi = \sqrt{av}xf(\eta), \eta = y\sqrt{\frac{a}{\nu}}, \theta(\eta) = \frac{T - T_\infty}{T_w - TT_\infty}, \phi(\eta) = \frac{C - C_\infty}{C_w - C_\infty}. \tag{17}$$

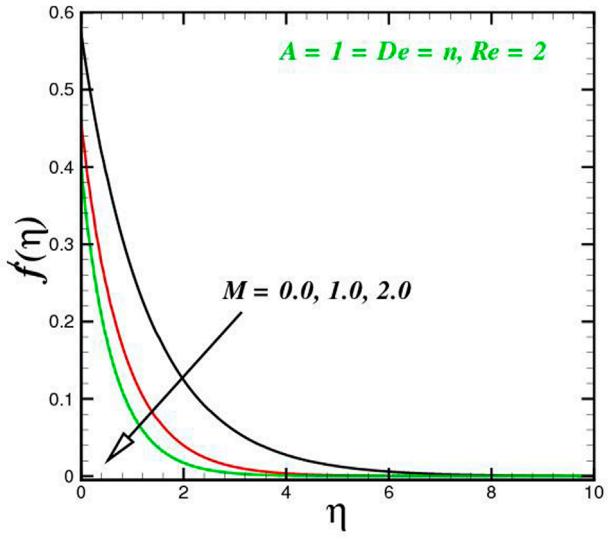

FIGURE 2
$f\prime(\eta)$, alteration *via* M.

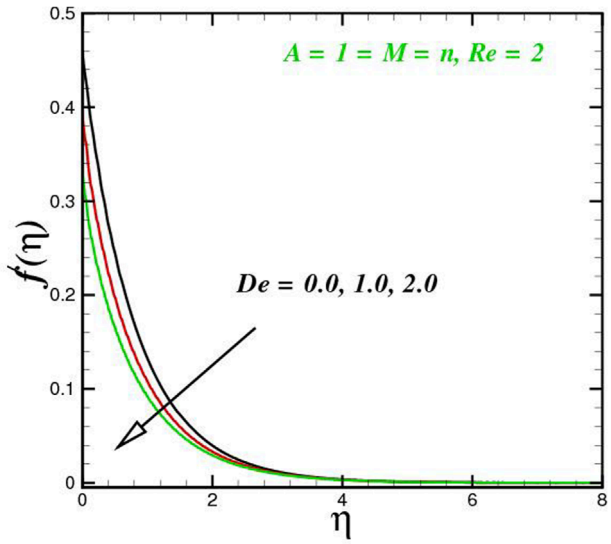

FIGURE 3
$f\prime(\eta)$, alteration *via* De.

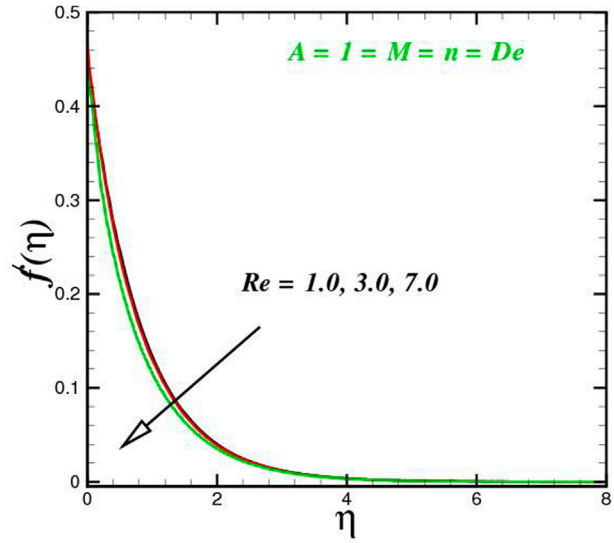

FIGURE 4
$f\prime(\eta)$, alteration *via* Re.

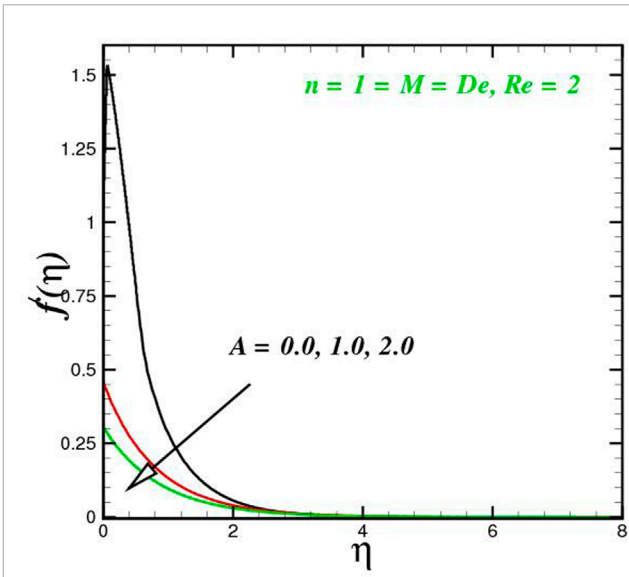

FIGURE 5
$f\prime(\eta)$, alteration *via* A.

Here, $f'(\eta)$, $\theta(\eta)$,and $\phi(\eta)$ represents the dimensionless stream function, dimensionless temperature and concentration. Making use of non-dimensional transformation, the leading Eqs. (4.12)–(4.14) reduced to

$$\left(1-\frac{1}{6}DeRef'^2\right)^n f''' - \frac{nDeRe}{3}\left(1-\frac{1}{6}DeRef'^2\right)^{n-1} f''f'^2 + ff' - f'^2 - Mf' = 0 \tag{18}$$

$$\left(1+\frac{4}{3}R\right)\theta'' + Pr\left(f\theta' - f'\theta\right) + Pr\left(N_b\theta'\phi' + N_t\theta'^2\right) - Prs_t f' + PrQ\theta = 0, \tag{19}$$

$$h'' + Lef\phi' - Le\phi f' + \frac{N_b}{N_t}\theta'' - LeS_c f' = 0 \tag{20}$$

$$f(0) = 1, f'(0) = 1 + Af'(0)\left[1-\frac{1}{6}DeRef'^2(0)\right]^n, \quad \theta(0) = 1 - S_t, \phi(0) = 1 - S_c, \ at\ \eta = 0, \tag{21}$$

$$f'(\infty) = 0, \theta(\infty) = 0, \phi(\infty) = 0\ as\ \eta \to \infty \tag{22}$$

where η is the similarity variables and the prime denotes differentiation with respect toη. The dimensionless parameters

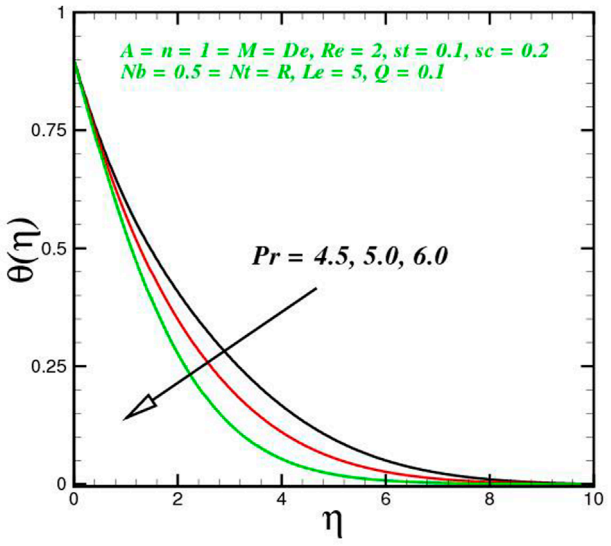

FIGURE 6
θ(η), alteration *via* Pr.

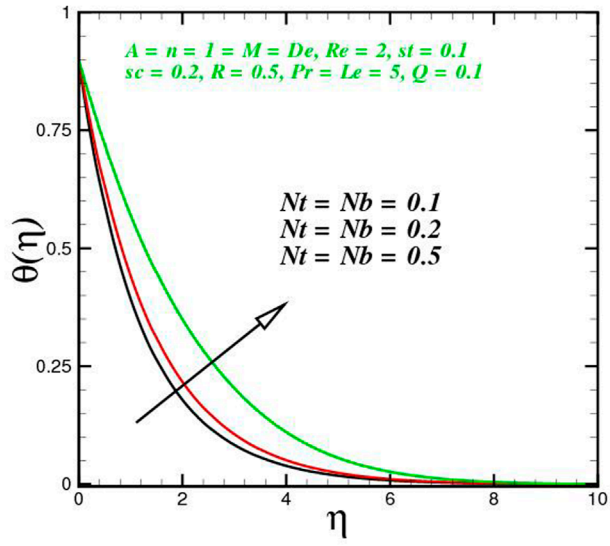

FIGURE 8
θ(η), alteration *via* Nt.

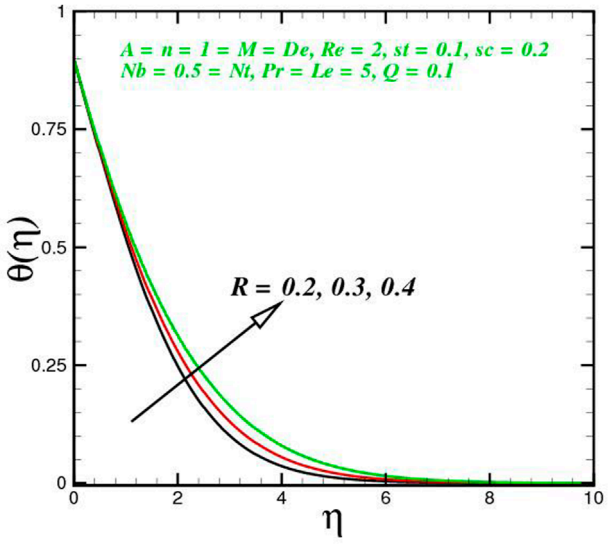

FIGURE 7
θ(η), alteration *via* R.

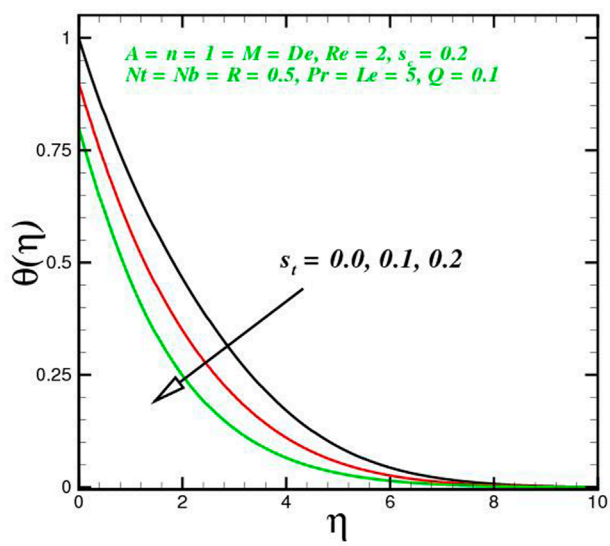

FIGURE 9
θ(η), alteration *via* S_t.

in the above equations are the Deborah number De, heat generation/absorption parameter Q, thermal stratification parameter s_t and solutal stratification parameter s_c, given as $De = a^2B^2, Q = \frac{Q_1}{\rho C_p a}, S_t = \frac{m_2}{m_1}, S_t = \frac{m_4}{m_3}$

$$C_f\sqrt{Rex} = \left[1 - \frac{1}{6}DeRef''(0)\right]^2 f''(0),$$
$$Nu_x\sqrt{Rex} = \left(\frac{1}{1-s_1}\right)Q'(1),$$
$$Sh_x\sqrt{Rex} = -\left(\frac{1}{1-S_2}\right)\phi'(1). \tag{23}$$

$$f = Z_1, f' = Z_2, f'' = Z_3, \theta = Z_4, \theta' = Z_5, \phi' = Z_7. \tag{24}$$

$$Z_1' = Z_2, Z_2' = Z_3, Z_3' = \frac{Z_2^2 - Z_1 z_2 + \mu Z_2}{A_1 - \frac{nDeRe}{3}A_2},$$
$$Z_5' = \frac{Pr\left(N_b Z_5 Z_7 - N_t Z_5^2 + Z_1 Z_5 - Z_2 Z_4 - Z_2 Z S_t Q Z_4\right)}{\left(1 + \frac{4}{3}R\right)}, \tag{25}$$
$$Z_7' = -LeZ_1 z_7 + LeZ_2 Z_6 + LeZ_2 S_c - \frac{N_b}{N_t}Z_5'$$

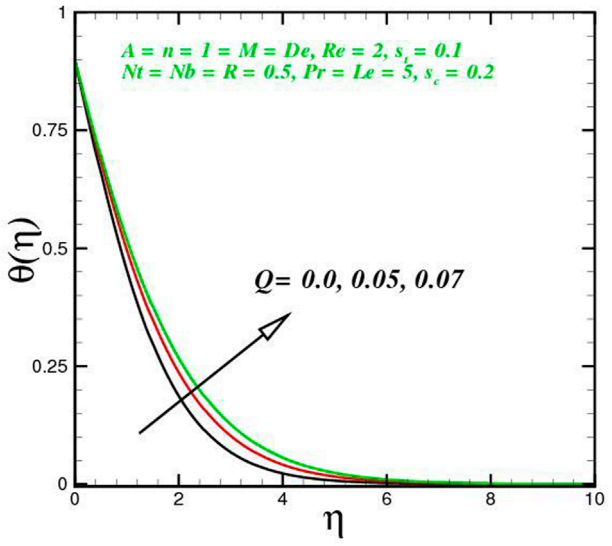

FIGURE 10
θ(η), alteration *via* Q.

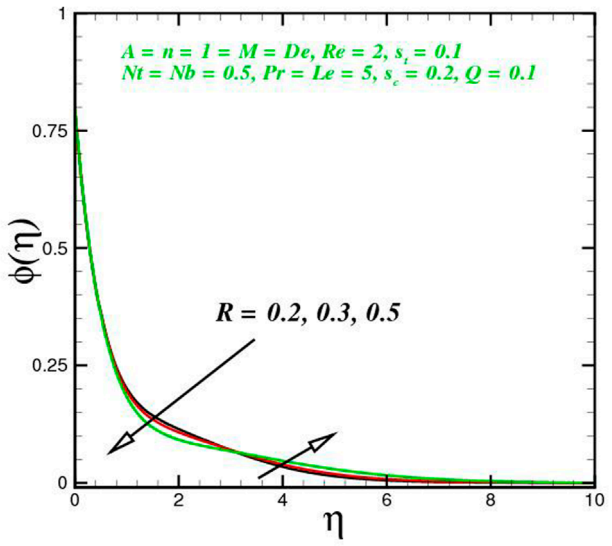

FIGURE 11
ϕ(η), alteration *via* R.

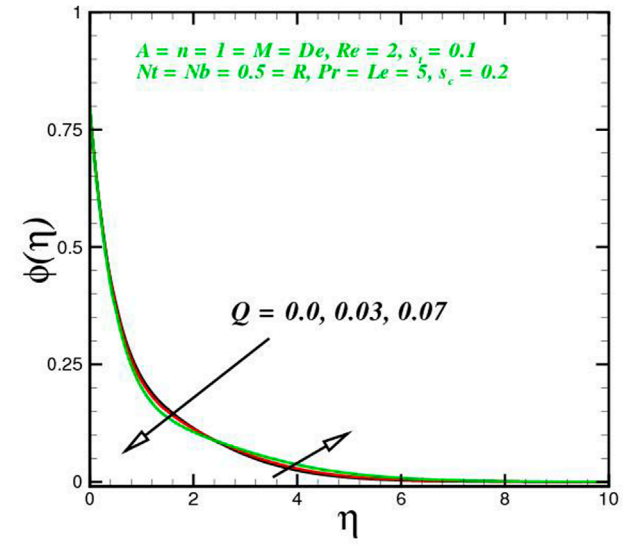

FIGURE 12
ϕ(η), alteration *via* Q.

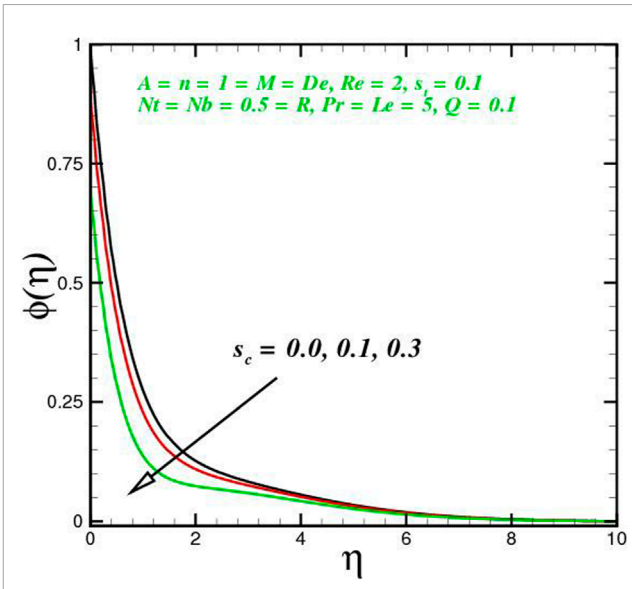

FIGURE 13
ϕ(η)), alteration *via* S_c.

along with boundary conditions

$$Z_1(0) = 0, Z_2(0) = 1 + AZ_3(0)\left[1 - \frac{1}{6}DeReZ_3^2(0)\right]^n,$$
$$Z_4(0) = 1 - S_t, Z_6(0) = 1 - S_c \tag{26}$$

$$Z_2(\infty) \to 0, Z_4(\infty) \to 0, Z_6(\infty) \to 0. \tag{27}$$

The above set of seven first-order ODEs Eq. 25 with boundary conditions Eqs 26 and 27 is numerically integrated by exercising the MATLAB routine bvp4c which is a finite difference code that uses the collocation method to execute the three - stage Labatto IIIa formula. The numerical analysis is performed by selecting a suitable finite value ($\eta_\infty = 10$) to fulfill the for field boundary conditions. The error tolerance of $10^{-6}$is set for computational purpose. The RFK45 procedure is adaptive because it modifies the number and location of grid points throughout each iteration, keeping the local error within acceptable ranges. The asymptotic boundary conditions in Eq. 27 are supplemented in the existing situation by a predefined limit in the range 10–15, based on the parameter values. To assure that all numerical results approach the asymptotic values accurately, infinity is desired. The choice of an appropriately large number for infinity is essential for maintaining desirable reliability in boundary layer

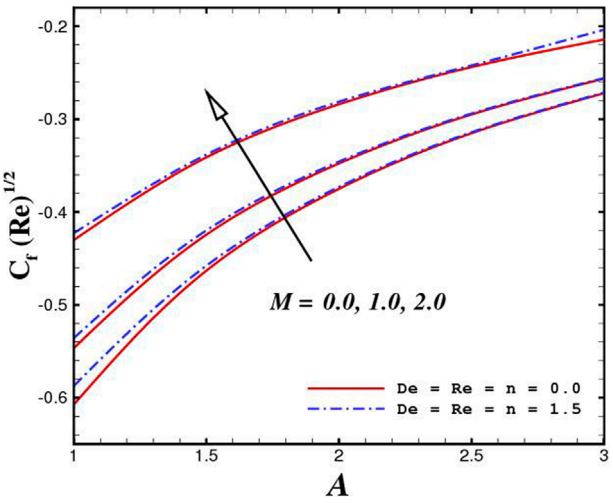

FIGURE 14
$skinC_f\sqrt{Re_x}$, sketch for frequent values M and A.

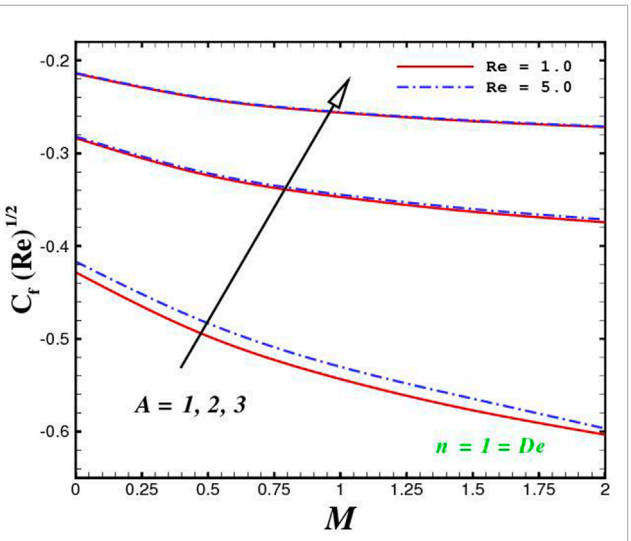

FIGURE 15
$skinC_f\sqrt{Re_x}$, sketch for frequent values of A and M.

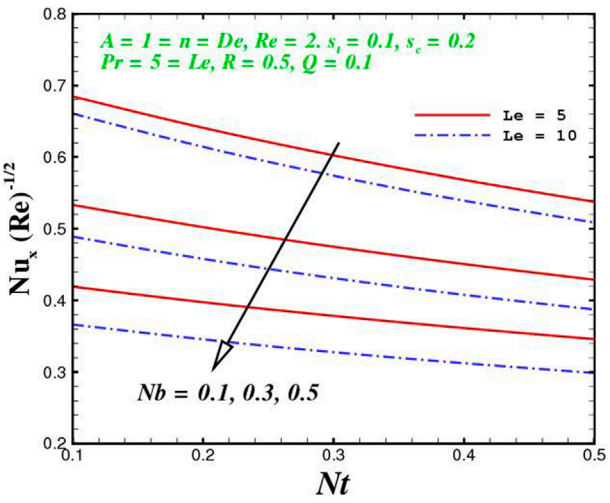

FIGURE 16
Nusslt $Nu_x\sqrt{Re_x}$, sketch for frequent values of Nb and Nt.

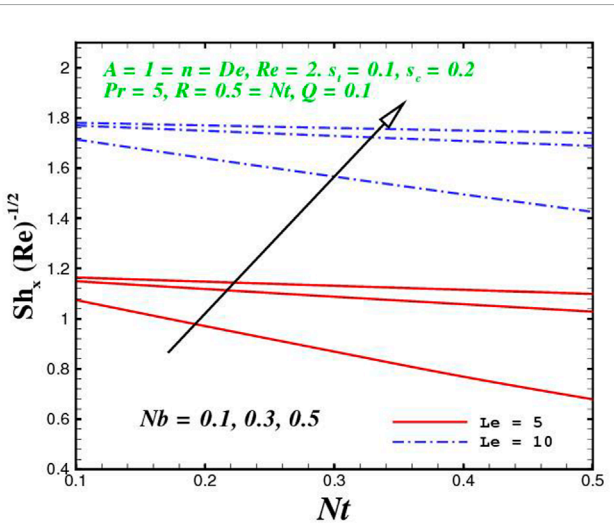

FIGURE 17
Shaerwood $Sh_x\sqrt{Re_x}$, sketch for frequent values of Nb and Nt.

flows, and it is a common blunder seen in many investigations. The stepped equations used to estimate Eq. 25, employing fifth–fourth-order Runge-Kutta-Fehlberg procedures under conditions Eqs 26 and 27 are listed below (Bég et al., 2020; Bég et al., 2022).

$K_0 = f(x_0, y_0)$.

$K_1 = f\left(x_0 + \frac{1}{4}h, y_0 + \frac{1}{4}K_0 h\right)$

$K_2 = f\left(x_0 + \frac{3}{8}h, y_0 + \left(\frac{3}{32}K_0 + \frac{9}{32}k_1\right)\right)$

$K_3 = f\left(x_0 + \frac{12}{13}h, y_0 + \left(\frac{1932}{2197}k_0 - \frac{7200}{2197}K_1 + \frac{7296}{2197}k_2\right)h\right)$

$K_4 = f\left(x_0 + h, y_0 + \left(\frac{439}{216}K_0 - 8K_1 + \frac{3860}{513}K_2 - \frac{845}{4104}K_3\right)h\right)$

$K_5 = f\left(x_0 + \frac{1}{2}h, y_0 + \left(\frac{8}{27}k_0 + 2K_1 - \frac{3544}{2565}K_2 - \frac{1859}{4104}K_3 - \frac{11}{40}K_4\right)h\right)$

$y_{i+1} + \left(\frac{25}{216}K_0 + \frac{1408}{2565}K_2 + \frac{2197}{4104}K_3 - \frac{11}{5}K_4\right)h$

$Z_{i+1} = Z_i + \left(\frac{16}{135}K_0 + \frac{6656}{12825}K_2 + \frac{28561}{56430}K_3 - \frac{9}{40}K_4 + \frac{2}{55}K_5\right)h$

The fourth-order Runge-Kutta component is denoted by y, and the fifth-order Runge-Kutta stage is denoted by Z. By subtracting the two values obtained, an estimate of the error can be obtained. The findings can be redone with a reduced step size if the deviation reaches a certain threshold. The following is an example of how to determine the new step size:

$$h_{new} = h_{old}\left[\frac{\epsilon h_{old}}{2\left(Z_{i+1} - y_{i+1}\right)}\right]^{\frac{1}{4}} \tag{28}$$

2.3 Results and discussion

The function of innovative quantities on flow profile pictures is investigated in this section for various values of emerging

parameters. Physical changes in temperature, concentration, skin friction, Nussselt and Sherwood, and velocity *versus* numerous parameters are reviewed in Figures 2–17. The variational curves of velocity towards M are shown in Figure 2. It is evident that velocity dwindle near the center and exhibits a reverse attitude across the walls. In fact, this means that increasing M values strengthens the retarding and Lorentz forces, which has an immediate effect on the fluid dynamics. The diminishing conduct of Sutterby fluid is exposed in Figure 3. De is a rheological term that describes the fluidity of substances under precise flow conditions. The escalation in De assist the delaying flow as witnessed in the paint. Physically, strengthened in De result in shear thickening rheology of the Sutterby fluid as a consequences the fluid flow dwindle. The reverse trend for $f'(\eta)$ against Reynolds Re is delineated in Figure 4. Physically, uplifting Re, result in denser liquid, as a consequences, depressing the flow rate. The flowing rate through the surface dwindle; Figure 5, addresses the slip A impact on velocity $f'(\eta)$. The flow structure is depressed with greater values of slip factor. In fact, velocity slip escalates the momentum boundary layer thickness. Figures 6–10), exhibits the temperature conduct *via* novel parameters. The Prandtl Pr consequences for temperature $\theta(\eta)$, is painted in Figure 6. Since the Prandtl number is inversely related to thermal diffusivity, boosting it cools the flow. This is justified by the fact that an escalation in Pr contracts the thermal boundary layer thickness; Figure 7 outlines the impact of the radiation parameter R on the temperature $\theta(\eta)$. The radiant parameter indicates how much heat transport through conduction contributes to thermal radiation. As an outcome, for increasing R values, there is a distinct rise in temperature curves. Optimizing thermal radiation entails transferring energy into the flow *via* radiating, which promotes the fluid's thermal performance. The joint action of Nt and Nb on thermal field is offered in Figure 8. Accelerating Brownian action caused quicker stochastic mobility of nanoparticles in a stream, resulting in an increase in thermal boundary layer thickness and a quicker spike in flow temperature. For increasing Nt values, a similar trend can be seen. As a function of the thermophoresis mechanism, more heated particles near the surface migrate away from hot regions into cold regions, raising temperature there, and the entire system temperature rises. The stratification parameter s_t attributed to temperature variation is indicated graphically in Figure 9. The thermally stratification process induces layer development owing to temperature variations; as the stratification parameter is strengthened, the temperature differential between the wall and the frame of reference declines, and the system's cools down. Positive values of Q, result in the highest temperature because more heat generated, which strengthens the thermal behavior. When the heat input parameter advances, the boundary layer relating to the temperature field thickens. The uplifting temperature curves can be witnessed from Figure 10. Figures 11–17) show how different flow characteristics can be used to map the decorum of dimensionless concentration. A substantial growth in radiant parameter R, the corresponding concentration of the nanoparticles depressed near the wall, while within the central region, the concentration boundary layer expand as clear from Figure 11. The physics behind the mechanism is that, the radiant parameter escalates the thermal and concentration boundary layer thickness, while adverse reaction happen near the wall of geometry. The influence of heat generation exhibits contrary conduct on concentration sketch $\phi(\eta)$. The heat producing/absorbing coefficient, Q, has little significance on the concentration distribution, $\phi(\eta)$, since the fluid's concentration remains unaffected as the heat in the fluid changes. The heat generation coefficient is responsible for increasing the fluid flow's heat gradient, although it has no effect on the fluid particle concentration levels. The fluid central regime is dwindle, while the concentration layer near the boundaries are little altered is visible in Figure 12. To be more explicit; Figure 11 exhibits the concentration distribution's descending tendency for positive values of the solutal stratified parameter s_c. The potential difference across wall surface and ambient fluid concentration$C_w - C_\infty$ drops as the potential difference between c surface wall and ambient fluid concentration upturns, dropping the thickness of the corresponding concentration boundary layer; Figure 14, offerings the dimension of skin friction against magnetic parameter and velocity slip. It is evident from the scenario that surface skin friction expand against velocity slip parameter, while the magnetic field strength weakens the surface skin friction. The shear strength at the wall drops significantly with an expansion in slip parameter when the surface is sufficiently smooth and fluid flows at nanoscales is predicted; Figure 17, reveal the same outcomes. The action of magnetic parameter in the existence of slip parameter is obvious. Magnetic parameter reduces the movement growth, as a result the skin friction diminished; Figure 16, testify that the heat transfer rate is shrink with the Brownian Nb and thermopheretic Nt phenomena in the flow region. This is justified by the fact that greater Brownian motion results in the intensification of large movements of nanoparticles, and consequently heat is transmitted into colder particles. This phenomenon depressed the nanoparticles' heat transfer rate. While on the other hand, mass transmission rate (Sherwood number) is significantly high with the growth of said phenomena as clear from Figure 17.

3 Conclusion

The investigation presented in this paper helps us to understand, physically as well as numerically, the aspects of activation energy on magnetized Sutterby nanoliquid subjected to heat generation/absorption through a Darcy porous medium. The well-established Buongiorno model is employed to examine the features of Brownian and thermophoresis diffusion of the nanofluid. The most significant outcomes noted from present research are described as follows.

- $g(\zeta)$ nanoliquid temperature deteriorates for larger S_1while it intensifies against Q.
- Positive values (heat generation) of Q, improve the temperature distribution while reverse trend is seen in case of negative values (heat absorption).
- Velocity$f'\zeta)$, is increasing function of n, and D_a and dwindle for large M.
- Opposite trend of $h(\zeta)$ is detected against N_b (Brownian moment parameter) and N_b (thermophoresis parameter).
- The solutal stratification parameter S_1, Le and γ (Chemical reaction rate) exhibitsdiminishing behavior for concentration of the nanofluid.

- Heat transfer rate is significantly rises with heat generating parameter.
- Large magnetic number reduces the skin friction of the nanofluid.

Data availability statement

The raw data supporting the conclusions of this article will be made available by the authors, without undue reservation.

Author contributions

There are six authors in this manuscript and each one has contributed properly. The mathematical model has been proposed by SA, all the numerical computations and their graphs have been carried out by UU. The discussion of graphs and their physical interpretation has been given by HK and KSN. The literature review and comparison of the present simulations with the classical data has been established by MY. The final review and amendments in the manuscript has been carried out by NU.

Funding

This study is supported *via* funding from Prince Sattam bin Abdulaziz University project number (PSAU/2023/R/1444).

Conflict of interest

The authors declare that the research was conducted in the absence of any commercial or financial relationships that could be construed as a potential conflict of interest.

Publisher's note

All claims expressed in this article are solely those of the authors and do not necessarily represent those of their affiliated organizations, or those of the publisher, the editors and the reviewers. Any product that may be evaluated in this article, or claim that may be made by its manufacturer, is not guaranteed or endorsed by the publisher.

References

Akram, J., Akbar, N. S., and Tripathi, D. (2021). A theoretical investigation on the heat transfer ability of water-based hybrid (Ag–Au) nanofluids and Ag nanofluids flow driven by electroosmotic pumping through a microchannel. *Arabian J. Sci. Eng.* 46, 2911–2927. doi:10.1007/s13369-020-05265-0

Akram, J., Akbar, N. S., and Tripathi, D. (2020). Comparative study on ethylene glycol based Ag-Al 2 O 3 and Al 2 O 3 nanofluids flow driven by electroosmotic and peristaltic pumping: A nano-coolant for radiators. *Phys. Scr.* 95 (11), 115208. doi:10.1088/1402-4896/abbd6b

Akram, J., Akbar, N. S., and Tripathi, D. (2020). Numerical simulation of electrokinetically driven peristaltic pumping of silver-water nanofluids in an asymmetric microchannel. *Chin. J. Phys.* 68, 745–763. doi:10.1016/j.cjph.2020.10.015

Akram, J., Akbar, N. S., and Tripathi, D. (2022). Thermal analysis on MHD flow of ethylene glycol-based BNNTs nanofluids via peristaltically induced electroosmotic pumping in a curved microchannel. *Arabian J. Sci. Eng.* 47, 7487–7503. doi:10.1007/s13369-021-06173-7

Andersson, H. (2002). Slip flow past a stretching surface. *Acta Mech.* 158, 121–125. doi:10.1007/bf01463174

Aziz, A. (2010). Hydrodynamic and thermal slip flow boundary layer over a flat plate with constant heat flux boundary condition. *Commun. Non-linear Sci. Numer. Simul.* 15, 80–573.

Bég, O. A., Bég, T., Khan, W. A., and Uddin, M. J. Multiple slip effects on nanofluid dissipative flow in a converging/diverging channel: A numerical study. *Heat. Transf.* 51(1) (2022)1040–1061. doi:10.1002/htj.22341

Bég, O. A., Uddin, M. J., Bég, T. A., Kadir, A., Shamshuddin, M. D., and Babaie, M. (2020). Numerical study of self-similar natural convection mass transfer from a rotating cone in anisotropic porous media with Stefan blowing and Navier slip. *Indian J. Phys.* 94(6), 863–877. doi:10.1007/s12648-019-01520-9

Buongiorno, J. (2006). Convective transport in nanofluids. *J. Heat. Transf.* 128 (3), 240–250. doi:10.1115/1.2150834

Chamkha, A. J., Rashad, A. M., and Al-Meshaiei, E. (2011). Melting effect on unsteady hydromagnetic flow of a nanofluid past a stretching sheet. *Int. J. Chem. React. Eng.*, 9, doi:10.2202/1542-6580.2613

Choi, S. U. S. (1995). Enhancing thermal conductivity of fluids with nanoparticles. *Am. Soc. Mech. Eng. Fluids Eng. Div. Fed.* 231, 99–105.

Daniel, Y. S., Aziz, Z. A., Ismail, Z., and Salah, F. (2017). Double stratification effects on unsteady electrical MHD mixed convection flow of nanofluid with viscous dissipation and Joule heating. *J. Appl. Res. Technol.* 15(5), 464–476. doi:10.1016/j.jart.2017.05.007

Das, K. (2012). Slip flow and convective heat transfer of nanofluids over a permeable stretching surface. *Comput. Fluids* 64, 34–42. doi:10.1016/j.compfluid.2012.04.026

Effect of heat generation (2012). Effect of heat generation/absorption on stagnation point flow of nanofluid over a surface with convective boundary conditions. *Comm. Nonlinear Sci. Num. Simul.* 17, 4210–4223.

El-Hakiem, M. A., and Rashad, A. M. (2007). Effect of radiation on non-Darcy free convection from a vertical cylinder embedded in a fluid-saturated porous medium with a temperature-dependent viscosity. *J. porous media* 10(2).

El-Kabeir, S. M. M., Chamkha, A., and Rashad, A. M. (2010). Heat and mass transfer by MHD stagnation-point flow of a power-law fluid towards a stretching surface with radiation, chemical reaction and Soret and Dufour effects. *Int. J. Chem. React. Eng.* 8. doi:10.2202/1542-6580.2396

El-Kabeir, S. M. M., Rashad, A. M., and Gorla, R. S. R. (2007). Unsteady MHD combined convection over a moving vertical sheet in a fluid saturated porous medium with uniform surface heat flux. *Math. Comput. Model.* 46 (3-4), 384–397. doi:10.1016/j.mcm.2006.11.010

Fang, T., S.YaoZhang, J., and Aziz, A. (2010). Viscous flow over a shrinking sheet with second order slip flow model. *Commun. Non-linear Sci. Numer. Simul.* 15, 42–831.

Fang, T., Zhang, J., and Yao, S. (2009). Slip MHD viscous flow over a stretching sheet–an exact solution. *Commun. Non-linear Sci. Numer. Simul.* 14, 3731–3737. doi:10.1016/j.cnsns.2009.02.012

Hamad, A., and Ferdows, M. (2012). Similarity solution of boundary layer stagnation-point flow towards a heated porous stretching sheet saturated with a nanofluid with heat absorption/generation and suction/blowing: A lie group analysis. *Nonlinear Sci. Numer. simulat.* 17, 132–140. doi:10.1016/j.cnsns.2011.02.024

Hayat, T., Khan, M., Imtiaz, M., and Alsaedi, A. (2017). Squeezing flow past a Riga plate with chemical reaction and convective conditions. *J Molec Liqs* 225, 569–576. doi:10.1016/j.molliq.2016.11.089

Hayat, T., Muhammad, T., Shehzad, S. A., and Alsaedi, A. (2015). Temperature and concentration stratification effects in mixed convection flow of an Oldroyd-B fluid with thermal radiation and chemical reaction. *PloS one* 10 (6), 0127646. doi:10.1371/journal.pone.0127646

Hayat, T., Qasim, M., and Mesloub, S. (2011). MHD flow and heat transfer over permeable stretching sheet with slip conditions. *Int. J. Numer. Meth Fluid.* 66, 963–975. doi:10.1002/fld.2294

Kuznetsov, A. V., and Nield, D. A. (2010). Natural convective boundary-layer flow of a nanofluid past a vertical plate. *Int. J. Therm. Sci.* 49, 243–247. doi:10.1016/j.ijthermalsci.2009.07.015

Lin, P., and Ghaffari, A. (2021). Heat and mass transfer in a steady flow of Sutterby nanofluid over the surface of a stretching wedge. *Phys. Scr* 96(6), 065003. doi:10.1088/1402-4896/abecf7

Mahantesh, M., Vajravelu, K., Abel, M. S., and Siddalingappa, M. N. (2012). Second order slip flow and heat transfer over a stretching sheet with non-linear Navier boundary condition. *Int. J. Therm. Sci.* 58, 50–142.

Mahanthesh, B., Gireesha, B. J., and Gorla, R. S. (2016). Nonlinear radiative heat transfer in MHD three-dimensional flow of water based nanofluid over a non-linearly stretching sheet with convective boundary condition. *J Niger. Mathem Soc.35(1)* 35, 178–198. doi:10.1016/j.jnnms.2016.02.003

Makinde, O. D., and Aziz, A. (2011). Boundary layer flow of a nanofluid past a stretching sheet with a convective boundary condition. *Int. J. Ther. Sci.* 50 (7), 1326–1332. doi:10.1016/j.ijthermalsci.2011.02.019

Mostafa, M., Hayat, T., Pop, I., Asghar, S., and Obaidat, S. (2011). Stagnation point flow of a nanofluid towards a stretching sheet. *Int. J. Heat. Mass Transf.* 54, 5588–5594. doi:10.1016/j.ijheatmasstransfer.2011.07.021

Muhammad, N., Nadeem, S., and Mustafa, T. (2017). Squeezed flow of a nanofluid with Cattaneo–Christov heat and mass fluxes. *Results Phys* 7, 862–869. doi:10.1016/j.rinp.2016.12.028

Nabwey, H. A., Khan, A. W., Rashad, A. M., Mabood, F., and Salah, T. (2022). Power-law nanofluid flow over a stretchable surface due to gyrotactic microorganisms. *Mathematics* 10 (18), 3285. doi:10.3390/math10183285

Nandi, S., Kumbhakar, B., and Sarkar, S. (2022). MHD stagnation point flow of Fe3O4/Cu/Ag-CH3OH nanofluid along a convectively heated stretching sheet with partial slip and activation energy: Numerical and statistical approach. *Int Commu Heat Mass Transf* 130, 105791. doi:10.1016/j.icheatmasstransfer.2021.105791

Bachok, N., Ishak, A., and Pop, I. (2012). Boundary layer stagnation-point flow and heat transfer over an exponentially stretching/shrinking sheet in a nanofluid. *Int. J. Heat. Transf.* 55, 8122–8128. doi:10.1016/j.ijheatmasstransfer.2012.08.051

Prakash, J., Balaji, R., Tripathi, D., Tiwari, A. K., and Sharma, R. K. (2022). "Composite nanofluids flow driven by electroosmosis through squeezing parallel plates in presence of magnetic fields," in *Advancements in nanotechnology for energy and environment* (Singapore: Springer Nature Singapore), 273–293.

Prakash, J., Sharma, A., and Tripathi, D. (2020). Convective heat transfer and double diffusive convection in ionic nanofluids flow driven by peristalsis and electromagnetohydrodynamics. *Pramana* 94, 4–17. doi:10.1007/s12043-019-1873-5

Ramzan, M., Bilal, M., and Chung, J. D. (2017). Radiative flow of Powell-Eyring magneto-nanofluid over a stretching cylinder with chemical reaction and double stratification near a stagnation point. *PloS one* 12 (1), 0170790. doi:10.1371/journal.pone.0170790

Reddy, S. R. R., Bala Anki Reddy, P., and Rashad, A. M. (2020). Activation energy impact on chemically reacting Eyring–Powell nanofluid flow over a stretching cylinder. *Arabian J. Sci. Eng.* 45, 5227–5242. doi:10.1007/s13369-020-04379-9

Rehman, K. U., Malik, M. Y., Salahuddin, T., and Naseer, M. (2016). Dual stratified mixed convection flow of Eyring-Powell fluid over an inclined stretching cylinder with heat generation/absorption effect. *AIP Adv.* 6 (7), 075112. doi:10.1063/1.4959587

Rehman, S. U., Mir, N. A., Farooq, M., Rafiq, N., and Ahmad, S. (2021). Analysis of thermally stratified radiative flow of Sutterby fluid with mixed convection. *Proc. Institution Mech. Eng. Part C*, 09544062211007887.J of Mech Engg Sci

Saleem, N., Munawar, S., Tripathi, D., Afzal, F., and Afzal, D. (2022). Cilia beating modulated radiating ternary nanofluids flow in a corrugated asymmetric channel with electromagnetohydrodynamic and momentum slip. *Heat. Transf.* 51(8), 7462–7486. doi:10.1002/htj.22652

Sutterby, J. L. (1966). Laminar converging flow of dilute polymer solutions in conical sections: Part I. Viscosity data, new viscosity model, tube flow solution. *Viscosity data, new viscosity Model., tube Flow. Solut.* 12, 63–68. doi:10.1002/aic.690120114

Sutterby, J. L. (1965). Laminar converging flow of dilute polymer solutions in conical sections. II. *Ii. Trans. Soc. Rheol.* 9, 227–241. doi:10.1122/1.549024

Tlili, I., Rashad, A. M., Khan, A. W., and el-Hakiem, A. M. A. (2019). *Indian J. Pure Appl. Phys. (IJPAP)* 57 (10), 773–782.

Tripathi, D., Prakash, J., and Bég, O. A. (2020). Peristaltic pumping of hybrid nanofluids through an asymmetric microchannel in the presence of electromagnetic fields. *J. Therm. Sci. Eng. Appl.*

Tripathi, D., Prakash, J., Gnaneswara Reddy, M., and Kumar, R. (2021). Numerical study of electroosmosis-induced alterations in peristaltic pumping of couple stress hybrid nanofluids through microchannel. *Indian J. Phys.* 95, 2411–2421. doi:10.1007/s12648-020-01906-0

Turkyilmazoglu, M. (2012). Exact analytical solutions for heat and mass transfer of MHD slip flow in nanofluids. *Chem. Eng. Sci.* 84, 182–187. doi:10.1016/j.ces.2012.08.029

Unyong, B., Vadivel, R., Govindaraju, M., Anbuvithya, R., and Gunasekaran, N. (2021). Entropy analysis for ethylene glycol hybrid nanofluid flow with elastic deformation, radiation, non-uniform heat generation/absorption, and inclined Lorentz force effects. *Case Stud. Therm Engg* 30, 101639. doi:10.1016/j.csite.2021.101639

Wang, C. Y. (2002). Flow due to a stretching boundary with partial slip-an exact solution of the Navier-Stokes equation. *Chem. Eng. Sci.* 57, 7–3745.

Wang, C. Y. (2006). Stagnation slip flow and heat transfer on a moving plate. *Chem. Eng. Sci.* 61, 7668–7672. doi:10.1016/j.ces.2006.09.003

Ibrahim, W., Shanker, B., and Mahantesh, M. (2013). MHD stagnation point flow and heat transfer due to nanofluid towards a stretching sheet. *Int. J. Heat. Mass Transf.* 56, 1–9. doi:10.1016/j.ijheatmasstransfer.2012.08.034

Wu, L. (2008). A slip model for rarefied gas flows at arbitrary Knudsen number. *Appl. Phys. Lett.* 93, 253103. doi:10.1063/1.3052923

Xuan, Y., and Li, Q. (2000). Heat transfer enhancement of nanofluids, int. *J. Heat fluid flow* 21(1), 58–64.

Glossary

x, y Cartesian Coordinates
D_a Darcy
u, v velocity components in x(y) directions
c_p specific heat ($JKg^{-1}k^{-1}$)
D mass diffusivity
D_b Brownian diffusion coefficient
D_t Thermophoretic diffusion coefficient
T_0 Reference temperature(K)
T_w wall temperature(K)
C_0 Concentration
E Activation energy J)
Q Heat generating absorbing J)
s_1 $\frac{b}{d}$ Thermal stratification
s_2 $\frac{c}{e}$ Solutal stratification
τ_{np} $\frac{(\rho c_p)_p}{(\rho c_p)_f}$ Ratio of the nano particle to fluid particle
K Thermal conductivity ($Wm^{-1}k^{-1}$)
t_w sheer stress on the wall

Dimensionless functions

η similarity variables
$h(\eta)$ represent the velocity component u
$g(\eta)$ represent the velocity component v
τ shear stress
Re Reynolds number
Pr Prandtl number
Le Lewis number
Sc Schmidth number
Sh Sherwood number
Nu Nusselt number
Nt Thermophoresis parameter
Nb Brownian motion parameter
Gr_x Grashof number along *x– axis*

Greek Letters

α Thermal diffusivity
β Sutterby fluid coefficient
γ Chemical reaction
ϵ Sutterby fluid
δ Temperature ratio
μ Viscosity (Nsm^{-2})
ρ Density (Kgm^{-1})
ν Kinematic viscosity ($m^{-2}s^{-1}$)

frontiers | Frontiers in Materials

TYPE Original Research
PUBLISHED 14 March 2023
DOI 10.3389/fmats.2023.1133133

OPEN ACCESS

EDITED BY
Hammad Khalil,
University of Education Lahore, Pakistan

REVIEWED BY
Feng Shizhe,
Hebei University of Technology, China
Basma Souayeh,
King Faisal University, Saudi Arabia

*CORRESPONDENCE
Sayed M. Eldin,
sayed.eldin22@fue.edu.eg
Anwar Saeed,
anwarsaeed769@gmail.com

SPECIALTY SECTION
This article was submitted to Colloidal Materials and Interfaces, a section of the journal Frontiers in Materials

RECEIVED 28 December 2022
ACCEPTED 20 February 2023
PUBLISHED 14 March 2023

CITATION
Algehyne EA, Lone SA, Raizah Z, Eldin SM, Saeed A and Galal AM (2023), Mechanical characteristics of MHD of the non-Newtonian magnetohydrodynamic Maxwell fluid flow past a bi-directional convectively heated surface with mass flux conditions.
Front. Mater. 10:1133133.
doi: 10.3389/fmats.2023.1133133

Mechanical characteristics of MHD of the non-Newtonian magnetohydrodynamic Maxwell fluid flow past a bi-directional convectively heated surface with mass flux conditions

Ebrahem A. Algehyne[1,2], Showkat Ahmad Lone[3], Zehba Raizah[4], Sayed M. Eldin[5]*, Anwar Saeed[6]* and Ahmed M. Galal[7,8]

[1]Department of Mathematics, Faculty of Science, University of Tabuk, Tabuk, Saudi Arabia, [2]Nanotechnology Research Unit (NRU), University of Tabuk, Tabuk, Saudi Arabia, [3]Department of Basic Sciences, College of Science and Theoretical Studies, Saudi Electronic University (Jeddah-M), Riyadh, Saudi Arabia, [4]Department of Mathematics, College of Science, Abha King Khalid University, Abha, Saudi Arabia, [5]Center of Research, Faculty of Engineering, Future University in Egypt New Cairo, New Cairo, Egypt, [6]Center of Excellence in Theoretical and Computational Science (TaCS-CoE), Science Laboratory Building, Faculty of Science, King Mongkut's University of Technology Thonburi (KMUTT), Bangkok, Thailand, [7]Department of Mechanical Engineering, College of Engineering in Wadi Alddawasir, Prince Sattam bin Abdulaziz University, Saudi Arabia, [8]Production Engineering and Mechanical Design Department, Faculty of Engineering, Mansoura University, Mansoura, Egypt

In engineering and manufacturing industries, stretching flow phenomena have numerous real-world implementations. Real-world applications related to stretched flow models are metalworking, crystal growth processes, cooling of fibers, and plastics sheets. Therefore, in this work, the mechanical characteristics of the magnetohydrodynamics of the non-Newtonian Maxwell nanofluid flow through a bi-directional linearly stretching surface are explored. Brownian motion, thermophoresis, and chemical reaction impacts are considered in this analysis. Additionally, thermal convective and mass flux conditions are taken into consideration. The mathematical framework of the existing problem is constructed on highly non-linear partial differential equations (PDEs). Suitable similarity transformations are used for the conversion of partial differential equations into ordinary differential equations (ODEs). The flow problem is tackled with the homotopy analysis method, which is capable of solving higher-order non-linear differential equations. Different flow profiles against various flow parameters are discussed physically. Heat and mass transference mechanisms for distinct flow factors are analyzed in a tabular form. The outcomes showed that both primary and secondary velocities are the declining functions of magnetic and Maxwell fluid parameters. The heat transfer rate rises with the cumulative values of the Brownian motion and thermal Biot number. In addition, the mass transfer rate decreases with the rising Schmidt number, Brownian motion parameter, and chemical reaction parameter, while it increases with the augmenting thermophoresis parameter. It has been highlighted that streamlines in the current work for Maxwell and Newtonian models are in fact different from one another.

KEYWORDS

Maxwell fluid, MHD, Brownian motion, thermophoresis, chemical reaction, convection and mass flux conditions, HAM

1 Introduction

The fluids that differ from Newtonian fluids in behavior and characteristics in the sense of not obeying Newtonian's law are termed as non-Newtonian fluids, which include honey, paste, ketchup, and grease lubricant. There are many applications of the non-Newtonian fluid flow in modern industries and technology such as printing technology, biological solution, polymer, braking and damping devices, production of foods, and reduction agents in dragging. These fluids are considered to be the most effective in heat transmission phenomena (Ogunseye, Salawu, Tijani, Riliwan, Sibanda; Salawu and Ogunseye, 2020). Sharma and Shaw (2022) calculated the nanofluid flow over an expanding surface by assuming viscous dissipation and non-linear radiation and have concluded that the drag force has been augmented by an upsurge in the magnetic factor. Kumar and Sahu (2022) inspected the non-Newtonian fluid flow past an elliptical rotary cylinder through a laminar flow stream and have investigated the flow phenomenon numerically. Khalil et al. (2022) inspected the influences of fluctuating fluid properties of the double-diffusive model over the dissipated non-Newtonian liquid flow on a stretched surface. Sneha et al. (2022) appraised the magnetohydrodynamic (MHD) radiated nanoliquid flow toward a stretchy and shrinking sheet subject to the impact of carbon nanotubes and concluded that the velocity of the fluid declined, while the temperature had an upsurge with growing values of the magnetic parameter. Hu et al. (2022) used non-Newtonian fluids in a square channel to discuss the polydispersal, migration, and formation chain of particles. Islam et al. (2020) inspected the impacts of the MHD radiated micropolar fluid flow in a channel with the influence of hybrid nanoparticles. Waini et al. (2022) investigated the thermally radiative flow across an extending sheet by using magnetic field effects.

The branch of science that deals with magnetic characteristics of electrically conducting materials is termed as magnetohydrodynamics (MHD). This field of science provides a basis for many scientific, industrial, and technological applications such as liquid metals, cooling systems for automobiles, cooling of electronic chips, and production of chemicals. Sohail et al. (2020) inspected the MHD Casson fluid flow and entropy production, subject to variable heat conductivities past a non-linear bi-directional stretched surface, and deduced that the upsurge values of the magnetic factor have supported concentration and thermal profiles. Reddy et al. (2022a) used the MHD fluid flow with a porous medium to use the influence of radiation, thermal, and velocity slips and highlighted that the width of the boundary layer weakened with the growth in slip and heat factor parameters. Mishra et al. (2022) numerically explored the Williamson MHD nanofluid flow, subject to variable viscosities over a wedge. Reddy et al. (2016) debated the effect of thermal radiation over the MHD nanoparticle-based liquid flow past an extending surface and compared their results with a fine agreement to those results established in the literature. Bejawada and Yanala (2021) inspected Soret and Dufour impacts upon the time-dependent MHD liquid flow past an inclined surface placed vertically. Reddy et al. (2022b) scrutinized the influence of different slip effects over the MHD liquid flow past a stretchy sheet subject to Soret and Dufour effects. Sandeep et al. (2022) discussed the influence of the non-linearly radiated MHD hybrid nanofluid fluid flow using a heat source and concluded that the fluid flow declined and the thermal flow had an upsurge with a growth in the magnetic factor. Sandeep and Ashwinkumar (2021) studied the impact of different nanoparticles' shapes upon the MHD fluid flow over a thin movable needle. Ashwinkumar et al. (2021) explained a 2D MHD hybrid nanoparticle flow using two different geometries of a cone and plate and proved that the flow and temperature incrimination are more visible in the case of the plate than that in the case of the cone. Mabood et al. (2022) inspected the influence of the non-linearly radiated 3D time-based MHD hybrid nanofluid flow. Readers can further study about the impact of MHD on mass and heat transmission in Sulochana et al. (2018), Alshehri et al. (2021), Mabood et al. (2021), Bejawada et al. (2022), Kumar et al. (2022), and Nalivela et al. (2022).

The mass and thermal flow problems with the impact of chemical reactions play a pivotal role in numerous fluid flow models. They have captivated more consideration due to its widespread utilization in many engineering and natural phenomena such as refrigeration, aerodynamic extrusions, and human transpiration. Sharma and Mishra (2020) documented the MHD nanoliquid flow using an internal thermal source. Singh et al. (2021) numerically solved the flow of a liquid past an enlarging sheet with the impact of chemical reactions and concluded that an upsurge in the stretching factor declined the diffusivities of heat and mass. Khan et al. (2021) discussed the bioconvection micropolar nanoparticle flow past a thin needle subject to binary chemical reactions and highlighted that mass diffusion declined with an upsurge in the chemical reaction factor and Brownian motion. Kodi et al. (2022) inspected the MHD Casson nanofluid flow past a vertically placed permeable plate subject to the impact of thermal diffusivity and chemical reactions. Kumar and Sharma (2022) discussed the influences of Stefan blowing on a fluid flow past a rotary disc subject to chemical reactions. Raghunath et al. (2022) inspected the time-dependent MHD flow of a liquid over an inclined permeable plate using magnetic impacts and chemical reactions.

Brownian motion and thermophoretic effects are responsible for controlling mass and thermal diffusivities subject to concentration and temperature gradients. Both these effects have numerous applications in different areas of science such as aerosol technology, nuclear safety phenomena, atmospheric pollution, aerospace technology, and hydrodynamics. Irfan (2021) considered the collective influence of Brownian and thermal diffusivity over the nanoparticle flow past a sheet with varying thickness, subject to slip conditions, and concluded that the augmentation of the Brownian number and thermophoresis factor has an upsurge in thermal profiles. Upreti et al. (2022) described the Casson fluid flow past a Riga plate subject to the effects of microorganisms. Saleem et al. (2022) studied the motion of water carrying three different types of nanoparticles subject to thermophoretic effects and the Brownian motion. Kiyani et al.

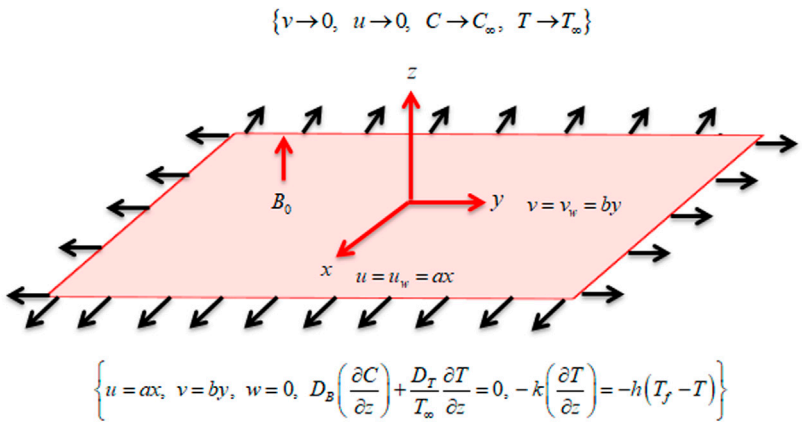

FIGURE 1
Geometry of the flow problem.

(2022) inspected the MHD micropolar nanoparticle flow past an exponentially radiated surface using thermal radiations, Brownian motion, and thermophoretic effects upon the fluid flow system. Mehta and Kataria (2022) inspected the MHD fluid flow through the shrinking surface along with thermal radiations. Tayyab et al. (2022) have numerically studied the three-dimensional rotary nanoliquid flow subject to bio-convective activation energy.

The boundary-layer flows of nanofluids caused by stretched surfaces have attracted researchers' attention recently (Andersson et al., 1994; Xu and Liao, 2009; Prasad et al., 2012; Mukhopadhyay, 2013). Their enormous significance in engineering and industrial applications has been the key driver behind this. These uses are particularly common in extrusion operations, paper and glass fiber manufacture, electronic chip manufacturing, paint application, food preparation, and the transfer of biological fluids. There is not a single constitutive connection between stress and the rate of strain that can be used to investigate all non-Newtonian fluids. The diversity of these fluids, their constitutive behavior, and simultaneous viscous and elastic properties make it nearly impossible to distinguish between effects resulting from a fluid's shear-dependent viscosity and effects resulting from the fluid's elasticity. A few mathematical models have been explained that closely match the experimental findings (Wu and Thompson, 1996). The Maxwell model is utilized for relaxation time in some highly concentrated polymeric fluids.

In this work, the authors have considered to present a semi-analytical solution of the Maxwell fluid flow over a bi-directional stretching sheet. Additionally, the thermal convective and mass flux conditions are taken into consideration. The mathematical framework of the existing problem is constructed on highly non-linear PDEs. Suitable similarity transformations are used for the conversion of PDEs into ODEs, which is presented in section 2. The flow problem is tackled with a homotopy analysis method, which is capable of solving higher-order non-linear differential equations, presented in section 3. The convergence of the HAM technique is also shown in section 4. Different flow profiles against various flow parameters are discussed physically, as shown in section 5. Finally, the concluding remarks are presented in section 6.

2 Model formulation

We consider the steady, laminar, and incompressible three-dimensional flow of a Maxwell fluid over a bi-directional linearly extending surface. The surface stretches along x and y directions and with velocity $v_w(x) = by$, where both a and b are constants. A magnetic field of strength B_0 is applied normal to the fluid flow. The surface temperature is denoted by T_w, T_f represents the reference temperature, and T_∞ shows the ambient temperature. In addition, the surface concentration is denoted by C_w and C_∞, showing the ambient concentration. Brownian motion, thermophoresis, and chemical reaction impacts are considered in this analysis. Additionally, the thermal convective and mass flux conditions are taken into consideration, as shown in Figure 1. Under the aforementioned suppositions, the principle equations are as follows (Bilal Ashraf et al., 2016; Dawar et al., 2021):

$$\frac{\partial u}{\partial x} + \frac{\partial v}{\partial y} + \frac{\partial w}{\partial z} = 0, \tag{1}$$

$$u\frac{\partial u}{\partial x} + w\frac{\partial u}{\partial z} + v\frac{\partial u}{\partial y} = \nu\frac{\partial^2 u}{\partial z^2} - \frac{\sigma B_0^2}{\rho}\left(u + \lambda w\frac{\partial u}{\partial z}\right) - \lambda\left(u^2\frac{\partial^2 u}{\partial x^2} + w^2\frac{\partial^2 u}{\partial z^2} + v^2\frac{\partial^2 u}{\partial y^2} + 2uv\frac{\partial^2 u}{\partial x \partial y} + 2uw\frac{\partial^2 u}{\partial x \partial z} + 2vw\frac{\partial^2 u}{\partial y \partial z}\right), \tag{2}$$

$$u\frac{\partial v}{\partial x} + w\frac{\partial v}{\partial z} + v\frac{\partial v}{\partial y} = \nu\frac{\partial^2 v}{\partial z^2} - \frac{\sigma B_0^2}{\rho}\left(v + \lambda w\frac{\partial v}{\partial z}\right) - \lambda\left(u^2\frac{\partial^2 v}{\partial x^2} + w^2\frac{\partial^2 v}{\partial z^2} + v^2\frac{\partial^2 v}{\partial y^2} + 2uv\frac{\partial^2 v}{\partial x \partial y} + 2vw\frac{\partial^2 v}{\partial y \partial z} + 2uw\frac{\partial^2 v}{\partial x \partial z}\right), \tag{3}$$

$$u\frac{\partial T}{\partial x} + w\frac{\partial T}{\partial z} + v\frac{\partial T}{\partial y} = \frac{k}{\left(\rho C_p\right)_f}\frac{\partial^2 T}{\partial z^2} + \frac{\left(\rho C_p\right)_p}{\left(\rho C_p\right)_f}\left(D_B\frac{\partial T}{\partial z}\frac{\partial C}{\partial z}\right) + \frac{D_T}{T_\infty}\left(\frac{\partial C}{\partial z}\right)^2, \tag{4}$$

$$u\frac{\partial C}{\partial x} + w\frac{\partial C}{\partial z} + v\frac{\partial C}{\partial y} + k_1\left(C - C_\infty\right) = D_B\frac{\partial^2 C}{\partial z^2}\frac{D_T}{T_\infty}\left(\frac{\partial^2 T}{\partial z^2}\right), \tag{5}$$

with boundary conditions, given as follows (Bilal Ashraf et al., 2016; Dawar et al., 2021):

$$\left\{\begin{array}{c} u = ax, v = by, w = 0, D_B\left(\frac{\partial C}{\partial z}\right) + \frac{D_T}{T_\infty}\frac{\partial T}{\partial z} = 0, -k\left(\frac{\partial T}{\partial z}\right) = -h\left(T_f - T\right), at \quad z = 0, \\ v \to 0, u \to 0, C \to C_\infty, T \to T_\infty \quad as \quad z \to \infty . \end{array}\right\} \tag{6}$$

In the aforementioned equations, $u, v,$ and w are the velocity components; $x, y,$ and z are the coordinate axes; σ is the electrical conductivity; ρ is the density; λ is the relaxation time; B_0 is the magnetic field strength; C_p is the specific heat; k is the thermal conductivity; D_B is the Brownian diffusion coefficient; D_T is the thermophoretic coefficient; T is the temperature; C is the concentration; k_1 is the chemical reaction coefficient; h is the heat transfer coefficient; and a and b are the velocity constants.

The similarity transformations are defined as follows (Bilal Ashraf et al., 2016; Dawar et al., 2021):

$$\left.\begin{array}{c} v = ayg'(\eta), u = axf'(\eta), w = -\sqrt{a\nu}\left(g(\eta) + f(\eta)\right), \\ \theta(\eta) = \frac{T - T_\infty}{T_f - T_\infty}, \phi(\eta) = \frac{C - C_\infty}{C_w - C_\infty} =, \eta = z\sqrt{\frac{a}{\nu}}. \end{array}\right\} \tag{7}$$

The leading equations are transformed by using similarity transformations defined in (7):

$$f'''(\eta) + (1 + M\beta)\left(f(\eta)f''(\eta) + g(\eta)f''(\eta)\right) - \left(f'(\eta)\right)^2 - Mf'(\eta) + \beta\left(\begin{array}{c} 2f(\eta)f'(\eta)f''(\eta) + 2g(\eta)f'(\eta)f''(\eta) - \\ f'''(\eta)\left(f(\eta)\right)^2 - f'''(\eta)\left(g(\eta)\right)^2 - 2f'''(\eta)g(\eta)f(\eta) \end{array}\right) = 0, \tag{8}$$

$$g'''(\eta) + (1 + M\beta)\left(f(\eta)g''(\eta) + g(\eta)g''(\eta)\right) - \left(g'(\eta)\right)^2 - Mg'(\eta) + \beta\left(\begin{array}{c} 2g''(\eta)f(\eta)g'(\eta) + 2g''(\eta)g(\eta)g'(\eta) - \\ g'''(\eta)\left(f(\eta)\right)^2 - g'''(\eta)\left(g(\eta)\right)^2 - 2g'''(\eta)f(\eta)g(\eta) \end{array}\right) = 0, \tag{9}$$

$$\frac{1}{Pr}\theta''(\eta) + g(\eta)\theta'(\eta) + f(\eta)\theta'(\eta) + Nb\theta'(\eta)\phi'(\eta) + Nt\left(\theta'(\eta)\right)^2 = 0, \tag{10}$$

$$\phi''(\eta) + Scf(\eta)\phi'(\eta) + Scg(\eta)\phi'(\eta) + \frac{Nt}{Nb}\theta''(\eta) - ScK\phi(\eta) = 0, \tag{11}$$

with boundary conditions given as follows:

$$\left\{\begin{array}{c} f(0) = 0, f'(0) = 1, g'(0) = \alpha, g(0) = 0, \theta'(0) = \gamma(\theta(0) - 1), \\ Nt\theta'(0) + Nb\phi'(0) = 0, g'(\infty) = 0, f'(\infty) = 0, \theta(\infty) = 0, \phi(\infty) = 0. \end{array}\right\} \tag{12}$$

The embedded parameters are discussed as follows:

$$\left\{\begin{array}{c} M = \frac{\sigma B_0^2}{\rho a}, \beta = \lambda a, Sc = \frac{\nu}{D_B}, \alpha = \frac{b}{a}, \Pr = \frac{\mu\left(C_P\right)_f}{k}, K = \frac{k_1}{a}, \\ \gamma = \frac{h_f}{k}\sqrt{\frac{\nu}{a}}, Nt = \frac{\left(\rho C_P\right)_p D_B\left(T_w - T_\infty\right)}{\left(\rho C_P\right)_f \gamma T_\infty}, Nb = \frac{\left(\rho C_P\right)_p D_B\left(C_w - C_\infty\right)}{\left(\rho C_P\right)_f \nu}. \end{array}\right\} \tag{13}$$

Here, M is the magnetic factor, β is the Deborah number, Sc is the Schmidt number, α is the stretching constant, Pr is the Prandtl number, K is the chemical reaction factor, γ is the thermal Biot number, Nt is the thermophoresis factor, and Nb is the Brownian motion factor.

The Nusselt, Sherwood, and density numbers are defined as follows:

$$\frac{Nu_x}{\sqrt{\mathrm{Re}_x}} = -\theta'(\eta)\big|_{\eta=0}, \quad \frac{Sh_x}{\sqrt{\mathrm{Re}_x}} = -\phi'(\eta)\big|_{\eta=0}, \tag{14}$$

where $\mathrm{Re}_x = \frac{xu_w(x)}{\nu}$ is the local Reynolds number.

3 HAM solution

For an analytical simulation of the existing model, the HAM technique is considered. The initial guesses are given as follows:

$$\left\{f_0(\eta) = 1 - e^{-\eta}, g(\eta) = \alpha\left(1 - e^{-\eta}\right), \theta_0(\eta) = \frac{\gamma}{\gamma + 1}e^{-\eta}, \phi_0(\eta) = -\frac{\gamma}{1 + \gamma}\frac{Nt}{Nb}e^{-\eta}.\right\} \tag{15}$$

The linear operators are taken as follows:

$$\mathbf{L}_f(\eta) = f''' - f', \mathbf{L}_g(\eta) = g''' - g', \mathbf{L}_\theta(\eta) = \theta'' - \theta, \mathbf{L}_\phi(\eta) = \phi'' - \phi, \tag{16}$$

with the following properties:

$$\left\{\begin{array}{c} \mathbf{L}_f\left(\mho_1 + \mho_2\, exp(\eta) + \mho_3\, exp(-\eta)\right) = 0, \\ \mathbf{L}_g\left(\mho_4 + \mho_5\, exp(\eta) + \mho_6\, exp(-\eta)\right) = 0, \\ \mathbf{L}_\theta\left(\mho_7\, exp(\eta) + \mho_8\, exp(-\eta)\right) = 0, \\ \mathbf{L}_\phi\left(\mho_9\, exp(\eta) + \mho_{10}\, exp(-\eta)\right) = 0, \end{array}\right\} \tag{17}$$

where $\mho_i\,(i = 1, 2, 3, \ldots, 10)$ are the constants.

$\Re \in [0 \quad 1]$ shows the entrenching factor, and $\hbar$ shows the auxiliary parameter. Then, the zero-order problems are constructed as follows:

$$(1 - \mathrm{A})L_f\left[f(\eta;\mathrm{A}) - f_0(\eta)\right] = \mathrm{A}\hbar_f N_f\left[f(\eta;\mathrm{A}), g(\eta;\mathrm{A})\right], \tag{18}$$

$$(1 - \mathrm{A})L_g\left[g(\eta;\mathrm{A}) - g_0(\eta)\right] = \mathrm{A}\hbar_g N_g\left[g(\eta;\mathrm{A}), f(\eta;\mathrm{A})\right], \tag{19}$$

$$(1 - \mathrm{A})L_\theta\left[\theta(\eta;\mathrm{A}) - \theta_0(\eta)\right] = \mathrm{A}\hbar_\theta N_\theta\left[\theta(\eta;\mathrm{A}), f(\eta;\mathrm{A}), g(\eta;\mathrm{A}), \phi(\eta;\mathrm{A})\right], \tag{20}$$

$$(1 - \mathrm{A})L_\phi\left[\phi(\eta;\mathrm{A}) - \phi_0(\eta)\right] = \mathrm{A}\hbar_\phi N_\phi\left[\phi(\eta;\mathrm{A}), f(\eta;\mathrm{A}), g(\eta;\mathrm{A}), \theta(\eta;\mathrm{A})\right], \tag{21}$$

$$\left\{\begin{array}{c} f(0;\mathrm{A}) = 0, g(0;\mathrm{A}) = 0, f'(0;\mathrm{A}) = 1, g'(0;\mathrm{A}) = \alpha, \\ \theta'(0;\mathrm{A}) = \gamma((0;\mathrm{A})\theta - 1), Nt\theta'(0;\mathrm{A}) + Nb\phi'(0;\mathrm{A}) = 0, \\ f'(\infty;\mathrm{A}) \to 0, \theta(\infty;\mathrm{A}) \to 0, g'(\infty;\mathrm{A}) \to 0, \phi(\infty;\mathrm{A}), \end{array}\right\} \tag{22}$$

$$N_f\left[f(\eta;\mathrm{A}), g(\eta;\mathrm{A})\right] = \frac{\partial^3 f(\eta;\mathrm{A})}{\partial\eta^3} + (1 + M\beta)\left(f(\eta;\mathrm{A})\frac{\partial^2 f(\eta;\mathrm{A})}{\partial\eta^2} + g(\eta;\mathrm{A})\frac{\partial^2 f(\eta;\mathrm{A})}{\partial\eta^2}\right) - M\frac{\partial f(\eta;\mathrm{A})}{\partial\eta} - \left(\frac{\partial f(\eta;\mathrm{A})}{\partial\eta}\right)^2 + \beta\left(\begin{array}{c} 2f(\eta)\frac{\partial f(\eta;\mathrm{A})}{\partial\eta}\frac{\partial^2 f(\eta;\mathrm{A})}{\partial\eta^2} + 2g(\eta;\mathrm{A})\frac{\partial f(\eta;\mathrm{A})}{\partial\eta}\frac{\partial^2 f(\eta;\mathrm{A})}{\partial\eta^2} \\ -(f(\eta;\mathrm{A}))^2\frac{\partial^3 f(\eta;\mathrm{A})}{\partial\eta^3} - (g(\eta;\mathrm{A}))^2\frac{\partial^3 f(\eta;\mathrm{A})}{\partial\eta^3} \\ -2g(\eta;\mathrm{A})f(\eta;\mathrm{A})\frac{\partial^3 f(\eta;\mathrm{A})}{\partial\eta^3} \end{array}\right), \tag{23}$$

$$N_g\left[g(\eta;\mathrm{A}), f(\eta;\mathrm{A})\right] = \frac{\partial^3 g(\eta;\mathrm{A})}{\partial\eta^3} + (1 + M\beta)\left(f(\eta;\mathrm{A})\frac{\partial^2 g(\eta;\mathrm{A})}{\partial\eta^2} + g(\eta;\mathrm{A})\frac{\partial^2 g(\eta;\mathrm{A})}{\partial\eta^2}\right) - \left(\frac{\partial g(\eta;\mathrm{A})}{\partial\eta}\right)^2 - M\frac{\partial g(\eta;\mathrm{A})}{\partial\eta} + \beta\left(\begin{array}{c} 2f(\eta;\mathrm{A})\frac{\partial g(\eta;\mathrm{A})}{\partial\eta}\frac{\partial^2 g(\eta;\mathrm{A})}{\partial\eta^2} + 2g(\eta;\mathrm{A})\frac{\partial g(\eta;\mathrm{A})}{\partial\eta}\frac{\partial^2 g(\eta;\mathrm{A})}{\partial\eta^2} \\ -(f(\eta;\mathrm{A}))^2\frac{\partial^3 g(\eta;\mathrm{A})}{\partial\eta^3} - (g(\eta;\mathrm{A}))^2\frac{\partial^3 g(\eta;\mathrm{A})}{\partial\eta^3} \\ -2f(\eta;\mathrm{A})g(\eta;\mathrm{A})\frac{\partial^3 g(\eta;\mathrm{A})}{\partial\eta^3} \end{array}\right), \tag{24}$$

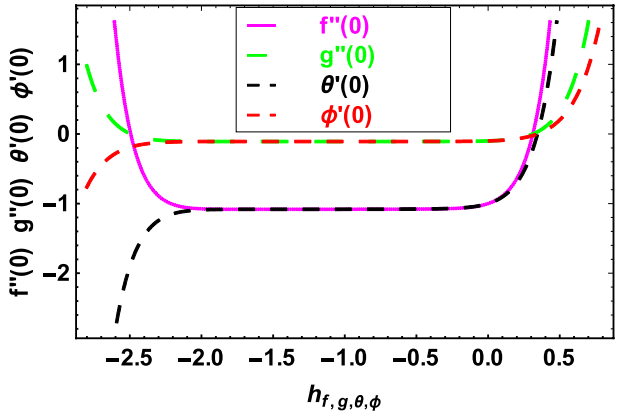

FIGURE 2
ħ– curves for $\hbar_f$, $\hbar_g$, $\hbar_\theta$, and $\hbar_\phi$.

$$N_\theta[\theta(\eta;\mathrm{A}), f(\eta;\mathrm{A}), g(\eta;\mathrm{A}), \phi(\eta;\mathrm{A})] = \frac{1}{Pr}\frac{\partial^2\theta(\eta;\mathrm{A})}{\partial\eta^2} + g(\eta;\mathrm{A})\frac{\partial\theta(\eta;\mathrm{A})}{\partial\eta} + f(\eta;\mathrm{A})\frac{\partial\theta(\eta;\mathrm{A})}{\partial\eta} + Nb\frac{\partial\theta(\eta;\mathrm{A})}{\partial\eta}\frac{\partial\phi(\eta;\mathrm{A})}{\partial\eta} + Nt\left(\frac{\partial\theta(\eta;\mathrm{A})}{\partial\eta}\right)^2, \tag{25}$$

$$N_\phi[\phi(\eta;\mathrm{A}), f(\eta;\mathrm{A}), g(\eta;\mathrm{A}), \theta(\eta;\mathrm{A})] = \frac{\partial^2\phi(\eta;\mathrm{A})}{\partial\eta^2} + Scf(\eta;\mathrm{A})\frac{\partial\phi(\eta;\mathrm{A})}{\partial\eta} + Scg(\eta;\mathrm{A})\frac{\partial\phi(\eta;\mathrm{A})}{\partial\eta} + \frac{Nt}{Nb}\frac{\partial^2\theta(\eta;\mathrm{A})}{\partial\eta^2} - ScK\phi(\eta;\mathrm{A}). \tag{26}$$

For $A = 0$ and $A = 1$, we obtain the following:

$$\left\{\begin{array}{l} f(\eta;0) = f_0(\eta), f(\eta;1) = f(\eta) \\ g(\eta;0) = g_0(\eta), g(\eta;1) = g(\eta) \\ \theta(\eta;0) = \theta_0(\eta), \theta(\eta;1) = \theta(\eta) \\ \phi(\eta;0) = \phi_0(\eta), \phi(\eta;1) = \phi(\eta) \end{array}\right\}. \tag{27}$$

Using the Taylor series, we obtain the following:

$$f(\eta;A) = f_0(\eta) + \sum_{\mathrm{X}=1}^{\infty} f_{\mathrm{X}}(\eta)\mathfrak{R}^{\mathrm{X}} \quad as\ f_{\mathrm{X}}(\eta) = \left.\frac{1}{\mathrm{X}!}\frac{\partial^{\mathrm{X}} f(\eta;\mathrm{A})}{\partial \mathrm{A}^{\mathrm{X}}}\right|_{A=0}, \tag{28}$$

$$g(\eta;A) = g_0(\eta) + \sum_{\mathrm{X}=1}^{\infty} g_{\mathrm{X}}(\eta)\mathfrak{R}^{\mathrm{X}} \quad as\ g_{\mathrm{X}}(\eta) = \left.\frac{1}{\mathrm{X}!}\frac{\partial^{\mathrm{X}} g(\eta;\mathrm{A})}{\partial \mathrm{A}^{\mathrm{X}}}\right|_{A=0}. \tag{29}$$

$$\theta(\eta;A) = \theta_0(\eta) + \sum_{\mathrm{X}=1}^{\infty} \theta_{\mathrm{X}}(\eta)\mathfrak{R}^{\mathrm{X}} \quad as\ \theta_{\mathrm{X}}(\eta) = \left.\frac{1}{\mathrm{X}!}\frac{\partial^{\mathrm{X}} \theta(\eta;\mathrm{A})}{\partial \mathrm{A}^{\mathrm{X}}}\right|_{A=0}. \tag{30}$$

$$\phi(\eta;A) = \phi_0(\eta) + \sum_{\mathrm{X}=1}^{\infty} \phi_{\mathrm{X}}(\eta)\mathfrak{R}^{\mathrm{X}} \quad as\ \phi_{\mathrm{X}}(\eta) = \left.\frac{1}{\mathrm{X}!}\frac{\partial^{\mathrm{X}} \phi(\eta;\mathrm{A})}{\partial \mathrm{A}^{\mathrm{X}}}\right|_{A=0}. \tag{31}$$

The X th-order deformation problems can be written as follows:

$$L_f[f_{\mathrm{X}}(\eta) - \lambda_{\mathrm{X}} f_{\mathrm{X}-1}(\eta)] = \hbar_f R_{\mathrm{X}}^f(\eta), \tag{32}$$

$$L_g[g_{\mathrm{X}}(\eta) - \lambda_{\mathrm{X}} g_{\mathrm{X}-1}(\eta)] = \hbar_g R_{\mathrm{X}}^g(\eta), \tag{33}$$

$$L_\theta[\theta_{\mathrm{X}}(\eta) - \lambda_{\mathrm{X}} \theta_{\mathrm{X}-1}(\eta)] = \hbar_\theta R_{\mathrm{X}}^\theta(\eta), \tag{34}$$

$$L_\phi[\phi_{\mathrm{X}}(\eta) - \lambda_{\mathrm{X}} \phi_{\mathrm{X}-1}(\eta)] = \hbar_\phi R_{\mathrm{X}}^\phi(\eta), \tag{35}$$

TABLE 1 Comparison of the present results of $-\theta(0)$ with the published results.

Pr	Chen (1998)	Present results
1.0	−0.58199	−0.58199
3.0	−1.16523	−1.16523
10.0	−2.30796	−2.30796

TABLE 2 Impacts of Nb, Nt, and γ on $\mathrm{Re}_x^{-\frac{1}{2}}Nu_x$.

Nb	Nt	γ	$\mathrm{Re}_x^{-\frac{1}{2}}Nu_x$
0.2			0.210766
0.4			0.210788
0.6			0.210794
0.8			0.210799
	0.1		0.160788
	0.3		0.180956
	0.5		0.200321
	0.7		0.220112
		0.2	0.512715
		0.4	0.516953
		0.6	0.701836
		0.8	0.787086

$$\left\{\begin{array}{c} f_{\mathrm{X}}(0) = f_{\mathrm{X}}'(0) = f_{\mathrm{X}}'(\infty) = 0, \\ g_{\mathrm{X}}(0) = g_{\mathrm{X}}'(0) = g_{\mathrm{X}}'(\infty) = 0, \\ \theta_{\mathrm{X}}'(0) - \gamma(\theta_{\mathrm{X}}(0) - 1) = \theta_{\mathrm{X}}(\infty) = 0, \\ Nb\phi_{\mathrm{X}}'(0) + Nt\theta_{\mathrm{X}}'(0) = \phi_{\mathrm{X}}(\infty) = 0, \end{array}\right\}, \tag{36}$$

$$R_{\mathrm{X}}^f(\eta) = f_{\mathrm{X}-1}'''(\eta) + (1+M\beta)\left(\sum_{n=0}^{\mathrm{X}-1}\left(f_{\mathrm{X}-1-j}(\eta)f_{\mathrm{X}-1}''(\eta)\right) + \sum_{n=0}^{\mathrm{X}-1}\left(g_{\mathrm{X}-1-j}(\eta)f_{\mathrm{X}-1}''(\eta)\right)\right) - \sum_{n=0}^{\mathrm{X}-1}\left(f_{\mathrm{X}-1-j}'(\eta)f_{\mathrm{X}-1}'(\eta)\right) - Mf_{\mathrm{X}-1}'(\eta) + \beta\left[2\sum_{n=0}^{\mathrm{X}-1} f_{\mathrm{X}-1-j}(\eta)\sum_{l=0}^{n} f_{\mathrm{X}-l}'(\eta)\sum_{p=0}^{l} f_{l-p}''(\eta) + 2\sum_{n=0}^{\mathrm{X}-1} g_{\mathrm{X}-1-j}(\eta)\sum_{l=0}^{n} f_{\mathrm{X}-l}'(\eta)\sum_{p=0}^{l} f_{l-p}''(\eta) + \sum_{n=0}^{\mathrm{X}-1} f_{\mathrm{X}-1-j}(\eta)\sum_{l=0}^{n} f_{\mathrm{X}-l}(\eta)\sum_{p=0}^{l} f_{l-p}'''(\eta) - \sum_{n=0}^{\mathrm{X}-1} g_{\mathrm{X}-1-j}(\eta)\sum_{l=0}^{n} g_{\mathrm{X}-l}(\eta)\sum_{p=0}^{l} f_{l-p}'''(\eta) - 2\sum_{n=0}^{\mathrm{X}-1} g_{\mathrm{X}-1-j}(\eta)\sum_{l=0}^{n} f_{\mathrm{X}-l}(\eta)\sum_{p=0}^{l} f_{l-p}'''(\eta)\right], \tag{37}$$

$$R_{\mathrm{X}}^g(\eta) = g_{\mathrm{X}-1}'''(\eta) + (1+M\beta)\left(\sum_{n=0}^{\mathrm{X}-1}\left(f_{\mathrm{X}-1-j}(\eta)g_{\mathrm{X}-1}''(\eta)\right) + \sum_{n=0}^{\mathrm{X}-1}\left(g_{\mathrm{X}-1-j}(\eta)g_{\mathrm{X}-1}''(\eta)\right)\right) - \sum_{n=0}^{\mathrm{X}-1}\left(g_{\mathrm{X}-1-j}'(\eta)g_{\mathrm{X}-1}'(\eta)\right) - Mg_{\mathrm{X}-1}'(\eta) + \beta\left[2\sum_{n=0}^{\mathrm{X}-1} f_{\mathrm{X}-1-j}(\eta)\sum_{l=0}^{n} g_{\mathrm{X}-l}'(\eta)\sum_{p=0}^{l} g_{l-p}''(\eta) + 2\sum_{n=0}^{\mathrm{X}-1} g_{\mathrm{X}-1-j}(\eta)\sum_{l=0}^{n} g_{\mathrm{X}-l}'(\eta)\sum_{p=0}^{l} g_{l-p}''(\eta) + \sum_{n=0}^{\mathrm{X}-1} f_{\mathrm{X}-1-j}(\eta)\sum_{l=0}^{n} g_{\mathrm{X}-l}(\eta)\sum_{p=0}^{l} g_{l-p}'''(\eta) - \sum_{n=0}^{\mathrm{X}-1} g_{\mathrm{X}-1-j}(\eta)\sum_{l=0}^{n} g_{\mathrm{X}-l}(\eta)\sum_{p=0}^{l} g_{l-p}'''(\eta) - 2\sum_{n=0}^{\mathrm{X}-1} g_{\mathrm{X}-1-j}(\eta)\sum_{l=0}^{n} g_{\mathrm{X}-l}(\eta)\sum_{p=0}^{l} g_{l-p}'''(\eta)\right], \tag{38}$$

$$R_{\mathrm{X}}^\theta(\eta) = \frac{1}{Pr}\theta_{\mathrm{X}-1}''(\eta) + \sum_{n=0}^{\mathrm{X}-1}\left(g_{\mathrm{X}-1-j}(\eta)\theta_{\mathrm{X}-1}'(\eta)\right) + \sum_{n=0}^{\mathrm{X}-1}\left(f_{\mathrm{X}-1-j}(\eta)\theta_{\mathrm{X}-1}'(\eta)\right) + Nb\sum_{n=0}^{\mathrm{X}-1}\left(\theta_{\mathrm{X}-1-j}'(\eta)\phi_{\mathrm{X}-1}'(\eta)\right) + Nt\sum_{n=0}^{\mathrm{X}-1}\left(\theta_{\mathrm{X}-1-j}'(\eta)\theta_{\mathrm{X}-1}'(\eta)\right), \tag{39}$$

TABLE 3 Impacts of Nb, Nt, Sc, and K on $\mathrm{Re}_x^{-\frac{1}{2}}Sh_x$.

Nb	Nt	Sc	K	$\mathrm{Re}_x^{-\frac{1}{2}}Sh_x$
0.2				0.232872
0.4				0.213886
0.4				0.203379
0.6				0.193220
	0.1			0.232172
	0.3			0.232196
	0.5			0.232297
	0.7			0.233299
		0.1		0.132872
		0.2		0.112196
		0.3		0.092297
		0.4		0.083299
			0.2	0.532872
			0.4	0.332196
			0.6	0.232297
			0.8	0.133299

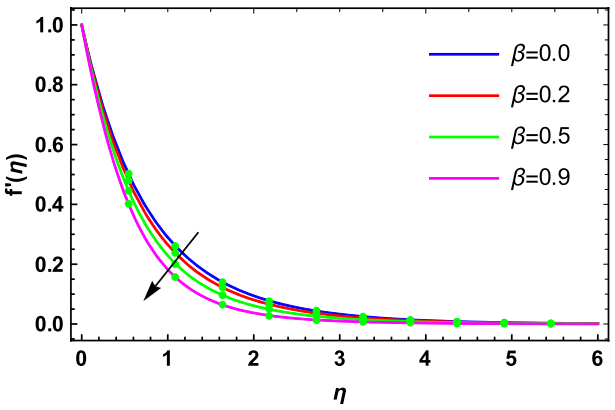

FIGURE 3
Influence of β on $f'(\eta)$.

$$R_{\mathrm{X}}^{\phi}(\eta) = \frac{1}{Pr}\phi''_{\mathrm{X}-1}(\eta) + Sc\sum_{n=0}^{\mathrm{X}-1}\left(f_{\mathrm{X}-1-j}(\eta)\phi'_{\mathrm{X}-1}(\eta)\right) + Sc \times \sum_{n=0}^{\mathrm{X}-1}\left(g_{\mathrm{X}-1-j}(\eta)\phi'_{\mathrm{X}-1}(\eta)\right) + \frac{Nt}{Nb}\theta''_{\mathrm{X}-1} + -ScK\phi_{\mathrm{X}-1}(\eta), \tag{40}$$

where

$$\lambda_{\mathrm{X}} = \begin{cases} 0, \mathrm{X} \le 1, \\ 1, \mathrm{X} > 1. \end{cases} \tag{41}$$

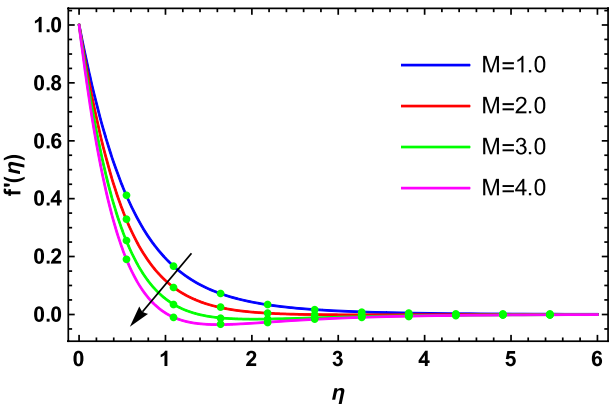

FIGURE 4
Influence of M on $f'(\eta)$.

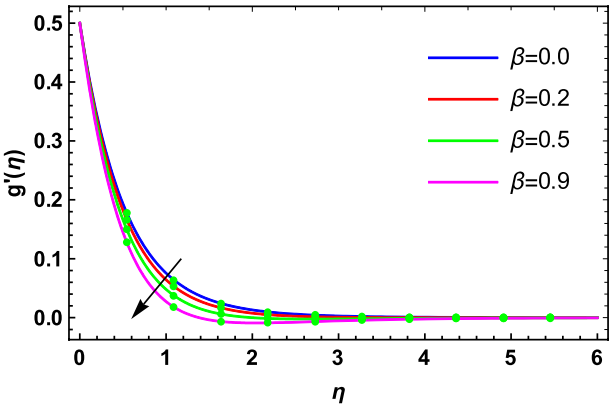

FIGURE 5
Influence of β on $g'(\eta)$.

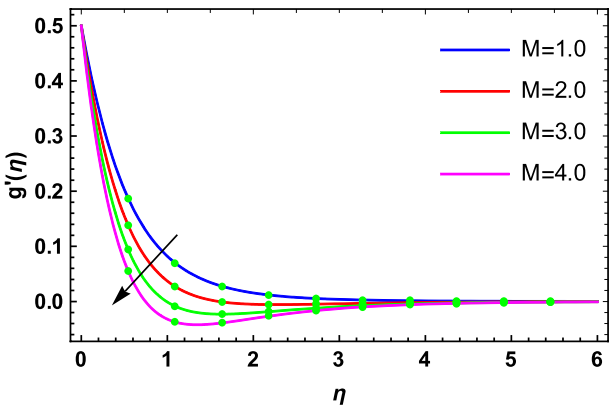

FIGURE 6
Influence of M on $g'(\eta)$.

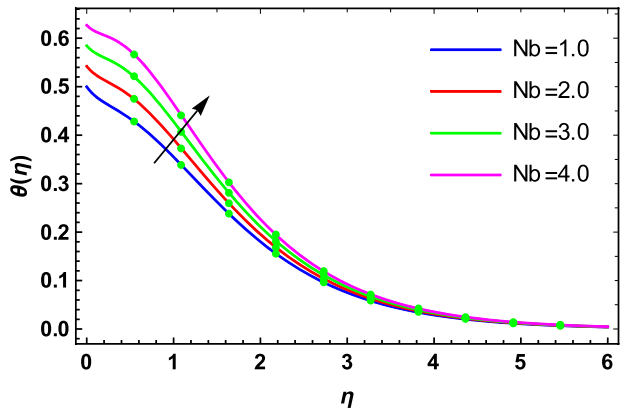

FIGURE 7
Influence of *Nb* on $\theta(\eta)$.

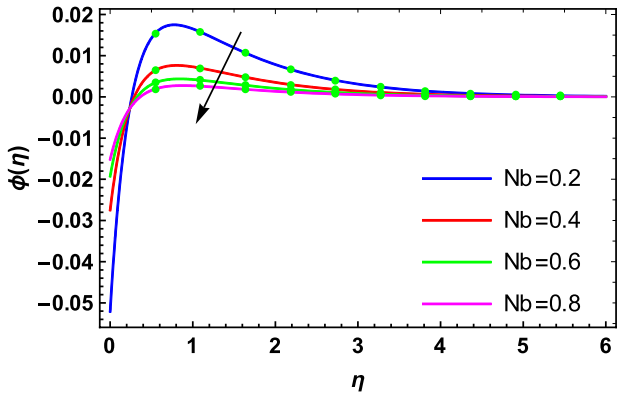

FIGURE 10
Influence of *Nb* on $\phi(\eta)$.

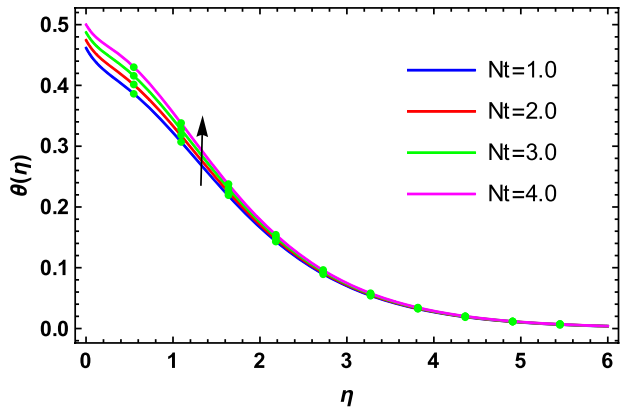

FIGURE 8
Influence of *Nt* on $\theta(\eta)$.

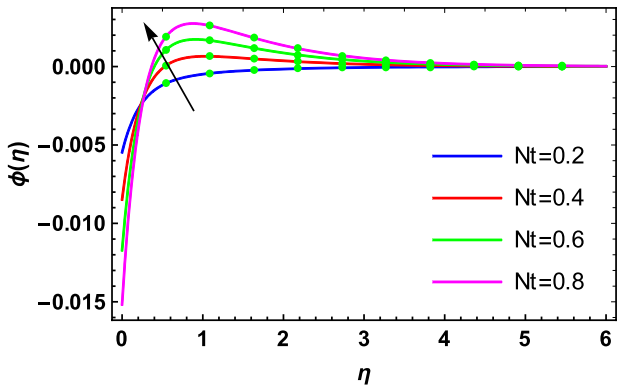

FIGURE 11
Influence of *Nt* on $\phi(\eta)$.

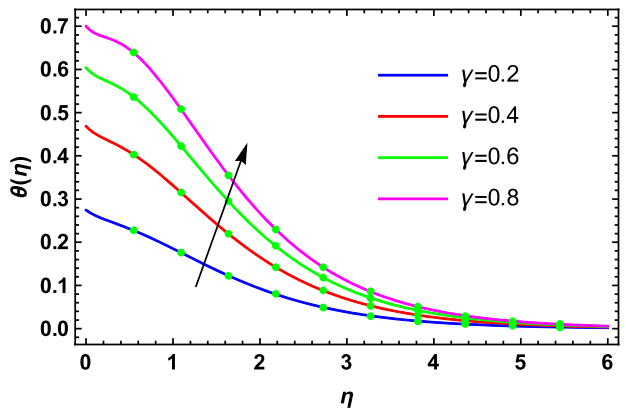

FIGURE 9
Influence of γ on $\theta(\eta)$.

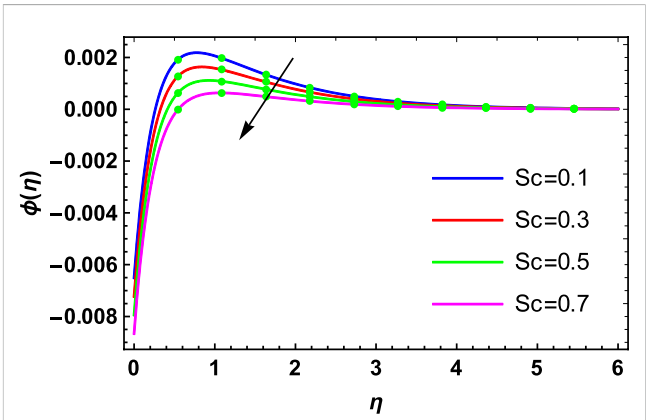

FIGURE 12
Influence of *Sc* on $\phi(\eta)$.

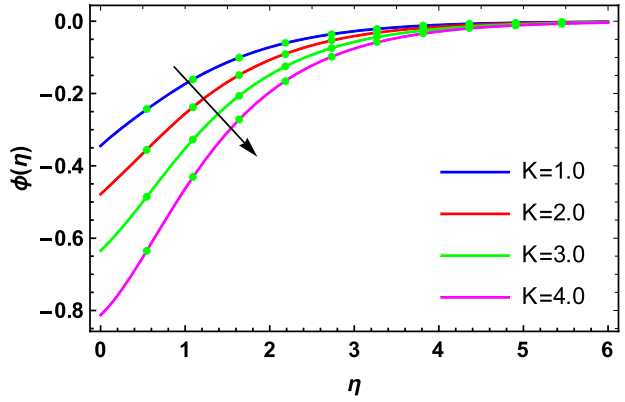

FIGURE 13
Influence of K on $\phi(\eta)$.

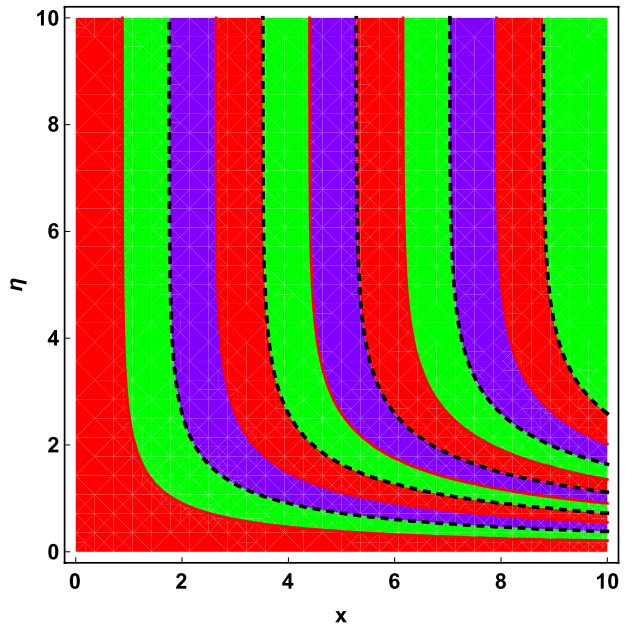

FIGURE 14
Streamlines for the Newtonian fluid.

4 HAM convergence

The factors $\hbar_f$, $\hbar_g$, $\hbar_\theta$, and $\hbar_\phi$ are called auxiliary factors, regulating the homotopic convergence. At the 23rd order of approximations, convergence regions for primary velocity, secondary velocity, temperature, and concentration distributions are shown in Figure 2. The convergence area of $f''(0)$ is $-2.1 \le \hbar_f \le 0.0$, $g''(0)$ is $-2.25 \le \hbar_g \le 0.2$, $\theta'(0)$ is $-2.1 \le \hbar_\theta \le 0.0$, and $\phi'(0)$ is $-2.25 \le \hbar_\phi \le 0.2$.

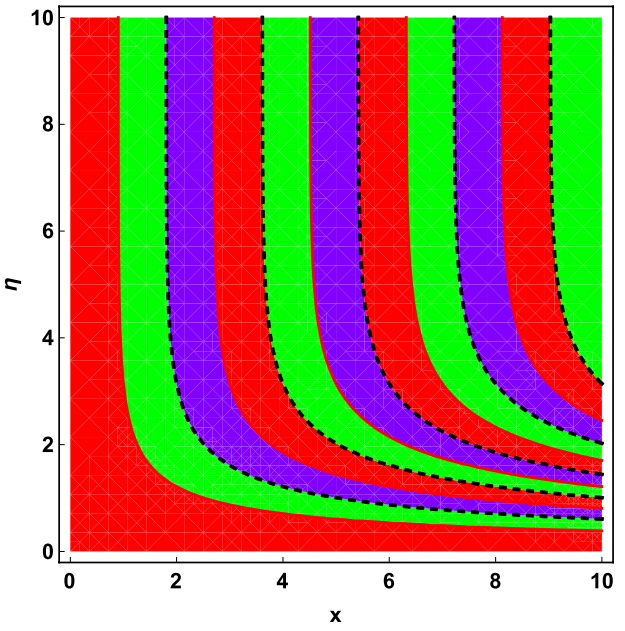

FIGURE 15
Streamlines for the Maxwell fluid.

5 Results and discussion

The physical investigation of the flow of the Maxwell fluid with the occurrence of the magnetic effect past an extending surface is explored in this section. With the occurrence of the thermal and mass diffusivity, the role of heat and mass transport is analyzed. The HAM procedure is used for the simulation of the existing model. Impacts of various flow parameters on flow distributions of the nanofluid are computed and discussed. Table 1 shows the validation of the present results with the published results. Here, a close relation between both the results is found, and we can validate our present analysis. The influences of Nb, Nt, and γ on the Nusselt number $\mathrm{Re}_x^{-\frac{1}{2}} Nu_x$ are investigated in Table 2. Table 2 shows that by increasing Nb, Nt, and γ, $\mathrm{Re}_x^{-\frac{1}{2}} Nu_x$ also increases. In Table 3, the variation in Sherwood number $\mathrm{Re}_x^{-\frac{1}{2}} Sh_x$ versus flow constraints such as Nb, Nt, Sc, and K is examined. In this analysis, it is observed that greater Nb, Sc, and K values decrease $\mathrm{Re}_x^{-\frac{1}{2}} Sh_x$, while increasing Nt augments $\mathrm{Re}_x^{-\frac{1}{2}} Sh_x$. Figures 3, 4 display variations in the primary velocity distribution of the nanofluid *via* the increasing Maxwell fluid factor β and magnetic parameter M, respectively. It is detected that the primary velocity distribution declines with growing values of β. Incidentally, increasing values of β correspond to the higher viscosity of the fluid, which, consequently, reduces the velocity of the fluid flow. Thus, the velocity distribution declines with the increase in β. Additionally, $\beta = 0.0$ corresponds to the Newtonian fluid. Thereafter, it is found that the Newtonian fluid is less viscous

than the non-Newtonian fluid. Figure 4 is drawn to determine the role of the primary velocity distribution against augmenting values of M. In this observation, a decreased performance in the primary velocity distribution is found for the increasing M value. With the increasing magnetic field, the Lorentz force shows a retarding behavior against the flow behavior. Therefore, the Lorentz force opposes the fluid motion, which, consequently, decreases the boundary layer thickness and velocity distribution of the fluid flow. Furthermore, the increase in the magnetic parameter shows an upsurge of frictional forces between particles of fluids. This explains why velocity distribution is lower for higher magnetic factors. The effects of β and M on secondary velocity distributions are analyzed in Figures 5, 6. Since, the surface stretches linearly along both $x-$ and $y-$ directions. Therefore, similar impacts of the Maxwell fluid parameter β and magnetic parameter M are also found along the secondary velocity distribution. Figures 7–9 are plotted for the assessment of nanoliquid temperatures against increasing values of Nb, Nt, and γ. The consequence of Nb on an energy profile is shown in Figure 7. An increase in the nanofluid temperature is examined for expanding the values of Nb. Brownian motion refers to the movement of particles; therefore, an increased production of heat occurs, which raises the energy profile. Figure 8 shows the effect of Nt on the temperature distribution. Figure 8 describes that the nanoliquid temperature is enhanced for intensifying values of Nt. In the case of thermophoresis, liquid elements are quickly transformed from the hot region to the cold region with a rising the thermophoresis parameter Nt which, consequently, shows a surge in the temperature distribution. The outcome of the nanoliquid temperature for increasing values of the thermal Biot number γ is observed in Figure 9. In this figure, the increasing behavior in the temperature distribution due to γ is observed. For greater values of γ, the heat transfer coefficient is enhanced because the heat transfer coefficient is directly related to the thermal Biot number γ. Therefore, the temperature distribution of the nanoliquid increases for the higher thermal Biot number γ. Figures 10–13 are displayed to discuss variations in the nanoliquid concentration distribution with respect to expanding values of Nb, Nt, Sc, and kr. The result of Nb on the concentration distribution is shown in Figure 10. It is examined that, a rise in Nb reduces the nanofluid concentration distribution. As Nb increases, the concentration gradually falls. The explanation behind this is because higher values of the Brownian parameter enhance fluid particle collisions and lower the viscosity of nanofluids. Figure 11 explains the role of Nt on the concentration distribution. In this figure, it is perceived that enhancing values of Nt increase the nanofluid concentration distribution. This is because the thermodiffusion coefficient and the thermophoresis parameter are closely related. Increased diffusion coefficients are implied by higher values of Nt, which intensify the concentration distribution. The impact of Sc on the concentration distribution is discussed in Figure 12. It is observed that the nanofluid concentration is lower with the expansion of the Schmidt number Sc. The Schmidt number Sc is the ratio of momentum diffusivity and mass diffusivity. So, the mass diffusivity of the fluid decreases with the increase of the Schmidt number Sc. This is because the Schmidt number and mass diffusivity are inversely related to each other. Thus, a decrease in mass diffusivity decreases the concentration distribution. The consequence of K on the concentration distribution is shown in Figure 13. It should be noted that the growth in the values of K decays the nanofluid concentration. Furthermore, it can be perceived that molecular diffusivity is lower for higher chemical reactions. Therefore, a lower molecular diffusivity decreases the boundary layer thickness and concentration distribution of the nanoliquid. Figures 14, 15 show streamline patterns of Newtonian and Maxwell fluids, respectively. It should be noted that the analysis streamlines for Maxwell and Newtonian models in the current study are indeed distinct from one another.

6 Conclusion

This article examines the 3D flow of a Maxwell nanofluid across a bi-directional stretching surface with magnetic field applications. In this approach, the effects of Brownian motion, thermophoresis, and chemical reactions are taken into account. The conditions for mass flux and thermal convection are also taken into account. The modeled problem is solved using the HAM technique. The HAM convergence is also demonstrated. Simulations and detailed discussions are carried out to determine the effects of various physical factors on flow profiles and quantities of interest. Key findings of the current problem are as follows:

- The magnetic and Maxwell fluid parameters determine the decreasing functions of primary and secondary velocities.
- The thermophoresis parameter, Brownian motion parameter, and thermal Biot number are the enhancing functions of the temperature distribution.
- The thermophoresis parameter has an enhancing effect on the concentration distribution, whereas Brownian motion, the Schmidt number, and chemical reaction parameters have a decreasing effect.
- The Nusselt number rises as the thermal Biot number, thermophoresis parameter, and Brownian motion parameter rise.
- The Sherwood number increases with the increasing thermophoresis parameter, while decreasing with the increasing Schmidt number, Brownian motion parameter, and chemical reaction parameter.
- It has been noted that the analysis streamlines for Maxwell and Newtonian models in the current study are indeed distinct from one another.

Data availability statement

The original contributions presented in the study are included in the article/Supplementary Material; further inquiries can be directed to the corresponding authors.

Author contributions

EA and SL: conceptualization, methodology, software, reviewing, and editing. ZR: data curation and writing—original draft preparation. SE: visualization and investigation. AS: software, validation, and supervision. AG: writing—reviewing and editing.

Acknowledgments

The author ZR extends her appreciation to the Deanship of Scientific Research at King Khalid University, Abha, Saudi Arabia, for funding this work through the Research Group Project under grant number (RGP.1/334/43).

Conflict of interest

The authors declare that the research was conducted in the absence of any commercial or financial relationships that could be construed as a potential conflict of interest.

Publisher's note

All claims expressed in this article are solely those of the authors and do not necessarily represent those of their affiliated organizations, or those of the publisher, the editors, and the reviewers. Any product that may be evaluated in this article, or claim that may be made by its manufacturer, is not guaranteed or endorsed by the publisher.

References

Alshehri, N. A., Abidi, A., Khan, M. R., Reddy, Y. D., Rasheed, S., Alali, E., et al. (2021). Unsteady convective MHD flow and heat transfer of a viscous nanofluid across a porous stretching/shrinking surface: Existence of multiple solutions. *Crystals* 11, 1359. doi:10.3390/cryst11111359

Andersson, H. I., Hansen, O. R., and Holmedal, B. (1994). Diffusion of a chemically reactive species from a stretching sheet. *Int. J. Heat. Mass Transf.* 37, 659–664. doi:10.1016/0017-9310(94)90137-6

Ashwinkumar, G. P., Samrat, S. P., and Sandeep, N. (2021). Convective heat transfer in MHD hybrid nanofluid flow over two different geometries. *Int. Commun. Heat. Mass Transf.* 127, 105563. doi:10.1016/j.icheatmasstransfer.2021.105563

Bejawada, S. G., Reddy, Y. D., Jamshed, W., Nisar, K. S., Alharbi, A. N., and Chouikh, R. (2022). Radiation effect on MHD Casson fluid flow over an inclined non-linear surface with chemical reaction in a Forchheimer porous medium, Alexandria Eng. *J.* 61, 8207–8220.

Bejawada, S. G., and Yanala, D. R. (2021). Finite element Soret Dufour effects on an unsteady MHD heat and mass transfer flow past an accelerated inclined vertical plate. *Heat. Transf.* 50, 8553–8578. doi:10.1002/htj.22290

Bilal Ashraf, M., Hayat, T., and Alhuthali, M. S. (2016). Three-dimensional flow of Maxwell fluid with soret and dufour effects. *J. Aerosp. Eng.* 29, 4015065. doi:10.1061/%28ASCE%29AS.1943-5525.0000551

Chen, C. H. (1998). Laminar mixed convection adjacent to vertical continuously stretching sheets. *Heat. mass Transf.* 33, 471–476. doi:10.1007/s002310050217

Dawar, A., Saeed, A., Islam, S., Shah, Z., Kumam, W., and Kumam, P. (2021). Electromagnetohydrodynamic bioconvective flow of binary fluid containing nanoparticles and gyrotactic microorganisms through a stratified stretching sheet. *Sci. Rep.* 11, 23159–23229. doi:10.1038/s41598-021-02320-0

Hu, X., Lin, P., Lin, J., Zhu, Z., and Yu, Z. (2022). On the polydisperse particle migration and formation of chains in a square channel flow of non-Newtonian fluids. *J. Fluid Mech.* 936, A5. doi:10.1017/jfm.2022.38

Irfan, M. (2021). Study of Brownian motion and thermophoretic diffusion on non-linear mixed convection flow of Carreau nanofluid subject to variable properties. *Surfaces Interfaces* 23, 100926. doi:10.1016/j.surfin.2021.100926

Islam, S., Khan, A., Deebani, W., Bonyah, E., Alreshidi, N. A., and Shah, Z. (2020). Influences of Hall current and radiation on MHD micropolar non-Newtonian hybrid nanofluid flow between two surfaces. *AIP Adv.* 10, 055015. doi:10.1063/1.5145298

Khalil, K. M., Soleiman, A., Megahed, A. M., and Abbas, W. (2022). Impact of variable fluid properties and double diffusive cattaneo–christov model on dissipative non-Newtonian fluid flow due to a stretching sheet. *Mathematics* 10, 1179. doi:10.3390/math10071179

Khan, A., Saeed, A., Tassaddiq, A., Gul, T., Mukhtar, S., Kumam, P., et al. (2021). Bio-convective micropolar nanofluid flow over thin moving needle subject to Arrhenius activation energy, viscous dissipation and binary chemical reaction. *Case Stud. Therm. Eng.* 25, 100989. doi:10.1016/j.csite.2021.100989

Kiyani, M. Z., Abbasi, A. M. K., Muhammad, T., Ahmad, I., Waqas, M., and Riaz, S. (2022). Rheology of magneto-micropolar nanoliquid toward radiative exponential surface subjected to Brownian motion, thermal radiation, thermophoresis and viscous dissipation. *Waves Random Complex Media* 2022, 1–15. doi:10.1080/17455030.2022.2048921

Kodi, R., Mopuri, O., Sree, S., and Konduru, V. (2022). Investigation of MHD Casson fluid flow past a vertical porous plate under the influence of thermal diffusion and chemical reaction. *Heat. Transf.* 51, 377–394. doi:10.1002/htj.22311

Kumar, D., and Sahu, A. K. (2022). Non-Newtonian fluid flow over a rotating elliptic cylinder in laminar flow regime. *Eur. J. Mech.* 93, 117–136. doi:10.1016/j.euromechflu.2022.01.005

Kumar, M. A., Reddy, Y. D., Goud, B. S., and Rao, V. S. (2022). An impact on non-Newtonian free convective MHD Casson fluid flow past a vertical porous plate in the existence of Soret, Dufour, and chemical reaction. *Int. J. Ambient. Energy* 43, 7410–7418. doi:10.1080/01430750.2022.2063381

Kumar, S., and Sharma, K. (2022). Impacts of stefan blowing on reiner–rivlin fluid flow over moving rotating disk with chemical reaction. *Arab. J. Sci. Eng.* 2022, 1–10. doi:10.1007/s13369-022-07008-9

Mabood, F., Ashwinkumar, G. P., and Sandeep, N. (2022). Effect of nonlinear radiation on 3D unsteady MHD stagnancy flow of Fe_3O_4/graphene–water hybrid nanofluid. *Int. J. Ambient Energy* 43, 3385–3395. doi:10.1080/01430750.2020.1831593

Mabood, F., Ashwinkumar, G. P., and Sandeep, N. (2021). Simultaneous results for unsteady flow of MHD hybrid nanoliquid above a flat/slendering surface. *J. Therm. Anal. Calorim.* 146, 227–239. doi:10.1007/s10973-020-09943-x

Mehta, R., and Kataria, H. R. (2022). Brownian motion and thermophoresis effects on MHD flow of viscoelastic fluid over stretching/shrinking sheet in the presence of thermal radiation and chemical reaction. *Heat. Transf.* 51, 274–295. doi:10.1002/htj.22307

Mishra, P., Kumar, D., Dharmendar Reddy, Y., and Shankar Goud, B. (2022). Numerical investigation of MHD flow of Williamson nanofluid with variable viscosity pasting a wedge within porous media: A non-Darcy model approach. *Heat. Transf.* 51 (7), 6071–6086. doi:10.1002/htj.22580

Mukhopadhyay, S. (2013). Casson fluid flow and heat transfer over a nonlinearly stretching surface. *Chin. Phys. B* 22, 074701. doi:10.1088/1674-1056/22/7/074701

Nalivela, N. R., Vempati, S. R., Ravindra Reddy, B., and Dharmendar Reddy, Y. (2022). Viscous dissipation and thermal radiation impact on MHD mass transfer natural convective flow over a stretching sheet. *Proc. Inst. Mech. Eng. Part E J. Process Mech. Eng.* 2022, 09544089221081339. doi:10.1177/09544089221081339

Ogunseye, H. A., Salawu, S. O., Tijani, Y. O., Riliwan, M., and Sibanda, P. (2019). Dynamical analysis of hydromagnetic Brownian and thermophoresis effects of squeezing Eyring–Powell nanofluid flow with variable thermal conductivity and chemical reaction, Multidiscip. *Model. Mat. Struct.* 15 (6), 1100–1120. doi:10.1108/MMMS-01-2019-0008

Prasad, K. V., Santhi, S. R., and Datti, P. S. (2012). Non-Newtonian power-law fluid flow and heat transfer over a non-linearly stretching surface. *Appl. Math.* 3, 35065. doi:10.4236/am.2012.35065

Raghunath, K., Gulle, N., Vaddemani, R. R., and Mopuri, O. (2022). Unsteady MHD fluid flow past an inclined vertical porous plate in the presence of chemical reaction with aligned magnetic field, radiation, and Soret effects. *Heat. Transf.* 51, 2742–2760. doi:10.1002/htj.22423

Reddy, N. N., Reddy, Y. D., Rao, V. S., Goud, B. S., and Nisar, K. S. (2022). Multiple slip effects on steady MHD flow past a non-isothermal stretching surface in presence of Soret, Dufour with suction/injection. *Int. Commun. Heat. Mass Transf.* 134, 106024. doi:10.1016/j.icheatmasstransfer.2022.106024

Reddy, Y. D., Mebarek-Oudina, F., Goud, B. S., and Ismail, A. I. (2022). Radiation, velocity and thermal slips effect toward MHD boundary layer flow through heat and mass transport of Williamson nanofluid with porous medium. *Arab. J. Sci. Eng.* 47, 16355–16369. doi:10.1007/s13369-022-06825-2

Reddy, Y. D., Ramya, D., and Babu, L. A. (2016). Effect of thermal radiation on MHD boundary layer flow of nanofluid and heat transfer over a non-linearly stretching sheet with transpiration. *J. Nanofluids* 5, 889–897. doi:10.1166/jon.2016.1284

Salawu, S. O., and Ogunseye, H. A. (2020). Entropy generation of a radiative hydromagnetic Powell-Eyring chemical reaction nanofluid with variable conductivity and electric field loading. *Results Eng.* 5, 100072. doi:10.1016/j.rineng.2019.100072

Saleem, S., Animasaun, I. L., Yook, S.-J., Al-Mdallal, Q. M., Shah, N. A., and Faisal, M. (2022). Insight into the motion of water conveying three kinds of nanoparticles shapes on a horizontal surface: Significance of thermo-migration and Brownian motion. *Surfaces Interfaces* 30, 101854. doi:10.1016/j.surfin.2022.101854

Sandeep, N., and Ashwinkumar, G. P. (2021). Impact of nanoparticle shape on magnetohydrodynamic stagnation-point flow of carreau nanoliquid: A comparative study. *Proc. Inst. Mech. Eng. Part E J. Process Mech. Eng.* 236 (3), 09544089211058427. doi:10.1177/09544089211058427

Sandeep, N., Ranjana, B., Samrat, S. P., and Ashwinkumar, G. P. (2022). Impact of nonlinear radiation on magnetohydrodynamic flow of hybrid nanofluid with heat source effect. *Proc. Inst. Mech. Eng. Part E J. Process Mech. Eng.* 236 (4), 09544089211070667. doi:10.1177/095440892110706

Sharma, R. P., and Mishra, S. R. (2020). Effect of higher order chemical reaction on magnetohydrodynamic micropolar fluid flow with internal heat source, Int. J. Fluid Mech. Res. *Inter. J. Fluid Mech. Res.* 47, 121–134. doi:10.1615/interjfluidmechres.2019027201

Sharma, R. P., and Shaw, S. (2022). MHD non-Newtonian fluid flow past a stretching sheet under the influence of non-linear radiation and viscous dissipation. *J. Appl. Comput. Mech.* 8, 949–961. doi:10.22055/JACM.2021.34993.2533

Singh, K., Pandey, A. K., and Kumar, M. (2021). Numerical solution of micropolar fluid flow via stretchable surface with chemical reaction and melting heat transfer using Keller-Box method. *Propuls. Power Res.* 10, 194–207. doi:10.1016/J.JPPR.2020.11.006

Sneha, K. N., Mahabaleshwar, U. S., Chan, A., and Hatami, M. (2022). Investigation of radiation and MHD on non-Newtonian fluid flow over a stretching/shrinking sheet with CNTs and mass transpiration. *Waves Random Complex Media* 2022, 1–20. doi:10.1080/17455030.2022.2029616

Sohail, M., Shah, Z., Tassaddiq, A., Kumam, P., and Roy, P. (2020). Entropy generation in MHD Casson fluid flow with variable heat conductance and thermal conductivity over non-linear bi-directional stretching surface. *Sci. Rep.* 10, 12530–12616. doi:10.1038/s41598-020-69411-2

Sulochana, C., Ashwinkumar, G. P., and Sandeep, N. (2018). Boundary layer analysis of persistent moving horizontal needle in magnetohydrodynamic ferrofluid: A numerical study. *J.* 57, 2559–2566. doi:10.1016/j.aej.2017.08.020

Tayyab, M., Siddique, I., Jarad, F., Ashraf, M. K., and Ali, B. (2022). Numerical solution of 3D rotating nanofluid flow subject to Darcy-Forchheimer law, bio-convection and activation energy. *South Afr. J. Chem. Eng.* 40, 48–56. doi:10.1016/j.sajce.2022.01.005

Upreti, H., Pandey, A. K., Uddin, Z., and Kumar, M. (2022). Thermophoresis and brownian motion effects on 3D flow of Casson nanofluid consisting microorganisms over a Riga plate using PSO: A numerical study. *Phys.* 78, 234–270. doi:10.1016/j.cjph.2022.06.019

Waini, I., Khashi'ie, N. S., Kasim, A. R. M., Zainal, N. A., Ishak, A., and Pop, I. (2022). Thermal analysis of non-Newtonian fluid flow past a permeable shrinking wedge with magnetohydrodynamic effects: Reiner–Philippoff model. *J. Therm. Anal. Calorim.* 147, 13561–13571. doi:10.1007/s10973-022-11508-z

Wu, J., and Thompson, M. C. (1996). Non-Newtonian shear-thinning flows past a flat plate. *J. Nonnewt. Fluid Mech.* 66, 127–144. doi:10.1016/s0377-0257(96)01476-0

Xu, H., and Liao, S.-J. (2009). Laminar flow and heat transfer in the boundary-layer of non-Newtonian fluids over a stretching flat sheet. *Comput. Math. Appl.* 57, 1425–1431. doi:10.1016/j.camwa.2009.01.029

Nomenclature

Symbol names

a **and** b positive constants

C concentration of the fluid

D_B Brownian diffusivity

$L_f, L_g, L_\theta,$ and L_ϕ linear operators $\hbar_f$, $\hbar_g$, $\hbar_\theta$, and $\hbar_\phi$ and auxiliary parameters

M magnetic term

T temperature

$u, v,$ and w velocity components

$x, y,$ and z coordinates

Greek letters

σ electrical conductivity

α stretching parameter

Subscripts

w at the surface

B_0 magnetic field

$f_0, g_0, \theta_0, and\ \phi_0$ initial guesses

K chemical reaction parameter

$\mho_1 - \mho_{10}$ arbitrary constants

Pr Prandtl number

Sc Schmidt number

$u_w(x) = ax$ stretching velocity along the $x-$ direction

$v_w(x) = by$ stretching velocity along the $y-$ direction

β Deborah number

ρ density

∞ free stream

frontiers | Frontiers in Materials

TYPE Original Research
PUBLISHED 28 March 2023
DOI 10.3389/fmats.2023.1144854

OPEN ACCESS

EDITED BY
Noor Saeed Khan,
University of Education Lahore, Pakistan

REVIEWED BY
Khadija Maqbool,
International Islamic University, Islamabad, Pakistan
Humaira Yasmin,
King Faisal University, Saudi Arabia

*CORRESPONDENCE
Zahir Shah,
zahir@ulm.edu.pk
Narcisa Vrinceanu,
vrinceanu.narcisai@ulbsibiu.ro

SPECIALTY SECTION
This article was submitted to Colloidal Materials and Interfaces, a section of the journal *Frontiers in Materials*

RECEIVED 15 January 2023
ACCEPTED 21 February 2023
PUBLISHED 28 March 2023

CITATION
Tang T-Q, Rooman M, Shah Z, Khan S, Vrinceanu N, Alshehri A and Racheriu M (2023), Numerical study of magnetized Powell–Eyring hybrid nanomaterial flow with variable heat transfer in the presence of artificial bacteria: Applications for tumor removal and cancer cell destruction.
Front. Mater. 10:1144854.
doi: 10.3389/fmats.2023.1144854

Numerical study of magnetized Powell–Eyring hybrid nanomaterial flow with variable heat transfer in the presence of artificial bacteria: Applications for tumor removal and cancer cell destruction

Tao-Qian Tang[1,2,3,4,5], Muhammad Rooman[6], Zahir Shah[6]*, Saima Khan[7], Narcisa Vrinceanu[8]*, Ahmed Alshehri[9] and Mihaela Racheriu[10,11]

[1]Department of Internal Medicine, E-Da Hospital, I-Shou University, Kaohsiung, Taiwan, [2]School of Medicine, College of Medicine, I-Shou University, Kaohsiung, Taiwan, [3]International Intercollegiate Ph.D. Program, National Tsing Hua University, Hsinchu, Taiwan, [4]Department of Family and Community Medicine, E-Da Hospital, I-Shou University, Kaohsiung, Taiwan, [5]Department of Engineering and System Science, National Tsing Hua University, Hsinchu, Taiwan, [6]Department of Mathematical Sciences, University of Lakki Marwat, Lakki Marwat, Pakistan, [7]Department of Physics, Abdul Wali Khan University, Mardan, Pakistan, [8]Department of Industrial Machines and Equipment, Faculty of Engineering, "Lucian Blaga" University of Sibiu, Sibiu, Romania, [9]Department of Mathematics, Faculty of Sciences, King Abdulaziz University, Jeddah, Saudi Arabia, [10]Medicine Faculty, Lucian Blaga University of Sibiu, Sibiu, Romania, [11]City Clinical Emergency Hospital, Sibiu, Romania

This investigation determined the effectiveness of an exterior magnetic field on bacteria enclosed by thousands of magnetite nanoparticles. Variable thermal conductivity and Joule heating were used in the interstitial nano liquid in which artificial bacteria were swimming in a biotic cell. The unsteady motions of a Powell–Eyring fluid in two dimensions were assumed. The porous extending wall was used as a bent surface shape. To convert the governing non-linear PDEs into non-linear ODEs, suitable transformations were exploited. The homotopy analysis technique (HAM) was utilized to resolve the semi-analytical results of non-linear ODEs. Plots were utilized to investigate the impact of significant parameters of velocity distribution, temperature profile, bacterial density field, nutrient concentration field, skin friction, Nusselt number, and nutrient concentration density. Clinical disease has shown that daring tumors have reduced blood flow. The results of this study showed that augmenting the values of unsteady parameters improved the blood velocity profile. The velocity distribution decreased for higher magnetite volume fraction values, as well as porosity and magnetic parameters. As the concentration of magnetite nanoparticles increased, so did the blood temperature distribution. As a result, the immersion of magnetite nanoparticles improved the physical characteristics of the blood. These findings also demonstrated that magnetic parameters and Eckert number play an essential role in increasing heat transfer rates.

KEYWORDS

Powell–Eyring fluid, blood flow, magnetite nanoparticles, porous medium, curved biological boundary, joule heating, artificial bacteria

1 Introduction

Radiotherapy and chemotherapy are frequently applied to treat patients with cancer. However, the combination of these treatments may be inadequate to achieve a cure in some cases. Thus, the development of advanced and novel tactics may provide oncologists with additional therapeutic possibilities. A laboratory in Spain recently produced an artificial magnetic bacterium that, when consumed, can trigger a charged magnetism compass to mark and destroy tumors because the compass rotation speed heats and melts tumors. This method is based on hyperthermia caused by magnets, which is an exploratory treatment method in which magneto-nanoparticle-saturated tumors are subjected to a discontinuous magnetic field. This treatment begins by immersing a tumor in iron magneto-nanoparticles. Every cell in the body requires oxygen to function, and tumors cannot grow beyond the size of a sugar pill without it. Thus, tumors produce hormones that permit them to obtain oxygen-rich blood by hijacking surrounding blood vessels. Moreover, because blood arteries grow in tumors in an unorganized and faster manner, they are porous and defective. When ferromagnetic iron nanoparticles are infused into blood circulation, they travel throughout the body, avoiding healthy blood vessels unless they enter the leakages that nourish tumors. Mathuriya et al. (2015) reported that these vaccinated magnetic iron nanomaterials eventually pass through the blood unless they reach a tumor's blood generator, in which these particles accumulate. Magnetic nanoparticles show potential as a drug conveyance module because of their large surface area, high viability, low toxicity, and volume proportions. Furthermore, magnetic hyperthermia uses magnetic nanoparticles to reduce tumor volume and to target and eliminate malignant cells. Magnetic bio partitioning is useful for detaching a specific atom from a catalog of molecules. One example is the magnetic bio partitioning used to restrict viral RNA for further investigation by polymerase chain reaction. Furthermore, magnetic particles exhibit imaging characteristics, making them useful for multimodal theranostics. These characteristics of magnetic nanomaterials allow simultaneous treatment and diagnostics (Anik et al. (2021). Kong et al. (2014) and Cui et al. (2012) used an unsteady applied magnetic field impact to examine the movement of magnetotactic bacteria (MTB) in a Newtonian fluid. The authors addressed the swimming motion of MTB from a fluid dynamics standpoint in conjunction with an entire three-dimensional Stokes flow. Vincenti et al. (2018) scrutinized the effect of a magnetic field on micro-swimmer suspensions in liquid. Furthermore, Nagaraj et al. (2018) reported on the joint effect of electric and magnetic fields on the synovial fluid in a biological context. Bhatti (2021) recently investigated nanomedicine utilizing suspensions of magnetized gold (Au) nanoparticles. Afridi et al. (2019) explored the effect of thermal dissipation and entropy formation on the flow of a hybrid nanofluid across a curved sheet. Moreover, it is practical to use a spreading twisted surface for interstitial nanoparticle flow, in which artificial magnetic bacteria swim within biological cells. Shukla et al. (2019) examined the effects of viscoelasticity factors on second-order fluid in carotid artery blood flow. The HAM was used to initiate an entropy creation evaluation of time-dependent second-grade nanoliquid and heat transfer under the influence of a magnetic field. The authors discovered that increasing the second-order viscoelastic and magnetic values increased the entropy production number.

Many studies have proposed strategies for mathematical models within the human body, including the flow of fluid across a curved surface. Several investigators have also considered abdominal fluid flowing through biological cells as a non-Newtonian Powell–Eyring fluid. Saleem and Munawar (2016) examined blood flow *via* a stenotic artery in a constant magnetic field by assuming that blood within the artery was an Powell–Eyring fluid. Hina et al. (2016) investigated the heat transfer characteristics of a Powell–Eyring fluid in peristaltic flow within a curved channel with compliant walls. According to Riaz et al. (2019), the heat transfer procedure in the human body is a complex process that includes heat movement in tissues, membrane pores, electromagnetic radiation emitted by cell phones, exterior interface, metabolic heat production, and arterial-venous blood circulation. Their research aimed to determine the impact of bioheat and mass transfer in the peristaltic movement of an Powell–Eyring liquid in a three-dimensional rectangular cross section in the context of the human thermoregulation framework and thermotherapy. Hussain et al. (2020) numerically explored flow and explained blood flow behavior through tapered arteries as a non-Newtonian Powell–Eyring fluid. Asha and Sunitha (2018), Gholinia et al. (2019), Mallick and Misra (2019), Sultan et al. (2019), and Basha and Sivaraj (2021) conducted relevant research on this model. In the presence of a magnetic field generated using magnetite (Fe_3O_4), Yasmin (2022), Alyousef et al. (2023), Yasmin et al. (2023a), Yasmin et al. (2023b), and Yasmin et al. (2023c) performed biomedical investigations of fluid flow and studied nanofluid flow and hybrid nanofluids experimentally and theoretically, with stability analysis in the context of energy storage and other applications.

Based on these previous findings, the present study considered the growth of artificial magnetic bacteria in a non-Newtonian Powell–Eyring nanofluid on a stretching curved surface using a porous medium. The variable fluid thermal conductivity of the nanofluid was considered. As shown in Figure 1, curvilinear coordinates were used to model mathematical expressions across the curved biological boundary. This investigation also used magnetite nanoparticles. The temperature, concentration, and velocity of magnetite/blood in biological cells were acquired by the homotopy analysis method (HAM) *via* MATHEMATICA and depicted in a set of plots. Additionally, different scenarios were developed by varying the impact of dimensionless parameters, and distinct cases were constructed to obtain maximum reference data. The magnetic bacterium function as a magnetically charged compass to mark and abolish tumors by revolving at such a high rate that tumors heat and melt. Section 2 provides the mathematical formulas and all relevant details. Section 3 presents the physical quantities and the solution method, and its convergence with the validation of the results is shown in Sections 4 and 5. Section 6 includes the results and discussion. Finally, Section 7 contains the conclusions.

2 Mathematical formulas

We assumed a two-dimensional unsteady boundary layer Powell–Eyring nanofluid flow on a strained curved surface using a

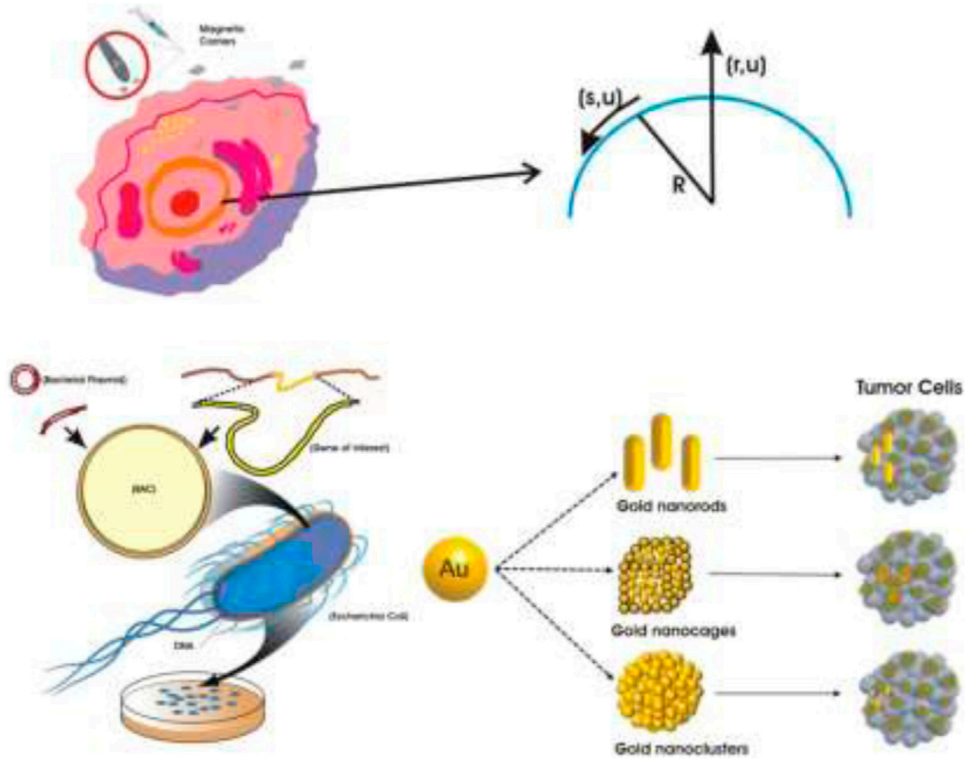

FIGURE 1
Fluid flow configuration and coordinate system.

porous medium that was a spiral in a circle with radius R around the curvilinear coordinates. The stretching surface in the $s-direction$ had a velocity $u = U_w$ and was vertical to the $r-direction$. A magnetic field of intensity $B(t)$ was applied in the vertical direction. The nanofluid was embedded in the porous medium, and its flow behavior in the porous medium was accounted for by using the Brinkman model. The effects of variable thermal conductivity, heat generation/absorption, and joule dissipation were all considered. We used reaction–diffusion equations to explicitly model the dynamics of the bacterial density ρ_n and nutrient concentration n.

2.1 Formal model and geometry

Figure 1 shows the geometry of the flow problem along with the coordinate system, velocity field, and other details.

2.1.1 Governing equations and boundary conditions after applying assumptions

Navier–Stokes flow is a type of fluid movement in which the spinning speed of the flow, U_w, is extremely low and the typical dimension a is slight. The Stokes estimate is commonly used to describe the motion of magnetic bacteria because it ignores the inertial term in the Navier–Stokes equation by using a low Reynolds number. Thus, the Navier–Stokes and continuity equations govern the fluid speed produced by swimming magnetotactic bacteria. The theory of rate mechanisms was utilized to deduce the Powell–Eyring model (1994) to define shear in non-Newtonian flow. The shear tensor in the Powell–Eyring fluid model is given by (Riaz et al. (2019)

$$\boldsymbol{\tau} = \mu\nabla\boldsymbol{V} + \frac{1}{\beta_1}\sinh^{-1}\left(\frac{1}{c_1}\nabla\boldsymbol{V}\right) \tag{1}$$

and

$$\sinh^{-1}\left(\frac{1}{c_1}\nabla\boldsymbol{V}\right) \approx \left(\frac{1}{c_1}\nabla\boldsymbol{V}\right) - \frac{1}{6}\left(\frac{1}{c_1}\nabla\boldsymbol{V}\right)^3, \quad \left|\frac{1}{c_1}\nabla\boldsymbol{V}\right| \ll 1. \tag{2}$$

The appropriate governing equations to examine the foregoing fluid flow are as follows:

$$\bar{r}\frac{\partial v}{\partial r} + r + R\frac{\partial u}{\partial s} = 0, \tag{3}$$

$$\frac{u^2}{\bar{r}} = \frac{1}{\rho_{nf}}\frac{\partial p}{\partial r}, \tag{4}$$

$$\rho_{nf}\left(\frac{\partial u}{\partial t} + v\frac{\partial u}{\partial r} + \frac{R}{\bar{r}}u\frac{\partial u}{\partial s} + uv\right) = -\frac{R}{\bar{r}}\frac{\partial p}{\partial s} + \left(\mu_{nf} + \frac{1}{\beta_1 c_1}\right)\frac{\partial}{\partial r}\left(\frac{\partial u}{\partial r} + \frac{u}{\bar{r}}\right) - \frac{1}{6\beta_1 c_1^3}\frac{\partial}{\partial r}\left(\frac{\partial u}{\partial r} + \frac{u}{\bar{r}}\right)^3 - \sigma_{nf}B^2(t)u - \frac{\mu_{nf}}{k_1}u, \tag{5}$$

$$\left(\rho C_p\right)_{nf}\left(\frac{\partial T}{\partial t} + v\frac{\partial T}{\partial r} + \frac{R}{\bar{r}}u\frac{\partial T}{\partial s}\right) = \frac{1}{\bar{r}}\frac{\partial}{\partial r}\left(\bar{r}k_{nf}(T)\frac{\partial T}{\partial r}\right) + \sigma_{nf}B^2(t)u^2 + Q^*(T - T_\infty), \tag{6}$$

$$\left(\frac{\partial \rho_n}{\partial t} + v\frac{\partial \rho_n}{\partial r} + \frac{R}{\bar{r}}u\frac{\partial \rho_n}{\partial s}\right) = D_n\left(\frac{\partial^2 \rho_n}{\partial r^2} + \frac{1}{\bar{r}}\frac{\partial \rho_n}{\partial r}\right) + A(n,t)\rho_n, \tag{7}$$

TABLE 1 Thermophysical characteristics of Fe_3O_4 magnetite nanoparticles and blood (Alyousef et al., 2023; Yasmin et al., 2023a).

Thermophysical property	$\rho\ (kg/m^3)$	$C_p\ (J/kg\,K)$	$k\ (W/m\,K)$	$\sigma\ (S/m)$
Blood	1,000	4,180	0.543	0.0109
Iron oxide Fe_3O_4	5,180	670	9.7	25,000

$$\left(\frac{\partial n}{\partial t}+v\frac{\partial n}{\partial r}+\frac{R}{\bar{r}}u\frac{\partial n}{\partial s}\right)=D_n\left(\frac{\partial^2 n}{\partial r^2}+\frac{1}{\bar{r}}\frac{\partial n}{\partial r}\right)-\frac{A(n,t)}{Y}\rho_n. \tag{8}$$

subject to the boundary condition (Elgazery et al., 2022)

$$\left.\begin{aligned} &u=U_w=\frac{as}{1-ct},\quad v=0,\ T=T_w,\ \rho_n=(\rho_n)_w,\ n=n_w\ at\ r\to 0\\ &u\to 0,\quad \frac{\partial u}{\partial r}\to 0,\ T\to T_\infty,\ \rho_n\to(\rho_n)_\infty,\ n\to n_\infty,\ as\ r\to\infty \end{aligned}\right\}. \tag{9}$$

Here, $\bar{r}=r+R, B(t)=\frac{B_0}{\sqrt{1-ct}}$, $Y=\frac{(\rho_n)_w-(\rho_n)_\infty}{n_w-n_\infty}$ is the conversion factor, $A(n,t)=a\lambda(t)\frac{n}{(K_m+n)}$ represents the variable nutrient bacterial growth rate, and $\lambda(t)=\frac{\lambda_0}{1-ct}$ represents the maximum growth rate. In this present discussion, we assume that n is greater than the Monod constant K_m and that $a>0$ and $c\geq 0$ with dimension $(time)^{-1}$.

2.1.2 Similarity transformations and modeled ODEs

Using the following dimensionless similarity transformations (Elgazery et al., 2022),

$$\left.\begin{aligned} &\xi=\sqrt{\frac{a}{\nu_f(1-ct)}}r,\\ &u=\frac{as}{1-ct}f'(\xi),\ p=\rho_f\left(\frac{as}{1-ct}\right)^2P(\xi),\ T=T_\infty+(T_w-T_\infty)\theta(\xi),\\ &\rho_n=(\rho_n)_\infty+\left((\rho_n)_w-(\rho_n)_\infty\right)\chi(\xi),\quad n=n_\infty+(n_w-n_\infty)\omega(\xi). \end{aligned}\right\} \tag{10}$$

and using the aforementioned dimensionless quantity, the equation of continuity is satisfied, and after pressure elimination the governing Eqs 7–12 can be written as follows:

$$\begin{aligned} &(\varphi_4+\alpha_1)\left[f^{IV}+\frac{2f'''}{\bar{\xi}}-\frac{f''}{(\bar{\xi})^2}+\frac{f'}{(\bar{\xi})^3}\right]-\varphi_3M\left(f''+\frac{f'}{\bar{\xi}}\right)-\varphi_4\beta_0\left(f''+\frac{f'}{\bar{\xi}}\right)\\ &-\alpha_2\left[\left(f''^2+\frac{2f'f''}{\bar{\xi}}+\frac{f'^2}{(\bar{\xi})^2}\right)f^{IV}+\left(f''^2-\frac{3f'f''}{\bar{\xi}}-\frac{f'^2}{(\bar{\xi})^2}\right)\frac{f''}{(\bar{\xi})^2}+\frac{3f'^3}{(\bar{\xi})^5}\right.\\ &\left.+2\left(f''+\frac{f'}{\bar{\xi}}\right)f'''^2+2\left(3f''^2+\frac{2f'f''}{\bar{\xi}}-\frac{f'^2}{(\bar{\xi})^2}\right)\frac{f'''}{\bar{\xi}}\right]\\ &+\varphi_1\left[\frac{K(ff'''-f'f'')}{\bar{\xi}}+\frac{K(ff''-f'^2)}{(\bar{\xi})^2}-\frac{Kff'}{(\bar{\xi})^3}-\frac{\gamma}{\bar{\xi}}\left(\frac{\xi}{2}f''+f'\right)\right.\\ &\left.-\frac{\gamma}{2}(\xi f'''+3f'')\right]=0, \end{aligned} \tag{11}$$

$$\varphi_5\left[(1+\beta\theta)\left(\theta''+\frac{\theta'}{\bar{\xi}}\right)+\beta(\theta')^2\right]+\varphi_3MPrEcf'^2+\varphi_2Pr\left[\left(\frac{Kf}{\bar{\xi}}-\frac{\gamma\xi}{2}\right)\theta'+\frac{Q}{\varphi_2}\theta\right]=0, \tag{12}$$

$$\chi''+\frac{\chi}{\bar{\xi}}+Lb\left[\left(\frac{Kf}{\bar{\xi}}-\frac{\gamma\xi}{2}\right)\chi'+\lambda(\Omega+\chi)\right]=0, \tag{13}$$

$$\omega''+\frac{\omega}{\bar{\xi}}+Lb\left[\left(\frac{Kf}{\bar{\xi}}-\frac{\gamma\xi}{2}\right)\omega'+\lambda(\Omega+\chi)\right]=0. \tag{14}$$

Similarly, pressure can be expressed as follows:

$$\begin{aligned} P(\xi)=&\frac{\bar{\xi}}{2K}(\varphi_4+\alpha_1)\left[f'''+\frac{f''}{\bar{\xi}}-\frac{f'}{(\bar{\xi})^2}\right]\\ &+\frac{\varphi_1}{2}\left[ff''-f'^2+\frac{ff'}{\bar{\xi}}-\frac{\bar{\xi}}{K}\gamma\left(\frac{\xi}{2}f''+f'\right)\right]\\ &-\frac{\bar{\xi}}{2K}(\varphi_3M+\varphi_1\beta_0)f'+\frac{\bar{\xi}}{2K}\alpha_2\left(f''+\frac{f'}{\bar{\xi}}\right)^2\left(f'''+\frac{f''}{\bar{\xi}}-\frac{f'}{(\bar{\xi})^2}\right). \end{aligned} \tag{15}$$

subject to the boundary conditions

$$\begin{aligned} &f'(0)=\theta(0)=\chi(0)=\omega(0)=1,\quad f(0)=0,\\ &f'(\infty)=f''(\infty)=\theta(\infty)=\chi(\infty)=\omega(\infty)=0, \end{aligned} \tag{16}$$

where $\bar{\xi}=\xi+K, K=\sqrt{\frac{a}{\nu_f(1-ct)}}R, M=\frac{\sigma_f B_0^2}{\rho_f a}, \Omega=\frac{(\rho_n)_w}{(\rho_n)_w-(\rho_n)_\infty}, \alpha_1=\frac{\mu_f}{\beta_1 c_1}$, $\alpha_2=\frac{a^3s^2}{\beta_1 c_1^3\rho_f\nu_f^2(1-ct)^3}$, $\beta_0=\frac{\mu_f(1-ct)}{\rho_f k_1 a}$, $Lb=\nu_f/D_n$, $Q=\frac{1-ct}{a(\rho C_P)_f}Q^*$, and $Pr=\frac{\nu(\rho C_P)_f}{k_0}$ $(Pr\approx 21\ for\ blood)$.

2.1.3 Thermo-physical characteristics of nanofluid

The thermo-physical characteristics of an effective nanofluid can be expressed as follows (Mallick and Misra, 2019; Yasmin, 2022; Alyousef et al., 2023):

$$\mu_{nf}=\varphi_1\mu_f, \rho_{nf}=\varphi_2\rho_f,\quad (\rho C_P)_{nf}=\varphi_3(\rho C_P)_f,\ \sigma_{nf}=\varphi_5\sigma_f, \tag{17}$$

where

$$\left.\begin{aligned} &\varphi_2=(1-\phi)+\frac{\rho_P}{\rho_f}\phi,\quad \varphi_3=(1-\phi)+\phi\frac{(\rho C_P)_P}{(\rho C_P)_f}\\ &\varphi_5=\frac{(\sigma_P+2\sigma_f+2\phi(\sigma_P-\sigma_f))}{(\sigma_P+2\sigma_f-\phi(\sigma_P-\sigma_f))},\quad \varphi_1=(1-\phi)^{-2.5} \end{aligned}\right\}. \tag{18}$$

Here, the index f represents the base fluid and P refers to the nanoparticles (Fe_3O_4). The thermophysical characteristics of magnetite nanoparticles are given in Table 1. Moreover, the nanoliquid variable thermal conductivity can be considered as follows (Yasmin, 2022):

$$\kappa_{nf}(T)=\varphi_4\kappa_0(1+\beta\theta(\eta)), \tag{19}$$

where $\varphi_4=\left(\frac{k_P+2k_f+2\phi(k_P-k_f)}{k_P+2k_f-\phi(k_P-k_f)}\right)$, k_0 represents the constant thermal conductivity of the base fluid and β is a parameter used for variable thermal conductivity.

3 Physical quantities

The physical quantities of concern in the current research are expressed as follows:

$$C_f=\frac{\tau_w}{\rho_f U_w^2},\quad Nu_s=\frac{sq_w}{k_f(T_w-T_\infty)}, Nn_s=\frac{sq_n}{D_n(n_w-n_\infty)}, \tag{20}$$

TABLE 2 Tables 2(a-d).

ξ	HAM solution	Numerical solution	Absolute error
(a) Validations of the HAM with a numerical method for $f'(\xi)$			
0.0	1.000000	1.000000	0.000000
0.5	0.654935	0.656548	0.001613
1.0	0.466136	0.469411	0.003275
1.5	0.346991	0.351120	0.004129
2.0	0.256295	0.260327	0.004032
2.5	0.180685	0.183972	0.003287
3.0	0.119248	0.121564	0.002315
3.5	0.073023	0.074451	0.001428
4.0	0.041167	0.041928	0.000762
4.5	0.021032	0.021363	0.000331
5.0	0.009352	0.009439	0.000087
(b) Validation of the HAM with the numerical method for $p(\xi)$			
0.0	1.000000	1.000000	0.000000
0.5	0.622007	0.622523	0.000516
1.0	0.402824	0.403989	0.001165
1.5	0.262053	0.263350	0.001297
2.0	0.169004	0.170127	0.001122
2.5	0.107701	0.108555	0.000854
3.0	0.067856	0.068458	0.000602
3.5	0.042343	0.042748	0.000405
4.0	0.026223	0.026486	0.000264
4.5	0.016145	0.016313	0.000168
5.0	0.009897	0.010003	0.000105
(c) Validation of the HAM with the numerical method for $\theta(\xi)$			
0.0	1.000000	1.000000	0.000000
0.5	0.644781	0.644908	0.000127
1.0	0.410030	0.410170	0.000141
1.5	0.257583	0.257698	0.000115
2.0	0.160285	0.160368	0.000083
2.5	0.099048	0.099105	0.000057
3.0	0.060908	0.060945	0.000037
3.5	0.037330	0.037354	0.037354
4.0	0.022829	0.022844	0.000015
4.5	0.013942	0.013951	9.44×10^{-6}
5.0	0.008507	0.008513	5.89×10^{-6}

(Continued in next column)

TABLE 2 (*Continued*)

ξ	HAM solution	Numerical solution	Absolute error
(d) Validation of the HAM with the numerical method for $\chi(\xi)$			
0.0	1.000000	1.000000	0.000000
0.5	0.657530	0.658168	0.000637
1.0	0.424080	0.424782	0.000703
1.5	0.269068	0.269642	0.000574
2.0	0.168602	0.169017	0.000416
2.5	0.104703	0.104985	0.000283
3.0	0.064615	0.064801	0.000185
3.5	0.039707	0.039826	0.000119
4.0	0.024333	0.024409	0.000075
4.5	0.014886	0.024409	0.000047
5.0	0.009097	0.009126	0.000029

where C_f signifies the skin friction, Nu_s denotes the Nusselt number, and Nn_s represents the nutrient concentration. Moreover, τ_w, q_w, and q_n are the surface shear stress, heat flux, and wall nutrient concentration flux, respectively. These are defined as follows:

$$\tau_{rs} = \left[\left(\mu_{nf} + \frac{1}{\beta c}\right)\left(\frac{\partial u}{\partial r} + \frac{u}{\bar{r}}\right) - \frac{1}{6\beta c^3}\left(\frac{\partial u}{\partial r} + \frac{u}{\bar{r}}\right)^3\right]_{r=R},$$
$$q_w = -k_{nf}\left[\frac{\partial T}{\partial r}\right]_{r=0}, \quad q_s = -D_n. \tag{21}$$

These quantities can be written in non-dimensional form as follows:

$$C_f (Re_s)^{1/2} = (\varphi_1 + \alpha_1)\left(f''(0) + \frac{f'(0)}{\bar{\xi}}\right) - \alpha_2\left(f''(0) + \frac{f'(0)}{\bar{\xi}}\right)^3,$$
$$Nu_s (Re_s)^{-1/2} = -\theta'(0), \quad Nn_s (Re_s)^{-1/2} = -\omega'(0), \tag{22}$$

where $(Re_s)^{1/2} = \sqrt{\frac{a}{\nu_f (1-ct)}}s$ represents the local Reynolds number.

4 Solution methods

To find the solution to the system of Eqs 11–14 under the boundary constraints (16), a HAM (Liao, 2004) approach was used and figures were sketched for convergence. The complete procedure is shown in Eqs 23–45.

The initial guesses were selected as follows:

$$f_0(\eta) = 1 - e^{-\eta}, \theta_0(\eta) = e^{-\eta}, \chi_0(\eta) = e^{-\eta}, \omega_0(\eta) = e^{-\eta}. \tag{23}$$

The linear operators are taken as L_f, L_θ, L_χ, and L_ω:

$$L_f(f) = f''' - f', L_\theta(\theta) = \theta'' - \theta, L_\chi(\chi) = \chi'' - \chi, L_\omega = \omega'' - \omega, \tag{24}$$

which have the following properties:

$$L_f\left(c_1+c_2\eta+c_3e^{-\eta}+c_4e^{\eta}\right)=0,\quad L_\theta\left(c_5e^{\eta}+c_6e^{-\eta}\right)=0,\\ L_\chi\left(c_7e^{-\eta}+c_8e^{\eta}\right)=0,\quad L_\omega\left(c_9e^{-\eta}+c_{10}e^{\eta}\right)=0, \tag{25}$$

where $c_i\,(i=1-10)$ are the constants in the general solution.

The resultant non-linear operatives $N_f, N_\theta, N_\chi,$ and N_ω are given as follows:

$$N_f[f(\eta;p)]=(\varphi_4+\alpha_1)\left[\frac{\partial^4 f(\eta;p)}{\partial\eta^4}+\frac{2}{\xi}\frac{\partial^3 f(\eta;p)}{\partial\eta^3}-\frac{1}{\xi^2}\frac{\partial^2 f(\eta;p)}{\partial\eta^2}+\frac{1}{\xi^3}\frac{\partial f(\eta;p)}{\partial\eta}\right]$$

$$-\varphi_3 M\left(\frac{\partial^2 f(\eta;p)}{\partial\eta^2}+\frac{1}{\xi}\frac{\partial f(\eta;p)}{\partial\eta}\right)-\varphi_4\beta_0\left(\frac{\partial^2 f(\eta;p)}{\partial\eta^2}+\frac{1}{\xi}\frac{\partial f(\eta;p)}{\partial\eta}\right)$$

$$-\alpha_2\begin{bmatrix}\left(\left(\frac{\partial^2 f(\eta;p)}{\partial\eta^2}\right)^2+\frac{2}{\xi}\frac{\partial f(\eta;p)}{\partial\eta}\frac{\partial^2 f(\eta;p)}{\partial\eta^2}+\frac{2}{\xi^2}\left(\frac{\partial f(\eta;p)}{\partial\eta}\right)^2\right)\frac{\partial^4 f(\eta;p)}{\partial\eta^4}\\ +\left(\left(\frac{\partial^2 f(\eta;p)}{\partial\eta^2}\right)^2-\frac{3}{\xi}\frac{\partial f(\eta;p)}{\partial\eta}\frac{\partial^2 f(\eta;p)}{\partial\eta^2}-\frac{2}{\xi^2}\left(\frac{\partial f(\eta;p)}{\partial\eta}\right)^2\right)\frac{1}{\xi^2}\frac{\partial^2 f(\eta;p)}{\partial\eta^2}\\ +\frac{3}{\xi^5}\left(\frac{\partial f(\eta;p)}{\partial\eta}\right)^3+2\left(\frac{\partial^2 f(\eta;p)}{\partial\eta^2}+\frac{1}{\xi}\frac{\partial f(\eta;p)}{\partial\eta}\right)\left(\frac{\partial^3 f(\eta;p)}{\partial\eta^3}\right)^2\\ +2\left(3\left(\frac{\partial^2 f(\eta;p)}{\partial\eta^2}\right)^3+\frac{2}{\xi}\frac{\partial f(\eta;p)}{\partial\eta}\frac{\partial^2 f(\eta;p)}{\partial\eta^2}-\frac{1}{\xi^2}\left(\frac{\partial f(\eta;p)}{\partial\eta}\right)^2\right)\frac{1}{\xi}\frac{\partial^3 f(\eta;p)}{\partial\eta^3}\end{bmatrix}$$

$$\times\varphi_1\begin{bmatrix}\frac{k}{\xi}\left(f(\eta;p)\frac{\partial^3 f(\eta;p)}{\partial\eta^3}-\frac{\partial f(\eta;p)}{\partial\eta}\frac{\partial^2 f(\eta;p)}{\partial\eta^2}\right)+\frac{k}{\xi^2}\left(f(\eta;p)\frac{\partial^2 f(\eta;p)}{\partial\eta^2}-\left(\frac{\partial f(\eta;p)}{\partial\eta}\right)^2\right)\\ \frac{k}{\xi^3}f(\eta;p)\frac{\partial f(\eta;p)}{\partial\eta}-\frac{\gamma}{\xi}\left(\frac{\xi}{2}\frac{\partial^2 f(\eta;p)}{\partial\eta^2}-\frac{\partial f(\eta;p)}{\partial\eta}\right)-\frac{\gamma}{2}\left(\xi\frac{\partial^3 f(\eta;p)}{\partial\eta^3}+3\frac{\partial^2 f(\eta;p)}{\partial\eta^2}\right)\end{bmatrix}, \tag{26}$$

TABLE 3 Comparison of skin friction.

M	Present results	Imtiaz et al. (2019)
0.0	−3.035213606332084	−3.03837
0.2	−3.426597847646775	−3.42970
0.5	−3.8509138382373056	−3.85035

$$N_\theta[f(\eta;p),\theta(\eta;p)]=\varphi_5\left[\left(1+\beta\frac{\partial\theta(\eta;p)}{\partial\eta}\right)\left(\frac{\partial^2\theta(\eta;p)}{\partial\eta^2}+\frac{1}{\xi}\frac{\partial\theta(\eta;p)}{\partial\eta}\right)+\beta\left(\frac{\partial\theta(\eta;p)}{\partial\eta}\right)^2\right]-\varphi_3 MPrEc\left(\frac{\partial f(\eta;p)}{\partial\eta}\right)^2+\varphi_2 Pr\left[\left(\frac{k_f}{\xi}-\frac{\gamma\xi}{2}\right)\frac{\partial\theta(\eta;p)}{\partial\eta}+\frac{Q}{\varphi_2}\theta(\eta;p)\right], \tag{27}$$

$$N_\omega[f(\eta;p),\omega(\eta;p)]=\frac{\partial^2\omega(\eta;p)}{\partial\eta^2}+\frac{1}{\xi}\frac{\partial\omega(\eta;p)}{\partial\eta}+Lb\begin{bmatrix}\left(\frac{K}{\xi}f(\eta;p)-\frac{\gamma\xi}{2}\right)\frac{\partial\omega(\eta;p)}{\partial\eta}\\ +\lambda(\Omega+\chi(\eta;p))\end{bmatrix}, \tag{28}$$

$$N_\chi[f(\eta;p),\chi(\eta;p)]=\frac{\partial^2\chi(\eta;p)}{\partial\eta^2}+\frac{1}{\xi}\frac{\partial\chi(\eta;p)}{\partial\eta}+Lb\left[\left(\frac{K}{\xi}f(\eta;p)-\frac{\gamma\xi}{2}\right)\frac{\partial\chi(\eta;p)}{\partial\eta}+\lambda(\Omega+\chi(\eta;p))\right]. \tag{29}$$

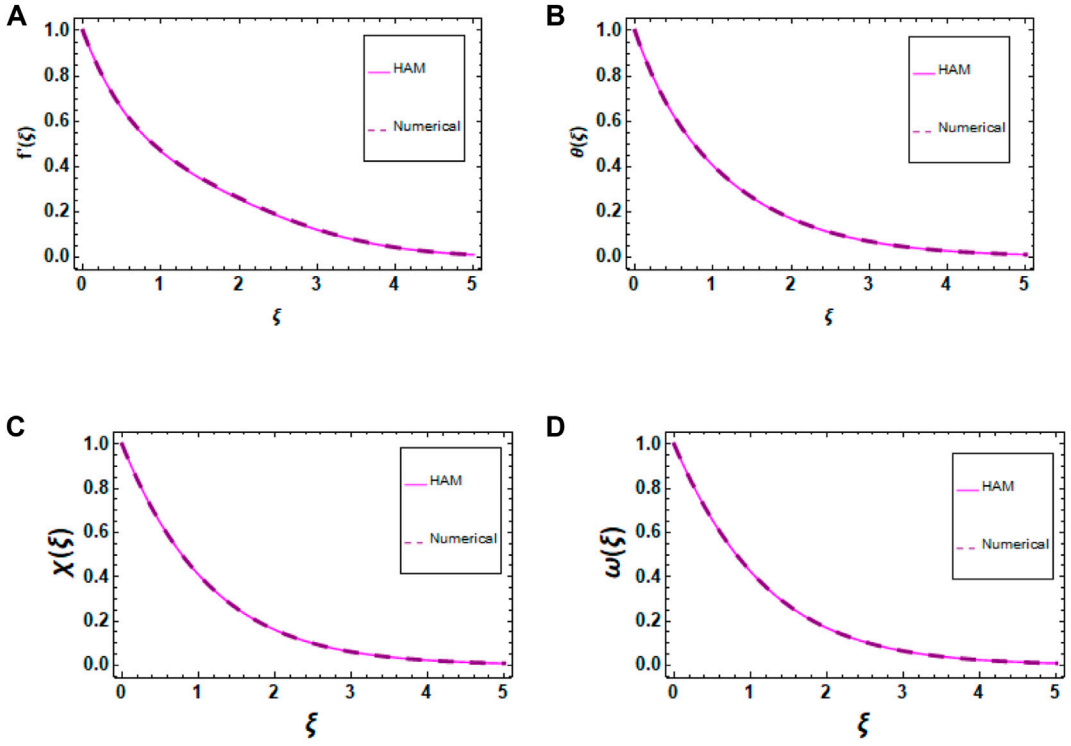

FIGURE 2
(A–D) Graphical validations of the HAM with numerical methods for $f'(\xi)$, $p(\xi)$, $\theta(\xi)$, and $\chi(\xi)$.

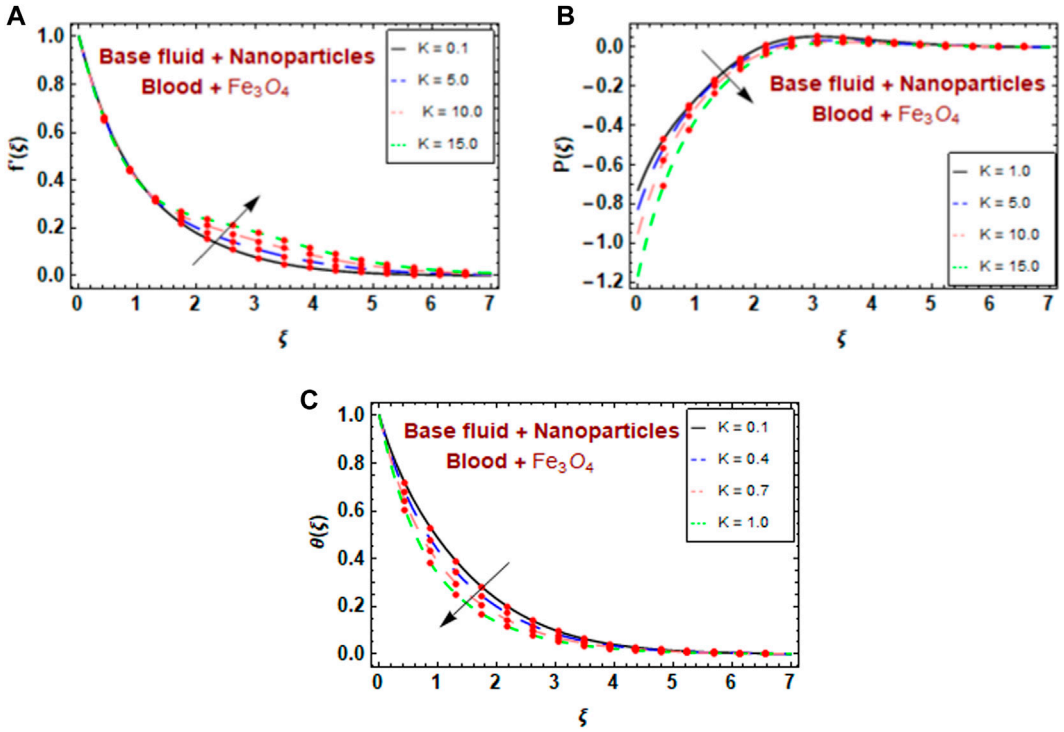

FIGURE 3
(A–C) Variations in $f'(\xi)$, $p(\xi)$, and $\theta(\xi)$ for distinct numbers of K.

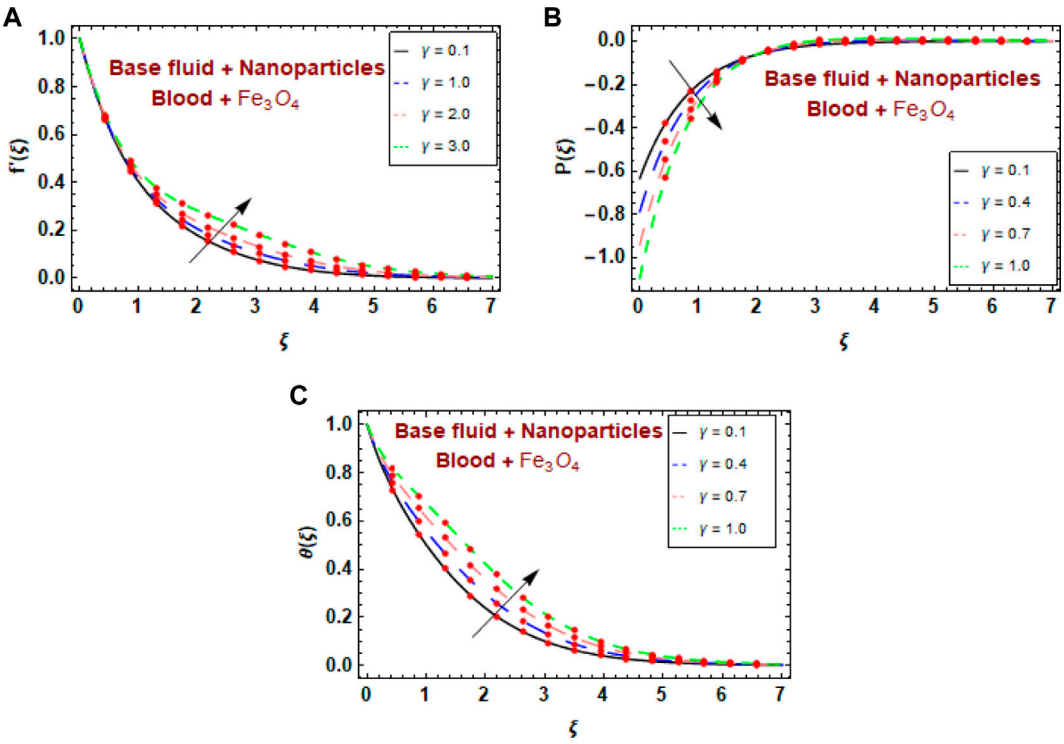

FIGURE 4
(A–C) Variations in $f'(\xi)$, $p(\xi)$, and $\theta(\xi)$ for distinct numbers of γ.

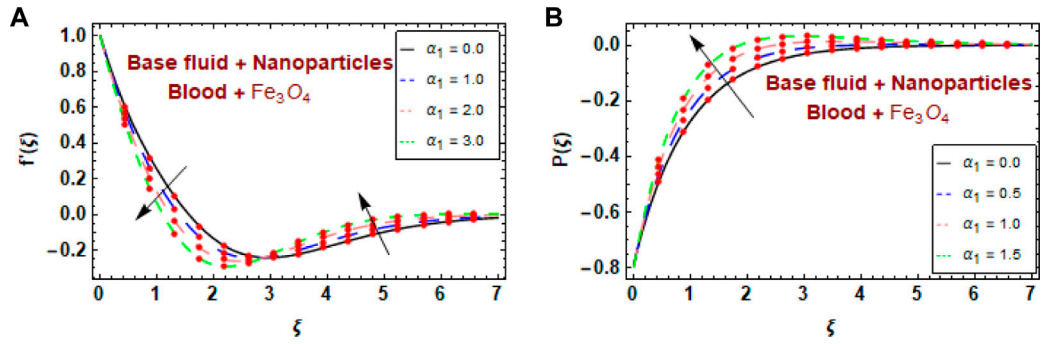

FIGURE 5
(A,B) Variations in $f'(\xi)$ and $p(\xi)$ for distinct numbers of α_1.

The fundamental concept of HAM is characterized in Cui et al. (2012), Kong et al. (2014), Mathuriya et al. (2015), and Anik et al. (2021). The zeroth-order problems from Eqs 9–12 are as follows:

$$(1-p)L_f[f(\eta;p)-f_0(\eta)] = p\hbar_f N_f[f(\eta;p)], \tag{30}$$
$$(1-p)L_\theta[\theta(\eta;p)-\theta_0(\eta)] = p\hbar_\theta N_\theta[f(\eta;p),\theta(\eta;p)], \tag{31}$$
$$(1-p)L_\omega[\omega(\eta;p)-\omega_0(\eta)] = p\hbar_\omega N_\omega[f(\eta;p),\omega(\eta;p)], \tag{32}$$
$$(1-p)L_\chi[\chi(\eta;p)-\chi_0(\eta)] = p\hbar_\chi N_\chi[f(\eta;p),\omega(\eta;p),\chi(\eta;p)]. \tag{33}$$

The equivalent boundary conditions are as follows:

$$\begin{aligned} &f(\eta;p)\big|_{\eta=0} = 0, \quad \frac{\partial f(\eta;p)}{\partial\eta}\Big|_{\eta=0} = 1, \frac{\partial f(\eta;p)}{\partial\eta}\Big|_{\eta\to\infty} = 0,\\ &\theta(\eta;p)\big|_{\eta=0} = 0, \quad \theta(\eta;p)\big|_{\eta=\infty} = 0,\\ &\omega(\eta;p)\big|_{\eta=0} = 0, \quad \omega(\eta;p)\big|_{\eta=\infty} = 0,\\ &\chi(\eta;p)\big|_{\eta=0} = 0, \quad \chi(\eta;p)\big|_{\eta=\infty} = 0, \end{aligned} \tag{34}$$

where $p \in [0,1]$ is the imbedding parameter and $\hbar_f, \hbar_\theta, \hbar_\omega,$ and $\hbar_\chi$ are used to control the convergence of the solution. When $p = 0$ and $p = 1$,

$$f(\eta;1) = f(\eta), \quad \theta(\eta;1) = \theta(\eta), \omega(\eta;1) = \omega(\eta), \chi(\eta;1) = \chi(\eta). \tag{35}$$

and expanding $f(\eta;p), \theta(\eta;p), \omega(\eta;p),$ and $\chi(\eta;p)$ in the Taylor's series about $p = 0$,

$$\begin{aligned} f(\eta;p) &= f_0(\eta) + \sum_{m=1}^{\infty} f_m(\eta)p^m,\\ \theta(\eta;p) &= \theta_0(\eta) + \sum_{m=1}^{\infty} \theta_m(\eta)p^m,\\ \omega(\eta;p) &= \omega_0(\eta) + \sum_{m=1}^{\infty} \omega_m(\eta)p^m,\\ \chi(\eta;p) &= \chi_0(\eta) + \sum_{m=1}^{\infty} \chi_m(\eta)p^m, \end{aligned} \tag{36}$$

where

$$\begin{aligned} f_m &= \frac{1}{m!}\frac{\partial f(\eta;p)}{\partial\eta}\Big|_{p=0}, \quad \theta_m = \frac{1}{m!}\frac{\partial\theta(\eta;p)}{\partial\eta}\Big|_{p=0},\\ \omega_m &= \frac{1}{m!}\frac{\partial\omega(\eta;p)}{\partial\eta}\Big|_{p=0}, \quad \chi_m = \frac{1}{m!}\frac{\partial\chi(\eta;p)}{\partial\eta}\Big|_{p=0}. \end{aligned} \tag{37}$$

The secondary constraints $\hbar_f, \hbar_\theta, \hbar_\omega,$ and $\hbar_\chi$ are selected so that the series (27) converges at $p = 1$; substituting $p = 1$ in (27), we obtain:

$$\begin{aligned} f(\eta) &= f_0(\eta) + \sum_{m=1}^{\infty} f_m(\eta),\\ \theta(\eta) &= \theta_0(\eta) + \sum_{m=1}^{\infty} \theta_m(\eta),\\ \omega(\eta) &= \omega_0(\eta) + \sum_{m=1}^{\infty} \omega_m(\eta),\\ \chi(\eta) &= \chi_0(\eta) + \sum_{m=1}^{\infty} \chi_m(\eta). \end{aligned} \tag{38}$$

The $m^{th}-order$ problem satisfies the following:

$$\begin{aligned} L_f[f_m(\eta) - \chi_m f_{m-1}(\eta)] &= \hbar_f R_m^f(\eta),\\ L_\theta[\theta_m(\eta) - \chi_m \theta_{m-1}(\eta)] &= \hbar_\theta R_m^\theta(\eta),\\ L_\omega[\omega_m(\eta) - \chi_m \omega_{m-1}(\eta)] &= \hbar_\omega R_m^\omega(\eta),\\ L_\chi[\chi_m(\eta) - \chi_m \chi_{m-1}(\eta)] &= \hbar_\chi R_m^\chi(\eta). \end{aligned} \tag{39}$$

The following are the corresponding boundary conditions:

$$\begin{aligned} &f_m(0) = f_m'(0) = \theta_m(0) = \omega_m(0) = \chi_m(0) = 0,\\ &f_m'(\infty) = \theta_m(\infty) = \omega_m(\infty) = \chi_m(\infty) = 0. \end{aligned} \tag{40}$$

Here,

$$\begin{aligned} R_m^f(\eta) &= (\varphi_4+\alpha_1)\left[f_{m-1}'''' + \frac{2}{\xi}f_{m-1}''' - \frac{1}{\xi^2}f_{m-1}'' + \frac{1}{\xi^3}f_{m-1}'\right]\\ &\quad -\varphi_3 M\left(f_{m-1}'' + \frac{1}{\xi}f_{m-1}'\right) - \varphi_4\beta_0\left(f_{m-1}'' + \frac{1}{\xi}f_{m-1}'\right)\\ &\quad -\alpha_2\left(\begin{array}{c} \left(\begin{array}{c} \sum_{k=0}^{m-1} f_{m-1-k}''\sum_{l=0}^{k} f_{k-l}''f_l'''' + \frac{2}{\xi}\sum_{k=0}^{m-1} f_{m-1-k}'\sum_{l=0}^{k} f_{k-l}''f_l''' \\ +\frac{2}{\xi^2}\sum_{k=0}^{m-1} f_{m-1-k}'\sum_{l=0}^{k} f_{k-l}'f_l'''' \end{array}\right) + \\ \left(\frac{1}{\xi^2}\sum_{k=0}^{m-1} f_{m-1-k}''\sum_{l=0}^{k} f_{k-l}''f_l'' - \frac{3}{\xi^2}\sum_{k=0}^{m-1} f_{m-1-k}'\sum_{l=0}^{k} f_{k-l}''f_l'' - \frac{2}{\xi^4}\sum_{k=0}^{m-1} f_{m-1-k}'\sum_{l=0}^{k} f_{k-l}'f_l'\right) \\ +\frac{3}{\xi^5}\sum_{k=0}^{m-1} f_{m-1-k}'\sum_{l=0}^{k} f_{k-l}'f_l' + 2\left(\sum_{k=0}^{m-1} f_{m-1-k}''\sum_{l=0}^{k} f_{k-l}'''f_l'' + \frac{1}{\xi}\sum_{k=0}^{m-1} f_{m-1-k}'\sum_{l=0}^{k} f_{k-l}'''f_l'''\right) \\ +2\left(\frac{3}{\xi}\sum_{k=0}^{m-1} f_{m-1-k}''\sum_{l=0}^{k} f_{k-l}''f_l''' + \frac{2}{\xi^2}\sum_{k=0}^{m-1} f_{m-1-k}'\sum_{l=0}^{k} f_{k-l}'''f_l'' - \frac{1}{\xi^3}\sum_{k=0}^{m-1} f_{m-1-k}'\sum_{l=0}^{k} f_{k-l}'f_l'''\right) \end{array}\right)\\ &\quad +\varphi_1\left(\begin{array}{c} \frac{k}{\xi}\left(\sum_{k=0}^{m-1} f_{m-1-k}'f_k''' - \sum_{k=0}^{m-1} f_{m-1-k}'''f_k''\right) + \frac{k}{\xi^2}\left(\sum_{k=0}^{m-1} f_{m-1-k}''f_k'' - \sum_{k=0}^{m-1} f_{m-1-k}''f_k'\right) \\ -\frac{k}{\xi^3}\sum_{k=0}^{m-1} f_{m-1-k}'f_k' - \frac{\gamma}{\xi}\left(\frac{\xi}{2}f_m''' - f_m'' + \frac{1}{2}\left(\xi f_{m-1}'' + 3f_m'\right)\right) - \frac{\gamma}{2}\left(\xi f_{m-1}''' + 3f_m''\right) \end{array}\right), \end{aligned} \tag{41}$$

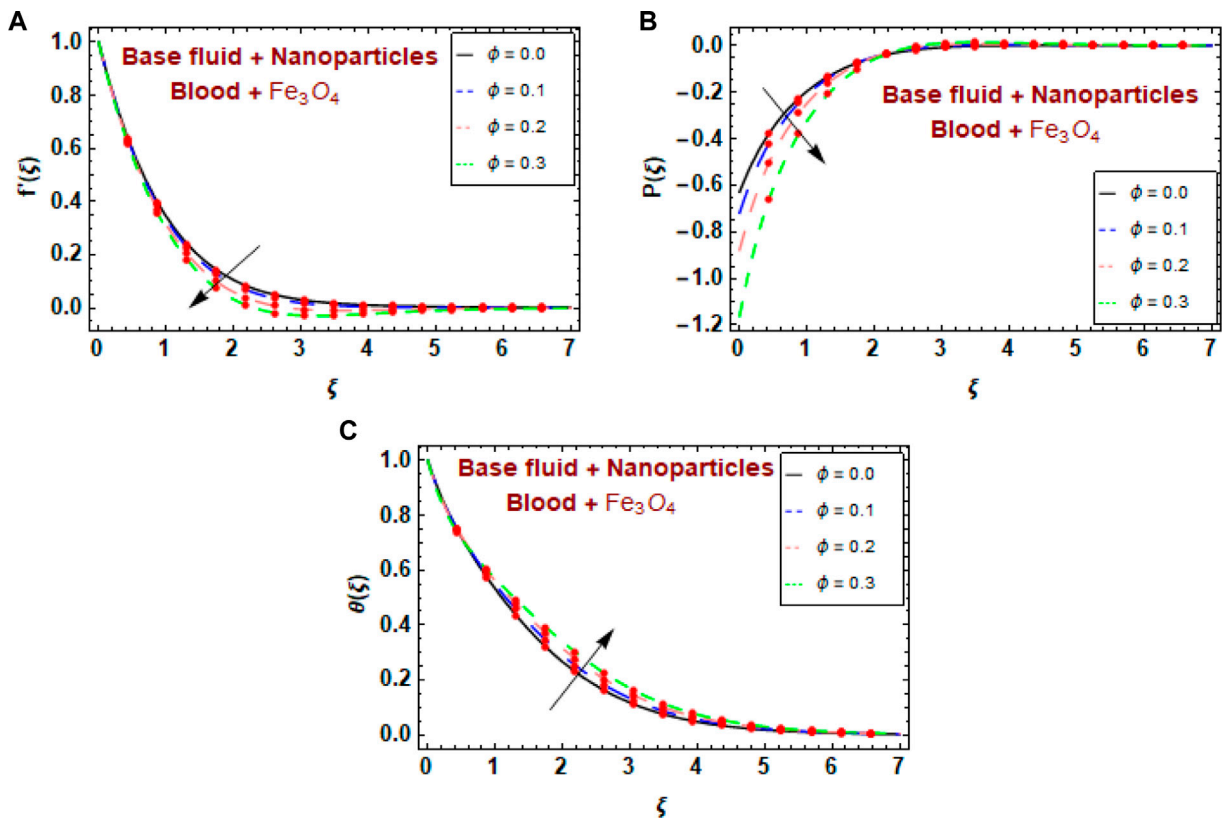

FIGURE 6
(A–C) Variations in $f'(\xi)$, $p(\xi)$, and $\theta(\xi)$ for distinct numbers of ϕ.

$$R_m^{\theta}(\eta) = \varphi_5\left(\left(\theta''_{m-1} + \frac{1}{\xi}\theta'_{m-1}\right) + \beta\left(\sum_{k=0}^{m-1}\theta'_{m-1-k}\theta''_k + \frac{1}{\xi}\sum_{k=0}^{m-1}\theta'_{m-1-k}\theta'_k\right) + \beta\sum_{k=0}^{m-1}\theta'_{m-1-k}\theta'_k) - \varphi_3 MPrEc\sum_{k=0}^{m-1} f'_{m-1-k}\, f'_k + \varphi_2 Pr\left(\left(\frac{k_f}{\xi} - \frac{\gamma\xi}{2}\right)\theta'_{m-1} + \frac{Q}{\varphi_2}\theta_{m-1}\right), \tag{42}$$

$$R_m^{\omega}(\eta) = \omega''_{m-1} + \frac{1}{\xi}\omega'_{m-1} + Lb\left[\left(\frac{K}{\xi}\sum_{k=0}^{m-1} f_{m-1-k}\omega_k - \frac{\gamma\xi}{2}\omega'_{m-1}\right) + \lambda(\Omega + \chi_{m-1})\right], \tag{43}$$

$$R_m^{\chi}(\eta) = \chi''_{m-1} + \frac{1}{\xi}\chi'_{m-1} + Lb\left[\left(\frac{K}{\xi}\sum_{k=0}^{m-1} f_{m-1-k}\chi_k - \frac{\gamma\xi}{2}\chi'_{m-1}\right) + \lambda(\Omega + \chi_{m-1})\right], \tag{44}$$

where

$$\chi_m = \begin{cases} 0, & if\ p \le 1, \\ 1, & if\ p > 1. \end{cases} \tag{45}$$

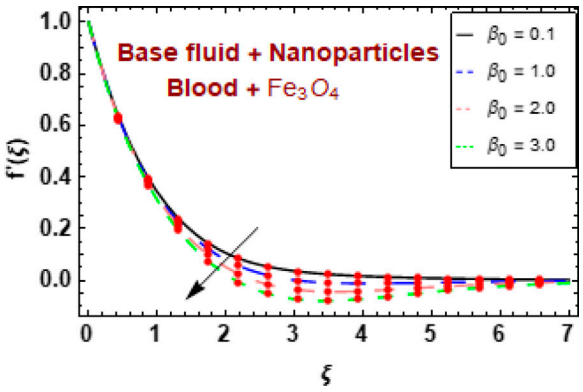

FIGURE 7
Variations in $f'(\xi)$ for distinct numbers of β_0.

5 Validations of the results

This section shows the result validations graphically and numerically. The results obtained using the semi-analytical HAM

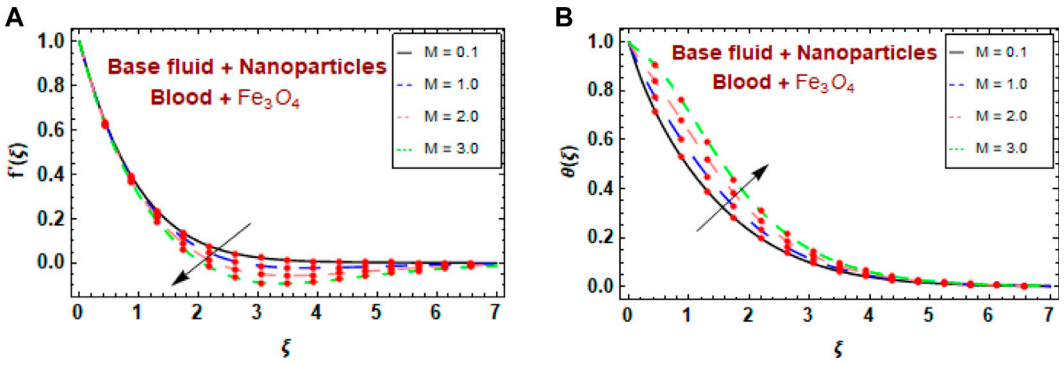

FIGURE 8
(A,B) Variations in $f'(\xi)$ and $\theta(\xi)$ for distinct numbers of *M*.

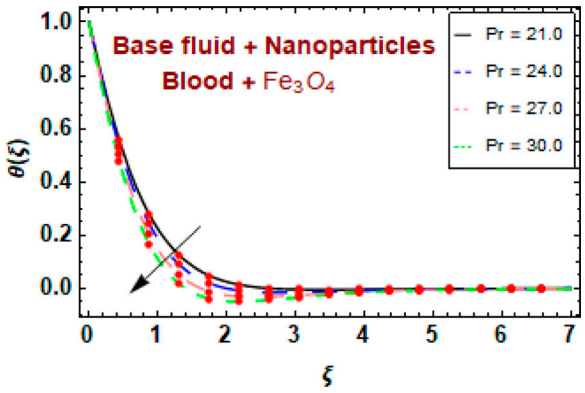

FIGURE 9
Variations in $\theta(\xi)$ for distinct numbers of *Pr*.

method are compared to the numerical (ND-Solved) techniques for temperature $\theta(\xi)$, pressure $p(\xi)$, velocity $f'(\xi)$, bacterial density field $\chi(\xi)$, and nutrient concentration $\omega(\xi)$.

Table 2(a–d) shows the results of the HAM solutions, numerical solutions, and the absolute errors for temperature $\theta(\xi)$, pressure $p(\xi)$, velocity $f'(\xi)$, bacterial density field $\chi(\xi)$, and nutrient concentration $\omega(\xi)$. We observed excellent agreement between the results for all profiles. Table 3 shows a comparison between the current and previous results (Elgazery et al., 2022) for skin friction and it was found that both results agreed. Figures 2A–D show comparison between HAM and numerical solutions for the temperature $\theta(\xi)$, pressure $p(\xi)$, velocity $f'(\xi)$, the bacterial density field $\chi(\xi)$, nutrient concentration $\omega(\xi)$. An excellent agreement is found between both results for all profile.

6 Results and discussion

This investigation used HAM to graphically explore the efficacy of numerous governing factors, such as the curvature factor *K*, volume fraction ϕ, maximum bacteria growth rate λ, fluid parameter α_1, unsteady parameter γ, magnetic parameter *M*, porosity parameter β_0, non-dimensional bacterial density difference Ω, non-dimensional generation/absorption coefficient, bioconvection Lewis number *Lb*, and variable thermal conductivity β, on the temperature $\theta(\xi)$, pressure $p(\xi)$, velocity $f'(\xi)$, bacterial density field $\chi(\xi)$, nutrient concentration $\omega(\xi)$, Nusselt number, skin friction, and density of nutrient concentration.

Figures 3A–C show how the curvature factor K affects the velocity $f'(\xi)$, pressure $P(\xi)$, and temperature $\theta(\xi)$ curves, in which increases in velocity and decreases in pressure resulted in increased curvature parameter values. Tumor blood flow usually decreases as tumors grow larger; however, mathematical examination predicted that enhancing the curvature parameter would boost tumor blood flow, which may enhance medical treatment.

Furthermore, as shown in Figures 4A, B increasing the curvature parameter value increased the radius of the curved surface, which increased the velocity and decreased the pressure. Due to vascular damage, the environment within the tumors became hypoxic, acidic, and nutritionally deficient when heated. These suboptimal environmental changes enhance the tumor cell hyperthermia response, inhibit thermal damage repair, and interfere with the development of thermal tolerance. At high temperatures, the acidic environment enhances the tumor cell response to certain drugs. As shown in Figure 4C, the temperature decreased as the curvature factor increased, and increased with increasing unsteady parameter. In medical treatment, to enhance the tumor cell response to magnetic magnetite nanoparticles, γ should be increased, thus increasing the environmental temperature of the nanofluid. Figures 4A, B show increased velocity and decreased pressure with increasing unsteady parameter γ.

Figures 5A, B show the effect of the fluid parameter α_1 on velocity and pressure. Figure 5A shows that the blood velocity first decreased and then gradually increased as the fluid parameter value increased. Figure 5B shows that the blood pressure curves increased for large fluid parameter values.

Figures 6A–C show how the magnetite nanoparticle volume fraction parameter ϕ affects the velocity $f'(\xi)$, pressure $P(\xi)$, and temperature $\theta(\xi)$ curves. As the volume fraction of magnetite nanoparticles increased, the velocity profile and pressure distribution decreased. The mathematical explanation showed that magnetite nanoparticles reduced blood flow pressure, which

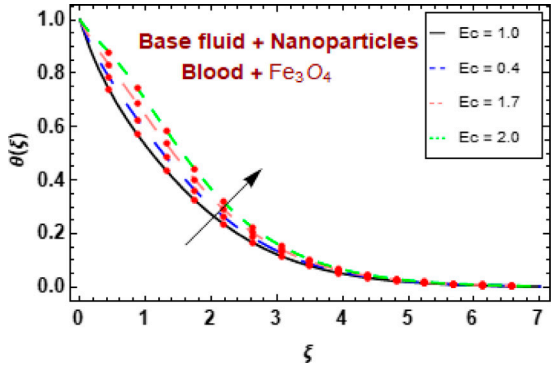

FIGURE 10
Variations in $\theta(\xi)$ for distinct numbers of *Ec*.

is a beneficial outcome in the medical treatment of cancer, thus demonstrating the potential effectiveness of magnetite nanoparticles in medical therapy. As the concentration of magnetite nanoparticles increased, so did the blood temperature distribution. Therefore, passing magnetite nanoparticles through the blood improves its physical properties.

The impact of the porosity parameter on blood velocity is shown in Figure 7, in which the blood velocity decreased as the porosity increased. This effect occurred because increasing blood porosity increased the interactions and fraction between the flow and blood cells, resulting in decreased velocity.

The exploration of the magnetic factor M showed that opposition in artificial magnetic bacteria swimming within the blood flow was a major factor. Figures 8A, B show the effects of M on the velocity $f'(\xi)$ and temperature $\theta(\xi)$, respectively. When the magnetic factor M increased, $f'(\xi)$ decreased and $\theta(\xi)$ increased. The changes in magnetite/blood velocity were inversely related to the magnetic factor. Thus, applying a magnetic field to an electrically conducting liquid created a resistive Lorentz force that tended to diminish the fluid flow while increasing the temperature.

Figure 9 depicts the influence of the Prandtl number *Pr* on the temperature $\theta(\xi)$. As *Pr* increased, the temperature decreased. The thermal boundary layer thickness decreased as the Prandtl number increased. The Prandtl number is the momentum diffusivity/thermal diffusivity ratio and it governs the relative thickening of the momentum and thermal boundary layers in heat transfer.

Figure 10 shows the temperature distribution for various Eckert number *Ec* values. The relationship between heat enthalpy difference and flow kinetic energy is known as the Eckert number *Ec*. Therefore, increasing the Eckert number increases the kinetic energy. Furthermore, temperature is defined as the

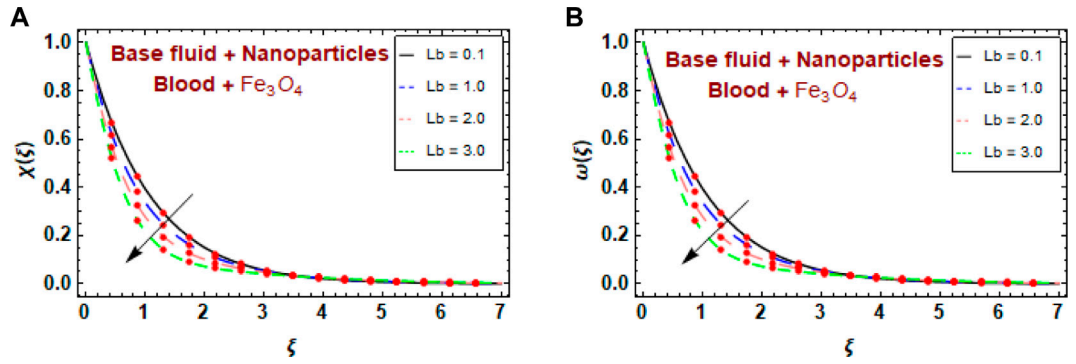

FIGURE 11
(A,B) Variations in $\chi(\xi)$ and $\omega(\xi)$ for distinct numbers of *Lb*.

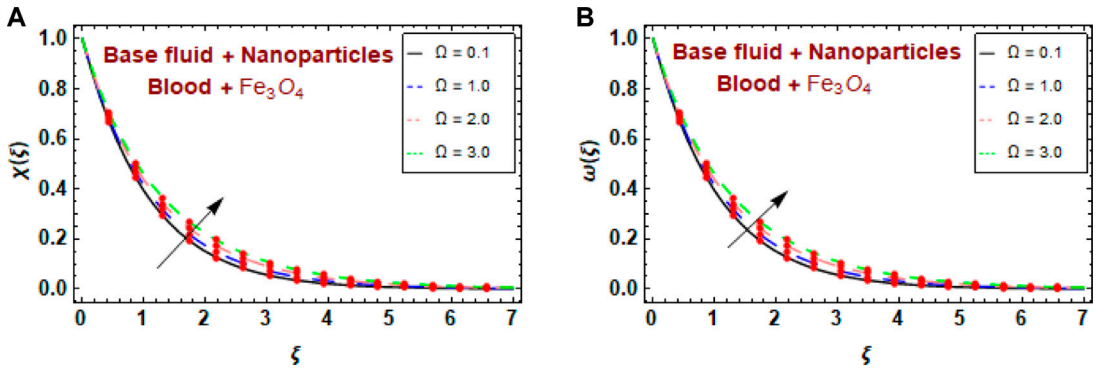

FIGURE 12
(A,B) Variations in $\chi(\xi)$ and $\omega(\xi)$ for distinct numbers of Ω.

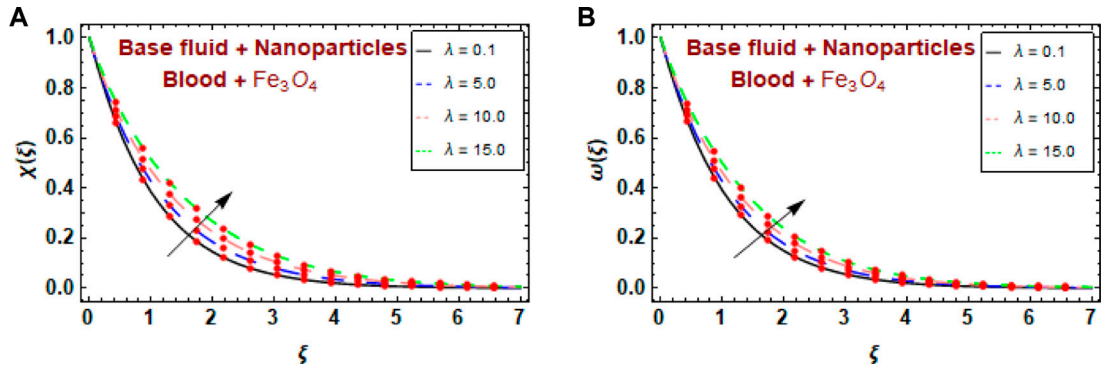

FIGURE 13
(A,B) Variations in $\chi(\xi)$ for distinct numbers of λ.

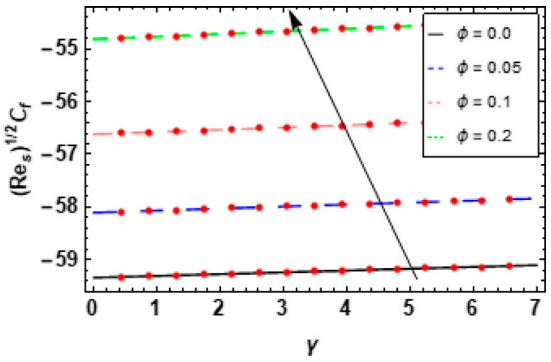

FIGURE 14
Influences of γ and ϕ on skin friction.

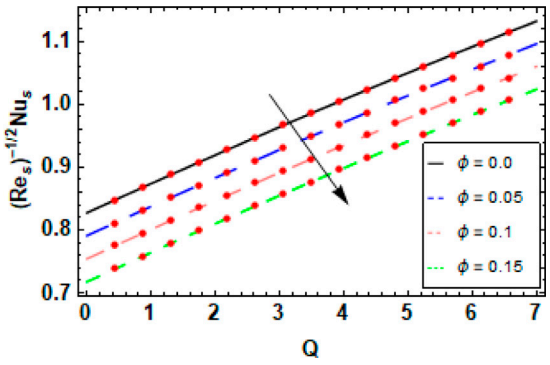

FIGURE 16
Effects of Q and ϕ on $Nu_s\,(Re_s)^{-1/2}$.

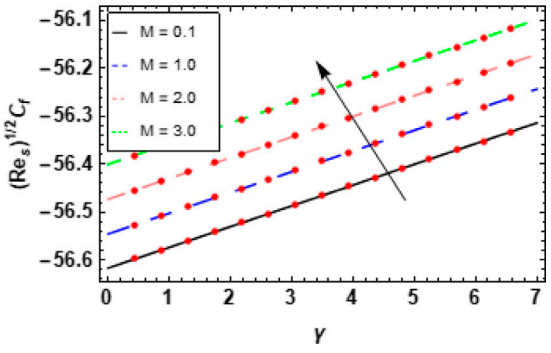

FIGURE 15
Influences of γ and M on skin friction.

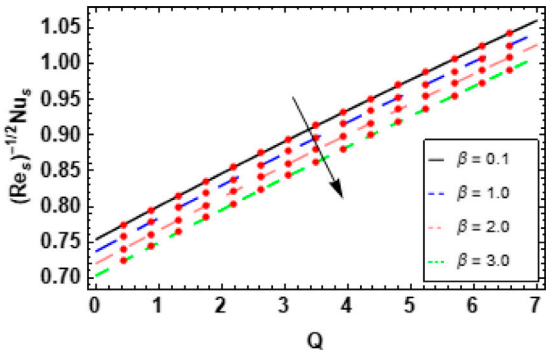

FIGURE 17
Effects of Q and β on $Nu_s\,(Re_s)^{-1/2}$.

average kinetic energy. Consequently, the temperature of the fluid increased with increasing Eckert number *Ec*.

Figures 11A, B show the effect of the bioconvection Lewis number *Lb* on the bacterial density $\chi(\xi)$ and nutrient concentration $\omega(\xi)$, in which both bacterial density and nutrient concentration decreased with increasing bioconvection Lewis number *Lb*.

Figures 12A, B show the influence of the bacterial difference density parameter Ω on the bacterial density field $\chi(\xi)$ and nutrient

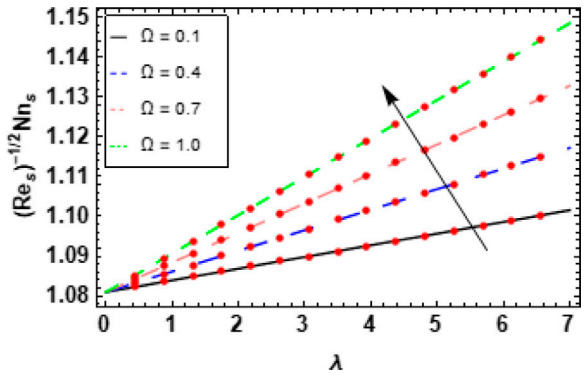

FIGURE 18
Influences of Ω and λ on $Nn_s\,(Re_s)^{-1/2}$.

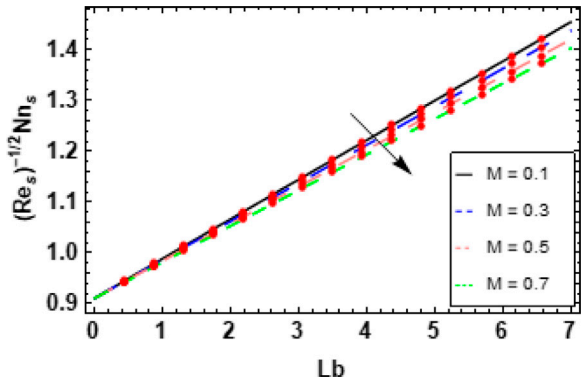

FIGURE 19
Influences of *Lb* and *M* on $Nn_s\,(Re_s)^{-1/2}$.

concentration $\omega(\xi)$. As the Ω increased, so did the bacterial density and nutrient concentration.

The effects of the bacteria maximum growth rate λ on the bacterial density and nutrient concentration are shown in Figures 13A, B, in which the bacterial density and nutrient concentration fields improved when the bacterial maximum growth rate increased.

6.1 Skin friction coefficients and Nusselt numbers

Figures 14, 15 show the effects of the nanoparticle volume fraction ϕ and magnetic factor M on the skin friction coefficient, with mainly significant influences on the unsteady constraint γ on skin friction. The skin friction increased with increasing ϕ and M.

Figure 16 shows the effects of the volume fraction ϕ and variable thermal conductivity constraint β on the Nusselt number. The Nusselt number decreased with increasing ϕ. Figure 17 shows the effects of β against Q on the Nusselt number distribution. The Nusselt number decreased with increasing β. Figure 18 shows the variation in the nutrient concentration density because of the bacterial difference density Ω and the optimum bacterial growth rate λ. When both the bacterial difference density and the optimum bacterial growth rate increased, the nutrient concentration density increased. These mathematical outcomes showed that in the medical treatment of cancer using magnetite nanoparticles and artificial bacteria, it is preferable to moderate the bacterial difference density and the bacterial growth rate to increase nutrients in normal cells while decreasing nutrient consumption in tumor cells. Figure 19 also shows the behavior of the nutrient concentration density as a function of the bioconvection Lewis number *Lb* and the magnetic parameter *M*. The nutrient concentration density value improved as the Lewis number increased but decreased as the magnetic parameter increased. Physically, in medical treatment, increasing the magnetic factor and decreasing the ratio of thermal diffusivity to mass diffusivity are recommended to increase nutrient consumption in normal cells while decreasing nutrient consumption in tumor cells.

7 Conclusion

This study aimed to determine the effectiveness of an external magnetic field on bacteria enclosed by thousands of magnetic magnetite nanoparticles. Variable thermal conductivity and Joule heating were used in the interstitial nanofluid, in which artificial bacteria swam in a biological cell. The unsteady motion of a Powell–Eyring fluid in two dimensions was considered. A porous stretching wall was used as a curved surface structure. To convert the governing non-linear PDEs into non-linear ODEs, suitable transformations were exploited. The HAM was used to resolve the semi-analytical results of non-linear ODEs. This mathematical procedure demonstrates unnatural magnetic bacterium that can function like a compass that is magnetically charged to mark and abolish tumors by spinning at such a high rate that tumors heat and melt. We discovered the following:

- The blood velocity improved at higher curvature parameter values and was unsteady when the velocity decreased for large magnetic factor, volume fraction, and porosity parameter values.
- The blood velocity profile began to decrease and then gradually increased with increasing fluid parameter values.
- The mathematical description revealed that magnetite nanoparticles lower blood pressure, which is a beneficial outcome in the clinical consideration of cancer, and demonstrates the effectiveness of magnetite nanoparticles in such medical therapy.
- The mathematical analysis showed that to enhance the reaction of tumor cells to several drugs in an acidic environment, temperatures should be raised by increasing the characteristics of the nearby environment, including the unsteady parameter, Eckert number, magnetite nanoparticles, and magnetic parameters.

- To increase nutrient consumption in normal cells while decreasing nutrient consumption in tumor cells, our mathematical outcomes showed that the bacterial difference density, bacterial growth rate, and Lewis number should be moderated in the medical treatment of cancer using magnetite nanoparticles and artificial bacteria.
- For the intensification of the unsteady parameter, applied magnetic fields should be considered.

Data availability statement

The original contributions presented in the study are included in the article/Supplementary Material. Further inquiries can be directed to the corresponding authors.

Author contributions

All authors listed have made substantial, direct, and intellectual contributions to the work and approved it for publication.

Funding

The project was financed by the Lucian Blaga University of Sibiu through research grant number LBUS-IRG-2022-08."

Conflict of interest

The authors declare that the research was conducted in the absence of any commercial or financial relationships that could be construed as a potential conflict of interest.

Publisher's note

All claims expressed in this article are solely those of the authors and do not necessarily represent those of their affiliated organizations, or those of the publisher, the editors, and the reviewers. Any product that may be evaluated in this article, or claim that may be made by its manufacturer, is not guaranteed or endorsed by the publisher.

References

Afridi, M. I., Alkanhal, T. A., Qasim, M., and Tlili, I. (2019). Entropy generation in Cu-Al2O3-H2O hybrid nanofluid flow over a curved surface with thermal dissipation. *Entropy* 21, 941. doi:10.3390/E21100941

Alyousef, H. A., Yasmin, H., Shah, R., Shah, N. A., El-Sherif, L. S., and El-Tantawy, S. A. (2023). Mathematical modeling and analysis of the steady electro-osmotic flow of two immiscible fluids: A biomedical application. *Coatings* 13, 115. doi:10.3390/coatings13010115

Anik, M. I., Hossain, M. K., Hossain, I., Mahfuz, A. M. U. B., Rahman, M. T., and Ahmed, I. (2021). Recent progress of magnetic nanoparticles in biomedical applications: A review. *Nano Sel.* 2, 6, 1146–1186. doi:10.1002/NANO.202000162

Asha, S. K., and Sunitha, G. (2018). Effect of joule heating and MHD on peristaltic blood flow of Eyring–Powell nanofluid in a non-uniform channel. *J. Taibah Univ. Sci.* 13 (1), 155–168. doi:10.1080/16583655.2018.1549530

Basha, H. T., and Sivaraj, R. (2021). Entropy generation of peristaltic Eyring–Powell nanofluid flow in a vertical divergent channel for biomedical applications. *Proc. Inst. Mech. Eng. Part E J. Process Mech. Eng.* 235 (5), 1575–1586. doi:10.1177/09544089211013926

Bhatti, M. M. (2021). Biologically inspired intra-uterine nanofluid flow under the suspension of magnetized gold (Au) nanoparticles: Applications in nanomedicine. *Invent* 6, 28. doi:10.3390/INVENTIONS6020028

Cui, Z., Kong, D., Pan, Y., and Zhang, K. (2012). On the swimming motion of spheroidal magnetotactic bacteria. *Fluid Dyn. Res.* 44 (5), 055508. doi:10.1088/0169-5983/44/5/055508

Elgazery, N. S., Elelamy, A. F., Bobescu, E., and Ellahi, R. (2022). How do artificial bacteria behave in magnetized nanofluid with variable thermal conductivity: Application of tumor reduction and cancer cells destruction. *Int. J. Numer. Methods Heat Fluid Flow* 32 (9), 2982–3006. doi:10.1108/HFF-11-2021-0722

Gholinia, M., Hosseinzadeh, K., Mehrzadi, H., Ganji, D. D., and Ranjbar, A. A. (2019). Investigation of MHD Eyring–Powell fluid flow over a rotating disk under effect of homogeneous–heterogeneous reactions. *Case Stud. Therm. Eng.* 13, 100356. doi:10.1016/J.CSITE.2018.11.007

Hina, S., Mustafa, M., Hayat, T., and Alsaedi, A. (2016). Peristaltic flow of powell-eyring fluid in curved channel with heat transfer: A useful application in biomedicine. *Comput. Methods Programs Biomed.* 135, 89–100. doi:10.1016/J.CMPB.2016.07.019

Hussain, A., Sarwar, L., Akbar, S., and Nadeem, S. (2020). Mathematical model for blood flow through the stenosed channel. *Phys. Scr.* 95 (2), 025206. doi:10.1088/1402-4896/AB43FF

Kong, D., Lin, W., Pan, Y., and Zhang, K. (2014). Swimming motion of rod-shaped magnetotactic bacteria: The effects of shape and growing magnetic moment. *Front. Microbiol.* 5, 8. doi:10.3389/FMICB.2014.00008

Liao, S. (2004). On the homotopy analysis method for nonlinear problems. *Appl. Math. Comput.* 147 (2), 499–513. doi:10.1016/S0096-3003(02)00790-7

Mallick, B., and Misra, J. C. (2019). Peristaltic flow of Eyring-Powell nanofluid under the action of an electromagnetic field. *Eng. Sci. Technol. Int. J.* 22 (1), 266–281. doi:10.1016/J.JESTCH.2018.12.001

Mathuriya, A. S., Yadav, K., and Kaushik, B. D. (2015). Magnetotactic bacteria: Performances and challenges. *Geomicrobiol. J.* 32 (9), 780–788. doi:10.1080/01490451.2014.986694

Nagaraj, C., Dinesh, P. A., and Kalavathi, G. K. (2018). Combined effects of electric field and magnetic field on electro hydrodynamic dispersion of macromolecular components in biological bearing. *Defect Diffus. Forum* 388, 361–377. doi:10.4028/www.scientific.net/ddf.388.361

Riaz, A., Ellahi, R., Bhatti, M. M., and Marin, M. (2019). Study of heat and mass transfer in the eyring–powell model of fluid propagating peristaltically through a rectangular compliant channel. *Heat. Transf. Res.* 50 (16), 1539–1560. doi:10.1615/HEATTRANSRES.2019025622

Saleem, N., and Munawar, S. (2016). A mathematical analysis of MHD blood flow of Eyring-Powell fluid through a constricted artery. *Int. J. Biomath.* 9 (2), 1650027. doi:10.1142/S1793524516500273

Shukla, N., Rana, P., and Bég, O. A. (2019). Unsteady MHD non-Newtonian heat transfer nanofluids with entropy generation analysis. *Nonlinear Eng.* 8 (1), 630–644. doi:10.1515/nleng-2017-0177

Sultan, F., Khan, N. A., Qasim, M., and Afridi, M. I. (2019). Numerical simulation of the flow of nano-eyring-powell fluid through a curved artery with time-variant stenosis and aneurysm. *Nihon Reoroji Gakkaishi* 47 (2), 75–85. doi:10.1678/RHEOLOGY.47.75

Vincenti, B., Douarche, C., and Clement, E. (2018). Actuated rheology of magnetic micro-swimmers suspensions: Emergence of motor and brake states. *Phys. Rev. Fluids* 3 (3), 033302. doi:10.1103/physrevfluids.3.033302

Yasmin, H. (2022). Design and research of biomaterials. *Coatings* 12, 1684. doi:10.3390/coatings12111684

Yasmin, H., Giwa, S. O., Noor, S., and Aybar, H. Ş. (2023). Influence of preparation characteristics on stability, properties, and performance of mono- and hybrid nanofluids: Current and future perspective. *Machines* 11, 112. doi:10.3390/machines11010112

Yasmin, H., Giwa, S. O., Noor, S., and Aybar, H. Ş. (2023). Reproduction of nanofluid synthesis, thermal properties and experiments in engineering: A research paradigm shift. *Energies* 16, 1145. doi:10.3390/en16031145

Yasmin, H., Giwa, S. O., Noor, S., and Sharifpur, M. (2023). Experimental exploration of hybrid nanofluids as energy-efficient fluids in solar and thermal energy storage applications. *Nanomaterials* 13, 278. doi:10.3390/nano13020278

Nomenclature

(r, s) curvilinear coordinates
(u, v) velocity components
p pressure
T temperature
R curvature radius
k thermal conductivity
k_1 permeability of the porous medium
t time
n nutrient concentration
D_n nutrient diffusivity
K curvature parameter
Pr Prandtl number
Lb bioconvection Lewis number
M magnetic parameter
Q generation/absorption coefficient

Greek terms

α_1, α_2 fluid parameters
μ dynamic viscosity
ν kinematic viscosity
ρ density
ρ_n bacterial density
β thermal conductivity parameter
β_0 porosity parameter
γ unsteady parameter
Ω bacterial difference density
λ bacteria maximum growth rate
ϕ nanoparticle volume fraction

Subscripts

nf nanofluid
f base fluid
p nanoparticles
w at the curved surface
∞ far from the surface

frontiers | Frontiers in Materials

TYPE Original Research
PUBLISHED 09 June 2023
DOI 10.3389/fmats.2023.1187986

OPEN ACCESS

EDITED BY
Noor Saeed Khan,
University of Education Lahore, Pakistan

REVIEWED BY
Humaira Yasmin,
King Faisal University, Saudi Arabia
Muhammad Sohail,
Khwaja Fareed University of Engineering and Information Technology (KFUEIT), Pakistan

*CORRESPONDENCE
Syed Ibrahim,
syed.ibrahim@riphah.edu.pk

RECEIVED 16 March 2023
ACCEPTED 18 April 2023
PUBLISHED 09 June 2023

CITATION
Ibrahim S, Khan Marwat DN, Ullah N and Nisar KS (2023), Investigation of fluid flow pattern in a 3D meandering tube. *Front. Mater.* 10:1187986. doi: 10.3389/fmats.2023.1187986

Investigation of fluid flow pattern in a 3D meandering tube

Syed Ibrahim[1]*, Dil Nawaz Khan Marwat[1], Naeem Ullah[1] and Kottakkaran Sooppy Nisar[2,3]

[1]Department of Mathematics, Islamia College Peshawar, University Campus, Peshawar, Pakistan, [2]Department of Mathematics, College of Science and Humanities in Alkharj, Prince Sattam Bin Abdulaziz University, Alkharj, Saudi Arabia, [3]School of Technology, Woxsen University-Hyderabad, Hyderabad, India

Several types of meandering channels and their mathematical simulation have been proposed and discussed widely in the open literature. In the present study, the impact of a novel meandering tube geometry on streamwise vortices and pressure losses have been determined. Using a simplified Poiseuille flow simulation approach with a sinusoidal wavy meandering tube of non-uniform radius, the onset flow separation, vertex formation, and the impact of Reynolds number on field variables and stream function has been analyzed. Moreover, the linear stability theory has been implemented to trace the vertex formation. A decrease in wavelength leads to flow separation near the tube's surface, but the flow becomes rectilinear with a sudden disturbance caused by the meander, becoming independent of vertex generating centrifugal forces. Novel insights are provided on the impact of meandering tube geometry on fluid flow and potential applications for enhancing flow conditions are suggested.

KEYWORDS

stream wise vortices, meandering tube, centrifugal forces, flow separation, instability

1 Introduction

The escalation process of heat and species transport in different flow phases with practical significance is an interesting and important subject in thermodynamics and fluid mechanics. Both the formation of fluid mixtures and changes in the functional thermophysical characteristics of the fluids fall within the category of escalation processes (Bergles and Webb, 1985; Jensen et al., 1997; Ligrani et al., 2003). Integrated heat exchangers that operate at low Reynolds numbers in case of laminar flows are treated specially for improved mixing (Webb and Bergles, 1981). It is often accepted that improved mixing may be achieved by driving a laminar-turbulent transformation under difficult conditions or by inserting vortex generators, which are efficient but have a substantial drag cost (Fiebig, 1995a; Fiebig, 1995b; Jacobi and Shah, 1995; Fiebig, 1998; Fiebig and Chen, 1999). In most cases, the hydrodynamic stabilities have been used for the transition of laminar flow to turbulent flow and, therefore, transverse grooves are used. However, a novel model has been demonstrated with the most accurate simulations, i.e., to shift laminar states without transiting to turbulent ones by using hydrodynamic instabilities. In this novel model, separating local flow is demonstrated well; the flow is driven by a slight oscillatory component and enters the resonant and stable separated shear layer (Patera and Mikic, 1986) Another type of bifurcation, i.e., centrifugal instability, has been taken into account and it produces simple vortices without suffering from the maximum drag cost associated with conventional vortex generators. Instability can improve vortex generators in limiting vortices decay, which decreases the minimum number of such generators even when the flow is only locally asymptotically stable. Both directly (by establishing a transverse transition) and indirectly (by creating a bypass transition), streamwise vortices can boost heat transfer. In

most cases, a three-dimensional flow field has been developed at the end and transverse shear layers with inflection points and rapidly expanding secondary instability are formed (Floryan, 1991). Recent investigations have reported an alternate approach being taken into account of a fluid of higher thermal conductivity used with properly shaped channels while, at the same time, flow pressure being reduced immediately (Mohammadi and Floryan, 2013). This technique has provided an alternative solution to the most common development programs used on macro channels (Xu et al., 2016).

It has been known for nearly 100 years that the rotating shear layers are subjected to centrifugal instabilities. This instability has been taken into account for the situation of simple geometry and canonical flow, providing an example where it is possible to forecast the curvature of lines with ease. Using the flow state between rotating cylinders, Rayleigh introduced the inviscid technique in 1920 and determined the necessary stabilization condition through circulating distribution (Rayleigh, 1917). In 1923, Taylor included the full viscous problem and identified the crucial conditions that emerge as a result of the secondary flow (Taylor, 1923). Similar instability in curved channels was examined by Dean (Dean, 1928). The occurrence of centrifugal instability in the context of boundary layers on concave surfaces was proved by Görtler (Görtler, 1941). If the streamwise velocity distribution is not monotonic (Floryan, 1986), demonstrated that the instability is active in flows over concave as well as convex surfaces. A clear relationship between the streamline curvature and the wall curvature was provided by all of these investigations where the wall curvature was either constant or had been approximated as a constant. As a result, the critical stability condition might be expressed in terms of one parameter.

There are very few theoretical investigations that can pinpoint the starting conditions for flows in complex geometries where the wall curvature varies spatially. However, there are large number of numerical models and experimental studies that offer qualitative data (Gschwind et al., 1995). used a meandering amplitude of the same order of magnitude as the channel height, and (Nishimura et al., 1990; Tatsuo et al., 1990) used a large amplitude compared to the channel height to demonstrate the existence of streamwise vortices attributed to the centrifugal instability in sinusoidal channels. Rush et al. (Rush et al., 1999) has qualitatively identified the additional types of instability for corresponding geometries. Theoretical investigations which employed two-dimensional models were able to identify the effect of flow separation on heat transfer (Metwally and Manglik, 2004; Zhang et al., 2004) and identify the conditions that led to either single or double Hopf bifurcations or self-sustained oscillations (Guzmán et al., 2009). These models failed to identify the formation of the vortices. In their 2012 study, (Sui et al., 2012), took into account a three-dimensional rectangular channel with a very large meandering amplitude and applied numerical simulations to find a complex pattern of Dean's vortices that changed over time and space. In the case of turbulent flow, consistent structures were found by (Pham et al., 2008). Other types of geometries, such as boundary layer flows over wavy surfaces (Saric and Ali, 1991) and Couette flows over wavy walls (Floryan, 2002), have also been found to demonstrate centrifugal instability. According to recent findings, streamwise vortices may be created by the placement of different triangular surface obstacles (Floryan and Asai, 2011) The transport of heat and fluid flow in various mediums and the studies considered the impact of magnetic fields, chemical reactions, porous media on fluid flow and thermal transport. The studies considered the impact of magnetic fields, chemical reactions, and porous media on fluid flow and thermal transport The results suggest that the addition of tri-hybrid nanoparticles and magnetic dipoles can enhance thermal transportation in Carreau Yasuda liquid, but may decrease the flow profile. This study also investigated the effects of different parameters on the peristaltic motion of hyperbolic tangent fluid in a curved compliant channel, which has potential applications in explaining blood transport dynamics. Numerical solutions and perturbation techniques were used to analyze and evaluate the results (Javed et al., 2021; Naseem et al., 2021; Wang et al., 2022). Different approaches related to the studies of fluid flow in microfluidic systems for biomedical engineering. This study analyzed the behavior of different types of fluids in different channel geometries by taking into account, convective conditions, thermal deposition effect, and chemical reactions. They investigated the impact of various parameters on flow quantities such as velocity, temperature, and concentration. This study also suggest the viability of electro-osmotic pumps for fluid flow in large osteoarticular implants (Hayat et al., 2015; Yasmin et al., 2020a; Yasmin et al., 2020b; Mehmood et al., 2020; Yasmin and Iqbal, 2021; Alyousef et al., 2023).

The main objective of the current analysis is to investigate the three-dimensional structure of the meandering geometries that cause the centrifugal force mechanism to produce streamwise vortices at the lowest possible cost as measured by pressure losses and without the interference of the traveling wave instability. This is the first comprehensive analysis of three-dimensional flow in a meandering tube that takes all potential instabilities into consideration. The new information would provide an accurate mathematical simulation for engineers and be a reasonable foundation upon which they may construct small heat exchangers that operate in the laminar flow domain. The study is divided into three main parts, specifically: i) mathematical modeling of flow in the meandering tube; ii) calculating the flow losses related to the meandering tube; and iii) identifying the geometric and flow characteristics that cause the centrifugal instability to predominate. The source in engineering procedures might be a mechanical pressure gradient. In this study, we look at the pressure gradient-driven (Poiseuille flow) flow of viscous fluid in a meandering tube with waves that is made up of fixed walls. A lot of interest has been shown in the flow of viscous fluid in a wavy meandering tube due to its applications in engineering and biological sciences, including regarding the development of muddy waves in river channels, the generation of wind waves on water and sandbanks in deserts, the movement of melting slides, rocket boosters, and the evaporation of film in burning chambers. Furthermore, physiologists and technicians have often attempted to create and explain blood and urine flow in terms of meandering channels (tubes).

2 Geometry of the problem

The flow of a viscous fluid in a meandering tube, whose geometry is shown in Figure 1, is the main focus of this paper.

The tube of variable radius is taken, whose radius is determined by $R^* = r_m^* (1 + \alpha\ sin\ \delta)$. The polar coordinate system (r, θ, z) is connected to the Cartesian coordinate system (x, y, z) for this particular problem in such a way that $x = \eta\ (1 + \alpha\ \sin\delta) \cos\theta$, $y =$

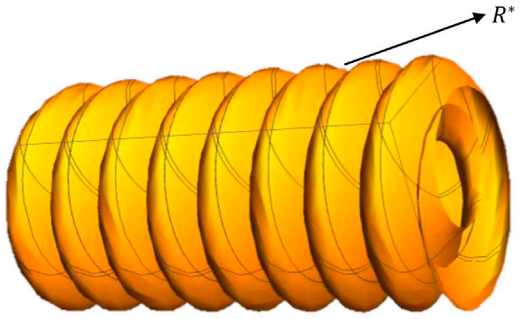

The radius R varies as

$$R = 1 + \alpha \sin(\delta)$$
$$x = \eta\left(1 + \alpha \sin(\delta)\right)\cos\theta$$
$$y = \eta\left(1 + \alpha \sin(\delta)\right)\sin\theta$$
$$z = z$$
$$\delta = \beta\theta + kz$$
$$\eta = \frac{r}{R}$$

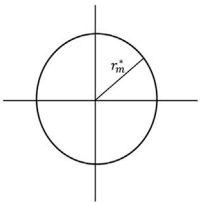

FIGURE 1
Geometry of the meandering tube under consideration and flow regime with coordinatex-axis.

$\eta\ (1 + \alpha\ \sin\delta)\sin\theta, z = z$ where $\delta = \beta\theta + kz$ and $= \frac{r}{R}$. Note that x, y, z, and η are dimensionless variables.

3 Governing equations

In order to express the current problem in proper coordinates, it is appropriate to choose a suitable coordinate system for the simulated problem. The well-established relationship between the Cartesian coordinates (x^*, y^*, z^*) and cylindrical ones (r^*, θ, z^*) has been presented above. For the meandering, we took the following transformation to define a tube of non-uniform radius (R^*) as:

$$R^* = r_m^*(1 + \alpha\ Sin\ \delta) \quad where \quad \delta = \beta\theta + k^*z^*$$

where r_m^* is the mean radius of the tube while "α" represents the dimensionless amplitude, "β" represents the number of helixes starts, and "k^*" represents the wave number in the axial direction of the wall of the tube.

The governing equations are non-dimensionalized by introducing dimensionless variables and the length is non-dimensionalized by r_m^* (mean radius), the velocity components (u^*, v^*, w^*) by v^*/r_m^*, the static pressure by $\rho^*(v^*/r_m^*)^2$, ∇^{*2} by $1/r_m^{*2}$, and $(\mathbf{V}^* \cdot \nabla^*)$ by v^*/r_m^{*2}.

Note that the asterisk "*" represents the dimensional quantities and v^* and ρ^* are kinematic viscosity and density of the fluid, respectively. The governing equations in cylindrical coordinates (r^*, θ, z^*) are:

Continuity equation, r^*, θ, and z^*- components of Navier-Stokes equations in cylindrical coordinates (r^*, θ, z^*) are given as:

$$\frac{\partial}{\partial r^*}(r^*u^*) + \frac{\partial}{\partial\theta}v^* + r^*\frac{\partial}{\partial z^*}w^* = 0 \tag{1}$$

$$(\mathbf{V}^* \cdot \nabla^*)u^* - \frac{v^{*2}}{r^*} = -\frac{1}{\rho^*}\frac{\partial P^*}{\partial r^*} + v^*\left(\nabla^{*2}u^* - \frac{u^*}{r^{*2}} - \frac{2}{r^{*2}}\frac{\partial v^*}{\partial\theta}\right) \tag{2}$$

$$(\mathbf{V}^* \cdot \nabla^*)v^* - \frac{u^*v^*}{r^*} = -\frac{1}{\rho^*r^*}\frac{\partial P^*}{\partial\theta} + v^*\left(\nabla^{*2}v^* - \frac{v^*}{r^{*2}} - \frac{2}{r^{*2}}\frac{\partial u^*}{\partial\theta}\right) \tag{3}$$

$$(\mathbf{V}^* \cdot \nabla^*)w^* = -\frac{1}{\rho^*}\frac{\partial P^*}{\partial z^*} + v^*\nabla^{*2}w^* \tag{4}$$

$$\mathbf{V}^* \cdot \nabla^* = u^*\frac{\partial}{\partial r^*} + \frac{1}{r^*}v^*\frac{\partial}{\partial\theta} + w^*\frac{\partial}{\partial z^*} \tag{5}$$

$$\nabla^{*2} = \frac{1}{r^*}\frac{\partial}{\partial r^*}\left(r^*\frac{\partial}{\partial r^*}\right) + \frac{1}{r^{*2}}\frac{\partial^2}{\partial\theta^2} + \frac{\partial^2}{\partial z^{*2}} \tag{6}$$

The no slip boundary conditions at the wall and the symmetry conditions at the center of the meandering tube are given as:

$$u^* = v^* = w^* = 0\ at\ r^* = R^* \text{ and } u^* = v^* = 0, w^* = U^* \text{ at } r^* = 0 \tag{7}$$

where U^* represents stream velocity at the center of the meandering tube.

By using the dimensionless variables as defined above, the continuity Eq. 1 is transformed as:

$$\frac{\partial}{r_m^*\partial\frac{r^*}{r_m^*}}r_m^*\left(\frac{r^*}{r_m^*}\right)\left(\frac{v^*}{r_m^*}\right)\frac{u^*}{\left(\frac{v^*}{r_m^*}\right)} + \frac{\partial}{\partial\theta}\left(\frac{v^*}{r_m^*}\right)\frac{v^*}{\left(\frac{v^*}{r_m^*}\right)} + r_m^*\left(\frac{r^*}{r_m^*}\right)\frac{\partial}{r_m^*\partial\frac{z^*}{r_m^*}}\left(\frac{v^*}{r_m^*}\right)\frac{w^*}{\left(\frac{v^*}{r_m^*}\right)} = 0 \tag{8}$$

From above definitions of dimensionless variables, we have:

$$\frac{u^*}{\left(\frac{v^*}{r_m^*}\right)} = v_r, \frac{v^*}{\left(\frac{v^*}{r_m^*}\right)} = v_\theta, \frac{w^*}{\left(\frac{v^*}{r_m^*}\right)} = v_z, r = \frac{r^*}{r_m^*}, z = \frac{z^*}{r_m^*} \tag{9}$$

where v_r, v_θ, and v_z represent the dimensionless velocity components in r, θ, and z directions, respectively:

$$\frac{\partial}{\partial r}(r\,v_r) + \frac{\partial}{\partial\theta}v_\theta + r\frac{\partial}{\partial z}v_z = 0 \tag{10}$$

$$(\mathbf{V}\cdot\nabla)v_r-\frac{1}{r}v_\theta^2=-\frac{\partial P}{\partial r}+\nabla^2 v_r-\frac{v_r}{r^2}-\frac{2}{r^2}\frac{\partial v_\theta}{\partial\theta} \tag{11}$$

$$(\mathbf{V}\cdot\nabla)v_\theta+\frac{v_r v_\theta}{r}=-\frac{1}{r}\frac{\partial P}{\partial\theta}+\nabla^2 v_\theta-\frac{v_\theta}{r^2}+\frac{2}{r^2}\frac{\partial v_r}{\partial\theta} \tag{12}$$

$$(\mathbf{V}\cdot\nabla)v_z=-\frac{\partial P}{\partial z}+\nabla^2 v_z \tag{13}$$

$$\mathbf{V}\cdot\nabla=\frac{r_m^{*2}}{v^\star}(\mathbf{V}^\star\cdot\nabla^\star) \tag{14}$$

$$\nabla^2=r_m^{*2}\nabla^{*2} \tag{15}$$

Where Eqs. 10–13 represent the dimensionless form of **continuity** and **components of Navier-Stokes** equations, respectively.

The dimensionless form of no slip boundary conditions at the wall and the symmetry conditions at the center of the meandering tube are obtained as:

$$v_r=v_\theta=v_z=0\ at\ r=R\ \text{and}\ v_r=v_\theta=0, v_z=Re\ \text{at}\ r=0$$

where $Re=\frac{\rho^\star U^\star r_m^\star}{v^\star}$ represents the Reynolds number.

4 Modal problem

The velocity vector $\boldsymbol{V}_b$ for the modeled problem is decomposed as $\boldsymbol{V}_b=\boldsymbol{V}_0+\boldsymbol{V}_1$ where the velocity $\boldsymbol{V}_0$, pressure P_0, the total volume flow rate Q_0, the stream function ψ_0, and the vorticity function ξ_0 for the fully developed flow in a straight duct (circular pipe) becomes purely radial in a pipe. The solution is obtained from the continuity equation, η, θ, and z momentum equations. Note that the fluid flow is directed in the direction along positive z-axis. The velocity field and other field quantities for fluid motion in the meandering tube are approximated as:

$$\begin{aligned}
&\boldsymbol{V}_b=\boldsymbol{V}_0+\boldsymbol{V}_1=[0,0,w_0(\eta)]+[u_1(\eta,\theta,z),v_1(\eta,\theta,z),w_1(\eta,\theta,z)]\\
&P_b=P_0(\eta)+P_1(\eta,\theta,z)\\
&\psi_b=\psi_0(\eta)+\psi_1(\eta,\theta,z)\\
&Q_b=Q_0(\eta)+Q_1(\eta,\theta,z)\\
&\xi_b=\xi_0(\eta)+\xi_1(\eta,\theta,z)
\end{aligned}$$

$$\begin{aligned}
\boldsymbol{V}_0(\eta,\theta,z)&=[u_0(\eta,\theta,z),\boldsymbol{v}_0(\eta,\theta,z),w_0(\eta,\theta,z)]\\
&=[0,0,Re(1-\eta^2)],P_0=-4Rez+c_0,Q_0=\frac{\pi Re}{2},\\
\psi_0&=-\frac{\eta^2}{2}Re\left(1-\frac{\eta^2}{2}\right)+c_1\ and\ \xi_0=2\,\eta\,Re
\end{aligned}$$

Further, the velocity vector $\boldsymbol{V}_b=[u_b,v_b,w_b]$ needs to be determined; therefore, an appropriate approximation technique is used to get this part of velocity $\boldsymbol{V}_b$.

5 Solution of the problem

Next, our aim is to determine the solution of dimensionless Eqs. (10 - 16). As these equations have a parameter α which may be a small quantity in many practical problems, we therefore consider the case of small amplitude waviness, i.e.; $\alpha\to 0$ and the flow domain has been regularized for the radial coordinate of the form when $\eta=\frac{r}{R}$ where $R=1+\alpha\sin(\delta)$ where $\delta=\beta\theta+kz$ (the tube or its wall is located at $\eta=1$ for this new variable), and the dimensionless governing equations are transformed from (r,θ,z) to (η,θ,z) such that the dimensionless continuity and Navier-Stokes Eqs. (10-13) in cylindrical coordinates (r,θ,z) take the form below:

$$\begin{aligned}
&(1+\alpha\sin\delta)u_b+\eta(1+\alpha\sin\delta)^2\frac{\partial w_b}{\partial z}+\frac{\partial v_b}{\partial\theta}+\eta\frac{\partial u_b}{\partial\eta}+\alpha\sin\delta\frac{\partial v_b}{\partial\theta}\\
&+\alpha\eta\sin\delta\frac{\partial u_b}{\partial\eta}-\alpha\eta\cos\delta\,\beta\frac{\partial v_b}{\partial\eta}+k\eta\alpha\eta\cos\delta(1+\alpha\sin\delta)\frac{\partial w_b}{\partial z}=0
\end{aligned} \tag{18}$$

$$\begin{aligned}
&-\eta(1+\alpha\sin\delta)^3{v_b}^2-(1+\alpha\sin\delta)^2\frac{\partial^2 u_b}{\partial\theta^2}+\eta^2(1+\alpha\sin\delta)^3\frac{\partial P_b}{\partial\eta}\\
&-2\alpha^2\beta^2\eta\cos^2\delta\frac{\partial u_b}{\partial\eta}-\alpha\beta^2\eta\sin\delta(1+\alpha\sin\delta)\frac{\partial u_b}{\partial\eta}+\eta^2(1+\alpha\sin\delta)^3u_b\frac{\partial u_b}{\partial\eta}\\
&+\eta^2(1+\alpha\sin\delta)^3w_b\left((1+\alpha\sin\delta)\frac{\partial u_b}{\partial z}-k\alpha\eta\cos\delta\frac{\partial u_b}{\partial\eta}\right)\\
&+\eta(1+\alpha\sin\delta)^2v_b\left((1+\alpha\sin\delta)\frac{\partial u_b}{\partial\theta}-\alpha\beta\eta\cos\delta\frac{\partial u_b}{\partial\eta}\right)\\
&+2(1+\alpha\sin\delta)\left((1+\alpha\sin\delta)\frac{\partial u_b}{\partial\theta}-\alpha\beta\eta\cos\delta\frac{\partial u_b}{\partial\eta}\right)\\
&+\alpha\beta\eta\cos\delta(1+\alpha\sin\delta)\frac{\partial^2 u_b}{\partial\eta\partial\theta}-\eta^2(1+\alpha\sin\delta)^3\left(\frac{\partial u_b}{\partial\eta}+\eta\frac{\partial^2 u_b}{\partial\eta^2}\right)\\
&+\alpha\beta\eta\cos\delta\left((1+\alpha\sin\delta)\frac{\partial^2 u_b}{\partial\eta\partial\theta}-\alpha\beta\eta\cos\delta\frac{\partial^2 u_b}{\partial\eta^2}\right)\\
&-(\eta+\alpha\eta\sin\delta)^2\left((1+\alpha\sin\delta)^2\frac{\partial^2 u_b}{\partial z^2}+\frac{1}{2}k\alpha\eta\left(k(3\alpha+\alpha\cos\delta+2\sin\delta)\frac{\partial u_b}{\partial\eta}\right.\right.\\
&\left.\left.+2\cos\delta\left(-2(1+\alpha\sin\delta)\frac{\partial^2 u_b}{\partial\eta\partial z}+k\alpha\eta\cos\delta\frac{\partial^2 u_b}{\partial\eta^2}\right)\right)\right)=0
\end{aligned} \tag{19}$$

$$\begin{aligned}
&-\eta(1+\alpha\sin\delta)^2v_b+\eta(1+\alpha\sin\delta)^3u_b\,v_b-(1+\alpha\sin\delta)^2\frac{\partial^2 v_b}{\partial\theta^2}\\
&+\eta(1+\alpha\sin\delta)^2\left((1+\alpha\sin\delta)\frac{\partial P_b}{\partial\theta}-\alpha\beta\eta\cos\delta\frac{\partial P_b}{\partial\eta}\right)\\
&-2(1+\alpha\sin\delta)\left((1+\alpha\sin\delta)\frac{\partial u_b}{\partial\theta}-\alpha\beta\eta\cos\delta\frac{\partial u_b}{\partial\eta}\right)\\
&-2\alpha^2\beta^2\eta\cos^2\delta\frac{\partial v_b}{\partial\eta}-\alpha\beta^2\eta\sin\delta(1+\alpha\sin\delta)\frac{\partial v_b}{\partial\eta}\\
&+\eta^2(1+\alpha\sin\delta)^3u_b\frac{\partial v_b}{\partial\eta}\\
&+\eta^2(1+\alpha\sin\delta)^3w_b\left((1+\alpha\sin\delta)\frac{\partial v_b}{\partial z}-k\alpha\eta\cos\delta\frac{\partial v_b}{\partial\eta}\right)\\
&+\eta(1+\alpha\sin\delta)^2v_b\left((1+\alpha\sin\delta)\frac{\partial v_b}{\partial\theta}-\alpha\beta\eta\cos\delta\frac{\partial v_b}{\partial\eta}\right)\\
&+\alpha\beta\eta\cos\delta(1+\alpha\sin\delta)\frac{\partial^2 v_b}{\partial\eta\partial\theta}-\eta^2(1+\alpha\sin\delta)^3\left(\frac{\partial v_b}{\partial\eta}+\eta\frac{\partial^2 v_b}{\partial\eta^2}\right)\\
&+\alpha\beta\eta\cos\delta\left((1+\alpha\sin\delta)\frac{\partial^2 v_b}{\partial\eta\partial\theta}-\alpha\beta\eta\cos\delta\frac{\partial^2 v_b}{\partial\eta^2}\right)\\
&-(\eta+\alpha\eta\sin\delta)^2((1+\alpha\sin\delta)^2\frac{\partial^2 v_b}{\partial\eta^2}\\
&+\frac{1}{2}k\alpha\eta\left(k(3\alpha+\alpha\cos\delta+2\sin\delta)\right.\\
&\left.\left.\frac{\partial v_b}{\partial\eta}+2\cos\delta\left(k\alpha\eta\cos\delta\frac{\partial^2 v_b}{\partial\eta^2}-2(1+\alpha\sin\delta)\frac{\partial^2 v_b}{\partial\eta\partial z}\right)\right)\right)=0
\end{aligned} \tag{20}$$

$$
\begin{aligned}
&-(1+\alpha\sin\delta)^2\frac{\partial^2 w_b}{\partial\theta^2}\\
&+\eta^2(1+\alpha\sin\delta)^3\left((1+\alpha\sin\delta)\frac{\partial P_b}{\partial z}-k\alpha\eta\cos\delta\frac{\partial p_b}{\partial\eta}\right)\\
&-2\alpha^2\beta^2\eta\cos^2\delta\frac{\partial w_b}{\partial\eta}-\alpha\beta^2\eta\sin\delta(1+\alpha\sin\delta)\frac{\partial w_b}{\partial\eta}\\
&+\eta^2(1+\alpha\sin\delta)^3u_b\frac{\partial w_b}{\partial\eta}\\
&+\eta^2(1+\alpha\sin\delta)^3w_b\left((1+\alpha\sin\delta)\frac{\partial w_b}{\partial z}-k\alpha\eta\cos\delta\frac{\partial w_b}{\partial\eta}\right)\\
&+\eta(1+\alpha\sin\delta)^2v_b\left((1+\alpha\sin\delta)\frac{\partial w_b}{\partial\theta}-\alpha\beta\eta\cos\delta\frac{\partial w_b}{\partial\eta}\right)\\
&+\alpha\beta\eta\cos\delta(1+\alpha\sin\delta)\frac{\partial^2 w_b}{\partial\eta\partial\theta}-\eta(1+\alpha\sin\delta)^2\left(\frac{\partial w_b}{\partial\eta}+\eta\frac{\partial^2 w_b}{\partial\eta^2}\right)\\
&+\alpha\beta\eta\cos\delta\left((1+\alpha\sin\delta)\frac{\partial^2 w_b}{\partial\eta\partial\theta}-\alpha\beta\eta\cos\delta\frac{\partial^2 w_b}{\partial\eta^2}\right)\\
&-(\eta+\alpha\eta\sin\delta)^2\left((1+\alpha\sin\delta)^2\frac{\partial^2 w_b}{\partial z^2}\right.\\
&+\frac{1}{2}k\alpha\eta\left(k(3\alpha+\alpha\cos 2\delta+2\sin\delta)\frac{\partial w_b}{\partial\eta}\right.\\
&\left.\left.+2\cos\delta\left(k\alpha\eta\cos\delta\frac{\partial^2 w_b}{\partial\eta^2}-2(1+\alpha\sin\delta)\frac{\partial^2 w_b}{\partial\eta\partial z}\right)\right)\right)=0
\end{aligned}
\tag{21}
$$

Similarly, the dimensionless Eq. 16 has transformed (by introducing $\eta=\frac{r}{R}$; $R=1+\alpha\sin\delta$ where $\delta=\beta\theta+kz$) into the following form:

$$
u_b=v_b=w_b=0\text{ at }\eta=1\text{ and }u_b=v_b=0,w_b=Re\text{ at }\eta=0 \tag{22}
$$

In the case of small amplitude waviness, i.e., $\alpha\to 0$, the velocity components, i.e., u_b, v_b, and w_b in η, θ, and z-directions, respectively, and the pressure term P_b are expanded in a series of α as:

$$
\begin{aligned}
&u_b=\hat{u}_0+\alpha\hat{u}_1+O(\alpha^2),v_b=\hat{v}_0+\alpha\hat{v}_1+O(\alpha^2),\\
&w_b=\hat{w}_0+\alpha\hat{w}_1+O(\alpha^2)\text{ and }P_b=\hat{P}_0+\alpha\hat{P}_1+O(\alpha^2)
\end{aligned}
\tag{23}
$$

where $u_0=\hat{u}_0, v_0=\hat{v}_0, w_0=\hat{w}_0, and\, P_0=\hat{P}_0$ and they are determined previously for the fully developed flow in straight duct.

The values of u_b, v_b, w_b, and P_b are substituted from Eq. 23 into the equations of continuity, motion, and the relevant boundary conditions, i.e., Eqs. 18–21 which are described by means of (η, θ, z), and terms of the same order of α are collected on each side of these equations.

6 Results and discussion

The solution of the zeroth-order system, which is obtained by putting value from Eq. 23 into Eqs 18–21 and equating like powers of α^0 on both sides of them, is given below:

$$
\begin{aligned}
&\hat{u}_0=\hat{v}_0=0,\hat{w}_0=Re(1-\eta^2),\hat{P}_0=-4Rez+c_0,\hat{Q}_1=\frac{\pi Re}{2},\\
&\psi_0=\hat{\psi}_0=-\frac{\eta^2}{2}Re\left(1-\frac{\eta^2}{2}\right)+c_1\, and\,\hat{\xi}_0=2\eta Re
\end{aligned}
\tag{24}
$$

Note that the solution in Eq. 24 for the fully developed flow in a straight duct has been reported in F.M. White (White and Majdalani, 2006) and Schlichting (Schlichting and Kestin, 1961).

Similarly, the first-order system is obtained by equating like powers of α^1 on both sides of Eqs 18–21 and then by substituting Eq. 24 into them. The unknowns in this system are further expressed by the following series:

$$
\begin{aligned}
&\hat{\psi}_1=f_a(\eta)\sin\delta+f_b(\eta)\cos\delta,\hat{w}_1=f_c(\eta)\sin\delta+f_d(\eta)\cos\delta,\\
&\hat{u}_1=\frac{1}{\eta}\left(\frac{\partial\hat{\psi}_1}{\partial\theta}-\frac{1}{2}kRe\eta^4\cos\delta\right),\hat{v}_1=-\frac{\partial\hat{\psi}_1}{\partial\eta}-\frac{1}{\beta}k\eta\hat{w}_1,\\
&f_a(\eta)=\sum_{p=0}^{\infty}a_p\eta^p,f_b(\eta)=\sum_{p=0}^{\infty}b_p\eta^p,f_c(\eta)=\sum_{p=0}^{\infty}c_p\eta^p\, and\\
&f_d(\eta)=\sum_{p=0}^{\infty}d_p\eta^p
\end{aligned}
$$

where the functions f_a, f_b, f_c, and f_d depend only on η and the coefficients a_p, b_p, c_p, and d_p are obtained by substituting the series into the first-order system. The coefficients of the above series are:

$$
\begin{aligned}
&a_0=0,a_1=0,a_2=0,a_3=0,a_4=\frac{12kRe+5kRe\beta^2}{2\beta(12+\beta^2)},\\
&a_5=\frac{54kRe\beta}{(12+\beta^2)(15+2\beta^2)},a_6=-\frac{2Re\beta(-576k+15k^3+2k^3\beta^2)}{(6+\beta^2)(12+\beta^2)(15+2\beta^2)},\\
&a_7=-\frac{2kRe\beta(-72000+k^2(2523+358\beta^2))}{(6+\beta^2)(12+\beta^2)(15+2\beta^2)(21+4\beta^2)},\\
&a_8=\frac{1}{(6+\beta^2)(12+\beta^2)(15+2\beta^2)(21+4\beta^2)(24+5\beta^2)}\\
&\{2kRe\beta(15552000+5k^4(315+102\beta^2+8\beta^4)\\
&-k^2(72(8409+1234\beta^2)+5Re^2(315+102\beta^2+8\beta^4)))\}
\end{aligned}
$$

Moreover, the coefficients a_I are recursively obtained as:

$$
\begin{aligned}
a_{I+4}=\frac{1}{(I+4)(\beta^2+3)-3\beta^2}&\left\{[(I+3)\{(I+1)(I+2)+1\}-1]a_{I+3}\right.\\
&-kRe(I-1)b_I-k^2(I+1)a_{I+2}+kRe(I+1)b_{I+2}\\
&+kRe(I+1)b_{I+1}-\frac{k}{\beta}(\beta^2+3)c_{I+2}+\frac{k}{\beta}\{(I+1)(I+3)+1\}c_{I+1}\\
&\left.-\frac{k^3}{\beta}c_I+\frac{k^2Re}{\beta}d_I-\frac{k^2Re}{\beta}d_{I-2}\right\}
\end{aligned}
$$

For $I=5,6,7,\ldots\ldots$

Furthermore, the coefficients of the second series in the expression of $\hat{\psi}_1$ are obtained as:

$$
\begin{aligned}
&b_0=0,b_1=0,b_2=0,b_3=0,b_4=0,b_5=0,\\
&b_6=-\frac{2k^2\mathrm{Re}^2\beta}{(\beta^2+6)(\beta^2+12)},\\
&b_7=-\frac{2k^2\mathrm{Re}^2\beta(2523+358\beta^2)}{(\beta^2+6)(\beta^2+12)(2\beta^2+15)(4\beta^2+21)},\\
&b_8=\frac{1}{(\beta^2-36)(\beta^2+6)(\beta^2+12)(2\beta^2+15)(4\beta^2+21)(5\beta^2+24)}\\
&\{2k^2\,\mathrm{Re}^2\beta(21580668+2489292\beta^2-105021\beta^4-762\beta^6+8\beta^8\\
&+10k^2(\beta-6)(\beta+6)(15+2\beta^2)(21+4\beta^2))\},
\end{aligned}
$$

The recursive formula for b_I is obtained as:

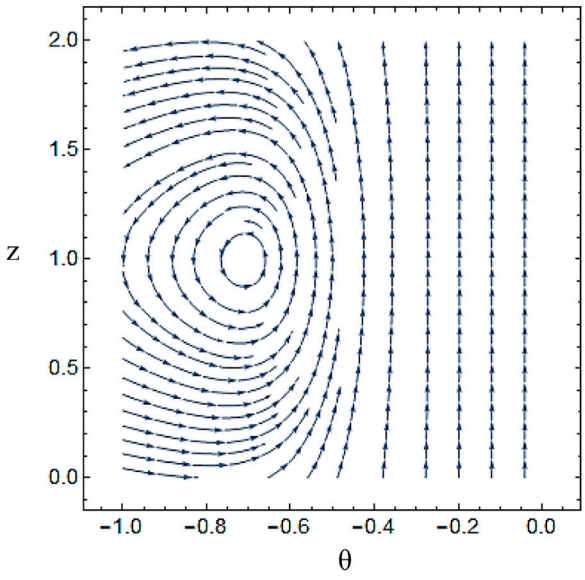

FIGURE 2
The stream lines are drawn by using u_b and w_b (components of velocity) and the stream contours are graphed for Re = 10, ß = 1, z = 1, and k = 10 in the domain $0 \le \theta \le 2$, $-1 \le \eta \le 0$ at the lower portion of the tube.

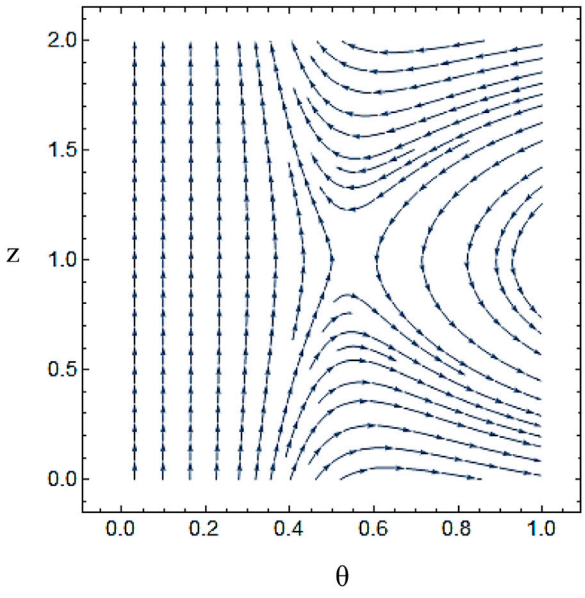

FIGURE 3
The stream lines are drawn by using u_b and w_b (components of velocity) and the stream contours are graphed for Re = 10, ß = 1, z = 1, and k = 10 in the domain $0 \le \theta \le 2$, $0 \le \eta \le 1$ at the upper portion of the tube.

$$b_{I+4} = \frac{1}{(\beta^2+3)(I+4)-3\beta^2}\left\{-kRe(I+1)a_{I+2} + kRe(I-1)a_I + [(I+3)\{(I+1)(I+2)+1\}-1]b_{I+3} - k^2(I+1)b_{I+2} - \frac{k}{\beta}(\beta^2+3)d_{I+2} + \frac{k}{\beta}\{(I+1)(I+3)+1\}d_{I+1} + \frac{k^3}{\beta}d_I\right\}$$

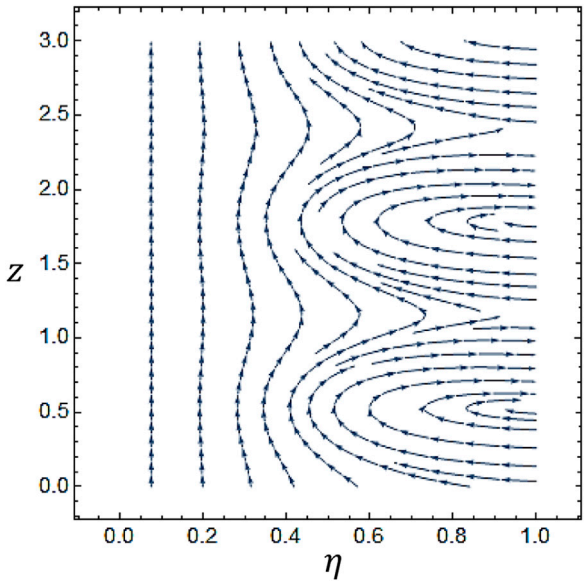

FIGURE 4
The stream lines are drawn by using v_b and w_b (components of velocity) and the stream contours are graphed for Re = 100, ß = 1, z = 1, and k = 0.1 in the domain $0 \le \theta \le$, $0 \le \eta \le 1$ at the upper portion of the tube.

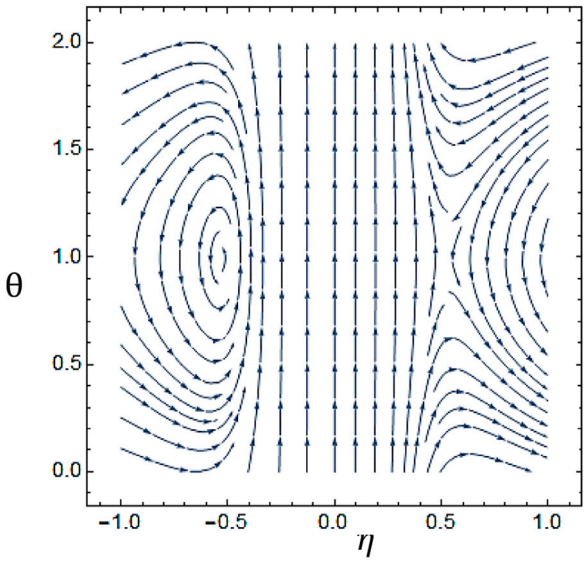

FIGURE 5
The stream lines are drawn by using u_b and w_b (components of velocity) and the stream contours are graphed for Re = 10, ß = 1, z = 1, and k = 10 in the domain $0 \le \theta \le 2$, $-1 \le \eta \le 1$ of the whole tube.

For $I = 5, 6, 7, \ldots\ldots$

$$c_0 = 0, c_1 = 0, c_2 = -2Re, c_3 = 0, c_4 = 0, c_5 = 0, c_6 = 0, c_7 = 0,$$

The recursive formula for c_I is obtained as:

$$c_{I+2} = \frac{1}{(I+2)^2-\beta^2}\{2Re\beta b_I + k^2 c_I - kRed_I + kRed_{I-2}\}$$

For $I = 6, 7, 8, \ldots\ldots$

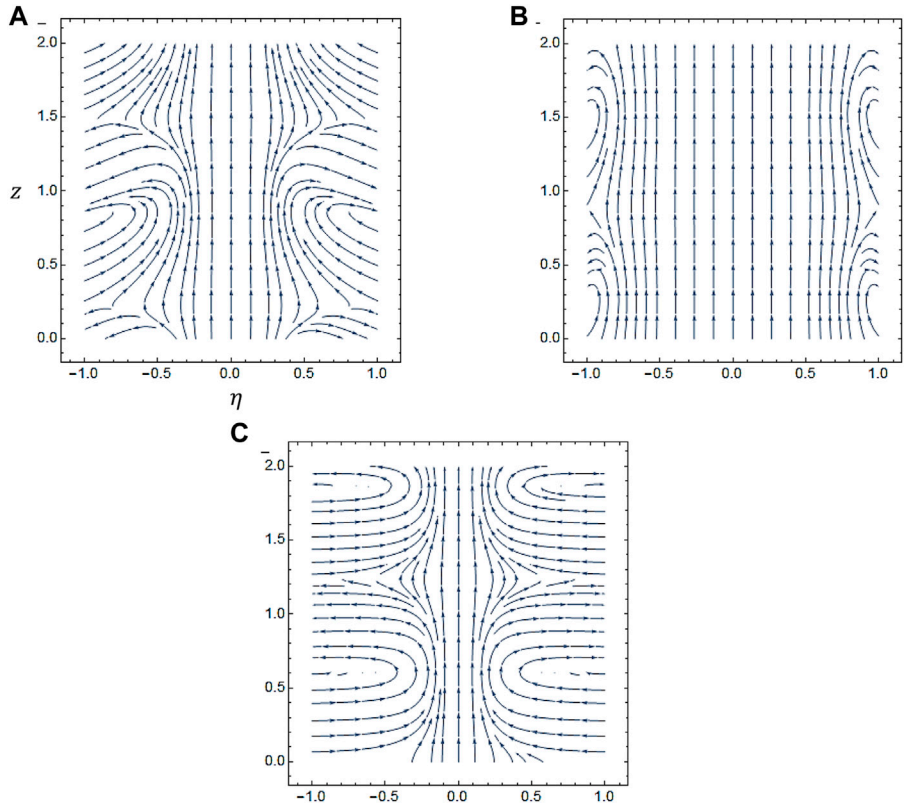

FIGURE 6
The stream lines are drawn by using v_b and w_b (components of velocity) and the stream contours are graphed for Re = 100, θ = 1, k = 5, **(A)** ß = 2, **(B)** ß = 5, and **(C)** ß = 0.1 in the domain $0 \le z \le 2$, $-1 \le \eta \le 1$ of the whole tube.

$$d_0 = 0, d_1 = 0, d_2 = -2Re, d_3 = 0, d_4 = 0, d_5 = 0,$$
$$d_6 = \frac{4k\mathrm{Re}^2\beta^2}{(\beta^2 - 36)(\beta^2 + 12)}, d_7 = \frac{108k\mathrm{Re}^2\beta^2}{(\beta^2 - 49)(\beta^2 + 12)(2\beta^2 + 15)},$$

And the recursive formula for d_I is obtained as:

$$d_{I+2} = \frac{1}{(I+2)^2 - \beta^2}\{-2Re\beta a_I + k^2 c_I + kRec_I + kRec_{I-2}\}$$

For $I = 6, 7, 8, \ldots\ldots$

Figure 2, Figure 3, Figure 4, Figure 5 describe the impact of meanders on the formation and behavior of vortices in the flow, producing complex patterns of stream contours. Vortices form near the wall of the tube and interact with the fluid flow. In Figure 6, fluid flow patterns are affected in several ways with variation in the number of helixes. As the number of helixes increases, the amplitude of the meanders increases, leading to more complex flow patterns with multiple recirculation zones near the wall of the tube. This also causes an increase in the pressure drop and the overall mixing in the flow.

7 Conclusion

In a meandering tube, streamwise vortices can improve the transportation of heat and species mass in a transverse direction. To create these vortices, a specific meandering wavelength is required, which can be measured using linear instability theory. Short wavelengths cause flow separation, while long wavelengths result in a rectilinear stream resembling a flat plate. Shear-driven instability also contributes to vortex formation. The effect of a steady laminar flow in a meandering tube with small amplitude wavy walls was studied. The governing equations were constructed using the continuity equation and Navier-Stokes equations with no slip boundary conditions. Suppositions were made to simplify the complex non-linear problem, including linear instabilities, uniform thermal characteristics, and laminar flow conditions. The equations were further simplified using available dimensionless variables and new transformations. The perturbation and power series approaches were used to solve the equations with the help of Mathematica, and the velocity profiles and stream contours were graphed using standard codes and definitions.

The flow in a meandering tube becomes unstable due to centrifugal impact, which results in the formation of streamwise vortices. This research has focused on identifying the lowest meandering amplitude that can create these vortices with minimal pressure loss. Two primary forms of vortex instability have been studied, with the most effective parameter being better for creating vortex instability than centrifugal instability. The meandering geometry that is most successful in producing vortices does not encourage traveling wave instability, which can delay the onset of laminar-turbulent transition. By using the reduced geometry model approach, the findings can be applied to various types of meandering tubes.

Further investigations can be conducted through experiments, simulations, and new applications. Experiments can provide valuable insights into the complex nature of the flow using advanced techniques like PIV, LDV, and HWA to measure velocities, turbulence, and vortices. Numerical simulations using CFD techniques can also be performed to investigate flow behavior, providing detailed information on velocity, pressure, and vortices, and help optimize tube design.

Data availability statement

The original contributions presented in the study are included in the article/supplementary material, further inquiries can be directed to the corresponding author.

Author contributions

The mathematical model has been proposed by DK, all the numerical computations and their graphs have been carried out by SI. The discussion of graphs and their physical interpretation has been given by DK and SI. The literature review and comparison of the present simulations with the classical data has been established by NU. The final review and amendments in the manuscript has been carried out by KN.

Funding

This study is supported via funding from Prince Sattam bin Abdulaziz University project number (PSAU/2023/R/1444).

Conflict of interest

The authors declare that the research was conducted in the absence of any commercial or financial relationships that could be construed as a potential conflict of interest.

Publisher's note

All claims expressed in this article are solely those of the authors and do not necessarily represent those of their affiliated organizations, or those of the publisher, the editors and the reviewers. Any product that may be evaluated in this article, or claim that may be made by its manufacturer, is not guaranteed or endorsed by the publisher.

References

Alyousef, H. A., Yasmin, H., Shah, R., Shah, N. A., El-Sherif, L. S., and El-Tantawy, S. A. (2023). Mathematical modeling and analysis of the steady electro-osmotic flow of two immiscible fluids: A biomedical application. *Coatings* 13 (1), 115. doi:10.3390/coatings13010115

Bergles, A. E., and Webb, R. L. (1985). *A guide to the literature on convective heat transfer augmentation*. Ames, Iowa: Iowa State University College of Engineering.

Dean, W. R. (1928). Fluid motion in a curved channel. *Proc. R. Soc. Lond. Ser. A, Contain. Pap. a Math. Phys. Character* 121, 402–420.

Fiebig, M., and Chen, Y. (1999). "Heat transfer enhancement by wing-type longitudinal vortex generators and their application to finned oval tube heat exchanger elements," in *Heat transfer enhancement of heat exchangers* (Dordrecht: Springer), 79–105.

Fiebig, M. (1995). Embedded vortices in internal flow: Heat transfer and pressure loss enhancement. *Int. J. Heat Fluid Flow* 16, 376–388. doi:10.1016/0142-727x(95)00043-p

Fiebig, M. (1995). Vortex generators for compact heat exchangers. *J. Enhanc. Heat Transf.* 2, 1–20. doi:10.1615/jenhheattransf.v24.i1-6.10

Fiebig, M. (1998). Vortices, generators and heat transfer. *Chem. Eng. Res. Des.* 76, 108–123. doi:10.1205/026387698524686

Floryan, J. M., and Asai, M. (2011). On the transition between distributed and isolated surface roughness and its effect on the stability of channel flow. *Phys. Fluids* 23, 104101. doi:10.1063/1.3644694

Floryan, J. M. (2002). Centrifugal instability of Couette flow over a wavy wall. *Phys. fluids* 14, 312–322. doi:10.1063/1.1416185

Floryan, J. M. (1986). Görtler instability of boundary layers over concave and convex walls. *Phys. fluids* 29, 2380–2387. doi:10.1063/1.865531

Floryan, J. M. (1991). On the Görtler instability of boundary layers. *Prog. Aerosp. Sci.* 28, 235–271. doi:10.1016/0376-0421(91)90006-p

Görtler, H. (1941). Instabilität laminarer Grenzschichten an konkaven Wänden gegenüber gewissen dreidimensionalen Störungen. *ZAMM-Journal Appl. Math. Mechanics/Zeitschrift für Angewandte Math. und Mech.* 21, 250–252. doi:10.1002/zamm.19410210408

Gschwind, P., Regele, A., and Kottke, V. (1995). Sinusoidal wavy channels with Taylor-Goertler vortices. *Exp. Therm. fluid Sci.* 11, 270–275. doi:10.1016/0894-1777(95)00056-r

Guzmán, A. M., Cárdenas, M. J., Urzúa, F. A., and Araya, P. E. (2009). Heat transfer enhancement by flow bifurcations in asymmetric wavy wall channels. *Int. J. Heat Mass Transf.* 52, 3778–3789. doi:10.1016/j.ijheatmasstransfer.2009.02.026

Hayat, T., Iqbal, M., Yasmin, H., Alsaadi, F. E., and Gao, H. (2015). Simultaneous effects of Hall and convective conditions on peristaltic flow of couple-stress fluid in an inclined asymmetric channel. *Pramana* 85, 125–148. doi:10.1007/s12043-014-0888-1

Jacobi, A. M., and Shah, R. K. (1995). Heat transfer surface enhancement through the use of longitudinal vortices: A review of recent progress. *Exp. Therm. Fluid Sci.* 11, 295–309. doi:10.1016/0894-1777(95)00066-u

Javed, M., Imran, N., Arooj, A., and Sohail, M. (2021). Meta-analysis on homogeneous-heterogeneous reaction effects in a sinusoidal wavy curved channel. *Chem. Phys. Lett.* 763, 138200. doi:10.1016/j.cplett.2020.138200

Jensen, M. K., Bergles, A. E., and Shome., B. (1997). The literature on enhancement of convective heat and mass transfer. *J. Enhanc. Heat Transf.* 4, 1–6. doi:10.1615/jenhheattransf.v4.i1.10

Ligrani, P. M., Oliveira, M. M., and Blaskovich, T. (2003). Comparison of heat transfer augmentation techniques. *AIAA J.* 41, 337–362. doi:10.2514/2.1964

Mehmood, O. U., Qureshi, A. A., Yasmin, H., and Uddin, S. (2020). Thermo-mechanical analysis of non Newtonian peristaltic mechanism: Modified heat flux model. *Phys. A Stat. Mech. its Appl.* 550, 124014. doi:10.1016/j.physa.2019.124014

Metwally, H. M., and Manglik, R. M. (2004). Enhanced heat transfer due to curvature-induced lateral vortices in laminar flows in sinusoidal corrugated-plate channels. *Int. J. Heat Mass Transf.* 47, 2283–2292. doi:10.1016/j.ijheatmasstransfer.2003.11.019

Mohammadi, A., and Floryan, J. M. (2013). Groove optimization for drag reduction. *Phys. Fluids* 25, 113601. doi:10.1063/1.4826983

Naseem, T., Nazir, U., and Sohail, M. (2021). Contribution of Dufour and Soret effects on hydromagnetized material comprising temperature-dependent thermal conductivity. *Heat. Transf.* 50 (7), 7157–7175. doi:10.1002/htj.22222

Nishimura, T., Yano, K., Yoshino, T., and Kawamura, Y. (1990). Occurrence and structure of Taylor–Goertler vortices induced in two-dimensional wavy channels for steady flow. *J. Chem. Eng. Jpn.* 23, 697–703. doi:10.1252/jcej.23.697

Patera, A. T., and Mikic, B. B. (1986). Exploiting hydrodynamic instabilities. Resonant heat transfer enhancement. *Int. J. heat mass Transf.* 29, 1127–1138. doi:10.1016/0017-9310(86)90144-4

Pham, M. V., Plourde, F., and Doan, S. K. (2008). Turbulent heat and mass transfer in sinusoidal wavy channels. *Int. J. Heat Fluid Flow* 29 (5), 1240–1257. doi:10.1016/j.ijheatfluidflow.2008.04.002

Rayleigh, L. (1917). On the dynamics of revolving fluids. *Proc. R. Soc. Lond. Ser. A, Contain. Pap. a Math. Phys. Character* 93, 148–154.

Rush, T. A., Newell, T. A., and Jacobi, A. M. (1999). An experimental study of flow and heat transfer in sinusoidal wavy passages. *Int. J. heat mass Transf.* 42, 1541–1553. doi:10.1016/s0017-9310(98)00264-6

Saric, W. S., and Ali, B. (1991). "Görtler vortices with periodic curvature," in *Boundary layer stability and transition to turbulence* (Berlin, Germany: Springer), 37–42.

Schlichting, H., and Kestin, J. (1961). *Boundary layer theory*. New York: McGraw-Hill.

Sui, Y., Teo, C. J., and Lee, P. S. (2012). Direct numerical simulation of fluid flow and heat transfer in periodic wavy channels with rectangular cross-sections. *Int. J. Heat Mass Transf.* 55, 73–88. doi:10.1016/j.ijheatmasstransfer.2011.08.041

Tatsuo, N., Shinichiro, M., Shingho, A., and Yuji, K. (1990). Flow observations and mass transfer characteristics in symmetrical wavy-walled channels at moderate Reynolds numbers for steady flow. *Int. J. Heat Mass Transf.* 33, 835–845. doi:10.1016/0017-9310(90)90067-5

Taylor, G. I. (1923). VIII. Stability of a viscous liquid contained between two rotating cylinders. *Philosophical Trans. R. Soc. Lond. Ser. A, Contain. Pap. a Math. or Phys. Character* 223, 605–615.

Wang, F., Sohail, M., Nazir, U., El-Zahar, E. R., Park, C., and Jabbar, N. (2022). An implication of magnetic dipole in Carreau Yasuda liquid influenced by engine oil using ternary hybrid nanomaterial. *Nanotechnol. Rev.* 11 (1), 1620–1632. doi:10.1515/ntrev-2022-0100

Webb, R. L., and Bergles, A. E. (1981). *Performance evaluation criteria for selection of heat transfer surface geometries used in low Reynolds number heat exchangers*. Ames, Iowa: Iowa State University College of Engineering.

White, F. M., and Majdalani, J. (2006). *Viscous fluid flow*. New York: McGraw-Hill, 433–434.

Xu, M., Lu, H., Gong, L., Chai, J. C., and Duan, X. (2016). Parametric numerical study of the flow and heat transfer in microchannel with dimples. *Int. Commun. Heat Mass Transf.* 76, 348–357. doi:10.1016/j.icheatmasstransfer.2016.06.002

Yasmin, H., and Iqbal, N. (2021). Convective mass/heat analysis of an electroosmotic peristaltic flow of ionic liquid in a symmetric porous microchannel with soret and dufour. *Math. Problems Eng.* 2021, 1–14. doi:10.1155/2021/2638647

Yasmin, H., Iqbal, N., and Hussain, A. (2020). Convective heat/mass transfer analysis on johnson-segalman fluid in a symmetric curved channel with peristalsis: Engineering applications. *Symmetry* 12 (9), 1475. doi:10.3390/sym12091475

Yasmin, H., Iqbal, N., and Tanveer, A. (2020). Engineering applications of peristaltic fluid flow with hall current, thermal deposition and convective conditions. *Mathematics* 8 (10), 1710. doi:10.3390/math8101710

Zhang, J., Kundu, J., and Manglik, M. (2004). Effect of fin waviness and spacing on the lateral vortex structure and laminar heat transfer in wavy-plate-fin cores. *Int. J. Heat Mass Transf.* 47, 1719–1730. doi:10.1016/j.ijheatmasstransfer.2003.10.006

10.3389/fmats.2023.1187986

Nomenclature

x, y, z	Cartesian coordinates
ρ	Density of the fluid
a_n, b_n, c_n, d_n	Coefficient of series
$\mathbf{V}$	Velocity vector
∇	Differential operator
ν^*	Kinematic velocity
L	Diameter of the pipe
α	Amplitude of tube
k	Wave number
β	Number of helixes Starts
r, θ, z	Cylindrical coordinates
Re	Reynold number
$\mathbf{P}$	Dimensionless pressure
R	Radius of the tube
μ	Dynamic viscosity
U^*	Characteristic Velocity
λ	Wavelength
r_m^*	Mean Radius of the tube
η	Dimensionless Redial length
δ	$\delta = \beta\theta + kz$

frontiers | Frontiers in Materials

TYPE Original Research
PUBLISHED 15 June 2023
DOI 10.3389/fmats.2023.1158644

OPEN ACCESS

EDITED BY
Mustafa Inc,
Firat University, Türkiye

REVIEWED BY
Francesco Costanzo,
The Pennsylvania State University (PSU), United States
Jawali C. Umavathi,
Gulbarga University, India

*CORRESPONDENCE
Ahmed M. Hassan,
ahmed.hassan.res@fue.edu.eg

RECEIVED 04 February 2023
ACCEPTED 01 June 2023
PUBLISHED 15 June 2023

CITATION
Swamy MS, Hanumagowda BN, Khan U, Vidyashree K, Hassan AM, Mohammed Saeed A and Kumar R (2023), Darcy–Benard–Oldroyd convection in anisotropic porous layer subject to internal heat generation.
Front. Mater. 10:1158644.
doi: 10.3389/fmats.2023.1158644

Darcy–Benard–Oldroyd convection in anisotropic porous layer subject to internal heat generation

Mahantesh S. Swamy[1], B. N. Hanumagowda[2], Umair Khan[3,4], K. Vidyashree[5], Ahmed M. Hassan[6]*, Abdulkafi Mohammed Saeed[7] and Ranvijay Kumar[8]

[1]Department of Mathematics, Government College (Autonomous), Kalaburagi, India, [2]Department of Mathematics, School of Applied Sciences, REVA University, Bangalore, India, [3]Department of Mathematical Sciences, Faculty of Science and Technology, Universiti Kebangsaan Malaysia, Bangi, Selangor, Malaysia, [4]Department of Mathematics and Social Sciences, Sukkur IBA University, Sukkur, Sindh, Pakistan, [5]Department of Mathematics, Sharnbasva University, Kalaburagi, India, [6]Mechanical Engineering, Future University in Egypt, New Cairo, Egypt, [7]Department of Mathematics, College of Science, Qassim University, Buraydah, Saudi Arabia, [8]University Centre for Research and Development and Department of Mechanical Engineering, Chandigarh University, Mohali, Punjab, India

An anisotropic horizontal porous layer saturated with viscoelastic liquids of the Oldroyd-B type is explored to determine how the internal heat source affects thermal convection. As a momentum equation, a modified Darcy–Oldroyd model is used that takes into account the anisotropy of the porous layer. The energy equation is formulated in such a way that the influence of internal heat sources and anisotropy in thermal diffusivity on the stability criterion may be easily identified. The effects of anisotropy, viscoelasticity, and internal heat generation on the onset of thermal convection are investigated using linear stability analysis. It is understood that convection begins via an oscillatory mode instead of a stationary mode because viscous relaxation, thermal diffusions, and internal heat generation mechanisms compete with one another. Both steady and unsteady finite-amplitude convections are studied using nonlinear stability analysis with the truncated Fourier series method. The effect of different governing parameters on the system's stability and on convective heat transfer is studied. The present investigation has been significantly validated by the recovery of several prior results as special situations. The findings presented in this work are anticipated to have significant implications for a number of real-world applications, including modeling of oil reservoirs, crude oil extraction, crystal growth, the pharmaceutical and medical industries, and the use of geothermal energy, among others.

KEYWORDS

thermal convection, internal heat generation, Rayleigh number, Oldroyd-B model, viscoelastic fluid

1 Introduction

Numerous real-world applications exist for the theoretical and practical analysis of convective heat transfer in porous media. Geothermal energy systems, hydrocarbon reserves, nuclear reactors, medicine, and the chemical industry are among the many examples. Ingham and Pop (2005), Nield and Bejan (2006), Vafai (2005), and Vadasz (2008) have documented the developments in porous medium thermal convection. An essential component of rheological

research is the study of the viscoelastic properties of the asthenospheric and mantle components of the Earth (see Lowrie, 2020). Snow systems and the rheology of food transport involve viscoelastic liquids saturated in porous media. Less research has been conducted on Rayleigh–Benard convection in liquids with viscoelastic properties than on thermal convection in a Newtonian fluid (refer to Li and Khayat, 2005).

Due to their coagulated viscosity, polymeric liquids are unaffected by flow and turbulence, whereas Newtonian fluids are affected. Moreover, oscillatory convection is believed to exist as viscoelastic fluids are characterized by their elasticity. According to Kim et al. (2003), the system is unstable due to its elasticity but stable due to its porosity. The oscillatory mode is appropriate for studying convection because convection reduced to supercritical and stable bifurcation forms does not vary with elasticity. However, few authors have investigated oscillatory convection in viscoelastic liquids, and many researchers have not addressed a comparable problem in porous media. Thermal convection in viscoelastic fluids was studied by O'Connell and Budiansky (1977), Griffiths (1987), Rudraiah et al. (1989), Yoon et al. (2004), Malashetty et al. (2006a), and Swamy et al. (2012).

When a porous medium exhibits anisotropy in its mechanical and thermal properties, the flow behavior is significantly altered. The assumption underlying Darcy's model is that the fluid flow is sufficiently slow for inertial effects to be negligible, and that the fluid complies with the laws of continuum mechanics. If the porous medium is anisotropic, then the medium's permeability will depend on the flow direction. In other words, the permeability of the porous medium will vary in different orientations. Darcy's law must be modified to account for the anisotropy of the medium in this instance. This can be accomplished by introducing a permeability tensor that describes the medium's permeability in various orientations. Numerous applications in the actual world involve anisotropic porous media. Anisotropy results from the incorrect orientation of a solid matrix or the asymmetries of the natural porous medium; it is also a characteristic of porous synthetic materials, such as the fibrous material utilized for insulation and pelleting, both of which are beneficial to chemical engineering processes.

McKibbin et al. (1985) and Storesletten (1998) have exhaustively documented the work pertaining to convection in anisotropic porous media. Govender (2006) described the effects of anisotropy on thermal convection in a porous layer. Malashetty et al. (2006b)presented a study on the effect of a time-periodic modulated temperature field on the stability of a viscoelastic fluid saturated within an anisotropic porous layer. Saravanan and Purusothaman (2009) studied non-Darcian effects in anisotropic porous media. Many pertinent studies on anisotropy have been conducted (Malashetty and Swamy, 2007a; Malashetty and Swamy, 2007b; Malashetty et al., 2009; Sivakumar and Saravanan, 2009; Malashetty and Swamy, 2010; Agarwal et al., 2011; Malashetty et al., 2011; Srivastava et al., 2011; Chandra and Satyamurty, 2012; Swamy et al., 2013; Swamy et al., 2014; Swamy, 2017; Swamy et al., 2019; Capone et al., 2020).

Understanding thermal convection in a porous stratum with internal heat generation is crucial in a variety of natural and artificial systems. The interior of the Earth provides an example of internal heat production. Due to the disintegration of radioactive isotopes and residual heat from the planet's formation, the Earth's core is thought to be the source of significant internal heating. This heat production is responsible for the elevated temperature of the Earth's interior and is one of the driving forces behind plate tectonics and volcanism. Electronic devices, such as computer processors, are another example of internal heat generation. A computer processor's electronic components generate heat due to the passage of electric current through them. If the generated heat is not effectively dissipated, the processor may malfunction or even fail. To prevent this, electronic devices are frequently equipped with cooling systems, such as heat sinks and fans, to dissipate heat and maintain secure component temperatures. Chemical reactions can also generate heat internally. Due to the exothermic nature of the combustion reaction, for example, heat is produced when fuel is consumed. This internal heat production can be utilized to generate electricity in power facilities or to heat industrial processes.

Internal heat generation results in a nonlinear temperature gradient. A temperature gradient is the temperature change over a specified distance. A nonlinear temperature gradient indicates that the change in temperature over a given distance is not constant. In other terms, the change in temperature is not linear. This refers to the fact that the system or material in question generates its own heat rather than receiving it from an external source. Therefore, thermal convection occurs even though the temperature difference between the lower and upper surfaces is insufficient for convection to begin. Consequently, the production of internal heat is an additional essential mechanism for regulating the onset of convection in the porous layer. Numerous researchers have conducted extensive research on thermal convection in absorbent layers with internal heat generation [refer to (Thirlby, 1970; Mahabaleshwar et al., 2017; Ahmed and Rashed, 2019; Yadav et al., 2021; Enagi et al., 2022; Raju et al., 2022; Upadhya et al., 2022)].

Now, let us see the physical mechanisms involved in the present problem. As a result of the internal heating, a temperature gradient is generated within the porous layer, with the temperature being higher near the heat source and decreasing toward the top surface of the layer. This temperature gradient creates density differences within the viscoelastic liquid, causing it to flow from the heat source toward the top surface. The fluid flow of the viscoelastic liquid is influenced by the anisotropy of the porous layer. If the porous layer is more permeable in one direction than in other directions, the fluid flow will be preferentially directed along the more permeable direction, resulting in anisotropic convection. The properties of the porous medium, such as its porosity, permeability, and tortuosity, also affect the rate of fluid flow and the way in which heat is transferred through the medium. For example, a higher porosity of the porous layer can increase the flow rate of the viscoelastic liquid, while a higher tortuosity can hinder the flow, leading to a slower rate of fluid motion. The viscoelasticity of the liquid can also influence the way in which fluid flow and heat transfer occur within the porous layer. A viscoelastic liquid has both viscous and elastic properties, which can lead to nonlinear behavior in fluid flow and heat transfer. For instance, the elasticity of the liquid can cause it to exhibit oscillatory behavior in response to the temperature gradient, resulting in oscillatory fluid flow and heat transfer. The heating of the bottom surface by an external means can also affect the flow of the viscoelastic liquid. For instance, uniformly heating the bottom surface can generate a temperature gradient that interacts with the temperature gradient generated by the internal heat source, resulting in a more complex flow pattern.

A stability analysis of an Oldroyd-B fluid in a porous medium with the combined influence of anisotropy and the internal heat source is rare. Such investigations are still greatly desired. The

TABLE 1 Comparison of the present result with the earlier published works.

Special case	Result recovered from Eq. 32	Previously published work
$\xi = \eta = 1$	$Ra^{st} = \delta^2(4\pi^2 - Ra_I)(\delta^2 - Ra_I)/4\pi^2k^2$	Gasser and Kazimi (1976)
$Ra_I = 0$	$Ra^{st} = \delta_1^2\delta_2^2/k^2$	Storesletten (1998)
$\xi = \eta = 1$, $Ra_I = 0$	$Ra^{st} = \delta^4/k^2$	Horton and Rogers (1945) and Lapwood (1948)

primary objective of this study is to determine how the viscoelastic parameters, internal heat generation coefficient, and anisotropy parameters impact the onset criterion of thermal convection and the heat transfer across the layer.

2 Mathematical formulation

A shallow horizontal anisotropic porous layer saturated with Oldroyd-B liquid is considered. The surfaces held at $z = 0$ and $z = h$ are regarded as being stress-free and isothermal. The gravitational force $g \equiv (0, 0, -g)$ is acting downward in the direction of the z-axis. The adverse temperature gradient ΔT between the two surfaces is maintained by heating the lower surface uniformly. Internal heat generation is considered as an additional source. The temperatures of the solid and liquid phases are assumed to have reached equilibrium. The conservation law of linear momentum is represented by a modified Darcy–Oldroyd model incorporating local time derivatives, Boussinesq approximation, and anisotropy. The convection velocities are expected to be negligible. Thus, the effects of Forchheimer inertia and advection are disregarded. Consequently, the pertinent mathematical model is

$$\nabla.\mathbf{v} = 0, \tag{1}$$

$$\left(1 + \Lambda_1\frac{\partial}{\partial t}\right)\left(\frac{\rho_0}{\varepsilon}\frac{\partial \mathbf{v}}{\partial t} + \nabla p - \rho\mathbf{g}\right) = -\mu\left(1 + \Lambda_2\frac{\partial}{\partial t}\right)\mathbf{K}\cdot\mathbf{v}_D, \tag{2}$$

$$\gamma\frac{\partial T}{\partial t} + (\mathbf{v}\cdot\nabla)T = \nabla\cdot(\boldsymbol{\kappa}\cdot\nabla T) + Q_I(T - T_0), \tag{3}$$

$$\rho = \rho_0(1 - \alpha(T - T_0)), \tag{4}$$

where $\mathbf{v} \equiv (v_1, v_2, v_3)$ denotes the velocity vector, $\mathbf{v}_D = \varepsilon\mathbf{v}$ is the seepage velocity, Λ_1 is the stress-relaxation time, Λ_2 is the strain-retardation time, ε is the porosity, μ is the viscosity, ρ is the density, α is

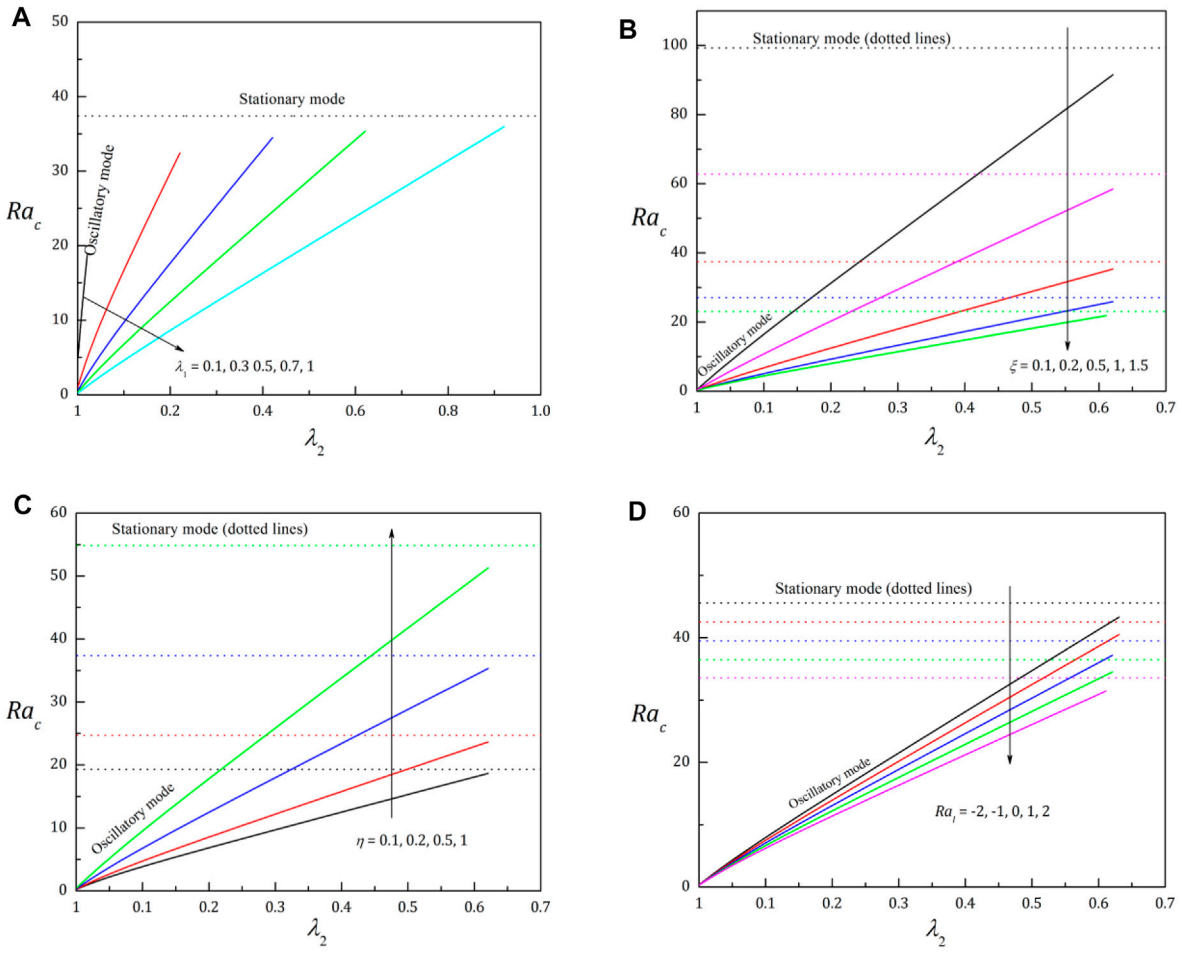

FIGURE 1
Plot of Ra_c *versus* λ_2 for varying **(A)** λ_1, **(B)** ξ, **(C)** η, and **(D)** Ra_I.

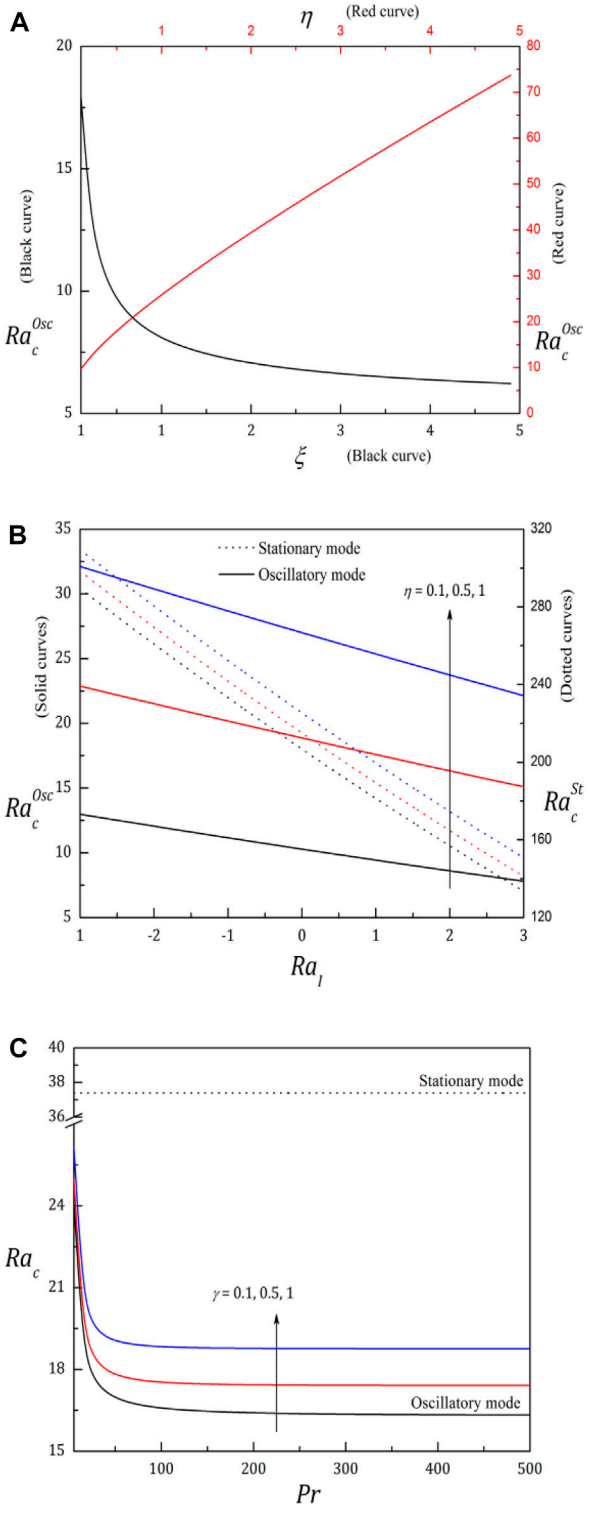

FIGURE 2
Plot of Ra_c as a function of **(A)** ξ and η, **(B)** Ra_I and η, and **(C)** Pr and γ.

the thermal expansion coefficient, $\gamma = (\varepsilon(\rho c)_f + (1-\varepsilon)(\rho c)_s)/(\rho c)_f$ is the ratio of specific heat capacities, $\mathbf{K} = (\mathbf{e_1 e_1} + \mathbf{e_2 e_2})\mathrm{K}_1^{-1} + (\mathbf{e_3 e_3})\mathrm{K}_3^{-1}$ and $\boldsymbol{\kappa} = (\mathbf{e_1 e_1} + \mathbf{e_2 e_2})\kappa_1 + (\mathbf{e_3 e_3})\kappa_3$ denote the anisotropy-induced permeability and thermal diffusivity tensor, respectively, with $\mathbf{e_1}, \mathbf{e_2}, \mathbf{e_3}$ being the unit vectors along the x, y, and z-axes, respectively. The last term in Eq. 3 is due to the presence of internal heat generation, where $\mathcal{Q}_I$ quantifies the amount of heat generation within the bulk of the porous layer

Because the fluid is at rest in the basic state, we can determine its mass, pressure, and temperature by

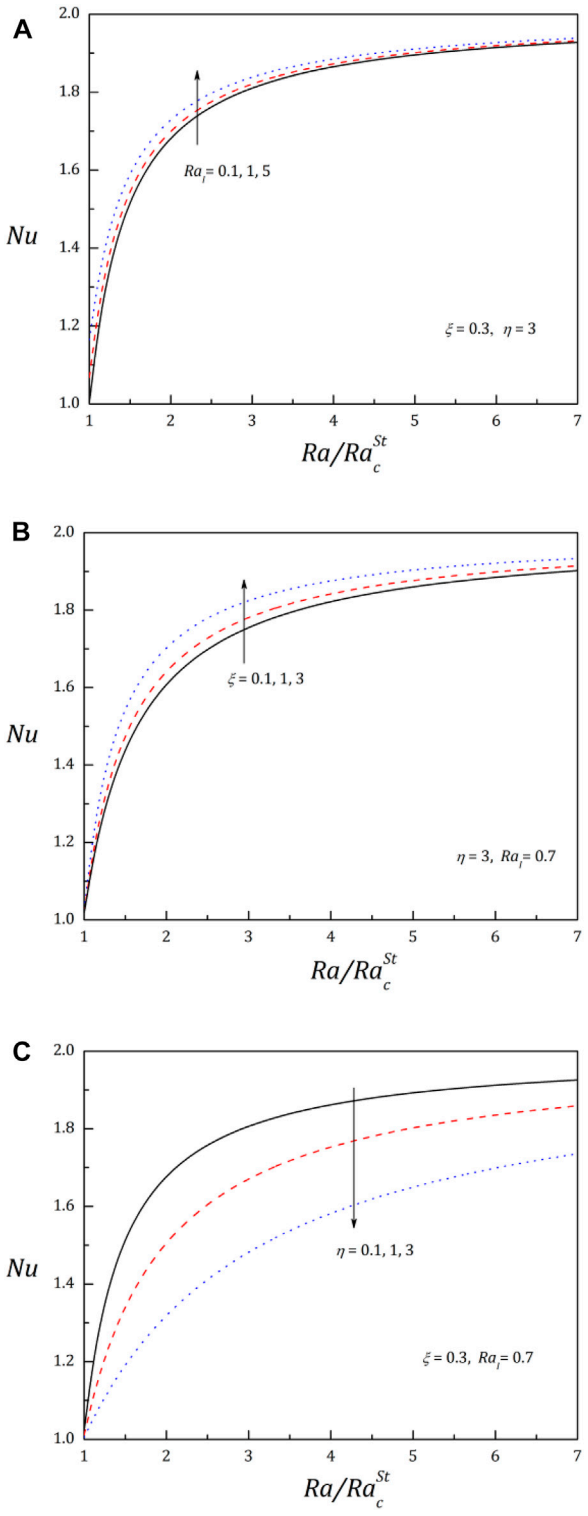

FIGURE 3
Plot of *Nu* against Ra/Ra_c^{St} for varying **(A)** Ra_l, **(B)** ξ and η, and **(C)** η.

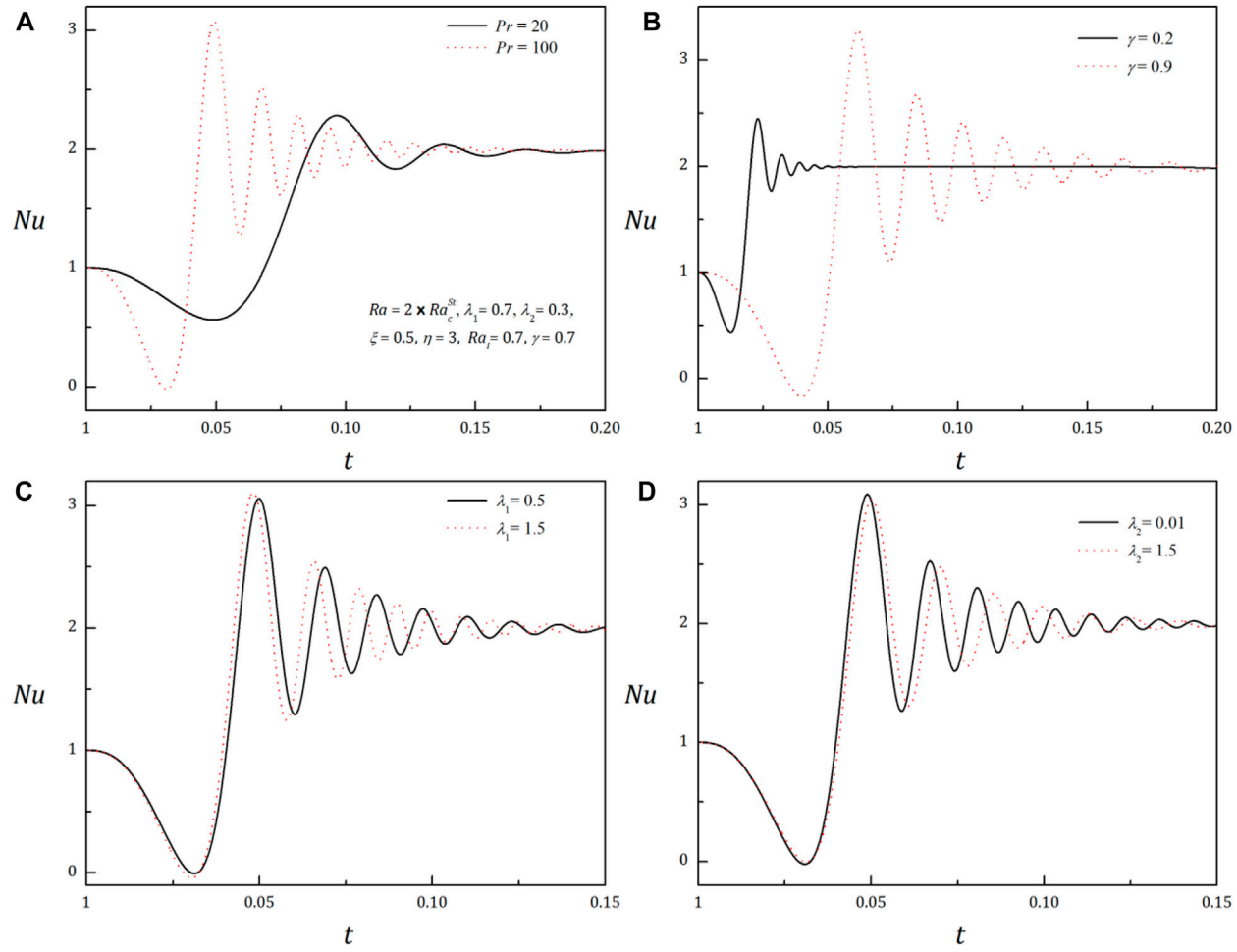

FIGURE 4
Nu versus t for varying **(A)** *Pr*, **(B)** γ,**(C)** λ_1, and **(D)** λ_2

$$\rho_b(z) = \rho_0\left(1 - \alpha\Delta T\left(\sin\left(\sqrt{\mathcal{Q}_I/k_3}\,h(1-z/h)\right)/\sin\left(\sqrt{\mathcal{Q}_I/k_3}\,h\right)\right)\right), \tag{5}$$

$$p_b(z) = \rho_0 g\left(z - \left(\alpha\Delta T/\sqrt{\mathcal{Q}_I/k_3}\right)\left(\cos\left(\sqrt{\mathcal{Q}_I/k_3}\,h(1-z/h)\right)/\sin\left(\sqrt{\mathcal{Q}_I/k_3}\,h\right)\right)\right), \tag{6}$$

$$T_b(z) = T_0 + \Delta T\left(\sin\left(\sqrt{\mathcal{Q}_I/k_3}\,h(1-z/h)\right)/\sin\left(\sqrt{\mathcal{Q}_I/k_3}\,h\right)\right). \tag{7}$$

The stability of the system is studied by imposing the perturbations on the basic state.

$$\mathbf{v} = \mathbf{v}', \rho = \rho_b(z) + \rho', T = T_b(z) + T', \tag{8}$$

where prime represents the quantity in the perturbed state. We use Eqs. 5–8 in the governing Eqs. 1–4 and eliminate p'. Furthermore, assume the flow to be two-dimensional and thus incorporate the stream function such that $(u', w') = (\partial/\partial_z, -\partial/\partial x)\Psi'$. Then, use $(x, z) = h(x^*, z^*), t = (h^2/k_3)t^*, \Psi = k_3\Psi^*$ and $T' = (\Delta T)T^*$ to express the equations in the nondimensional form as follows:

$$\left(1 + \lambda_1\frac{\partial}{\partial t}\right)\left(\frac{1}{\mathrm{Pr}}\frac{\partial}{\partial t}\left(\nabla^2\Psi\right) + Ra\frac{\partial T}{\partial x}\right) = -\left(1 + \lambda_2\frac{\partial}{\partial t}\right)\nabla_1^2\Psi, \tag{9}$$

$$\gamma\frac{\partial T}{\partial t} + f(z)\frac{\partial\Psi}{\partial x} - \left(\frac{\partial\Psi}{\partial x}\frac{\partial T}{\partial z} - \frac{\partial\Psi}{\partial z}\frac{\partial T}{\partial x}\right) = \nabla_1^2 T + Ra_I T, \tag{10}$$

where $f(z) = \sqrt{Ra_I}\cos\left(\sqrt{Ra_I}\,(1-z)\right)/\sin\left(\sqrt{Ra_I}\right)$, $\nabla_1^2 = \partial^2/\partial x^2 + (1/\xi)(\partial^2/\partial z^2)$, and $\nabla_2^2 = \eta(\partial^2/\partial x^2) + \partial^2/\partial z^2$. $Ra = \rho_0\alpha g\Delta T h^3/\mu k_3$ denotes the thermal Rayleigh number, $Ra_I = \mathcal{Q}h^2/k_3$ is the internal Rayleigh number, $Pr = \mu h^2/\varepsilon\rho_0 k_3 K_3$ is the Darcy–Prandtl number, $\lambda_1 = \Lambda_1 k_3/h^2$ is the Deborah number or stress-relaxation parameter, $\lambda_2 = \Lambda_2 k_3/h^2$ is the strain-retardation parameter, and $\xi = K_1/K_3$ and $\eta = k_1/k_3$ denote mechanical and thermal anisotropy parameters, respectively. Because the boundaries are assumed to be stress-free and isothermal, the relevant boundary conditions are

$$\Psi = D^2\Psi = T = 0 \text{ at } z = 0, 1. \tag{11}$$

3 Galerkin weighted-residual technique

In the linear stability theory, the imposed perturbations are anticipated to be infinitesimal, and hence, the nonlinear terms in Eqs. 9–11 can be ignored. The normal mode analysis is used to solve

the resulting eigenvalue problem. Thus, it is supposed that the infinitesimal perturbations are the periodic waves of form

$$(\Psi, T) = (\Psi(z), \Theta(z))e^{i(\omega t + kx)}, \tag{12}$$

where the real variable k is the wavenumber, and the complex variable ω is the temporal growth rate. It decides whether these tiny-recurrent-perturbations either enlarge or degenerate. In thermal convection, wavenumber is a term used to describe the spatial variation of temperature and fluid flow patterns that arise due to temperature differences within the fluid. Wavenumber is a measure of the number of waves that occur in a given distance. The concept of wavenumber is closely related to the concept of wavelength, which is the distance between successive peaks or troughs of a wave. The wavelength and wavenumber are related by the formula $k = 2\pi/\lambda$, where λ is the wavelength of the wave. This shows that the wavenumber is inversely proportional to the wavelength; that is, waves with shorter wavelengths have larger wavenumbers, and waves with longer wavelengths have smaller wavenumbers.

In natural convection, the spatial variation of temperature and fluid flow patterns can take on different wavelengths, depending on factors such as the geometry of the system, the temperature differences within the fluid, and the properties of the fluid itself. The wavelength of these patterns can be quantified in terms of the wavenumber, and the behavior of natural convection can be analyzed in terms of the relationship between the wavenumber and other parameters such as the Rayleigh number.

On substituting Eq. 12 into linearized Eqs. 9–11, we obtain

$$\left(\frac{i\omega}{\mathrm{Pr}}(1 + i\omega\lambda_1)(D^2 - k^2) + (1 + \lambda_2 i\omega)\left(\frac{1}{\xi}D^2 - k^2\right)\right)\Psi + Ra(1 + i\omega\lambda_1)ik\Theta = 0, \tag{13}$$

$$(D^2 - \eta k^2 - i\omega\gamma + Ra_I)\Theta - \mathrm{i}k\, f(z)\Psi = 0, \tag{14}$$

$$\Psi = D^2\Psi = \Theta = 0 \mathrm{at}\, z = 0, 1. \tag{15}$$

According to the Galerkin method, we choose

$$(\Psi(z), \Theta(z)) = (A_1\Psi_1(z), B_1\Theta_1(z)), \tag{16}$$

where A_1 and B_1 are constants, and $\Psi_1(z), \Theta_1(z)$ are so designated that they satisfy the boundary conditions (15). On multiplying Eqs. 13, 14, respectively, by $\Psi_1(z), \Theta_1(z)$ and integrating the resultant equations w. r. t. z between the limits 0 and 1, we acquire

$$\left(\frac{i\omega}{\mathrm{Pr}}(1 + i\omega\lambda_1)X_0 + (1 + i\omega\lambda_2)X_1\right)A_1 + ikRa(1 + i\omega\lambda_1)X_2B_1 = 0, \tag{17}$$

$$ikX_4A_1 + \left((i\omega\gamma - Ra_I)X_5 - X_6\right)B_1 = 0, \tag{18}$$

where $X_0 = \langle\Psi_1(D^2 - k^2)\Psi_1\rangle$, $X_1 = \langle\Psi_1(\frac{1}{\xi}D^2 - k^2)\Psi_1\rangle$, $X_2 = \langle\Psi_1\Theta_1\rangle$, $X_4 = \langle f(z)\Theta_1\Psi_1\rangle$, $X_5 = \langle\Theta_1^2\rangle$, and $X_6 = \langle\Theta_1(D^2 - \eta k^2)\Theta_1\rangle$. The angular brackets denote the integral w. r. t. z between the limits 0 and 1. The requirement for the existence of a non-trivial solution of Eqs. 17 and 18 yield the expression for Rayleigh number:

$$Ra = \frac{N_r + i\omega N_i}{k^2X_2X_4\left(1 + \omega^2\lambda_1^2\right)}. \tag{19}$$

Because $\omega = \omega_r + i\omega_i$, the case $\omega_r < 0$ specifies a stable state, while $\omega_r > 0$ corresponds to the unstable mode. A neutral state is attained for $\omega_r = 0$. The steady-marginal stability can be observed for $\omega = 0$ (i.e., $\omega_r = \omega_i = 0$), with which Eq. 19 abridges to the expression of stationary Rayleigh number:

$$Ra^{st} = X_1(Ra_IX_5 + X_6)/k^2X_2X_4. \tag{20}$$

The trial functions that satisfy the boundary conditions (15) are obviously

$$(\Psi_1(z), \Theta_1(z)) = (\sin\pi z, \sin\pi z).$$

On using these, one can estimate X_1, X_2, X_4, X_5 and X_6 value and then substituting into Eq. 20 to get

$$Ra^{st} = \frac{\delta_1^2}{4\pi^2k^2}(4\pi^2 - Ra_I)(\delta_2^2 - Ra_I), \tag{21}$$

where $\delta_1^2 = k^2 + \pi^2/\xi$ and $\delta_2^2 = \eta k^2 + \pi^2$. Eq. 21 is free from viscoelasticity, so it resembles the equation obtained for a viscous Newtonian fluid. The validity of our work can be ascertained through Table 1, wherein we recovered the previous classical results as a special case of Eq. 21

Now, we discuss the behavior of Eq. 19 with the nonzero growth rate, that is, $\omega \neq 0$. As Ra portrays a physical phenomenon, it should not be imaginary and hence, Eq. 19 admits $N_i = 0$ as $\omega \neq 0$. This affords the expression forω^2:

$$\omega^2 = \frac{X_1(X_5(\gamma + \lambda_1Ra_I) - \lambda_2(X_6 + X_5Ra_I) + \lambda_1X_6) - Pr^{-1}X_0(X_6 + X_5Ra_I).}{\lambda_1(\lambda_1Pr^{-1}X_0(X_6 + X_5Ra_I) - \gamma\lambda_2X_1X_5)} \tag{22}$$

The real part of Eq. 19 then symbolizes the expression for the oscillatory Rayleigh number:

$$Ra^{Osc} = \frac{N_r}{k^2X_2X_4\left(I + \omega^2\lambda_1^2\right)}. \tag{23}$$

To estimate Ra_c^{Osc} , we minimize (23) w. r. t. k, after substituting $\omega^2\,(>0)$ from Eq. 22.

4 Weak nonlinear theory

Nonlinear stability analysis is preferred to measure convection amplitudes and heat transfer. This facilitates comprehension of the physical mechanism with a little mathematical labor. This is a basic step toward grasping the full nonlinearity of the problem. Because the perturbations are assumed to be of finite amplitude, it is reasonable to represent them in the form of a limited Fourier series, as follows:

$$\Psi = \mathrm{A}_{11}(t)\sin(kx)\sin(\pi z), \tag{24}$$

$$T = B_{11}(t)\cos(kx)\sin(\pi z) + B_{02}(t)\sin(2\pi z). \tag{25}$$

The finite amplitudes of A and B subscripts for unsteady nonlinear convection are to be assessed by the dynamics of the system. Using Eqs. 24 and 25 in Eqs. 9 and 10 and comparing the coefficients of like terms, the following fourth-order Lorenz system of autonomous nonlinear differential equations is obtained:

$$d/dt(\mathrm{A}_{11}, G_1, B_{11}, B_{12}) = (\mathrm{G}_1, D_1, G_2, D_2), \tag{26}$$

where

$$D_1 = -\Pr\delta^{-2}\left(\lambda_1^{-1}\left(\delta_1^2\left(A_{11}+\lambda_2 G_1\right)+\left(\delta^2\Pr^{-1}G_1+RakB_{11}\right)\right)+RakG_2\right),$$

$$G_2 = -\gamma^{-1}\left(kf\left(z\right)A_{11}+\delta_2^2 B_{11}-Ra_I B_{11}+2\pi k A_{11}B_{02}\right),$$

$$D_2 = -\gamma^{-1}\left(\left(4\pi^2-Ra_I\right)B_{02}-\pi k A_{11}B_{11}/2\right).$$

There is no suitable analytical method to obtain a closed-form solution of the aforementioned system. Thus, a competent numerical technique is recommended. Although it may not be possible to make precise quantitative predictions, there are several qualitative insights that can be gleaned from the available data or theoretical models. As system of Eq. 26 is homogeneously bounded with time, it retains numerous features of the full problem. For $Ra_I < (0.5)\delta_2^2 + 2\pi^2$, the velocity field possesses a constant negative divergence; that is,

$$\nabla\cdot\left(d/dt\left(A_{11},G_1,B_{11},B_{12}\right)\right) = -\lambda_1^{-1}\left(\Pr\lambda_2\delta_1^2\delta^{-2}+1\right) - \gamma^{-1}\left(\delta_2^2+4\pi^2-2Ra_I\right). \quad (27)$$

This implies that the system is constrained. In dynamical systems theory, a system is said to be constrained if it is subject to certain limitations or conditions. These constraints can arise due to physical, mathematical, or other reasons. For example, a mechanical system may be constrained by rigid walls or other physical barriers that restrict the motion of its components. When a system is constrained, the possible states that it can occupy are limited to a subset of its phase space. The phase space is the space of all possible states of the system, and it is often represented as a high-dimensional space in which each dimension corresponds to a particular variable or parameter of the system. Because the system is constrained, the phase space paths are drawn toward a set of measure zero or a fixed point. A set of measure zero is a subset of the phase space that has zero volume or probability. In other words, it is a set of states that is extremely unlikely to be reached by the system. A fixed point, on the other hand, is a state of the system that does not change over time. When the phase space paths are drawn toward a set of measure zero or a fixed point, this can result in volume shrinkage in the phase space. This means that the volume of the phase space that is accessible to the system becomes smaller over time as the system is forced to occupy a smaller subset of the phase space due to the constraints. This is revealed by Eq. 28 through the fact that if a set of preliminary points in space fills a volume $V(0)$ at t = 0, then after time t, the endpoints of the corresponding paths will occupy a region

$$V(t) = V(0)\exp\left(-\left(\lambda_1^{-1}\left(\Pr\lambda_2\delta_1^2\delta^{-2}+1\right)-\gamma^{-1}\left(\delta_2^2+4\pi^2-2Ra_I\right)\right)t\right). \quad (28)$$

The larger values of the Darcy–Prandtl number and strain-retardation number and smaller values of the Deborah number and heat-capacities ratio are used to emphasize the exponential deterioration of volume with time.

Upon switching from qualitative exploration, we now look into the existence of an analytical solution. As the finite amplitude instability can be well explored analytically using the truncated model shown in Eqs. 24 and 25, a closed-form solution of Eq. 26 is used for the steady case. The following expression is obtained by Eq. 26 after removing all terms except A_{11}:

$$\left(\delta_1^2 - Rak^2 f\left(z\right)\left(\left(\delta_2^2-Ra_I\right)+\left(2\pi^2k^2/\left(\pi^2-Ra_I/4\right)\right)\left(A_{11}^2/8\right)\right)^{-1}\right)A_{11} = 0.$$

The solution $A_{11} = 0$ symbolizes the pure conduction state. Thus, the second option guarantees the likelihood of finite amplitude steady convection by offering the value of the finite-amplitude $A_{11}^2/8$ of convective motions in the form

$$A_{11}^2/8 = \left(\left(\pi^2-Ra_I/4\right)/2\pi^2k^2\right)\left(Rak^2 f\left(z\right)\delta_1^{-2}-\left(\delta_2^2-Ra_I\right)\right). \quad (29)$$

Rather than merely defining the onset criterion, the impact of the Rayleigh number can be swiftly documented by analyzing its effect on heat transport. In the study of convection, determining the quantity of heat transported past the layer is of utmost importance. Because the basic state is immobile, heat transfer in this state is limited to conduction. However, as the Rayleigh number exceeds the threshold, convection develops. The Nusselt number is used to describe the convection-heat transport throughout the stratum.

$$Nu = 1+\left(\int_0^{2\pi/k_c}\left(\partial T/\partial z\right)dx\Big/\int_0^{2\pi/k_c}\left(\partial T_b/\partial z\right)dx\right)_{z=0}$$

By using Eqs. 28 and 7, one can obtain

$$Nu = 1-2\pi\left(\left(\tan\sqrt{Ra_I}\right)\Big/\sqrt{Ra_I}\right)\left(B_{02}\right)_{z=0}.$$

Substituting the value of B_{02} at $z = 0$ gives

$$Nu = 1-2\pi\left(\frac{\tan\sqrt{Ra_I}}{\sqrt{Ra_I}}\right) \times\left(\frac{-\pi k^2 f\left(0\right)}{\left(\left(\pi^2-Ra_I/4\right)\left(\delta_2^2-Ra_I\right)+2\pi^2k^2\left(A_{11}^2/8\right)\right)}\left(A_{11}^2/8\right)\right).$$

This can be further simplified as

$$Nu = 1+2\pi^2k^2\left(A_{11}^2/8\right)\Big/ \times\left(\left(\pi^2-Ra_I/4\right)\left(\delta_2^2-Ra_I\right)+2\pi^2k^2\left(A_{11}^2/8\right)\right). \quad (30)$$

This analysis is valid for Rayleigh numbers close to their threshold value. By including more terms in the Fourier expansion, one can anticipate better outcomes. The Runge–Kutta–Gill method is used to clarify the unsteady Eq. 26. The calculated amplitude values for various time intervals are then used to estimate Nu as a function of t.

5 Results and discussion

The onset of convection refers to the point at which fluid motion due to buoyancy forces begins to occur in a fluid that is initially at rest. This occurs when a fluid is subjected to a temperature difference that is large enough to cause density variations within the fluid, which in turn generate buoyancy forces that drive fluid motion. The onset of convection can be characterized by a critical value of a dimensionless parameter called the Rayleigh number. The Rayleigh number represents the ratio of buoyancy forces to viscous forces in the fluid. For a fluid layer that is initially at rest, the onset of convection occurs when the Rayleigh number exceeds a critical value that is specific to the geometry and boundary conditions of the system. Above this critical value, the buoyancy forces overcome the viscous forces and initiate fluid motion. The critical Rayleigh number can be determined through theoretical analysis or experimental observation. The onset of convection is an

important phenomenon in many natural and industrial systems, including geophysical flows, crystal growth, and industrial heat transfer processes. Understanding the onset of convection is important for predicting the behavior of these systems and for designing efficient heat transfer systems.

The primary objective of investigating a convection problem is to determine the smallest possible Rayleigh number that demonstrates convection. Fine-tuning the parameters that define the Rayleigh number is advantageous for deferring or accelerating convective motions. This study examines the interaction between variable permeability, thermal diffusivity, and internal heat generation. The point (k_c, Ra_c) at which the marginal stability curve reaches the least signifies the convection threshold. The detailed behavior of this critical value is deliberated as a function of the strain-retardation number. Figures 1A–D display the dependence of critical Ra on the strain-retardation parameter λ_2. It has already been mentioned that Ra_c^{St} is independent of viscoelasticity. This fact is justified by a horizontal dotted line (corresponding to Ra_c^{St}) in Figure 1A, which is invariant with respect to λ_2, λ_1 and located at the higher level. All the Ra^{Osc} curves lie at the lower level, indicating that the onset of convection is through oscillatory mode. It is observed that Ra_c^{Osc} increases with λ_2. Thus, the strain-retardation parameter makes the system more stable, but this stabilizing effect is retarded by λ_1 because there is a significant decrease in Ra_c^{Osc} w.r.t. λ_1. We note that the influence of λ_2 on Ra_c^{Osc} is constrained to a specific range depending on the value of λ_1. Beyond this range, the oscillatory convection ceases to occur.

In Figure 1B, the effect of the mechanical anisotropy parameter, which signifies heterogeneity in the permeability of the porous layer, is expressed. The values of both Ra_c^{St} and Ra_c^{Osc} decline with ξ. This indicates that the onset of convection can be advanced by increasing the anisotropy in permeability. Figure 1C exhibits the impact of anisotropy in thermal diffusivity on the threshold of convection. It portrays that by choosing larger values for η, one can enhance the values of Ra_c^{St} and Ra_c^{Osc}. Hence, stabilization can be achieved through increasing η. Figure 1D depicts the variation of Ra_c with the internal Rayleigh number. Convective motions in both steady and oscillatory modes vary considerably with the aid of internal heating. This is revealed through the fact that when Ra_I is increased, the Ra_c curves are shifted downward in both stationary and oscillatory cases. This confirms that internal heating favors the onset of convection.

One of the main objectives of the present paper is to analyze the significance of controlling the convection by the anisotropic nature of the porous layer. The detailed behavior of Ra_c^{Osc} as a function of anisotropy parameters is demonstrated via Figure 2A. The black solid curve with regards to the left-side axis shows that the value of Ra_c^{Osc} decreases with ξ. Therefore, the anisotropy in permeability causes the oscillatory convective motions to occur at the earlier stage. However, note that this destabilization is more sensitive for the small and moderate values of ξ. Furthermore, the red curve drawn with reference to the right-side axis makes us aware of the stabilizing role of anisotropic thermal diffusivity. The value of Ra_c^{Osc} increases almost linearly with η.

The impact of Ra_I, which signifies the strength of the internal heat source, is expressed through the curves in the (Ra_c, Ra_I) plane (see Figure 2B). Both Ra_c^{St} and Ra_c^{Osc} plummet with Ra_I. This indicates that onset of convection can be brought forward by increasing the rate of internal heating. The figure also exhibits that these critical curves are shifted upward when we increase the thermal anisotropy parameter. So, the heterogeneity of thermal diffusivity retards the destabilization caused by an internal heat source.

To explore the activity of Ra_c with respect to the varying Prandtl number, we plot the critical curves in the (Ra_c, Pr) plane in Figure 2C. For smaller values of Pr, there is a swift decrease in the value of Ra_c^{Osc}. This trend continues up to some specific value of Pr, beyond which Ra_c^{Osc} becomes independent of Pr. Thus, a destabilizing effect is reported for smaller values of Pr. The dotted horizontal line, which corresponds to the stationary case, shows that Ra_c^{St} is not influenced by the varying Prandtl number. Furthermore, the value of Ra_c^{St} is much larger than Ra_c^{Osc}. Another fact that can be noticed through this figure is the enhancement in the values of Ra_c^{Osc} with respect to the increasing heat capacities ratio. Therefore, the destabilization caused by increasing Pr can be suppressed by γ. Linear stability analysis, which provided us with a glimpse of the convection threshold, is followed by weak nonlinear stability analysis.

This study helped us to measure the amplitude of convective motions and the amount of heat transfer. The Nusselt number (Nu) that signifies the extent of convective heat transfer is calculated. The control of Rayleigh number over Nu is presented in Figures 3A–C. The value of Nu is found to be 1 at the onset, while as the Ra_c increases to about three times the value of the critical Rayleigh number, the Nusselt number also increases. Thereafter, Nu becomes less sensitive to Ra_c. Thus, one can conclude that in the vicinity of the onset of convection, the enhancement of heat transfer occurs, and the same magnitude is maintained even after the further increase in Ra_c.

From Figures 3A,B, Nu is found to upsurge for the higher Ra_I and ξ. Therefore, heat transport is amplified by introducing an internal source within the porous layer and by choosing the anisotropy in permeability. Furthermore, through Figure 3C, we notice that there is a significant reduction in the value of Nu w.r.t. the thermal anisotropy parameter. The heat transfer across the layer decreases considerably with increasing anisotropy in thermal diffusivity.

In unsteady finite-amplitude analysis, the fourth-order Lorenz model has been solved numerically using the Runge–Kutta–Gill method. The amplitudes are obtained as the functions of t and then substituted into the expression of Nu. In general, the Nusselt number is a function of several parameters, including the fluid velocity, temperature, and physical properties of the fluid, and it can vary with time during transient heat transfer processes. The behavior of the heat transfer coefficient with respect to time is displayed through the curves in the (Nu, t) plane, as shown in Figures 4A–D. One can observe from these figures that at the onset of natural convection, heat transfer initially occurs through conduction alone, and Nu has a value of 1, which corresponds to purely conductive heat transfer. As the fluid flow starts to develop, convective heat transfer becomes dominant, and the Nusselt number becomes sensitive to time. The behavior of the Nusselt number during this transient phase is oscillatory, with the value of Nu fluctuating about a mean value. This means that the heat transfer coefficient, which is related to the Nusselt number, varies periodically in time, with some oscillations. However, as time progresses, the oscillatory behavior of the Nusselt

number starts to decay, and after a short period of time, the heat transfer process reaches a steady state. At this point, the Nusselt number reaches a mean value that is similar to the value of Nu obtained in the steady-state, finite-amplitude case. Thus, in general, these figures display that the behavior of the Nusselt number during a transient heat transfer process is initially oscillatory and sensitive to time but eventually reaches a steady-state mean value. This behavior is a result of the interplay between conduction and convection heat transfer mechanisms during the transient phase of the process.

Figures 4A, B depict a considerable enhancement in the value of the heat transfer coefficient with the Prandtl number and the heat capacities ratio. It also shows that the sensitivity of *Nu* with respect to *t* increases with increasing *Pr* and γ. Figure 4C shows that the amount of convective heat transfer rises with Deborah's number. However, the strain-retardation parameter shows a decrease in the heat-transfer coefficient (see Figure 4D). This justifies the fact that the influence of retardation time is to inhibit the heat transfer.

6 Conclusion

The aforementioned results support the subsequent conclusions. Due to a competition between thermal diffusion, viscoelastic relaxation, anisotropy in permeability, thermal diffusivity, and internal heat generation, the conduction state degenerated into convective motions via the oscillatory mode. Viscoelasticity, the heat capacity ratio, and the Prandtl number have no effect on stationary convection. Increasing anisotropy in permeability, the coefficient of internal heat generation, and stress-relaxation parameters are associated with an early onset. It has been discovered that anisotropy in thermal diffusivity and heat capacity ratios delays convection. Strain-retardation time reinforces oscillatory case stability. The range of retardation parameter values within which oscillatory convection occurs is determined by the magnitude of the relaxation time. Beyond this range, oscillatory convection ceases, and stationary mode instability is then established. The Prandtl number indicates the effect of destabilization on oscillatory convection. The coefficient of heat transfer increases with the Rayleigh number, the internal Rayleigh number, the Deborah number, the Prandtl number, anisotropy in permeability, and the heat capacity ratio. Increasing values of the strain-retardation parameter and anisotropy in thermal diffusivity indicate an inverse trend. It is possible to promote or inhibit convection in a given system by adjusting the relevant parameters in accordance with practical application. In other words, the onset and intensity of convection can be manipulated by adjusting the system's controlling parameters, such as temperature gradients, fluid properties, and geometrical factors. Several of the prior results were obtained through the use of special cases. This provides substantial support for the results of the current investigation (Eswaramoorthi et al., 2023).

Data availability statement

The original contributions presented in the study are included in the article/Supplementary Material. Further inquiries can be directed to the corresponding authors.

Author contributions

MS, BH, AS: conceptualization, methodology, software, formal analysis, and writing—original draft. AH: writing—original draft, data curation, investigation, visualization, and validation. UK: conceptualization, writing—original draft, writing—review and editing, supervision, and resources. RK: validation, investigation, writing—review and editing, and formal analysis. VK: writing—review and editing, data curation, validation, and resources. All authors contributed to the article and approved the submitted version.

Funding

This work was partially funded by the research center of the Future University in Egypt 2023.

Acknowledgments

The authors would like to express their gratitude to the reviewers for their constructive remarks and insightful suggestions, which have significantly improved the current work.

Conflict of interest

The authors declare that the research was conducted in the absence of any commercial or financial relationships that could be construed as a potential conflict of interest.

Publisher's note

References

Agarwal, S., Bhadauria, B. S., and Siddheshwar, P. G. (2011). Thermal instability of a nanofluid saturating a rotating anisotropic porous medium. *Spec. Top. Rev. Porous Media* 2 (1), 53–64. doi:10.1615/specialtopicsrevporousmedia.v2.i1.60

Ahmed, S. E., and Rashed, Z. Z. (2019). MHD natural convection in a heat generating porous medium-filled wavy enclosures using Buongiorno's nanofluid model. *Case Stud. Therm. Eng.* 14, 100430. doi:10.1016/j.csite.2019.100430

Capone, F., De Luca, R., and Gentile, M. (2020). Thermal convection in rotating anisotropic bidispersive porous layers. *Mech. Res. Comm.* 110, 103601. doi:10.1016/j.mechrescom.2020.103601

Chandra, P., and Satyamurty, V. V. (2012). Effect of anisotropy on natural convective flow through a rectangular porous slab. *J. Porous Media* 15 (6), 595–605. doi:10.1615/jpormedia.v15.i6.70

Eswaramoorthi, S., Loganathan, K., Faisal, M., Botmart, T., and Shah, N. A. (2023). Analytical and numerical investigation of Darcy-Forchheimer flow of a nonlinear-radiative non- Newtonian fluid over a Riga plate with entropy optimization. *Ain Shams Eng. J.* 14 (3), 101887. doi:10.1016/j.asej.2022.101887

Gasser, R. D., and Kazimi, M. S. (1976). Onset of convection in a porous medium with internal heat generation. *J. Heat. Transf.* 98 (1), 49–54. doi:10.1115/1.3450468

Govender, S. (2006). Effect of anisotropy on stability of convection in a rotating porous layer distant from the center of rotation. *J. Porous Media* 9 (7), 651–662. doi:10.1615/jpormedia.v9.i7.40)

Griffiths, R. W. (1987). Effects of earth's rotation on convection in magma chambers. *Earth Planet Sci. Lett.* 85, 525–536. doi:10.1016/0012-821x(87)90146-4

Horton, C. W., and Rogers, F. T. (1945). Convection currents in a porous medium. *J. Al. Phys.* 16, 367–370. doi:10.1063/1.1707601

Ingham, D. B., and Pop, I. (2005). *Transport phenomena in porous media, III*. Amsterdam, Netherlands: Elsevier.

Kim, M. C., Lee, S. B., Kim, S., and Chung, B. J. (2003). Thermal instability of viscoelastic fluids in porous media. *Int. J. Heat. Mass Transf.* 46, 5065–5072. doi:10.1016/s0017-9310(03)00363-6

Lapwood, E. R. (1948). Convection of a fluid in a porous medium. *Proc. Camb. Phil. Soc.* 44, 508–521. doi:10.1017/s030500410002452x

Li, Z., and Khayat, R. E. (2005). Finite-amplitude Rayleigh–Benard convection and pattern selection for viscoelastic fluids. *J. Fluid Mech.* 529, 221–251. doi:10.1017/s0022112005003563

Lowrie, W. (2020). *Fundamentals of geophysics*. Cambridge, United Kingdom: Cambridge University Press.

Mahabaleshwar, U. S., Basavaraja, D., Wang, S., Lorenzini, G., and Lorenzini, E. (2017). Convection in a porous medium with variable internal heat source and variable gravity. *Int. J. Heat. Mass Transf.* 111, 651–656. doi:10.1016/j.ijheatmasstransfer.2017.04.030

Malashetty, M. S., Shivakumara, I. S., Kulkarni, S., and Swamy, M. (2006a). Convective instability of Oldroyd-B fluid saturated porous layer heated from below using a thermal non-equilibrium model. *Transp. Porous Med.* 62, 123–139. doi:10.1007/s11242-005-1893-0

Malashetty, M. S., Siddheshwar, P. G., and Swamy, M. (2006b). Effect of thermal modulation on the onset of convection in a viscoelastic fluid saturated porous layer. *Transp. Porous Media* 62, 55–79. doi:10.1007/s11242-005-4507-y

Malashetty, M. S., Swamy, M. S., and Sidram, W. (2011). Double diffusive convection in a rotating anisotropic porous layer saturated with viscoelastic fluid. *Int. J. Therm. Sci.* 50, 1757–1769. doi:10.1016/j.ijthermalsci.2011.04.006

Malashetty, M. S., and Swamy, M. (2007b). The effect of rotation on the onset of convection in a horizontal anisotropic porous layer. *Int. J. Therm. Sci.* 46, 1023–1032. doi:10.1016/j.ijthermalsci.2006.12.007

Malashetty, M. S., and Swamy, M. (2010). The onset of convection in a binary fluid saturated anisotropic porous layer. *Int. J. Therm. Sci.* 49, 867–878. doi:10.1016/j.ijthermalsci.2009.12.008

Malashetty, M. S., and Swamy, M. (2007a). The onset of convection in a viscoelastic liquid saturated anisotropic porous layer. *Transp. Porous Media* 67, 203–218. doi:10.1007/s11242-006-9001-7

Malashetty, M. S., Tan, W. C., and Swamy, M. (2009). The onset of double diffusive convection in a binary viscoelastic fluid saturated anisotropic porous layer. *Phys. Fluids* 21 (8), 084101. doi:10.1063/1.3194288

McKibbin, R. (1985). "Thermal convection in layered and anisotropic porous media: A review," in *Convective flows in porous media*. Editors R. A. Wooding and I. White (Wellington, NZ: Department of Scientific and Industrial Research), 113–127.

Nield, D. A., and Bejan, A. (2006). *Convection in porous media*. New York, NY, United States: Springer.

Enagi, N. K., Chavaraddi, K. B., Kulkarni, S., and Ramesh, G. K. (2022). Effect of maximum density and internal heating on the stability of rotating fluid saturated porous layer using LTNE model. *Heliyon* 8, e09620. doi:10.1016/j.heliyon.2022.e09620

O'Connell, R. J., and Budiansky, B. (1977). Viscoelastic properties of fluid saturated cracked solids. *J. Geophys. Res.* 82, 5719–5735. doi:10.1029/jb082i036p05719

Raju, C. S. K., Ahammad, N. A., Sajjan, K., Shah, N. A., Yook, S. J., and Kumar, M. D. (2022). Nonlinear movements of axisymmetric ternary hybrid nanofluids in a thermally radiated expanding or contracting permeable Darcy Walls with different shapes and densities: Simple linear regression. *Int. Comm. Heat. Mass* 135, 106110. doi:10.1016/j.icheatmasstransfer.2022.106110

Rudraiah, N., Kaloni, P. N., and Radhadevi, P. V. (1989). Oscillatory convection in a viscoelastic fluid through a porous layer heated from below. *Rheol. Acta* 28, 48–53. doi:10.1007/bf01354768

Saravanan, S., and Purusothaman, A. (2009). Floquet instability of a gravity modulated Rayleigh–Benard problem in an anisotropic porous medium. *Int. J. Therm. Sci.* 48, 2085–2091. doi:10.1016/j.ijthermalsci.2009.04.001

Sivakumar, T., and Saravanan, S. (2009). Effect of gravity modulation on the onset of convection in a horizontal anisotropic porous layer. *AIP Conf. Proc.* 1146, 472–478.

Srivastava, A. K., Bhadauria, B. S., and Kumar, J. (2011). Magnetoconvection in an anisotropic porous layer using thermal nonequilibrium model. *Spec. Top. Rev. Porous Media* 2 (1), 1–10. doi:10.1615/specialtopicsrevporousmedia.v2.i1.10

Storesletten, L. (1998). "Effects of anisotropy on convective flow through porous media," in *Transport phenomena in porous media* (Oxford, United Kingdom: Pergamon Press), 261–283.

Swamy, M. S. (2017). Combined effect of thermal modulation and AC electric field on the onset of electrothermoconvection in anisotropic porous layer. *Am. J. Heat Transf.* 4 (3), 95–114. doi:10.7726/ajhmt.2017.1011

Swamy, M. S., Naduvinamani, N. B., and Sidram, W. (2012). Onset of Darcy-Brinkman convection in a binary viscoelastic fluid saturated porous layer. *Transp. Porous Med.* 94, 339–357. doi:10.1007/s11242-012-0008-y

Swamy, M. S., Patil, S., and Pallavi, S. P. (2019). Soret and dufour effect induced double- diffusive reaction-convection in anisotropic porous layer. *J. Nanofluids* 8, 1329–1337. doi:10.1166/jon.2019.1688

Swamy, M. S., Shivakumara, I. S., and Naduvinamani, N. B. (2014). Effect of gravity modulation on electrothermal convection in dielectric fluid saturated anisotropic porous layer. *J. Heat. Transf.* 136, 032601.

Swamy, M. S., Shivakumara, I. S., and Sidram, W. (2013). The onset of convection in a gravity-modulated viscoelastic fluid-saturated anisotropic porous layer. *Spec. Top. Rev. Porous Media* 4 (1), 69–80. doi:10.1615/specialtopicsrevporousmedia.v4.i1.70

Thirlby, R. (1970). Convection in an internally heated layer. *J. Fluid Mech.* 44, 673–693. doi:10.1017/s0022112070002082

Upadhya, S. M., Raju, S. V. S. R., Raju, C. S. K., Shah, N. A., and Chung, J. D. (2022). Importance of entropy generation on Casson, Micropolar and Hybrid magneto-nanofluids in a suspension of cross diffusion. *Chin. J. Phys.* 77 (2022), 1080–1101. doi:10.1016/j.cjph.2021.10.016

Vadasz, P. (2008). *Emerging topics in heat and mass transfer in porous media*. New York, NY, United States: Springer.

Vafai, K. (2005). *Handbook of porous media*. Boca Raton, Florida, United States: Taylor and Francis.

Yadav, D., Mahabaleshwar, U. S., Wakif, A., and Chand, R. (2021). Significance of the inconstant viscosity and internal heat generation on the occurrence of Darcy Brinkman convective motion in a couple-stress fluid saturated porous medium an analytical solution. *Int. Comm. Heat. Mass Transf.* 122, 105165. doi:10.1016/j.icheatmasstransfer.2021.105165

Yoon, D. Y., Kim, M. C., and Choi, C. K. (2004). The onset of oscillatory convection in a horizontal porous layer saturated with viscoelastic liquid. *Transp. Porous Media* 55, 275–284. doi:10.1023/b:tipm.0000013328.69773.a1

frontiers | Frontiers in Materials

TYPE Original Research
PUBLISHED 29 June 2023
DOI 10.3389/fmats.2023.1216757

OPEN ACCESS

EDITED BY
Noor Saeed Khan,
University of Education Lahore, Pakistan

REVIEWED BY
M. D. Shamshuddin,
SR University, India
Zafar Mahmood,
Hazara University, Pakistan

*CORRESPONDENCE
Umair Khan,
umairkhan@iba-suk.edu.pk

RECEIVED 04 May 2023
ACCEPTED 19 June 2023
PUBLISHED 29 June 2023

CITATION
Tanuja TN, Kavitha L, Varma SVK, Khan U, Sherif E-SM, Hassan AM, Pop I, Sarada K and Gill HS (2023), Flow and heat transfer analysis on micropolar fluid through a porous medium between a clear and Al_2O_3 – Cu/H_2O in conducting field. *Front. Mater.* 10:1216757. doi: 10.3389/fmats.2023.1216757

Flow and heat transfer analysis on micropolar fluid through a porous medium between a clear and Al_2O_3 – Cu/H_2O in conducting field

T. N. Tanuja[1], L. Kavitha[1], S. V. K. Varma[1], Umair Khan[2,3]*, El-Sayed M. Sherif[4], Ahmed M. Hassan[5], Ioan Pop[6], K. Sarada[7] and Harjot Singh Gill[8]

[1]Department of Mathematics, School of Applied Sciences, REVA University, Bengaluru, Karnataka, India, [2]Department of Mathematical Sciences, Faculty of Science and Technology, Universiti Kebangsaan Malaysia, Selangor, Malaysia, [3]Department of Mathematics and Social Sciences, Sukkur IBA University, Sukkur, Sindh, Pakistan, [4]Mechanical Engineering Department, College of Engineering, King Saud University, Riyadh, Saudi Arabia, [5]Mechanical Engineering, Future University in Egypt, New Cairo, Egypt, [6]Department of Mathematics, Babes-Bolyai University, Cluj-Napoca, Romania, [7]Department of Mathematics, Government City College, Nayapul, Hyderabad, India, [8]Department of Mechanical Engineering and University Centre for Research and Development, Chandigarh University, Mohali, Punjab, India

The current study is focused on the flow of micropolar liquid in a saturated permeable medium sandwiched between clear and hybrid nanofluid filled in an inclined channel, with radiation and dissipation effects. Copper and Aluminium oxide nanoparticles is considered along with base (water) fluid. The solution for velocity, micro rotational velocity, and temperature are determined by applying the regular perturbation technique to the dimensionless version of the governing equations. The heat transport rate at the left $y = -1$ and right $y = 2$ plate is also calculated, as well as shear stress expressed in terms of skin-friction coefficient and Nusselt number. The result obtained for various physical parameters are analyzed through several graphs and tables. Results reveal that an increase in the material parameter of micropolar fluid, the motion of the fluid flow decreases. The heat transport rate is enhanced and the velocity is degraded by the magnetic parameter. The Hybrid nanofluid temperature is greater when compared to clear and binary hybrid nanofluid. This work establishes the mechanisms for heat transport enhancement on micropolar liquid through a porous medium between a clear and hybrid nanofluid in conducting field.

KEYWORDS

micropolar fluid, three-phase flow, hybrid nanofluids, inclined channel, numerical solutions

1 Introduction

Micropolar fluids are special non-Newtonian fluids with microscopic effects like micro rotational and rotational inertia. Eringen has put out the theory of micropolar fluids (Eringen, 1964), (Eringen, 1996). Many academics studied micropolar fluids by outlining many practical uses. Micropolar liquids may be utilized as lubricants since they have lesser friction coefficients than Newtonian liquids (Bansal et al., 2020), (Khonsari, 1990). The

significance of micropolar fluids exists in various industries such as the metallic plate cooling, colonial and suspension solutions, liquid crystals, blood (Ikbal et al., 2009), and nuclear power plant (Siddiqa et al., 2021). Recently, nanofluids have so many applications in many industrial sectors, In connection to this, many fluid dynamics experts are currently exhibiting a significant interest in studying them. As the volume percentage of the suspended nanoparticles increases, the thermal conductivity of nanofluids rises (Lee and Eastman, 1999; Wang et al., 1999; Li and Xuan, 2000; Mintsa et al., 2009). Additionally, Wang & Mujumdar's (Wang and Mujumdar, 2007) comparison of their data with other sources shows that the rate of thermal conduction of nanofluids improves as the size of the particles decreases. As temperature rises, the thermal conductivity likewise rises (Das et al., 2003), (Hayat et al., 2019) and (Gopal et al., 2020). Anwar et al. (Bég et al., 2019) swotted the two-phase stream of a fluids in the presence of a permeable medium. Under the isothermal condition, Kumar et al. (Kumar et al., 2010) carried out the scrutiny of the two-phase stream of micropolar and Newtonian fluid in the channel. The study of two-layered non-miscible liquids in flat mini channels was swotted by Khaled et al. (Khaled and Vafai, 2014) and Umavathi et al. (Umavathi and Anwar Bég, 2020a). Chamkha (Chamkha, 2000) scrutinized the influence of a permeable medium in a two-phase stream of heat-generating or absorbing materials.

Three-phase flows of a couple of stress fluids squeezed between Newtonian fluids are analytically studied by Umavathi et al. (Umavathi et al., 2005). It was noticed that the fluid flow is increased by the pair stress parameter. Umavathi et al. (Umavathi et al., 2008) investigated the three-phase flow of Micropolar fluid. Dragiša et al. (Nikodijevic et al., 2014) analytically studied the three immiscible region flows of Newtonian fluid and all three regions are electrically conducting. Abdul Rauf and Memoona Naz (Abdul and Naz, 2020) investigated the one-dimensional flow of three immiscible region flows in a cylindrical. Hasnain et al. (Hasnain et al., 2022) studied the three-phase flow of Casson liquid with a porous medium squeezed between hybrid nanofluid with clear fluid. They noticed that copper (Cu) nanoparticles increase the temperature. Kumar et al. (Kumar Yadav et al., 2018) analytically studied the three-phase flow of micropolar fluid between clear and hybrid nanofluid. Engineering applications for three-phase flows in porous media include oil production, biofluid transfer, radiator coolant circulation, and more (Dey et al., 2017; Fan et al., 2017; Vamvakidis et al., 2018). Modern methods such as the machine learning are adopted by El-Amin et al. (El-Amin et al., 2023) to study the effect of Nanoparticles in two-phase flow in permeable medium and demonstrated that machine learning approach gives better results than some of the numerical methods. Immiscible fluid flow in different geometries was considered to study flow and heat transfer rate (Umavathi and Anwar Bég, 2020b), (Chen and Jian, 2022). Abdullah et al. (Alzahrani et al., 2023) studied the effect of viscous-Casson fluid in a rotating two-phase flow channel with a chemical reaction and performed a comparative study of different numerical methods.

There is a fascinating new class of sophisticated fluids known as hybrid nanofluids. These nanofluids combine the advantages of traditional nanofluids with those of hybrid materials. They are manufactured by dispersing nanoparticles and other functional components in a base fluid, which results in the creation of a medium that is unique, adaptable, and with increased qualities. In their study, Shamshuddin et al. (Shamshuddin et al., 2023a) educed the HNF model and the development of entropy across a stretchy disk. Shamshuddin et al. (Shamshuddin et al., 2023b) investigated the effects of radiation and other influencing factors on magnetized nanoliquid flow in a permeable cylindrical annulus. They used molybdenum disulfide and magnetite nanoparticles in their research. Shamshuddin et al. (Shamshuddin et al., 2023c) conducted research on a micropolar liquid medium channel while assuming heat radiation and species reactive agents were present. Researchers Shamshuddin et al. (Shahzad et al., 2022) investigated the thermal features of ternary hybrid nanofluids. Additionally, aluminum oxide, copper oxide, silver, and water nano-molecules were used in the research. Taking into account the Hall effect and radiation impacts Shamshuddin et al. (Shamshuddin et al., 2023d) investigated the energy transition that occurs in order to improve the heat transport rate during the flow of a ternary hybrid nanofluid across the surface of a rotating disk. Moreover, this examination is focused on the characteristics of two different kinds of metallic nanoparticles, including Cu and Al_2O_3. In this framework, Cu nanomaterials are used/exercised in a wide variety of products, including heat transfer, antimicrobial materials, catalysts, super solid materials, and sensors [see Refs. (Ahmed et al., 2016; Khan et al., 2021; Khan et al., 2022)]. The advantages or benefits of Cu nanomaterials are competitive, inflated yields under delicate reaction circumstances or situations, and exact reaction durations that seem differently from traditional catalysts (Khan and Alshomrani, 2017). In addition, the Al_2O_3 nanomaterials are widely used in the ceramics, mechanical, and personal care industries (Khan et al., 2017). In recent times, numerous researchers explored the hybrid nanofluids past diverse surfaces (Kavya et al., 2022; Lou et al., 2022; Raju et al., 2022; Upadhya et al., 2022).

In further study, they can use the different nanoparticle with different base fluids. They can study the mass transfer with Soret effect and Dufour effect with non-linear thermal radiation. The aforementioned works' wide-ranging implications in science and technology have led to the discussion of the three-phase flow of micropolar fluid compressed between transparent fluid and hybrid nanofluid subject to heat radiation and electromagnetic influence. The perturbation technique is carried out to solve the differential equation in our study.

2 Problem formulation

The flow configuration of the problem is schematically shown in Figure 1. In the presence of a magnetic field and electric field, steady and laminar fluid flow through a channel is considered. The fluid flow in the inclined channel is assumed to be a constant pressure gradient. The wall y = −1 is kept at T_{w2}, while y = 2 is maintained at T_{w1}. The inclined channel is separated into three regions, Region-1 consists of clear fluid and Region-3 consists of a hybrid nanofluid. Both regions are considered in the presence of viscous, Joules and Darcy dissipation region 2 is of a porous medium and consists of micropolar fluid. Density is considered to be constant in all the regions and thermal conductivity and viscosity only with temperature. Copper, Aluminium Oxide—water hybrid nanofluid are considered. The properties of the nanoparticles involved in the study are mentioned in Table 1. Nanoparticles are assumed to be spherical (q = 3) and platelets (q = 5.7) shape for the fluid flow.

TABLE 1 Thermophysical properties of base fluids and nanoparticles (Hayat and Nadeem, 2017).

Property	Water	Aluminium oxide (Al_2O_3)	Copper
$\rho(kg/m^2)$	997.1	3,970	8,933
$k(W/mK)$	0.613	756	401
$C_p(J/kgK)$	4,179	40	385
$\sigma(simens/m)$	0.05	0.85×10^{-5}	5.96×10^{7}
$\beta(1/K)$	21×10^{-5}	1.07×10^{-6}	1.67×10^{-5}

These presumptions allow us to write the steady, microrotation velocity, one-dimensional velocity and temperature governing equations (Umavathi et al., 2008), (Ghasemi and Aminossadati, 2009; Muthtamilselvan et al., 2010; Vajravelu et al., 2013) as follows.

Region 1:

$$\mu_f \frac{d^2u_1'}{dy'^2} + \left(\rho_f g\beta_f\right)(T_1 - T_{w2})\cos(\omega) - \frac{\partial p}{\partial x} - \sigma_f\left(E_0 + B_0u_1'\right)B_0 = 0 \tag{1}$$

$$k_f \frac{d^2T_1}{dy'^2} + \mu_f\left(\frac{du_1'}{dy'}\right)^2 - \frac{\partial q^*}{\partial y} + \sigma_f\left(E_0 + B_0u_1'\right)^2 = 0 \tag{2}$$

Region 2:

$$\left(\mu_{mf} + k\right)\frac{d^2u_2'}{dy'^2} + k\frac{dn}{dy'} + \left(\rho_f g\beta_f\right)(T_2 - T_{w2})\cos(\omega) - \frac{\mu_{mf}}{\kappa}u_2' - \frac{\partial p}{\partial x} - \sigma_{mf}\left(E_0 + B_0u_2'\right)B_0 = 0 \tag{3}$$

$$\gamma\frac{d^2n}{dy'^2} - k\left(2n + \frac{du_2'}{dy'}\right) = 0 \tag{4}$$

$$k_{mf}\frac{d^2T_2}{dy'^2} + \mu_{mf}\left(\frac{du_2'}{dy'}\right)^2 + \frac{\mu_{mf}}{\kappa}u_2'2 - \frac{\partial q^*}{\partial y} + \sigma_{mf}\left(E_0 + B_0u_2'\right)^2 = 0 \tag{5}$$

Region 3:

$$\mu_{hnf}\frac{d^2u_3'}{dy'^2} + \left(\rho_{hnf}g\beta_{hnf}\right)(T_3 - T_{w2})\cos(\omega) - \frac{\partial p}{\partial x} - \sigma_{ehnf}\left(E_0 + B_0u_3'\right)B_0 = 0 \tag{6}$$

$$k_{hnf}\frac{d^2T_3}{dy'^2} + \mu_{hnf}\left(\frac{du_3'}{dy'}\right)^2 - \frac{\partial q^*}{\partial y} + \sigma_{ehnf}\left(E_0 + B_0u_3'\right)^2 = 0 \tag{7}$$

Boundary and Interface conditions are assumed to be:

$$u_1'(-h) = 0,\ u_1'(0) = u_2'(0),$$
$$\mu_f\frac{du_1'(0)}{dy'} = \mu_{mf}(1+K)\frac{du_2'(0)}{dy'} + \mu_{mf}KN_m, u_2'(h) = u_3'(h),$$
$$u_3'(2h) = 0,\ \mu_{mf}(1+K)\frac{du_2'(h)}{dy'} + \mu_{mf}KN_m = \mu_{hnf}\frac{du_3'(h)}{dy'},$$
$$\frac{dN_m(0)}{dy} = 0,\ \frac{dN_m(1)}{dy} = 0$$
$$T_1(-h) = T_{w2}, T_1(0) = T_2(0), k_f\frac{dT_1(0)}{dy'} = k_{mf}\frac{dT_2(0)}{dy'}, T_2(h) = T_3(h), T_3(2h) = T_{w1}, k_{mf}\frac{dT_2(h)}{dy'} = k_{hnf}\frac{dT_3(h)}{dy'} \tag{8}$$

To convert Eqs 1, 2, 3, 4, 5, 6, 7, 8 into dimensionless equations, we use the following dimensionless parameters

$$y = \frac{y'}{h},\ u_i = u_i'\left(\frac{\rho_f}{\mu_f}\right)h,\ \theta_i = \frac{T_i - T_{w2}}{T_{w1} - T_{w2}},$$
$$G_r = \frac{g\beta_f(T_{w1} - T_{w2})h^3}{\nu_f^2}\cos(\omega),\ M^2 = \frac{B_0^2h_1^2\sigma}{\mu_f},\ E = \frac{E_0\rho_f h}{B_0\mu_f},$$
$$Br = \frac{\mu_f^3}{\rho_f^2h^2(T_{w1} - T_{w2})k_f},\ \sigma = \frac{h}{\sqrt{\kappa}}, P = -\frac{\rho_f h^3}{\mu_f^2}\frac{\partial p}{\partial x},\ \nu_f = \frac{\mu_f}{\rho_f},$$
$$\frac{\partial q}{\partial y} = 4\alpha^2(T_i - T_{w2}),\ N = 2\alpha\frac{h}{\sqrt{k_f}},\ K = \frac{k}{\mu_{mf}},\ n = \frac{Nh}{\mu_{mf}}$$

The thermophysical properties of hybrid nanofluids are given by (Hayat and Nadeem, 2017):

$$\rho_{hnf} = \left[(1-\phi_{s1})\rho_f + \phi_{s1}\rho_{s1}\right](1-\phi_{s2}) + \rho_{s2}\phi_{s2}, \alpha_{hnf} = \frac{k_{hnf}}{\left(\rho C_p\right)_{hnf}}$$

$$(\rho\beta)_{hnf} = \left[(1-\phi_{s1})(\rho\beta)_f + \phi_{s1}(\rho\beta)_{s1}\right](1-\phi_{s2}) + (\rho\beta)_{s2}\phi_{s2}, \mu_{hnf} = \frac{\mu_f}{\sqrt{(1-\phi_{s1})^5(1-\phi_{s2})^5}}$$

$$\left(\rho C_p\right)_{hnf} = \left(\rho C_p\right)_f(1-\phi_{s2})\left[(1-\phi_{s1}) + \phi_{s1}\frac{\left(\rho C_p\right)_{s1}}{\left(\rho C_p\right)_f}\right] + \phi_{s2}\left(\rho C_p\right)_{s2}$$

$$\sigma_{hnf} = \sigma_{nf}\left[\frac{\sigma_{s2} + 2\sigma_{nf} - 2\phi_{s2}\left(\sigma_{nf} - \sigma_{s2}\right)}{\sigma_{s2} + 2\sigma_{nf} + \phi_{s2}\left(\sigma_{nf} - \sigma_{s2}\right)}\right],$$
$$\sigma_{nf} = \sigma_f\left[\frac{\sigma_1 + 2\sigma_f - 2\phi_1\left(\sigma_f - \sigma_1\right)}{\sigma_1 + 2\sigma_f + \phi_1\left(\sigma_f - \sigma_1\right)}\right] \tag{9}$$

The thermophysical properties of the nanofluid, base fluid and nanoparticles are denoted by the subscripts nf, f, s_1 and s_2 respectively. According to Maxwell thermal conductivity of hybrid nanofluid k_{hnf} is considered as:

$$k_{hnf} = k_{bf}\left[\frac{k_{s2} + (q-1)k_{bf} - (q-1)\phi_2\left(k_{bf} - k_{s2}\right)}{k_{s2} + (q-1)k_{bf} + \phi_2\left(k_{bf} - k_{s2}\right)}\right],$$
$$k_{bf} = k_f\left[\frac{k_{s1} + (q-1)k_f - (q-1)\phi_1\left(k_f - k_{s1}\right)}{k_{s1} + (q-1)k_f + \phi_1\left(k_f - k_{s1}\right)}\right] \tag{10}$$

2.1 Non—dimensionalized equations

Region 1

$$\frac{d^2u_1}{dy^2} + G_r\theta_1 + P - M^2(E + u_1) = 0 \tag{11}$$

$$\frac{d^2\theta_1}{dy^2} + Br\left(\frac{du_1}{dy}\right)^2 - N^2\theta_1 + BrM^2(E + u_1)^2 = 0 \tag{12}$$

Region 2

$$(1+K)\frac{d^2u_2}{dy^2} + K\frac{dN_m}{dy} + G_r\theta_2 - \sigma^2u_2 + P - M^2(E + u_2) = 0 \tag{13}$$

$$\frac{d^2\theta_2}{dy^2} + Br\left(\left(\frac{du_2}{dy}\right)^2 + \sigma^2{u_2}^2\right) - N^2\theta_2 + BrM^2(E + u_2)^2 = 0 \tag{14}$$

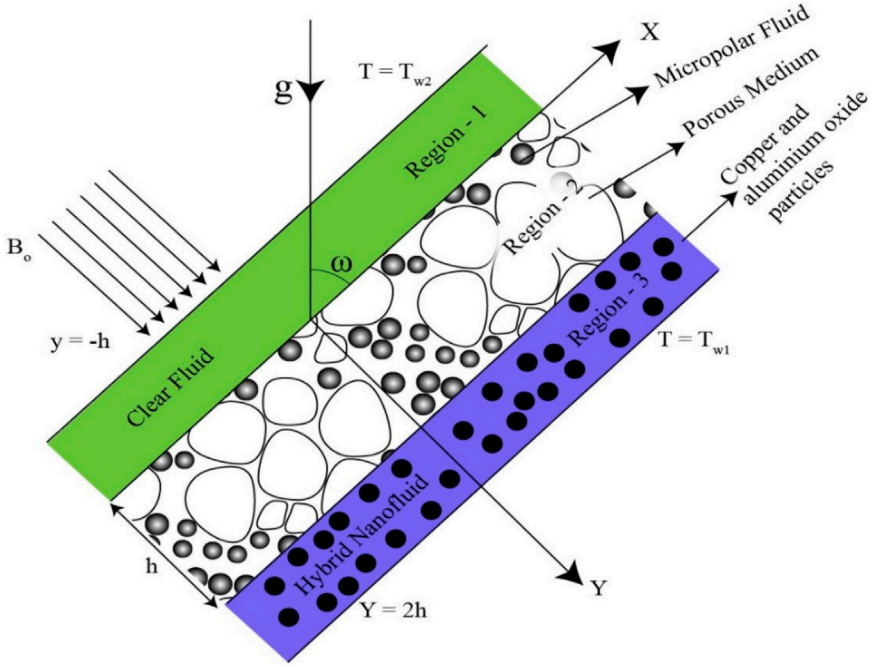

FIGURE 1
A physical model of the problem.

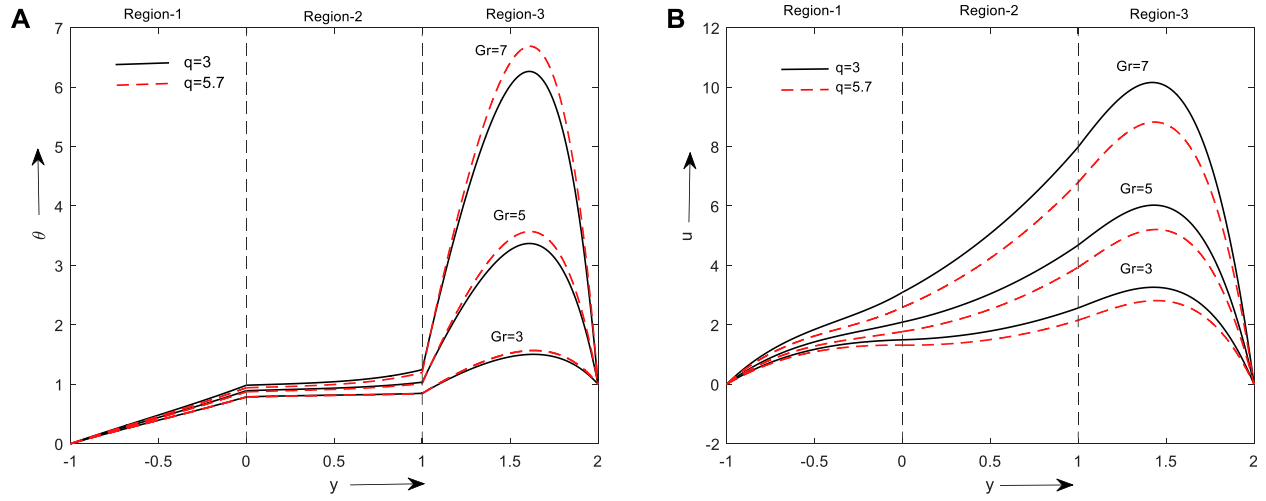

FIGURE 2
Depicts the effect of thermal grashof number on **(A)** temperature **(B)** Velocity.

$$\frac{d^2N_m}{dy^2} - \frac{2K}{2+K}\left(2N_m + \frac{du_{30}}{dy}\right) = 0 \tag{15}$$

Region 3

$$\frac{d^2u_3}{dy^2} + A_6Gr\theta_3 + A_{41}P - A_{51}M^2(E+u_3) \tag{16}$$

$$\frac{d^2\theta_3}{dy^2} + BrA_4\left(\frac{du_3}{dy}\right)^2 - \frac{N^2}{A_3}\theta_3 + A_5BrM^2(E+u_3)^2 = 0 \tag{17}$$

Boundary and interface conditions are:

$$\left.\begin{aligned} &u_1(-1)=0, u_1(0)=u_2(0), \mu_f\frac{du_1(0)}{dy}=\mu_{mf}(1+K)\frac{du_2(0)}{dy}+\mu_{mf}KN_m, u_2(1)=u_3(1),\\ &\mu_{mf}(1+K)\frac{du_2(1)}{dy}+\mu_{mf}KN_m=\mu_{hnf}\frac{du_3(1)}{dy}, u_2(1)=0, \frac{dN_m(0)}{dy}=0, \frac{dN_m(1)}{dy}=0\\ &\theta_1(-1)=0, \theta_1(0)=\theta_2(0), \frac{d\theta_1(0)}{dy}=\frac{k_{mf}}{k_f}\frac{d\theta_2(0)}{dy}, \theta_2(1)=\theta_3(1), \frac{d\theta_2(1)}{dy}=\frac{k_{hnf}}{k_{mf}}\frac{d\theta_3(1)}{dy}, \theta_2(1)=1 \end{aligned}\right\} \tag{18}$$

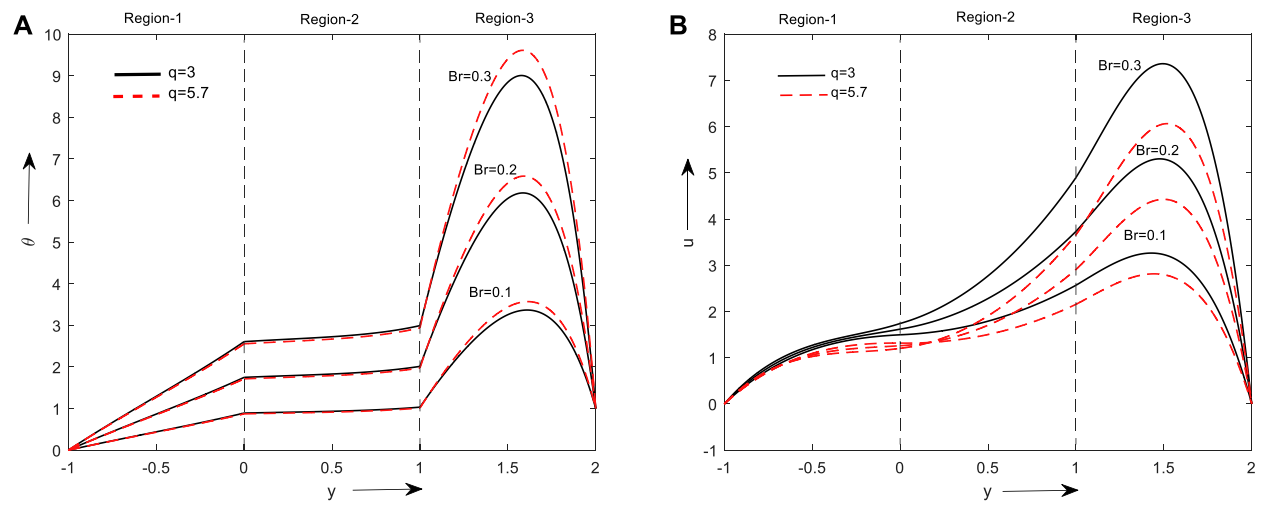

FIGURE 3
Depicts the effect of Brinkman number on **(A)** temperature **(B)** Velocity.

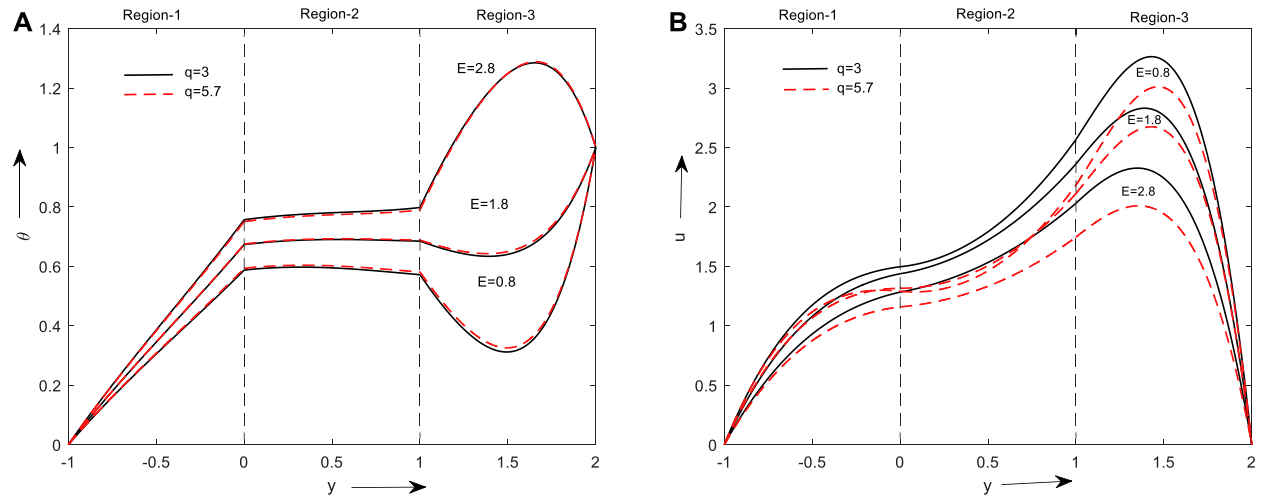

FIGURE 4
Depicts the effect of the Electric field on **(A)** temperature **(B)** Velocity.

2.2 Solution of the problem

The dimensionless governing Eqs 11, 12, 13, 14, 15, 16, 17 which are nonlinear and coupled are solved using the boundary and interface constraints Eq. 18 for flow. We form an asymptotic analysis by representing the velocity and temperature as:

$$u_i(y) = u_{i0}(y) + Bru_{i1}(y) + (Br)^2 u_{i2}(y) + \ldots\ldots \quad (19)$$

$$\theta_i(y) = \theta_{i0}(y) + Br\theta_{i1}(y) + (Br)^2 \theta_{i2}(y) + \ldots\ldots \quad (20)$$

The perturbation parameter is assumed to be Br, by replacing Eqs 19, 20 in Eqs 11, 12, 13, 14, 15, 16, 17, then equating the same powers and ignoring higher order terms we get:

2.3 Zeroth order equations

Region 1

$$\frac{d^2u_{10}}{dy^2} + G_r\theta_{10} + P - M^2(E + u_{10}) = 0 \quad (21)$$

$$\frac{d^2\theta_{10}}{dy^2} - N^2\theta_{10} = 0 \quad (22)$$

Region 2

$$(1+K)\frac{d^2u_{20}}{dy^2} + K\frac{dN_m}{dy} + G_r\theta_{20} + P - M^2(E + u_{20}) - \sigma^2 u_{20} = 0 \quad (23)$$

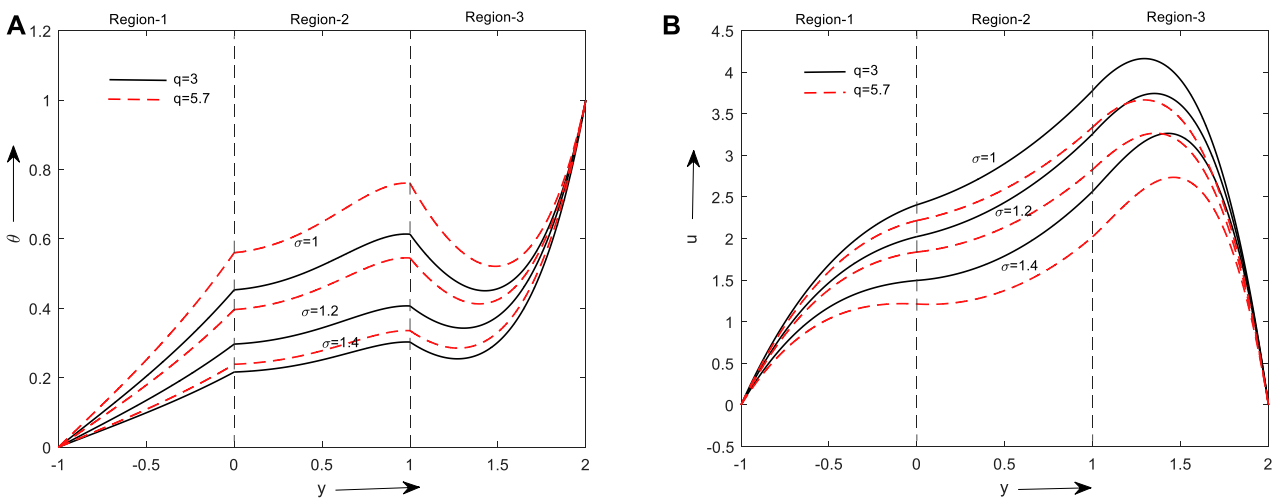

FIGURE 5
Depicts the effect of porosity on **(A)** temperature **(B)** Velocity.

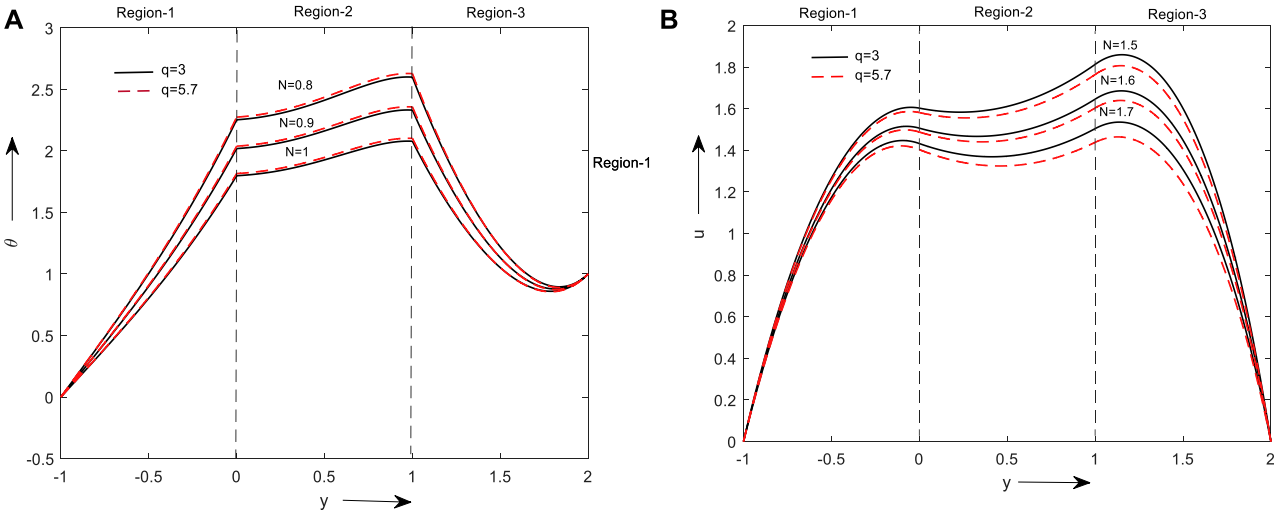

FIGURE 6
Depicts the effect of thermal radiation on **(A)** temperature **(B)** Velocity.

$$\frac{d^2N_m}{dy^2} - \frac{2K}{2+K}\left(2N_m + \frac{du_{20}}{dy}\right) = 0 \tag{24}$$

$$\frac{d^2\theta_{20}}{dy^2} - N^2\theta_{20} = 0 \tag{25}$$

Region 3

$$\frac{d^2u_{30}}{dy^2} + A_6Gr\theta_{30} + A_{41}P - A_{51}M^2(E + u_{30}) = 0 \tag{26}$$

$$\frac{d^2\theta_{30}}{dy^2} - \frac{N^2}{A_3}\theta_{30} = 0 \tag{27}$$

The boundary and interface conditions are

$$\left.\begin{aligned} &u_{10}(-1) = 0, u_{10}(0) = u_{20}(0), \mu_f\frac{du_{10}(0)}{dy} = \mu_{mf}(1+K)\frac{du_{20}(0)}{dy} + \mu_{mf}KN_m, u_{20}(1) = u_{30}(1),\\ &\mu_{mf}(1+K)\frac{du_{20}(1)}{dy} + \mu_{mf}KN_m = \mu_{hnf}\frac{du_{30}(1)}{dy}, u_{30}(2) = 0, \frac{dN_m(0)}{dy} = 0, \frac{dN_m(1)}{dy} = 0,\\ &\theta_{10}(-1) = 0, \theta_{10}(0) = \theta_{20}(0), \frac{d\theta_{10}(0)}{dy} = \frac{k_{nf}}{k_f}\frac{d\theta_{20}(0)}{dy}, \theta_{20}(1) = \theta_{30}(1), \frac{d\theta_{20}(1)}{dy} = \frac{k_f}{k_{nf}}\frac{d\theta_{30}(1)}{dy}, \theta_{30}(2) = 1 \end{aligned}\right\} \tag{28}$$

2.4 First-order equations

Region 1

$$\frac{d^2u_{11}}{dy^2} + G_r\theta_{11} - M^2u_{11} = 0 \tag{29}$$

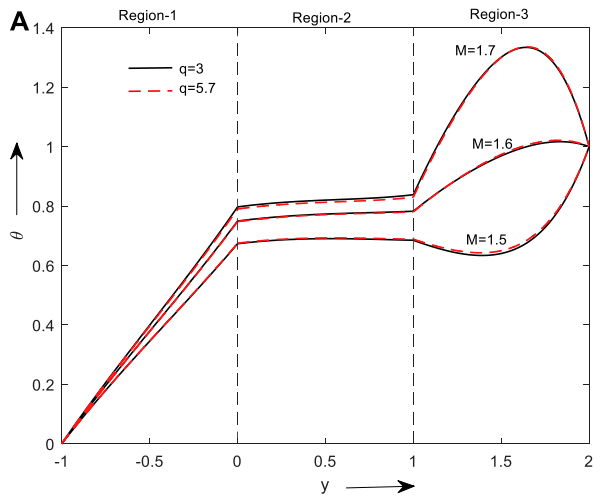

FIGURE 7
Depicts the effect of magnetic field on **(A)** temperature **(B)** Velocity.

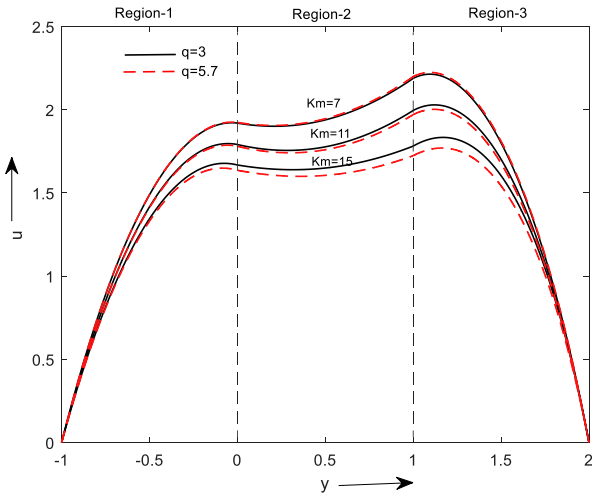

FIGURE 8
Depicts the effect of micropolar parameter on Velocity.

$$\frac{d^2\theta_{11}}{dy^2}+\left(\frac{du_{10}}{dy}\right)^2-N^2\theta_{11}+M^2\left(E+u_{10}\right)^2=0 \tag{30}$$

Region 2

$$G_r\theta_{21}+(1+K)\frac{d^2u_{21}}{dy^2}-\sigma^2u_{21}-M^2u_{21}=0 \tag{31}$$

$$-\frac{2K}{2+K}\frac{du_{21}}{dy}=0 \tag{32}$$

$$\frac{d^2\theta_{21}}{dy^2}+\left(\frac{du_{20}}{dy}\right)^2+\sigma^2u_{20}^2-N^2\theta_{21}+M^2\left(E^2+u_{20}^2+2Eu_{20}\right)=0 \tag{33}$$

Region 3

$$\frac{d^2u_{31}}{dy^2}+A_6Gr\theta_{31}-A_{51}M^2u_{31}=0 \tag{34}$$

$$\frac{d^2\theta_{31}}{dy^2}+A_4\left(\frac{du_{30}}{dy}\right)^2-\frac{N^2}{A_3}\theta_{31}+A_5M^2\left(E+u_{30}\right)^2=0 \tag{35}$$

The boundary and interface conditions are

$$\left.\begin{aligned}&u_{11}(-1)=0,u_{11}(0)=u_{21}(0),\mu_f\frac{du_{11}(0)}{dy}=\mu_{mf}(1+K)\frac{du_{21}(0)}{dy}+\mu_{mf}KN_m,u_{21}(1)=u_{31}(1),\\&\mu_{mf}(1+K)\frac{du_{21}(1)}{dy}+\mu_{mf}KN_m=\mu_{hnf}\frac{du_{31}(1)}{dy},u_{31}(2)=0,\frac{dN_m(0)}{dy}=0,\frac{dN_m(1)}{dy}=0,\\&\theta_{11}(-1)=0,\theta_{11}(0)=\theta_{21}(0),\frac{d\theta_{11}(0)}{dy}=\frac{k_{nf}}{k_f}\frac{d\theta_{21}(0)}{dy},\theta_{21}(1)=\theta_{31}(1),\frac{d\theta_{21}(1)}{dy}=\frac{k_f}{k_{nf}}\frac{d\theta_{31}(1)}{dy},\theta_{31}(2)=0\end{aligned}\right\} \tag{36}$$

Solving Eqs 21, 22, 23, 24, 25, 26, 27, 29, 30, 31, 32, 33, 34, 35 by using boundary conditions Eqs 28, 36, we obtain.

Region 1

$$u_1=u_{10}+Bru_{11}$$

$$u_1=\begin{pmatrix}(c_7\cosh[My]+c_8\sinh[My])-\left(\frac{G_rc_1}{N^2-M^2}\cosh[Ny]+\frac{G_rc_2}{N^2-M^2}\sinh[Ny]-\frac{P}{M^2}+E\right)\\+Br\begin{pmatrix}(b_{41}\cosh[My]+b_{42}\,\mathrm{Sinh}[My])-(L_{170}\cosh[Ny]+L_{171}\sinh[Ny])\\+\begin{pmatrix}L_{172}+L_{173}\cosh[2My]+L_{174}+L_{175}\cosh[2My]+L_{165}\cosh[(M-N)y]\\+L_{166}\sinh[(M-N)y]+L_{167}\sinh[(M+N)y]+L_{168}\cosh[(M+N)y]\\+L_{176}-L_{177}\cosh[2Ny]+L_{169}\sinh[2Ny]-L_{178}-L_{179}\sinh[2Ny]-L_{180}\\-L_{181}\cosh[2Ny]+L_{182}y\cosh[My]+L_{183}y\sinh[My]+L_{184}\sinh[2My]\\+L_{185}\cosh[Ny]+L_{186}y\sinh[Ny]-L_{187}+L_{188}\sinh[Ny]+L_{189}y\cosh[Ny]\end{pmatrix}\end{pmatrix}\end{pmatrix} \tag{37}$$

$$\theta_1=\theta_{10}+Br\theta_{11}$$

$$\theta_1=\begin{pmatrix}(c_1\cosh[Ny]+c_2\sinh[Ny])+Br\,(b_{11}\cosh[Ny]+b_{12}\sinh[Ny])\\-Br\begin{pmatrix}L_{76}[N^2\cosh(2My)+4M^2-N^2]+L_{77}[N^2\cosh(2My)-4M^2+N^2]\\+\cosh[(M-N)y]L_{78}+\sinh[My-Ny]L_{79}+\sinh[(M+N)y]L_{80}\\+L_{81}\cosh[(M+N)y]+L_{82}(-3+\cosh[2Ny])+L_{83}\sinh[2Ny]\\+L_{84}(3+\sinh[2Ny])+L_{85}(3+\cosh[2Ny])+L_{86}(L_{12}\cosh[My]+L_{13}\sinh[My])\\+L_{87}(L_{14}+L_1)\sinh[2My]+L_{881}(y\sinh[Ny])+L_{88}(y\cosh[Ny])+L_{89}\end{pmatrix}\end{pmatrix} \tag{38}$$

Region 2

$$u_2=u_{20}+Bru_{21}$$

$$u_2=\begin{pmatrix}c_9\cosh[Z_9y]+c_{91}\sinh[Z_9y]+c_{10}\cosh[Z_{10}y]+c_{101}\sinh[Z_{10}y]+Z_{16}\cosh[Ny]\\+Br\begin{pmatrix}Z_{651}\cosh[Ny]+Z_{661}\sinh[Ny]+Z_{671}-Z_{681}\cosh(2Z_9y)-Z_{69}\sinh(2Z_9y)\\-Z_{70}\cosh(Z_9+Z_{10})y+Z_{71}\cosh(Z_9-Z_{10})y-Z_{72}\sinh(Z_{10}+Z_9)y\\+Z_{73}\sinh(Z_9-Z_{10})y-Z_{74}\cosh(2Z_{10}y)-Z_{75}\sinh(2Z_{10}y)-Z_{76}\cosh(Z_9+N)y\\+Z_{77}\cosh(N-Z_9)y-Z_{78}\sinh(N+Z_9)y+Z_{79}\sinh(Z_9-N)y-Z_{80}\cosh(Z_{10}+N)y\\+Z_{81}\cosh(N-Z_{10})y-Z_{82}\sinh(N+Z_{10})y+Z_{83}\sinh(Z_{10}-N)y-Z_{84}\cosh(2Ny)\\-Z_{85}\sinh(yZ_9)+Z_{86}\sinh(2Ny)-Z_{87}\,\mathrm{Cosh}(yZ_9)-Z_{88}\,\mathrm{Cosh}(yZ_{10})-Z_{89}\sinh(yZ_{10})\\-Z_{90}y\cosh[Ny]+Z_{91}\sinh[Ny]-Z_{92}\cosh[Ny]+Z_{93}y\sinh[Ny]+_{51}\,\mathrm{Cosh}(Z_{96})y\\+b_{52}\,\mathrm{Sinh}(Z_{96})y\end{pmatrix}\end{pmatrix} \tag{39}$$

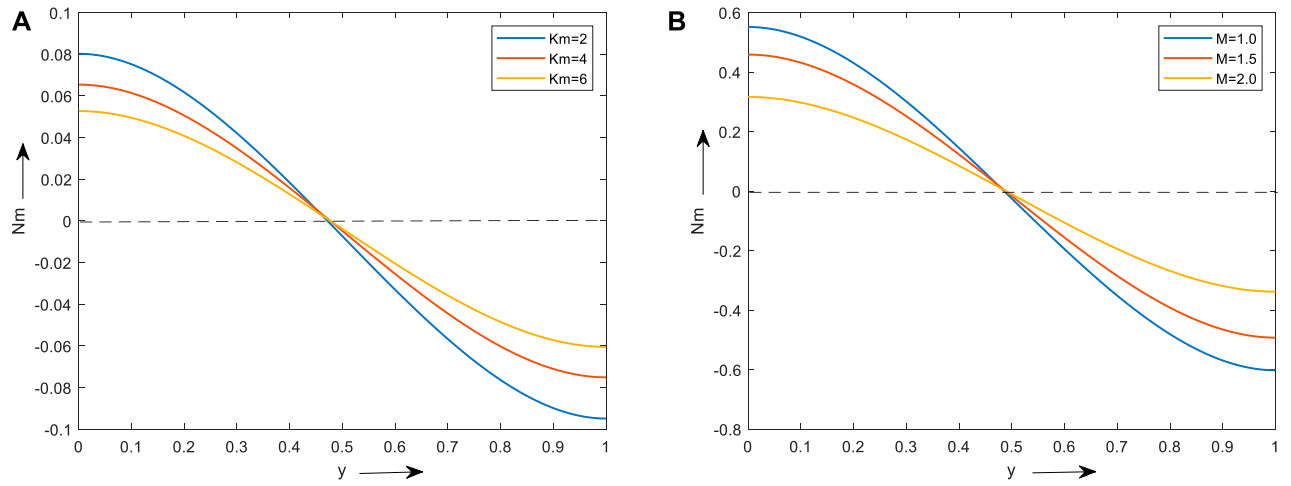

FIGURE 9
Depicts the impact of the material parameter **(A)** and magnetic parameter **(B)** on the micro rotational velocity.

$$\theta_2 = \theta_{20} + Br\theta_{21}$$

$$\theta_2 = \begin{pmatrix} (c_3\cosh[Ny] + c_4\sinh[Ny]) + Br(b_{21}\cosh[Ny] + b_{22}\sinh[Ny]) \\ -Br\begin{pmatrix} Z_{36} + Z_{37}\cosh(2Z_9 y) + Z_{38}\sinh(2Z_9 y) + Z_{39}\cosh(Z_9 + Z_{10})y - Z_{40}\cosh(Z_9 - Z_{10})y \\ +Z_{41}\sinh(Z_{10} + Z_9)y - Z_{42}\sinh(Z_9 - Z_{10})y + Z_{43}\cosh(2Z_{10} y) + Z_{44}\sinh(2Z_{10} y) \\ +Z_{45}\cosh(Z_9 + N)y - Z_{46}\cosh(N - Z_9)y + Z_{47}\sinh(N + Z_9)y - Z_{48}\sinh(Z_9 - N)y \\ +Z_{49}\cosh(Z_{10} + N)y - Z_{50}\cosh(N - Z_{10})y + Z_{51}\sinh(N + Z_{10})y - Z_{52}\sinh(Z_{10} - N)y \\ +Z_{53}\cosh(2Ny) + Z_{54}\sinh(yZ_9) - Z_{55}\sinh(2Ny) + Z_{56}\mathrm{Cosh}(yZ_9) + Z_{57}\mathrm{Cosh}(yZ_{10}) \\ +Z_{58}\sinh(yZ_{10}) + Z_{59}y\,\mathrm{Cosh}(yN) - Z_{60}y\sinh(yN) \end{pmatrix} \end{pmatrix} \quad (40)$$

Region 3

$$u_3 = u_{30} + Bru_{31}$$

$$u_3 = \begin{pmatrix} \begin{pmatrix} c_{11}\cosh[A_8 y] \\ +c_{12}\sinh[A_8 y] \end{pmatrix} - \left(\frac{GrA_6c_5}{A_7^2 - A_8^2}\cosh[A_7 y] + \frac{GrA_6c_6}{A_7^2 - A_8^2}\sinh[A_7 y] - \frac{A_{41}P}{A_8^2} + \frac{A_{51}M^2E}{A_8^2}\right) \\ +Br\begin{pmatrix} b_{61}\cosh[A_{53}y] + b_{62}\sinh[A_{53}y] - A_{54}\cosh[yA_{42}] - A_{55}\sinh[yA_{42}] \\ +A_{56}\sinh[yA_7] + A_{57}y\cosh[yA_7] + A_{58}\cosh[yA_8] + A_{59}\cosh[yA_7] \\ +A_{60}y\sinh[yA_7] - A_{61} + A_{62}\sinh[2yA_7] + A_{63}\sinh[2yA_8] + A_{64}\cosh[2yA_8] \\ +A_{65}\cosh[2yA_7] + A_{66}\cosh[y(A_7 + A_8)] + A_{67}\cosh[y(A_7 - A_8)] \\ +A_{68}\sinh[y(A_7 + A_8)] + A_{69}\sinh[y(A_7 - A_8)] \end{pmatrix} \end{pmatrix} \quad (41)$$

$$\theta_3 = \theta_{30} + Br\theta_{31}$$

$$\theta_3 = \begin{pmatrix} (c_5\cosh[A_7 y] + c_6\sinh[A_7 y]) + (b_{31}\cosh[A_{42}y] + b_{32}\sinh[A_{42}y]) \\ -Br\begin{pmatrix} A_{43}y\cosh[yA_7] + A_{44}\cosh[yA_8] + A_{45} + A_{46}y\sinh[yA_7] + A_{47}\sinh[2yA_7] \\ +A_{48}\sinh[2yA_8] + A_{49}\cosh[2yA_8] + A_{50}\cosh[2yA_7] + A_{511}\cosh(A_7 + A_8)y \\ +A_{52}\cosh(A_7 - A_8)y + A_{53}\sinh(A_8 + A_7)y + A_{54}\sinh(A_7 - A_8)y \end{pmatrix} \end{pmatrix} \quad (42)$$

2.5 Derived quantities

2.5.1 Nusselt number

$$(Nu)_{y=-1} = \left(\frac{d\theta_1}{dy}\right)_{y=-1}$$

$$= \begin{pmatrix} (-c_1 N\sinh[N] + c_2 N\cosh[N]) + Br(-b_{11}N\sinh[N] + b_{12}N\cosh[N]) \\ -Br\begin{pmatrix} L_{76}\left[-2MN^2\sinh(2M)\right] + L_{77}\left[-2MN^2\sinh(2M)\right] \\ -(M-N)\sinh[(M-N)]L_{78} + (M-N)\cosh[M-N]L_{79} \\ +(M+N)\cosh[(M+N)]L_{80} - L_{81}(M+N)\sinh[(M+N)] \\ -L_{82}(2N\sinh[2N]) + L_{83}2N\cosh[2N] + L_{84}(2N\cosh[2Ny]) \\ -L_{85}2N(\sinh[2N]) + L_{86}(-L_{12}M\sinh[M] + L_{13}M\cosh[M]) \\ +L_{87}(L_{14} + L_1)2M\cosh[2M] + L_{881}(-\sinh[N] - N\cosh[N]) \\ +L_{88}(\cosh[N] + N\sinh[Ny]) \end{pmatrix} \end{pmatrix}$$

$$(Nu)_{y=2} = -\left(\frac{d\theta_3}{dy}\right)_{y=2}$$

$$= \begin{pmatrix} (c_5A_7\sinh[2A_7] + c_6A_7\cosh[2A_7]) \\ -Br\begin{pmatrix} A_{43}(\cosh[2A_7] + 4A_7\sinh[2A_7]) + A_{44}A_8\sinh[2A_8] \\ +A_{46}\sinh[2A_7] + 4A_{46}A_7\cosh[2A_7] + A_{47}2A_7\cosh[4A_7] \\ +A_{48}2A_8\cosh[4A_8] + A_{53}(A_8 + A_7)\cosh[2(A_8 + A_7)] \\ +A_{511}(A_7 + A_8)\sinh[2(A_7 + A_8)] + b_{31}A_{42}\sinh[2A_{42}] \\ +A_{52}(A_7 - A_8)\sinh[2(A_7 - A_8)] + b_{32}A_{42}\cosh[2A_{42}] \\ +A_{49}2A_8\sinh[4A_8] + A_{50}2A_7\sinh[4A_7] \\ +A_{54}(A_7 - A_8)\cosh[2(A_7 - A_8)] \end{pmatrix} \end{pmatrix}$$

2.5.2 Skin friction

$$(\tau)_{y=-1} = \left(\frac{du_1}{dy}\right)_{y=-1}$$

$$= \begin{pmatrix} \begin{pmatrix} -c_7M\sinh[M] \\ +c_8M\cosh[M] \end{pmatrix} - \begin{pmatrix} \frac{G_rNc_1}{N^2 - M^2}\sinh[N] \\ +\frac{G_rNc_2}{N^2 - M^2}\cosh[N] \end{pmatrix} \\ +Br\begin{pmatrix} (-L_{170}N\sinh[N] + L_{171}N\cosh[N]) - L_{173}2M\sinh[2M] \\ -L_{175}2M\sinh[2M] - L_{165}(M-N)\sinh[(M-N)] \\ +L_{166}(M-N)\cosh[(M-N)] + L_{167}(M+N)\cosh[(M+N)] \\ -L_{168}(M+N)\sinh[(M+N)] + L_{177}2N\sinh[2N] \\ +L_{169}2N\cosh[2N] - L_{179}2N\cosh[2N] + L_{181}2N\sinh[2N] \\ -b_{41}M\sinh[M] + L_{182}(\cosh[M] + M\sinh[M]) + b_{42}M\cosh[M] \\ +L_{183}(-\sinh[M] - M\cosh[M]) + L_{184}2M\cosh[2M] \\ -L_{185}N\sinh[N] + L_{186}(-\sinh[N] - N\cosh[N]) + L_{188}N\cosh[N] \\ +L_{189}(\cosh[N] + N\sinh[N]) \end{pmatrix} \end{pmatrix}$$

$$(\tau)_{y=2} = -\left(\frac{du_3}{dy}\right)_{y=2}$$

$$= \begin{pmatrix} c_{11}A_8\sinh[2A_8] + c_{12}A_8\cosh[2A_8] - \frac{GrA_6A_7c_5}{A_7^2 - A_8^2}\sinh[2A_7] \\ +Br\begin{pmatrix} -\frac{GrA_6A_7c_6}{Br(A_7^2 - A_8^2)}\cosh[2A_7] + b_{61}A_{53}\sinh[2A_{53}] + b_{62}A_{53}\cosh[2A_{53}] \\ -A_{54}A_{42}\sinh[2A_{42}] - A_{55}A_{42}\cosh[2A_{42}] + A_{56}A_7\cosh(2A_7) \\ +A_{57}\cosh(2A_7) + 2A_{57}A_7\sinh(2A_7) + A_{58}[2A_8]\sinh[2A_8] \\ +A_{62}2A_7\cosh[4A_7] + A_{59}A_7\sinh(2A_7) + A_{60}\begin{pmatrix} \sinh(2A_7) \\ +A_7\cosh(2A_7) \end{pmatrix} \\ +A_{63}2A_8\cosh[4A_8] + A_{64}2A_8\sinh[4A_8] + A_{65}2A_7\sinh[4A_7] \\ +A_{66}(A_7 + A_8)\sinh[2(A_7 + A_8)] + A_{67}(A_7 - A_8)\sinh[2(A_7 - A_8)] \\ +A_{68}(A_7 + A_8)\cosh[2(A_7 + A_8)] + A_{69}(A_7 - A_8)\cosh[2(A_7 - A_8)] \end{pmatrix} \end{pmatrix}$$

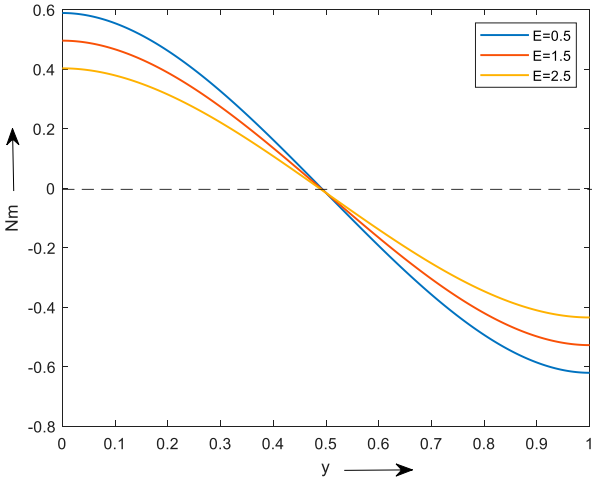

FIGURE 10
Depicts the effect of the Electric field on the micro rotational velocity.

3 Results and discussions

Before embarking on the discussion of the results, we make some comments on the flow parameters that are considered in this study such as Gr, Br, E, M, N, σ &Km influencing the convective heat and mass transport. The flow is considered as follows the first region consists of clear fluid, the second region has micropolar fluid with porous medium and the third region has hybrid nanofluid. Also, sphere and platelet shapes of nanoparticles are considered in the current study, they have a sphericity ψ as 1 & 0.526 respectively.

Figures 2A, B are the plots of temperature and velocity for varied thermal Grashof number (Gr) and nanoparticle shape factor (q) values. Here, as Gr & q upsurges, the temperature and velocity of the fluid flow also increase. The temperature and velocity can be observed to be maximum in region-3. Figure 2A portrays the temperature change, a small difference can be observed in clear fluid & micropolar fluid regions whereas a large difference is observed in the hybrid nanoliquid region, it is due to the higher thermal conductivity property of hybrid nanoliquid which surpasses the property of porous medium and micropolar fluid, hence a major difference is observed in all the regions. The platelet shape of

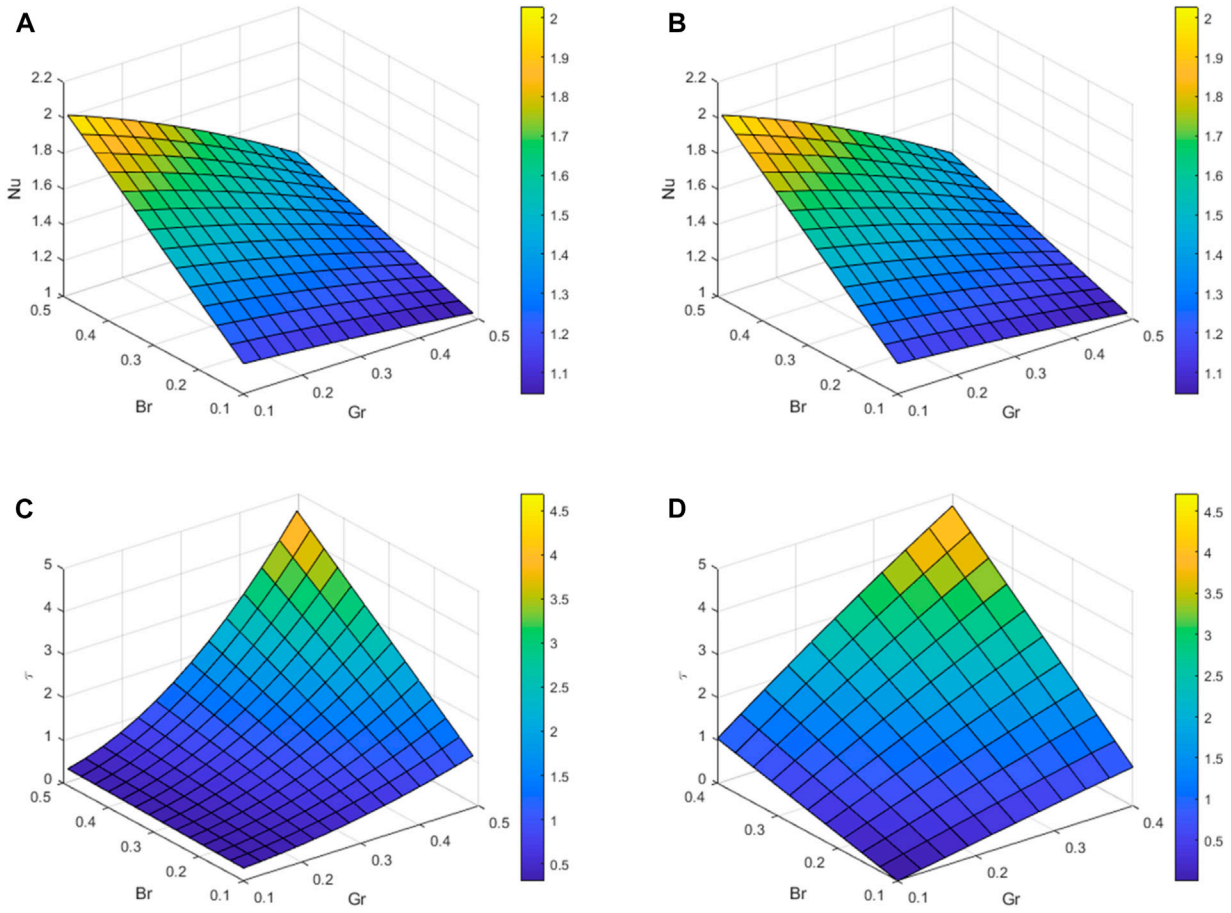

FIGURE 11
Nu graphs for variation in Br and Gr **(A)** at the left plate **(B)** at the right plate & Skin friction **(C)** at the left plate **(D)** at the right plate.

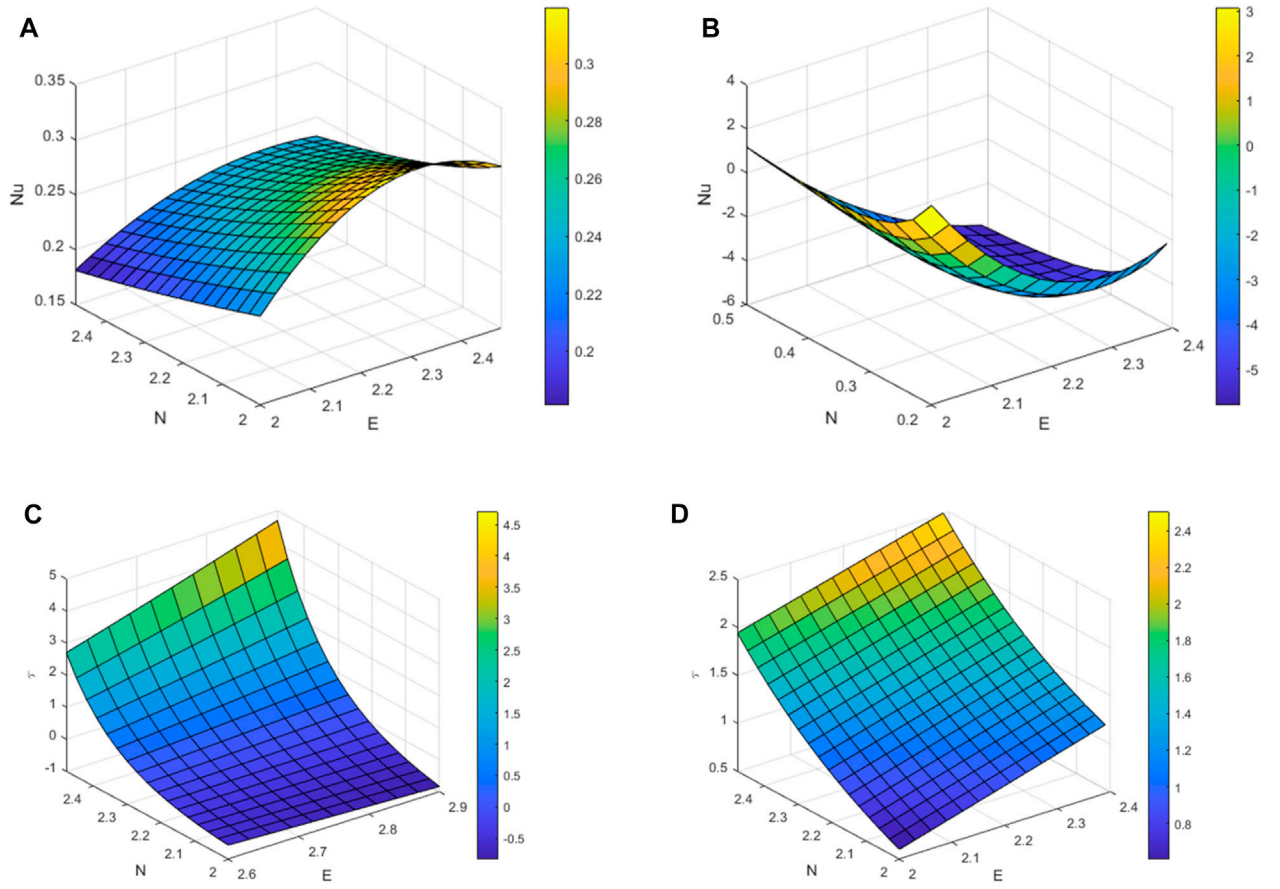

FIGURE 12
Nu graphs for variation in N and E **(A)** at the left plate **(B)** at the right plate & Skin friction **(C)** at the left plate **(D)** at the right plate.

the hybrid nanoparticle exhibits a higher temperature than the sphere shape. A similar observation can be made for a change in velocity from Figure 2B but the sphere shape has a higher velocity than the platelet shape.

The flow and thermal distributions for different base liquids and nanoparticles is shown in Figures 3A, B. The ratio of heat transfer by viscous dissipation to molecular conduction is Br's physical interpretation. Consequently, the slowdown the viscous dissipation resulting in greater temperature enhancement due to increase in Br is shown in Figures 3A, B. As Br increases, a velocity increment can be noticed. Furthermore, velocity rise is more prevalent in the hybrid nanofluid region than in the clear & micropolar fluid region, it is due to higher thermal conductivity, temperature enhancement is more and fluid thickness reduction which increases the fluid velocity which is visible in Figure 3B.

The consequence of the electric field on the temperature and velocity of fluid can be observed in Figures 4A, B. Graphs are plotted for increasing values of electric field & shape factor parameters in both cases. But the outcome of the variation is different in both. Velocity declines and temperature grows with increases in the electric field. Because of the resistance force induced by the electric field, molecules for a group move in a haphazard manner which reduces the velocity and a temperature rise is observed.

Figures 5A, B reveal the influence of the σ on thermal and velocity respectively. Figure 5A exemplifies that the temperature decrement σ is increased in all the regions. In contrast to the micropolar and hybrid nanofluid zones, the impact of suppression is dominant in the clear fluid region. This is a typical outcome that is seen when the channels are filled with various fluids that have a wide range of thermal conductivities.

Figures 6A, B show the consequence of thermal radiation on the velocity and thermal behaviours. Here, both the fields within the boundary are seen to decrease with an increase in N. This is for all combinations of nanofluids, thermal conductivity declines as the radiation parameter rise, hence temperature and velocity decrease.

We examine the effect of Lorentz force on temperature and velocity distribution from Figures 7A, B. The clear fluid zone has a higher momentum compared to the nanofluid region in the velocity profile, which can be seen in Figure 7B. The temperature is enhanced and the velocity is degraded by the magnetic parameter. This is because of the Hartmann effect, which is a ratio of viscous force to electromagnetic force. Thus, as the magnetic field is strengthened, the viscosity also grows, dampening the flow's velocity and raising its temperature.

Figure 8 is plotted for the micropolar parameter on velocity. From the above fig, it is noticed that an increase in the material parameter decreases the flow velocity. The flow of regions 1 and 3 don't affect by an increase in the material parameter value. This is because a material

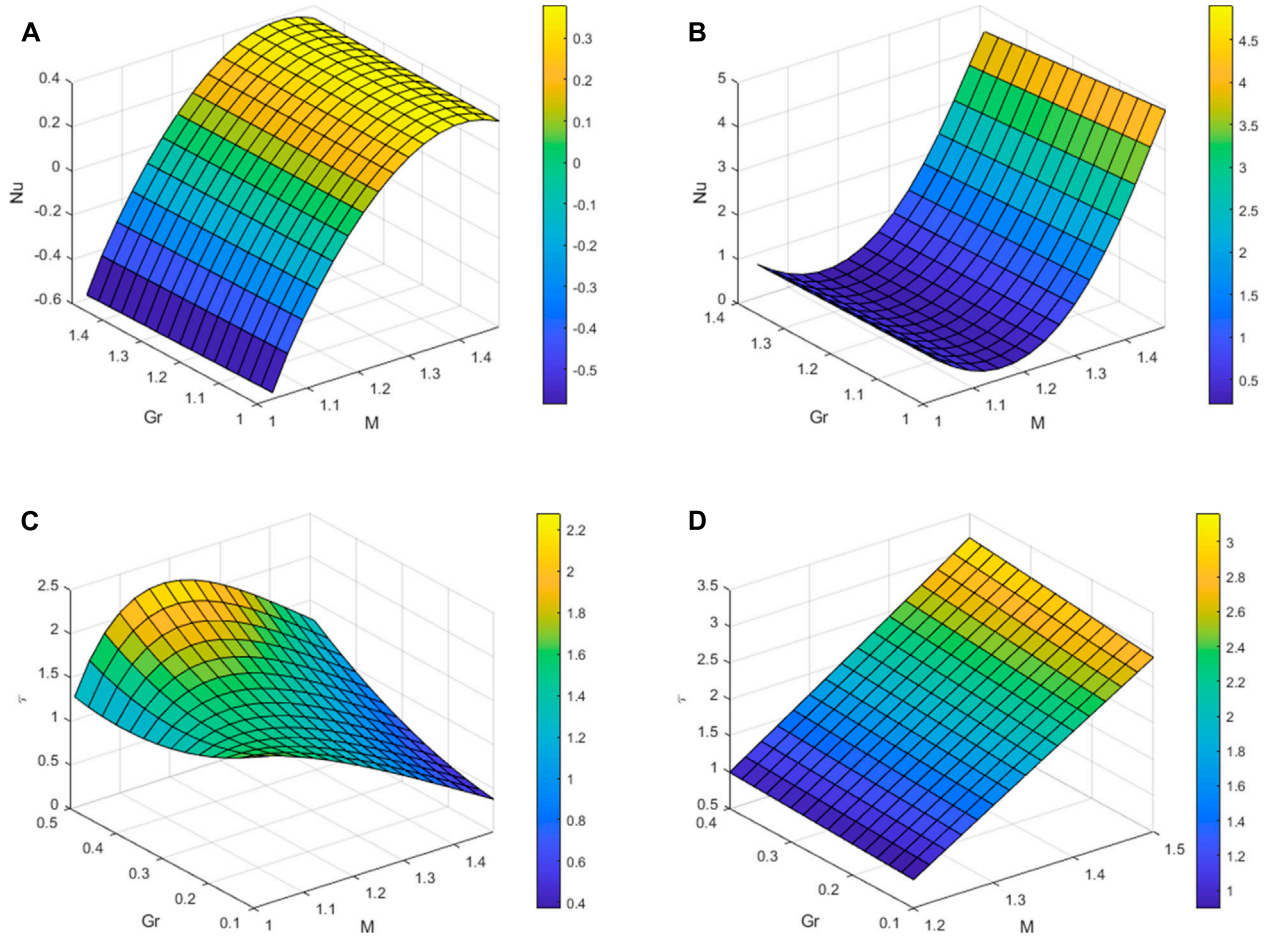

FIGURE 13
Nu graphs for variation in Gr and M **(A)** at the left plate **(B)** at the right plate & Skin friction **(C)** at the left plate **(D)** at the right plate.

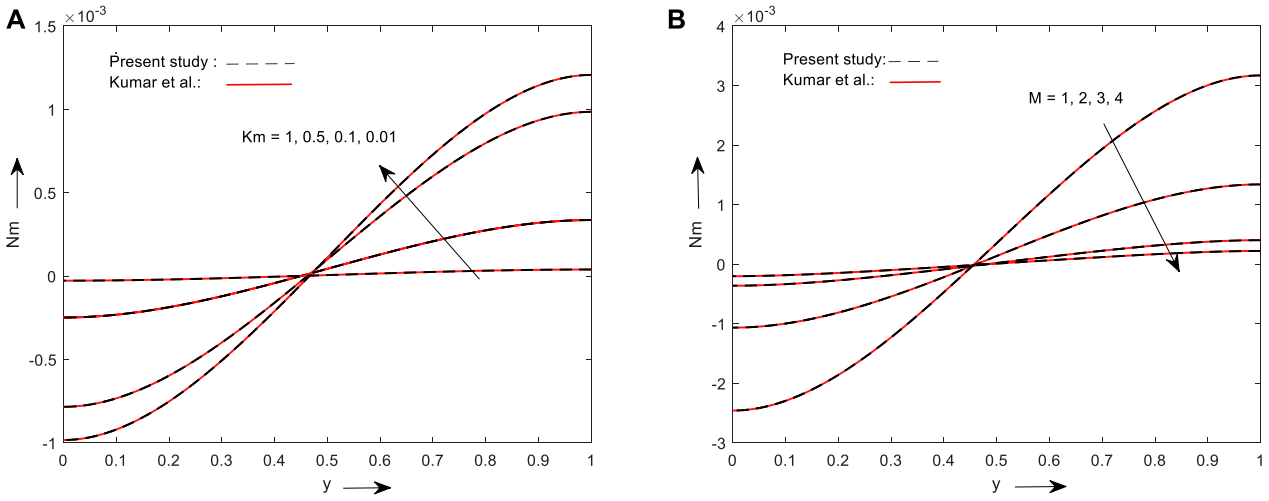

FIGURE 14
Depicts the comparison of the present outcomes for the impact of the material parameter **(A)** and magnetic parameter **(B)** on the micro rotational velocity with prior research work.

parameter, which only applies to micropolar fluids and specifies the micro rotational features of fluid flow, is the cause of the problem.

The outcome of material parameter and magnetic field on micro rotational velocity in region 2 is shown in Figures 9A, B. It is observed that the above y = 0.5, velocity decreases with the material parameter and magnetic parameter, and below y = 0.5 velocity increases with the material parameter and magnetic parameter, this trend is observed on both graphs.

From Figure 10, it is clear that Region 2 is affected by the electric field's influence on a micropolar fluid's rotational velocity. Figure 10 illustrates how the electric field changes with micro rotational velocity below and above y = 0.5. Below y = 0.5, it has been noted that a larger value of micro rotational velocity is higher for a lower value of an electric field. For smaller levels of the electric field, the micro rotational velocity reaches a minimum value above y = 0.5.

Figures 11A–D display the surface graphs of Nu and τ for different values of Br and Gr. Figures 11A, B are plotted for y = −1 and Figures 11C, D are plotted for y = 2. Skin friction increases by increasing both Br and Gr for y = −1 and y = 2 respectively. By keeping Gr values constant and increasing Br values, it is observed that the rate of heat transfer is maximum in both plates (y = −1, y = 2).

Nusselt number and skin friction graph for variation in thermal radiation and Electric field are shown in Figures 12A–D. From Figures 12A, B, Nu increases gradually by increasing the values of N and E, at y = −1 and for smaller values of N and E rate of heat transfer is higher at y = 2. By simultaneously increasing the values of N and E, an upward skin friction co-efficient is observed.

Graphs for Nusselt number and Skin friction for various values of Gr and M are shown in Figures 13A–D. By increasing the values of Gr and M, the rate of heat transfer increases in the left (y = −1) and right plates (y = 2). Figures 13C, D also give similar observations for skin friction.

4 Validation of results

validation of the current study is carried out by comparing our results with Kumar et al. (Kumar Yadav et al., 2018). Kumar et al. considered a horizontal channel with three regions with finite lengths where the middle region is micropolar and is bounded by Newtonian fluid. By considering $P = -0.7$, $Gr = 0$, $\sigma = 1.1$, $\phi_1 = \phi_2 = 0$ and, Figures 14A, B are plotted. It is noticed that our results are in good agreement with the Kumar et al. paper.

5 Conclusion

Three-phase flows for clear fluid, micropolar fluid and hybrid nanofluid are studied. Here the effects of the magnetic field, electric field, thermal radiation and permeability parameter on the physical study of fluid's velocity and temperature profile with the Cu/H_2O and Al_2O_3/H_2O hybrid nanoparticles are studied.

Some observations noticed from this study are.

- The electric and magnetic fields decline the velocity and increase the temperature distribution.
- The Hybrid nanofluid temperature is greater when compared to nano and clear fluid.
- By increasing material parameters, the velocity of the micropolar liquid decreases.
- Velocity and thermal profiles of the fluid flow increase by increasing the Grashof number and Brinkman number. By increasing porous parameters and thermal radiation, the fluid's velocity and temperature distribution decrease.
- The heat transport rate is enhanced by up surging the Grashof number and magnetic field.
- Skin friction can be increased by increasing thermal radiation and electric field.
- The effect of the Brinkman number and Grashof number increases heat flux marginally.

Data availability statement

The original contributions presented in the study are included in the article/supplementary material, further inquiries can be directed to the corresponding author.

Author contributions

All authors listed have made a substantial, direct and intellectual contribution to the work and approved it for publication. TNN, LK, KS, SVKV and UK wrote the original draft, E-SMS, AMH, IP and HSG done the mathematical analysis, language editing and study validation.

Funding

This work was funded by the Researchers Supporting Project number (RSP2023R33), King Saud University, Riyadh, Saudi Arabia.

Acknowledgments

The authors are thankful for the support of Researchers Supporting Project number (RSP2023R33), King Saud University, Riyadh, Saudi Arabia.

Conflict of interest

The authors declare that the research was conducted in the absence of any commercial or financial relationships that could be construed as a potential conflict of interest.

Publisher's note

References

Abdul, R., and Naz, M. (2020). Simultaneous flow of three immiscible fractional Maxwell fluids with the clear and homogeneous porous cylindrical domain. *J. Appl. Comput. Mech.* 6, 1324–1334. doi:10.22055/JACM.2020.33464.2230

Ahmed, J., Begum, A., Shahzad, A., and Ali, R. (2016). MHD axisymmetric flow of power-law fluid over an unsteady stretching sheet with convective boundary conditions. *Results Phys.* 6, 973–981. doi:10.1016/j.rinp.2016.11.013

Alzahrani, A. K., Abbas, Z., and Ullah, M. Z. (2023). Chemically reactive two-phase flow of viscous-Casson fluids in a rotating channel. *Alexandria Eng. J.* 62, 403–413. doi:10.1016/j.aej.2022.07.036

Bansal, P., Saraswat, M., Sharma, K., and Chauhan, N. (2020). Effect of Poisson's ratio for liner material on performance of journal bearing under micropolar lubrication. *Int. J. Eng. Trends Technol.* 68 (8), 58–61. doi:10.14445/22315381/IJETT-V68I8P211S

Bég, O. A., Zaman, A., Ali, N., Gaffar, S. A., and Bég, E. T. (2019). Numerical computation of nonlinear oscillatory two-immiscible magnetohydrodynamic flow in dual porous media system: FTCS and FEM study. *Heat Transfer-Asian Res.* 48 (4), 1245–1263. doi:10.1002/htj.21429

Chamkha, A. J. (2000). Flow of two-immiscible fluids in porous and nonporous channels. *J. Fluids Eng.* 122 (1), 117–124. doi:10.1115/1.483233

Chen, X., and Jian, Y. (2022). Entropy generation minimization analysis of two immiscible fluids. *Int. J. Therm. Sci.* 171, 107210. doi:10.1016/j.ijthermalsci.2021.107210

Das, S. K., Putra, N., Thiesen, P., and Roetzel, W. (2003). Temperature dependence of thermal conductivity enhancement for nanofluids. *J. Heat. Transf.* 125 (4), 567–574. doi:10.1115/1.1571080

Dey, C., Baishya, K., Ghosh, A., Goswami, M. M., Ghosh, A., and Mandal, K. (2017). Improvement of drug delivery by hyperthermia treatment using magnetic cubic cobalt ferrite nanoparticles. *J. Magn. Magn. Mater* 427, 168–174. doi:10.1016/j.jmmm.2016.11.024

El-Amin, M., Alwated, B., and Hoteit, H. (2023). Machine learning prediction of nanoparticle transport with two-phase flow in porous media. *Energies (Basel)* 16 (2), 678. doi:10.3390/en16020678

Eringen, A. C. (1996). Theory of micropolar fluids. *J. Math. Mech.* 16, 1–18. doi:10.1512/iumj.1967.16.16001

Eringen, A. C. (1964). Simple micro fluids. *Int. J. Eng. Sci.* 2 (2), 205–217. doi:10.1016/0020-7225(64)90005-9

Fan, H., Xing, X., Yang, Y., Li, B., Wang, C., and Qiu, D. (2017). Triple function nanocomposites of porous silica-CoFe $_2$ O $_4$ -MWCNTs as a carrier for pH-sensitive anti-cancer drug-controlled delivery. *Dalton Trans.* 46 (43), 14831–14838. doi:10.1039/C7DT02424J

Ghasemi, B., and Aminossadati, S. M. (2009). Natural convection heat transfer in an inclined enclosure filled with a water-cuo nanofluid. *Numeri Heat. Transf. A Appl.* 55 (8), 807–823. doi:10.1080/10407780902864623

Gopal, D., Naik, S. H. S., Kishan, N., and Raju, C. S. K. (2020). The impact of thermal stratification and heat generation/absorption on MHD carreau nano fluid flow over a permeable cylinder. *SN Appl. Sci.* 2 (4), 639. doi:10.1007/s42452-020-2445-5

Hasnain, J., Abid, N., O Alansari, M., and Zaka Ullah, M. (2022). Analysis on Cattaneo-Christov heat flux in three-phase oscillatory flow of non-Newtonian fluid through porous zone bounded by hybrid nanofluids. *Case Stud. Therm. Eng.* 35, 102074. doi:10.1016/j.csite.2022.102074

Hayat, T., and Nadeem, S. (2017). Heat transfer enhancement with Ag–CuO/water hybrid nanofluid. *Results Phys.* 7, 2317–2324. doi:10.1016/j.rinp.2017.06.034

Hayat, T., Nadeem, S., and Khan, A. U. (2019). Numerical analysis of Ag–CuO/water rotating hybrid nanofluid with heat generation and absorption. *Can. J. Phys.* 97 (6), 644–650. doi:10.1139/cjp-2018-0011

Ikbal, Md. A., Chakravarty, S., and Mandal, P. K. (2009). Two-layered micropolar fluid flow through stenosed artery: Effect of peripheral layer thickness. *Comput. Math. Appl.* 58 (7), 1328–1339. doi:10.1016/j.camwa.2009.07.023

Kavya, S., Nagendramma, V., Ahammad, N. A., Ahmad, S., Raju, C. S. K., and Shah, N. A. (2022). Magnetic-hybrid nanoparticles with stretching/shrinking cylinder in a suspension of MoS4 and copper nanoparticles. *Int. Commun. Heat Mass Transf.* 136, 106150. doi:10.1016/j.icheatmasstransfer.2022.106150

Khaled, A.-R. A., and Vafai, K. (2014). Heat transfer enhancement by layering of two immiscible co-flows. *Int. J. Heat. Mass Transf.* 68, 299–309. doi:10.1016/j.ijheatmasstransfer.2013.09.040

Khan, M., and Alshomrani, A. S. (2017). Numerical simulation for flow and heat transfer to carreau fluid with magnetic field effect: Dual nature study. *J. Magnetism Magnetic Mater.* 443, 13–21. doi:10.1016/j.jmmm.2017.06.135

Khan, U., Waini, I., Ishak, A., and Pop, I. (2021). Unsteady hybrid nanofluid flow over a radially permeable shrinking/stretching surface. *J. Mol. Liq.* 331, 115752. doi:10.1016/j.molliq.2021.115752

Khan, U., Zaib, A., Ishak, A., Waini, I., Raizah, Z., Prasannakumara, B. C., et al. (2022). Dynamics of bio-convection agrawal axisymmetric flow of water-based Cu-TiO2 hybrid nanoparticles through a porous moving disk with zero mass flux. *Chem. Phys.* 561, 111599. doi:10.1016/j.chemphys.2022.111599

Khan, Z. H., Qasim, M., Haq, R. U., and Al-Mdallal, Q. M. (2017). Closed form dual nature solutions of fluid flow and heat transfer over a stretching/shrinking sheet in a porous medium. *Chin. J. Phys.* 55, 1284–1293. doi:10.1016/j.cjph.2017.07.001

Khonsari, M. M. (1990). On the self-excited whirl orbits of a journal in a sleeve bearing lubricated with micropolar fluids. *Acta Mech.* 81 (3–4), 235–244. doi:10.1007/BF01176991

Kumar, J. P., Umavathi, J. C., Chamkha, A. J., and Pop, I. (2010). Fully-developed free-convective flow of micropolar and viscous fluids in a vertical channel. *Appl. Math. Model* 34 (5), 1175–1186. doi:10.1016/j.apm.2009.08.007

Kumar Yadav, P., Jaiswal, S., Asim, T., and Mishra, R. (2018). Influence of a magnetic field on the flow of a micropolar fluid sandwiched between two Newtonian fluid layers through a porous medium. *Eur. Phys. J. Plus* 133 (7), 247. doi:10.1140/epjp/i2018-12071-5

Lee, S. U. S. ChoiS. Li, and Eastman, J. A. (1999). Measuring thermal conductivity of fluids containing oxide nanoparticles. *J. Heat. Transf.* 121 (2), 280–289. doi:10.1115/1.2825978

Li, Q., and Xuan, Y. (2000). Heat transfer enhancement of nanofluids. *Int. J. Heat. Fluid Flow.* 21, 58–64. doi:10.1016/s0142-727x(99)00067-3

Lou, Q., Ali, B., Rehman, S. U., Habib, D., Abdal, S., Shah, N. A., et al. (2022). Micropolar dusty fluid: Coriolis force effects on dynamics of MHD rotating fluid when Lorentz force is significant. *Mathematics* 10 (15), 2630. doi:10.3390/math10152630

Mintsa, H. A., Roy, G., Nguyen, C. T., and Doucet, D. (2009). New temperature dependent thermal conductivity data for water-based nanofluids. *Int. J. Therm. Sci.* 48 (2), 363–371. doi:10.1016/j.ijthermalsci.2008.03.009

Muthtamilselvan, M., Kandaswamy, P., and Lee, J. (2010). Heat transfer enhancement of copper-water nanofluids in a lid-driven enclosure. *Commun. Nonlinear Sci. Numer. Simul.* 15 (6), 1501–1510. doi:10.1016/j.cnsns.2009.06.015

Nikodijevic, D., Stamenkovic, Z., Jovanovic, M., Kocic, M., and Nikodijevic, J. (2014). Flow and heat transfer of three immiscible fluids in the presence of uniform magnetic field. *Therm. Sci.* 18 (3), 1019–1028. doi:10.2298/TSCI1403019N

Raju, C. S. K., Ahammad, N. A., Sajjan, K., Shah, N. A., Yook, S.-J., and Kumar, M. D. (2022). Nonlinear movements of axisymmetric ternary hybrid nanofluids in a thermally radiated expanding or contracting permeable Darcy Walls with different shapes and densities: Simple linear regression. *Int. Commun. Heat Mass Transf.* 135, 106110. doi:10.1016/j.icheatmasstransfer.2022.106110

Shahzad, F., Jamshed, W., El Din, S. M., Shamshuddin, M., Ibrahim, R. W., Raizah, Z., et al. (2022). Second-order convergence analysis for Hall effect and electromagnetic force on ternary nanofluid flowing via rotating disk. *Sci. Rep.* 12 (1), 18769. doi:10.1038/s41598-022-23561-7

Shamshuddin, M. D., Akkurt, N., Saeed, A., and Kumam, P. (2023d). Radiation mechanism on dissipative ternary hybrid nanoliquid flow through rotating disk encountered by Hall currents: HAM solution. *Alexandria Eng. J.* 65, 543–559. doi:10.1016/j.aej.2022.10.021

Shamshuddin, M. D., Mabood, F., Khan, W. A., and Rajput, G. R. (2023c). Exploration of thermal Péclet number, vortex viscosity, and Reynolds number on two-dimensional flow of micropolar fluid through a channel due to mixed convection. *Heat. Transf.* 52 (1), 854–873. doi:10.1002/htj.22719

Shamshuddin, M. D., Saeed, A., Asogwa, K. K., and Jamshed, W. (2023a). A semi-analytical approach to investigate the entropy generation in a tangent hyperbolic magnetized hybrid nanofluid flow upon a stretchable rotating disk. *J. Magn. Magn. Mater* 574, 170664. doi:10.1016/j.jmmm.2023.170664

Shamshuddin, M. D., Salawu, S. O., Asogwa, K. K., and Srinivasa Rao, P. (2023b). Thermal exploration of convective transportation of ethylene glycol based magnetized nanofluid flow in porous cylindrical annulus utilizing MOS2 and Fe3O4 nanoparticles with inconstant viscosity. *J. Magn. Magn. Mater* 573, 170663. doi:10.1016/j.jmmm.2023.170663

Siddiqa, S., Begum, N., Hossain, Md. A., Abrar, M. N., Gorla, R. S. R., and Al-Mdallal, Q. (2021). Effect of thermal radiation on conjugate natural convection flow of a micropolar fluid along a vertical surface. *Comput. Math. Appl.* 83, 74–83. doi:10.1016/j.camwa.2020.01.011

Umavathi, J. C., and Anwar Bég, O. (2020a). Effects of thermophysical properties on heat transfer at the interface of two immisicible fluids in a vertical duct: Numerical study. *Int. J. Heat. Mass Transf.* 154, 119613. doi:10.1016/j.ijheatmasstransfer.2020.119613

Umavathi, J. C., and Anwar Bég, O. (2020b). Effects of thermophysical properties on heat transfer at the interface of two immisicible fluids in a vertical duct: Numerical

study. *Int. J. Heat. Mass Transf.* 154, 119613. doi:10.1016/j.ijheatmasstransfer.2020.119613

Umavathi, J. C., Chamkha, A. J., Manjula, M. H., and Al-Mudhaf, A. (2005). Flow and heat transfer of a couple-stress fluid sandwiched between viscous fluid layers. *Can. J. Phys.* 83 (7), 705–720. doi:10.1139/p05-032

Umavathi, J. C., Kumar, J. P., and Chamkha, A. J. (2008). Flow and heat transfer of a micropolar fluid sandwiched between viscous fluid layers. *Can. J. Phys.* 86 (8), 961–973. doi:10.1139/p08-022

Upadhya, S. M., Raju, S. V. S. R., Raju, C. S. K., Shah, N. A., and Chung, J. D. (2022). Importance of entropy generation on Casson, Micropolar and Hybrid magneto-nanofluids in a suspension of cross diffusion. *Chin. J. Phys.* 77, 1080–1101. doi:10.1016/j.cjph.2021.10.016

Vajravelu, K., Prasad, K. V., and Abbasbandy, S. (2013). Convective transport of nanoparticles in multi-layer fluid flow. *Appl. Math. Mech.* 34 (2), 177–188. doi:10.1007/s10483-013-1662-6

Vamvakidis, K., Mourdikoudis, S., Makridis, A., Paulidou, E., Angelakeris, M., and Dendrinou-Samara, C. (2018). Magnetic hyperthermia efficiency and MRI contrast sensitivity of colloidal soft/hard ferrite nanoclusters. *J. Colloid Interface Sci.* 511, 101–109. doi:10.1016/j.jcis.2017.10.001

Wang, X.-Q., and Mujumdar, A. S. (2007). Heat transfer characteristics of nanofluids: A review. *Int. J. Therm. Sci.* 46 (1), 1–19. doi:10.1016/j.ijthermalsci.2006.06.010

Wang, X., Xu, X., and Choi, S. U. S. (1999). Thermal conductivity of nanoparticle - fluid mixture. *J. Thermophys. Heat. Trans.* 13 (4), 474–480. doi:10.2514/2.6486

Nomenclature

Roman letters

Br →	Brinkman number
E →	Electric parameter
g →	gravitational force
Gr →	thermal Grashof number
k →	thermal conductivity
κ →	Porosity
Km →	material parameter
M →	Magnetic parameter
N →	Thermal radiation
Nu →	Nusselt number
s →	solid particle
v →	kinematic viscosity
w →	condition at the surface

Greek words

ω →	angle of inclination
ϕ →	solid volume fraction
ρ →	the density of the fluid
θ →	dimensionless temperature
τ →	skin friction
μ →	dynamic viscosity of hybrid nanofluid
σ →	porous medium parameter
β →	thermal expansion coefficient

Subscripts

nf →	Nanofluid
f →	base fluid
hnf →	hybrid nanofluid

frontiers | Frontiers in Materials

TYPE Original Research
PUBLISHED 26 July 2023
DOI 10.3389/fmats.2023.1183175

OPEN ACCESS

EDITED BY
Noor Saeed Khan,
University of Education Lahore, Pakistan

REVIEWED BY
M. Riaz Khan,
Quaid-i-Azam University, Pakistan
Nilankush Acharya,
Jadavpur University, India

*CORRESPONDENCE
Syed Ibrahim,
syed.ibrahim@riphah.edu.pk

RECEIVED 09 March 2023
ACCEPTED 29 May 2023
PUBLISHED 26 July 2023

CITATION
Ibrahim S, Khan Marwat DN, Ullah N, Nisar KS, Kamran (2023), Flow and heat transfer in a meandering channel. *Front. Mater.* 10:1183175. doi: 10.3389/fmats.2023.1183175

Flow and heat transfer in a meandering channel

Syed Ibrahim[1,2]*, Dil Nawaz Khan Marwat[1], Naeem Ullah[1], Kottakkaran Sooppy Nisar[3,4] and Kamran[1]

[1]Department of Mathematics, Islamia College Peshawar, University Campus, Peshawar, Khyber Pakhtunkhwa, Pakistan, [2]Riphah International University, Chakdara, Khyber Pakhtunkhwa, Pakistan, [3]Department of Mathematics, College of Science and Humanities in Alkharj, Prince Sattam Bin Abdulaziz University, Alkharj, Saudi Arabia, [4]School of Technology, Woxsen University, Hyderabad, India

Fluid flows occur due to internal or external forces such as wind, gravity, pressure gradients, side-wall motion, MHD, and free convection. This study examines how meanders impact heat transfer by studying the behavior of viscous fluid flow with streamwise vortices in a sinusoidal wavy meandering channel of non-uniform radius. The study simplifies the motion and energy equations governing the fluid flow using novel transformations and a regular perturbation method. By plotting graphs for different parameter values, such as Pr, Re, and Ec, it reveals that decreasing the wavelength leads to flow separation near the channel surface. However, the stream moves forward with a sudden meander disturbance, causing the flow to become rectilinear and independent of vertex-generating centrifugal forces. The study identifies a stream function using standard and established relations. The fluid flow patterns and temperature distribution behavior are shown in various plots, highlighting the significant impact of meanders on fluid flow.

KEYWORDS

stream wise vortices, meandering channel, flow separation, instability, nonuniform radius

1 Introduction

There are infinitely many possible types of meanders, and here we consider only a special type of meandering channel, i.e., the sinusoidal meandering channel. These channels are influenced by various agents that cause fluid motion, with the most common being the pressure gradient. In some cases, the pressure gradient may be mechanical in nature. The flows within these channels are predominantly induced by the pressure gradient, and they have numerous practical applications (Webb and Bergles, 1981; Bergles and Webb, 1985; Jensen et al., 1997; Ligrani et al., 2003). The partition of escalation structures can be performed on those that are responsible for necessary changes in the thermal and physical properties of fluids under consideration and the ones marked by perfection in fluid maxing (Fiebig, 1995a; Fiebig, 1995b; Jacobi and Shah, 1995). Mixing with improved mechanics is the point of attention in engineering devices functioning at small Reynolds numbers (Re) with laminar patterns (Fiebig, 1998). Commonly, it is understood that improved mixing can be done via compelling the fluid from the laminar state into a turbulent one or by the formation vortex generators. Vortex generators are functional but have significant pressure in their drag drawback (Patera and Mikic, 1986; Fiebig and Chen, 1999).

For nearly a century, centrifugal instability has been observed in shear layers. Previous studies focused on simple geometries and canonical flows, making it easy to calculate the curvature or meander of flow patterns. One example is the flow of fluid motion between rotating cylinders, where (Floryan, 1991) investigated the stability states of the distribution of rotation in an inviscid mechanism. In (Mohammadi and Floryan, 2013), addressed a highly

viscous problem was addressed, and the critical conditions of the secondary flow onset were determined. In (Xu et al., 2016), comparable instability in curved channels was analyzed, and (Rayleigh, 1917) presented a case of boundary layer flows on concave sheets, taking into account centrifugal instability. In (Taylor, 1923), it was found that the special type of instability is prominent for fluid flow over concave and convex sheets, subject to the condition that the velocity components are non-monotonic in nature. In (Ghalambaz et al., 2016; Hayat et al., 2017; Srinivasacharya and Sibanda, 2020; Mahmud and Uddin, 2021), numerical simulation and analysis of different types of nanofluids flowing past various types of surfaces in the context of fluid flow and heat transfer in different channels was performed (Khan and Ahmed, 2015; Alsaedi et al., 2016; Nadeem et al., 2016; Izadi and Pourmehran, 2017; Khan et al., 2017; Sheikholeslami et al., 2017). These studies explore the impact of various factors such as thermal radiation, magnetic fields, bioconvection, entropy optimization, and chemical reactions on flow and heat transfer characteristics. As such, these articles are highly relevant for those interested in studying the behavior of nanofluids. All of these results apply to constant meanders and establish a clear relationship between streamline meanders and the wall meander. Consequently, the demonstration of this special type of stability revealed that it is represented by a single parameter, which is one possible way to describe this meandering with a single parameter.

The main objective of this study is to investigate the flow of a viscous fluid in a meandering channel with wavy walls driven by a pressure gradient. The equations of motion, including the conservation of the mass and momentum equations and the energy equation, are utilized to analyze the fluid flow and temperature distribution within the channel. The boundary conditions are imposed on the channel walls and at the center of the channel to maintain symmetry. Dimensionless variables are used to transform the governing equations into a dimensionless form for easy tracking of units. Additionally, the study explores special types of instabilities and their significance. In the first part, an assumption of fixed pressure gradient is imposed, assuming direct channel flow with parallel plates, and sinusoidal channel flow is driven by an identical pressure gradient. Flow rate variation is used to supplement the flow losses associated with the meandering channel. The generalized model is solved using perturbation method, and the stream function is calculated and examined using other techniques. The temperature distribution behavior is illustrated through various plots depicting different dimensionless parameters, such as Pr, Re, and Ec.

2 Geometry of the problem

Consider the flow of a viscous fluid in a meandering channel, which consists of two wavy walls separated by a fixed gap. The classical model for laminar flows in channels, tubes, and ducts is provided by Poiseuille. The flow in such a channel is primarily induced by a pressure gradient. There are various types of flows that pass through ducts and channels, and they have significant practical importance. The classification of scaling structures can be conducted based on those that have variations in the effective thermophysical properties of fluids, and the pursuit of optimal fluid mixing can lead to an infinite number of possible meander types. In this study, we will focus on the simplest sinusoidal channel, whose geometry is illustrated in Figure 1, where the superscript H denotes the upper and G denotes the lower walls of the channel. The channel extends along the *x-axis* from negative infinity to positive infinity, and the flow is driven by a pressure gradient.

3 Governing equations and their non-dimensional form

The general form of continuity equation for incompressible viscous flow is:

$$\mathrm{div}\mathbf{V} = \mathbf{0} \tag{1}$$

The velocity vector, denoted as $\mathbf{V}$, has three components for three-dimensional flow. Similarly, the general form of the Navier–Stokes equations applies to steady and viscous flows of constant viscosity.

$$\rho(\mathbf{V}\cdot\nabla)\mathbf{V} = -\nabla \mathrm{P} + \mu\nabla^2\mathbf{V}, \tag{2}$$

The variables ρ, μ, and P represent density, viscosity, and pressure of the fluid, respectively. To define the dimensionless variables, we use asterisks and reference length L and velocity U, as follows:

$$\nabla^* = \mathrm{L}\nabla, \mathrm{V}^* = \frac{\mathbf{V}}{U}, \textit{and}\ \mathrm{P}^* = \frac{P}{\rho \mathrm{U}^2}, \tag{3}$$

After substituting the non-dimensional variables, which are defined in Eq. 3, into Eqs 1, 2, we obtain the dimensionless continuity and Navier–Stokes equations:

$$\mathrm{div}\mathrm{V}^* = \mathbf{0}, \tag{4}$$

$$\frac{\rho U^2}{L}\mathrm{V}^*\cdot(\nabla^*\mathrm{V}^*) = -\frac{\rho \mathrm{U}^2}{L}\nabla^*\mathrm{P}^* + \frac{\mu \mathrm{U}}{L^2}\nabla^{*2}\mathrm{V}^*, \tag{5}$$

The above equation is multiplied by $\frac{L}{\rho \mathrm{U}^2}$, and when simplified we get:

$$\Rightarrow (\mathrm{V}^*\cdot\nabla^*)\,\mathrm{V}^* = -\nabla^*\mathrm{P}^* + \frac{1}{Re}\nabla^{*2}\mathrm{V}^*. \tag{6}$$

where $Re = \frac{\rho \mathrm{UL}}{\mu}$ represents the Reynold's number.

4 Modeling of the problem

Let us consider that for flow in a straight channel and for two-dimensional flow, the velocity is represented by the velocity $\boldsymbol{V_0}$, pressure by P_0, the stream function of the flow is denoted by ψ_0, and Q_0 is the flow rate representative. Then, the continuity equation in two dimensional is transformed to:

$$\frac{\partial u_0}{\partial x} + \frac{\partial v_0}{\partial y} = 0, \tag{7}$$

The x- component of the Navier–Stoke equations is:

$$\rho\left(\frac{\partial u_0}{\partial t} + u_0\frac{\partial u_0}{\partial x} + v_0\frac{\partial u_0}{\partial y}\right) = -\frac{\partial P_0}{\partial x} + \mu\left\{\frac{\partial^2 u_0}{\partial x^2} + \frac{\partial^2 u_0}{\partial y^2}\right\}, \tag{8}$$

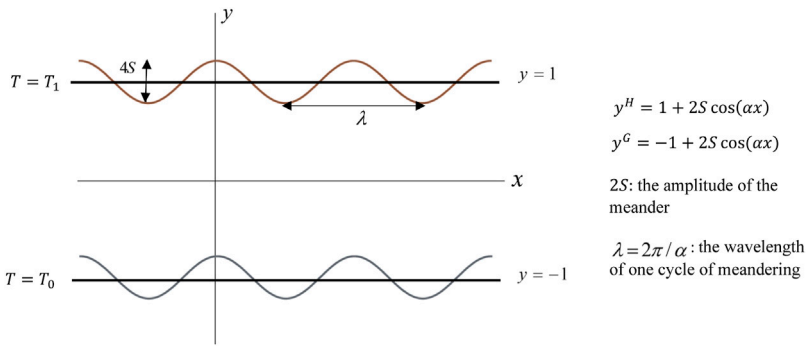

FIGURE 1
Geometry of meandering channel and flow field under consideration.

The y- component of the Navier–Stoke equations is:

$$\rho\left(\frac{\partial v_0}{\partial t}+u_0\frac{\partial v_0}{\partial x}+v_0\frac{\partial v_0}{\partial y}\right)=-\frac{\partial P_0}{\partial y}+\mu\left\{\frac{\partial^2 v_0}{\partial x^2}+\frac{\partial^2 v_0}{\partial y^2}\right\}, \tag{9}$$

The boundary conditions for the problem are established by utilizing the no-slip condition, along with considering the geometry of the problem. Thus, the boundary conditions can be written as:

$$u_0 = 0 \; at \; y = \pm\ 1. \tag{10}$$

Equations 7–9 represent the continuity and the $x\,\&\,y$-momentum equations, respectively, for a one-dimensional straight channel. These equations can be greatly simplified by making certain assumptions, namely, that $(u_0 \neq 0 \; and \; v_0 = 0)$. With this assumption, the solution for the governing equations for straight channel flow can be obtained by combining the axial velocity (u_0), normal velocity (v_0), and pressure $(\mathcal{P}_0)$, which can be expressed as follows:

$$\begin{aligned} \boldsymbol{V}_0 &= [u_0(\eta), 0] = [1-\eta^2, 0] \\ \mathcal{P}_0 &= \frac{-2\xi}{Re}+C_1, \end{aligned} \tag{11}$$

Note that Eqs 1–11 for the fully developed flow in a straight channel has been reported in F.M. White [31] and Schlichting [32].

The volume flow rate for the channel flow of fixed width is:

$$Q_0 = \int_{-1}^{1} u_0(\eta)d\eta = \frac{4}{3}. \tag{12}$$

The stream function (ψ_0) is simply evaluated as:

$$\frac{\partial \psi_0}{\partial \eta} = u_0(\eta) \Rightarrow \psi_0 = -\frac{\eta^3}{3}+\eta+C_2. \tag{13}$$

In a meandering channel, where the fluid flow moves in the positive x-axis direction, the Reynolds number is defined based on the maximum x-velocity and channel half-height.

The velocity field and other related field quantities for the fluid motion in the meandering channel can be expressed as follows:

$$\begin{aligned} \boldsymbol{V}_b &= \boldsymbol{V}_0 + \boldsymbol{V}_1 = [u_0(\eta), 0] + [u_1(\xi,\eta), v_1(\xi,\eta)], \\ \mathcal{P}_b(\xi,\eta) &= \mathcal{P}_0(\xi) + \mathcal{P}_1(\xi,\eta), \\ \psi_b &= \psi_0(\eta) + \psi_1(\xi,\eta), Q_b = Q_0 + Q_1, \end{aligned} \tag{14}$$

In the context of the meandering channel geometry, the velocity $\boldsymbol{V_1}$, pressure $\mathcal{P}_1$, stream function ψ_1, and flow rate Q_1 are dimensionless quantities that are adjusted accordingly. Additionally, the velocity vector $\boldsymbol{V}_b = (u_b, v_b)$ is decomposed. These components are further decomposed as follows:

$$u_b = [u_0(\eta), u_1(\xi,\eta)] \; and \; v_b = [0, v_1(\xi,\eta)], \tag{15}$$

This is achieved by substituting the new variables for the velocity field in the dimensionless governing equations, i.e., Eqs 4, 6, and eliminating pressure term.

The continuity equation Eq. 4 in the new variable is:

$$\frac{\partial u_b}{\partial \xi}+\frac{\partial v_b}{\partial \eta} = 0, \tag{16}$$

and now using the decomposed forms of u_b and v_b from Eq. 15, we have:

$$\Rightarrow \frac{\partial u_1}{\partial \xi}+\frac{\partial v_1}{\partial \eta} = 0, \tag{17}$$

Note that u_0 and v_0 are defined in Eq. 15, and some derivatives vanish:

$$\frac{\partial u_0}{\partial \xi} = \frac{\partial v_0}{\partial \xi} = 0,$$

The dimensionless $x-$ momentum Eq. 6 for new variables becomes:

$$\begin{aligned} &\left\{\frac{\partial}{\partial \eta}\left(u_0\frac{\partial u_1}{\partial \xi}\right)+\frac{\partial}{\partial \eta}\left(u_1\frac{\partial u_1}{\partial \xi}\right)+\frac{\partial}{\partial \eta}\left(v_1\frac{\partial u_0}{\partial \eta}\right)+\frac{\partial}{\partial \eta}\left(v_1\frac{\partial u_1}{\partial \eta}\right)\right\} \\ &= -\frac{\partial^2 \mathcal{P}_1}{\partial \xi \partial \eta}+Re^{-1}\left\{\frac{\partial^3 u_1}{\partial \xi^2 \partial \eta}+\frac{\partial^3 u_1}{\partial \eta^3}\right\}, \end{aligned} \tag{18}$$

The dimensionless $y-$ momentum Eq. 6 for new variables becomes:

$$\begin{aligned} &\left\{\frac{\partial}{\partial \xi}\left(u_0\frac{\partial v_1}{\partial \xi}\right)+\frac{\partial}{\partial \xi}\left(u_1\frac{\partial v_1}{\partial \xi}\right)+\frac{\partial}{\partial \xi}\left(v_1\frac{\partial v_1}{\partial \eta}\right)\right\} \\ &= -\frac{\partial^2 \mathcal{P}_1}{\partial \xi \partial \eta}+Re^{-1}\left\{\frac{\partial^3 v_1}{\partial \xi^3}+\frac{\partial^3 v_1}{\partial \xi \partial \eta^2}\right\}, \end{aligned} \tag{19}$$

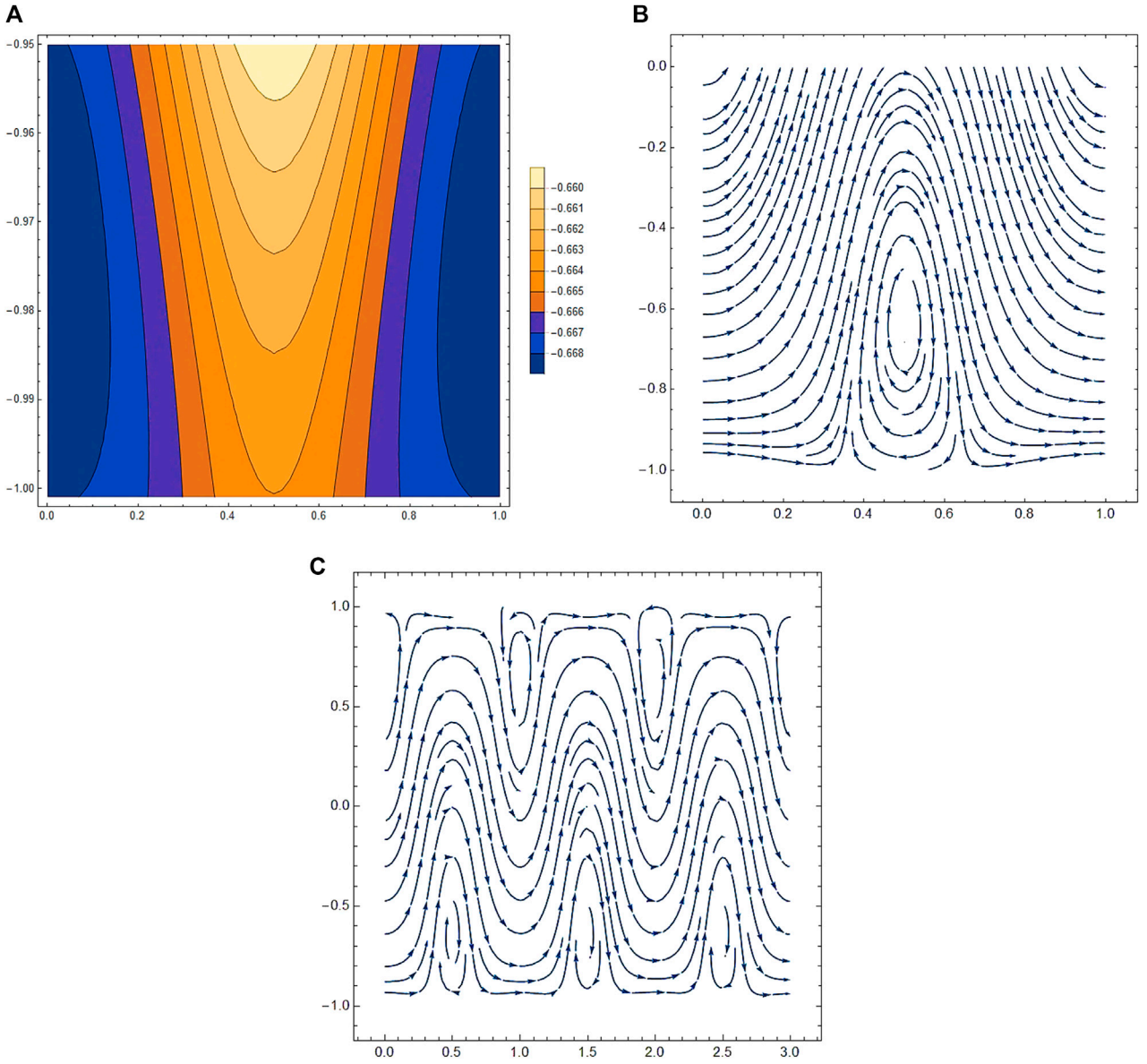

FIGURE 2
The streamlines in the area adjacent to the lower wall are shown in **(A,B)** where S = 5 (amplitude), Re = 1, and α = 10, while **(C)** is plotted for the whole channel.

The pressure term is eliminated by expending the terms

$$\frac{\partial}{\partial \eta}\left(u_0\frac{\partial u_1}{\partial \xi}\right),\frac{\partial}{\partial \eta}\left(v_1\frac{\partial u_1}{\partial \eta}\right),\frac{\partial}{\partial \xi}\left(u_0\frac{\partial v_1}{\partial \xi}\right).$$

in Eqs 18, 19, and then by subtracting Eq. 19 from Eq. 18, we get:

$$\left\{\frac{\partial u_0}{\partial \eta}\ \frac{\partial u_1}{\partial \xi}+u_0\frac{\partial^2 u_1}{\partial \xi \partial \eta}+\frac{\partial}{\partial \eta}\left(u_1\frac{\partial u_1}{\partial \xi}+v_1\frac{\partial u_1}{\partial \eta}\right)+\frac{\partial v_1}{\partial \eta}\ \frac{\partial u_0}{\partial \eta}\right.$$
$$\left.+v_1\frac{\partial^2 u_0}{\partial \eta^2}-u_0\frac{\partial^2 v_1}{\partial \xi^2}-\frac{\partial}{\partial \xi}\left(u_1\frac{\partial v_1}{\partial \xi}+v_1\frac{\partial v_1}{\partial \eta}\right)\right\}$$
$$=Re^{-1}\left\{\frac{\partial^3 u_1}{\partial \xi^2 \partial \eta}+\frac{\partial^3 u_1}{\partial \eta^3}-\frac{\partial^3 v_1}{\partial \xi^3}-\frac{\partial^3 v_1}{\partial \xi \partial \eta^2}\right\}, \quad (20)$$

We define a stream function (ψ_b) such that:

$$u_b=\frac{\partial \psi_b}{\partial \eta}\ and\ v_b=-\frac{\partial \psi_b}{\partial \xi}\Rightarrow(u_0+u_1)=\frac{\partial}{\partial \eta}\left(\psi_0+\psi_1\right)and\ v_1=\frac{\partial \psi_1}{\partial \eta}. \quad (21)$$

Substituting in Eq. 20, we get:

$$\Rightarrow u_0\frac{\partial}{\partial \xi}\nabla^2\psi_1-\frac{\partial^2 u_0}{\partial \eta^2}\frac{\partial \psi_1}{\partial \xi}-Re^{-1}\nabla^4\psi_1$$
$$=\frac{\partial}{\partial \xi}\left(u_1\frac{\partial v_1}{\partial \xi}+v_1\frac{\partial v_1}{\partial \eta}\right)-\frac{\partial}{\partial \eta}\left(u_1\frac{\partial u_1}{\partial \xi}+v_1\frac{\partial u_1}{\partial \eta}\right), \quad (22)$$

$$where\nabla^2\psi_1=\frac{\partial^2 \psi_1}{\partial \eta^2}+\frac{\partial^2 \psi_1}{\partial \xi^2}\ \&\nabla^4\psi_1=\frac{\partial^4 \psi_1}{\partial \eta^4}+2\frac{\partial^4 \psi_1}{\partial \xi^2 \partial \eta^2}+\frac{\partial^4 \psi_1}{\partial \xi^4}.$$

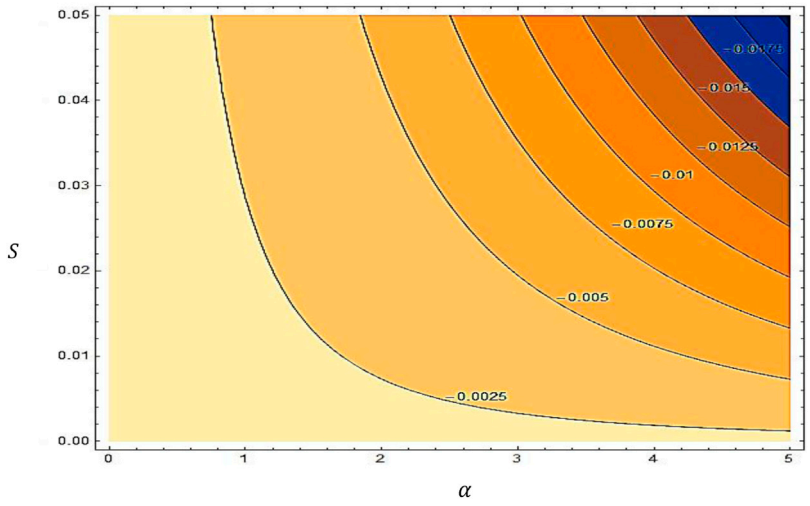

FIGURE 3
Variations of the pressure gradient correction Re[(dP_1)/dx] = -0.002.

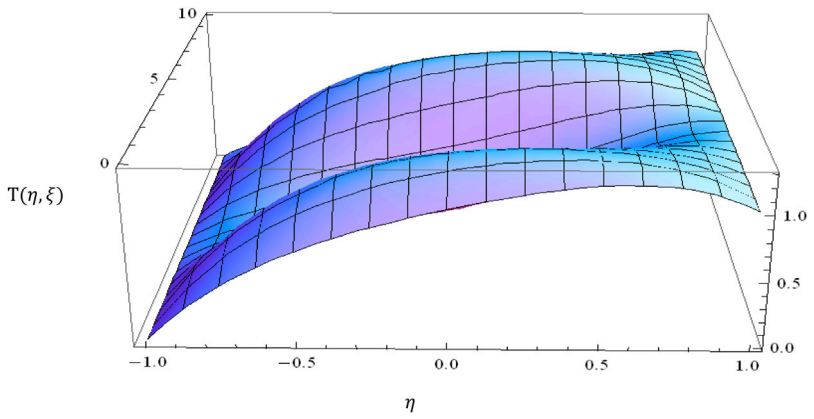

FIGURE 4
Temperature distribution is uniform and smooth from 0 to 1 in the direction of η, whereas its behavior in ξ direction is periodic in nature. For fixed values of S = 0.0125, Re = 10, α = 0.1, Pr = 1, and Ec = 1.

From the above continuity Eq. 22, we have:

$$\frac{\partial u_1}{\partial \xi}+\frac{\partial v_1}{\partial \eta}=0\Rightarrow u_1\left(\frac{\partial u_1}{\partial \xi}+\frac{\partial v_1}{\partial \eta}\right)=v_1\left(\frac{\partial u_1}{\partial \xi}+\frac{\partial v_1}{\partial \eta}\right)=0. \quad (23)$$

By substituting in Eq. 22, we have:

$$u_0\frac{\partial}{\partial \xi}\nabla^2\psi_1-\frac{\partial^2 u_0}{\partial \eta^2}\frac{\partial \psi_1}{\partial \xi}-Re^{-1}\nabla^4\psi_1 = \frac{\partial}{\partial \xi}\left\{\frac{\partial}{\partial \xi}\left(u_1v_1\right)+\frac{\partial}{\partial \eta}\left(v_1v_1\right)\right\}-\frac{\partial}{\partial \eta}\left(\frac{\partial}{\partial \xi}\left(u_1u_1\right)+\frac{\partial}{\partial \eta}\left(u_1v_1\right)\right). \quad (24)$$

The no slip boundary conditions:

$$u_0\left(y_U\left(\xi\right)\right)+u_1\left(\xi,y_U\left(\xi\right)\right)=0, v_1\left(\xi,y_U\left(\xi\right)\right)=0,$$
$$u_0\left(y_L\left(\xi\right)\right)+u_1\left(\xi,y_L\left(\xi\right)\right)=0, v_1\left(\xi,y_L\left(\xi\right)\right)=0. \quad (25)$$

Reconsidering the total stream function:

$$\psi_0\left(y_U\left(\xi\right)\right)+\psi_1\left(\xi,y_U\left(\xi\right)\right)=\frac{3}{4}.$$
$$\psi_0\left(y_L\left(\xi\right)\right)+\psi_1\left(\xi,y_L\left(\xi\right)\right)=0. \quad (26)$$

Floryan (1997) used the Fourier expansion for the simplification of the above equation:

$$\psi_1\left(\xi,\eta\right)=\sum_{n=-\infty}^{n=\infty}\phi^n\left(\eta\right)e^{in\alpha\xi}, \quad (27)$$

where $\phi^n=\phi^{(-n)^*}$ represents the conditions, and the star identifies the complex conjugate.

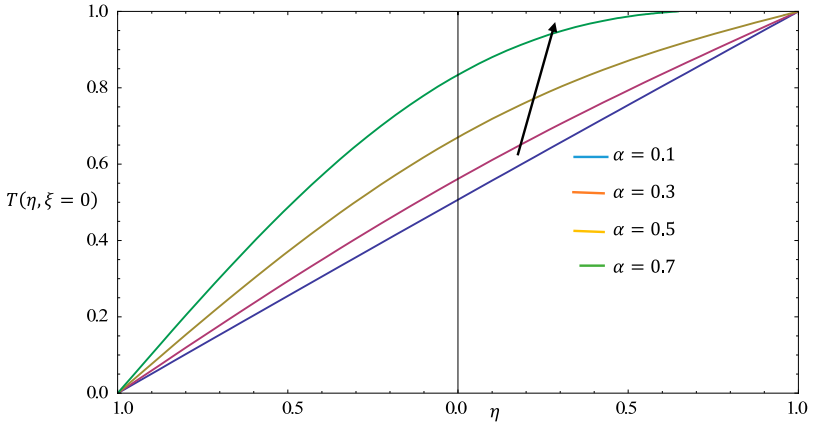

FIGURE 5
Temperature distribution $T(\eta, \xi)$ is plotted against "η" for fixed values of $\xi = 0$, $S = 0.0125$, $Re = 1$, $Pr = 2$, and $Ec = 0.0001$ and different values of α. Note that the Prandtl and Eckert numbers are the choice for water. The temperature profile is increasing with α, whereas each profile changes uniformly. Moreover, the profile is either linear or close to linear for small values of α.

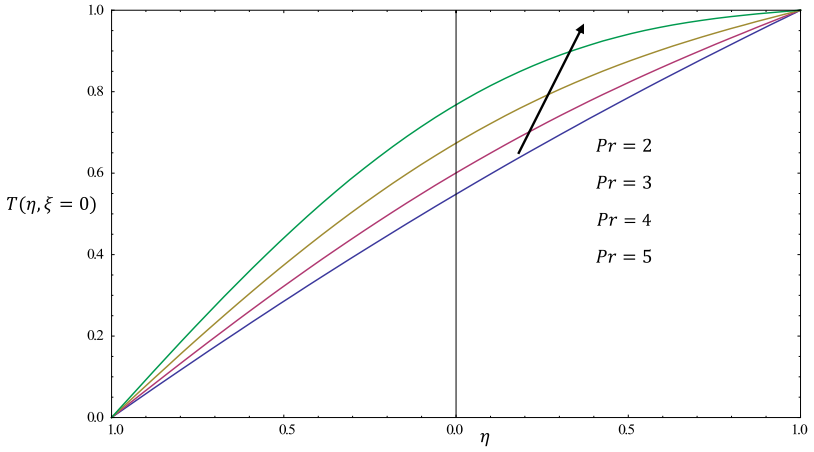

FIGURE 6
Temperature distribution $T(\eta, \xi)$ is plotted against "η" for fixed values of $\xi = 0$, S = 0.0125, $Re = 1$, $\alpha = 0.25$, $Br = 0.01$, and different values of Pr. The range of Pr in water is $2 \leq Pr \geq 7$, and Br = $PrEc$, the different values for the Prandtl numbers is Pr, the Eckert number becomes $Ec = 0.0085, 0.0056, 0.00425, 0.0034$. Note that the Prandtl and Eckert numbers are the choice for water. The temperature profile is increasing in Pr, whereas each profile changes uniformly. Moreover, the profile is either linear or close to linear for small values of Pr.

By substituting Eq. 27 into Eq. 24, we get:

$$\Rightarrow D^4\phi^0 + 2\alpha\, Re\, Im\left(\sum_{k=1}^{k=\infty} kD^2\left(\phi^{(k)^*} D\phi^k\right)\right) = 0, \tag{28}$$

where $D = \frac{\partial}{\partial \eta}$, Im represents the imaginary part. Integrating Eq. 28 w.r.t. 'η' we get:

$$\Rightarrow D^3\phi^0 + 2\alpha\, Re\, Im\left(\sum_{k=1}^{k=\infty} kD\left(\phi^{(k)^*} D\phi^k\right)\right) = A\, Re,$$
$$where\ A = \left.\frac{\partial p_1}{\partial \xi}\right|_{mean} \tag{29}$$

The equations of the model are valid for a constant pressure gradient, where both the straight and sinusoidal channels are driven by the same gradient. The flow rate variation is taken into account and measured due to the extra flow losses that occur in the meandering channel. Additionally, it is assumed that in Eq. 26, A is equal to zero, and the correction for the flow rate, Q_1, can be easily calculated as per Floryan's work in 1997.

5 Solution of the modified equations

Let us assume that the wavelength is a large quantity, denoted as $\alpha \to 0$. We can then obtain a solution for the

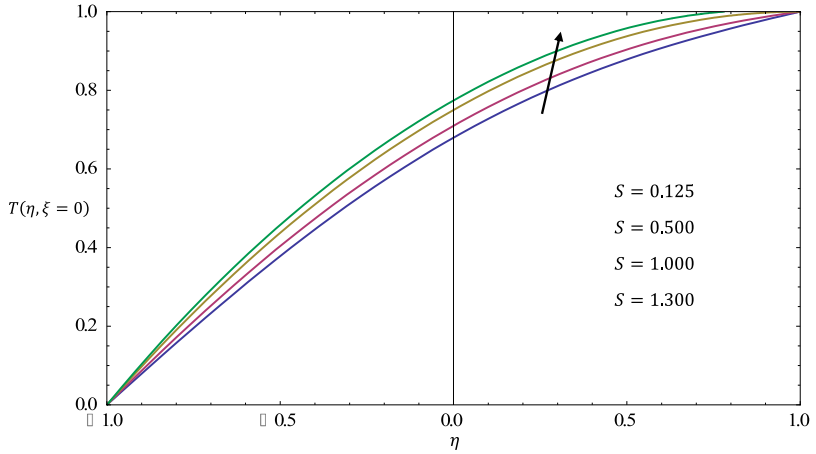

FIGURE 7
Temperature distribution $T(\eta, \xi)$ is plotted against $"\eta"$ for fixed values of $\xi = 0$, $\alpha = 0.5$, $Re = 1$, $Pr = 2$, and $Ec = 0.0001$ and different values of S. Note that the Prandtl and Eckert numbers are the choice for water. The temperature profile is increased in S, whereas each profile changes uniformly. Moreover, the profile is either linear or close to linear for small values of S.

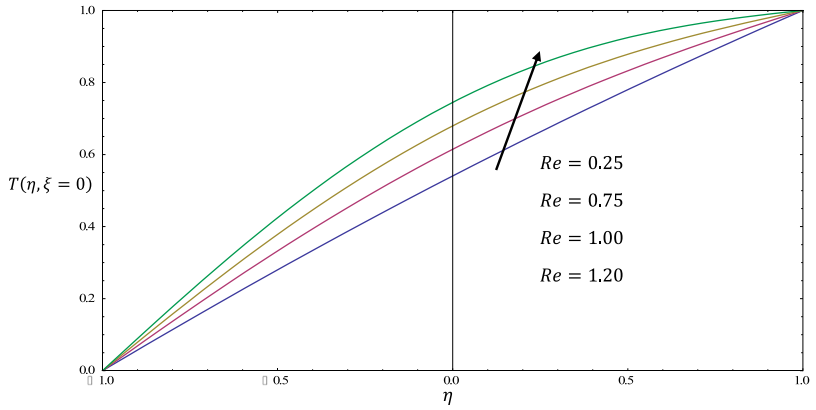

FIGURE 8
Temperature distribution $T(\eta, \xi)$ is plotted against $"\eta"$ for fixed values of $\xi = 0$, $\alpha = 0.5$, $S = 0.125$, $Pr = 2$, and $Ec = 0.000$, and different values of Re. Note that the Prandtl and Eckert numbers are the choice for water. The temperature profile is increased in Re, whereas each profile changes uniformly. Moreover, the profile is either linear or close to linear for small values of Re.

problem. To regularize the flow domain, transformation $\theta = (\eta - 2S\cos\sigma)$ is applied, where $\sigma = \alpha\xi$ represents a slow scale. With these new variables, the governing equations in dimensionless form, denoted as Eqs 4, 6, are transformed into the following set of field equations given as:

$$\alpha\frac{\partial u_b}{\partial \sigma} + 2S\alpha\sin\sigma\frac{\partial u_b}{\partial \theta} + \frac{\partial v_b}{\partial \theta} = 0, \tag{30}$$

$$\begin{aligned} &-\left(1 + 4S^2\alpha^2 sin^2\,\sigma\right)\frac{\partial^2 u_b}{\partial \theta^2} - \alpha^2\frac{\partial^2 u_b}{\partial \sigma^2} - 4S\alpha^2\sin\sigma\frac{\partial^2 u_b}{\partial \theta \partial \sigma} \\ &- 2S\alpha^2\cos\sigma\frac{\partial u_b}{\partial \theta} + 2S\alpha Re\sin\sigma u_b\frac{\partial u_b}{\partial \theta} + Re\,v_b\frac{\partial u_b}{\partial \theta} \\ &+ \alpha\,Re\,u_b\frac{\partial u_b}{\partial \sigma} + \alpha\,Re\frac{\partial p_b}{\partial \sigma} + 2S\alpha Re\sin\sigma\frac{\partial p_b}{\partial \theta} = 0, \end{aligned} \tag{31}$$

$$\begin{aligned} &-\left(1 + 4S^2\alpha^2 sin^2\,\sigma\right)\frac{\partial^2 v_b}{\partial \theta^2} - \alpha^2\frac{\partial^2 v_b}{\partial \sigma^2} - 4S\alpha^2\sin\sigma\frac{\partial^2 v_b}{\partial \theta \partial \sigma} - 2S\alpha^2\cos\sigma\frac{\partial v_b}{\partial \theta} \\ &+ 2S\alpha Re\sin\sigma u_b\frac{\partial v_b}{\partial \theta} + Re\,v_b\frac{\partial v_b}{\partial \theta} + \alpha\,Re\,u_b\frac{\partial v_b}{\partial \sigma} + Re\frac{\partial p_b}{\partial \theta} = 0, \end{aligned} \tag{32}$$

The no-slip boundary and free-stream conditions with the total flow rate given in Eq. 25 is reduced to the following simplest form:

$$u_b = v_b = 0\ at\ \theta = \pm 1,\ \ u_b = 1\ at\ \theta = 0,\ \ Q_b = \int_{-1}^{1} u_b(\sigma, \theta)d\eta = \frac{4}{3}. \tag{33}$$

In Eqs 30–32 are three unknown quantities, i.e., u_b, v_b, and P_b that we need to determine by using the perturbation method. These unknown quantities are expanded in terms of α by using the following series:

$$u_b = \hat{u}_0 + \alpha\hat{u}_1 + \alpha^2\hat{u}_2 + \alpha^3\hat{u}_3 + O(\alpha^4),$$
$$v_b = \hat{v}_0 + \alpha\hat{v}_1 + \alpha^2\hat{v}_2 + \alpha^3\hat{v}_3 + O(\alpha^4),$$
$$\mathcal{P}_b = \alpha^{-1}\hat{\mathcal{P}}_{-1} + \hat{\mathcal{P}}_0 + \alpha\hat{\mathcal{P}}_1 + \alpha^2\hat{\mathcal{P}}_2 + O(\alpha^3). \quad (34)$$

Substituting the values of u_b, v_b, and $\mathcal{P}_b$ from Eq. 34 into Eqs 30–32, we have:

$$\alpha\frac{\partial}{\partial\sigma}(\hat{u}_0 + \alpha\hat{u}_1 + \alpha^2\hat{u}_2 + \alpha^3\hat{u}_3) + 2S\alpha\sin\sigma\frac{\partial}{\partial\theta}(\hat{u}_0 + \alpha\hat{u}_1 + \alpha^2\hat{u}_2 + \alpha^3\hat{u}_3) + \frac{\partial}{\partial\theta}(\hat{v}_0 + \alpha\hat{v}_1 + \alpha^2\hat{v}_2 + \alpha^3\hat{v}_3) = 0, \quad (35)$$

$$\begin{aligned}
&-(1 + 4S^2\alpha^2 sin^2\sigma)\frac{\partial^2}{\partial\theta^2}(\hat{u}_0 + \alpha\hat{u}_1 + \alpha^2\hat{u}_2 + \alpha^3\hat{u}_3)\\
&-\alpha^2\frac{\partial^2}{\partial\sigma^2}(\hat{u}_0 + \alpha\hat{u}_1 + \alpha^2\hat{u}_2 + \alpha^3\hat{u}_3)\\
&-4S\alpha^2\sin\sigma\frac{\partial^2}{\partial\theta\partial\sigma}(\hat{u}_0 + \alpha\hat{u}_1 + \alpha^2\hat{u}_2 + \alpha^3\hat{u}_3)\\
&-2S\alpha^2\cos\sigma\frac{\partial}{\partial\theta}(\hat{u}_0 + \alpha\hat{u}_1 + \alpha^2\hat{u}_2 + \alpha^3\hat{u}_3)\\
&+2S\alpha Re\sin\sigma(\hat{u}_0 + \alpha\hat{u}_1 + \alpha^2\hat{u}_2 + \alpha^3\hat{u}_3)\frac{\partial}{\partial\theta}(\hat{u}_0 + \alpha\hat{u}_1 + \alpha^2\hat{u}_2 + \alpha^3\hat{u}_3)\\
&+Re(\hat{v}_0 + \alpha\hat{v}_1 + \alpha^2\hat{v}_2 + \alpha^3\hat{v}_3)\frac{\partial}{\partial\theta}(\hat{u}_0 + \alpha\hat{u}_1 + \alpha^2\hat{u}_2 + \alpha^3\hat{u}_3)\\
&+\alpha Re(\hat{u}_0 + \alpha\hat{u}_1 + \alpha^2\hat{u}_2 + \alpha^3\hat{u}_3)\frac{\partial}{\partial\sigma}(\hat{u}_0 + \alpha\hat{u}_1 + \alpha^2\hat{u}_2 + \alpha^3\hat{u}_3)\\
&+\alpha Re\frac{\partial}{\partial\sigma}(\alpha^{-1}\hat{\mathcal{P}}_{-1} + \hat{\mathcal{P}}_0 + \alpha\hat{\mathcal{P}}_1 + \alpha^2\hat{\mathcal{P}}_2)\\
&+2S\alpha Re\sin\sigma\frac{\partial}{\partial\theta}(\alpha^{-1}\hat{\mathcal{P}}_{-1} + \hat{\mathcal{P}}_0 + \alpha\hat{\mathcal{P}}_1 + \alpha^2\hat{\mathcal{P}}_2) = 0,
\end{aligned} \quad (36)$$

$$\begin{aligned}
&-(1 + 4S^2\alpha^2 sin^2\sigma)\frac{\partial^2}{\partial\theta^2}(\alpha\hat{v}_1 + \alpha^2\hat{v}_2 + \alpha^3\hat{v}_3)\\
&-\alpha^2\frac{\partial^2}{\partial\sigma^2}(\alpha\hat{v}_1 + \alpha^2\hat{v}_2 + \alpha^3\hat{v}_3)\\
&-4S\alpha^2\sin\sigma\frac{\partial^2}{\partial\theta\partial\sigma}(\alpha\hat{v}_1 + \alpha^2\hat{v}_2 + \alpha^3\hat{v}_3)\\
&-2S\alpha^2\cos\sigma\frac{\partial}{\partial\theta}(\alpha\hat{v}_1 + \alpha^2\hat{v}_2 + \alpha^3\hat{v}_3)\\
&+2S\alpha Re\sin\sigma(\hat{u}_0 + \alpha\hat{u}_1 + \alpha^2\hat{u}_2 + \alpha^3\hat{u}_3)\frac{\partial}{\partial\theta}(\alpha\hat{v}_1 + \alpha^2\hat{v}_2 + \alpha^3\hat{v}_3)\\
&+Re(\hat{v}_0 + \alpha\hat{v}_1 + \alpha^2\hat{v}_2 + \alpha^3\hat{v}_3)\frac{\partial}{\partial\theta}(\alpha\hat{v}_1 + \alpha^2\hat{v}_2 + \alpha^3\hat{v}_3)\\
&+\alpha Re(\hat{u}_0 + \alpha\hat{u}_1 + \alpha^2\hat{u}_2 + \alpha^3\hat{u}_3)\frac{\partial}{\partial\sigma}(\alpha\hat{v}_1 + \alpha^2\hat{v}_2 + \alpha^3\hat{v}_3)\\
&+Re\frac{\partial}{\partial\theta}(\alpha^{-1}\hat{\mathcal{P}}_{-1} + \hat{\mathcal{P}}_0 + \alpha\hat{\mathcal{P}}_1 + \alpha^2\hat{\mathcal{P}}_2) = 0.
\end{aligned} \quad (37)$$

6 Analysis of heat transfer in a meandering channel

The analysis of heat transfer in a meandering channel involves studying the heat transfer mechanisms that occur due to meanders in the channel. Heat transfer occurs in three modes: conduction, convection, and radiation. In the present study, a case of heat transfer through conduction and convection is taken into account. Conduction occurs when heat flows from regions of high temperature to regions of low temperature through a solid material. In a meandering channel, heat is conducted through the walls of the channel. The rate of heat transfer through conduction is proportional to the temperature gradient, the thermal conductivity of the material, and the cross-sectional area of the channel. Convection occurs when heat is transferred by the movement of fluids, either liquids or gases. In a meandering channel, heat is transferred through convection due to the flow of fluid through the channel. The rate of heat transfer through convection is proportional to the temperature difference between the fluid and the channel wall, the velocity of the fluid, and the heat transfer coefficient of the fluid. The heat transfer is analyzed by using the energy equation, which relates the rate of heat transfer to the temperature distribution in the channel. The energy equation is taken into account to study the conduction and convection mechanisms of heat transfer and the thermal properties of the meandering channel in the flow of fluids.

7 Formulation of the problem

The problem is modeled using the Navier–Stokes equations, along with the continuity and energy equations. To obtain a non-linear, simple partial differential equation, a defined set of transformations is applied. The regular perturbation technique is utilized to expand the heat transfer, T_b, in terms of " α " in the meandering channel.

The energy equation is:

$$\rho c_p\frac{DT}{Dt} = k\nabla^2 T + \Phi, \quad (38)$$

where T is the temperature distribution, ρ is density, c_p is specific heat, k is thermal conductivity, and Φ is the dissipation term. The boundaries condition of the problem is at the upper wall, $T = T_1$, and at the lower wall , $T = T_0$.

Consider the following dimensionless variables in order to transform the energy equation into dimensionless form:

$$T^* = \frac{T - T_0}{T_1 - T_0}, \Phi^* = \frac{L^2\Phi}{U^2\mu}, \quad (39)$$

The dimensionless numbers that appear in Eq. 38 are the Reynolds and Prandtl numbers, which are defined as:

$$Re = \frac{\rho UL}{\mu}, Pr = \frac{\mu c_p}{k}, Re.Pr = \frac{\rho ULc_p}{k}, \frac{1}{RePr} = \frac{k}{\rho ULc_p}, \quad (40)$$

$$u^*\frac{\partial T^*}{\partial x^*} + v^*\frac{\partial T^*}{\partial y^*} = \frac{1}{RePr}\left[\frac{\partial^2 T^*}{\partial x^{*2}} + \frac{\partial^2 T^*}{\partial y^{*2}}\right] + \frac{Ec}{Re}\Phi^*, \quad (41)$$

Equation 41 is the dimensionless form of the energy equation. On the other hand, the boundaries conditions for the temperature distribution in the dimensionless form are obtained, and the dimensional boundary conditions are given by taking:

$$T^*(x, y) = \frac{T - T_0}{T_1 - T_0}, \quad (42)$$

The temperature at the upper wall is $T = T_1$, so using definition from Eq. 42:

$$y = 1, T = T_1, T^*(x, y) = \frac{T - T_0}{T_1 - T_0} = \frac{T_1 - T_0}{T_1 - T_0}, T^*(x, y) = 1, \quad (43)$$

The temperature at the lower wall is $T = T_0$, so using definition from Eq. 42:

10.3389/fmats.2023.1183175

$$y=-1, T=T_0, T^*(x,y)=\frac{T-T_0}{T_1-T_0}=\frac{T_0-T_0}{T_1-T_0}, T^*(x,y)=0, \quad (44)$$

The temperature of a flow in a straight channel is denoted by $\hat{T}_0$, and so we have:

$$u_0\frac{\partial \hat{T}_0}{\partial x}+v_0\frac{\partial \hat{T}_0}{\partial y}=\frac{1}{RePr}\left[\frac{\partial^2 \hat{T}_0}{\partial x^2}+\frac{\partial^2 \hat{T}_0}{\partial y^2}\right]+\frac{Ec}{Re}\left[2\left(\frac{\partial u_0}{\partial x}\right)^2+2\left(\frac{\partial v_0}{\partial y}\right)^2+\left(\frac{\partial v_0}{\partial x}+\frac{\partial u_0}{\partial y}\right)^2\right], \quad (45)$$

The boundaries condition for the temperature at the upper wall, $\hat{T}_0=1$, and at the lower wall, $\hat{T}_0=0$.

Putting Eq. 11 into Eq. 45, after simplification we have:

$$\frac{\partial^2 \hat{T}_0}{\partial y^2}=-4PrEcy^2, \quad (46)$$

Integrating Eq. 46 twice w.r.t "y", we get:

$$\hat{T}_0(y)=-\frac{PrEcy^4}{3}+C_1y+C_2, \quad (47)$$

where C_1 and C_2 are the constant of integration, which can be determined by using the boundary conditions imposed at the upper wall of the channel, $\hat{T}_0(1)=1$, and at lower wall of the channel, $\hat{T}_0(-1)=0$.

$$\hat{T}_0(y)=\frac{PrEc}{3}(1-y^4)+\frac{1}{2}(1+y), \quad (48)$$

As the $\boldsymbol{V}_b(\boldsymbol{X})=\boldsymbol{V}_0(\boldsymbol{X})+\boldsymbol{V}_1(\boldsymbol{X})$ and $T_b(\boldsymbol{X})=T_0(\boldsymbol{X})+T_1(\boldsymbol{X})$, where $\boldsymbol{V}_b(\boldsymbol{X})=(u_b\hat{\boldsymbol{i}}+v_b\hat{\boldsymbol{j}})$ and $T_b(\boldsymbol{X})$ are the velocity and temperature of the total flow, respectively, and $\boldsymbol{V}_1(\boldsymbol{X})=(u_1\hat{\boldsymbol{i}}+v_1\hat{\boldsymbol{j}})$ and $T_1(\boldsymbol{X})$ are the velocity and temperature induced by the channel geometry, respectively.

It is assumed that α is a small quantity, and for this choice of α we expand the unknown quantities of $\hat{T}_b$ by using the regular perturbations to find $\hat{T}_b$. The dimensionless form of the energy equation is transformed and expanded using the following transformation and expansion:

$$\eta=y-2scas(\xi), \xi=\alpha x, \quad (49)$$

$$\hat{T}_b=\hat{T}_0+\alpha\hat{T}_1+\alpha^2\hat{T}_2+O(\alpha^3), \quad (50)$$

We get:

$$\begin{aligned}
&u_0\left[2S\alpha\sin(\xi)\left(\frac{\partial \hat{T}_0}{\partial\eta}+\alpha\frac{\partial \hat{T}_1}{\partial\eta}+\alpha^2\frac{\partial \hat{T}_2}{\partial\eta}\right)+\alpha\left(\frac{\partial \hat{T}_0}{\partial\xi}+\alpha\frac{\partial \hat{T}_1}{\partial\xi}+\alpha^2\frac{\partial \hat{T}_2}{\partial\xi}\right)\right]\\
&+\alpha^2u_2\left[2S\alpha\sin(\xi)\left(\frac{\partial \hat{T}_0}{\partial\eta}+\alpha\frac{\partial \hat{T}_1}{\partial\eta}+\alpha^2\frac{\partial \hat{T}_2}{\partial\eta}\right)+\alpha\left(\frac{\partial \hat{T}_0}{\partial\xi}+\alpha\frac{\partial \hat{T}_1}{\partial\xi}+\alpha^2\frac{\partial \hat{T}_2}{\partial\xi}\right)\right]\\
&+\alpha v_1\left[\frac{\partial \hat{T}_0}{\partial\eta}+\alpha\frac{\partial \hat{T}_1}{\partial\eta}+\alpha^2\frac{\partial \hat{T}_2}{\partial\eta}\right]\\
&=\frac{1}{RePr}\left[4S^2\alpha^2\sin^2(\xi)\left(\frac{\partial^2 \hat{T}_0}{\partial\eta^2}+\alpha\frac{\partial^2 \hat{T}_1}{\partial\eta^2}+\alpha^2\frac{\partial^2 \hat{T}_2}{\partial\eta^2}\right)\right.\\
&+\alpha^2\left(\frac{\partial^2 \hat{T}_0}{\partial\xi^2}+\alpha\frac{\partial^2 \hat{T}_1}{\partial\xi^2{}_1}+\alpha^2\frac{\partial^2 \hat{T}_2}{\partial\xi^2}\right)+4\alpha^2S\sin(\xi)\left(\frac{\partial^2 \hat{T}_0}{\partial\eta\partial\xi}+\alpha\frac{\partial^2 \hat{T}_1}{\partial\eta\partial\xi}+\alpha^2\frac{\partial^2 \hat{T}_2}{\partial\eta\partial\xi}\right)\\
&\left.+2S\alpha^2\cos(\xi)\left(\frac{\partial \hat{T}_0}{\partial\eta}+\alpha\frac{\partial \hat{T}_1}{\partial\eta}+\alpha^2\frac{\partial \hat{T}_2}{\partial\eta}\right)+\left(\frac{\partial^2 \hat{T}_0}{\partial\eta^2}+\alpha\frac{\partial^2 \hat{T}_1}{\partial\eta^2}+\alpha^2\frac{\partial^2 \hat{T}_2}{\partial\eta^2}\right)\right]\\
&+\frac{Ec}{Re}\left[\left(\frac{\partial u_0}{\partial\eta}\right)^2+\alpha^2\left(8S^2\sin^2(\xi)\left(\frac{\partial u_0}{\partial\eta}\right)^2+2\left(\frac{\partial u_0}{\partial\eta}\right)\left(\frac{\partial u_2}{\partial\eta}\right)\right.\right.\\
&+4S\sin(\xi)\left(\frac{\partial u_0}{\partial\eta}\right)\left(\frac{\partial v_1}{\partial\eta}\right)+2\left(\frac{\partial v_1}{\partial\eta}\right)^2+8S\sin(\xi)\left(\frac{\partial u_0}{\partial\eta}\right)\left(\frac{\partial u_0}{\partial\xi}\right)\\
&\left.\left.+2\left(\frac{\partial u_0}{\partial\xi}\right)+2\left(\frac{\partial u_0}{\partial\eta}\right)\left(\frac{\partial v_1}{\partial\xi}\right)\right)+O(\alpha^3)\right],
\end{aligned} \quad (51)$$

The boundaries condition on the upper wall is $y=h=1$, and the boundaries condition on the lower wall is $y=-h=-1$ for the small α.

$$\hat{T}_0(1)=1, \hat{T}_1(1)=0, \hat{T}_2(1)=0, \quad (52)$$

$$\hat{T}_0(-1)=0, \hat{T}_1(-1)=0, \hat{T}_2(-1)=0, \quad (53)$$

8 Results and discussion

With the solution represented as a power expansion in terms of σ and by equating the coefficients, we have:

$$\hat{u}_0(\theta)=1-\theta^2,\ \hat{u}_1(\sigma,\theta)=0,\ \hat{u}_2(\sigma,\theta)=\frac{4}{3}S\theta\cos\sigma(1-\theta^2),$$

$$\hat{u}_3(\sigma,\theta)=\frac{2}{315}ReS\,\theta\sin\sigma(\theta^2-1)(\theta^4+21S\theta(\theta^2-4)\cos\sigma+\theta^2-34),$$

$$\hat{v}_0(\sigma,\theta)=0, \hat{v}_1=-2S\sin\sigma(1-\theta^2), \hat{v}_2(\sigma,\theta)=0,$$

$$\hat{v}_3(\sigma,\theta)=\frac{1}{3}S(\theta^2-1)(\theta^2-1+8S\theta\cos\sigma)\sin\sigma,$$

$$\hat{\mathcal{P}}_{-1}(\sigma)=-\frac{2\sigma}{Re}+C_0, \hat{\mathcal{P}}_0=C_1,$$

$$\hat{\mathcal{P}}_1(\sigma,\theta)=-4Re^{-1}S(2S\sigma-\theta\sin\sigma-S\sin2\sigma),$$

$$\hat{\mathcal{P}}_2(\sigma,\theta)=2S\cos\sigma\left(\theta-\frac{2\theta^3}{3}+\frac{\theta^5}{5}\right)+\frac{11}{15}S^2\cos2\sigma,$$

$$\hat{T}_0(\eta)=\frac{PrEc}{3}(1-\eta^4)+\frac{1}{2}(1+\eta),$$

$$\hat{T}_1(\eta)=\frac{1}{1260}\sin(\xi)PrRe(-1+S)(-1+\eta^2)[-105(-5+\eta^2)+8EcPr\eta(-11-11\eta^2+10\eta^4)],$$

And

$$\begin{aligned}
\hat{T}_2=\frac{1}{1260}\Big[&\frac{105}{2}pr^2Re^2(-1+S)cos(\xi)(-\eta^4+1)\\
&+1176EcPrS(-\eta^5+\eta)cos(\xi)+4EcPr^3Re^2(-1+S)(\eta^7-\eta)cos(\xi)\\
&+\frac{10}{9}EcPr^3Re^2(-1+S)(-\eta^9+\eta)cos(\xi)\\
&+88EcPr^3Re^2(-1+S)^2(\eta^2-1)sin^2(\xi)\\
&+420Pr^2Re^2(-1+S)^2(\eta^3-\eta)sin^2(\xi)\\
&+\frac{4}{3}EcPr(11Pr^2Re^2(1+S)^2+3780S^2)(-\eta^4+1)sin^2(\xi)\\
&+56EcPr^3Re^2(-1+S)^2(-\eta^6+1)sin^2(\xi)\\
&+20Pr^2Re^2(-1+S)^2(\eta^7-\eta)sin^2(\xi)\\
&+50EcPr^3Re^2(-1+S)^2(\eta^8-1)sin^2(\xi)\\
&+\frac{112}{9}EcPr^3Re^2(-1+S)^2(-\eta^{10}+1)sin^2(\xi)\\
&+84PrRe(-1+S)(-\eta^5+\eta)sin(\xi)\{-Scos(\xi)+2PrRe(-1+S)sin(\xi)\}\\
&+\frac{7}{2}Pr^2Re(-1+S)(\eta^6-1)cos(\xi)\{Re-32EcSsin(\xi)\}\\
&+\frac{4}{3}Pr(-\eta^3+\eta)cos(\xi)\{Ec(-11Pr^2Re^2(-1+S)-2100S)\\
&+630Re(-1+S)Ssin(\xi)\}\\
&+\frac{1}{2}(-\eta^2+1)cos(\xi)\{105(-5Pr^2Re^2(-1+S)+24S)\\
&-352EcPr^2Re(-1+S)Ssin(\xi)\}\\
&+20EcPr^2Re(-1+S)S(-\eta^8+1)sin(2\xi)\Big].
\end{aligned}$$

Stream function $\psi(\sigma, \theta)$

The stream function $\psi(\sigma,\theta)$ is used to define the velocity components such that:

$$u_b = \frac{\partial \psi(\sigma,\theta)}{\partial \theta}, v_b = -2\alpha S \sin\sigma \frac{\partial \psi(\sigma,\theta)}{\partial \theta} + \frac{\partial \psi(\sigma,\theta)}{\partial \sigma}, \quad (54)$$

By integrating u_b with 'θ' and after finding the constant of integration, we get:

$$\begin{aligned}\psi(\sigma,\theta) = \frac{1}{1260}(&420S\alpha^2(-1+\theta^2)^2\cos\sigma \\ &+ reS\alpha^3(-1+\theta^2)^2(-67+2\theta^2+\theta^4)\sin\sigma \\ &+ 4(1+\theta)^2(-105(-2+\theta) \\ &+ reS^2\alpha^3(10-20\theta+30\theta^2-12\theta^3-6\theta^4+3\theta^5)\sin 2\sigma)).\end{aligned} \quad (55)$$

The streamlines in the area adjacent to the lower wall are shown in Figures 2A, B, where $S = 5$ (amplitude), (Reynolds number) = 1 , $\alpha = 10$, while Figures 2C is plotted for the whole channel, which determines that a diminution of the meandering wavelength results in the establishment of separation zones in the troughs. Figure 3 illustrates the variations of the pressure losses as a function of S and α. From Figure 2, the area adjacent to the lower wall is complex and exhibits a variety of behaviors. The fluid experiences both pressure and shear forces. The pressure forces result from the changes in the height of the channel, while the shear forces arise due to the velocity gradient near the channel walls. As a result of these forces, the streamlines in the area adjacent to the lower wall exhibit the behaviors of separation and reattachment. As the fluid flows over the wave crest, the pressure forces cause the flow to separate from the lower wall, resulting in a region of recirculating flow or eddies. As the fluid flows over the wave trough, the pressure forces cause the flow to reattach to the lower wall, resulting in a region of reversed flow. In addition to the primary flow along the channel axis, the pressure and shear forces are also induced the secondary flows perpendicular to the channel axis. These secondary flows create complex patterns of vortices and recirculation zones, as shown in Figure 2, which affect the overall flow behavior. The complex flow behavior in the area adjacent to the wall also leads to flow instability, such as the formation of Kelvin–Helmholtz instability waves, which can cause the flow to break down into smaller-scale vortices. Overall, the streamlines in the area adjacent to the lower wall of a meandering channel in a viscous fluid flow exhibit a variety of complex behaviors, which have an important implication for fluid transport and mixing in microfluidic and other applications.

9 Conclusion

The periodicity of the meandering channel affects the flow pattern and turbulence intensity of the fluid. A higher periodicity leads to a more regular flow pattern, while a lower periodicity leads to a more chaotic flow pattern. The presence of periodicity also leads to the development of secondary flows, such as Dean vortices, which affect the mixing and heat transfer characteristics of the flow. The Prandtl number relates the momentum diffusivity to the thermal diffusivity of a fluid. In a meandering channel, a higher Prandtl number results in a thicker thermal boundary layer, which affects the heat transfer characteristics of the flow. A lower Prandtl number, on the other hand, results in a thinner thermal boundary layer and a more efficient heat transfer. As shown in the Figures 4–8, the Eckert number relates the kinetic energy of a fluid to its thermal energy. In a meandering channel, a higher Eckert number results in a more energetic flow, which can lead to an increase in turbulence intensity and mixing. A lower Eckert number results in a less energetic flow, which leads to a more laminar flow pattern and reduced mixing. The Reynolds number represents the inertial forces to the viscous forces in a fluid. In a meandering channel, a higher Reynolds number results in a more turbulent flow pattern, with increased mixing and heat transfer. A lower Reynolds number results in a more laminar flow pattern, with reduced mixing and heat transfer. The effects of periodicity and the Prandtl number, Eckert number, and Reynolds number on fluid flow in a meandering channel are complex and interrelated.

In future, the flow and heat transfer in wavy meandering channels could include investigating the thermal profiles, skin friction, and Nusselt number calculations for various flow parameters. This could provide insights into the heat transfer characteristics of the flow and help optimize the design of such channels for specific applications. Additionally, examining the effects of different geometries and materials on the flow and heat transfer could yield valuable results.

Data availability statement

The original contributions presented in the study are included in the article/Supplementary material, further inquiries can be directed to the corresponding author.

Author contributions

DK proposed the mathematical model. SI performed all numerical computations and created the corresponding graphs. DK and SI provided the discussion of the graphs and their physical interpretation. NU conducted the literature review and compared the present simulations with classical data. KN and K carried out the final review and made amendments to the manuscript.

Funding

This study was supported by funding from Prince Sattam bin Abdulaziz University, project number (PSAU/2023/R/1444).

Conflict of interest

The authors declare that the research was conducted in the absence of any commercial or financial relationships that could be construed as a potential conflict of interest.

Publisher's note

References

Alsaedi, A., Rashad, A. M., and Hayat, T. (2016). Bioconvective Darcy–Forchheimer flow of the Ree–Eyring nanofluid through a stretching sheet with velocity and thermal slips. *J. Mol. Liq.* 220, 803–811.

Bergles, A. E., and Webb, Ralph L. (1985). *A guide to the literature on convective heat transfer augmentation*. Ames, IA, USA: Iowa State University College of Engineering.

Fiebig, Martin, and Chen, Yuwen (1999). Heat transfer enhancement by wing-type longitudinal vortex generators and their application to finned oval tube heat exchanger elements. *Heat Transf. Enhanc. Heat Exch.* 42, 79–105.

Fiebig, Martin. (1995). Embedded vortices in internal flow: Heat transfer and pressure loss enhancement. *Int. J. Heat Fluid Flow* 16 (5), 376–388. doi:10.1016/0142-727x(95)00043-p

Fiebig, Martin. (1995). Vortex generators for compact heat exchangers. *J. Enhanc. Heat Transf.* 2, 1–20. doi:10.1615/jenhheattransf.v24.i1-6.10

Fiebig, M. (1998). Vortices, generators and heat transfer. *Chem. Eng. Res. Des.* 76 (2), 108–123. doi:10.1205/026387698524686

Floryan, J. M. (1991). On the Görtler instability of boundary layers. *Prog. Aerosp. Sci.* 28 (3), 235–271. doi:10.1016/0376-0421(91)90006-p

Ghalambaz, M., Rostami, B., and Rashidi, M. M. (2016). Thermal analysis of a radiative nanofluid over a stretching/shrinking cylinder with viscous dissipation. *J. Mol. Liq.* 224, 87–93.

Hayat, T., Ahmad, B., Alsaedi, A., and Rasool, N. (2017). Theoretical analysis of the thermal characteristics of Ree–Eyring nanofluid flowing past a stretching sheet due to bioconvection. *J. Mol. Liq.* 242, 758–764.

Izadi, M., and Pourmehran, O. (2017). Formation of hydrogen bonding during the Homann flow over a cylindrical disk of variable visco-elastic nano-materials in presence of activation energy. *Int. J. Hydrogen Energy* 42 (28), 18003–18016.

Jacobi, A. M., and Shah, R. K. (1995). Heat transfer surface enhancement through the use of longitudinal vortices: A review of recent progress. *Exp. Therm. Fluid Sci.* 11 (3), 295–309. doi:10.1016/0894-1777(95)00066-u

Jensen, Michael K., Bergles, Arthur E., and Shome., Biswadip (1997). The literature on enhancement of convective heat and mass transfer. *J. Enhanc. Heat Transf.* 4, 1–6. doi:10.1615/jenhheattransf.v4.i1.10

Khan, M., Saleem, S., and Rehman, K. U. (2017). Energy and mass transport through hybrid nanofluid flow passing over an extended cylinder with the magnetic dipole using a computational approach. *J. Magnetism Magnetic Mater.* 427, 107–114.

Khan, W. A., and Ahmed, S. (2015). Significance of activation energy and entropy optimization in radiative stagnation point flow of nanofluid with cross-diffusion and viscous dissipation. *Results Phys.* 5, 301–311.

Ligrani, Phil M., Oliveira, Mauro M., and Tim Blaskovich (2003). Comparison of heat transfer augmentation techniques. *AIAA J.* 41 (3), 337–362. doi:10.2514/2.1964

Mahmud, S., and Uddin, M. J. (2021). Numerical simulations for optimised flow of second-grade nanofluid due to rotating disk with nonlinear thermal radiation: Chebyshev spectral collocation method analysis *J. Therm. Analysis Calorim.* 145 (2), 1087–1100.

Mohammadi, A., and Floryan, J. M. (2013) Groove optimization for drag reduction *Phys. Fluids* 25 (11), 113601 doi:10.1063/1.4826983

Nadeem, S., Akbar, N. S., and Lee, C. (2016) Numerical analysis of a time-dependent aligned MHD boundary layer flow of a hybrid nanofluid over a porous radiated stretching/shrinking surface *J. Mol. Liq.* 220, 945–954.

Patera, A. T., and Mikic, B. B. "Exploiting hydrodynamic instabilities. Resonant heat transfer enhancement" *Int. J. heat mass Transf.* 29 8 (1986): 1127–1138.doi:10.1016/0017-9310(86)90144-4

Rayleigh, Lord. (1917). On the dynamics of revolving fluids. *Proc. R. Soc. Lond. Ser. A, Contain. Pap. a Math. Phys. Character* 93 (648), 148–154.

Schlichting, H., and Kestin, J. (1961). *Boundary layer theory*. New York, NY, USA: McGraw-Hill.

Sheikholeslami, M., Rokni, H. B., and Ganji, D. D. (2017). Numerical investigation of Darcy–Forchheimer hybrid nanofluid flow with energy transfer over a spinning fluctuating disk under the influence of chemical reaction and heat source. *J. Therm. Analysis Calorim.* 128 (2), 913–924.

Srinivasacharya, D., and Sibanda, P. (2020). Investigation of hydromagnetic bioconvection flow of Oldroyd-B nanofluid past a porous stretching surface. *J. Therm. Analysis Calorim.* 139 (1), 237–247.

Taylor, Geoffrey Ingram. "VIII. Stability of a viscous liquid contained between two rotating cylinders." *Philosophical Trans. R. Soc. Lond. Ser. A, Contain. Pap. a Math. or Phys. Character* 223.605–615. (1923).

Webb, R. L., and Bergles, A. E. (1981). *Performance evaluation criteria for selection of heat transfer surface geometries used in low Reynolds number heat exchangers*. Ames, IA, USA: Iowa State University College of Engineering.

White, F. M., and Majdalani, J. (2006). *Viscous fluid flow*. New York, NY, USA: McGraw-Hill, 433–434.

Xu, Minghai, Lu, H., Gong, L., Chai, J. C., and Duan, X. (2016). Parametric numerical study of the flow and heat transfer in microchannel with dimples. *Int. Commun. Heat Mass Transf.* 76, 348–357. doi:10.1016/j.icheatmasstransfer.2016.06.002

10.3389/fmats.2023.1183175

Nomenclature

V	Velocity of the flow profile
μ	Dynamic viscosity
η, ξ	Similarity transformation
v	Kinematic viscosity
$2S$	Amplitude of the meandering
ψ	Stream function
$\lambda = \frac{2\pi}{\alpha}$	Wavelength of one cycle
x, y	Cartesian coordinates
h	Half-length of the channel
$2h$	Total length of the channel
u, v	Velocity of the components
η, ξ	Transformed coordinates
ρ	Fluid density
p	Pressure
T	Temperature distribution
Pr	Prandtl number
Ec	Eckert number
Re	Reynolds number
∇^2	$\partial/\partial x^2 + \partial/\partial y^2$
∇	$\partial/\partial x\boldsymbol{i} + \partial/\partial y\boldsymbol{j}$

frontiers | Frontiers in Materials

TYPE Original Research
PUBLISHED 17 August 2023
DOI 10.3389/fmats.2023.1253090

OPEN ACCESS

EDITED BY
Noor Saeed Khan,
University of Education Lahore, Pakistan

REVIEWED BY
Ali Zabihi,
Rowan University, United States
Asad Ullah,
University of Lakki Marwat, Pakistan

*CORRESPONDENCE
Ahmed M. Hassan,
ahmed.hassan.res@fue.edu.eg

RECEIVED 04 July 2023
ACCEPTED 04 August 2023
PUBLISHED 17 August 2023

CITATION
Nagaraja KV, Vinutha K, Madhukesh JK, Khan U, Singh Chohan J, Sherif E-SM, Sarris IE, Hassan AM and Shanker B (2023), Thermal conductivity performance in sodium alginate-based Casson nanofluid flow by a curved Riga surface.
Front. Mater. 10:1253090.
doi: 10.3389/fmats.2023.1253090

Thermal conductivity performance in sodium alginate-based Casson nanofluid flow by a curved Riga surface

K. V. Nagaraja[1], K. Vinutha[2], J. K. Madhukesh[1], Umair Khan[3,4,5], Jasgurpreet Singh Chohan[6], El-Sayed M. Sherif[7], Ioannis E. Sarris[8], Ahmed M. Hassan[9]* and B. Shanker[10]

[1]Department of Mathematics, Amrita School of Engineering, Amrita Vishwa Vidyapeetham, Bengaluru, India, [2]Department of Studies in Mathematics, Davangere University, Davangere, India, [3]Department of Mathematical Sciences, Faculty of Science and Technology, Universiti Kebangsaan Malaysia, Bangi, Selangor, Malaysia, [4]Department of Computer Science and Mathematics, Lebanese American University, Byblos, Lebanon, [5]Department of Mathematics and Social Sciences, Sukkur IBA University, Sukkur, Sindh, Pakistan, [6]Department of Mechanical Engineering and University Centre for Research and Development, Chandigarh University, Mohali, Punjab, India, [7]Mechanical Engineering Department, College of Engineering, King Saud University, Riyadh, Saudi Arabia, [8]Department of Mechanical Engineering, University of West Attica, Athens, Greece, [9]Mechanical Engineering, Future University in Egypt, New Cairo, Egypt, [10]Department of Mathematics, CVR College of Engineering, Rangareddy, India

This study examines the effects of a porous media and thermal radiation on Casson-based nano liquid movement over a curved extending surface. The governing equations are simplified into a system of ODEs (ordinary differential equations) using the appropriate similarity variables. The numerical outcomes are obtained using the shooting method and Runge-Kutta Fehlbergs fourth-fifth order (RKF-45). An analysis is conducted to discuss the impact of significant nondimensional constraints on the thermal and velocity profiles. The findings show that the rise in curvature constraint will improve the velocity but diminish the temperature. The increased values of the modified Hartmann number raise the velocity, but a reverse trend is seen for increased porosity parameter values. Thermal radiation raises the temperature, while modified Hartmann numbers and the Casson factor lower the velocity but raise the thermal profile. Moreover, the existence of porous and solid fractions minimizes the surface drag force, and radiation and solid fraction components enhance the rate of thermal dispersion. The findings of this research may have potential applications in the design of heat exchangers used in cooling electronic devices like CPUs and GPUs, as well as microscale engines such as microturbines and micro-heat engines.

KEYWORDS

curved stretching sheet, Riga plate, casson nanofluid, thermal radiation, porous medium

1 Introduction

Fluid flow past a curved stretching sheet (CSS) is a classical fluid mechanics problem with numerous applications in engineering and physics. Investigating nanofluid flow over curved stretched sheets has become an attractive field of study due to its many useful applications, such as cooling in electronic devices, heat exchangers, processing of materials, solar collectors, synthesis of polymers, and microelectronic devices. The behavior of the fluid in this scenario depends on several factors, including the geometry of the surface, the velocity

of the stretching motion, and the properties of the fluid itself. Madhukesh et al. (Madhukesh et al., 2021) investigated the Newtonian heating (NH) and non-Fourier heat flux (NFHF) effect on the CSS in the presence of HNF (hybrid nanofluid). Multiple slippages on hydro-magnetic dissipative fluid across a CSS were addressed by Aihem et al. (Duraihem et al., 2023) and discussed their enhanced thermal and mass transmission properties. The impact of Cross dispersion on MHD Casson liquid movement along a CSS was inspected by Lakshmi et al. (Lakshmi et al., 2022). Sakkaravarthi et al. (Sakkaravarthi and Reddy, 2023) made a numerical investigation on entropy formation over a CHNF circulation over CSS. Simulation and theoretical inquiry on CNF over a CSS with the impact of a magnetic field and chemical processes were examined by Kumar et al. (Varun Kumar et al., 2022).

An electromagnetic actuator is a tool used in fluid mechanics to produce an effective liquid motion. A planar surface known as the Riga plate (RP) comprises alternating permanent magnets and electrodes. The magnetic field on the RP is not uniform, producing a Lorentz force that propels the fluid flow. In 1999, Gailitis and Lielausis (Gailitis and Lielausis, 1961) presented the electromagnetic actuator's basic theory for the first time. In contrast to typical techniques, they showed that employing electrodes and permanent magnets on a Riga plate may considerably increase the fluid flow rate and mixing capabilities. The advantage of employing an electromagnetic actuator to produce liquid flow is that it can do so without the need for mechanical actuators or movable components, which may be costly and prone to failure. Consequently, it is a viable solution for various practical purposes such as improving the exchange of heat, combining, and liquid flow. Asogwa et al. (Asogwa et al., 2022) examined analytical approaches to cross-diffusion and convection effects in the presence of CF over a porous RP. Hussain et al. (Hussain et al., 2022) investigated the impact of the Navier slip on an upward RP with CF displacement. Madhukesh et al. (Madhukesh et al., 2022a) investigated TPD and heat generation of Newtonian NF in an RP. Alshehri as al. (Mohammed Alshehri et al., 2021). Investigated Buoyancy implications in a Micropolar solution over an upward RP.

A nanofluid is a liquid with individual nanoparticles suspended in a solvent. Increased transfer of heat efficiency is a significant benefit of nanofluids over more traditional fluids. Increased thermal conductivity due to nanoparticles in the base fluid makes nanofluids excellent for thermal transfer medium. Nanofluids remain an intriguing field of study because of their revolutionary effects on a wide range of businesses and technology. The use of the change of variables approaches in the hydrothermal investigation of MHD compressing nanofluid circulation in parallel plates was studied by Zabihi et al. (Zabihi et al., 2022). Rizk et al. (Rizk et al., 2022) assessed the influence of the KKL correlation hypothesis on the production of thermal energies in a nanofluid comprising GO and ZnO dissolved in water passing via a permeable vertically spinning substrate. Shah et al. (Shah et al., 2021) researched mesoscopic modelling for magnetized nanofluid movement inside a porous three-dimensional tank. Ullah et al. (Ullah et al., 2022) scrutinized a magnetized 2D nanofluid that included blood, Go, and ZnO nanoparticles and moved via a perforated tube. The computational estimation of mixed convective entropy optimized in Darcy-Forchheimer circulation of Cross nanofluids via an upward plane plate with inconsistent heat source/sink was explored by Hussain et al. (Hussain et al., 2023).

When non-Newtonian behavior and nanofluids are combined, the result is a non-Newtonian nanofluid. Non-Newtonian fluids have a viscosity that varies as a function of the shear or stress rate. The temperature, nanoparticle concentration, and nanoparticle kind may impact this behavior. Khan et al. (Khan et al., 2023) investigated the effects of irregular heat source/sink on the aiding and opposing movements of the Eyring-Powell liquid on wall jet nanoparticles. Alharbi et al. (Alharbi et al., 2022) assessed the influence of viscous dissipation and Coriolis impacts on the mass and heat transmission evaluation of the 3D non-Newtonian flow of liquids. Khan et al. (Khan S. et al., 2021) investigated the study of the movement of a non-Newtonian liquid through a stretching/shrinking permeable material while considering the transmission of heat and mass. Some of the noticeable works on non-Newtonian fluids are found in (Algehyne et al., 2023; Alsulami et al., 2023).

The Casson nanofluid (CNF) idea is built on the assumption that the Casson equation governs liquid circulation and particle motion, a rheological model that explains the momentum behavior of non-Newtonian liquids. The Casson model considers yield stress and plastic solution viscosity, essential factors in various real-world scenarios such as blood circulation, coating layout, and liquid processing. Because of its improved thermal conductivity and specific heat capacity, CNF can considerably improve a fluid's ability to transmit temperature. Nanoparticles can also affect the fluid's rheological properties, such as viscosity and yield stress. Madhukesh et al. (Madhukesh et al., 2023) used the Cattaneo–Christov theory to investigate the heat transport of an MHD CMNF (Casson—Maxwell nanofluid) between two porous discs. Mabood et al. (Mabood et al., 2020) studied the free convective movement of time-dependent CNF in a permeable stretched surface. Madhukesh et al. (Madhukesh et al., 2022b) scrutinized the circulation of MHD MCNF in the presence of permeable discs using CCHF and slip impacts. Rasheed et al. (Rasheed et al., 2022) considered the homotopic solutions for the unsteady MHD CNF in a vertical cylinder with viscous dissipation impacts. The exact solution of a CF using Prabhakar-fractional simulations while also experiencing the effects of magnetohydrodynamic and sinusoidal thermal conditions was examined by Raza et al. (Raza et al., 2023).

Because of its temperature, a body emits a specific sort of electromagnetic radiation known as thermal radiation (TR). This radiation is formed by the thermal movement of the molecules and atoms inside the body, and it can go freely into space as there is no requirement for a medium to conduct it. The Stefan-Boltzmann equation describes the relationship between the temperature of a blackbody (an idealized object that absorbs all radiation incident on it) and the intensity of the thermal radiation it emits. Thermal radiation has important practical applications in various fields, including engineering, physics, astronomy, electronics, and energy conversion. Lone et al. (Lone et al., 2022) inspected MHD micropolar nanofluid hybrids circulating across a flat surface exposed to TR and mixed convection. Khan et al. (Khan U. et al., 2021) inspected the nonlinear T-R-influenced entropy production in the presence of NF with mixed convection effects. Naqvi et al. (Raza Shah Naqvi et al., 2022) examined numerical simulations to study the movement of hybrid nanofluids while considering the consequences of TR and entropy formation.

Ramesh et al. (Ramesh et al., 2023) scrutinized the hybrid-based CNT movement over a rotating sphere object in the presence of T-R and TPD. Magnetite-based liquid nanofluid three-dimensional layer movement involving non-linear TR and couple stress responses were studied by Ullah et al. (Ullah et al., 2021). The thermal study of slip and magnetohydrodynamic consequences for unstable sheet extending was investigated by Benos et al. (Benos et al., 2019).

The liquid and porous medium's features affect the rheological behavior of a fluid moving through them. When a non-Newtonian fluid, like a CNF, travels through a porous media, the pores' porosity, permeability, size, and shape can all impact how the fluid behaves. There has been a rise in interest in CNF flowing through porous media in recent years because of its potential applications in various industries, including increased oil recovery and geothermal energy generation. Understanding Casson nanofluid behavior is crucial for optimizing these processes since the characteristics of the porous medium can significantly impact how they behave. Alrehili et al. (Alrehili et al., 2022) made a numerical investigation of linear radiation and Soret impacts on MHD CNF over a vertical surface with a porous medium. Rallabandi et al. (Rallabandi, 2022) investigated the CNF flow over an inclined permeable stretched surface. Yogeesha et al. (Yogeesha et al., 2022) studied the Dufour and Soret effects to evaluate the dusty TNF circulation across an unstable stretched sheet. Raza et al. (Raza et al., 2022) inspected the activation energy, magnetic field, and binary chemical reaction impact on NF- and HNF through a porous area. Shoaib et al. (Shoaib et al., 2022) made soft computing to investigate the thermal energy's effects on the MHD CF as it passes over a porous material with an inclined non-linear surface.

The RKF-45, or Runge Kutta Fehlberg 4th 5th order, is a numerical method employed to solve complex systems of differential equations governing fluid flow problems. Many problems arise from simple laminar to complex turbulent flows in fluid mechanics. In mathematics, many of these situations may be modelled using ordinary differential equations, partial differential equations, or a hybrid of the two. Due to its high order accuracy and flexible step size capacity, RKF-45 is a popular numerical approach for modelling fluid dynamics. RKF-45 continuously controls the step size to reach the required level of precision while minimizing computational cost by calculating two estimates of the solution with varying orders of accuracy. The algorithm of the RKF-45 method is in detail given in (Mathews and Fink, 2004), and solving the differential equations using the RKF-45 algorithm was explained in (Abell and Braselton, 2000). Some works that implemented and used the RKF-45 algorithm are provided in (Sarris et al., 2002; Arifeen et al., 2021; Madhukesh et al., 2022b; Yogeesha et al., 2022; Hussain et al., 2023; Madhukesh et al., 2023).

The consider examination originality comes from its emphasis on the as-yet-unstudied subject of Casson-based nanofluid flow over a CSS in the presence of a porous medium and thermal radiation effects. In today's energy-conscious world, this study has the potential to help create more effective and sustainable thermal energy systems. Overall, studying the fluid flow past a CSS is an important area of research in fluid mechanics, with a significant impact on the development of microscale machines, including microfluidic devices, microscale engines, microsensors, and microscale reactors.

2 Mathematical formulation of the problem

As schematically seen in Figure 1, the flow pattern under study is a two-dimensional, incompressible, non-Newtonian Casson nanofluid flowing over a curved Riga surface. The radius of the curved surface is represented by R_1, and its curvilinear coordinates are marked by s_1& r_1. The uniform velocity of the Riga surface is $u_1 = U_{w1} = as_1$. Let T_{w1}& T_∞, respectively, stands for the wall and far-field temperatures. Suppose that the Riga surface is being affected by an electromagnetic force, denoted by F_m, in order to model the behavior of the fluid flow. A surface-mounted array of electrodes and permanent magnets are used to build the Riga surface. The previously derived governing equations for the fluid flow under these hypotheses are provided in the references (Hayat et al., 2018; Ahmad et al., 2019; Abbas et al., 2020; AdnanZaidi et al., 2020). These equations account for the influence of porous medium, TR, and CNF rheology on fluid flow across the curved Riga surface as follow:

$$R_1\frac{\partial u_1}{\partial s_1} + \frac{\partial}{\partial r_1}\left(v_1\left(R_1 + r_1\right)\right) = 0, \tag{1}$$

$$\frac{u_1^2}{\left(R_1 + r_1\right)} = \frac{1}{\rho_{nf}}\frac{\partial p_1}{\partial r_1}, \tag{2}$$

$$\begin{aligned}\frac{R_1}{\left(R_1 + r_1\right)}u_1\frac{\partial u_1}{\partial s_1} + v_1\frac{\partial u_1}{\partial r_1} + \frac{u_1 v_1}{\left(R_1 + r_1\right)} &= -\frac{1}{\rho_{nf}}\frac{R_1}{\left(R_1 + r_1\right)}\frac{\partial p_1}{\partial r_1} \\ &+ \exp\left(\frac{-\pi r_1}{c_1}\right)\frac{\pi j_0 M_0}{8\rho_{nf}} - \frac{\nu_{nf}}{k_1^*}u_1 + \nu_{nf}\left(1 + \frac{1}{\beta_1}\right) \\ &\left[\frac{\partial^2 u_1}{\partial r_1^2} + \frac{\partial u_1}{\partial r_1}\frac{1}{\left(R_1 + r_1\right)} - \frac{u_1}{\left(R_1 + r_1\right)^2}\right],\end{aligned} \tag{3}$$

$$\begin{aligned}\frac{R_1}{\left(R_1 + r_1\right)}u_1\frac{\partial T_1}{\partial s_1} + v_1\frac{\partial T_1}{\partial r_1} &= -\frac{k_{nf}}{\left(\rho Cp\right)_{nf}}\left[\frac{\partial^2 T_1}{\partial r_1^2} + \frac{\partial T_1}{\partial r_1}\frac{1}{\left(R_1 + r_1\right)}\right] \\ &- \frac{1}{\left(\rho Cp\right)_{nf}}\left[\frac{\partial}{\partial r_1}\left(\left(R_1 + r_1\right)q_r\right)\right]\frac{1}{\left(R_1 + r_1\right)}\end{aligned} \tag{4}$$

in Eq. 4, the term q_r is given by: $q_r = \frac{-16\sigma^* T_\infty^3}{3k^*}\frac{\partial T_1}{\partial r_1}$, [see (Hayat et al., 2018)].

The respective boundary conditions for the consider model are

$$\left.\begin{aligned} &r_1 = 0\text{: } u_1 = U_{w1}, v_1 = 0, T_1 = T_{w1}, \\ &r_1 \to \infty : u_1 \to 0, \frac{\partial u_1}{\partial r_1} \to 0, T_1 \to T_\infty. \end{aligned}\right\} \tag{5}$$

Furthermore, to ease the analysis of the consider investigation, the following similarity variables are introduced as [see (Abbas et al., 2020; AdnanZaidi et al., 2020)]:

$$\left.\begin{aligned} &\zeta = \left(\frac{U_1}{\nu_f s_1}\right)^{0.5} r_1, u_1 = U_1 h'(\zeta), v_1 = -\frac{R_1}{\left(R_1 + r_1\right)}\sqrt{\frac{U_1\nu_f}{s_1}}h(\zeta), \\ &p_1 = \rho_f {U_1}^2 P_1(\zeta), K_1 = \left(\frac{U_1}{\nu_f s_1}\right)^{0.5} R_1, \theta = \frac{T_1 - T_\infty}{T_{w1} - T_\infty}. \end{aligned}\right\} \tag{6}$$

Therefore, with the help of the above similarity variables stated in Eqs 1, 6 is satisfied and Eqs 2, 3 take the following form as:

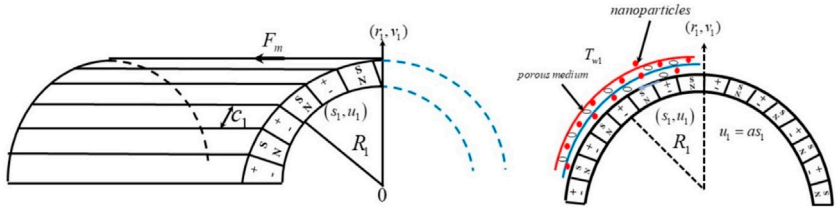

FIGURE 1
Geometry of the flow problem.

$$P_1' = \frac{h'^2 G_2}{\zeta + K_1}, \tag{7}$$

$$\frac{2K_1}{\zeta + K_1}\frac{P_1}{G_2} = \left(1 + \frac{1}{\beta_1}\right)\left[h''' + \frac{1}{\zeta + K_1}h'' - \frac{h'}{(\zeta + K_1)^2}\right]\frac{1}{G_1 G_2} + \frac{K_1}{\zeta + K_1}\left(hh'' - (h')^2\right) + \frac{K_1}{(\zeta + K_1)^2}h'h + \frac{Q_1 e^{-z\zeta}}{G_2} - \frac{\lambda_1}{G_1 G_2}h'. \tag{8}$$

here, $Q_1 = \frac{\pi j_0 M_0}{8\rho_f U_1 a}$ is the modified Hartmann number, $\lambda_1 = \frac{\nu_f}{k^*_1 a}$ is the porous parameter, and $z = \sqrt{\frac{\pi^2 \nu_f}{a c_1^2}}$ is the parameter related to the width of the magnets and electrodes.

Moreover, to eliminate the pressure terms in Eqs 7, 8, we get

$$\left(1 + \frac{1}{\beta_1}\right)\left[\frac{h'}{(\zeta + K_1)^3} - \frac{h''}{(\zeta + K_1)^2} + \frac{2}{\zeta + K_1}h''' + h''''\right]\frac{1}{G_1 G_2} + \frac{K_1}{\zeta + K_1}(hh''' - h'h'') + \frac{K_1}{(\zeta + K_1)^2}\left(hh'' - h'^2\right) - \frac{K_1}{(\zeta + K_1)^3}h'h + w_2\frac{Q_1 e^{-z\zeta}}{G_2} - \frac{\lambda_1}{G_1 G_2}\left(h'' + \frac{h'}{\zeta + K_1}\right) = 0. \tag{9}$$

After utilizing the similarity variables, the energy Eq. 4 reduces to the form as:

$$\left[\frac{k_{nf}}{k_f} + \frac{4}{3}Nr\right]\frac{1}{\mathrm{Pr}G_3}\left(\theta'' + \frac{1}{\zeta + K_1}\theta'\right) + \frac{K_1}{\zeta + K_1}h\theta' = 0, \tag{10}$$

with simplified boundary conditions are

$$\left.\begin{array}{l}\zeta = 0\text{: } h'(\zeta) = 1, h(\zeta) = 0, \theta(\zeta) = 1.\\ \zeta \to \infty : h'(\zeta) = 0, h''(\zeta) = 0, \theta(\zeta) = 0.\end{array}\right\} \tag{11}$$

in aforesaid Eqs 9–11, the term $w_2 = (\frac{1}{\zeta + K_1} - z)$ is called a dimensionless quantity, $\mathrm{Pr}\frac{\nu_f (\rho C p)_f}{k_f}$, & $Nr = \frac{4\phi^* T_\infty^3}{k^* k_f}$ refer the Prandtl number, and radiation parameter, respectively.

The important engineering quantities and its reduced form [see (Abbas et al., 2020; AdnanZaidi et al., 2020)]:

$$Cf = \frac{\mu_{nf}}{\rho_f U_{w1}^2}\left(1 + \frac{1}{\beta_1}\right)\left(\frac{\partial u_1}{\partial r_1} - \frac{u_1}{(R_1 + r_1)}\right)_{r_1 = 0} \Rightarrow \sqrt{\mathrm{Re}}Cf = \frac{1}{G_1}\left(1 + \frac{1}{\beta_1}\right)\left(h''(0) - \frac{h'(0)}{\zeta + K_1}\right), \tag{12}$$

$$Nu = \frac{-s_1}{k_f (T_{w1} - T_\infty)}\left(k_{nf} + \frac{16\phi^* T_\infty^3}{3k^*}\right)\left(\frac{\partial T_1}{\partial r_1}\right)_{r_1 = 0} \Rightarrow \frac{Nu}{\sqrt{\mathrm{Re}}} = \left[\frac{k_{nf}}{k_f} + \frac{4}{3}Nr\right]\theta'(0). \tag{13}$$

TABLE 1 Thermophysical properties of base fluid and nanoparticles.

Properties	$SA(C_6H_9NaO_7)$	TiO_2
$\rho(kgm^{-3})$	989	4250
$C_p(Jkg^{-1}K^{-1})$	4175	686.2
$k(kgms^{-3}K^{-1})$	0.6376	8.9528
Pr	6.45	-

TABLE 2 Comparison of $-Cf$ values of current numerical implementation with the work of (Sajid et al., 2010) in the absence of $G_1, G_2, (1 + \frac{1}{\beta_1})$ and $Q_1 = 0$.

Parameter	Sajid et al. (2010)	Present work
$K = 20$	0.9357	0.93588
$K = 30$	0.9568	0.95612
$K = 40$	0.9675	0.96787
$K = 50$	0.9740	0.97445
$K = 100$	0.9870	0.98797

Hence, $\mathrm{Re} = \frac{U_1 s_1}{\nu_f}$ is the local Reynolds number.

The thermophysical properties of nanofluid are given as follows [see (Khan et al., 2018; Alwawi et al., 2019)].

The effective thermophysical characteristics of nanofluid are given as follows [see (Acharya et al., 2019)]

$$\mu_{nf} = \frac{\mu_f}{G_1}\left(G_1 = (1 - \phi^*)^{2.5}\right), \tag{14}$$

$$\rho_{nf} = \rho_f G_2\left(G_2 = \left(1 - \phi^* + \frac{\phi^* \rho_s}{\rho_f}\right)\right), \tag{15}$$

$$(\rho C p)_{nf} = (\rho C p)_f G_3\left(G_3 = \left(1 - \phi^* + \frac{\phi^* \rho_s C p_s}{\rho_f C p_f}\right)\right), \tag{16}$$

$$\frac{k_{nf}}{k_f} = \frac{k_s - 2\phi^*\left(k_f - k_s\right) + 2k_f}{k_s + \phi^*\left(k_f - k_s\right) + 2k_f}. \tag{17}$$

3 Numerical method and code validation

The higher order and two-point boundary conditions in the governing equations for the fluid flow over the curved Riga

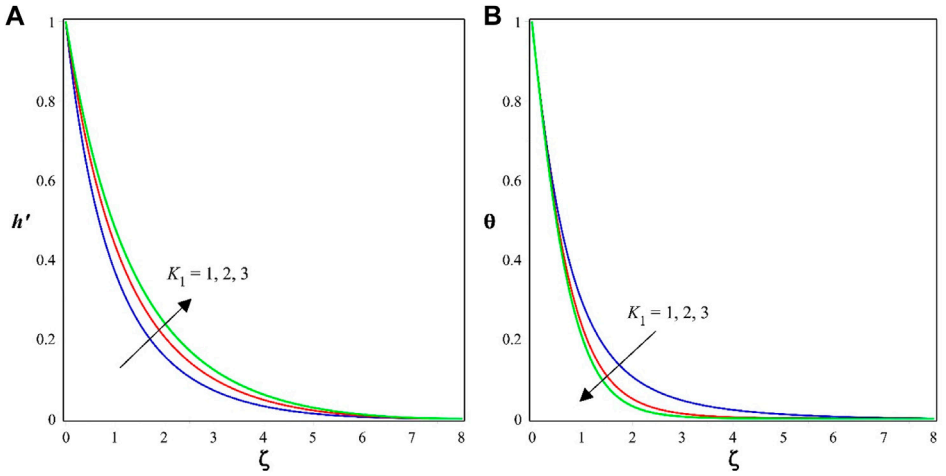

FIGURE 2
Significance of K_1 on **(A)** velocity profile **(B)** temperature profile.

surface make them challenging to solve analytically. We must transform these into first-order differential equations to achieve a numerical solution. Applying appropriate transformations will allow the higher-order differential equations to be represented as a set of first-order differential equations. Let us take,

$$\begin{matrix}[h, h', h'', h'''] = [\kappa_1, \kappa_2, \kappa_3, \kappa_4] \\ [\theta, \theta'] = [\kappa_5, \kappa_6]\end{matrix}, \tag{18}$$

$$h'''' = \frac{-G_1G_2}{\left(1+\frac{1}{\beta_1}\right)}\left(\begin{array}{l}\left(\left(1+\frac{1}{\beta_1}\right)\frac{1}{G_1G_2}\left(\frac{2}{\zeta+K_1}\kappa_4 - \frac{\kappa_3}{(\zeta+K_1)^2}+\frac{\kappa_2}{(\zeta+K_1)^3}\right)\right. \\ \left. + \frac{K_1}{\zeta+K_1}(\kappa_1\kappa_4-\kappa_2\kappa_3)+\frac{K_1}{(\zeta+K_1)^2}(\kappa_1\kappa_3-\kappa_2{}^2)\right) \\ \left. - \frac{K_1}{(\zeta+K_1)^3}\kappa_2\kappa_1 + w_2\frac{Q_1e^{-z\zeta}}{G_2} - \frac{\lambda_1}{G_1G_2}\left(\kappa_3+\frac{\kappa_2}{\zeta+K_1}\right)\right)\end{array}, \tag{19}$$

$$\theta'' = -\frac{\mathrm{PrG_3}}{\left[\frac{k_{nf}}{k_f}+\frac{4}{3}Nr\right]}\left(\frac{K_1}{\zeta+K_1}\kappa_1\kappa_6 + \frac{1}{\zeta+K_1}\kappa_6\frac{1}{\mathrm{PrG_3}}\left[\frac{k_{nf}}{k_f}+\frac{4}{3}Nr\right]\right), \tag{20}$$

with the boundary constraints become

$$\left.\begin{matrix}\kappa_1(0) = 0, \kappa_2(0) = 1, \kappa_3(0) = \chi_1, \kappa_4(0) = \chi_2, \\ \kappa_5(0) = 1, \kappa_4(0) = \chi_3.\end{matrix}\right\} \tag{21}$$

The Runge-Kutta Fehlberg 45-order approach was then used to solve the transformed Eq. 19 numerically and (20) as well as the boundary conditions (21). Since the boundary conditions contain unknowns, we employed a shooting technique to find the solution that meets the conditions at infinity. Further, utilised a step size of 0.001 and set the error tolerance to 10^{-6} to achieve accurate findings. By substituting appropriate values for the dimensionless variables and using the thermophysical properties of the nanofluid (see Table 1) solutions are obtained. We discovered that our findings were in strong accord with prior work (Sajid et al., 2010), demonstrating the accuracy and dependability of our numerical method (see Table 2).

4 Results and discussion

The purpose of this section is to describe how significant dimensionless parameters affect the temperature and velocity profiles. The RKF-45 method and shooting approach are used to numerically solve the reduced ODEs and boundary conditions acquired in the previous section. The acquired data are shown as graphs to illustrate the impact of various dimensionless parameters on the motion and temperature fields. Also, a discussion of the important technical variables that may have an impact on the system's flow and thermal transfer characteristics is included in this section. The current study offers useful insights for designing and optimising industrial applications employing Casson-based nanofluid movements over curved surfaces by taking these parameters into account.

Figures 2A, B show the impact of K_1 (curvature constraint) over velocity and temperature profiles, respectively. According to the findings, a rise in the curvature parameter improves the h' profile (Figure 2A) but lowers the θ profile (Figure 2B). This is explained by the fact that increasing the radius of the curved surface causes the fluid to move more quickly, which improves the velocity profile by reducing the thickness of both the momentum boundary layer (MBL) and thermal boundary layer (TBL). However, when the fluid moves more quickly, there is less time for temperature distribution, which reduces temperature.

Figure 3A, B display the variation of h' and θ profiles in the presence of Q_1 (modified Hartmann number). The improvement in the Q_1 will decreases the velocity profile (see Figure 3A) but improves the temperature profile (see Figure 3B). This is caused by a rise in the Q_1, which slows the liquid flow and lowers the velocity profile by increasing the magnetic strength and, consequently, the Lorentz force. Yet, this also improves the system's thermal distribution, leading to a better temperature profile.

The effect of the porosity constraint λ_1 on the h' profile is illustrated in Figure 4A. It has been found that a higher λ_1 causes the velocity profile to drop. This is due to the presence of a porous

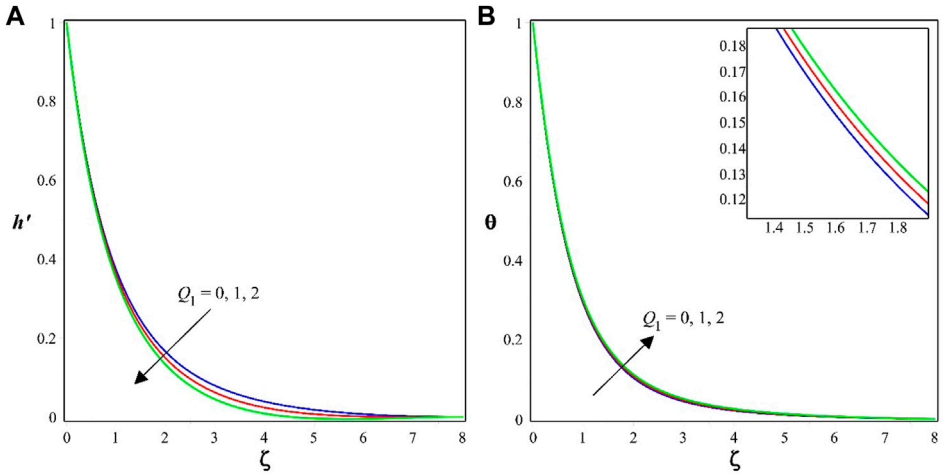

FIGURE 3
Significance of Q_1 on **(A)** velocity profile **(B)** temperature profile.

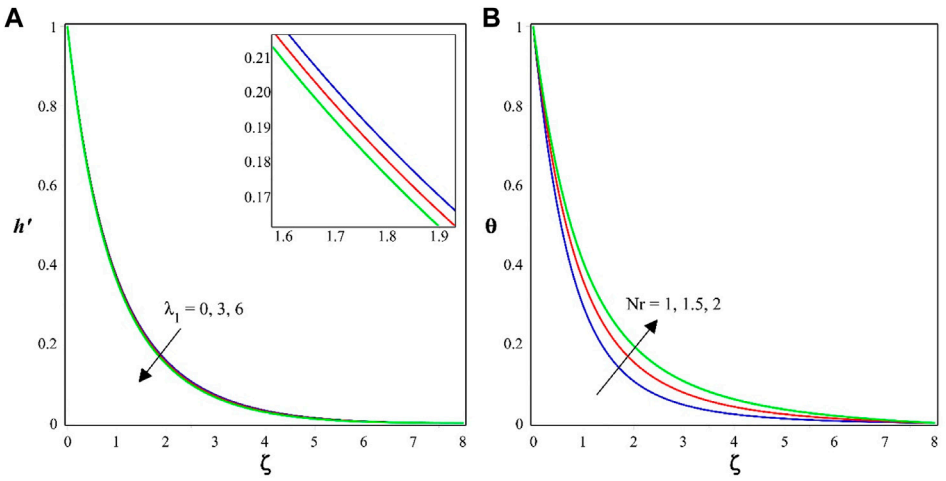

FIGURE 4
(A) Significance of λ_1 on velocity profile **(B)** Significance of *Nr* on temperature profile.

medium, which restricts the movement of fluids by providing a barrier against the motion of the fluids. The h' profile is decreased when the resistance rises along with the porous parameter. Figure 4B displayed the influence of the thermal radiation Nr parameter on θ profile. The rise in Nr will improve the temperature profile. An increase in the value of Nr denotes a rise in the system's thermal radiation output. The energy from the radiation is absorbed by the fluid, raising its temperature, which improves the temperature profile.

The consequence of the Casson parameter β_1 on the h' profile is represented in Figure 5A. It is evident that a rise in the values of β_1 causes the velocity profile to fall. This is because a greater β_1 causes the fluid's yield stress to flow initiation and decrease the h' profile. This leads to decline in the overall velocity of the liquid near the boundary as the circulation is impeded by increasing yield stress. Figure 5B displays the variation of θ profile for numerous values of the Casson parameter β_1. The rise in the values of β_1 will advance the temperature distribution. As explained in Figure 5A, the reduction in the velocity will lead to the liquid's residence time near the surface. When the β_1 increases, it implies a larger yield stress, meaning that the liquid requires more energy to commence flow. As a result of the higher flow resistance, more energy is released as heat inside the fluid. The temperature profile rises as a result of this phenomena.

Figure 6A represents the effect of skin friction on the porous parameter λ_1 for the rise in the values of solid volume fraction ϕ^*. It is observed that surface drag force decreases with improved values of λ_1 and ϕ^*. This is due to the fact that raising these parameters generates an increase in the MBL's thickness, which in turn causes a reduction in the fluid flow at the surface. As a direct consequence of this, the force of surface drag is decreased. Figure 6B shows the variation in Nusselt number for improved values of Nr and ϕ^*.

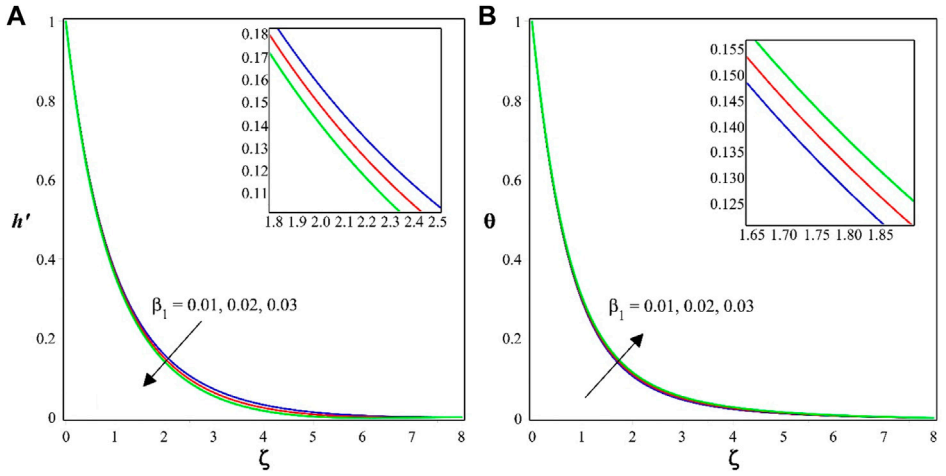

FIGURE 5
Significance of β_1 on **(A)** velocity profile **(B)** temperature profile.

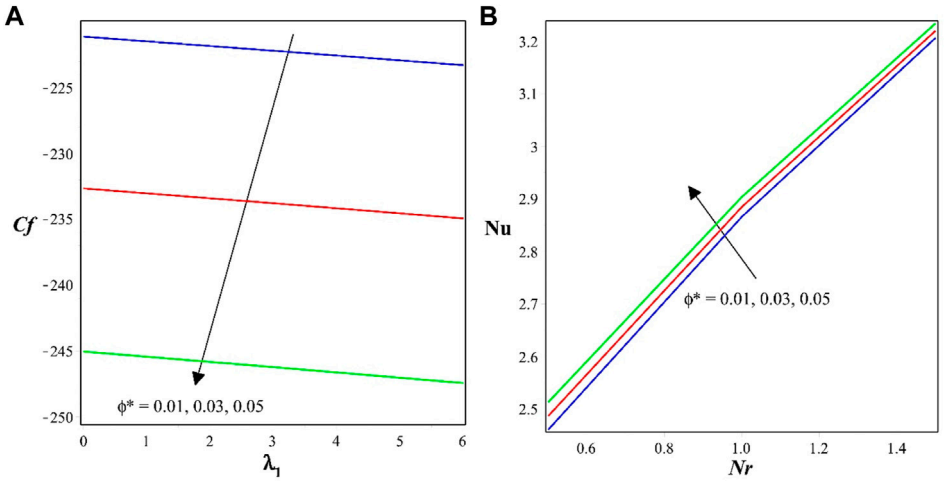

FIGURE 6
(A) Impact of *Cf* on λ_1 for different values of ϕ^* **(B)** Impact of *Cf* on *Nr* for different values of ϕ^*.

When these two criteria are improved, the rate at which thermal energy is distributed will increase. However, because nanoparticles are present in the fluid, the thermal conductivity is boosted, which results in an increase in the total heat transfer rate. This offsets the fact that the surface area that is accessible for heat transmission decreases as the percentage rises.

5 Final remarks

The present study investigates Casson-based nanofluid movement over a curved stretching surface in the presence of porous medium and thermal radiation effects. The ODEs and BCs are obtained by applying suitable similarity constraints to the PDEs. The numerical calculations are done with the aid of RKF-45 and shooting techniques. The outcomes are visualized using a graphical representation. The discussions on important dimensionless constraints are presented. The main conclusions of the study are as follows:

- ❖ The improvement in the modified Hartman number and porosity factors will decrease the velocity. An increase in these components indicates stronger magnetic impacts and increased permeability. As a result, the velocity of the flow of nanofluid reduces.
- ❖ With an increase in the curvature parameter, the velocity rises but the temperature decreases. The surface becomes increasingly curved when the curvature parameter is increased. This causes higher liquid flow along the curved surface, which causes velocity to go up. The temperature, on the other hand, falls as the liquid moves more and releases heat owing to the increasing surface area.

- ❖ Thermal radiation and modified Hartmann numbers will improve the temperature. Thermal radiation and modified Hartmann numbers facilitates the distribution of heat from liquid to the surrounding and improves the thermal distribution due to strong magnetic effects.
- ❖ The Casson factor will decline the velocity but improve the thermal profile. The rise in Casson factor will denotes the higher yield stress and more resistance to flow of the liquid. This results in decrease in velocity and improved thermal profile.
- ❖ The surface drag force reduces with increase in the values of porous and solid fractions. Porous medium act as a barrier and slows down the fluid flow and adding of solid particles also influence on the surface drag force by increasing thickness of momentum boundary layer.
- ❖ The rate of thermal distribution advances with radiation and solid fraction factors. Heat transport is facilitated by radiation, and the thermal distribution is improved by the presence of solid fractions, which encourage better mixing and dispersion of thermal energy.

Data availability statement

The original contributions presented in the study are included in the article/Supplementary Material, further inquiries can be directed to the corresponding author.

Author contributions

Conceptualization, AH, BS, KN, KV, and JM; methodology, KN, KV, and JM; software, KN, KV, and JM; validation, KN, KV, and JM; formal analysis, KN, KV, and JM; investigation, UK, JS, and IS; resources, IS; data curation, AH, BS, UK, JS, and IS; writing—original draft preparation, AH, BS, UK, JS, IS, and E-SS; writing—review and editing, AH, BS, UK, JS, IS, and E-SS; visualization, E-SS; supervision, E-SS; project administration, E-SS; funding acquisition, E-SS. All authors contributed to the article and approved the submitted version.

Funding

This work was funded by the Researchers Supporting Project number (RSP2023R33), King Saud University, Riyadh, Saudi Arabia.

Acknowledgments

The authors are thankful for the support of Researchers Supporting Project number (RSP2023R33), King Saud University, Riyadh, Saudi Arabia.

Conflict of interest

The authors declare that the research was conducted in the absence of any commercial or financial relationships that could be construed as a potential conflict of interest.

Publisher's note

References

Abbas, N., Malik, M. Y., and Nadeem, S. (2020). Transportation of magnetized micropolar hybrid nanomaterial fluid flow over a Riga curface surface. *Comput. Methods Programs Biomed.* 185, 105136. doi:10.1016/j.cmpb.2019.105136

Abell, M. L., and Braselton, J. P. (2000). *Differential equations with maple V*. Cambridge, Massachusetts, United States: Academic Press.

Acharya, N., Maity, S., and Kundu, P. K. (2019). Framing the hydrothermal features of magnetized TiO2–CoFe2O4 water-based steady hybrid nanofluid flow over a radiative revolving disk. *Multidiscip. Model. Mater. Struct.* 16, 765–790. doi:10.1108/mmms-08-2019-0151

AdnanZaidi, S. Z. A., Khan, U. N., Chu, Y. M., Mohyud-Din, S. T., Chu, Y.-M., Khan, I. K. S., et al. (2020). Impacts of freezing temperature based thermal conductivity on the heat transfer gradient in nanofluids: applications for a curved Riga surface. *Molecules* 25, 2152. doi:10.3390/molecules25092152

Ahmad, S., Nadeem, S., and Muhammad, N. (2019). Boundary layer flow over a curved surface imbedded in porous medium. *Commun. Theor. Phys.* 71, 344. doi:10.1088/0253-6102/71/3/344

Algehyne, E. A., Abdelmohsen, S. A. M., Gowda, R. J. P., Kumar, R. N., Abdelbacki, A. M. M., Gorji, M. R., et al. (2023). Mathematical modeling of magnetic dipole effect on convective heat transfer in Maxwell nanofluid flow: single and multi-walled carbon nanotubes. *Waves Random Complex Media* 33, 489–504. doi:10.1080/17455030.2022.2125598

Alharbi, K. A. M., Ullah, A., Ikramullah, Fatima, N., Khan, R., Sohail, M., et al. (2022). Impact of viscous dissipation and coriolis effects in heat and mass transfer analysis of the 3D non-Newtonian fluid flow. *Case Stud. Therm. Eng.* 37, 102289. doi:10.1016/j.csite.2022.102289

Alrehili, M. F., Goud, B. S., Reddy, Y. D., Mishra, S. R., Lashin, M. M. A., Govindan, V., et al. (2022). Numerical computing of Soret and linear radiative effects on MHD Casson fluid flow toward a vertical surface through a porous medium: finite element analysis. *Mod. Phys. Lett. B* 36, 2250170. doi:10.1142/s0217984922501706

Alsulami, M. D., Naveen Kumar, R., Punith Gowda, R. J., and Prasannakumara, B. C. (2023). Analysis of heat transfer using Local thermal non-equilibrium conditions for a non-Newtonian fluid flow containing Ti6Al4V and AA7075 nanoparticles in a porous media. *ZAMM - J. Appl. Math. Mech./ Zeitschrift Für Angewandte Math. Und Mech.* 103, e202100360. doi:10.1002/zamm.202100360

Alwawi, F. A., Alkasasbeh, H. T., Rashad, A. M., and Idris, R. (2019). Natural convection flow of Sodium Alginate based Casson nanofluid about a solid sphere in the presence of a magnetic field with constant surface heat flux. *J. Phys. Conf. Ser.* 1366, 012005. doi:10.1088/1742-6596/1366/1/012005

Arifeen, S. U., Haq, S., Ghafoor, A., Ullah, A., Kumam, P., and Chaipanya, P. (2021). Numerical solutions of higher order boundary value problems via wavelet approach. *Adv. Differ. Equ.* 2021, 347. doi:10.1186/s13662-021-03495-6

Asogwa, K. K., Alsulami, M. D., Prasannakumara, B. C., and Muhammad, T. (2022). Double diffusive convection and cross diffusion effects on Casson fluid over a Lorentz force driven Riga plate in a porous medium with heat sink: an analytical approach. *Int. Commun. Heat Mass Transf.* 131, 105761. doi:10.1016/j.icheatmasstransfer.2021.105761

Benos, L. Th., Mahabaleshwar, U. S., Sakanaka, P. H., and Sarris, I. E. (2019). Thermal analysis of the unsteady sheet stretching subject to slip and magnetohydrodynamic effects. *Therm. Sci. Eng. Prog.* 13, 100367. doi:10.1016/j.tsep.2019.100367

Duraihem, F. Z., Devi, R. L. V. R., Prakash, P., Sreelakshmi, T. K., Saleem, S., Durgaprasad, P., et al. (2023). Enhanced heat and mass transfer characteristics of multiple slips on hydro-magnetic dissipative Casson fluid over a curved stretching surface. *Int. J. Mod. Phys. B*, 2350229. doi:10.1142/s0217979223502296

Gailitis, A., and Lielausis, O. (1961). On a possibility to reduce the hydrodynamic resistance of a plate in aelectro-lyte. *Appl. Magnetohydrodyn.* 12, 143–146.

Hayat, T., Qayyum, S., Imtiaz, M., and Alsaedi, A. (2018). Double stratification in flow by curved stretching sheet with thermal radiation and joule heating. *J. Therm. Sci. Eng. Appl.* 10, 021010. doi:10.1115/1.4037774

Hussain, S. M., Khan, U., Zaib, A., Ishak, A., and Sarris, I. E. (2023). Numerical computation of mixed convective entropy optimized in Darcy-Forchheimer flow of Cross nanofluids through a vertical flat plate with irregular heat source/sink. *Tribol. Int.* 187, 108757. doi:10.1016/j.triboint.2023.108757

Hussain, S. M., Sharma, R., and Alrashidy, S. S. (2022). Numerical study of Casson nanofluid flow past a vertical convectively heated Riga-plate with Navier's slip condition. *AIP Conf. Proc.* 2435, 020002. doi:10.1063/5.0083603

Khan, A., Khan, D., Khan, I., Ali, F., ul Karim, F., and Imran, M. (2018). MHD flow of sodium alginate-based casson type nanofluid passing through A porous medium with Newtonian heating. *Sci. Rep.* 8, 8645. doi:10.1038/s41598-018-26994-1

Khan, S., Selim, M. M., Khan, A., Ullah, A., Abdeljawad, T., Ikramullah,, et al. (2021a). On the analysis of the non-Newtonian fluid flow past a stretching/shrinking permeable surface with heat and mass transfer. *Coatings* 11, 566. doi:10.3390/coatings11050566

Khan, U., Zaib, A., Ishak, A., Sherif, E.-S. M., Sarris, I. E., Eldin, S. M., et al. (2023). Analysis of assisting and opposing flows of the Eyring-Powell fluid on the wall jet nanoparticles with significant impacts of irregular heat source/sink. *Case Stud. Therm. Eng.* 49, 103209. doi:10.1016/j.csite.2023.103209

Khan, U., Zaib, A., Khan, I., and Nisar, K. S. (2021b). Entropy generation incorporating γ-nanofluids under the influence of nonlinear radiation with mixed convection. *Crystals* 11, 400. doi:10.3390/cryst11040400

Lakshmi, K. B., Sugunamma, V., Tarakaramu, N., Sivakumar, N., and Sivajothi, R. (2022). Cross-dispersion effect on magnetohydrodynamic dissipative Casson fluid flow via curved sheet. *Heat. Transf.* 51, 7822–7842. doi:10.1002/htj.22668

Lone, S. A., Alyami, M. A., Saeed, A., Dawar, A., Kumam, P., and Kumam, W. (2022). MHD micropolar hybrid nanofluid flow over a flat surface subject to mixed convection and thermal radiation. *Sci. Rep.* 12, 17283. doi:10.1038/s41598-022-21255-8

Mabood, F., Yusuf, T. A., and Sarris, I. E. (2020). Entropy generation and irreversibility analysis on free convective unsteady mhd casson fluid flow over a stretching sheet with soret/dufour in porous media. *STRPM* 11, 595–611. doi:10.1615/specialtopicsrevporousmedia.2020033867

Madhukesh, J. K., Naveen Kumar, R., Punith Gowda, R. J., Prasannakumara, B. C., Ramesh, G. K., Ijaz Khan, M., et al. (2021). Numerical simulation of aa7072-aa7075/water-based hybrid nanofluid flow over a curved stretching sheet with Newtonian heating: a non-fourier heat flux model approach. *J. Mol. Liq.* 335, 116103. doi:10.1016/j.molliq.2021.116103

Madhukesh, J. K., Prasannakumara, B. C., Kumar, R. S. V., Rauf, A., and Shehzad, S. A. (2022b). Flow of hydromagnetic micropolar-casson nanofluid over porous disks influenced by cattaneo-christov theory and slip effects. *JPM* 25, 35–49. doi:10.1615/jpormedia.2021039254

Madhukesh, J. K., Ramesh, G. K., Shehzad, S. A., Chapi, S., and Prabhu Kushalappa, I. (2023). Thermal transport of MHD Casson–Maxwell nanofluid between two porous disks with Cattaneo–Christov theory. *Numer. Heat. Transf. Part A Appl.*, 1–16. doi:10.1080/10407782.2023.2214322

Madhukesh, J. K., Varun Kumar, R. S., Punith Gowda, R. J., Prasannakumara, B. C., and Shehzad, S. A. (2022a). Thermophoretic particle deposition and heat generation analysis of Newtonian nanofluid flow through magnetized Riga plate. *Heat. Transf.* 51, 3082–3098. doi:10.1002/htj.22438

Mathews, J. H., and Fink, K. D. (2004). *Numerical methods using MATLAB*. Upper Saddle River, NJ, USA: Pearson Prentice Hall.

Mohammed Alshehri, A., Huseyin Coban, H., Ahmad, S., Khan, U., and Alghamdi, W. M. (2021). Buoyancy effect on a micropolar fluid flow past a vertical Riga surface comprising water-based SWCNT–MWCNT hybrid nanofluid subject to partially slipped and thermal stratification: cattaneo–christov model. *Math. Problems Eng.* 2021, 1–13. doi:10.1155/2021/6618395

Rallabandi, S. R. (2022). Finite element solutions of non-Newtonian dissipative Casson fluid flow past a vertically inclined surface surrounded by porous medium including constant heat flux, thermal diffusion, and diffusion thermo. *Int. J. Comput. Methods Eng. Sci. Mech.* 23, 228–242. doi:10.1080/15502287.2021.1949407

Ramesh, G. K., Madhukesh, J. K., Ali Shah, N., and Yook, S.-J. (2023). Flow of hybrid CNTs past a rotating sphere subjected to thermal radiation and thermophoretic particle deposition. *Alexandria Eng. J.* 64, 969–979. doi:10.1016/j.aej.2022.09.026

Rasheed, H. U., Khan, Z., El-Zahar, E. R., Shah, N. A., Islam, S., and Abbas, T. (2022). Homotopic solutions of an unsteady magnetohydrodynamic flow of Casson nanofluid flow by a vertical cylinder with Brownian and viscous dissipation effects. *Waves Random Complex Media* 0, 1–14. doi:10.1080/17455030.2022.2105979

Raza, A., Khan, U., Almusawa, M. Y., Hamali, W., and Galal, A. M. (2023). Prabhakar-fractional simulations for the exact solution of Casson-type fluid with experiencing the effects of magneto-hydrodynamics and sinusoidal thermal conditions. *Int. J. Mod. Phys. B* 37, 2350010. doi:10.1142/s0217979223500108

Raza, Q., Qureshi, M. Z. A., Khan, B. A., Kadhim Hussein, A., Ali, B., Shah, N. A., et al. (2022). Insight into dynamic of mono and hybrid nanofluids subject to binary chemical reaction, activation energy, and magnetic field through the porous surfaces. *Mathematics* 10, 3013. doi:10.3390/math10163013

Raza Shah Naqvi, S. M., Waqas, H., Yasmin, S., Liu, D., Muhammad, T., Eldin, S. M., et al. (2022). Numerical simulations of hybrid nanofluid flow with thermal radiation and entropy generation effects. *Case Stud. Therm. Eng.* 40, 102479. doi:10.1016/j.csite.2022.102479

Rizk, D., Ullah, A., Ikramullah,Elattar, S., Alharbi, K. A. M., Sohail, M., et al. (2022). Impact of the KKL correlation model on the activation of thermal energy for the hybrid nanofluid (GO+ZnO+Water) flow through permeable vertically rotating surface. *Energies* 15, 2872. doi:10.3390/en15082872

Sajid, M., Ali, N., Javed, T., and Abbas, Z. (2010). Stretching a curved surface in a viscous fluid. *Chin. Phys. Lett.* 27, 024703. doi:10.1088/0256-307x/27/2/024703

Sakkaravarthi, K., and Reddy, P. B. A. (2023). Entropy generation on Casson hybrid nanofluid over a curved stretching sheet with convective boundary condition: semi-analytical and numerical simulations. *Proc. Institution Mech. Eng. Part C J. Mech. Eng. Sci.* 237, 465–481. doi:10.1177/09544062221119055

Sarris, I. E., Lekakis, I., and Vlachos, N. S. (2002). Natural convection in a 2d enclosure with sinusoidal upper wall temperature. *Numer. Heat. Transf. Part A Appl.* 42, 513–530. doi:10.1080/10407780290059675

Shah, Z., Kumam, P., Ullah, A., Khan, S. N., and Selim, M. M. (2021). Mesoscopic simulation for magnetized nanofluid flow within a permeable 3D tank. *IEEE Access* 9, 135234–135244. doi:10.1109/access.2021.3115599

Shoaib, M., Kausar, M., Nisar, K. S., Asif Zahoor Raja, M., and Morsy, A. (2022). Impact of thermal energy on MHD casson fluid through a forchheimer porous medium with inclined non-linear surface: a soft computing approach. *Alexandria Eng. J.* 61, 12211–12228. doi:10.1016/j.aej.2022.06.014

Ullah, A., Ikramullah,Selim, M. M., Abdeljawad, T., Ayaz, M., Mlaiki, N., et al. (2021). A magnetite–water-based nanofluid three-dimensional thin film flow on an inclined rotating surface with non-linear thermal radiations and couple stress effects. *Energies* 14, 5531. doi:10.3390/en14175531

Ullah, I., Ullah, A., Selim, M. M., Khan, M. I., Saima,Khan, A. A., et al. (2022). Analytical investigation of magnetized 2D hybrid nanofluid (GO + ZnO + blood) flow through a perforated capillary. *Comput. Methods Biomechanics Biomed. Eng.* 25, 1531–1543. doi:10.1080/10255842.2021.2021194

Varun Kumar, R. S., Gunderi Dhananjaya, P., Naveen Kumar, R., Punith Gowda, R. J., and Prasannakumara, B. C. (2022). Modeling and theoretical investigation on Casson nanofluid flow over a curved stretching surface with the influence of magnetic field and chemical reaction. *Int. J. Comput. Methods Eng. Sci. Mech.* 23, 12–19. doi:10.1080/15502287.2021.1900451

Yogeesha, K. M., Megalamani, S. B., Gill, H. S., Umeshaiah, M., and Madhukesh, J. K. (2022). The physical impact of blowing, Soret and Dufour over an unsteady stretching surface immersed in a porous medium in the presence of ternary nanofluid. *Heat. Transf.* 51, 6961–6976. doi:10.1002/htj.22632

Zabihi, A., Akinshilo, A. T., Rezazadeh, H., Ansari, R., Sobamowo, M. G., and Tunc, C. (2022). Application of variation of parameter's method for hydrothermal analysis on MHD squeezing nanofluid flow in parallel plates. *Comput. Methods Differ. Equations* 10, 580–594. doi:10.22034/cmde.2021.41296.1794

frontiers | Frontiers in Materials

TYPE Original Research
PUBLISHED 19 September 2023
DOI 10.3389/fmats.2023.1242085

OPEN ACCESS

EDITED BY
Noor Saeed Khan,
University of Education Lahore, Pakistan

REVIEWED BY
Katta Ramesh,
Sunway University, Malaysia
Wasim Jamshed,
Capital University of Science & Technology, Pakistan

*CORRESPONDENCE
Ahmed M. Hassan,
ahmed.hassan.res@fue.edu.eg

RECEIVED 18 June 2023
ACCEPTED 31 August 2023
PUBLISHED 19 September 2023

CITATION
Alraddadi I, Ayub A, Hussain SM, Khan U, Hussain Shah SZ and Hassan AM (2023), The significance of ternary hybrid cross bio-nanofluid model in expanding/contracting cylinder with inclined magnetic field.
Front. Mater. 10:1242085.
doi: 10.3389/fmats.2023.1242085

The significance of ternary hybrid cross bio-nanofluid model in expanding/contracting cylinder with inclined magnetic field

Ibrahim Alraddadi[1], Assad Ayub[2,3], Syed Modassir Hussain[1], Umair Khan[4,5,6], Syed Zahir Hussain Shah[2] and Ahmed M. Hassan[7]*

[1]Department of Mathematics, Faculty of Science, Islamic University of Madinah, Madinah, Saudi Arabia, [2]Department of Mathematics & Statistics, Hazara University, Manshera, Pakistan, [3]Department of Mathematics, Government Post Graduate College Manshera, Manshera, Pakistan, [4]Department of Mathematical Sciences, Faculty of Science and Technology, Universiti Kebangsaan Malaysia, Bangi, Malaysia, [5]Department of Computer Science and Mathematics, Lebanese American University, Byblos, Lebanon, [6]Department of Mathematics and Social Sciences, Sukkur IBA University, Sukkur, Pakistan, [7]Faculty of Engineering, Future University in Egypt, New Cairo, Egypt

Significance: Bio-nanofluids have achieved rapid attention due to their potential and vital role in various fields like biotechnology and energy, as well as in medicine such as in drug delivery, imaging, providing scaffolds for tissue engineering, and providing suitable environments for cell growth, as well as being used as coolants in various energy systems, wastewater treatment, and delivery of nutrients to plants.

Objective: The present study proposes a novel mathematical model for the ternary hybrid cross bio-nanofluid model to analyse the behaviour of blood that passes through a stenosed artery under the influence of an inclined magnetic field. The model considers the effect of expanding/contracting cylinder, infinite shear rate viscosity, and bio-nanofluids.

Methodology: The considered model of the problem is bounded in the form of governing equations such as PDEs. These PDEs are transformed into ODEs with the help of similarity transformations and then solved numerically with the help of the bvp4c method.

Findings: The results show that the flow rate and velocity decrease as the inclination angle of the magnetic field increases. Additionally, research has found that the presence of nanoparticles in the bio-nanofluid has a significant impact on the velocity and flow rate. Therefore, the flow rate decreases, in general, as the stenosis becomes more severe.

Advantages of the study: The results obtained from this study may provide insights into the behaviour of blood flow in stenosed arteries and may be useful in the design of medical devices and therapies for the treatment of cardiovascular diseases.

KEYWORDS

numerical solutions, magnetohydrodynamics, expanding/contracting cylinder, ternary hybrid nanofluid (THN), cross fluid model

1 Introduction

Bio-nanofluids are a generally modern range of inquiries within the field of biomedicine, and they have been pulled into critical consideration due to their potential applications in well-dignified conveyance, imaging, and detecting. Specifically, the use of bio-nanofluids within the setting of blood has gotten much consideration as these liquids have the potential to upgrade the transport of drugs and other helpful operators within the circulatory system. Bio-nanofluids and suspension of nanoparticles in a natural liquid, such as blood, can essentially modify the physical and chemical properties of the liquid. The involvement of nanoparticles within bio-fluidity can improve the thickness of the liquid and modify the surface properties of the blood cells, which can influence their aptitude with other cells and with the dividers of blood vessels. Moreover, bio-nanofluids can improve the solvency and bio-availability of drugs and other restorative specialists, which can enhance their adequacy and decrease their side impacts. Bio-nanofluids have been utilized to upgrade blood stream in totally different ways. Therefore, it has been shown that adding nanoparticles, such as gold nanoparticles or carbon nanotubes, to the blood can reduce its viscosity and improve blood flow (Conrad and Wang, 2021). This can be achieved by reducing the interparticle spacing and increasing the Brownian motion of the particles. Another method is to modify the surface properties of the blood vessels. Bio-nanoparticles, such as liposomes and dendrimers, can be used to modify the surface properties of the blood vessels, which can reduce the resistance of the blood flow and improve its velocity (Ali et al., 2021). Ige et al. (Ige et al., 2023) made a numerical analysis related to mixed convection of blood flow with the hybrid fluid model under the influence of bio nanoparticles. In this study, Boussinesq approximation and transient Regime are incorporated. Latest studies regarding bio-nanoparticles in blood flow and their characteristics are investigated by (Ige et al., 2022; Yadav et al., 2022; Fatima et al., 2023).

The contracting/expanding stenosed arteries could be a common event in blood vessel maladies, such as atherosclerosis, where the supply route dividers thicken and limit the bloodstream. The harshness of the supply route leads to an increment in speed and turbulence of the bloodstream, which can cause different cardiovascular diseases, including myocardial dead tissue and stroke. Exact modelling of the bloodstream in stenosed courses is, hence, basic for understanding the instruments of these illnesses and creating viable treatment procedures. In the past, numerical models have been created to recreate the bloodstream in stenosed courses and explore the impacts of different components, such as the consistency of blood, the shape and estimate of the stenosis, and the nearness of attractive areas or nanoparticles. Stenosis has been broadly considered within the past few decades, and different computational models have been created to explore its impacts on the bloodstream. We utilised a computational show to re-enact expanding/contracting stenosis in a human carotid course and found that the degree of stenosis and the sufficiency of altered vessel breadth altogether influenced the speed and divider shear stretch of the bloodstream (Bath et al., 1999). Alghamdi et al. (Alghamdi et al., 2023) investigated a hybrid nanofluid to explore the effects of multiple ferromagnetic nanoparticles in co-axial disks for magnetized fluid. A computational study with Oldroyd-B nanofluid flow and magnetized gold-blood particles passing through the blood was conducted by (Tang et al., 2023a). Furthermore, literature regarding magnetized gold-blood nanofluid stenosis narrow arteries, blood flow via arteries with overlapping shaped stenosis, and vertical porous multiple stenoses can be traced by (Zain and Ismail, 2023a; Tang et al., 2023b; El Kot and Abd Elmaboud, 2023).

The magnetic field has appeared to have a critical effect on the conduct of the bloodstream in courses. In the past, we have found that the application of an attractive magnetic field to stenosed courses can improve the bloodstream and decrease the hazard of cardiovascular maladies. The reason behind this enhancement is credited to the impact of attractive areas on the attractive properties of blood cells, which changes the stream conduct of the blood. When an attractive magnetic field is connected at a point to the supply route, the speed and stream rate of blood are influenced, driving changes within the shear push and weight dispersion. These changes can have both positive and negative impacts on the cardiovascular framework, depending on the greatness and course of the attractive field. Hence, it is basic to consider the impacts of slanted attractive areas on the bloodstream in stenosed courses to get the superior potential benefits and dangers of using attractive areas within the treatment of cardiovascular diseases. In the past, there has been developing intrigue in considering the impact of a slanted attractive field on the bloodstream. A few considerations have illustrated that an attractive field can impact the rheological properties of blood, counting its thickness and stream characteristics. For example, a study by Dolui et al. (Dolui et al., 2023) found that an inclined magnetic field could reduce the resistance to flow in blood vessels, potentially improving circulation in patients with cardiovascular disease. Furthermore, Varshney et al. (Varshney et al., 2010) showed that a magnetic field applied at an angle to the direction of blood flow could alter the orientation of red blood cells, leading to changes in their deformation and aggregation behaviour. These findings suggest that an inclined magnetic field could have important implications for the diagnosis and treatment of various cardiovascular disorders. Zain et al. (Zain and Ismail, 2023b) explored the numerical results regarding the effects of MHD on blood flow by taking the mathematical model of power and the law fluid model. The latest study related to the influence of MHD, Dufour, and Soret effects on blood through a stenosed artery and keeping variable viscosity is established by Mishra et al. (Mishra et al., 2023).

1.1 Motivation

The inspiration for the "ternary hybrid cross bio-nanofluid in expanding/contracting stenosed arteries with interminable shear rate thickness and magnetic field" is to create a comprehensive numerical demonstration that considers numerous components that can influence the bloodstream in requisite posited stenosed supply routes. The motivation behind using a cross nanofluid is because of its capability to investigate the flow behaviour at a very high and low shear rate. The behavior of bloodstream flow in stenosed arteries became more understandable via adding the effects of expanding/contracting stenosis geometry, infinite shear rate consistency, and inclined magnetic field. Furthermore, thinking about the bio-nanofluid stream in stenosed supply routes may give bits of knowledge into the conduct of the bloodstream at the nanoscale level and the potential benefits of utilizing nanoparticles within the treatment of cardiovascular illnesses.

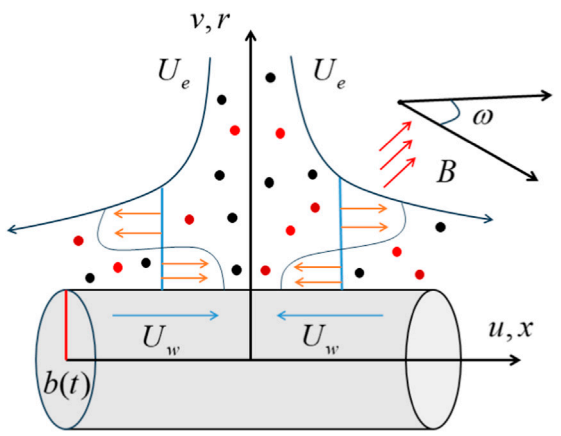

FIGURE 1
Physical shape of the flow problem.

1.2 Novelty

The "ternary hybrid cross bio-nanofluid model" considers various factors affecting blood flow in requisite posited stenosed arteries. The stenosis, viscosity, bio-nanofluid flow, and magnetic field influence have been simultaneously explored in the given model. This examination offers a novel model that sheds light on blood flow in narrowed arteries and the advantages of utilizing ternary nanofluids and magnetic fields to treat cardiovascular illnesses.

2 Mathematical formulation

Let us consider the two-dimensional stagnation-point flow of a ternary hybrid cross bio-nanofluids over a permeable expanding/contracting cylinder with influences of the inclined magnetic field. Also, the liquid (blood) is initiated by extension and withdrawal of a stenosed artery having a time-dependent radius $b(t) = b_0\sqrt{1-\beta t}$. So, β is called the constant of the expansion/contraction strength parameter, and the positive consistent b_0 incorporates a length measurement. However, when β is positive, the artery's sweep decreases over time, whereas in the case that β is negative, the radius develops as a result. Moreover, the problem is bounded by the corresponding x-axis and r-axis, as delineated in Figure 1. In this situation, the supply route is accepted to be contracting or developing at a rate determined by the time-dependent velocity $U_w(x,t) = \frac{2cx}{1-\beta t}$, where c may be a positive constant of dimension $(\text{time})^{-1}$ and the x-axis is the horizontal surface of the cylinder. It is assumed that T_w is the surface (body) temperature of the cylinder, and T_∞ is the temperature of the free stream. A non-uniform transverse attractive magnetic field $B(t) = \frac{B_0}{\sqrt{1-\beta t}}$ is applied perpendicular to the surface of the cylinder. The induced magnetic field is negligible due to a very small Reynolds number. The free stream velocity is denoted by $U_e(x,t) = \frac{2ax}{(1-\beta t)}$ where β is a positive acceleration and deceleration parameter.

The velocity and temperature field vectors are defined as:

$$V = [v(r,x,t), 0, u(r,x,t)], \quad T = T(r,x,t). \tag{1}$$

Furthermore, using the above-stated assumptions, the leading governing equations can take place as follows (see (Sumner et al., 1999; Ali et al., 2020a; Waqas, 2020; Ayub et al., 2022a)):

$$\frac{\partial}{\partial x}(ru) + \frac{\partial}{\partial r}(rv) = 0, \tag{2}$$

$$\left(\frac{\partial u}{\partial t} + u\frac{\partial u}{\partial x} + v\frac{\partial u}{\partial r}\right) = U_e\frac{\partial U_e}{\partial x} + \frac{\partial U_e}{\partial t} + \frac{1}{\rho_{thnf}}\frac{\mu_{thnf}}{r}\frac{\partial u}{\partial r}\left[\left(\beta^* + (1-\beta^*)\left(1+\left(\Gamma\frac{\partial u}{\partial r}\right)^n\right)\right)^{-1}\right] + \frac{1}{\rho_{thnf}}\mu_{thnf}\frac{\partial}{\partial r}\left[\frac{\partial u}{\partial r}\left(\beta^* + (1-\beta^*)\left(1+\left(\Gamma\frac{\partial u}{\partial r}\right)^n\right)\right)^{-1}\right] - \frac{\sigma_{thnf}\sin^2(\omega)B^2}{\rho_{thnf}}(u-U_e), \tag{3}$$

$$\rho(C_p)_{thnf}\left[\frac{\partial T}{\partial t} + v\frac{\partial T}{\partial r} + u\frac{\partial T}{\partial x}\right] = \frac{1}{r}\frac{\partial}{\partial r}\left[k^*_{thnf}(T)r\frac{\partial T}{\partial r}\right], \tag{4}$$

along with boundary conditions are (see (Ayub et al., 2022a)):

$$u = U_w(x,t) = \frac{2cx}{1-\beta t}, v = V_w(t) = -\frac{ab_0 s}{\sqrt{1-\beta t}}, T = T_w, \text{at } r = b(t), \tag{5}$$

$$u \to U_e(x,t), T \to T_\infty, \text{as } r \to \infty\,. \tag{6}$$

Here, β^* is the infinite shear rate viscosity parameter, u and v refer to the velocity components of blood along the axial and radial direction, respectively, T is the temperature of the THN, s is the suction parameter, b_0 is the positive constant, and c is called the stretching/shrinking rates. In addition, μ_{thnf} denotes the viscosity of the ternary hybrid nanofluid (THN), σ_{thnf} refers to the electrical conductivity of the THN, ρ_{thnf} represents the density of the THN, and $k^*_{thnf}(T)$ is the variable thermal conductivity (TCN) of the THN model. Also, the term $(C_p)_{thnf}$ is the specific heat. The variable TCN is defined as (see (Kaleem et al., 2022; Nazir et al., 2022; Babu et al., 2023; Bafakeeh et al., 2023)):

$$k^*_{thnf}(T) = k_{thnf}\left(1 + \varepsilon\left(\frac{T-T_\infty}{T_w - T_\infty}\right)\right), \tag{7}$$

where k_{thnf} is the TCN of the THN and its correlation is defined later in the given section, while ε is the thermal conductivity parameter.

Furthermore, the thermo-physical characteristics of the ternary nanofluid model are given as follows:

$$\frac{\mu_{thnf}}{\mu_f} = \frac{1}{(1-\varphi_{s1})^{2.5}(1-\varphi_{s2})^{2.5}(1-\varphi_{s3})^{2.5}}, \tag{8}$$

$$\frac{\rho_{thnf}}{\rho_f} = \left[(1-\varphi_{s1})(1-\varphi_{s2})(1-\varphi_{s3}) + \frac{\rho_{s3}}{\rho_f}\varphi_{s3} + \frac{\rho_{s2}}{\rho_f}\varphi_{s2} + \frac{\rho_{s1}}{\rho_f}\varphi_{s1}\right], \tag{9}$$

$$\frac{(\rho C_p)_{thnf}}{(\rho C_p)_f} = \left[(1-\varphi_1)(1-\varphi_2)(1-\varphi_3) + \frac{(\rho C_p)_{s3}}{(\rho C_p)_f}\varphi_{s3} + \frac{(\rho C_p)_{s2}}{(\rho C_p)_f}\varphi_{s2} + \frac{(\rho C_p)_{s1}}{(\rho C_p)_f}\varphi_{s1}\right]. \tag{10}$$

$$\frac{k_{thnf}}{k_{hnf}} = \frac{k_{s1} + 2k_{hnf} - 2\varphi_{s1}(k_{hnf} - k_{s1})}{k_{s1} + 2k_{hnf} + \varphi_{s1}(k_{hnf} - k_{s1})}, \tag{11}$$

TABLE 1 The thermophysical characteristics of base (blood) fluid and Au, TiO_2, and Al_2O_3 nanoparticles.

Properties	Blood	Au	TiO_2	Al_2O_3
$C_p\,(J/kgK)$	3,594	129	690	765
$\rho\,(kg/m^3)$	1,053	19,300	4,250	3,970
$k\,(W/mK)$	0.492	310	8.953	40
$\sigma\,(S/m)$	0.8	0.41×10^5	2.4×10^6	0.35×10^6
Pr	21	-		

$$\frac{k_{hnf}}{k_{nf}} = \frac{k_{s2} + 2k_{nf} - 2\varphi_{s2}\left(k_{nf} - k_{s2}\right)}{k_{s2} + 2k_{nf} + \varphi_{s2}\left(k_{nf} - k_{s2}\right)}, \tag{12}$$

$$\frac{k_{nf}}{k_f} = \frac{k_{s3} + 2k_f - 2\varphi_{s3}\left(k_f - k_{s3}\right)}{k_{s3} + 2k_f + \varphi_{s3}\left(k_f - k_{s3}\right)}, \tag{13}$$

and the electrical conductivity

$$\frac{\sigma_{thnf}}{\sigma_{hnf}} = \frac{\sigma_{s1} + 2\sigma_{hnf} - 2\varphi_{s1}\left(\sigma_{hnf} - \sigma_{s1}\right)}{\sigma_{s1} + 2\sigma_{hnf} + \varphi_{s1}\left(\sigma_{hnf} - \sigma_{s1}\right)}, \tag{14}$$

$$\frac{\sigma_{hnf}}{\sigma_{nf}} = \frac{\sigma_{s2} + 2\sigma_{nf} - 2\varphi_{s2}\left(\sigma_{nf} - \sigma_{s2}\right)}{\sigma_{s2} + 2\sigma_{nf} + \varphi_{s2}\left(\sigma_{nf} - \sigma_{s2}\right)}, \tag{15}$$

$$\frac{\sigma_{nf}}{\sigma_f} = \frac{\sigma_{s3} + 2\sigma_f - 2\varphi_{s3}\left(\sigma_f - \sigma_{s3}\right)}{\sigma_{s3} + 2\sigma_f + \varphi_{s3}\left(\sigma_f - \sigma_{s3}\right)}. \tag{16}$$

Here, in Equations 8–16, the solid nanoparticles volume fraction is denoted by φ_{si}, where $i = 1, 2, 3$. For this particular case, $\varphi_{si} = 0$, for $i = 1, 2, 3$; the equations are reduced to the regular base fluid. Moreover, the subscripts $thnf$, hmf, nf, f, and si, for $i = 1, 2, 3$ refer to the THNF, HNF, NF, base fluid, and the solid nanoparticles, respectively. The experimentation physical data of the base (blood) fluid and the three distinct nanoparticles are given in Table 1, see (Das et al., 2021; Tripathi et al., 2021; Sajid et al., 2023a).

3 Solution procedure

Furthermore, to ease the investigation of the problem, the following similarity variants are introduced for the conversion of PDEs into ODEs as:

$$u = \frac{2ax}{(1-\beta t)} f'(\eta), v = -\frac{ab_0}{\sqrt{1-\beta t}} \frac{f(\eta)}{\sqrt{\eta}}, \eta = \left(\frac{r}{b_0}\right)^2 (1-\beta t)^{-1},$$
$$\theta(\eta) = \frac{T - T_\infty}{T_w - T_\infty}. \tag{17}$$

Substituting Equation 17 in Equations 3, 4, we get the following reduced form of ODEs as:

$$\begin{aligned}
&\left[\beta^* + (1-\beta^*)\left(1 + (1-n)We^n\left(f''\right)^n\right)\right]\eta f''' \\
&+ \frac{A_1A_2}{2}\left(2 + (1-n)We^n\left(f''\right)^n\right)f'' \\
&+ A_1A_2\mathrm{Re}\left(ff'' - f'^2 + 1\right)\left(1 + We^n\left(f''\right)^n\right)^2 \\
&- A_1A_2A\left(\eta f'' + f' - 1\right)\left(1 + We^n\left(f''\right)^n\right)^2 \\
&- MSin^2(\omega)A_1A_2A_3\mathrm{Re}\left(1 + We^n\left(f''\right)^n\right)^2\left(f' - 1\right) \\
&= 0,
\end{aligned} \tag{18}$$

$$A_5(1 + \varepsilon\theta)\eta\theta'' + (1 + \varepsilon\theta)\theta' - A_4\mathrm{Pr}\,\mathrm{Re} f\theta' = 0, \tag{19}$$

with BCs are:

$$\begin{aligned}
&f'(1) = \lambda, f(1) = s, \theta(1) = 1, \\
&\theta(\eta) \to 0, f'(\eta) \to 1, as\ \eta \to \infty\,.
\end{aligned} \tag{20}$$

In addition, many different dimensionless parameters that are commonly used in this study are "We" (Weissenberg number), "Re" (Reynold number), "A" (unsteadiness parameter), "s" (suction parameter), and "Pr" (Prandtl number). The parameter obtained due to the ratio between the initial velocity and free stream velocity is λ; if $\lambda < 0$, it is called the shrinking case of the cylinder and $\lambda > 0$ is the stretching case of the cylinder.

$$\begin{aligned}
&\mathrm{Re} = \frac{ab_0^2}{2\upsilon_f}, A = \frac{\beta b_0^2}{4\upsilon_f}, \mathrm{Pr} = \frac{\upsilon_f}{\alpha_f}, \\
&We = \frac{2r\Gamma U_e}{b_0{}^2(1-\beta t)}, M = \frac{\sigma_f\beta_0^2}{2\rho a}, \lambda = \frac{c}{a}.
\end{aligned} \tag{21}$$

The skin friction coefficient C_f and local Nusselt number Nu for the practical point of view are defined as:

$$C_f = \frac{\tau_{rx}|_{r=b(t)}}{\frac{1}{2}\rho U_e^2} \text{ and } Nu = \frac{b(t)q_w|_{r=b(t)}}{2k(T_w - T_\infty)}, \tag{22}$$

where τ_{rx} exposes the wall shear stress and q_w is the wall heat flux, and both are defined as:

TABLE 2 The validity of the current model with old literature for limiting cases.

Parameters				Skin friction coefficient							
				Published work Azam et al. (2017)				Current results			
				$n = 0.5$		$n = 1.5$		$n = 0.5$		$n = 1.5$	
Re	A	M	**We**	$\lambda = -0.5$	$\lambda = 1.5$	$\lambda = -0.5$	$\lambda = 1.5$	$\lambda = -0.5$	$\lambda = 1.5$	$\lambda = -0.5$	$\lambda = 1.5$
1.0	2.0	1.0	1.0	4.07264	−1.646	5.3410	−1.918	4.07264	−1.646	5.35	−1.923
				6.65087	−2.822	10.377	−3.8678	6.65087	−2.822	10.38	−3.7998
				9.14835	−3.799	15.105	−5.6492	9.14835	−3.799	15.99	−5.5944

10.3389/fmats.2023.1242085

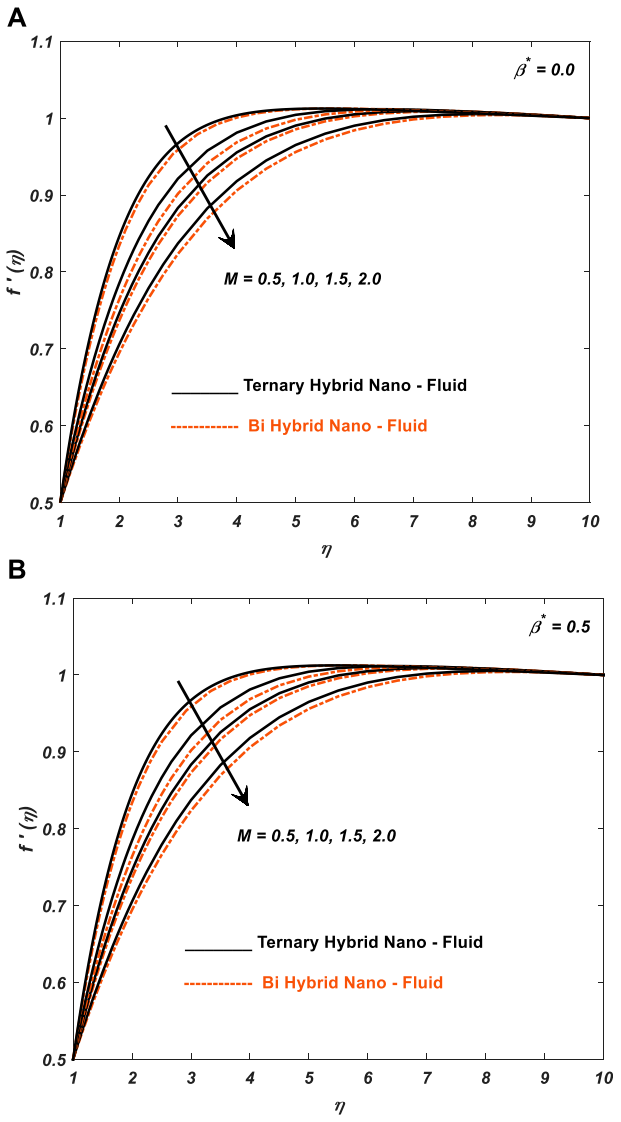

FIGURE 2
Pictorial interpretation of physically attached parameter M on $f'(\eta)$.

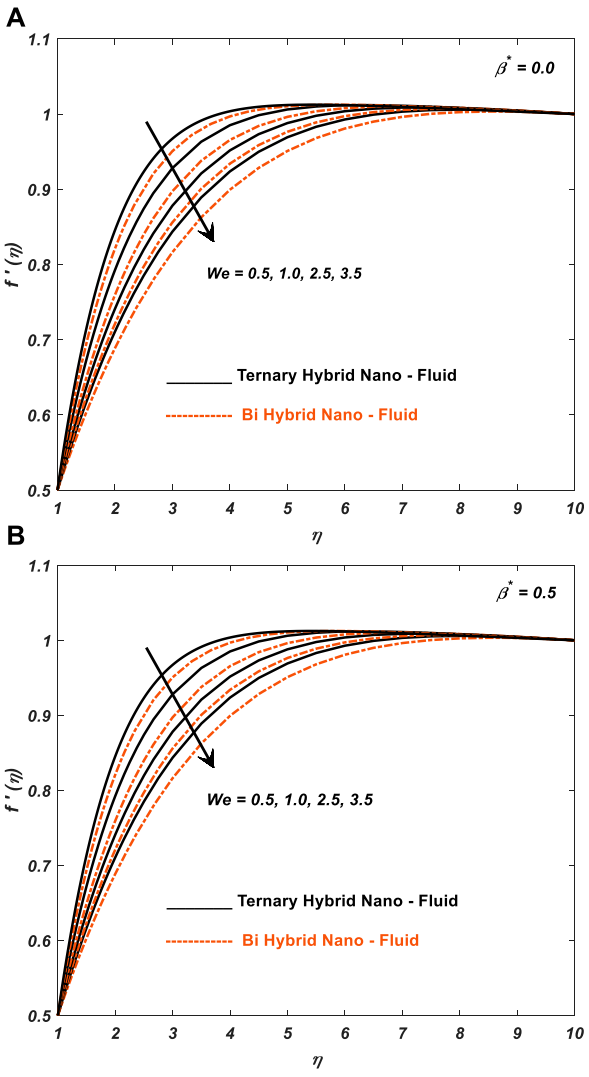

FIGURE 3
Pictorial interpretation of physically attached parameter We on $f'(\eta)$.

$$\tau_{rx} = \mu_{thnf}\frac{\partial u}{\partial r}\left[\frac{1}{\beta^\star + (1-\beta^\star)\left[1+\Gamma^n\left(\frac{\partial u}{\partial r}\right)^n\right]}\right]_{r=b(t)},$$
$$q_w = -k_{thnf}\frac{\partial T}{\partial r}\Big|_{r=b(t)}. \tag{23}$$

Implementing the similarity transformations in the above-stated equations, we get the reduced form of the skin friction and heat transfer rate as follows:

$$C_f Re\frac{x}{b(t)} = \frac{1}{A_1}\left[\frac{f''(1)}{\beta^\star + (1-\beta^\star)(1+(Wef''(1))^n)}\right]. \tag{24}$$

and

$$Nu = -A_5\theta'.$$

In which:

$$A_1 = \frac{1}{(1-\varphi_{s1})^{2.5}(1-\varphi_{s2})^{2.5}(1-\varphi_{s3})^{2.5}}, A_3 = \frac{\sigma_{thnf}}{k_f}, A_5 = \frac{k_{thnf}}{k_f}, \tag{25}$$

$$A_2 = (1-\varphi_{s1})(1-\varphi_{s2})(1-\varphi_{s3}) + \varphi_{s3}\frac{\rho_{s3}}{\rho_f} + \varphi_{s2}\frac{\rho_{s2}}{\rho_f} + \varphi_{s1}\frac{\rho_{s1}}{\rho_f}, \tag{26}$$

$$A_4 = (1-\varphi_{s1})(1-\varphi_{s2})(1-\varphi_{s3}) + \frac{(\rho C_p)_{s1}}{(\rho C_p)_f}\varphi_{s1} + \frac{(\rho C_p)_{s2}}{(\rho C_p)_f}\varphi_{s2} + \frac{(\rho C_p)_{s3}}{(\rho C_p)_f}\varphi_{s3}. \tag{27}$$

4 Numerical scheme

This portion of the work demonstrates the numerical solution procedure and the accuracy of the code. There are

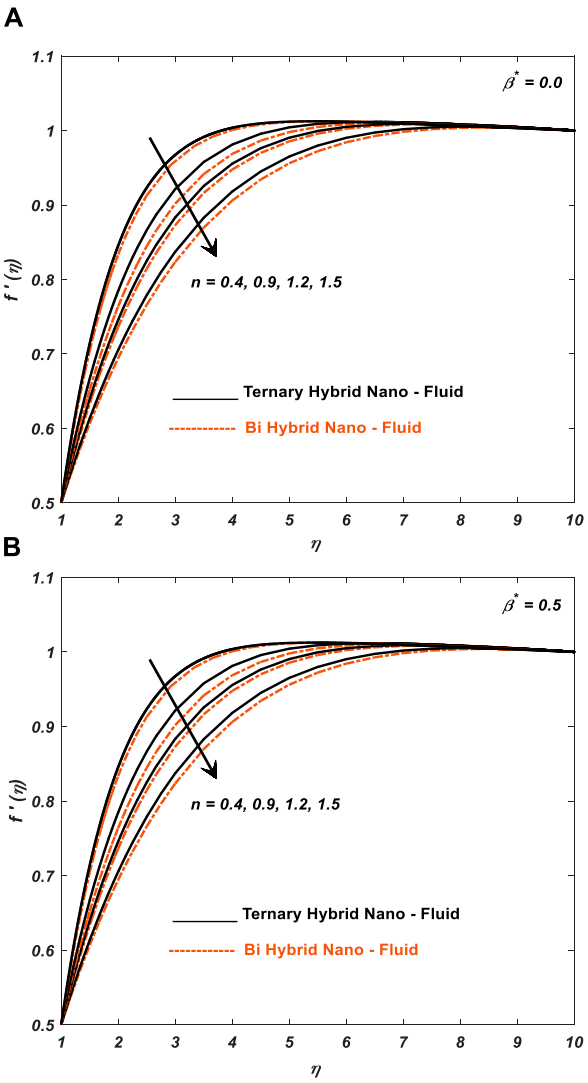

FIGURE 4
Pictorial interpretation of physically attached parameter n on $f'(\eta)$.

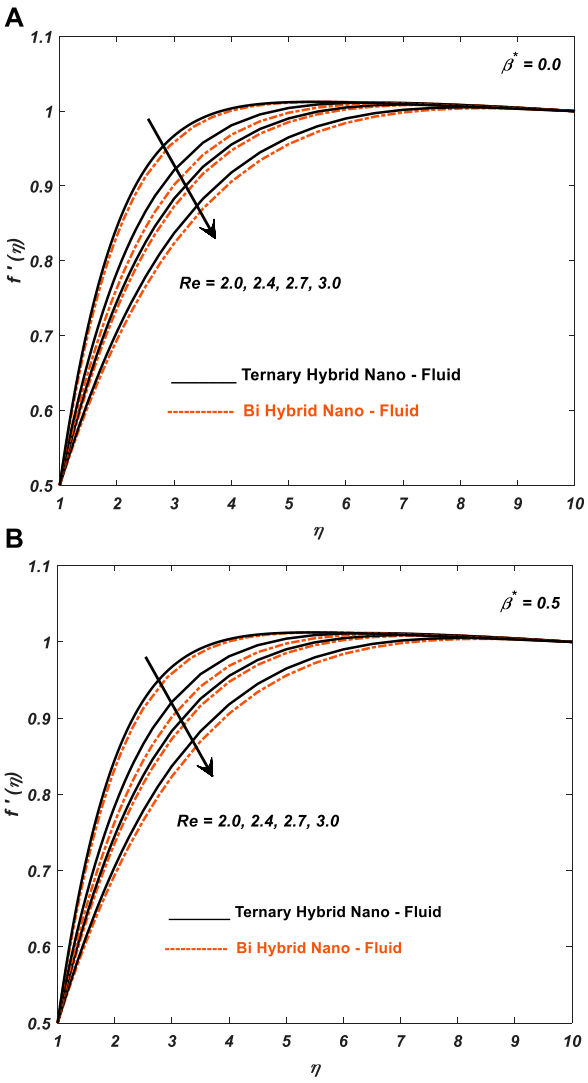

FIGURE 5
Pictorial interpretation of physically attached parameter Re on $f'(\eta)$.

several numerical schemes (Shah et al., 2021; Ayub et al., 2022b; Darvesh et al., 2022; El Din et al., 2022; Khan et al., 2022; Sajid et al., 2022; Wang et al., 2022; Darvesh et al., 2023) used to fetch the numerical results. To investigate such a framework, the bvp4c (Khan et al., 2023; Haider et al., 2021; Ayub et al., 2021a; Ayub et al., 2021b; han et al., 2022; Shah et al., 2021; Ayub et al., 2020) MATLAB command/function is utilized. To begin the process of the code, the boundary value problem (BVP) is changed into the initial value problem (IVP) and after that, bvp4c is utilized to get the unavailable results. This scheme is further based on the RK-4 method (Zaib et al., 2019; Ali et al., 2020b; Botmart et al., 2022a; Botmart et al., 2022b; Ayub et al., 2022c; Goud et al., 2022; Rasool et al., 2022) or finite difference scheme, which is only applicable to solve the initial value problems. Before starting the procedure, the MATLAB syntax is written with the help of the following substitution: $L_1 = f$, $L_2 = f'$, $L_3 = f''$, $L_4 = \theta$, and $L_5 = \theta'$. The MATLAB syntax is written as:

$$\begin{pmatrix} LL_1 \\ LL_2 \end{pmatrix} = \begin{pmatrix} \left(\begin{array}{l} -\frac{A_1 A_2}{2}\left(2+(1-n)We^n L_3{}^n L_3\right) - A_1 A_2 \mathrm{Re}\left(L_1 L_3 - L_2{}^2 + 1\right)\left(1+We^n L_3{}^n\right)^2 + \\ A_1 A_2 A\left(\eta L_3 + L_2 - 1\right)\left(1+We^n L_3{}^n\right)^2 + MSin^2(\omega) A_1 A_2 A_3 \mathrm{Re}\left(1+We^n L_3{}^n\right)^2\left(L_2 - 1\right) \end{array} \right) \\ \hline \left[\beta^* + (1-\beta^*)\left(1+(1-n)We^n L_3{}^n\right)\right]\eta \\ \frac{\left(-(1+\varepsilon L_4)L_5 + A_4 \mathrm{Pr}\,\mathrm{Re} L_1 L_5\right)}{\left(A_5(1+\varepsilon L_4)\eta\right)} \end{pmatrix} \tag{28}$$

and appropriate boundary conditions become:

$$\left.\begin{array}{l} L_2(1) = \lambda, L_1(1) = s, L_4(1) = 1, \text{at } \eta = 1 \\ L_2(\eta) \to 1, L_4(\eta) \to 0, \text{as } \eta \to \infty . \end{array}\right\} \tag{29}$$

The procedure mentioned is used to solve Eqs. 28, 29 to find the missing slopes. The step size between two mesh points is 0.01 and the point $\eta_{\max}$ representing infinity is chosen appropriately such that BCs are attained in an asymptotic manner. From the figures, it can be seen that all BCs are attained asymptotically, which is a sign of the convergence of results. For further details of the method

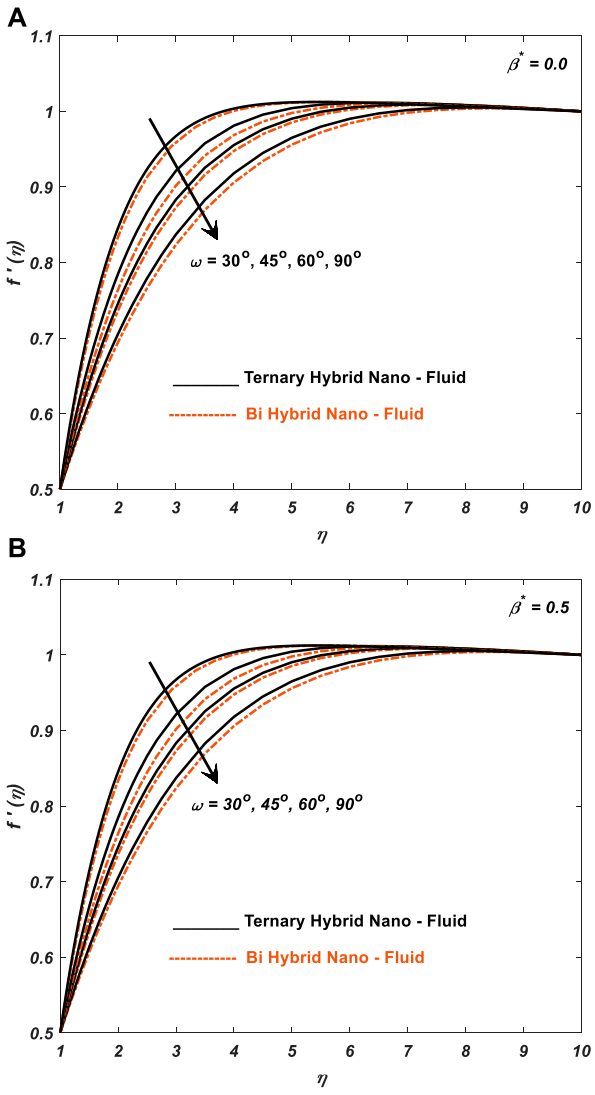

FIGURE 6
Pictorial interpretation of physically attached parameter ω on $f'(\eta)$.

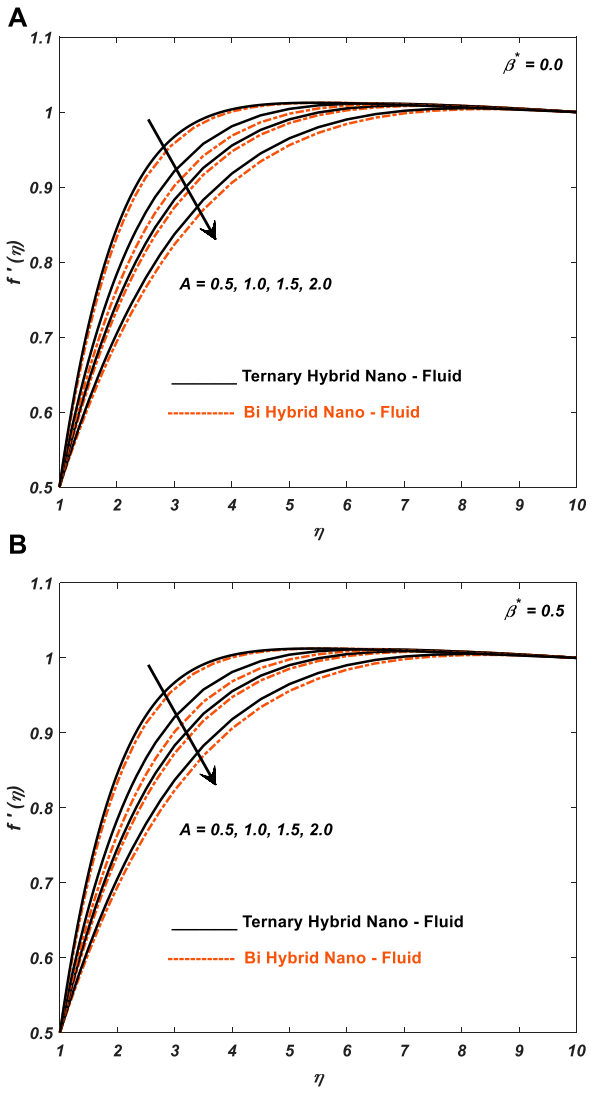

FIGURE 7
Pictorial interpretation of physically attached parameter A on $f'(\eta)$.

considered that have been documented by various researchers, see refs. (Shahzad et al., 2022; AlBaidani et al., 2023; Althoey et al., 2023; Assiri et al., 2023; Sajid et al., 2023b; Rafique et al., 2023). Moreover, the authors have utilized the mentioned numerical method for the following reasons:

a) The bvp4c is a robust method capable of solving varied nonlinear differential equations and initial conditions. It uses the finite difference method for stiff problems.
b) The user can adjust the error tolerance as needed when employing this technique.
c) It efficiently solves systems that are challenging to address using analytical methods.
d) Compared to other known methods, this approach significantly cuts the time required to find the solution.

4.1 Validity of the scheme

The current scheme intersects with old literature while fixing some of the influential parameters such as $A_1 = A_2 = A_3 = A_4 = 1$. This attempt shows that the validity of the mathematical model and numerical scheme used to solve this model are correct. The outcomes of the given work with prior research work are shown in Table 2.

5 Results and discussion

The ternary hybrid cross bio-nanofluid model is a promising approach for studying the fluid dynamics of expanding/contracting cylinders with inclined magnetic field effects. This model combines

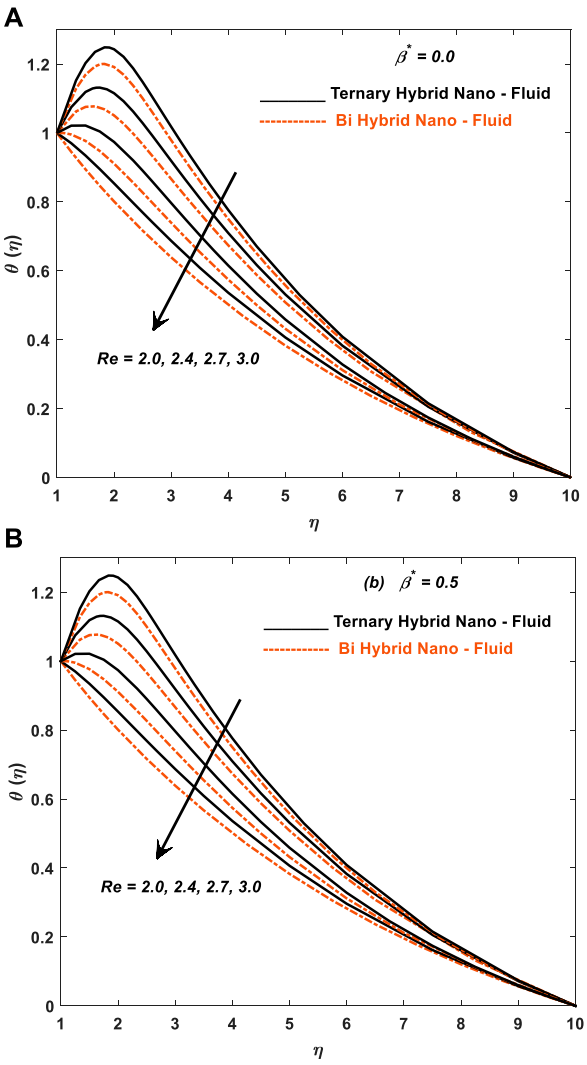

FIGURE 8
Pictorial interpretation of physically attached parameter *Re* on $\theta'(\eta)$.

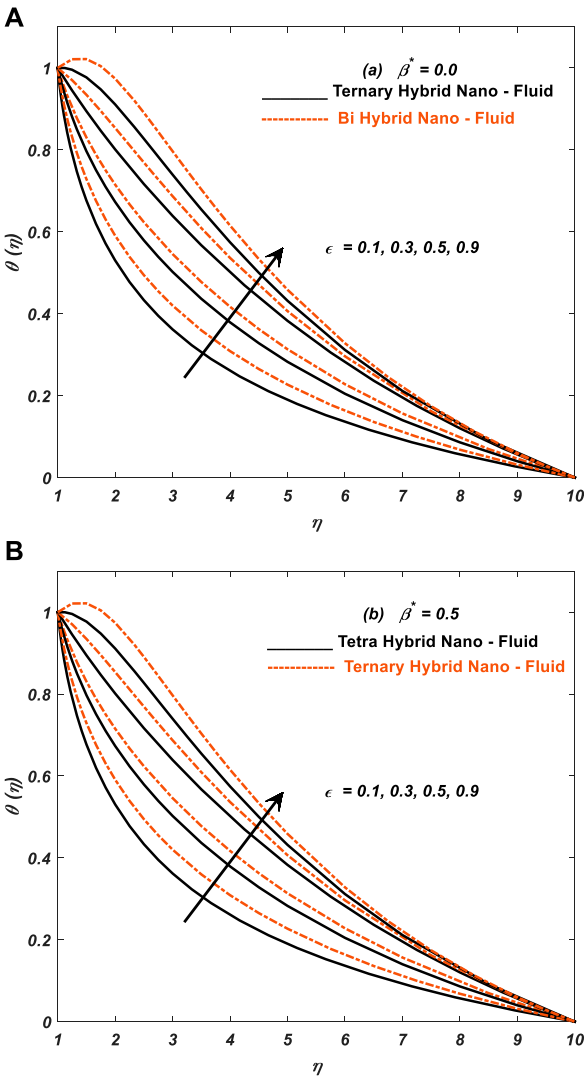

FIGURE 9
Pictorial interpretation of physically attached parameter ε on $\theta'(\eta)$.

the three different types of nanoparticles (Cu, Al_2O_3, and TiO_2) with biological components (blood) to create a unique bio-nanofluid. The model also considers the effects of stenosis (narrowing of the artery) and the expansion/contraction of the cylinder, which are important factors that can affect blood flow and lead to considerable cardiovascular diseases. By incorporating these elements, the ternary hybrid cross bio-nanofluid model provides a more realistic and comprehensive understanding of blood flow in stenosed arteries. Furthermore, this model has the potential to inform the development of novel therapies and interventions for cardiovascular diseases, by providing insights into the mechanisms underlying blood flow abnormalities. Overall, the ternary hybrid cross bio-nanofluid model is a valid and valuable tool for studying the fluid dynamics of expanding/contracting stenosed arteries.

This section investigates the impact of several involved physical parameters on the velocity and temperature of the blood flow in the presence and absence of the infinite shear rate viscosity parameter ($\beta^* = 0/\beta^* \neq 0$). Figures 2–7 are established for velocity distribution and Figures 8–10 are presented to discuss the temperature profiles keeping fixed the variation of parameters like $\mathrm{Pr} \in [18, 21]$, $M \in [0.1, 5.1]$, $\mathrm{We} \in [0.1, 4]$, $n \in [0, 1]$ and $\omega = 30^\circ, 45^\circ, 60^\circ, 90^\circ$.

Figures 2–4 give a pictorial interpretation of the physically attached parameter M and We on $f'(\eta)$. From the pictures, it is seen that a greater value of M, We, and n shows a lower velocity in the presence and absence ($\beta^* = 0/\beta^* \neq 0$) of the infinite shear rate viscosity parameter. The magnetic parameter is the strength of the magnetic field. From the physical point of view, the higher magnetic field strengths can lead to a lower blood flow rate as the charged particles in the blood experience Lorentz force and are pushed along more slowly (see Figure 2). However, extremely high magnetic fields can also be harmful to the body, so it is important to use magnetic fields within safe limits.

Figure 3 shows that the impact of the Weissenberg number on the blood flow rate will depend on the specific flow conditions and geometry of the blood vessel being considered. In the current study, higher Weissenberg numbers (indicating more elastic fluids) can

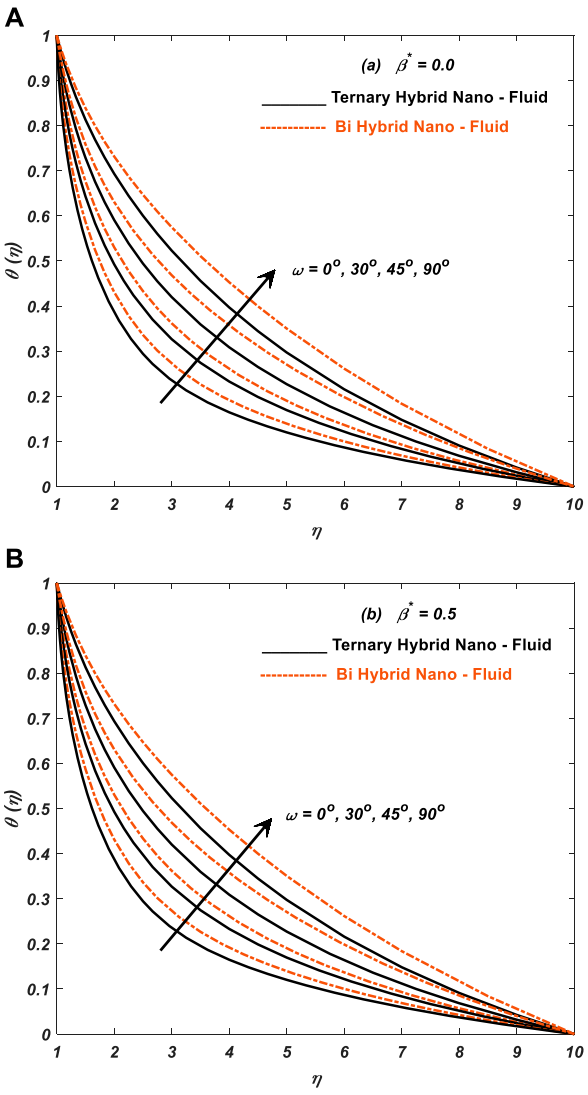

FIGURE 10
Pictorial interpretation of physically attached parameter of ω on $\theta'(\eta)$.

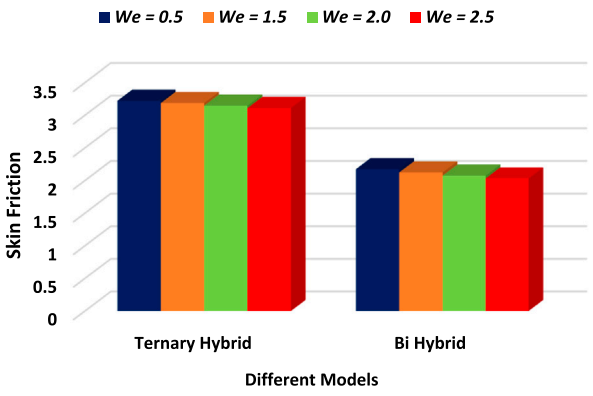

FIGURE 11
Statistical interpretation for We on the skin friction coefficient.

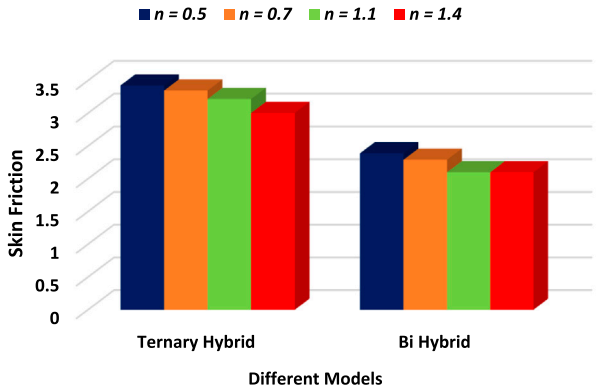

FIGURE 12
Statistical interpretation for cross fluid index "n" on the skin friction coefficient.

lead to more complex flow patterns and changes in blood flow rate, especially in regions where the blood vessel is constricted or curved, and as a result, velocity decreases.

Figure 4 displays that increasing the cross-fluid index (n) by adding a layer of fluid with a higher viscosity to a blood vessel wall can lead to changes in the flow patterns of the blood, including the formation of vortices and eddies, and due to these facts, the velocity of blood decreases. These changes in flow patterns can affect the shear stress experienced by the endothelial cells lining the blood vessel wall, which can in turn impact the development of atherosclerosis and other vascular diseases.

Figure 5 reveals the interpretation of Re on $f'(\eta)$. When the Reynolds number is low, viscous forces dominate and the flow is characterized as laminar. When the Reynolds number is high, inertial forces dominate and the flow is characterized as turbulent. Blood flow in the human body is laminar, with low Reynolds numbers. However, in certain situations, such as in regions of high flow rate or where blood vessels are narrowed, the Reynolds number may increase, and blood flow may become turbulent.

Figure 6 shows the attachment of ω on $f'(\eta)$. Inclined angle produces Lorentz force and hence flow rate decreases in the presence and absence $(\beta^* = 0/\beta^* \neq 0)$ of infinite shear rate viscosity parameter. Moreover, the solution gap between the curves is slightly better in the given figure compared to other graphs.

Figure 7 presents the impact of A on $f'(\eta)$. The unsteadiness of blood flow refers to variations in flow rate and pressure over time. The blood flow in the circulatory system is inherently unsteady due to the pulsatile nature of the heart, as well as other factors such as changes in vessel diameter and blood viscosity. The impact of unsteady flow on blood flow rate is complex and depends on several factors. While unsteady flow is a natural aspect of blood flow, certain conditions, such as disease states or variations in vessel geometry, can lead to increased unsteadiness and potentially negative impacts on the circulatory system.

Figure 8 depicts the impact of Re on $\theta'(\eta)$. Temperature distribution becomes lower as the value of Re increases in the presence and absence $(\beta^* = 0/\beta^* \neq 0)$ of infinite shear rate

TABLE 3 Tabular representation of physical quantities.

Physical quantities	Parameters	Values	Different models	
			Ternary hybrid	Bi hybrid
Nusselt Number	ε	1.2	3.190876	1.914275
		1.4	3.216756	2.000062
		1.6	3.487645	2.189296
		1.8	3.674576	2.454216
Skin Friction	n	0.5	3.425684	2.390192
		0.7	3.347868	2.291753
		1.1	3.218974	2.100597
		1.4	3.004874	2.099045
	We	0.5	3.221867	2.173991
		1.5	3.187872	2.124295
		2.0	3.146792	2.074216
		2.5	3.109867	2.030597

viscosity parameter. Reynolds number has an impact on the temperature profile of blood flow through several mechanisms. When the Reynolds number is high, turbulent flow can cause energy dissipation and mixing within the fluid, leading to decreased heat transfer between the blood and the surrounding tissue. This can result in a more uniform temperature within the fluid.

Figure 9 describes the influence of ε on $\theta'(\eta)$. Increased thermal conductivity parameter causes obvious increases in the temperature of blood flow in the presence and absence ($\beta^* = 0/\beta^* \neq 0$) of infinite shear rate viscosity parameter. Blood has a relatively low thermal conductivity compared to other materials, such as metals or ceramics. This means that blood is a poor conductor of heat, and heat transfer within the fluid is primarily driven by convective processes.

Figure 10 shows the physics of ω on $\theta'(\eta)$. A gradual increase in the inclined angle reduces velocity and, hence, increases the temperature. When charged particles experience the Lorentz force and move through a magnetic field, they transfer some of their kinetic energy to the surrounding fluid as heat. This process can cause localized heating of the fluid, including the blood.

Figures 11, 12 are established for statistical analysis of skin friction and Nusselt number corresponding to Table 3 with different parameters. In blood flow, the Nusselt number can impact the heat transfer between the blood and the vessel walls. This is important because the temperature of the blood can have significant effects on physiological processes, and the heat transfer between blood and the walls of blood vessels can affect the temperature profile. The drag force can impact the flow rate of blood and can have implications for the development of cardiovascular disease. Tabulations of all these results are presented in Table 3. For example, high drag forces can lead to turbulence in the flow of blood, which can increase the likelihood of plaque formation and blockages in blood vessels.

6 Conclusion

The expanding/contracting stenosed artery refers to the narrowing and widening of an artery due to the accumulation of plaque, which can impede blood flow and lead to cardiovascular disease. The inclusion of an infinite shear rate viscosity suggests that the model is accounting for the high levels of shear stress that occur at the site of a stenosis. Additionally, the inclined magnetic field may suggest that the model is considering the effects of magnetic fields on blood flow, which have been shown to have potential therapeutic applications for cardiovascular diseases. The main outcomes of the considered model are given as follows.

1. Greater value of M, We, and n gives lower velocity in ternary nanofluid compared to bi-hybrid nanofluid. Higher magnetic field strengths can lead to lower blood flow rates, as the charged particles in the blood experience Lorentz force and are pushed along more slowly.
2. Gradual increase in inclined angle reduces velocity and hence increases the temperature in ternary nanofluid compared to bi-hybrid nanofluid.
3. Heat transport is rapid in ternary nanofluid compared to bi-hybrid nanofluid.
4. Higher Weissenberg numbers (indicating more elastic fluids) can lead to more complex flow patterns and changes in blood flow rate.
5. When the Reynolds number is low, viscous forces dominate and the fluid flow is characterized as laminar.
6. The inclined angle produces Lorentz force and hence flow rate decreases.

7. When the Reynolds number is high, turbulent flow can cause energy dissipation and mixing within the fluid, leading to decreased heat transfer between the blood and the surrounding tissue.

6.1 Advantages of the significant outcomes

i. Greater heat transport regulates the physiological functions in the human body like temperature regulation (distribution of excess heat generated during physical activity), prevention of overheating, and improved oxygen delivery.
ii. Parameters like M, We, and n give lower velocity of blood and slower blood flow rate within capillaries allowing for more efficient exchange of nutrients, gases, and waste products between the blood and surrounding tissues, and lower blood velocity requires less energy expenditure from the heart.

6.2 Future direction

The current study considers the effects of multiple physical parameters on blood flow in stenosed arteries, but there are many other factors that could also be investigated in future research work which are as follows.

1. The effects of blood rheology, flow rate, and vessel compliance could be explored to gain a more complete understanding of the Casson and Power Law fluidic model.
2. Future research could launch the accuracy and predictive power of the ternary hybrid cross/Carreau bio-nanofluid model with the numerical technique of artificial neural networks.
3. The entropy generation for the non-Newtonian models can also be implemented in future research work.

Data availability statement

The raw data supporting the conclusion of this article will be made available by the authors, without undue reservation.

Author contributions

All authors listed have made a substantial, direct, and intellectual contribution to the work and approved it for publication.

Acknowledgments

The researchers wish to extend their sincere gratitude to the Islamic University of Madinah, Saudi Arabia for the support provided to this research work.

Conflict of interest

The authors declare that the research was conducted in the absence of any commercial or financial relationships that could be construed as a potential conflict of interest.

Publisher's note

References

AlBaidani, M. M., Mishra, N. K., Ahmad, Z., Eldin, S. M., Haq, E. U., and Ul Haq, E. (2023). Numerical study of thermal enhancement in ZnO-SAE50 nanolubricant over a spherical magnetized surface influenced by Newtonian heating and thermal radiation. *Case Stud. Therm. Eng.* 45, 102917. doi:10.1016/j.csite.2023.102917

Alghamdi, M., Akbar, N. S., Hussain, M. F., Akhtar, S., and Muhammad, T. (2023). Thermodynamic study of hybrid nanofluid to explore synergistic effects of multiple ferromagnetic nanoparticles in co-axial disks for magnetized fluid. *Tribol. Int.* 188, 108867. doi:10.1016/j.triboint.2023.108867

Ali, A., Bukhari, Z., Umar, M., Ismail, M. A., and Abbas, Z. (2021). Cu and Cu-swcnt nanoparticles' suspension in pulsatile Casson fluid flow via Darcy–forchheimer porous channel with compliant walls: A prospective model for blood flow in stenosed arteries. *Int. J. Mol. Sci.* 22 (12), 6494. doi:10.3390/ijms22126494

Ali, M., Shahzad, M., Sultan, F., Khan, W. A., and Shah, S. Z. H. (2020b). Characteristic of heat transfer in flow of Cross nanofluid during melting process. *Appl. Nanosci.* 10, 5201–5210. doi:10.1007/s13204-020-01532-6

Ali, M., Sultan, F., Khan, W. A., Shahzad, M., and Arif, H. (2020a). Important features of expanding/contracting cylinder for Cross magneto-nanofluid flow. *Chaos, Solit. Fractals* 133, 109656. doi:10.1016/j.chaos.2020.109656

Althoey, F., Akhter, M. N., Nagra, Z. S., Awan, H. H., Alanazi, F., Khan, M. A., et al. (2023). Prediction models for marshall mix parameters using bio-inspired genetic programming and deep machine learning approaches: A comparative study. *Case Stud. Constr. Mater.* 18, e01774. doi:10.1016/j.cscm.2022.e01774

Assiri, T. A., Aziz Elsebaee, F. A., Alqahtani, A. M., Bilal, M., Ali, A., and Eldin, S. M. (2023). Numerical simulation of energy transfer in radiative hybrid nanofluids flow influenced by second-order chemical reaction and magnetic field. *AIP Adv.* 13 (3). doi:10.1063/5.0141532

Ayub, A., Darvesh, A., Altamirano, G. C., and Sabir, Z. (2021b). Nanoscale energy transport of inclined magnetized 3D hybrid nanofluid with Lobatto IIIA scheme. *Heat. Transf.* 50, 6465–6490. doi:10.1002/htj.22188

Ayub, A., Sabir, Z., Shah, S. Z. H., Mahmoud, S. R., Algarni, A., Sadat, R., et al. (2022c). Aspects of infinite shear rate viscosity and heat transport of magnetized Carreau nanofluid. *Eur. Phys. J. Plus* 137 (2), 247–317. doi:10.1140/epjp/s13360-022-02410-6

Ayub, A., Sabir, Z., Wahab, H. A., Balubaid, M., Mahmoud, S. R., Ali, M. R., et al. (2022a). Analysis of the nanoscale heat transport and Lorentz force based on the time-dependent Cross nanofluid. *Eng. Comput.* 39, 2089–2108. doi:10.1007/s00366-021-01579-1

Ayub, A., Sajid, T., Jamshed, W., Zamora, W. R. M., More, L. A. V., Talledo, L. M. G., et al. (2022b). Activation energy and inclination magnetic dipole influences on carreau nanofluid flowing via cylindrical channel with an infinite shearing rate. *Appl. Sci.* 12 (17), 8779. doi:10.3390/app12178779

Ayub, A., Wahab, H. A., Sabir, Z., and Arbi, A. (2020). "A note on heat transport with aspect of magnetic dipole and higher order chemical process for steady micropolar fluid," in *Fluid-structure interaction* (London, England: IntechOpen).

Ayub, A., Wahab, H. A., Shah, S. Z., Shah, S. L., Darvesh, A., Haider, A., et al. (2021a). Interpretation of infinite shear rate viscosity and a nonuniform heat sink/source on a 3D radiative cross nanofluid with buoyancy assisting/opposing flow. *Heat. Transf.* 50 (5), 4192–4232. doi:10.1002/htj.22071

Azam, M., Khan, M., and Alshomrani, A. S. (2017). Unsteady radiative stagnation point flow of MHD Carreau nanofluid over expanding/contracting cylinder. *Int. J. Mech. Sci.* 130, 64–73. doi:10.1016/j.ijmecsci.2017.06.010

Babu, M. S., Sankar, G. R., Velpula, V. R., Chu, Y. M., Khan, M. I., Raju, C. S. K., et al. (2023). Chemically reactive flow of viscous thermophoretic fluid over wedge with variable thermal conductivity and viscosity. *Case Stud. Therm. Eng.* 45, 102924. doi:10.1016/j.csite.2023.102924

Bafakeeh, O. T., Al-Khaled, K., Khan, S. U., Abbasi, A., Ganteda, C., Khan, M. I., et al. (2023). On the bioconvective aspect of viscoelastic micropolar nanofluid referring to variable thermal conductivity and thermo-diffusion characteristics. *Bioengineering* 10 (1), 73. doi:10.3390/bioengineering10010073

Bathe, M., and Kamm, R. D. (1999). A fluid-structure interaction finite element analysis of pulsatile blood flow through a compliant stenotic artery. *J. Biomech. Eng.* 121, 361–369. doi:10.1115/1.2798332

Botmart, T., Ayub, A., Sabir, Z., weera, W., Sadat, R., and Ali, M. R. (2022a). Infinite shear rate aspect of the cross-nanofluid over a cylindrical channel with activation energy and inclined magnetic dipole effects. *Waves Random Complex Media*, 1–21. doi:10.1080/17455030.2022.2160028

Botmart, T., Shah, S. Z. H., Sabir, Z., Weera, W., Sadat, R., Ali, M. R., et al. (2022b). The inclination of magnetic dipole effect and nanoscale exchange of heat of the Cross nanofluid. *Waves Random Complex Media*, 1–16. doi:10.1080/17455030.2022.2128225

Conrad, S. A., and Wang, D. (2021). Evaluation of recirculation during venovenous extracorporeal membrane oxygenation using computational fluid dynamics incorporating fluid-structure interaction. *Asaio J.* 67 (8), 943–953. doi:10.1097/mat.0000000000001314

Darvesh, A., Altamirano, G. C., Sánchez-Chero, M., Zamora, W. R., Campos, F. G., Sajid, T., et al. (2023). Variable chemical process and radiative nonlinear impact on magnetohydrodynamics cross nanofluid: an approach toward controlling global warming. *Heat. Transf.* 52, 2559–2575. doi:10.1002/htj.22795

Darvesh, A., Sajid, T., Jamshed, W., Ayub, A., Shah, S. Z. H., Eid, M. R., et al. (2022). Rheology of variable viscosity-based mixed convective inclined magnetized cross nanofluid with varying thermal conductivity. *Appl. Sci.* 12 (18), 9041. doi:10.3390/app12189041

Das, S., Pal, T. K., Jana, R. N., and Giri, B. (2021). Significance of Hall currents on hybrid nano-blood flow through an inclined artery having mild stenosis: homotopy perturbation approach. *Microvasc. Res.* 137, 104192. doi:10.1016/j.mvr.2021.104192

Dolui, S., Bhaumik, B., and De, S. (2023). Combined effect of induced magnetic field and thermal radiation on ternary hybrid nanofluid flow through an inclined catheterized artery with multiple stenosis. *Chem. Phys. Lett.* 811, 140209. doi:10.1016/j.cplett.2022.140209

El Din, S. M., Darvesh, A., Ayub, A., Sajid, T., Jamshed, W., Eid, M. R., et al. (2022). Quadratic multiple regression model and spectral relaxation approach for carreau nanofluid inclined magnetized dipole along stagnation point geometry. *Sci. Rep.* 12 (1), 17337–17418. doi:10.1038/s41598-022-22308-8

El Kot, M. A., and Abd Elmaboud, Y. (2023). Model of LDL-C concentration of blood flow through a vertical porous microchannel with multiple stenoses: computational simulation. *J. Taibah Univ. Sci.* 17 (1), 2176194. doi:10.1080/16583655.2023.2176194

Fatima, N., Alayyash, K., Alfwzan, W. F., Ijaz, N., Riaz, A., Saleem, N., et al. (2023). Mathematical model for numerical simulations of thermal energy of nano-fluid in a complex peristaltic transport within a curved passage: pharmacological and engineering biomedical application. *Case Stud. Therm. Eng.* 45, 102897. doi:10.1016/j.csite.2023.102897

Goud, J. S., Srilatha, P., Kumar, R. V., Kumar, K. T., Khan, U., Raizah, Z., et al. (2022). Role of ternary hybrid nanofluid in the thermal distribution of a dovetail fin with the internal generation of heat. *Case Stud. Therm. Eng.* 35, 102113. doi:10.1016/j.csite.2022.102113

Haider, A., Ayub, A., Madassar, N., Ali, R. K., Sabir, Z., Shah, S. Z., et al. (2021). Energy transference in time-dependent Cattaneo–Christov double diffusion of second-grade fluid with variable thermal conductivity. *Heat. Transf.* 50 (8), 8224–8242. doi:10.1002/htj.22274

han, U., Zaib, A., Ishak, A., Elattar, S., Eldin, S. M., Raizah, Z., et al. (2022). Impact of irregular heat sink/source on the wall Jet flow and heat transfer in a porous medium induced by a nanofluid with slip and buoyancy effects. *Symmetry* 14 (10), 2212. doi:10.3390/sym14102212

Ige, E. O., Falodun, B. O., Adebiyi, D. O., and Khan, S. U. (2022). Computational analysis of mixed convection in a blood-based hybrid nanoliquid under Boussinesq approximation in a transient Regime. *J. Comput. Biophysics Chem.* 22, 347–359. doi:10.1142/s2737416523400094

Ige, E. O., Falodun, B. O., Adebiyi, D. O., and Khan, S. U. (2023). Computational analysis of mixed convection in a blood-based hybrid nanoliquid under Boussinesq approximation in a transient Regime. *J. Comput. Biophysics Chem.* 22 (03), 347–359. doi:10.1142/s2737416523400094

Kaleem, M. M., Usman, M., Asjad, M. I., and Eldin, S. M. (2022). Magnetic field, variable thermal conductivity, thermal radiation, and viscous dissipation effect on heat and momentum of fractional Oldroyd-B bio nano-fluid within a channel. *Fractal Fract.* 6 (12), 712. doi:10.3390/fractalfract6120712

Khan, U., Zaib, A., Ishak, A., Elattar, S., Eldin, S. M., Raizah, Z., et al. (2022). Impact of irregular heat sink/source on the wall Jet flow and heat transfer in a porous medium induced by a nanofluid with slip and buoyancy effects. *Symmetry* 14 (10), 2212. doi:10.3390/sym14102212

Khan, U., Zaib, A., Ishak, A., Eldin, S. M., Alotaibi, A. M., Raizah, Z., et al. (2023). Features of hybridized AA7072 and AA7075 alloys nanomaterials with melting heat transfer past a movable cylinder with Thompson and Troian slip effect. *Arabian J. Chem.* 16 (2), 104503. doi:10.1016/j.arabjc.2022.104503

Mishra, N. K., Sharma, M., Sharma, B. K., and Khanduri, U. (2023). Soret and Dufour effects on MHD nanofluid flow of blood through a stenosed artery with variable viscosity. *Int. J. Mod. Phys. B*, 2350266. doi:10.1142/s0217979223502661

Nazir, U., Sohail, M., Mukdasai, K., Singh, A., Alahmadi, R. A., Galal, A. M., et al. (2022). Applications of variable thermal properties in Carreau material with ion slip and Hall forces towards cone using a non-Fourier approach via FE-method and mesh-free study. *Front. Mater.* 9, 1054138. doi:10.3389/fmats.2022.1054138

Rafique, K., Mahmood, Z., Saleem, S., Eldin, S. M., and Khan, U. (2023). Impact of nanoparticle shape on entropy production of nanofluid over permeable MHD stretching sheet at quadratic velocity and viscous dissipation. *Case Stud. Therm. Eng.* 45, 102992. doi:10.1016/j.csite.2023.102992

Rasool, G., Shah, S. Z. H., Sajid, T., Jamshed, W., Cieza Altamirano, G., Keswani, B., et al. (2022). Spectral relaxation methodology for chemical and bioconvection processes for cross nanofluid flowing around an oblique cylinder with a slanted magnetic field effect. *Coatings* 12 (10), 1560. doi:10.3390/coatings12101560

Sajid, T., Ayub, A., Shah, S. Z. H., Jamshed, W., Eid, M. R., El Din, E. S. M. T., et al. (2022). Trace of chemical reactions accompanied with arrhenius energy on ternary hybridity nanofluid past a wedge. *Symmetry* 14 (9), 1850. doi:10.3390/sym14091850

Sajid, T., Jamshed, W., Eid, M. R., Altamirano, G. C., Aslam, F., Alanzi, A. M., et al. (2023a). Magnetized cross tetra hybrid nanofluid passed a stenosed artery with nonuniform heat source (sink) and thermal radiation: novel tetra hybrid tiwari and das nanofluid model. *J. Magnetism Magnetic Mater.* 569, 170443. doi:10.1016/j.jmmm.2023.170443

Sajid, T., Jamshed, W., Shahzad, F., Ullah, I., Ibrahim, R. W., Eid, M. R., et al. (2023b). Insightful into dynamics of magneto Reiner-Philippoff nanofluid flow induced by triple-diffusive convection with zero nanoparticle mass flux. *Ain Shams Eng. J.* 14 (4), 101946. doi:10.1016/j.asej.2022.101946

Shah, S. Z. H., Fathurrochman, I., Ayub, A., Altamirano, G. C., Rizwan, A., Núñez, R. A. S., et al. (2021a). Inclined magnetized and energy transportation aspect of infinite shear rate viscosity model of Carreau nanofluid with multiple features over wedge geometry. *Heat. Transf.* 51, 1622–1648. doi:10.1002/htj.22367

Shah, S. Z., Wahab, H. A., Ayub, A., Sabir, Z., haider, A., and Shah, S. L. (2021b). Higher order chemical process with heat transport of magnetized cross nanofluid over wedge geometry. *Heat. Transf.* 50 (4), 3196–3219. doi:10.1002/htj.22024

Shahzad, F., Jamshed, W., Ibrahim, R. W., Aslam, F., Tag El Din, E. S. M., ElSeabee, F. A. A., et al. (2022). Galerkin finite element analysis for magnetized radiative-reactive Walters-B nanofluid with motile microorganisms on a Riga plate. *Sci. Rep.* 12 (1), 18096. doi:10.1038/s41598-022-21805-0

Sumner, D., Wong, S. S. T., Price, S. J., and Paidoussis, M. P. (1999). Fluid behaviour of side-by-side circular cylinders in steady cross-flow. *J. Fluids Struct.* 13 (3), 309–338. doi:10.1006/jfls.1999.0205

Tang, T. Q., Rooman, M., Shah, Z., Jan, M. A., Vrinceanu, N., and Racheriu, M. (2023a). Computational study and characteristics of magnetized gold-blood Oldroyd-B nanofluid flow and heat transfer in stenosis narrow arteries. *J. Magnetism Magnetic Mater.* 569, 170448. doi:10.1016/j.jmmm.2023.170448

Tang, T. Q., Rooman, M., Shah, Z., Jan, M. A., Vrinceanu, N., and Racheriu, M. (2023b). Computational study and characteristics of magnetized gold-blood Oldroyd-B nanofluid flow and heat transfer in stenosis narrow arteries. *J. Magnetism Magnetic Mater.* 569, 170448. doi:10.1016/j.jmmm.2023.170448

Tripathi, J., Vasu, B., Bég, O. A., and Gorla, R. S. R. (2021). Unsteady hybrid nanoparticle-mediated magneto-hemodynamics and heat transfer through an overlapped stenotic artery: biomedical drug delivery simulation. *Proc. Institution Mech. Eng. Part H J. Eng. Med.* 235 (10), 1175–1196. doi:10.1177/09544119211026095

Varshney, G., Katiyar, V., and Kumar, S. (2010). Effect of magnetic field on the blood flow in artery having multiple stenosis: A numerical study. *Int. J. Eng. Sci. Technol.* 2 (2), 967–982. doi:10.4314/ijest.v2i2.59142

Wang, F., Sajid, T., Ayub, A., Sabir, Z., Bhatti, S., Shah, N. A., et al. (2022). Melting and entropy generation of infinite shear rate viscosity carreau model over riga plate with erratic thickness: A numerical keller box approach. *Waves Random Complex Media*, 1–25. doi:10.1080/17455030.2022.2063991

Waqas, M. (2020). Simulation of revised nanofluid model in the stagnation region of cross fluid by expanding-contracting cylinder. *Int. J. Numer. Methods Heat Fluid Flow* 30 (4), 2193–2205. doi:10.1108/hff-12-2018-0797

Yadav, M., Pareek, N., and Vivekanand, V. (2022). "Eggshell and fish/shrimp wastes for synthesis of bio-nanoparticles," in *Agri-waste and microbes for production of sustainable nanomaterials* (Amsterdam, Netherlands: Elsevier), 259–280.

Zaib, A., Khan, U., Khan, I., Seikh, H., and Sherif, M. (2019). Entropy generation and dual solutions in mixed convection stagnation point flow of micropolar Ti6Al4V nanoparticle along a Riga surface. *Processes* 8 (1), 14. doi:10.3390/pr8010014

Zain, N. M., and Ismail, Z. (2023a). Numerical solution of magnetohydrodynamics effects on a generalised power law fluid model of blood flow through a bifurcated artery with an overlapping shaped stenosis. *Plos one* 18 (2), e0276576. doi:10.1371/journal.pone.0276576

Zain, N. M., and Ismail, Z. (2023b). Numerical solution of magnetohydrodynamics effects on a generalised power law fluid model of blood flow through a bifurcated artery with an overlapping shaped stenosis. *Plos one* 18 (2), e0276576. doi:10.1371/journal.pone.0276576

10.3389/fmats.2023.1242085

Nomenclature

$k^*(T)$	Variable thermal conductivity (W/m.K)
$U_w(x,t)$	Velocity at the wall surface of the cylinder (m/s)
$U_e(x,t)$	Free-stream velocity (m/s)
T_w	Temperature at the wall surface (K)
T_∞	Ambient temperature (K)
a, c	Arbitrary constants
k_f	Thermal conductivity of the base fluid (W/m.K)
x, r	Cylindrical coordinates (m)
u, v	Velocity components (m/s)
s	Suction parameter
Pr	Prandtl number
B	Variable magnetic field (Tesla)
C_p	Specific heat capacitance at constant pressure (J/Kg. K)
n	Power-law index
T	Temperature of fluid (K)
M	Magnetic parameter
We	Weissenberg number
A	Unsteadiness parameter
Re	Reynolds number
Nu	Local Nusselt number
C_f	Skin friction coefficient
Greek Symbols	
μ	Absolute viscosity (Pa.sec)
ρ	Density (Kg/m^3)
λ	Stretching/Shrinking parameter
η	Pseudo-similarity variable
Γ	Relaxation time constant (sec)
ϕ	Solid nanoparticle volume fraction
σ	Electrical conductivity (S/m)
Subscripts	
$thnf$	Ternary hybrid nanofluid
hnf	Hybrid Nanofluid
nf	Nanofluid
f	Base fluid
w	Wall condition
∞	Ambient condition
s_1, s_2, s_3	Three distinct solid nanoparticles
Superscripts	
$(')$	Derivatives with respect to η

Frontiers in Materials

Investigates the discovery and design of materials for future application

A multidisciplinary journal that explores the breadth of materials science, engineering and mechanics - from carbon-based materials to smart materials.

Discover the latest Research Topics

See more →

Frontiers

Avenue du Tribunal-Fédéral 34
1005 Lausanne, Switzerland
frontiersin.org

Contact us

+41 (0)21 510 17 00
frontiersin.org/about/contact